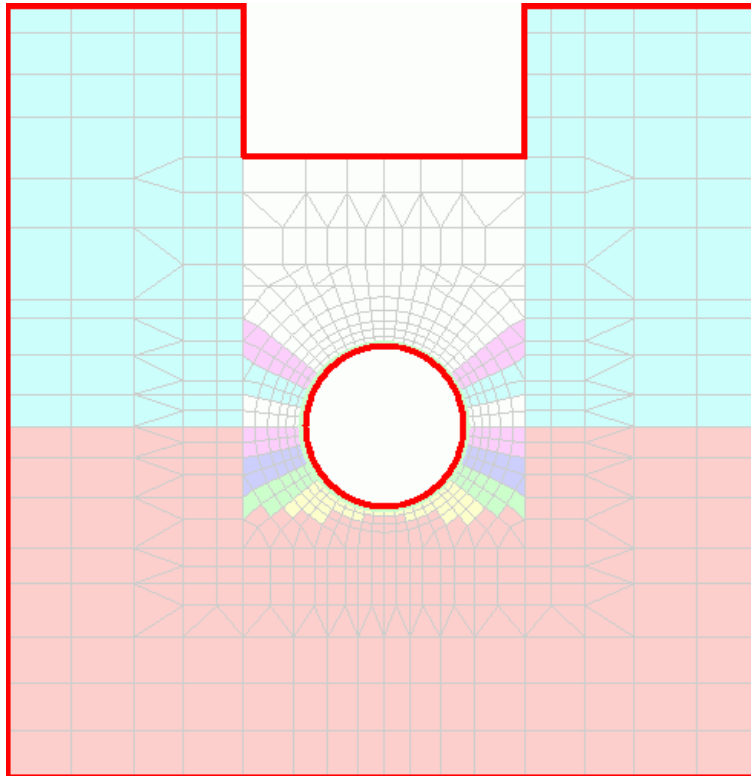


CANDE-2022

Culvert Analysis and Design

Solution Methods and Formulations

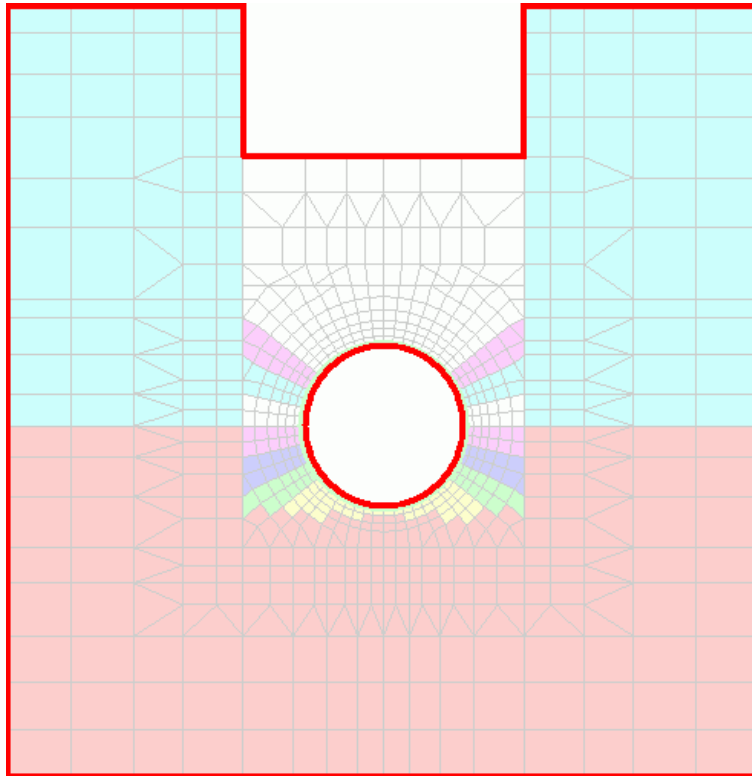


Originally Developed under National Cooperative Highway Research Project NCHRP 15-28

Updated by Michael G Katona
January, 2022

CANDE-2022

Culvert Analysis and Design Solution Methods and Formulations



Originally Developed under National Cooperative Highway Research Project NCHRP 15-28

Updated by Michael G. Katona with new capabilities.
January, 2022

Table of Contents

Table of Contents.....	iii
New Capabilities – 2022.....	vii
1 SOLUTION LEVELS AND ASSUMPTIONS.....	1-1
1.1 Elasticity Solution.....	1-1
1.1.1 Conceptual model.....	1-1
1.1.2 Nonlinear aspects.....	1-3
1.1.3 Utility of Level 1.....	1-4
1.2 Finite Element Methodology.....	1-4
1.2.1 Element types.....	1-5
1.2.2 Global assembly and incremental construction.....	1-7
1.2.3 Nonlinear solution strategy.....	1-7
2 BEAM-COLUMN ELEMENTS – PIPE TYPE MODELS.....	2-1
2.1 General Form.....	2-1
2.1.1 Beam kinematics.....	2-1
2.1.2 Incremental stress-strain model.....	2-2
2.1.3 Internal thrust and moment increments.....	2-3
2.1.4 Beam-column virtual work.....	2-4
2.1.5 Finite element interpolation functions.....	2-5
2.1.6 Element stiffness matrices.....	2-6
2.1.7 Transformation to global coordinates.....	2-7
2.1.8 Equation solving and recovery of structural responses.....	2-8
2.1.9 Nonlinear solution strategy.....	2-9
2.2 Corrugated Metal.....	2-10
2.2.1 Overview of corrugated metal pipe type.....	2-10
2.2.2 Design criteria for corrugated metal.....	2-10
2.2.3 Nonlinear model for corrugated metal.....	2-11
2.3 Reinforced Concrete.....	2-17
2.3.1 Overview of reinforced concrete pipe type.....	2-17
2.3.2 Design criteria for reinforced concrete.....	2-17
2.3.3 Nonlinear model for reinforced concrete.....	2-19
2.4 Thermoplastic Pipe.....	2-27
2.4.1 Overview of thermoplastic pipe type.....	2-27
2.4.2 Design criteria for thermoplastic pipe.....	2-27
2.4.3 Nonlinear model for local buckling in profile plastic pipe.....	2-28
2.5 Basic Pipe Type.....	2-31
2.6 Conrib Pipe Type.....	2-31
2.6.1 Overview of CONRIB Model.....	2-32
2.6.2 Design Criteria for CONRIB Reinforced Concrete.....	2-32
2.6.3 CONRIB concrete model.....	2-34
2.6.4 Reinforcement steel model.....	2-36
2.6.5 Concrete cross-section geometry.....	2-37
2.6.6 Nonlinear solution strategy.....	2-38
2.6.7 CONRIB Model Behavior and Parameter Identification.....	2-42
2.6.8 Derivation of moment capacity in pure bending.....	2-42
2.6.9 Model parameter identification.....	2-45
2.7 Contube Pipe Type.....	2-48
2.7.1 Overview of CONTUBE Model.....	2-48
2.7.2 Design Criteria for Concrete and Tube.....	2-49
2.7.3 Concrete stress-strain model.....	2-50
2.7.4 Tube stress-strain model.....	2-52
2.7.5 Section stiffness properties for CONTUBE.....	2-52
2.7.6 Nonlinear solution strategy.....	2-54
2.7.7 Simple Illustrative Example.....	2-57
3 SOIL MODELS.....	3-1

3.1	Continuum Elements	3-1
3.1.1	Triangle elements	3-1
3.1.2	Quadrilateral elements.....	3-2
3.1.3	Finite element development	3-2
3.2	Isotropic Linear Elastic	3-4
3.3	Orthotropic Linear Elastic.....	3-5
3.3.1	Orthotropic properties from testing specimens	3-5
3.3.2	Orthotropic properties for reinforced soil.....	3-5
3.4	Overburden Dependent Soil Model.....	3-8
3.4.1	Input data for overburden dependent model.....	3-8
3.4.2	Overburden model development	3-9
3.4.3	Overburden dependent secant moduli data tables in CANDE.....	3-10
3.5	Duncan and Duncan/Selig Soil Models.....	3-11
3.5.1	Plane-strain constitutive matrix.....	3-11
3.5.2	Duncan Young's modulus development.....	3-12
3.5.3	Bulk modulus formulations.....	3-15
3.5.4	Summary of Original Duncan and Duncan/Selig soil models.....	3-17
3.5.5	Behavioral characteristics and special considerations	3-18
3.5.6	Implementation of soil models and nonlinear solution strategy	3-19
3.5.7	Recommended Duncan and Duncan/Selig parameters for standard soils.....	3-22
3.5.8	Modified Duncan/Selig models for plastic deformation (Katona)	3-23
3.5.9	Performance of Modified Duncan/Selig model.....	3-27
3.6	Extended Hardin Soil Model	3-30
3.6.1	Hardin shear modulus development	3-31
3.6.2	Poisson ratio development.....	3-34
3.6.3	Summary of extended Hardin soil model functions	3-36
3.6.4	Implementation of Harden model and nonlinear solution strategy.....	3-37
3.7	Mohr/Coulomb Plasticity Model with Tension Cutoff.....	3-41
3.7.1	Pros and Cons of Mohr/Coulomb Model	3-41
3.7.2	Basic Plasticity Concepts	3-41
3.7.3	Stress and Strain Components for Plane Strain Plasticity	3-42
3.7.4	Plastic failure surface of Mohr/Coulomb Model.....	3-43
3.7.5	Flow Rule – Associative and Non-associative.	3-46
3.7.6	Development of Elastic-Plastic Constitutive Relationship.....	3-46
3.7.7	Development of Tension Cutoff Methodology	3-48
3.7.8	Nonlinear Solution Strategy for Mohr-Coulomb Plasticity with Tension Cutoff.....	3-51
3.8	Comparison of Duncan/Selig and Mohr/Coulomb Soil Models	3-57
3.8.1	Experimental Data Suite.....	3-57
3.8.2	Parameter Identification	3-58
3.8.3	Compare Soil Models with Experiments.....	3-60
4	INTERFACE AND LINK ELEMENTS	4-1
4.1	Interface Element Introduction.....	4-1
4.2	Interface Virtual Work and Constraint Equations	4-2
4.2.1	Constraint equations general form.....	4-3
4.2.2	Global virtual work statement with constraints	4-4
4.2.3	General element constraint matrix and load vector	4-4
4.3	Interface Element Matrix and Load Vector.....	4-5
4.3.1	Definition of interface element.....	4-5
4.3.2	Incremental and total responses (notation).....	4-6
4.3.3	Element constraint matrices and load vectors for three interface states.	4-7
4.4	Interface Nonlinear Solution Strategy.....	4-10
4.4.1	Selecting a new trial interface state	4-10
4.4.2	Computing load vector parameters for next iteration	4-11
4.4.3	Algorithm summary and convergence.....	4-12
4.4.3	Interface element with initial gap	4-13
4.5	Link Element Introduction	4-14

4.6	Link Virtual Work and Constraint Equations.....	4-14
4.6.1	Constraint equations.....	4-15
4.6.2	Constraint forces and virtual work.....	4-16
4.6.3	Global virtual work statement with constraints.....	4-17
4.6.4	General constraint matrix.....	4-17
4.7	Simple Link Elements.....	4-17
4.7.1	Rigid link constraint matrix.....	4-17
4.7.2	Pinned link constraint matrix.....	4-18
4.8	Composite Link Element.....	4-19
4.8.1	Composite constraint development.....	4-20
4.8.2	Composite constraint forces and solution approach.....	4-23
4.8.3	Transverse composite link constraint matrix.....	4-24
4.8.4	Longitudinal composite link constraint matrix.....	4-26
4.8.5	Revised Nonlinear Solution Strategy.....	4-29
4.8.6	Interpreting CANDE output for beams with composite link elements.....	4-33
4.9	Link Element Death.....	4-36
4.9.1	Procedure for element death.....	4-36
4.9.2	Programming strategy.....	4-36
5	LARGE DEFORMATIONS AND BUCKLING.....	5-1
5.1	Updated Lagrange Formulation.....	5-1
5.1.1	Coordinates and incremental relationships.....	5-1
5.1.2	Bernoulli-Euler beam kinematics.....	5-1
5.1.3	Total Lagrangian strain for large rotations.....	5-1
5.1.4	Updated Lagrangian strain increments.....	5-2
5.1.5	Incremental stress-strain model.....	5-2
5.1.6	Internal thrust and moment increments.....	5-3
5.1.7	Virtual work for beam-column element.....	5-3
5.2	Finite Element Development.....	5-5
5.2.1	Finite element interpolation functions.....	5-5
5.2.2	Element matrices and vectors.....	5-6
5.2.3	Transformation and global assembly.....	5-7
5.3	Solution Strategy.....	5-8
5.3.1	Iterative methodology.....	5-8
5.3.2	Recovery of element forces.....	5-8
5.3.3	Update coordinates.....	5-9
5.4	Buckling Capacity.....	5-10
5.5	Illustration – Simply Supported Beam.....	5-11
5.5.1	Development of closed-form solution.....	5-11
5.5.2	Example test problem for closed-form solution.....	5-12
5.5.3	CANDE model of test problem.....	5-13
5.5.4	CANDE simulating total Lagrange approach.....	5-14
5.5.5	CANDE Solution for updated Lagrange approach.....	5-15
5.6	Illustration -- Soil-Structure Interaction.....	5-16
5.6.1	CANDE soil-structure model and parameters.....	5-16
5.6.2	Study # 1 -- Linear soil and bonded interface.....	5-17
5.6.3	Study # 2 -- Nonlinear soil and bonded interface.....	5-21
5.6.4	Study # 3 -- Linear soil and frictionless interface.....	5-25
5.6.5	Comparing Studies #1, #2 and #3 with design criteria.....	5-27
6	DESIGN CRITERIA AND LRFD DESIGN METHODOLOGY.....	6-1
6.1	Service Loads for Performance Criteria.....	6-2
6.2	LRFD Loads for Strength-limit States.....	6-3
6.2.1	Load Factors.....	6-3
6.2.2	Load Modifiers.....	6-4
6.2.3	LRFD load factors and nonlinear soil models.....	6-4
6.3	Design Criteria for Culvert Materials.....	6-5
6.3.1	Corrugated metal.....	6-5

6.3.2	Reinforced concrete.....	6-6
6.3.3	Plastic pipe	6-7
6.4	Illustration of LRFD Factors and Evaluation with CANDE	6-9
6.4.1	Construction increment number 1.	6-9
6.4.2	Construction increment numbers 2 through 8	6-9
6.4.3	Construction increment number 9 (live load).....	6-10
6.4.4	Final evaluation of LRFD design criteria	6-11
7	BANDWIDTH MINIMIZATION.....	7-1
7.1	Background and Objectives	7-1
7.2	Bandwidth Minimization Methodology in CANDE	7-2
7.2.1	Element connectivity matrix	7-2
7.2.2	Algorithm Cycle.....	7-2
7.2.3	Post algorithm-cycle updates.....	7-4
7.3	Transparency of Node Numbers in Solution Output.....	7-5
7.4	Illustration of Bandwidth Minimization.....	7-6
8	MODELING TECHNIQUES.....	8-1
8.1	Live Loads.....	8-1
8.1.1	Specifying Live Loads for 2D Plane Strain.....	8-1
8.1.2	Live Load 2D Problems and Remedies	8-3
8.1.3	Elasticity Based Method (EBM) for Load Spreading.....	8-4
8.1.4	AASHTO Ad-hoc Method (AAM) for Load Spreading.....	8-7
8.1.5	Two-wheel Interaction and Soil Depth H_{int}	8-11
8.1.6	Reduced Surface Load (RSL) Procedure.....	8-13
8.1.7	Continuous Load Scaling (CLS) Procedure	8-15
8.1.8	Pavements and Live Loads (RSL and CLS).....	8-18
8.1.9	3D Stiffness Effects and Live Loads (RSL and CLS)	8-26
8.1.10	Big Picture Summary for Live Loads.....	8-34
8.2	Pipe Group Connections and Combinations.....	8-37
8.2.1	Connections among element types	8-38
8.2.2	Stiffeners and culvert rehabilitation with parallel pipe groups.....	8-39
8.2.3	Illustrations of pipe group combinations	8-41
8.3	Construction Increments	8-43
8.3.1	Rules and insights for construction increments.....	8-43
8.3.2	Techniques for initial construction increment	8-44
8.3.3	Soil compaction and construction increments	8-45
9	REFERENCES.....	9-1
10	CANDE ANALYSIS SOURCE CODE.....	10-1
10.1	Overview of CANDE Analysis Engine Architecture.....	10-1
10.2	Executive Routine (Cande_dll).....	10-1
10.3	Pipe-type Subroutines	10-2
10.4	Solution-level Subroutines	10-4
10.4.1	Elasticity solution Level 1.....	10-4
10.4.2	Finite element solutions Level 2 and Level 3.....	10-4
10.5	Extensions to New Pipe Types, Soil Models and Canned Meshes.....	10-7
10.5.1	New pipe-type model	10-7
10.5.2	New soil models	10-7
10.5.3	New canned mesh for Level 2.....	10-8
11	CANDE GUI Source Code.....	11-1
11.1	Overview of CANDE GUI Architecture.....	11-1
11.2	CANDE Files.....	11-3
11.2.1	CANDE Input Definition	11-3
11.2.2	CANDE analysis XML output files	11-5
11.2.3	CANDE table of contents files.....	11-5
11.2.4	CANDE help files	11-6

New Capabilities – 2022

The table below lists the new capabilities in the CANDE-2022 program that do not exist in the CANDE-2007 /2011 program distributed at the TRB website. The theoretical formulation and input instructions for each new capability are documented in the new CANDE-2022 manuals as identified in the last two columns of the table below.

Description of new CANDE capabilities since TRB version	User Manual input, Chapter 5, Section number and (line tag)	Solution and Formulation Manual, Section number
CONRIB pipe type. CONRIB has been added to CANDE’s pipe-type library that provides the capability of modeling rib-shaped reinforced/concrete cross-sections as well as standard rectangular cross sections. Moreover, the concrete constitutive model has been extended to include the simulation of fiber reinforced concrete.	5.3.2 (A-2) and 5.4.5 (B-1 to B-6)	2.6
CONTUBE pipe type. This special pipe type provides the capability of modeling circular shaped concrete cross sections encased in fiber-reinforced plastic (FRP) tubes spaced at uniform distances.	5.3.2 (A-2) and 5.4.6 (B-1 to B-6)	2.7
Link elements with death option. Two simple options are, (1) connect any two nodes with a pinned connection; or, (2) connect two beam nodes with a fixed-moment connection. <u>The link-element death option</u> is an extremely useful capability allowing the removal of any link element and its forces at any specified load step.	5.5.6.4 (C-4)	4.9
Deeply corrugated steel structures. Updated steel pipe type to accommodate the recently adopted AASHTO requirement for a combined moment-thrust design criterion that applies to deeply corrugated steel structures as well a new AASHTO equation to predict the global buckling resistance. These new design criteria may be activated at the user’s discretion.	5.5.4.1 (B-1) and 5.5.4.2 (B-2)	2.2.2
Plastic pipe type variable profile properties. The plastic pipe subroutine has been revised to allow variable profile geometries around the structure. This applies to all types of plastic including HDPE, PVC, and PP. Useful for analyzing storm-water chambers.	5.4.3.4 (B-3, B3b)	2.4.3
Mohr/Coulomb plasticity model. The classical Mohr/Coulomb elastic-perfectly plastic model is now included in the suite of available constitutive models that may be assigned to continuum elements to describe soil behavior. Up to five material parameters are required to define the model (E , ν , c , ϕ and ψ for non-associative flow rule). Also, the user has control of the tension cut-off stress level with improved convergence algorithms.	5.6.9 (D-2)	3.7 (3.8)
Modified Duncan/Selig soil model. The new modified Duncan/Selig model produces permanent deformations upon unloading similar to advanced plasticity models. No new material parameters are introduced into the new formulation; thus, the existing data base of Duncan/Selig parameters remains valid for the modified formulation. The user has the option to use either the Original or Modified version.	5.6.4.1 (D-2)	3.58 to 3.59 (3.8)
Continuous Load Scaling (CLS). A new improved procedure for simulating longitudinal load spreading and 3D stiffness effects resulting from 2D modeling of live loads. CLS provides a superior alternative to the traditional method of reducing surface loads (RSL) to approximately account for longitudinal effects.	5.5.6.2 (C-2) and 5.5.6.3 (C-2b)	8.1.1 to 8.1.5

<p>Composite Link Element. The composite link element is used to combine two colinear beam element groups to react as a composite bending unit as if the two beam groups are welded together along the common interface. Or, at the user' discretion, a reduction factor may be specified to simulate an interface condition somewhere between fully composite and simple tandem action.</p>	<p>5.5.6.6 (C-4) 5.6.8 (D-2)</p>	<p>4.8</p>
<p>Full benefit of pavements for load rating. It is well known that inserting a stiff pavement over a 2D soil-culvert model will significantly reduce the culvert's structural distress from live loads. However, this is only the in-plane portion of the actual full benefits provided by pavements. There is also an out-of-plane load spreading benefit that can be accurately simulated in CANDE using the revised load spreading theory called AAMP-θ^*, which produces more realistic load rating factors.</p>	<p>5.5.6.4 (C-2c) See also CANDE Tool Box – Option 3</p>	<p>8.1.8</p>

1 SOLUTION LEVELS AND ASSUMPTIONS

This document focuses on the engineering mechanics and methods that lie behind the capabilities in CANDE-2022. Each chapter is essentially a stand-alone reference that describes the theory and engineering approximations used for the solution methods and nonlinear models employed in the program. The reader is referred to *CANDE-2022 User Manual and Guideline* for an overall understanding of CANDE capabilities and architecture from a user's perspective.

Two distinct solution methods are contained in CANDE. The first is called Level 1 and is an extension of a closed-form elasticity solution by Burns and Richard (Reference 7). The second is a finite element methodology modified and extended from Herrmann (Reference 8). Input for the finite element method has two input options called Level 2 and Level 3. Level 2 offers a completely automated mesh generation scheme but it is restricted to basic culvert shapes and symmetric installations, whereas Level 3 is virtually unrestricted in modeling capability, but requires the user to define the mesh topology.

Fundamental to both the closed form solution and the finite element methodology is the assumption of plane strain geometry, two-dimensional loading, and real-time independence. Naturally, the elasticity solution is more restrictive than the finite element solutions for Levels 2 and 3. Detailed capabilities and restrictions of the solution methods are discussed in the following sections.

1.1 Elasticity Solution

The elasticity formulation provides an exact solution for an elastic cylindrical conduit encased in an isotropic, homogeneous, infinite, elastic medium (soil) with a uniformly distributed pressure acting on horizontal planes at an infinite distance. Thin-shell theory is assumed for the conduit, and continuum elastic theory is employed for the surrounding infinite medium. The conduit-medium interface is modeled with a choice of two boundary conditions: bonded interface, where both normal and tangential forces are transmitted across the interface, and frictionless interface, where only normal forces are transmitted across the interface. Table 1.1-1 identifies the parameters that describe the idealized boundary value problem and summarizes the elasticity solutions of key structural responses for the two interface assumptions. Key structural responses, including radial and tangential soil pressure on conduit, radial and tangential displacements of conduit wall, along with moment, thrust and shear resultants are given as a function of the angle theta measured counterclockwise from the springline. The solutions in Table 1.1-1 are expressed in terms of the dimensionless parameters alpha and beta. Alpha is a measure of the conduit's hoop stiffness relative to the soil's ability to resist uniform compression, and beta is a measure of the conduits bending stiffness relative to the soil's ability to resist ovaling deformation. The expressions in Table 1.1-1 are developed in References 9 and 10.

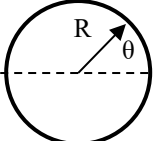
1.1.1 Conceptual model

At first encounter, the applicability of the infinite regions described above to model culvert systems with finite burial depths may seem questionable. However, it has been shown that the interaction between conduit and medium (or pipe and soil) occurs primarily within a three-radius area of the pipe center. Beyond this area, the soil response is practically unaffected by the pipe inclusion for overburden loading. Therefore, the pipe-soil system can be visualized with the finite boundaries and overburden loading as shown in Figure 7.1.1. In this representation, P_o is the equivalent overburden pressure of the fill soil above the pipe given by $P_o = \gamma H$, where the parameters are identified in the figure. The elasticity solution becomes progressively less valid when H , the depth of cover, is less than $3R$ and should not be used for cover depths less than $2R$.

Table 1.1.1-1 Elasticity parameters and solutions for bonded and frictionless interfaces.

Elasticity Solution Parameters		
<p>Soil Properties</p> <p>P_0 = Overburden pressure</p> <p>G = Shear modulus</p> <p>K = Lateral pressure coeff. $K = \mu/(1 - \mu)$, where μ is Poisson ratio of soil</p>	<p>Pipe Properties</p> <p>R = Average radius</p> <p>A = Wall thrust area per unit length</p> <p>I = Wall moment of inertia per unit length</p> <p>E = Young's modulus in plane strain form $E = E_{\text{pipe}}/(1 - \mu_{\text{pipe}}^2)$</p>	<p>Dimensionless Parameters</p> <p>θ = Angle in polar coord.</p> <p>$\alpha = EA/(2GR)$ (Relative hoop stiffness)</p> <p>$\beta = EI/(2GR^3)$ (Relative bend stiffness)</p>

Bonded Interface: Structural Response Solutions

Structural Response	Common Factor	Bonded Interface – Expression to be multiplied by common factor
	Common Factor	Denominator term: $D = (1+K) + 3(5-K)\beta + (3+K)\alpha + 12(3-K)\alpha\beta$
Radial pressure on pipe	P_0	$\alpha/(1 + \alpha) - \{(1-K)(-2\alpha + 18\beta + 24\alpha\beta)/D\}\cos 2\theta$
Tangential pressure on pipe	P_0	$0 + \{(1-K)(4\alpha + 24\alpha\beta)/D\}\sin 2\theta$
Radial displacement of pipe	$P_0 R/(2G)$	$1/(1 + \alpha) - \{(1-K)(2 + 4\alpha)/D\}\cos 2\theta$
Tangential displacement of pipe	$P_0 R/(2G)$	$0 + \{(1-K)(2 + 2\alpha + 6\beta)/D\}\sin 2\theta$
Moment in pipe wall per unit length	$P_0 R^2$	$\beta/(1 + \alpha) + \{(1-K)(6\beta + 12\alpha\beta)/D\}\cos 2\theta$
Thrust force in pipe wall Per unit length	$P_0 R$	$\alpha/(1 + \alpha) + \{(1-K)(2\alpha + 6\beta + 24\alpha\beta)/D\}\cos 2\theta$
Shear force in pipe wall per unit length	$P_0 R$	$0 - \{(1-K)(12\beta + 24\alpha\beta)/D\}\sin 2\theta$

Frictionless Interface: Structural Response Solutions

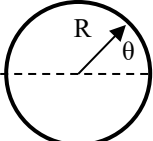
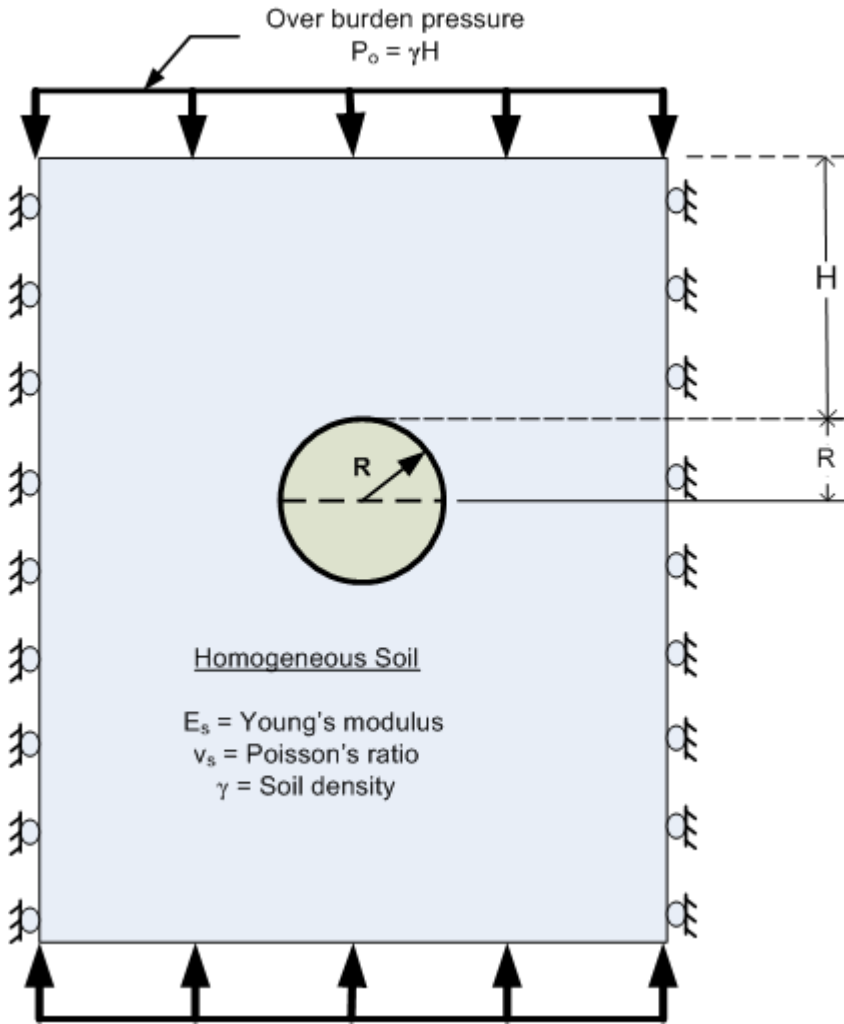
Structural Response	Common Factor	Frictionless Interface -- Expression to be multiplied by common factor
	Common Factor	Denominator term: $D = (1+K) + 3(5-K)\beta$
Radial pressure on pipe	P_0	$\alpha/(1 + \alpha) - \{(1-K)(18\beta)/D\}\cos 2\theta$
Tangential pressure on pipe	P_0	0.0
Radial displacement of pipe	$P_0 R/(2G)$	$1/(1 + \alpha) - \{(1-K)2/D\}\cos 2\theta$
Tangential displacement of pipe	$P_0 R/(2G)$	$0 + \{(1-K)/D\}\sin 2\theta$
Moment in pipe wall per unit length	$P_0 R^2$	$\beta/(1 + \alpha) + \{(1-K)(6\beta)/D\}\cos 2\theta$
Thrust force in pipe wall Per unit length	$P_0 R$	$\alpha/(1 + \alpha) + \{(1-K)(6\beta)/D\}\cos 2\theta$
Shear force in pipe wall per unit length	$P_0 R$	$0 - \{(1-K)(12\beta)/D\}\sin 2\theta$

Figure 1.1.1-1 Conceptual view of elasticity solution with finite boundaries.



1.1.2 Nonlinear aspects

Although Level 1 is based on a linear elasticity solution, a fair degree on nonlinear modeling is achieved for both soil and pipe in the following manner. First the overburden pressure, P_o , may be divided into “ n ” load increments, ΔP_i , for $i = 1$ to n , and each load increment is applied in a series of load steps. During each load step the material properties of the soil may be redefined in accordance with current overburden pressure. The structural responses as presented in Table 1.1-1, with P_o replaced by ΔP_i , are summed in a running total thereby providing a load-deformation history record. The concept of overburden-dependent soil properties is elaborated in a later chapter on soil models.

With regard to nonlinear behavior of the pipe, each pipe type model (discussed later) can create changes in the effective bending stiffness EI and the effective hoop stiffness EA at each point around the pipe periphery. These modified properties are used directly to predict stress and strain at each pipe point based on the moment, thrust and shear at that point. However, an average value of the modified properties is used in the closed-form equations to predict the primary unknowns (displacements, moment, thrust, and shear) at each point on the pipe periphery.

1.1.3 Utility of Level 1

The Level 1 approach does not have the versatility and generality of the Level 2 and 3 counterparts. Nonetheless its efficiency and applicability particularly for design is quite remarkable. From a design viewpoint, the exact nature of the soil system, loading and boundary conditions may not be known with enough certainty to warrant a finite element solution. Thus, the simplifying assumptions of Level 1 are often commensurate with knowledge of the design problem. It follows that the simple data preparation and quick computer time make Level 1 an attractive and powerful design tool for routine applications for deep burial loading.

1.2 Finite Element Methodology

As previously mentioned, Level 2 and Level 3 share a common finite element solution program and differ only with respect to the mode of input: automatic or user-defined. Although the development and formulation of the finite element method is well established in the literature, an overview will be given herein as it applies to culvert installations.

A static, displacement-based finite element formulation is developed based on incremental virtual work. Incremental virtual work is ideally suited for characterizing buried structures problems because the load may be applied in a series of steps representing increments of overburden pressure, temporary construction loading and live loads from vehicles. In the case of culvert-soil systems, the incremental approach takes on a larger meaning than just incremental load steps. To wit, not only the load, but also the structural system may be assembled in increments. This process is termed the "incremental construction" technique and is the mathematical analogue of the physical process of constructing the soil system in a series of compacted layers or lifts. The structural predictions from an incremented system are more realistic than an equivalent monolith system. Another advantage of the incremental virtual work formulation is the relative ease of incorporating and solving various nonlinear models, which are discussed throughout this document.

For a general structural-continuum system, incremental virtual work may be expressed in matrix notation as:

$$\int_V \delta \boldsymbol{\varepsilon}^T \Delta \boldsymbol{\sigma} dV = \int_S \delta \mathbf{u}^T \Delta \boldsymbol{\tau} dS + \int_V \delta \mathbf{u}^T \Delta \mathbf{f} dV \quad \text{Equation 1-1}$$

Where, $\boldsymbol{\sigma}$ = stress vector
 $\boldsymbol{\varepsilon}$ = strain vector
 \mathbf{u} = displacement vector
 $\boldsymbol{\tau}$ = surface-traction vector
 \mathbf{f} = body-force vector
 $\delta \mathbf{x}$ = small virtual variation of any vector \mathbf{x} , δ is an operator
 $\Delta \mathbf{x} = \mathbf{x}_{i+1} - \mathbf{x}_i$, incremental change in any vector \mathbf{x} from load step i to $i+1$, Δ is an operator
 S = surface area of traction loads at load step $i + 1$
 V = volume of structural system at load step $i + 1$

The physics behind the above incremental virtual work statement is as follows. We assume that the structural system is in equilibrium at load step i , and we are in the process of applying incremental loads to reach load step $i + 1$. With this understanding, Equation 1-1 states, "The increment of internal virtual-strain-energy is equal to the increment of external virtual work of body and traction loads as the system undergoes a virtual movement compatible with the kinematical constraints of the system."

To express the virtual work statement in a displacement formulation, the stress vector is expressed in terms of strains by using an incremental constitutive relationship, symbolized as;

$$\Delta \boldsymbol{\sigma} = \underline{\mathbf{C}} \Delta \boldsymbol{\varepsilon} \quad \text{Equation 1-2}$$

Where, $\underline{\mathbf{C}}$ is the constitutive function (matrix) that relates stress and strain increments from load step i to load step $i + 1$. In general, the coefficients may be nonlinear and dependent on the total stress and strain history.

Next, the strain increments are expressed in terms of displacement increments as;

$$\Delta \underline{\varepsilon} = \underline{\Delta Q}(\underline{u}) = \underline{Q}(\Delta \underline{u}) \quad \text{Equation 1-3}$$

where, \underline{Q} is an operator matrix composed of partial derivatives. For small-deformation theory, the operator matrix contains linear operations so that \underline{Q} is commutative with Δ and δ operators. In a later chapter, the strain-displacement operator is extended to include large deformations, however for present purposes small-deformation theory is assumed.

Using the above relationships, the incremental virtual work may be expressed in terms of displacement fields over the entire domain as;

$$\int_V \underline{Q}(\delta \underline{u})^T \underline{C} \underline{Q}(\Delta \underline{u}) dV = \int_S \delta \underline{u}^T \Delta \tau dS + \int_V \delta \underline{u}^T \Delta f dV \quad \text{Equation 1-4}$$

The components of \underline{C} and \underline{Q} are dependent on element type, material behavior, and kinematical assumptions. Later, a nonlinear form of the \underline{Q} operator is used to formulate large deformation analysis. The specific forms will be developed in subsequent chapters, for now, the concern is with the general formulation.

At this juncture, the finite element approximation is introduced by subdividing the domain V into a discrete set of elements interconnected at common nodal points. The unknown displacement fields within each element are approximated with prescribed functions such that continuity is maintained at the nodes and along the boundaries between elements. The assemblage of elements and nodes is termed the finite element mesh or topology.

The unknown displacement fields within each element are approximated by specified interpolation functions with unknown nodal-point displacements values, symbolically expressed as;

$$\underline{u}_e = \underline{N} \hat{\underline{u}}_e \quad \text{Equation 1-5}$$

where, \underline{u}_e = displacement vector-field within element

\underline{N} = matrix of prescribed interpolation functions (spatial variables)

$\hat{\underline{u}}_e$ = nodal-point displacement vector (unknown degrees of freedom)

The subscript “e” implies the above relationship holds within a given element. The form of the interpolation matrix and nodal displacement vector is dependent on element type.

1.2.1 Element types

The heart of any finite element formulation is the description of the elements themselves. The basic element types employed in the CANDE program are described below:

- Quadrilateral and triangular elements: for in-situ soil, bedding material, fill soil, pavement, etc.
- Interface element: for interfaces such as between pipe and soil.
- Link element: for special nodal connections along with death option.
- Beam-column element: for culvert structure like pipes, boxes, arches, etc.

The *quadrilateral* element is a nonconforming element developed by Herrmann (Reference 11) that has superior qualities in all basic deformation modes. The quadrilateral is composed of two triangles with complete quadratic interpolation functions initially specified within each triangle. Upon applying appropriate constraints and static condensation procedures a four-node quadrilateral with an 8 x 8 stiffness matrix is formed, wherein each node has two degrees of

freedom representing horizontal and vertical displacements. Associated with the quadrilateral/triangle element are five choices for material characterization: (1) linear elastic, isotropic or anisotropic; (2) incremental elastic, dependent on overburden pressure; (3) hyperbolic soil models by Duncan and Duncan & Selig, (4) variable modulus soil model by Hardin, and (5) plasticity model based on Mohr-Coulomb formulation. Specific derivations of the quadrilateral/triangular element are given in Section 7.3 in conjunction with the constitutive models for soil.

The *interface* element allows consideration of two subassemblies meeting at a common interface such that under loading the subassemblies may slip relative to each other with Coulomb friction, or separate, or re-bond. A natural application of this element is simulating the pipe-soil interface, other applications include trench soil-to-in-situ soil interface. The interface element is composed of two nodes, each associated with one subassembly and initially meeting at a common contact point. Each contact node has two degrees of freedom, horizontal and vertical displacement. In addition, a third node is assigned to the "interior" of the contact point to represent normal and tangential interface forces. The three nodes produce a 6 x 6 element "stiffness" matrix in a mixed formulation. Actually, the element stiffness is a set of constraint equations with Lagrange multipliers. Constraint equations impose conditions on normal and tangential displacements, and Lagrange multipliers are interface forces. The interface element derivation is presented in Chapter 4.

The *simple link* elements, like the interface element, is formulated with constraint equations that forces any two nodes to deform with same the translational degrees of freedom like a pinned connection, or with same translational and rotational degrees of freedom like a fixed moment connection. The *composite link* element are special constraint elements to join to separate beam-element groups into composite bending behavior. All link element includes a death option that permits modeling the removal of temporary supports, simulating the loss of culvert material by erosion, creation of a void in the soil, and soil excavation. The link element derivation is presented in the last portion of Chapter 4.

Lastly, the *beam-column* element is the familiar structural-matrix element for two-dimensional bending and axial deformation. It is defined by two nodes with three degrees of freedom per node, horizontal and vertical displacement and a rotation. Bending deformation is approximated by a cubic interpolation function and axial deformation is represented by a linear interpolation function. The beam-column element derivation employs a general nonlinear stress-strain model that is specialized to the material behavior of different pipe types. Specifically, elastic-plastic behavior for corrugated metal, tensile cracking and compressing yielding for reinforced concrete, and local buckling of wall profile elements for thermoplastic pipes. The beam-column element derivation is presented in Chapter 2 for each pipe type.

With the above background on specific element types, we continue with the general finite element formulation, wherein the global integrations expressed in Equation 1-4 may now be obtained as a summation of all element integrations. Specifically, within each element we replace the global displacement vector Δu by $\underline{N}\Delta\hat{u}_e$ and δu by $\underline{N}\delta\hat{u}_e$. Since $\Delta\hat{u}_e$ and $\delta\hat{u}_e$ are nodal-point parameters, they may be factored out of the element integrations. Thus, the element integrations are performed over known interpolation functions resulting in the so-called element stiffness matrix and load vector, expressed as;

$$\underline{k}_e = \int_{V_e} \underline{Q}(\underline{N})^T \underline{C} \underline{Q}(\underline{N}) dV_e \quad \text{Equation 1-6}$$

$$\Delta \underline{p}_e = \int_{S_e} \underline{N}^T \Delta \tau dS_e + \int_{V_e} \underline{N}^T \Delta f dV_e \quad \text{Equation 1-7}$$

Where, \underline{k}_e = element stiffness matrix

V_e = volume of element

$\Delta \underline{p}_e$ = element load vector

S_e = surface of element where traction is applied

1.2.2 Global assembly and incremental construction.

Each element is assigned a construction increment number, which corresponds to the load step number that the element stiffness matrix and load vector is assembled into the global system. Once an element stiffness enters the system it remains active for all subsequent load steps (there is no element death option except for link elements). Of course, the element body-load vector is only applied during the load step corresponding to the element construction increment number; it is not reapplied on subsequent load steps. Similarly, surface pressure and/or point loads (i.e., force boundary conditions) are also assigned a particular construction increment number and are only applied during the corresponding load step. Likewise, displacement boundary conditions are applied during the load step they are specified and remain fixed for all subsequent load steps.

To facilitate the global assemblage of elements, the current list of all active nodal degrees of freedom are aligned in a particular sequence order corresponding to the numerical sequence of the number-tag assigned to each node. Each active node is assigned two sequential positions in the global list for the horizontal and vertical nodal degrees of freedom. For those nodes that have a beam-column element attached, a third sequential position is assigned to the global list for the rotational degree of freedom. The global displacement vector, \hat{u}_G , represents the ordered list of all active degrees of freedom.

With the above understanding, the finite-element equivalent of Equation 1-4 is obtained by summing all active element contributions and assembling them into the global incremental virtual work statement. Since $\delta\hat{u}_G$ is an arbitrary virtual movement of all active degrees of freedom, the virtual work statement requires that the following set equilibrium equations be satisfied for each load step.

$$\underline{K}_G \Delta\hat{u}_G = \Delta P_G \quad \text{Equation 1-8}$$

where, $\underline{K}_G = \sum_{\text{elements}} \underline{k}_e$ = incremental global stiffness matrix

$$\Delta P_G = \sum_{\text{elements}} \Delta p_e = \text{incremental global load vector}$$

$\Delta\hat{u}_G$ = increment of global displacement vector (unknown degrees of freedom)

If the global system is linear, (that is, linear models are selected for the pipe materials, soil zones, interface conditions, and deformation theory), then the global stiffness matrix is directly calculable and constant for each load step. With this simplifying assumption, Equation 1-8 represents a set of linear algebraic equations that may be solved by standard methods such as Gauss Elimination to obtain $\Delta\hat{u}_G$. The running summation of each $\Delta\hat{u}_G$ over all load steps provides the total solution for the global displacement vector. More commonly, most culvert problems exhibit some type of nonlinear behavior so that the global stiffness matrix is not constant during the load step, requiring a nonlinear solution strategy discussed next.

1.2.3 Nonlinear solution strategy

CANDE employs a solution strategy known as the direct iterative method, or more simply called trial and error. This method has proven to be robust and readily accommodates the wide variety of nonlinear models such as tensile cracking and elastic-plastic behavior of pipe models, hyperbolic constitutive laws for soil models, frictional sliding and separation for interface models, and geometric nonlinearity for large deformation analysis. Most importantly, the solution accuracy is not too dependent on the magnitude of load increments; that is, a large load increment will often produce essentially the same results as the case where the load increment is divided into two or more sub-increments.

To illustrate the strategy, we start with the assumption that a valid (converged) solution is in hand for load step i , and we seek to increment the solution from load step i to $i+1$. That is, we know the mechanical responses (displacements, stresses,

strains, etc.) at load step i and we seek to update the mechanical responses at load step $i+1$. The global set of equations for load step $i+1$ is expressed with an iteration counter k as;

$$\underline{\mathbf{K}}_{Gk} \Delta \hat{\mathbf{u}}_{Gk} = \Delta \mathbf{P}_{Gk} \quad \text{Equation 1-9}$$

where, $\underline{\mathbf{K}}_{Gk}$ = global stiffness matrix for iteration k , (assembly of active elements)

$\Delta \hat{\mathbf{u}}_{Gk}$ = increment of global displacement vector for iteration k (active dof)

$\Delta \mathbf{P}_{Gk}$ = incremental global load vector for iteration k

k = iteration counter; 1, 2, 3, ...

For the first iteration $k=1$, the global stiffness matrix is assumed to remain the same as computed at the end of the previous iteration cycle for the step i , except for the addition of new elements entering the system for the first time at load step $i+1$. Note, if load step $i+1$ happens to be the first step, meaning the initial configuration, then the global stiffness matrix is constructed based on unloaded, linear-elastic elements belonging to the initial configuration prior to loading.

With the above understanding, the set of linear-like equations (Equation 1-9 for $k = 1$) is solved by a standard Gauss elimination scheme for the first trial solution $\Delta \hat{\mathbf{u}}_{G1}$. The trial solution is temporarily added to the known mechanical responses at load step i to form a new and better estimate of the displacements, stresses and strains at load step $i+1$. Next, all the nonlinear models for each element are re-evaluated based on current estimate of mechanical response for load step $i+1$, typically requiring small modifications to the element's stiffness matrices.

The process is repeated for $k = 2, 3, 4 \dots$ until convergence is witnessed. That is, iteration k produces a trial solution $\Delta \hat{\mathbf{u}}_{Gk}$ that is based on the revised stiffness matrix from the previous iteration $\Delta \hat{\mathbf{u}}_{Gk-1}$. When two consecutive iterations produce the same stiffness matrices for all elements within small error limits, then the solution has converged and we proceed to the next load step. The mechanics behind updating each element stiffness during the iteration cycle depends on the particular nonlinear model, discussed in subsequent chapters.

Once a converged solution increment has been found, all the mechanical responses are updated based on the last iteration solution, all intermediate iteration solutions are discarded. Thus prior to starting the next load step, the mechanical responses are permanently updated as symbolically shown below

$$\mathbf{q}_{i+1} = \mathbf{q}_i + \Delta \mathbf{q} \quad \text{Equation 1-10}$$

where q stands for all structural responses such as displacements, stresses, strains, moments, thrusts, etc. The data is saved in the program and the output file thereby providing a load-response history record.

As a final comment, it must be recognized that convergence is never guaranteed to occur. Sometimes convergence does not and should not occur because the system or portion of the system is physically incapable of carrying additional loading (singular system). In the normal default mode, CANDE will terminate on non-convergence with a message describing what nonlinear models are not converging. However, CANDE also offers the user control over the number of iterations with a special command to continue processing load steps even after a non-convergence load step has been encountered. In this way the user may inspect the post-convergent results to ascertain the cause of the problem.

2 BEAM-COLUMN ELEMENTS – PIPE TYPE MODELS

Presented in this section is a complete development of the beam-column elements used for modeling corrugated metal, reinforced concrete and thermoplastic pipe materials (or any two-dimensional structure). The initial development is focused on the general finite-element formulation that is applicable to all pipe-type material models. Subsequent developments describe specific stress-strain models that distinguish one pipe-type material from another.

2.1 General Form

The major assumptions and limitations used for the beam-column element are listed below:

1. Two-dimensional framework in a plane strain formulation.
2. Bernoulli-Euler beam kinematics without shear deformation.
3. Small deformation theory (this restriction removed in Chapter 5).
4. Material nonlinearity is a function of normal stress and strain and their history.
5. Incremental virtual work formulation with incremental stress-strain relationships.

2.1.1 Beam kinematics.

Based on the assumption that cross-sectional planes remain plane in bending and axial deformation, the Bernoulli-Euler assumption for displacement increments Δu at any station x along the beam length and at any point y in the beam's cross section may be expressed as an increment from load step i to $i+1$ as,

$$\Delta u(x, y) = \Delta a(x) + (y^* - y)\Delta v' \tag{Equation 2-1}$$

where, $\Delta u(x, y)$ = displacement in x direction from column and bending deformation.

$\Delta a(x)$ = uniform displacement in x direction from column action, independent of y .

$\Delta v(x)$ = displacement in y direction as function of x , independent of y .

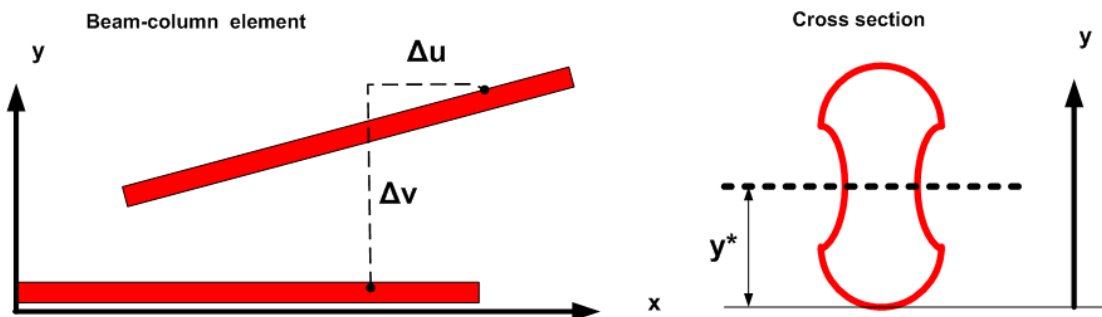
$\Delta v' = d(\Delta v)/dx$, derivative of Δv with respect to x (local deformation slope).

y^* = reference plane in the beam cross-section at $y = y^*$, yet to be specified.

$\Delta q = q_{i+1} - q_i$ = incremental change in any function q from load step i to $i+1$.

The Bernoulli-Euler assumption states that Δu at any point in the cross-section may be described by a uniform displacement Δa plus a rotational-like motion due to the slope of the transverse displacement increment. Note that the axis, y^* , is not specifically fixed in cross-section under these assumptions. Figure 2.1.1-1 illustrates the beam-column element in local beam coordinates, wherein x is aligned with the longitudinal axis and y is in the transverse direction locating positions in the beam's cross section.

Figure 2.1.1-1 Local coordinates for beam element and cross section.



Applying small strain theory to the above displacement functions produces one non-zero strain component, which is the strain normal to the beam cross section, $\Delta\varepsilon=d(\Delta u)/dx$. In terms of the Bernoulli-Euler functions, the incremental normal strain function is given by:

$$\Delta\varepsilon(x,y) = \Delta a' + (y^*-y)\Delta v'' \tag{Equation 2-2}$$

where $()' = d()/dx$, prime symbol denotes derivative of any quantity with respect to x.

2.1.2 Incremental stress-strain model

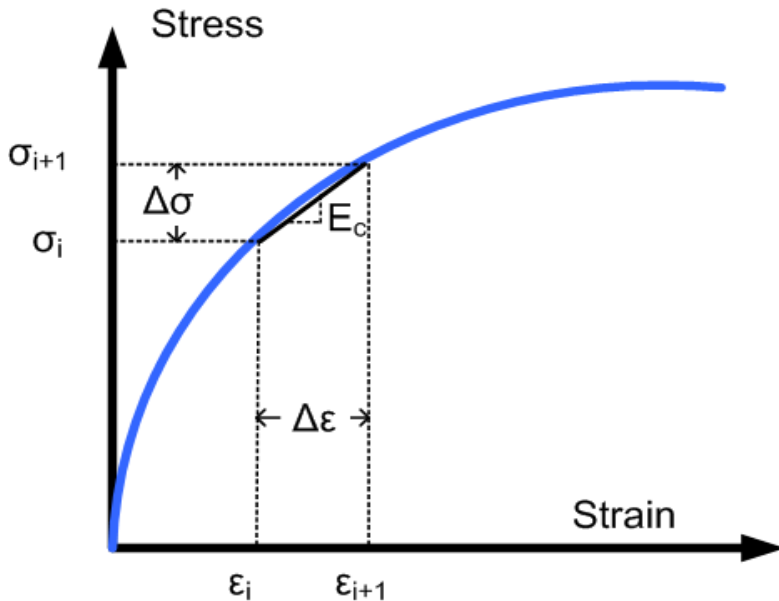
The nonlinear stress-strain laws used in CANDE are specific to each pipe material such as corrugated metal, reinforced concrete, and profile plastic pipe, which are presented in subsequent sections. However, all pipe materials stress-strain models conform to the same generic form expressed as;

$$\Delta\sigma = E_c \Delta\varepsilon \tag{Equation 2-3}$$

where, $\Delta\sigma$ = increment of axial stress from load step i to i + 1, ($\Delta\sigma = \sigma_{i+1} - \sigma_i$)
 $\Delta\varepsilon$ = increment of axial strain from load step i to i + 1, ($\Delta\varepsilon = \varepsilon_{i+1} - \varepsilon_i$)
 E_c = chord modulus of total stress-strain curve from load step i to i + 1

The chord modulus is dependent on the type of material and is generally dependent on the history of stress and strain throughout all loading steps. It is determined iteratively during each load step by repeating the solution process until the value of E_c converges for each point within the element to a small tolerance of error. The chord modulus is illustrated in Figure 2.1.2-1 for a generic, nonlinear stress-strain relationship.

Figure 2.1.2-1. Generic incremental stress-strain relationship.



Replacing $\Delta\varepsilon$ in Equation 2-3 with Equation 2-2, the fundamental stress-displacement relationship may be expressed as,

$$\Delta\sigma = E_c(\Delta a' + (y^*-y)\Delta v'') \tag{Equation 2-4}$$

Next, we will use the above equation to define the internal thrust and internal moment acting on the cross section at any station x.

2.1.3 Internal thrust and moment increments

As is customary, we define the thrust increment as the integral of $\Delta\sigma$ over the cross-section area A, and the moment increment as the integral of $\Delta\sigma (y^*-y)$ over the cross-section area A. Specifically,

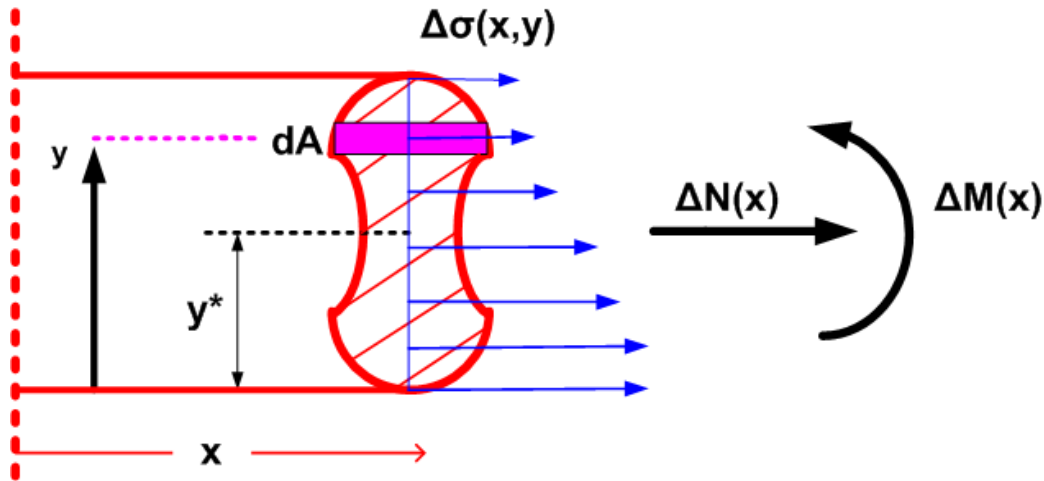
$$\Delta N = \int_A \Delta\sigma \, dA = \int_A E_c(\Delta a' + (y^*-y)\Delta v'') \, dA \tag{Equation 2-5}$$

$$\Delta M = \int_A \Delta\sigma (y^*-y) \, dA = \int_A E_c(\Delta a' + (y^*-y)\Delta v'') (y^*-y) \, dA \tag{Equation 2-6}$$

where, ΔN = thrust increment from load step i to i + 1, ($\Delta N = \Delta N(x)$)
 ΔM = moment increment from load step i to i + 1, ($\Delta M = \Delta M(x)$)
 $dA = b(y)dy$, a differential area of cross section where $b(y)$ is the width

Figure 2.1.3-1 shows the incremental thrust and moment resultants for an arbitrary cross-section with the coordinate y measured from bottom.

Figure 2.1.3-1 Thrust and moment increments from integration of stress distribution



The location of the arbitrary reference position y^* is now conveniently selected so that the first moment of integration is zero, i.e., $\int_A E_c (y^*-y) \, dA = 0$. Therefore, the location of y^* measured from the bottom of the cross section is,

$$y^* = \left(\int_A E_c \, y \, dA \right) / \left(\int_A E_c \, dA \right) \tag{Equation 2-7}$$

With the above definitions for y^* , the thrust and moment increments simplify to the following equations,

$$\Delta N = EA^* \Delta a' \quad \text{Equation 2-8}$$

$$\Delta M = EI^* \Delta v'' \quad \text{Equation 2-9}$$

where, $EA^* = \int_A E_c dA$ = effective axial stiffness of beam element

$$EI^* = \int_A E_c (y^*-y)^2 dA = \text{effective bending stiffness of beam element}$$

In the above equations, the thrust expression is written in the familiar linear form as the product of axial stiffness and column strain; likewise, the moment expression is written in the familiar form as the product of bending stiffness and beam curvature. Although the equations for thrust and moment increments may appear linear-like, the integrals defining y^* , EA^* , and EI^* depend on the nonlinear chord modulus, which in turn depends on the stress-strain state at each point in the cross-section in advancing from load step i to $i+1$.

From an analytical viewpoint, the only difference between one nonlinear pipe material and another is calculation of y^* , EA^* , and EI^* along with the associated convergence criteria. Except for these calculations, the fundamental beam-column formulation is identical for all pipes as presented in the remainder of this section.

2.1.4 Beam-column virtual work.

The general framework of incremental virtual work as previously presented is now specialized for the beam-column element. Specifically, the increment of internal virtual-strain-energy is written as,

$$\delta \Delta U_e = \int_V (\delta a' + (y^*-y) \delta v'') \Delta \sigma dV \quad \text{Equation 2-10}$$

where the virtual strain is expressed in terms of the Bernoulli-Euler functions prescribed in Equation 2-2, and V represents the volume of the beam-column element.

Separating the volume integral into area and length integrals, $dV = dA dx$, we arrive at,

$$\delta \Delta U_e = \int_x \left\{ \delta a' \int_A \Delta \sigma dA + \delta v'' \int_A \Delta \sigma (y^*-y) dA \right\} dx \quad \text{Equation 2-11}$$

Since the two area integrals in the above expression have been identified as ΔN and ΔM , the above expression may be equivalently written as,

$$\delta \Delta U_e = \int_x \{ \delta a' \Delta N + \delta v'' \Delta M \} dx \quad \text{Equation 2-12}$$

Lastly, replacing ΔN and ΔM by Equations 2-8 and 2-9, we arrive at the desired displacement form for internal virtual strain energy of the beam-column element,

$$\delta \Delta U_e = \int_x \{ \delta a' EA^* \Delta a' + \delta v'' EI^* \Delta v'' \} dx \quad \text{Equation 2-13}$$

In a similar manner, the incremental external virtual work for body loads is specialized for the beam-column element as,

$$\delta W_e = \int_x (\delta a \Delta F_x + \delta v \Delta F_y) dx \quad \text{Equation 2-14}$$

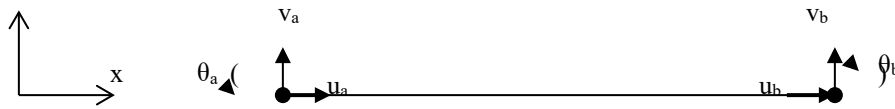
where, $\Delta F_x = \int_A f_x dA$ = axial body force per unit beam length in local x -direction,

$$\Delta F_y = \int_A f_y dA = \text{transverse body force per unit beam length in local } y\text{-direction.}$$

The body force per unit volume is assumed to be generated by gravity acting in the global vertical direction so that f_x and f_y are the component body forces per unit volume in local beam coordinates. Recall that all surface tractions and pressures are incorporated in the system at the global level, not at the element level.

2.1.5 Finite element interpolation functions.

To utilize the internal and external virtual work expressions in a finite element formulation for the beam-column, elements, we introduce specific interpolation functions for the displacement functions that become exact as the element lengths become small. The interpolation functions are expressed in terms of unknown nodal variables shown in the sketch below.



where, $\Delta u_a, \Delta u_b$ = incremental nodal displacements in x direction at nodes a and b
 $\Delta v_a, \Delta v_b$ = incremental nodal displacements in y direction at nodes a and b
 $\Delta \theta_a, \Delta \theta_b$ = incremental nodal rotations in counter-clockwise direction at nodes

The incremental axial displacement function is approximated with a linear interpolation function given by,

$$\Delta a(x) = \varphi_1(x) \Delta u_a + \varphi_2(x) \Delta u_b \quad \text{Equation 2-15a}$$

Or in vector notation,

$$\Delta a(x) = \langle \varphi_1 \ \varphi_2 \rangle \langle \Delta u_a \ \Delta u_b \rangle^T \quad \text{Equation 2-15b}$$

where, $\varphi_1(x) = 1 - x/L$ = first interpolation function defined over beam length L.
 $\varphi_2(x) = x/L$ = second interpolation function defined over beam length L.

The incremental vertical displacement function is approximated by a cubic polynomial, known as a Hermitian interpolation function, and is expressed in vector notation by,

$$\Delta v(x) = \langle \gamma_1 \ \gamma_2 \ \gamma_3 \ \gamma_4 \rangle \langle \Delta v_a \ \Delta \theta_a \ \Delta v_b \ \Delta \theta_b \rangle^T \quad \text{Equation 2-16}$$

where, $\gamma_1(x) = 1 - 3(x/L)^2 + 2(x/L)^3$ = Hermitian interpolation function one,
 $\gamma_2(x) = L(1 - x/L)^2 x/L$ = Hermitian interpolation function two,
 $\gamma_3(x) = 3(x/L)^2 - 2(x/L)^3$ = Hermitian interpolation function three,
 $\gamma_4(x) = L(x/L - 1)(x/L)^2$ = Hermitian interpolation function four.

The above interpolation functions for axial deformation and bending lead to the element stiffness matrices developed next.

2.1.6 Element stiffness matrices.

Taking the necessary derivatives of the interpolation functions for $\Delta u(x)$ and $\Delta v(x)$ and inserting them into the two internal virtual work terms of Equation 2-13, we arrive at the following expressions for internal virtual work in terms of axial virtual work and bending virtual work.

$$\delta\Delta U_e = \delta\langle\Delta u_a \Delta u_b\rangle \underline{K}_a \langle\Delta u_a \Delta u_b\rangle^T + \delta\langle\Delta v_a \Delta\theta_a \Delta v_b \Delta\theta_b\rangle \underline{K}_b \langle\Delta v_a \Delta\theta_a \Delta v_b \Delta\theta_b\rangle^T$$

$$\text{where, } \underline{K}_a = (EA^*) \int_0^L [\langle\phi'_1 \ \phi'_2\rangle^T \langle\phi'_1 \ \phi'_2\rangle] dx \quad (\text{axial stiffness}) \quad \text{Equation 2-17}$$

$$\text{and, } \underline{K}_b = (EI^*) \int_0^L [\langle\gamma''_1 \ \gamma''_2 \ \gamma''_3 \ \gamma''_4\rangle^T \langle\gamma''_1 \ \gamma''_2 \ \gamma''_3 \ \gamma''_4\rangle] dx \quad (\text{bending stiffness}) \quad \text{Equation 2-18}$$

Performing the integrations with respect to x over the element length L , we arrive at the final evaluation for the axial stiffness and bending stiffness as recorded below.

$$\underline{K}_a = (EA^*/L) \begin{pmatrix} 1 & -1 \\ -1 & 1 \end{pmatrix} \quad \text{Equation 2-19}$$

$$\underline{K}_b = (EI^*/L) \begin{pmatrix} 12/L^2 & 6/L & -12/L^2 & 6/L \\ 6/L & 4 & -6/L & 2 \\ -12/L^2 & -6/L & 12/L^2 & -6/L \\ 6/L & 2 & -6/L & 4 \end{pmatrix} \quad \text{Equation 2-20}$$

For linear materials EA^* and EI^* are constant and remain the same throughout the analysis. For nonlinear materials the stiffness factors EA^* and EI^* are determined iteratively for each load step wherein the factors are computed from the average moment and thrust at the center of the element. This implies that the elements will be sufficiently small so that thrust and moment do not vary substantially over any one element.

The above two matrices are combined into a single 6 x 6 matrix by re-grouping the nodal unknowns into a single vector as expressed below

$$\Delta\hat{u}_e = \langle\Delta u_a \ \Delta v_a \ \Delta\theta_a \ \Delta u_b \ \Delta v_b \ \Delta\theta_b\rangle^T \quad \text{Equation 2-21}$$

where, $\Delta\hat{u}_e$ is a vector of the six nodal unknowns in element coordinates. Accordingly, the 6x 6 element stiffness matrix is formed from the adding \underline{K}_a and \underline{K}_b to get the complete element stiffness matrix, \underline{K}_e .

$$\underline{K}_e = \frac{EA^*}{L} \begin{pmatrix} 1 & 0 & 0 & -1 & 0 & 0 \\ 0 & 0 & 0 & 0 & 0 & 0 \\ 0 & 0 & 0 & 0 & 0 & 0 \\ -1 & 0 & 0 & 1 & 0 & 0 \\ 0 & 0 & 0 & 0 & 0 & 0 \\ 0 & 0 & 0 & 0 & 0 & 0 \end{pmatrix} + \frac{EI^*}{L} \begin{pmatrix} 0 & 0 & 0 & 0 & 0 & 0 \\ 0 & 12/L^2 & 6/L & 0 & -12/L^2 & 6/L \\ 0 & 6/L & 4 & 0 & -6/L & 2 \\ 0 & 0 & 0 & 0 & 0 & 0 \\ 0 & -12/L^2 & -6/L & 0 & 12/L^2 & -6/L \\ 0 & 6/L & 2 & 0 & -6/L & 4 \end{pmatrix}$$

2.1.7 Transformation to global coordinates.

The last step before adding the element's contribution into the entire system is to transform the nodal variables from local coordinates to global coordinates.

Let β = angle from global X-axis to local x-axis, then the local nodal variables may be expressed as global nodal variables by,

$$\Delta \hat{u}_e = \underline{T} \Delta \hat{u}_E \quad \text{Equation 2-22}$$

where, $\Delta \hat{u}_e = \langle \Delta u_a \Delta v_a \Delta \theta_a \Delta u_b \Delta v_b \Delta \theta_b \rangle^T$ = local nodal variables for element

$\Delta \hat{u}_E = \langle \Delta u_A \Delta v_A \Delta \theta_A \Delta u_B \Delta v_B \Delta \theta_B \rangle^T$ = global nodal variables for element

$$\underline{T} = \begin{pmatrix} \cos\beta & \sin\beta & 0 & 0 & 0 & 0 \\ -\sin\beta & \cos\beta & 0 & 0 & 0 & 0 \\ 0 & 0 & 1 & 0 & 0 & 0 \\ 0 & 0 & 0 & \cos\beta & \sin\beta & 0 \\ 0 & 0 & 0 & -\sin\beta & \cos\beta & 0 \\ 0 & 0 & 0 & 0 & 0 & 1 \end{pmatrix} = \text{transformation matrix}$$

With the above transformation matrix, the global element stiffness matrix may be expressed in global coordinates as,

$$\underline{K}_E = \underline{T}^T \underline{K}_e \underline{T} \quad = \text{global element stiffness matrix} \quad \text{Equation 2-23}$$

It should be clear that lower-case subscripts are used for element quantities that are in expressed in local coordinates, whereas upper-case subscripts are used for element quantities that are in expressed in global coordinates.

The element load vector due to body weight may be directly expressed in global coordinates because gravity operates in the global Y direction (negative). Thus, the element's weight is divided equally to both nodes and acting in the -Y direction associated with Δv_A and Δv_B as expressed below.

$$\Delta p_E = -\rho AL \begin{pmatrix} 0 \\ 1/2 \\ 0 \\ 0 \\ 1/2 \\ 0 \end{pmatrix} = \text{global element load vector} \quad \text{Equation 2-24}$$

where, ρ is the density of the beam-column material, A is the cross-sectional area and L is the length. The element stiffness matrix K_E and load vector Δp_E are in the proper form for global assembly.

2.1.8 Equation solving and recovery of structural responses.

After the entire set of elements is assembled and solved by Gauss elimination as described in Sections 1.2.2 and 1.2.3, the solution (or trial solution) gives numerical results for the incremental displacements at all nodes. Using these results, other key structural responses of the beam-column element are calculated (recovered) based the previously developed relationships. Key responses include internal thrust, moment and shear resultants and stress and strain distributions.

First, the internal force and moment increments at the ends of the beam-column element are recovered by multiplying the element stiffness matrix by the calculated incremental displacements (transformed to local coordinates) as shown below.

$$\langle \Delta N_a \ \Delta Q_a \ \Delta M_a \ \Delta N_b \ \Delta Q_b \ \Delta M_b \rangle^T = \underline{K}_e \hat{\Delta u}_e \quad \text{Equation 2-25}$$

where, $\Delta N_a, \Delta N_b$ = thrust force increments (local x_i direction) at nodes a and b

$\Delta Q_a, \Delta Q_b$ = shear force increments (local y_i direction) at nodes a and b

$\Delta M_a, \Delta M_b$ = moment increments at nodes a and b (invariant to x-y coordinates)

The fact that the incremental end forces can be recovered by multiplying the current element stiffness matrix times the incremental displacements is a direct result of applying incremental virtual work to a free-body beam-column element cut just short of the end nodes. Said another way, the incremental forces and moments at the cut ends are the additional end forces that are required to hold the free-body element in equilibrium as a result of the incremental load. As a result of the assumed interpolation functions, thrust and shear forces are constant within the element and the moment varies linearly from end to end. Thus, ΔN and ΔM are known at every point x along the element length.

Next, the incremental strain, defined by Equation 2-2, may be evaluated at any point (x,y) by using Equation 2-8 to evaluate the constant axial strain increment ($\Delta a' = \Delta N/EA^*$) and Equation 2-9 to evaluate the bending curvature ($\Delta v'' = \Delta M/EI^*$) as shown below. The strain distribution over any cross-section is always linear irrespective of the material stress-strain model.

$$\Delta \varepsilon(x,y) = \Delta N/EA^* + (y^*-y)\Delta M/EI^* \quad \text{Equation 2-26}$$

Knowing the strain distribution, the stress increment at any point (x,y) may be calculated using the incremental stress-strain relationship (chord modulus) defined by Equation 2-3, which is dependent on the particular type of material.

$$\Delta \sigma(x,y) = E_c \Delta \varepsilon(x,y) \quad \text{Equation 2-27}$$

where, $E_c = E_c(\sigma(x,y))$ = chord modulus as a function of total stress and stress history

Unlike the linear strain distribution, the incremental stress distribution is, in general, nonlinear over the cross-section because the chord modulus is dependent on the total stress magnitude and history.

After the incremental structural responses have been computed, the total structural responses at load step $i + 1$ are computed by adding the incremental values to the values of previous load step as indicated below.

$$q_{i+1} = q_i + \Delta q \quad \text{Equation 2-28}$$

where q stands for any structural responses such as displacements, stresses, strains, moments, thrusts, and so on. If the solution represents a converged load step (or a linear system), then the q_{i+1} values are printed to the output file and permanently stored in the computer in preparation for the next load step. On the other hand, if the solution has not converged, the q_{i+1} values are used temporarily to compute improved estimates of the element stiffness matrices and then discarded.

2.1.9 Nonlinear solution strategy

The key section properties, EA^* , y^* and EI^* , are the heart of the nonlinear algorithm, and they are computed at every node for every iteration. Shown below is a summary of the key section property definitions.

$$EA^* = \int_A E_c \, dA \quad = \text{effective axial stiffness of beam element} \quad \text{Equation 2-29a}$$

$$y^* = \left(\int_A E_c \, y \, dA \right) / \left(\int_A E_c \, dA \right) = \text{reference axis} \quad \text{Equation 2-29b}$$

$$EI^* = \int_A E_c \, (y^* - y)^2 \, dA \quad = \text{effective bending stiffness of beam element} \quad \text{Equation 2-29c}$$

To perform the above area integrations, the chord modulus, E_c , must be estimated at each point in the cross-section. As previously illustrated in Figure 2.1.2-1, the chord modulus for nonlinear materials is dependent on the known stress-strain state at load step i and the unknown stress-strain at load step $i + 1$, thereby requiring an iterative solution strategy as outlined below.

1. For the first iteration, the chord moduli are assumed to remain unchanged from the converged results of load step i . Thus, the key section properties and element stiffness also remain the same as they were. Based on these known element stiffness matrices, the first trial solution is obtained for the new incremental load vector from load step i to load step $i+1$.
2. Using the first trial solution, the recovery process discussed above provides estimates for σ_{i+1} and ε_{i+1} , which, in turn, provides new estimates for the chord moduli depending on the particular stress-strain model assigned to the element.
3. Knowing the new estimates for the chord moduli, the area integrations in Equations 2-29a,b,c are performed to provide new estimates for the key section properties, EA^* , y^* and EI^* , and hence, revised element stiffness matrices.
4. After assembling the revised element stiffness matrices, the next trial solution is obtained, which leads to new estimates for σ_{i+1} , ε_{i+1} , and E_c , for each point in the cross-section. Once again, the area integrals are evaluated to provide better estimates of the key section properties at each nodal location, and so on.

- The above process is repeated for each iteration until two successive solutions produce essentially the same section properties for every element within 1% relative difference. When this occurs, the solution is said to have converged and all the updated structural responses are printed and saved for the next load step.

The area integrations for section properties, EA^* , y^* and EI^* , are accomplished in each pipe-type subroutine. In some cases, the integrations are done numerically and in other cases the integrations are accomplished in a semi-analytical manner depending on the stress-strain model of the pipe material. In subsequent sections of this chapter the calculation procedure to obtain EA^* , y^* and EI^* for each pipe material are presented for each pipe-type material.

2.2 Corrugated Metal

2.2.1 Overview of corrugated metal pipe type

Corrugated metal applies to both corrugated steel and corrugated aluminum. Both metals are represented by the same fundamental models and differ only with respect to the numerical values of key parameters such as modulus and yield stress. Wall properties of corrugated metal are characterized by cross-sectional area, moment of inertia and section modulus, which represent the geometry of the corrugation's waveform per unit length. The aluminum pipe-type subroutine and the steel pipe-type subroutine have built-in tables for commercially available corrugation sizes as well as realistic default values for all linear and nonlinear material properties. Steel and aluminum material behavior is simulated with a bilinear stress-strain model with an initial elastic response up to yield stress followed a hardening plastic response, identical in tension and compression. All unloading is assumed linear elastic.

2.2.2 Design criteria for corrugated metal

Design criteria for corrugated metal includes strength limits for thrust stress against material yielding in hoop compression, global buckling and seam strength rupture. Although not yet required by AASHTO, another meaningful strength criterion is a limit on the amount of plastic penetration through the cross section. For deep corrugations with corrugation heights ≥ 5.0 inches, the combined thrust-moment criterion is more stringent than the separate requirements of the thrust stress and plastic penetration criterions. Finally, a performance limit on the allowable deflection completes the set of design criteria. The design criteria are summarized in the following table.

TABLE 2.2.2-1 Corrugated Metal Design Criteria.

Design Criterion (Strength limits)	Demand	Capacity
(1) Thrust stress (psi)	$\sigma_{\max} = N_{\max} / A$	$f_y = \text{yield strength}$
(2) Global Buckling (psi)	$\sigma_{\max} = N_{\max} / A$	$f_b = \text{buckling capacity:}$ *AASHTO Eq. 12.7.2.4-1, or *AASHTO Eq. 12.8.9.6-1, or * CANDE prediction.
(3) Seam strength (psi)	$\sigma_{\max} = N_{\max} / A$	$f_s = \text{seam strength}$
(4) Plastic Penetration (%)	pp = percent of cross-section plastically deformed.	failure = 100%
(5) Combined Moment- Thrust Criterion (ratio). (For deep corrugations only)	$\text{Ratio} = \frac{ M_{\max} }{M_z} + \left(\frac{N_{\max}}{A f_y} \right)^2$	Ratio Limit = 1.00
(Performance Limits) (At Service Load)		
(5) Allowable deflection (%)	$\Delta_{\max} = \text{computed deflect \%}$	Allowable = 5% (Long Spans = 2%)

N_{\max} = max thrust force, M_{\max} = max moment, A = area, M_z = plastic moment

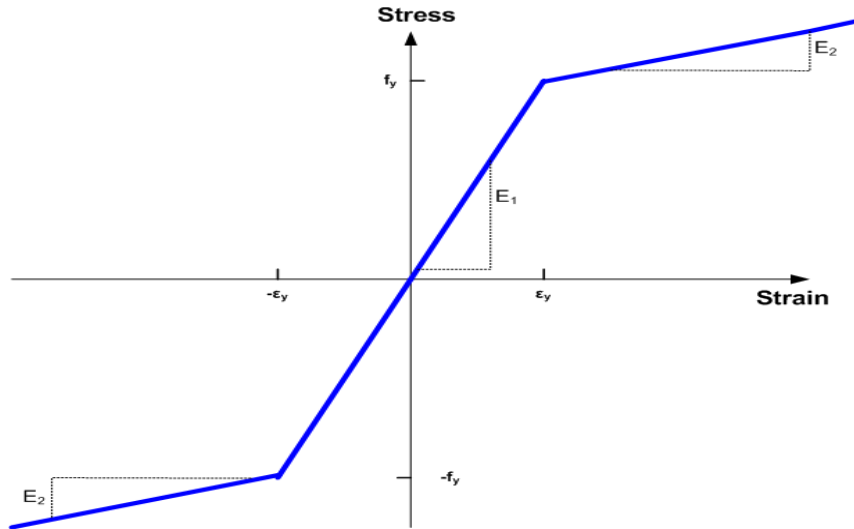
The above design criteria are equally applicable to working stress or LRFD design methodologies. For the working stress approach, the demand and the capacity quantities are unfactored, and the design evaluation is given by safety factors defined as capacity divided by demand. Typically, safety factors on the order of 2.0 are desirable for strength-related criteria. For the LRFD approach the demand and the capacity quantities are factored (see Chapter 6), and the design evaluation is given by ratios of demand-to-capacity. Demand-to-capacity ratios less than or equal to 1.0 are acceptably safe. Further discussion on the design criteria is provided below.

1. *Thrust stress.* Thrust-stress demand is determined by finding the element with the largest thrust force, N_{\max} , and dividing by the cross-sectional area. The corresponding yield-strength capacity is typically 33,000 psi for steel and 24,000 psi for aluminum.
2. *Global buckling.* For the buckling-strength capacity, CANDE-2022 offers the user three choices; (1) an approximate and generally conservative estimate based on the simplified AASHTO LRFD equations 12.7.2.4-1-2, (2) another approximate AASHTO LRFD equation 12.8.9.6-1 intended for deep corrugations, and (3) a much more accurate solution based on CANDE's large deformation formulation with linearized buckling prediction.
3. *Seam strength.* If longitudinal bolted seams are present in the corrugated metal culvert, the seam-strength capacity is typically less than the material yield strength. In the absence of experimental test data, seam-strength capacity is often specified as 67% of material yield-strength capacity.
4. *Plastic penetration.* On the demand side, the percentage of the cross-section that is strained into the plastic range from thrust and bending is calculated directly from the nonlinear corrugated metal model. The limit of plastic penetration is 100% of the cross section, meaning cross section is incapable of carrying any additional load. Note that some amount of plastic yielding is expected to occur in the outer fibers of most well-designed corrugated metal culverts under service loading. Although AASHTO does not specify a limit on the percent of plastic penetration for standard corrugations, the plastic penetration design criterion offers a precaution against full 100% yielding of the entire cross section without restricting moderate amounts of outer fiber yielding.
5. *Combined moment & thrust.* This relatively new AASHTO criterion is intended for deep corrugations whose corrugation height is greater or equal to 5.0 inches. For LRFD evaluation the ratio defining the combined moment-thrust criterion implies that numerators include load factors and the denominators include resistance factors, whereas for working stress evaluation they do not.
6. *Allowable deflection.* Computed deflection is the relative vertical movement between the top and bottom of the culvert structure, and the percent deflection is relative the vertical distance. The service load limit for allowable deflection is generally taken as 5% for all corrugated metal structures except long spans, which are usually limited to 2% of the vertical rise.

2.2.3 Nonlinear model for corrugated metal

The one-dimensional stress-strain relationship for metal is approximated by a bilinear curve as shown in the figure below.

Figure 2.2.3-1 Stress-strain relationship for metal culverts



The model is identical in tension and compression and applies to both steel and aluminum, which differ only in parametric values as shown in the table below.

Table 2.2.3-1 Typical material parametric values for steel and aluminum

Metal type	Yield strength psi	Elastic Young's modulus, E ₁ psi	Upper curve modulus, E ₂ psi
Aluminum	24,000	10,000,000	500,000
Steel	33,000	29,000,000	0.0

The following material constants are used for plane strain conditions:

$$E_e = E_1 / (1 - \nu^2) = \text{Effective plane strain modulus in elastic zone}$$

ν = Poisson ratio of metal

$$r = E_2 / E_1 = \text{Ratio of upper-curve modulus to initial modulus}$$

$$r E_e = \text{Effective plane strain modulus for upper-curve zone.}$$

Initial section properties are defined (input) as follows:

A_0 = Cross-sectional area of corrugation per unit length

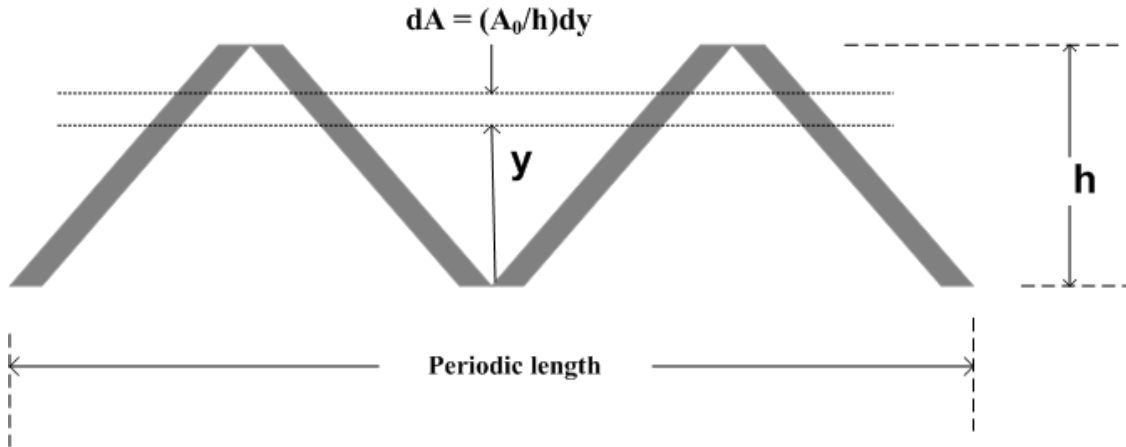
I_0 = Moment of inertia of corrugation about mid-height

$S_0 = I_0 / (h/2) = \text{Section modulus of corrugation}$

h = Total height of corrugation

Within the framework of the general nonlinear model, the objective is to determine the integral quantities EA^* , y^* , and EI^* defined by Equations 2-29a,b, & c. To accomplish this, the chord modulus E_c must be determined consistently with the bi-linear model, and, secondly, the area of integration must be defined. With regard to the latter, a manageable integration area can be obtained by approximating the actual corrugation geometry by a saw-tooth pattern, such that the same area A_0 and depth of section h is preserved, as shown in Figure 2.2.3-2

Figure 2.2.3-2 Saw-tooth approximation of corrugation for integrating in nonlinear range



Saw-tooth geometric properties:

$$\text{Area} = (A_0/h) \int_h dy = A_0$$

$$\text{Centroid} = (A_0/h) \int_h y dy / A_0 = h/2$$

$$\text{Moment inertia} = (A_0/h) \int_h (y-h/2)^2 dy = A_0 h^2 / 12$$

Correction factor for moment of inertia:

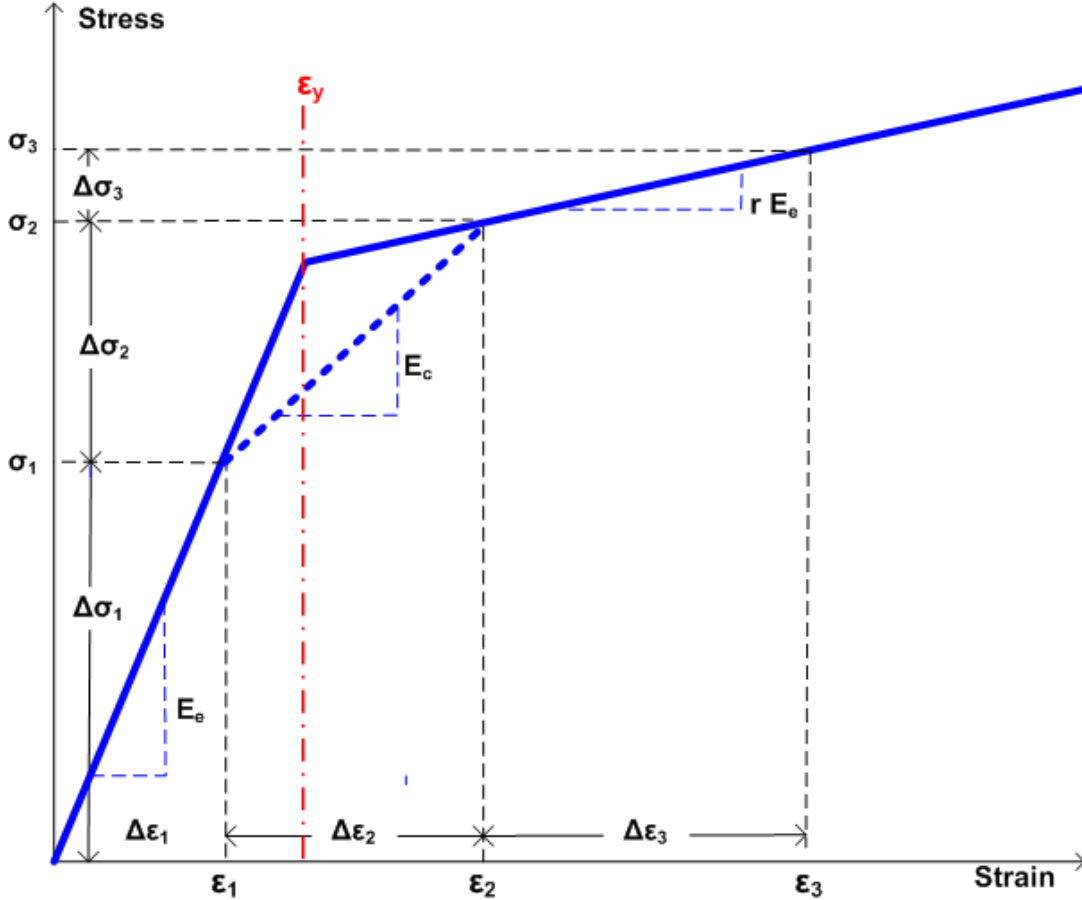
$$C_0 = I_0 / (A_0 h^2 / 12)$$

$$\text{Moment inertia} = C_0 (A_0/h) \int_h (y-h/2)^2 dy = I_0$$

As shown in the above figure, integration of the saw-tooth approximation yields the correct area and centroid location, however, the moment of inertia = $A_0 h^2 / 12$ is an approximation of actual corrugations, which are more rounded at the top and bottom than the saw-tooth approximation. By inspecting sectional properties of standard corrugation tables, the moment of inertias from the saw-tooth approximation are 5 to 10% lower than the reported moment of inertia values. To correct for this discrepancy, integrations for the effective bending stiffness will be multiplied by the correction factor C_0 defined in the above figure in order to reproduce the correct moment of inertia. Of course, if the metal is not yielding anywhere in the cross section, the chord modulus has the constant value E_c and may be removed from inside the integral and integrations need not be performed since the section properties are already known.

Recalling the chord modulus relates increments of stress to increments of strain, $\Delta\sigma = E_C \Delta\varepsilon$, the bilinear model results in three distinct zones as illustrated in Figure 2.2.3-3. Case 1 occurs when the strain increment lies entirely in the elastic zone, bounded by the yield strain, as illustrated by $\Delta\varepsilon_1$. Case 2 occurs when the strain increment starts in the elastic region and exceeds the yield strain, as illustrated by $\Delta\varepsilon_2$. Finally, Case 3 occurs when the strain increment starts at a strain greater than yield strain and ends at a greater value, as illustrated by $\Delta\varepsilon_3$. All other cases wherein the strain increment starts from a large strain value and ends with a smaller strain value is elastic unloading and treated the same as Case 1.

Figure 2.2.3-3 Illustration of strain increments in three zones; elastic, transition and plastic



With the above understanding the general chord modulus can be defined in term of the bilinear model for the elastic, transition and plastic zones as follows;

$$E_C = E_e \quad \text{(Elastic zone)} \quad \text{Equation 2.2-1a}$$

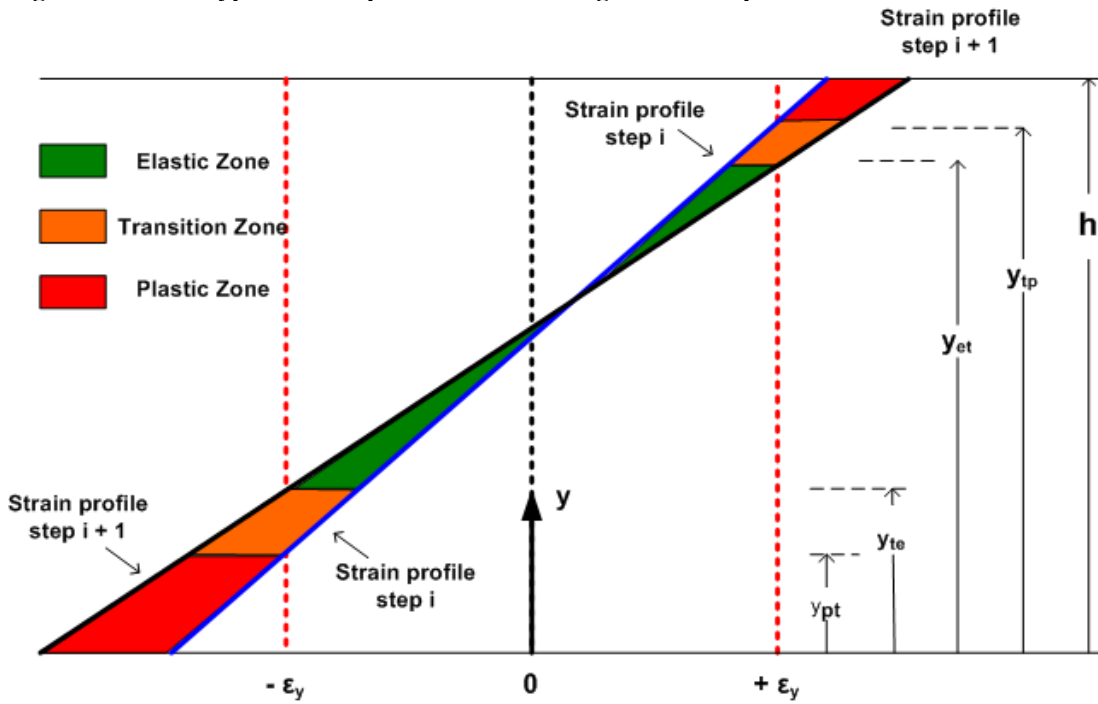
$$E_C = E_e [(\epsilon_y - \epsilon_i) / (\Delta\epsilon_{i+1}) + r (\epsilon_{i+1} - \epsilon_y) / (\Delta\epsilon_{i+1})] \quad \text{(Transition zone)} \quad \text{Equation 2.2-1b}$$

$$E_C = r E_e \quad \text{(Plastic zone)} \quad \text{Equation 2.2-1c}$$

In the above, the transition zone chord modulus is defined generally from load step i to $i+1$ where $\epsilon_i < \epsilon_y < \epsilon_{i+1}$.

The foregoing considered the stress-strain relationship at a point. To obtain EA^* , y^* , and EI^* , the stress-strain relationship must be defined over the cross-sectional area. To this end we take great advantage of the fact the strain profile always remains linear due to Bernoulli-Euler kinematics. Figure 2.2.3-4 illustrates two typical strain distributions at load step i and at load step $i+1$. The cross-section depth is divided into the regions; elastic, transition, and plastic. The elastic region is that portion which remains totally elastic during the load step. The transition region is the zone that begins elastic and becomes plastic during the load step. And finally, the yield region signifies the zone where the material remains plastic.

Figure 2.2.3-4 Typical strain profiles and resulting zone descriptions



Knowing the strain profile at step i and having obtained a trial strain profile at step $i+1$, it is a simple matter to locate the elastic-transition boundaries and the transition-plastic boundaries using straight-line equations as indicated in the above figure. The elastic-transition boundaries are located where the strain profile at step $i+1$ intersects the yield strain limits, and the transition-plastic boundaries are located where the strain profile at step i intersects the yield strain limits.

The chord modulus in the elastic and plastic zones is a constant value, however in the transition zones, the chord modulus varies with y because the strain increments vary with y . To simplify the integrations of the chord modulus in the transition zones, an average value of E_c is computed from Equation 2.2-1b based on the strain increment in the center of the transition zones. Letting z_{t1} and z_{t2} be the y -distance to the centroid of the lower and upper transition zones and computing the strain increments at these levels, we can express the chord moduli as,

$$E_{C1} = \alpha_1 E_e \quad \text{Average chord modulus in lower transition zone} \quad \text{Equation 2.2-2a}$$

$$E_{C2} = \alpha_2 E_e \quad \text{Average chord modulus in upper transition zone} \quad \text{Equation 2.2-2b}$$

where, $\alpha_1 = [(\epsilon_y - \epsilon_i) / (\Delta\epsilon_{i+1}) + r (\epsilon_{i+1} - \epsilon_y) / (\Delta\epsilon_{i+1})]$, with $\Delta\epsilon_{i+1}$ evaluated at lower transition center.

$\alpha_2 = [(\epsilon_y - \epsilon_i) / (\Delta\epsilon_{i+1}) + r (\epsilon_{i+1} - \epsilon_y) / (\Delta\epsilon_{i+1})]$, with $\Delta\epsilon_{i+1}$ evaluated at upper transition center.

The alpha terms are constants and are within the range, $r < \alpha < 1.0$, depending on the transition zone boundaries, which may be truncated at the top and bottom of the cross-section. This transition zone integration technique has proven to be very accurate. The following table summarizes the data that is required to compute the key section properties.

Table 2.2.3-2 Zone integration parameters to compute key section properties

Zone Number	Zone Description	Zone Thickness	Distance to zone centroid	Zone weight due to nonlinear modulus
1	Elastic	Δh_1	z_1	$w_1 = 1.0$
2	Lower transition	Δh_2	z_2	$w_2 = \alpha_1$
3	Upper transition	Δh_3	z_3	$w_3 = \alpha_2$
4	Lower plastic	Δh_4	z_4	$w_4 = r$
5	Upper plastic	Δh_5	z_5	$w_5 = r$

It should be understood that not all five zones might be active at any given time. Un-active zones are characterized with $\Delta h_j = 0$, so that $h = \sum_{j=1}^5 \Delta h_j$ always hold true.

With the above understanding, the effective axial stiffness for trial load step $i+1$ is given by,

$$EA^* = \int_A E_C dA = E_e A^* \quad \text{Equation 2.2-3a}$$

where, $A^* = (A_0/h) \sum_{j=1}^5 w_j \Delta h_j$ Equation 2.2-3b

The current reference axis is given by,

$$y^* = \left(\int_A E_C y dA \right) / \left(\int_A E_C dA \right) = \left(\sum_{j=1}^5 w_j z_j \Delta h_j \right) / A^* \quad \text{Equation 2.2-4}$$

And finally, the effective bending stiffness is given by,

$$EI^* = \int_A E_C (y^* - y)^2 dA = E_e I^* \quad \text{Equation 2.2-5a}$$

where, $I^* = C_0 (A_0/h) \sum_{j=1}^5 w_j (\Delta h_j^3 / 12 + \Delta h_j (z_j - y^*)^2)$ Equation 2.2-5b

Unloading. The forgoing elastic-plastic stiffness properties are replaced with simple elastic properties whenever elastic unloading is encountered. Elastic unloading is triggered by either one of two events, one event related to thrust reversal and the other to moment reversal. Thrust reversal occurs when the average strain at the beginning of the load step exceeds the yield strain, and the average strain decreases at the end of the load step. Moment reversal occurs when the depth of the elastic zone increases from the beginning to the end of the load step.

In CANDE-2022 the above computations are carried out in Subroutine EMOD wherein convergence is achieved when two successive trial solutions produce A^* , y^* and I^* within 1% of the previous trial solution for all elements.

2.3 Reinforced Concrete

2.3.1 Overview of reinforced concrete pipe type

Wall sections for reinforced concrete culverts are defined by the concrete wall thickness with up to two rows of reinforcing steel, typically placed near the inner and outer surface with specified cover depths. In tension, concrete behavior is characterized by cracking when tension stress levels exceed the tensile strain limit. When this occurs, the pre-existing tensile stresses are redistributed to the uncracked section, and the cracked location is assumed not to heal for any subsequent tensile loading. In compression, concrete is simulated with a tri-linear stress-strain curve. Initially, the concrete response is linear up to a specified strain level after which the concrete exhibits plastic-hardening behavior. When the compressive stress reaches the ultimate strength limit (f_c'), the stress-strain response becomes perfectly plastic with no increase in stress as compressive strain increases. Reinforcing steel behavior is characterized by an elastic-plastic stress-strain model, which becomes perfectly plastic when the steel yield stress is reached in tension or compression.

2.3.2 Design criteria for reinforced concrete

Design criteria for reinforced concrete culverts include strength limits for yielding of steel reinforcement, crushing of concrete in compression, diagonal cracking due to shear failure, and radial cracking due to curved tension steel (also called bowstringing). Finally, a performance limit on the allowable flexure crack width, typically taken as 0.01 inches, completes the set of design criteria. It is believed that the proposed design criteria faithfully represent the intent and, in some cases, improve the clarity of the criteria as presented in the AASHTO LRFD specifications.

Table 2.3.2-1 Reinforced Concrete Design Criteria.

Design Criterion (Strength limits)	Demand	Capacity
(1) Steel yielding (psi)	f_{\max} = max steel stress	f_y = yield strength
(2) Concrete crushing (psi)	σ_{\max} = max compression	f_c' = compressive strength
(3) Shear failure (lb/in)	V_{\max} = max shear force	V_{ult} = concrete shear capacity
(4) Radial tension failure (psi)	t_{\max} = max radial stress	t_{ult} = ultimate radial strength
(Performance Limits) (At Service Load)		
(5) Allowable crack width* (in)	CW_{\max} = max crack width	CW_{Allow} = allowable CW (0.01 inch)

The above design criteria are equally applicable to working stress or LRFD design methodologies. For the working stress approach, the demand and the capacity quantities are unfactored, and the design evaluation is given by safety factors defined as capacity divided by demand. Typically, safety factors on the order of 2.0 are desirable for strength-related criteria. For the LRFD approach the demand and the capacity quantities are factored (see Chapter 6), and the design evaluation is given by ratios of demand-to-capacity. Demand-to-capacity ratios less than or equal to 1.0 are acceptably safe. Further discussion on the design criteria is provided below.

1. *Steel yielding.* The maximum steel-stress demand is computed directly from the nonlinear reinforced concrete model. On the capacity side, the steel yield strength is an input or default value, nominally 60,000 psi for deformed bars and 65,000 psi for smooth wire fabric.
2. *Concrete crushing.* On the demand side, the maximum outer-fiber concrete compressive stress is determined directly from the reinforced concrete model as a result of thrust and compression bending. The ultimate compressive strength or capacity is an input or default value typically in the range of 4000 to 6000 psi.
3. *Shear failure.* The maximum shear-force demand is computed directly from the beam-column internal forces. Shear-force capacity is the shear force causing diagonal tension failure at a given cross-section. AASHTO LRFD specifications prescribe three different shear-force capacities depending on structural shape and burial depth.

- For concrete pipes and arches, the shear capacity is specified by V_{\max} = Equations 12.10.4.2.5, which yield variable values for shear capacity dependent on the values for moment, thrust and shear around the culvert wall.
- For boxes and 3-sided structures with 2 or more feet of soil cover, the shear capacity is specified by V_{\max} = Equations 5.14.5.3-1 wherein the value is dependent on moment and shear (not thrust).
- For boxes and 3-sided structures with less than 2 feet of soil cover, the shear capacity is specified by equations in Section 5.8.3.3 that, in some cases, depend on the nature of the traverse reinforcement (stirrups).

Clearly there is a need to unify the AASHTO shear-capacity equations because rational mechanics indicates that shear capacity should be a function of the cross-section properties and state of loading, not on the culvert shape or depth of burial. CANDE allows the user to select among the three choices for shear-force capacity, however, Equation 12.10.4.2.5 is considered the best predictor of shear-force capacity because of the large experimental data base (Reference 14). CANDE also provides the option to choose the classical shear-strength method where shear-strength = $\beta \sqrt{f'_c}$, where β is a specified factor, typically = 2.0.

4. *Radial tension failure.* On the demand side, the concrete radial tensile stress is caused by tensile forces in curved inner cage reinforcement steel as it tends to straighten out and exerts radial tensile stresses on the interior concrete cover thickness. The phenomenon is sometimes called bow stringing. CANDE predicts the radial tensile stress by dividing the interior cage steel force (maximum tensile force per unit length) by the radius of curvature of the steel cage, or letting A_s = steel area per unit length., we have;

$$t_{\max} = A_s f_{s\max} / \text{Radius} \quad \text{Equation 2.3-1}$$

The ultimate radial stress is related to the tension strength of concrete and the structure span. The radial tensile strength capacity is adapted from AASHTO LRFD Equation 12.10.4.2.4c-1. and restated in psi units as:

$$t_{\text{ult}} = 37.92 \sqrt{f'_c / 1000} F_{rt} \quad \text{Equation 2.3-2}$$

where F_{rt} is a scale factor dependent on structure span, specified in the contents of Equation 12.10.4.2.4c-1.

5. *Allowable crack width.* The allowable crack width at service loading is generally taken as 0.01 inches in accordance with AASHTO LRFD specification 12.10.3. CANDE offers three empirical formulas to predict crack width; the traditional Gergely-Lutz formula (Reference 16), the recently developed Heger-McGrath formula (Reference 15), and a simple concrete strain-based formula proposed by the author.

The Gergely-Lutz and Heger-McGrath equations are similar in form and are driven by the computed tension steel stress when it exceeds f_0 , the threshold stress for initial cracking. Their crack width predictions are concisely stated in the equation below,

$$CW = S(f_s - f_0) > 0 \quad \text{Equation 2.3-3}$$

where, CW = the crack width in inches,
 f_s = computed tension steel stress in psi,
 S and f_0 = model parameters specified in the table below.

Table 2.3.2-1 Crack width model parameters S and f_0

Gergely-Lutz (Reference 16)	Heger-McGrath (Reference 15)
$S = (0.122 \times 10^{-6}) (2t_b^2 s_1)^{1/3}$ where, t_b = concrete cover thickness (inches) s_1 = spacing between rows of steel reinforcement (inches)	$S = (0.333 \times 10^{-6}) (t_b s_1 / 2n)^{1/3}$ where, t_b = concrete cover thickness (inches) s_1 = spacing between rows of steel reinforcement (inches) n = number of steel reinforcement layers in the tension zone (1 or 2)
$f_0 = 5,000.$	$f_0 = 31.6 C_1 (h/d)^2 \sqrt{f'_c} / \rho$ where, $C_1 = 1.0$ for smooth wire, 1.5 for welded wire fabric, and 1.9 for deformed wire/bars. h/d = total concrete thickness –to- effective height (tension steel to other face) ρ = reinforcement area ratio (A_s/h).

The Heger-McGrath prediction is well calibrated for predicting crack widths near 0.01 inches; however, it tends to underestimate the prediction of smaller crack widths. The Gergely-Lutz formula is more accurate in predicting smaller crack widths.

The concrete strain-based crack width prediction is given by,

$$CW = L_s (\epsilon_{\text{tension}} - \epsilon_{\text{crack}}) \quad \text{Equation 2.3-4}$$

where, $\epsilon_{\text{tension}}$ = computed tensile strain in outer fiber of concrete.

ϵ_{crack} = tensile strain at initial concrete cracking, a concrete model property.

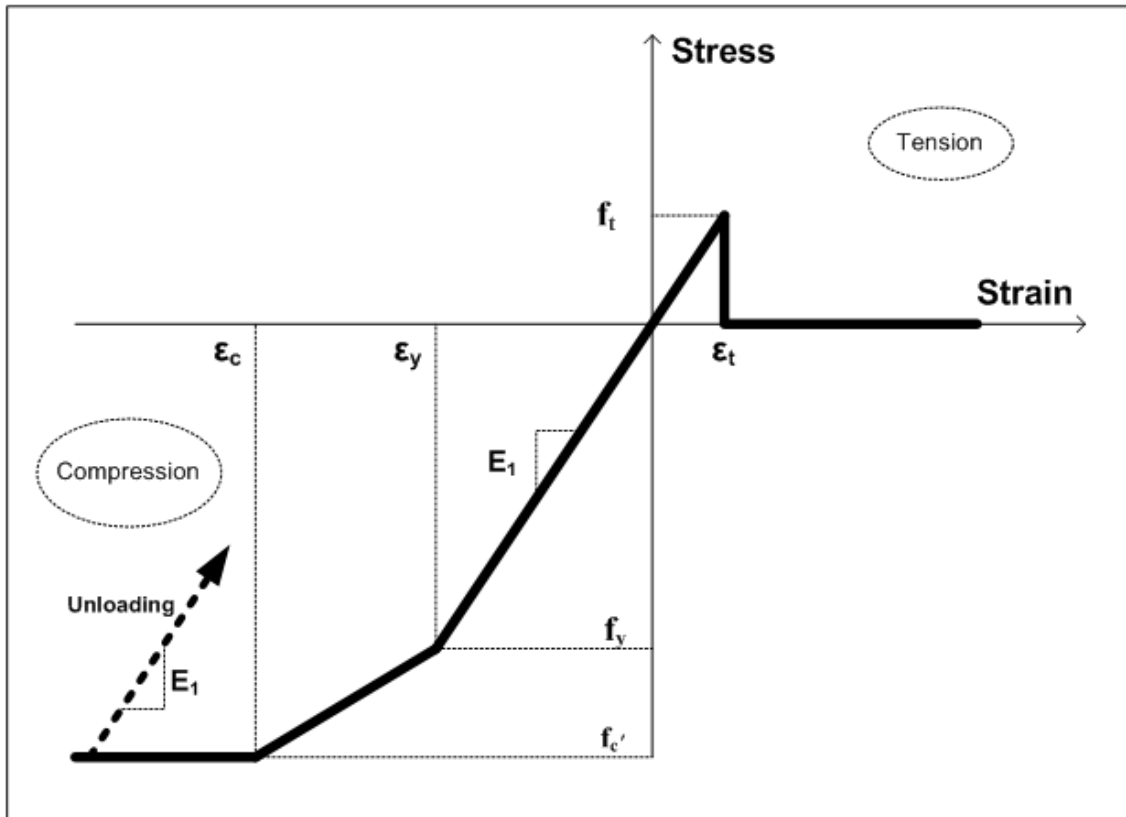
L_s = characteristic length for crack spacing, nominally about 10 inches.

This crack width prediction is useful for fiber-reinforced and plain concrete or when there is no tension steel to drive the Heger-McGrath or Gergely-Lutz crack width predictions.

2.3.3 Nonlinear model for reinforced concrete

Concrete model. The concrete constitutive model was originally developed in References 3 and 17. As shown in Figure 2.3.3-1, the model for plain concrete is a tri-linear curve in compression and an abrupt tension rupture at initial tension cracking.

Figure 2.3.3-1 Concrete stress-strain model and parameters.



Primary model input parameters are defined below along with typical values shown in parenthesis

ϵ_t = concrete strain at initial tensile cracking (0.0001 in/in)

ϵ_y = concrete strain at initial elastic limit in compression (0.0006 in/in)

ϵ_c = concrete strain at onset of unconfined compressive strength (0.002 in/in)

f'_c = unconfined compressive strength of concrete (4,000 psi)

E_1 = Young's modulus of concrete in linear zone (3,800,000 psi)

Using the above input variables, three additional parameters are derived as follows:

$E_2 = (f'_c - E_1 \epsilon_y) / (\epsilon'_c - \epsilon_y)$ = Young's modulus in compression yielding zone

$f_{yc} = E_1 \epsilon_y$ = compressive stress at initial yielding (2,000 psi)

$f_t = E_1 \epsilon_t$ = tensile strength at initial cracking and rupture (380 psi)

The following material constants are used for plane strain conditions:

$E_c = E_1 / (1 - \nu_c^2)$ = effective plane strain modulus of concrete in elastic zone

ν_c = Poisson ratio for concrete

$r = E_2/E_1 =$ ratio of compression yielding modulus to initial modulus

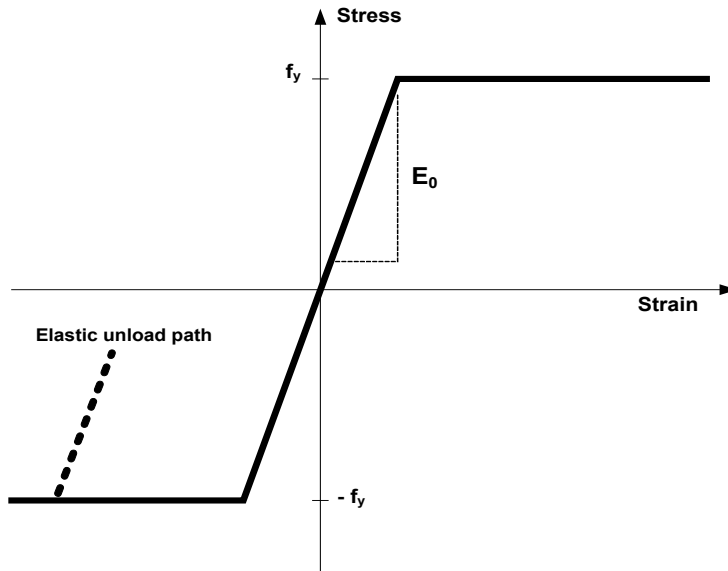
$r E_c =$ effective plane strain modulus for compression yielding zone.

The above model has the following behavior characteristics. In tension, the concrete is linear until the initial tensile strain exceeds the cracking strain limit ϵ_t . When cracking occurs, the tensile stress becomes abruptly zero (redistributed to non-cracked portions of concrete). Once a point in the cross section is cracked, the crack is assumed not to heal so that there is no future tensile strength. Thus, after initial cracking, the tensile strength parameter f_t is set to zero for all subsequent reloading in tension.

For initial compression loading, the concrete behaves linearly until the stress level reaches the initial yield strength f_{yc} after which plastic hardening begins to occur in the yield zone. Perfect plasticity occurs when the stress level reaches compressive strength f_c' . Unloading is elastic and with permanent plastic strain, and reloading is elastic until the stress reaches its previous maximum value after which it follows the original stress-strain curve.

Steel model. The assumed stress-strain behavior for reinforcing steel is shown in Figure 2.3.3-2.

Figure 2.3.3-2 Stress-strain model for reinforcing steel.



Steel behavior is assumed to be elastic-perfectly plastic defined by the input variables:

$E_0 =$ Young's modulus for steel

$f_y =$ steel yield strength

Behavior in compression and tension is identical so that material is elastic whenever the stress magnitude is less than the yield strength. Non-hardening plastic flow occurs when the stress attempts to exceed the yield strength. Unloading from the plastic range is elastic and results in permanent plastic strains.

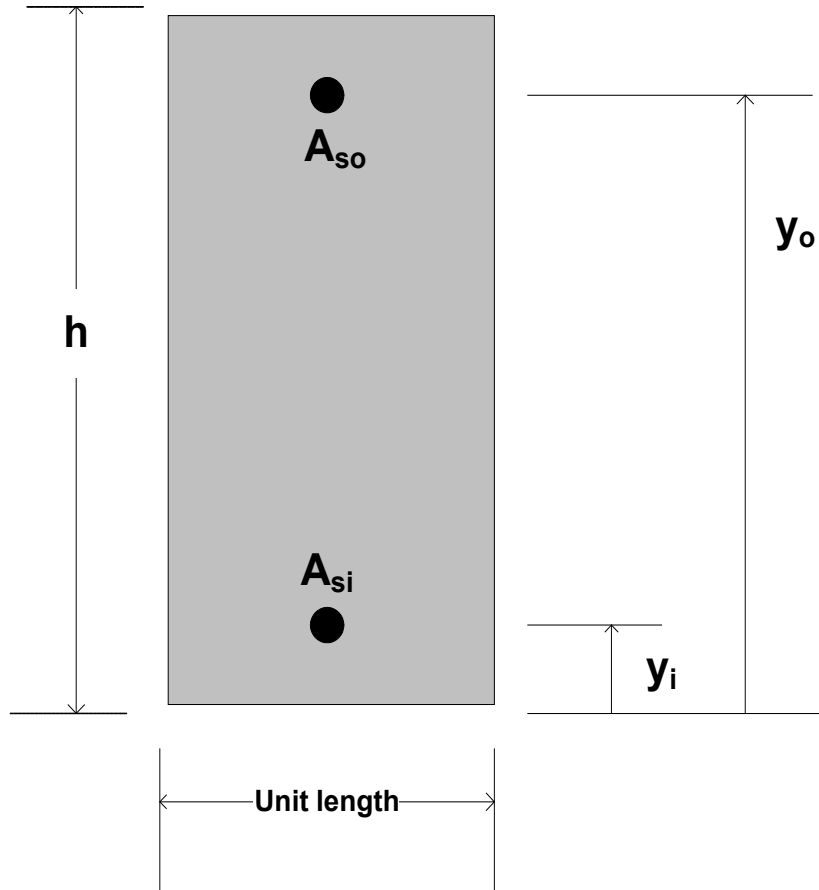
For the purposes of a plane-strain formulation, the steel modulus is denoted as;

$E_s = E_0/(1-\nu_s^2) =$ effective plane-strain modulus of steel

$\nu_s =$ Poisson ratio for steel

Section geometry. Figure 2.3.3-3 shows a unit width of concrete wall with steel reinforcement located near the inner face (bottom) and the outer face (top).

Figure 2.3.3-3 Section geometry of reinforced concrete wall



Geometric measures of the reinforced concrete section are defined below:

h = concrete wall thickness

A_{si} = area of steel for inner cage per unit length of wall

A_{so} = area of steel for outer cage per unit length of wall

y_i = distance to centroid of A_{si} from bottom face

y_o = distance to centroid of A_{so} from bottom face

The uncracked, transformed, elastic section properties are computed as,

$$EA^* = E_c (h + (n-1)(A_{si} + A_{so})) \quad \text{Equation 2.3.3-1}$$

$$y^* = (h^2/2 + (n-1)(y_i A_{si} + y_o A_{so})) / A^* \quad \text{Equation 2.3.3-2}$$

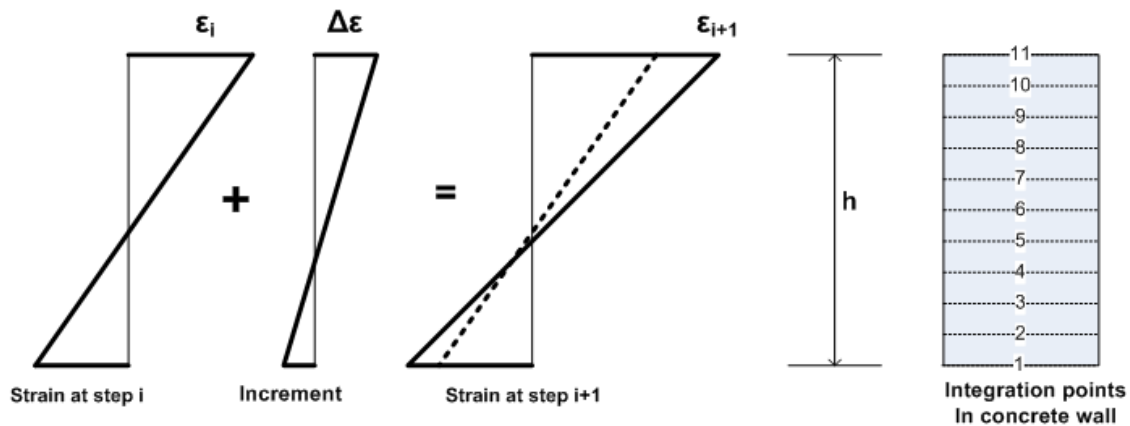
$$EI^* = E_c [h^3/12 + h(h/2 - y^*)^2 + (n-1)(A_{si}(y_i - y^*)^2 + A_{so}(y_o - y^*)^2)] \quad \text{Equation 2.3.3-3}$$

where, $n = E_s/E_c =$ ratio of steel modulus to concrete modulus (transform method).

The uncracked, transformed elastic section properties are used for the first iteration of the first load step to obtain a trial solution. If the loading does not cause cracking, concrete yielding or steel yielding, then the section properties as currently computed are correct, and the next load step is considered. More generally however, nonlinear responses are observed and iteration within the load step is required to obtain the solution as described next.

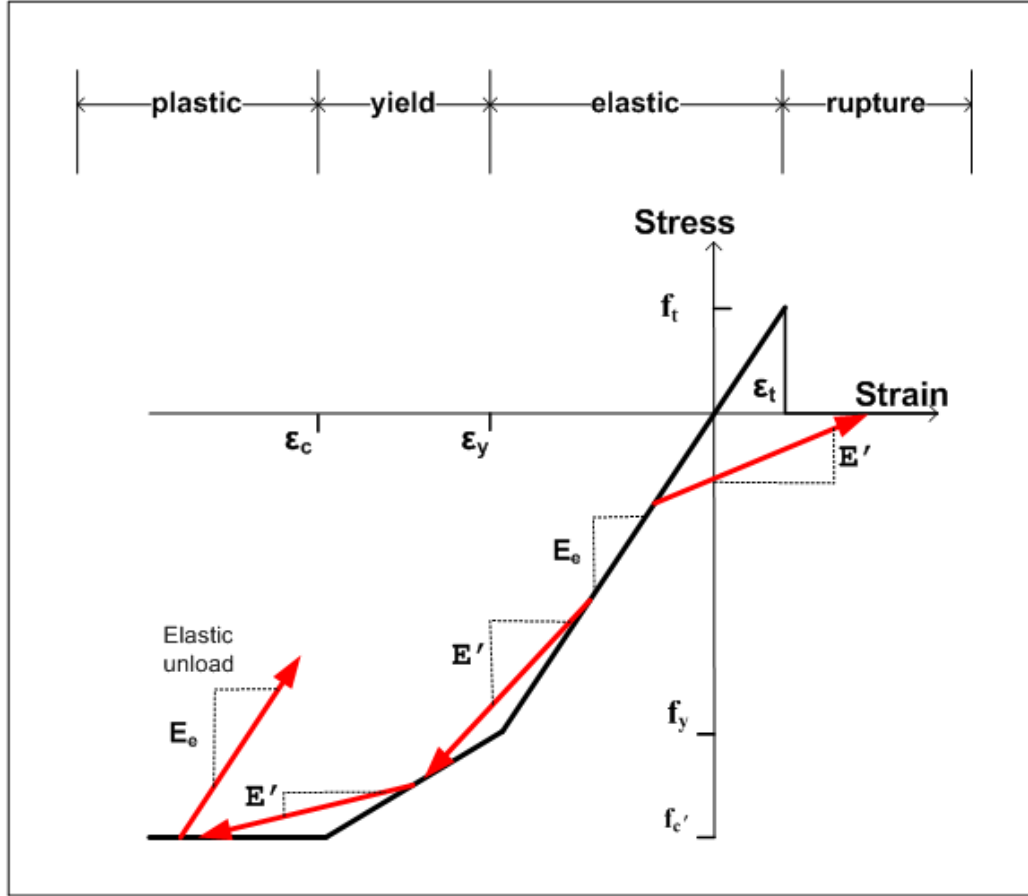
Nonlinear Strategy. We assume we have a converged solution at load step i and we seek an incremental solution for load step $i + 1$. Using the values of EA^* , y^* and EI^* from the previous load step, a trial solution is obtained for the first iteration thereby providing new estimates of the strain distribution at each reinforced concrete cross-section. To compute the next estimate for EA^* , y^* and EI^* , numerical integration is used over the concrete wall section to cope with nonlinear chord modulus as illustrated in the figure below.

Figure 2.3.3-4 Strain profile from step i to $i+1$ and 11-point Simpson integration



Concrete chord modulus. The effective chord modulus, E' , from the known stress-strain state (σ_i, ϵ_i) to the estimated stress-strain state $(\sigma_{i+1}, \epsilon_{i+1})$ is computed at each integration point using the concrete stress-strain curve as indicated in Figure 2.3.3-5 and quantified in Table 2.3.3-1.

Figure 2.3.3-5 Illustration of concrete chord moduli from σ_i, ϵ_i to $\sigma_{i+1}, \epsilon_{i+1}$



The above figure implies the chord modulus, E' , connects the known starting point (σ_i, ϵ_i) to the estimated end point $(\sigma_{i+1}, \epsilon_{i+1})$ where ϵ_{i+1} is obtained from the trial solution and σ_{i+1} is the corresponding stress determined from the stress-strain relationship as quantified in the table below.

Table 2.3.3-1. Concrete chord modulus and modulus ratio for specified starting and ending zones.

Starting Zone ϵ_i	Ending Zone ϵ_{i+1}	Corresponding Stress	Chord modulus E'	Modulus ratio $F'(y) = E'/E_c$
elastic	elastic	σ_{i+1}	E_c	1.0
elastic	yield	$\sigma_i + rE_c(\epsilon_{i+1} - \epsilon_y)$	$rE_c(\epsilon_{i+1} - \epsilon_y) / \Delta\epsilon$	< 1.0
elastic	plastic	f'_c	$(f'_c - \sigma_i) / \Delta\epsilon$	< 1.0
yield	yield	$\sigma_i + rE_c\Delta\epsilon$	rE_c	r
yield	plastic	f'_c	$(f'_c - \sigma_i) / \Delta\epsilon$	< 1.0
plastic	plastic	f'_c	0.0	0.0
any compress zone	unloading	$\sigma_i + E_c\Delta\epsilon$	E_c	1.0
elastic	rupture	0.0	$-\sigma_i / \Delta\epsilon$	< 1.0
rupture	rupture	0.0	0.0	0.0

In the above table, the concrete-modulus ratio is defined as the chord modulus divided by the initial elastic modulus, $F'(y) = E'/E_c$. Thus, F' varies through the cross-section in the range, $0 \leq F'(y) \leq 1$.

Elastic unloading occurs from any compression zone whenever $|\varepsilon_{i+1}| < |\varepsilon_i|$ with the provision that neither strain is in the rupture zone.

For the case when the starting strain is tensile but not yet at initial crack strength, $0 < \varepsilon_i < \varepsilon_t$, and the ending strain is in the rupture zone causing initial concrete cracking, we set $E' = 0$ (instead of a negative softening modulus) and the pre-existing tensile stress is distributed to the uncracked portion of the cross section by adjusting the thrust and moment increment to compensate for the loss of stress at the cracked location. Once a point in the cross section is cracked the tensile strength is set to zero for all future loading conditions implying the crack does not heal. Crack depth is directly predicted from the concrete model.

The above algorithm requires maintaining data records at each integration point to keep track of the cracking history as well as the maximum compressive stress encountered during the loading schedule to properly simulate unloading and reloading.

Steel chord modulus. Reinforcing steel is lumped at the inner and outer cage locations, measured by y_i and y_o . The chord modulus for steel at either location is easily deduced from the elastic-plastic relationship as shown in the following table.

Table 2.3.3-2. Steel chord modulus and modulus ratio for specified starting and ending zones.

Starting Zone ε_i	Ending Zone ε_{i+1}	Corresponding Stress σ_{i+1}	Chord modulus E_s'	Modulus ratio $W' = E_s' / E_s$
elastic	elastic	$\sigma_i + E_s \Delta \varepsilon$	E_s	1.0
elastic	plastic	f_y	$(f_y - \sigma_i) / \Delta \varepsilon$	< 1.0
plastic	plastic	f_y	0.0	0.0
unloading	elastic	$\sigma_i + E_s \Delta \varepsilon$	E_c	1.0

In the above table, the steel-modulus ratio is defined as the chord modulus divided by the initial elastic steel modulus, $W' = E_s' / E_s$, where the ratio is in the range, $0 \leq W' \leq 1$.

To summarize, the relationships for chord moduli of concrete and steel are listed below:

$$E'(y) = E_c F'(y) = \text{concrete chord modulus at location } y \text{ in cross section} \quad \text{Equation 2.3.3-4}$$

$$E'_{si} = E_s W'_i = \text{steel chord modulus at inner cage location, } y_i. \quad \text{Equation 2.3.3-5}$$

$$E'_{so} = E_s W'_o = \text{steel chord modulus at outer cage location, } y_o. \quad \text{Equation 2.3.3-6}$$

Re-expressing the steel chord moduli with concrete-transform parameters, we have

$$E'_{si} = n_i E_c W'_i \quad \text{Equation 2.3.3-7}$$

$$E'_{so} = n_o E_c W'_o \quad \text{Equation 2.3.3-8}$$

where, $n_i, n_o = E_s / E_c - 1$, if concrete is not cracked around the steel

$$n_i, n_o = E_s / E_c, \quad \text{if concrete is cracked around the steel}$$

The transform method expresses the elastic steel modulus as a multiple “n” of the concrete elastic modulus with the understanding that the uncracked concrete area needs to be reduced by the steel area. On the other hand, if the concrete is already cracked then further reduction of concrete area by the steel area is not required.

Key section properties. The equations for the key section properties are expressed in transformed parameters as:

$$EA^* = E_c \left(\int_0^h F'(y) dy + n_i W'_i A_{si} + n_o W'_o A_{so} \right) \quad \text{Equation 2.3.3-9}$$

$$y^* = \left(\int_0^h F'(y)y dy + n_i W_i A_{si} y_i + n_o W_o A_{so} y_o \right) / A^* \quad \text{Equation 2.3.3-10}$$

$$EI^* = E_c \left(\int_0^h F'(y)(y-y^*)^2 dy + n_i W_i A_{si} (y_i - y^*)^2 + n_o W_o A_{so} (y_o - y^*)^2 \right) \quad \text{Equation 2.3.3-11}$$

The integrals over the concrete wall thickness are achieved with 11-point Simpson integration to evaluate the following three sums where $F'(y_i)$ is the concrete modulus ratio at integration point i .

$$S_1 = \int_0^h F'(y) dy = (h/30)[F'(y_1) + 4F'(y_2) + 2F'(y_3) + \dots + F'(y_{11})] \quad \text{Equation 2.3.3-12}$$

$$S_2 = \int_0^h F'(y)y dy = (h/30)[F'(y_1)y_1 + 4F'(y_2)y_2 + 2F'(y_3)y_3 + \dots + F'(y_{11})y_{11}] \quad \text{Equation 2.3.3-13}$$

$$S_3 = \int_0^h F'(y)y^2 dy = (h/30)[F'(y_1)y_1^2 + 4F'(y_2)y_2^2 + 2F'(y_3)y_3^2 + \dots + F'(y_{11})y_{11}^2] \quad \text{Equation 2.3.3-14}$$

Using the above integration results, the final results for the key section properties are expressed as,

$$EA^* = E_c (S_1 + n_i W_i A_{si} + n_o W_o A_{so}) \quad \text{Equation 2.3.3-15}$$

$$y^* = (S_2 + n_i W_i A_{si} y_i + n_o W_o A_{so} y_o) / A^* \quad \text{Equation 2.3.3-16}$$

$$EI^* = E_c (y^{*2} S_1 - 2y^* S_2 + S_3 + n_i W_i A_{si} (y_i - y^*)^2 + n_o W_o A_{so} (y_o - y^*)^2) \quad \text{Equation 2.3.3-17}$$

Iterations with in the load step continue until successive calculations for EA^* , y^* and EI^* are within 1% relative error for all cross section.

2.4 Thermoplastic Pipe

2.4.1 Overview of thermoplastic pipe type

Thermoplastic materials include high-density polyethylene (HDPE), polyvinyl chloride (PVC) and polypropylene (PP). CANDE-2022 provides three options to characterize the wall sections for thermoplastic pipe: smooth, general or profile. Smooth refers to a uniform wall (gun barrel) whose cross-section properties are completely defined by the wall thickness. General refers to an arbitrary property described generically by the wall's area and moment of inertia per unit length. Profile refers to the majority of manufactured plastic pipe whose wall section properties are characterized by the geometry of profile elements including web, valley, crest, liner, and link elements.

Material properties are assumed linear elastic with default values provided for high-density polyethylene, polyvinyl chloride and polypropylene for both short-term and long-term loading conditions. Short-term properties are generally used when vehicular loading is dominant and long-term properties are used when earth loading is dominant. A nonlinear local buckling algorithm is provided for the profile option wherein the profile's section properties are reduced in proportion to the amount of compressive strain computed in the sub elements due to local buckling.

2.4.2 Design criteria for thermoplastic pipe

Design criteria for thermoplastic pipes include strength limits for thrust stress against material failure in hoop compression and global buckling. Another strength state is a limit on the maximum outer fiber combined strain (hoop plus bending strain). Performance limit states include allowable vertical deflection and maximum allowable tensile strain, dependent on type of plastic. The design criteria are summarized in the following table.

Table 2.4.2-1 Thermoplastic Design Criteria.

Design Criterion (Strength limits)	Demand	Capacity
(1) Thrust stress (psi)	$\sigma_{\max} = N_{\max} / A$	$f_u = \text{ultimate strength}$
(2) Global Buckling (psi)	$\sigma_{\max} = N_{\max} / A$	$f_b = \text{buckling capacity}$
(3) Combined strain (in/in)	$\epsilon_{\max} = \text{bending} + \text{thrust}$	$\epsilon_{\text{ult}} = \text{ultimate strain}$
(Performance Limits) (At Service Load)		
(4) Allowable tensile strain	$\epsilon_{t-\max} = \text{max tensile strain}$	$\epsilon_{t-\text{allow}} = \text{allowable tensile strain}$
(5) Allowable deflection *(%)	$\Delta_{\max} = \text{computed deflect \%}$	Allowable = 5% (recommended)

The above design criteria are equally applicable to working stress or LRFD design methodologies. For the working stress approach, the demand and the capacity quantities are unfactored, and the design evaluation is given by safety factors defined as capacity divided by demand. Typically, safety factors on the order of 2.0 are desirable for strength-related criteria. For the LRFD approach the demand and the capacity quantities are factored (see Chapter 6), and the design evaluation is given by ratios of factored demand-to-factored capacity. Ratios less than or equal to 1.0 are acceptably safe. Further discussion on the design criteria is provided below.

1. *Thrust stress.* Thrust-stress demand is computed by the dividing the maximum thrust force in the culvert by the cross-sectional area. The ultimate strength for thrust stress is dependent on the type plastic and the load duration. Nominal values, taken from the ASSHTO LRFD specifications and elsewhere, are shown in the table below.

Table 2.4.2-2 Recommended plastic properties for short and long-term loading

Type of plastic	Effective Young's Modulus (PE)		Ultimate strength (PU)	
	Short-term (ksi)	Long-term (ksi)	Short-term (ksi)	Long-term (ksi)
HDPE –	110.0	22.0	3.00	0.90
PVC –	400.0	140.0	6.00	2.60
PP –	135.0	27.0	3.10	1.00

2. **Global buckling.** The thrust stress level that causes global buckling may be conservatively approximated from the simplified AASHTO LRFD equations 12.7.2.4-1-2. A more accurate alternative is to utilize the new large deformation formulation with buckling capacity prediction available in CANDE-2022 (see Chapter 5).
3. **Combined strain.** Combined strain means the maximum outer-fiber strain from thrust and bending and the demand is the largest combined strain anywhere in the culvert. The combined strain limit value (or capacity) as recommended by AASHTO LRFD specifications is equal to 1.5 times the long-term strength divided by the long-term modulus. Accordingly, HDPE = 0.06 in/in, PVC = 0.028 in/in. and PP = 0.045 in/in.
4. **Allowable tensile strain.** This criterion is intended to preclude cracking and crazing under service load due the maximum outer-fiber tensile strain. The allowable tensile strain as recommended by AASHTO LRFD specifications is 0.05 in/in for HDPE and 0.035 or 0.05 in/in for PVC depending on cell class.
5. **Allowable deflection.** Computed deflection is the relative vertical movement between the top and bottom of the culvert structure, and the percent deflection is relative the vertical distance. The service load value for allowable deflection is generally taken as 5% of the diameter for all plastic pipes; however, the deflection limit is not directly specified in the AASHTO LRFD design specifications.

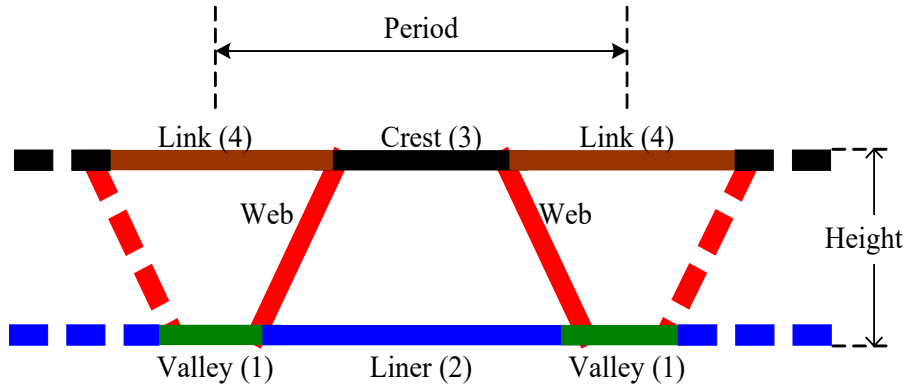
Local Buckling. Local buckling is not a direct design criterion for plastic pipe, but it does influence the demands and capacities of the design criteria listed above. Similar to corrugated metal pipe wherein some amount of outer fiber yielding is permitted, some amount of local buckling is permitted in plastic profile pipe. The nonlinear model to account for local buckling in profile plastic pipe is presented next.

2.4.3 Nonlinear model for local buckling in profile plastic pipe

Although the stress-strain models for all thermoplastic pipe materials are assumed linear and characterized by the elastic moduli in the above table, local buckling is a nonlinear phenomenon. Local buckling is caused by compressive strains that induce the elements of profile wall pipe to deform out-of-plane in a wrinkled pattern. Section 12.12.3.5.3 of AASHTO LRFD specifications provides a methodology to simulate the effect of local buckling by reducing the effective area of the profile elements dependent upon the average level of compressive strain in each element. This AASHTO methodology is incorporated into CANDE-2022 as described below.

The geometry of the profile wall is defined with two web elements and up to four horizontal elements (valley, liner, crest and link) as shown in the figure below. Older versions of CANDE assumed the profile configuration was constant for the entire pipe group; however, the newer versions permit varying the profile geometric properties within the pipe group.

Figure 2.4.3-1 Profile wall geometry and sub elements



The web element lengths, which form a mirror symmetric pair within each period, are defined to span the distance between the valley and crest element so that the web elements offer support to the ends of the crest and valley elements. Hence, the defined length of the crest element is the unsupported span between the web supports plus the length of the web supports, taken as twice the web thickness. Similarly, the defined length of the valley element is twice the web thickness plus the unsupported valley span between the web supports. The defined length of the liner element is the horizontal distance between two valley elements so that the liner’s defined length and unsupported length are identical. Similarly, the defined length of the link element is the horizontal distance between two crest elements so that the crest’s defined length and unsupported length are identical.

Given the defined lengths and thicknesses of all elements, the angle of the web elements, and the overall height of the profile wall, it is a straightforward matter to calculate the initial section properties of the profile wall. The area per unit length, A^* , is equal to the sum of all element areas (lengths multiplied by thickness) divided by the period length. The wall centroid, y^* , is the first area moment taken about the bottom fiber divided by the area. And finally, the moment inertia per unit length, I^* , is the second area moment taken about y^* divided by the period length. Thus, in the absence of local buckling, the beam-column section properties are initially known for the first iteration of the first load step to provide the first trial solution.

The AASHTO LRFD methodology, which accounts for local buckling by reducing the effective length of the elements due to compressive strain, is achieved by using the following two equations.

$$\lambda = (w/t)\sqrt{(\varepsilon/k)} > 0.673 \quad \text{Equation 2.4-1}$$

where, λ = measure of propensity to buckle, called slenderness ratio
 w = unsupported length of element
 t = thickness of element
 ε = average compressive strain in element
 k = edge support coefficient (typically taken as 4.0 for fix-ended elements)

$$\rho = (1/\lambda)(1 - 0.22/\lambda) < 1.0 \quad \text{Equation 2.4-2}$$

where, ρ = reduction factor applied to w
 ρw = remaining unsupported length of element

Each profile element (web, valley, liner, crest and link) is evaluated with above equations. Equation 2.4-1 is evaluated to compute λ using the predicted compressive strain at each element’s centroid as determined from the trial solution. If $\lambda <$

0.673, then the compressive strain is not large enough to trigger local buckling for the element under consideration so that ρ remains = 1. Otherwise, if $\lambda > 0.673$, we evaluate Equation 2.4.2 producing a value for ρ less than 1.0 wherein ρ is the fraction of the element's unsupported length that remains effective in the cross section. Note that the total effective length for the crest and valley elements also includes the web support thicknesses. The element length measures are clarified in the table below:

Table 2.4.3-1 Local buckling profile dimensions

Element length measures	Symbol	Derivation	Description
Defined length	L	Defined by user (input)	The actual length of the element
Unsupported length	w	$w = L$, (for web, liner and link) $w = L - 2t_{web}$, (for crest & valley)	The free distance between supports where buckling can occur
Effective length	L_{eff}	$L_{eff} = \rho L$, (for web, liner and link) $L_{eff} = \rho w + 2t_{web}$, (for crest & valley)	The effective remaining length of element after local buckling

Since the central portion of each element is the most prone to local buckling damage, we assume the original element length has effective gap length equal to $L - L_{eff}$ located in the central portion of the element. This assumption is needed to compute the effective moment of inertia.

Once the effective lengths of the elements have been determined and the location of the gaps understood, it is, once again, a straightforward matter to calculate the new section properties for the next trial solution as;

- $A^* =$ Sum of all effective element areas (effective lengths times thicknesses)
- $y^* =$ Centroid of A^* measured from bottom fiber
- $I^* =$ Sum of all effective element moment of inertias about y^*

The above process dovetails with the general nonlinear solution strategy described in Section 2.19 by forming EA^* and EI^* where E is the appropriate linear elastic modulus (Table 2.4.2-2). When two successive trial solutions produce the same compressive strain values within a 0.1% tolerance level for all elements at all nodes, the load step is said to converge and we proceed to the next load step.

2.5 Basic Pipe Type

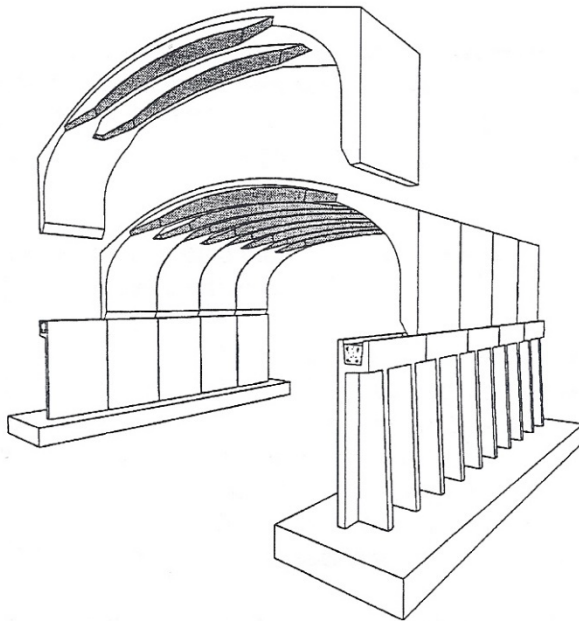
The so-called basic pipe-type is not associated with any particular pipe material. Therefore, it is restricted to linear material behavior, and it is not associated with any design criteria for evaluating its safety or performance. The material model is defined by an elastic Young's modulus and Poisson's ratio, and the cross-sectional properties are defined an area and moment of inertia.

If desired, each element in the basic pipe-type group may be assigned different elastic and cross-sectional properties, and the element group has the option to include large deformation theory and buckling capacity predictions. In addition to academic studies, the basic pipe-type groups are useful for modeling struts and braces and discrete reinforcement in the soil mass.

Lastly, if it is desired to use only continuum elements without beam-column elements in particular problem in the CANDE-2022 program, the basic pipe type is declared in the input with zero elements assigned to the group.

2.6 Conrib Pipe Type

The figure below represents one example of the potential use of the CONRIB pipe type for modeling precast arch units with ribbed stiffeners along the crown as well as T-shaped stiffeners cast into the supporting pedestal walls. These ribbed and/or T-shaped stiffeners cannot be modeled with the standard CONCRETE pipe type. Another special feature of the CONRIB pipe type is an advanced concrete constitutive model that is capable of simulating fiber reinforced concrete in addition to standard concrete with traditional steel reinforcement.



This section provides a detailed formulation of the CONRIB pipe type using the same presentation outline that is used for all other pipe-types in this chapter. The reader is referred to the beginning of Chapter 2 to review the general background development for the beam-column element, which is applicable to all pipe types. Although some of the aspects of the CONRIB model are similar or nearly identical to the CONCRETE pipe type, the following development is self-contained without referring the reader the CONCRETE model write-up. The ultimate goal is to derive the incremental stiffness matrices and nonlinear solution strategy even though some of the derivation is repetitive of the CONCRETE write-up.

2.6.1 Overview of CONRIB Model

Concrete cross sections are composed of a uniform slab and a rib stiffener periodically spaced along the slab. The rib geometry may be specified to form a trapezoid shape, a tee shape, or a smooth wall at the discretion of the user. One cage of reinforcing steel may be specified for the rib and another for the slab. Reinforcing steel behavior is characterized by an elastic-plastic stress-strain model, which becomes perfectly plastic when the steel yield stress is reached in tension or compression.

The concrete stress model is nonlinear in compression, simulated with a tri-linear stress-strain curve. Initially, the concrete response is linear up to a specified strain level after which the concrete exhibits plastic-hardening behavior. When the compressive stress reaches the ultimate strength limit (f_c'), the stress-strain response becomes perfectly plastic with no increase in stress as compressive strain increases.

In tension, concrete behavior is linear up to a specified tensile cracking strain limit. Thereafter tensile stress is released at a rate dependent on another tensile strain parameter called the rupture strain, which introduces some ductility (strain softening) into the tension side of the model. When tensile strain exceeds the rupture strain, all tensile stress has been released and the concrete is no longer capable of sustaining any further tensile stress. If the rupture strain is set equal to the initial tensile cracking strain, then the loss of tensile stress occurs abruptly, which is typical of ordinary plain concrete. On the other hand, if the rupture strain is specified much larger than the tensile cracking strain, say by an order of magnitude, the stress loss is gradual and adequately simulates the behavior of concrete mixed with steel fibers.

In summary the CONRIB concrete stress-strain model is identical to the CONCRETE stress-strain model except for the tension ductility range controlled by the rupture strain parameter. The rupture strain parameter allows the CONRIB model to simulate the behavior of fiber reinforced concrete, which cannot be simulated with the CONCRETE model.

2.6.2 Design Criteria for CONRIB Reinforced Concrete.

Design criteria for reinforced concrete culverts remain the same irrespective of which concrete stress-strain model is used, CONRIB or CONCRETE. Specifically, the design criteria include strength limits for yielding of steel reinforcement, crushing of concrete in compression, diagonal cracking due to shear failure, and radial cracking due to curved tension steel (also called bowstringing). Finally, a performance limit on the allowable flexure crack width, typically taken as 0.01 inches, completes the set of design criteria. These design criteria as explicitly listed in Table 2.6.2-1 faithfully represent the intent and, in some cases, improve the clarity of the design criteria as presented in the AASHTO LRFD specifications as explained in Reference 23.

Table 2.6.2-1 Reinforced concrete design criteria (CONRIB and CONCRETE).

Design Criterion (Strength limits)	Demand	Capacity
(1) Steel yielding (psi)	$f_{\max} = \text{max steel stress}$	$f_y = \text{yield strength}$
(2) Concrete crushing (psi)	$\sigma_{\max} = \text{max compression}$	$f'_c = \text{compressive strength}$
(3) Shear failure (lb/in)	$V_{\max} = \text{max shear force}$	$V_{\text{ult}} = \text{concrete shear capacity}$
(4) Radial tension failure (psi)	$t_{\max} = \text{max radial stress}$	$t_{\text{ult}} = \text{ultimate radial strength}$
(Performance Limits) (At Service Load)		
(5) Allowable crack width (in)	$CW_{\max} = \text{max crack width}$	$CW_{\text{Allow}} = \text{allowable (0.01 inch)}$

The above design criteria are equally applicable to working stress or LRFD design methodologies. For the working stress approach, the demand and the capacity quantities are unfactored, and the design evaluation is given by safety factors defined as capacity divided by demand. Typically, safety factors on the order of 2.0 are desirable for strength-related criteria. For the LRFD approach the demand and the capacity quantities are factored and the design evaluation is given by ratios of demand-to-capacity. Demand-to-capacity ratios less than or equal to 1.0 are acceptably safe. Further discussion on the design criteria is provided below.

1. Steel yielding. The maximum steel-stress demand is computed directly from the nonlinear reinforced concrete model. On the capacity side, the steel yield strength is an input or default value, nominally 60,000 psi for deformed bars and 65,000 psi for smooth wire fabric.
2. Concrete crushing. On the demand side, the maximum outer-fiber concrete compressive stress is determined directly from the reinforced concrete model as a result of thrust and compression bending. The ultimate compressive strength or capacity is an input or default value typically in the range of 4000 to 6000 psi.
3. Shear failure. The maximum shear-force demand is computed directly from the beam-column internal forces. Shear-force capacity is the shear force causing diagonal tension failure at a given cross-section. AASHTO LRFD specifications prescribe three different shear-force capacities depending on structural shape and burial depth.
 - For concrete pipes and arches, the shear capacity is specified by V_{\max} = Equations 12.10.4.2.5, which yield variable values for shear capacity dependent on the values for moment, thrust and shear around the culvert wall.
 - For boxes and 3-sided structures with 2 or more feet of soil cover, the shear capacity is specified by V_{\max} = Equations 5.14.5.3-1 wherein the value is dependent on moment and shear (not thrust).
 - For boxes and 3-sided structures with less than 2 feet of soil cover, the shear capacity is specified by equations in Section 5.8.3.3 that, in some cases, depend on the nature of the transverse reinforcement (stirrups).

Clearly there is a need to unify the AASHTO shear-capacity equations because rational mechanics indicates that shear capacity should be a function of the cross-section properties and state of loading, not on the culvert shape or depth of burial. CANDE allows the user to select among the three choices for shear-force capacity, however, Equation 12.10.4.2.5 is considered the best predictor of shear-force capacity because of the large experimental database (Reference 14).

CANDE also provides the option to choose the traditional shear-strength method where shear-strength = $\beta \sqrt{f'_c}$ where β is a specified factor, typically = 2.0.

4. Radial tension failure. On the demand side, the concrete radial tensile stress is caused by tensile forces in curved inner cage reinforcement steel as it tends to straighten out and exerts radial tensile stresses on the interior concrete cover thickness. The phenomenon is sometimes called bow stringing. CANDE predicts the radial tensile stress by dividing the interior cage steel force (maximum tensile force per unit length) by the radius of curvature of the steel cage, i.e., letting A_s = steel area per unit length., we have;

$$t_{\max} = A_s f_{\max} / \text{Radius} \quad \text{Equation 2.6-1}$$

The ultimate radial stress is related to the tension strength of concrete and the structure span. The radial tensile strength capacity is adapted from AASHTO LRFD Equation 12.10.4.2.4c-1. and restated in psi units as:

$$t_{\text{ult}} = 37.92 \sqrt{f'_c / 1000} F_{rt} \quad \text{Equation 2.6-2}$$

where F_{rt} is a scale factor dependent on structure span, specified in the contents of AASHTO LRFD Equation 12.10.4.2.4c-1.

5. Allowable crack width. The allowable crack width at service loading is generally taken as 0.01 inches in accordance with AASHTO LRFD specification 12.10.3. CANDE offers three empirical formulas to predict crack width; the traditional Gergely-Lutz formula (Reference 16), the recently developed Heger-

McGrath formula (modified form from Reference 15), and a simple concrete strain-based formula proposed by Katona.

The Gergely-Lutz and Heger-McGrath equations are similar in form and are driven by the computed tension steel stress when it exceeds f_0 , the threshold stress for initial cracking. Their crack width predictions are concisely stated in the equation below,

$$CW = S(f_s - f_0) > 0 \quad \text{Equation 2.6-3}$$

where, CW = the crack width in inches,
 f_s = computed tension steel stress in psi,
 S and f_0 = model parameters specified in the table below.

Table 2.6.2-2 Crack width model parameters S and f_0

Gergely-Lutz	Heger-McGrath
$S = (0.122 \times 10^{-6}) (2t_b s_1)^{1/3}$ where, t_b = concrete cover thickness (inches) s_1 = spacing between rows of steel (inches).	$S = (0.333 \times 10^{-6}) (t_b s_1 / 2n)^{1/3}$ where, t_b = concrete cover thickness (inches) s_1 = spacing between rows of steel (inches) n = number of steel layers in the tension zone (1 or 2)
$f_0 = 5,000.$	$f_0 = 31.6 C_1 (h/d)^2 \sqrt{f'_c} / \rho$ where, $C_1 = 1.0$ for smooth wire, 1.5 for welded wire fabric, and 1.9 for deformed wire/bars. h/d = total concrete thickness –to- effective height (tension steel to other face) ρ = reinforcement area ratio (A_s/h).

The Heger-McGrath prediction is well calibrated for predicting crack widths near 0.01 inches; however, it tends to underestimate the prediction of smaller crack widths. The Gergely-Lutz formula is more accurate in predicting smaller crack widths.

The concrete strain-based crack width prediction is given by,

$$CW = L_S (\epsilon_{\text{tension}} - \epsilon_{\text{crack}}) \quad \text{Equation 2.6-4}$$

where, $\epsilon_{\text{tension}}$ = computed tensile strain in outer fiber of concrete.
 ϵ_{crack} = tensile strain at initial concrete cracking, a concrete model property.
 L_S = characteristic length for crack spacing, nominally about 10 inches.

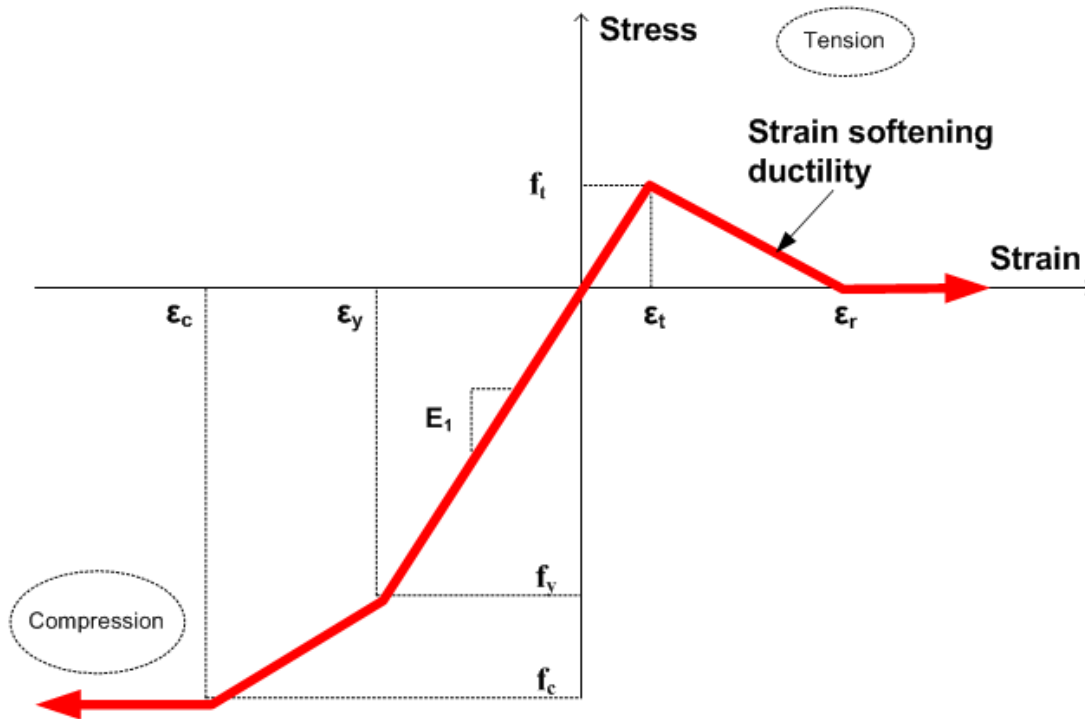
This crack width prediction is useful for fiber-reinforced and plain concrete or when there is no tension steel to drive the Heger-McGrath or Gergely-Lutz crack width predictions.

2.6.3 CONRIB concrete model.

As shown in Figure 2.6.3-1, the CONRIB concrete model is a tri-linear curve in compression exactly the same as the CONCRETE model for plain concrete. In the tension zone, however, the CONRIB model has the capability of simulating varying amounts of ductility depending on the values assigned to the initial cracking strain and rupture strain parameters.

If the rupture strain parameter is set equal to the initial tension cracking strain, then there is no ductility and the CONRIB model behaves like plain concrete with an abrupt loss of all tensile stress once the initial cracking strain is reached. On the other hand, if the rupture strain parameter is assigned a value larger than the initial cracking strain, the model exhibits a ductile behavior with a gradual loss of tensile stress such that the larger the value of the rupture strain the greater the amount of ductility.

Figure 2.6.3-1 Concrete stress-strain model and parameters.



Primary model input parameters are defined below along with typical values shown in parenthesis

- ϵ_c = concrete strain at onset of unconfined compressive strength (0.002 in/in)
- ϵ_y = concrete strain at initial elastic limit in compression (0.0006 in/in)
- ϵ_t = concrete strain at initial tensile cracking (0.0001 in/in)
- ϵ_r = concrete strain at tensile rupture (0.0001 to .01 in/in)
- f_c' = unconfined compressive strength of concrete (4,000 psi)
- E_1 = Young's modulus of concrete in linear zone (3,800,000 psi)

Using the above input variables, four additional parameters are derived as follows:

- $E_2 = (f_c' - E_1 \epsilon_y) / (\epsilon_c' - \epsilon_y)$ = Young's modulus in compression yielding zone
- $f_{yc} = E_1 \epsilon_y$ = compressive stress at initial yielding (2,000 psi)
- $f_t = E_1 \epsilon_t$ = tensile strength at initial cracking and rupture (380 psi)
- $E_3 = -f_t / (\epsilon_r - \epsilon_t)$ = tension-softening modulus (negative)

The following material constants are used for plane strain conditions:

- ν_c = Poisson ratio for concrete

$$E_c = E_1 / (1 - \nu_c^2) = \text{effective plane strain modulus of concrete in elastic zone}$$

$$E_c = E_2 / (1 - \nu^2) = \text{effective plane strain modulus in concrete yield zone}$$

$$E_s = E_3 / (1 - \nu^2) = \text{effective plane strain modulus in ductile softening zone}$$

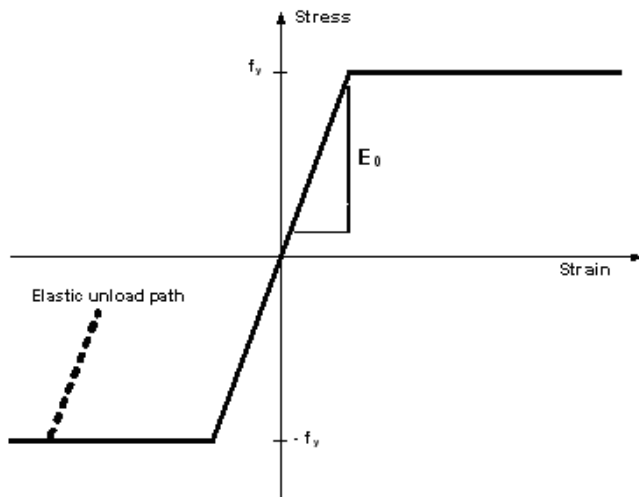
The above model has the following behavior characteristics. For initial compression loading, the concrete behaves linearly until the stress level reaches the initial yield strength f_{yc} after which plastic hardening begins to occur in the yield zone. Perfect plasticity occurs when the stress level reaches compressive strength f_c' . Unloading is elastic and with permanent plastic strain, and reloading is elastic until the stress reaches its previous maximum value after which it follows the original stress-strain curve.

In tension, the concrete is linear until the initial tensile strain exceeds the cracking strain limit ϵ_i . After tensile cracking occurs, the tensile stress is reduced in the softening range at a rate depending on the softening modulus (negative value). Finally, when the strain exceeds the rupture strain all stress is released inferring that all fibers bridging the crack are broken or pulled out. When this occurs, the crack is assumed not to heal so that there is no future tensile strength at this point. However, if the strain is reversed prior to reaching the rupture strain, then the remaining tension stress is preserved and the ductile zone is characterized with a reduced tensile strength for future tensile loading.

2.6.4 Reinforcement steel model

The assumed stress-strain behavior for reinforcing steel is shown in Figure 2.6.4-1.

Figure 2.6.4-1 Stress-strain model for reinforcing steel.



Steel behavior is assumed to be elastic-perfectly plastic defined by the input variables:

$$E_0 = \text{Young's modulus for steel}$$

$$f_y = \text{steel yield strength}$$

Behavior in compression and tension is identical so that material is elastic whenever the stress magnitude is less than the yield strength. Non-hardening plastic flow occurs when the stress attempts to exceed the yield strength. Unloading from the plastic range is elastic and results in permanent plastic strains.

For the purposes of a plane-strain formulation, the steel modulus is denoted as;

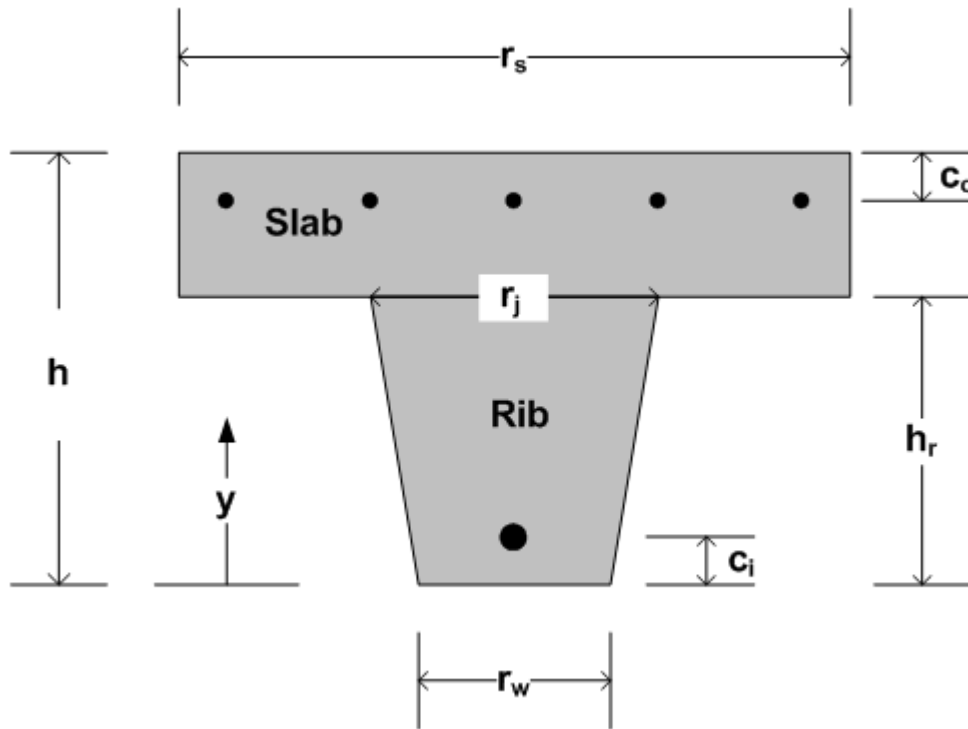
$$E_{st} = E_0 / (1 - \nu_{st}^2) = \text{effective plane-strain modulus of steel}$$

ν_{st} = Poisson ratio for steel

2.6.5 Concrete cross-section geometry

Figure 2.6.5-1 shows one period of concrete rib wall with steel reinforcement located near the inner face (bottom) and the outer face (top). Although not shown, the alternative orientation is with the rib pointing in the outward direction, which is developed in the same manner as the orientation shown below.

Figure 2.6.5-1 Section geometry of reinforced concrete rib wall



Geometric measures of the general concrete rib section are defined below. (Note that a smooth wall section is obtained by setting $r_s = r_w = r_j$.)

- r_s = rib spacing on centers along culvert length
- r_w = rib width at bottom
- r_j = rib width at junction with slab
- h = total concrete wall thickness, rib plus slab
- h_r = concrete rib thickness
- $h_s = h - h_r$ = concrete slab thickness

Steel reinforcement parameters are defined below.

- \tilde{A}_{si} = area of steel in rib divided by actual rib width through steel centroid
- A_{so} = area of steel in slab per unit length of slab
- $y_i = c_i$ = distance to centroid of A_{si} from bottom face
- $y_o = h - c_o$ = distance to centroid of A_{so} from bottom face

Note that for ease of input, the steel area in the rib \tilde{A}_{si} is defined as area per unit length of rib, not per unit length of the period. Therefore, the rib area as input is corrected to the common rib spacing value for computing section properties as follows.

$$A_{si} = (r_c / r_s) \tilde{A}_{si} \quad \text{Equation 2.6.5-1}$$

where, $r_c = r_w + (y_i/h)(r_j - r_w) =$ rib width at level of steel centroid.

With the above understandings, the uncracked, transformed, elastic section properties for area stiffness, neutral axis and bending stiffness are computed as follows.

$$EA^* = E_c \left(h_s + \frac{r_j + r_w}{2r_s} h_r + (n-1)(A_{si} + A_{so}) \right) \quad \text{Equation 2.6.5-2}$$

$$y^* = \left(h_s (h + h_s / 2) + \frac{r_j + r_w}{3r_s} h_r^2 + (n-1)(y_i A_{si} + y_o A_{so}) \right) / A^* \quad \text{Equation 2.6.5-3}$$

$$EI^* = E_c \left[(h^3 - h_r^3) / 3 - y^*(h^2 - h_r^2) + y^{*2}(h - h_r) + \frac{3r_j + r_w}{12r_s} h_r^3 - y^* \frac{2r_j + r_w}{3r_s} h_r^2 + y^{*2} \frac{r_j + r_w}{2r_s} h_r + (n-1)(A_{si}(y_i - y^*)^2 + A_{so}(y_o - y^*)^2) \right] \quad \text{Equation 2.6.5-4}$$

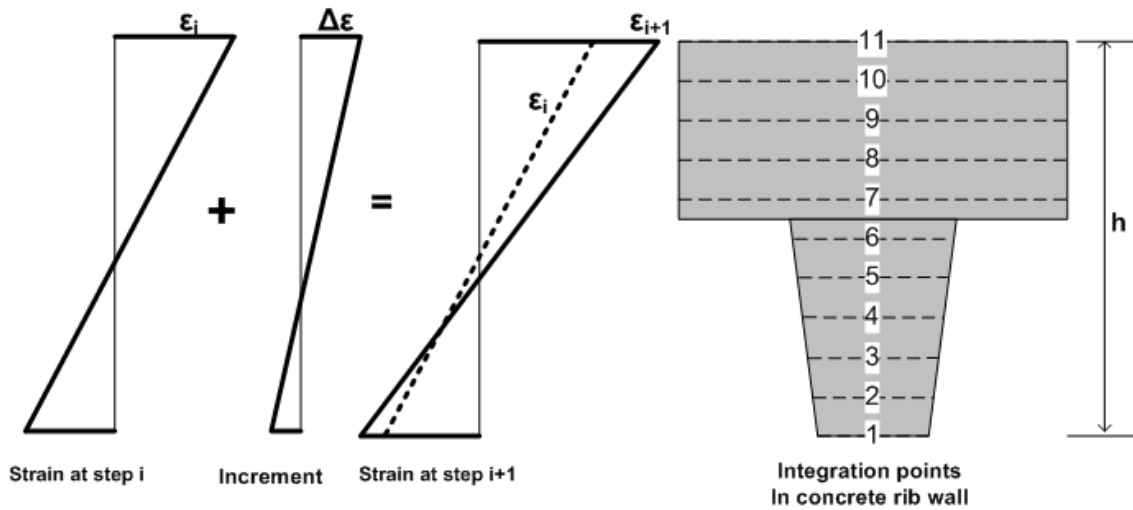
where, $n = E_{st}/E_c =$ ratio of steel modulus to concrete modulus (transform method).

The uncracked, transformed elastic section properties are used for the first iteration of the first load step to obtain a trial solution. If the loading does not cause cracking, concrete yielding or steel yielding, then the section properties as currently computed are correct, and the next load step is considered. More generally however, nonlinear responses are observed and iteration within the load step is required to obtain the solution as described next.

2.6.6 Nonlinear solution strategy.

We assume we have a converged solution at load step i and we seek an incremental solution for load step $i + 1$. Using the values of EA^* , y^* and EI^* from the previous load step, a trial solution is obtained for the first iteration thereby providing new estimates of the strain distribution at each reinforced concrete cross-section. To compute the next estimate for EA^* , y^* and EI^* , numerical integration is used over the concrete wall section to cope with nonlinear chord modulus as illustrated in the figures below.

Figure 2.6.6-1 Strain profile from step i to i+1 and 11-point Simpson integration



Concrete chord modulus. The effective chord modulus, E' , from the known stress-strain state (σ_i, ϵ_i) to the estimated stress-strain state $(\sigma_{i+1}, \epsilon_{i+1})$ is computed at each integration point using the concrete stress-strain curve previously illustrated in Figure 2.6.3-1. As discussed in the following sections, the chord modulus is determined iteratively.

The Figure 2.6.6-2 illustrates various chord moduli, E' , which connects a known starting point (σ_i, ϵ_i) to the estimated end point $(\sigma_{i+1}, \epsilon_{i+1})$. Here, ϵ_{i+1} is obtained from the trial incremental solution, $\epsilon_{i+1} = \epsilon_i + \Delta\epsilon$, and σ_{i+1} is the corresponding stress determined from the stress-strain relationship as quantified in the Table 2.6.6-1.

Figure 2.6.6-2 Illustration of concrete chord moduli in zone transitions

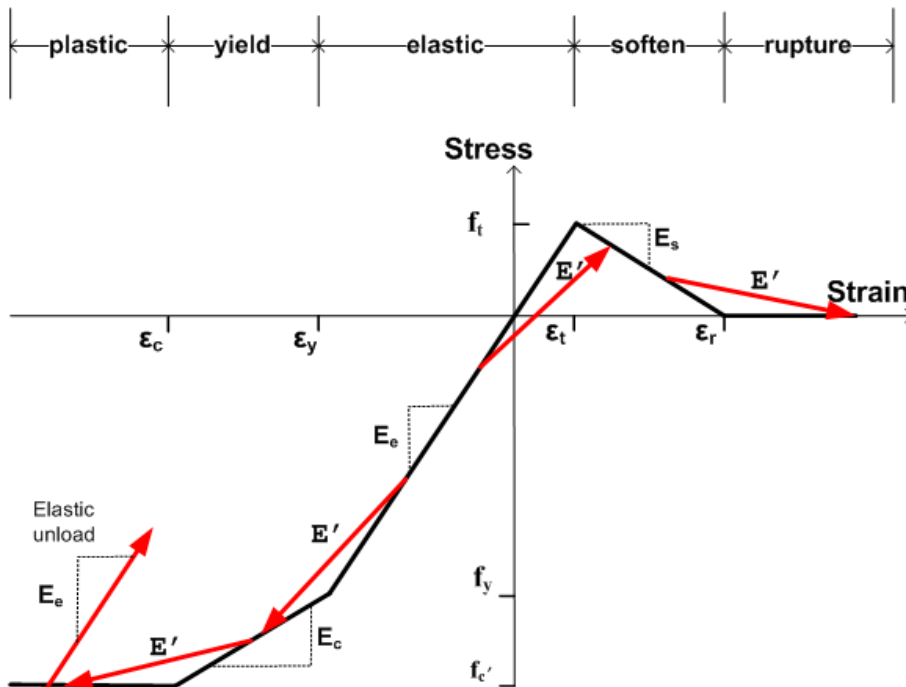


Table 2.6.6-1. Concrete chord modulus and ratio for specified starting and ending zones.

Starting Zone ε_i	Ending Zone ε_{i+1}	Corresponding Stress σ_{i+1}	Chord modulus E'	Modulus ratio $F'(y) = E'/E_c$
elastic	elastic	$\sigma_i + E_c \Delta \varepsilon$	E_c	$= 1.0$
elastic	yield	$f_y + E_c(\varepsilon_{i+1} - \varepsilon_y)$	$(\sigma_{i+1} - \sigma_i) / \Delta \varepsilon$	< 1.0
elastic	plastic	f'_c	$(f'_c - \sigma_i) / \Delta \varepsilon$	< 1.0
yield	more yield	$\sigma_i + E_c \Delta \varepsilon$	E_c	$= E_c / E_c$
yield	plastic	f'_c	$(f'_c - \sigma_i) / \Delta \varepsilon$	$< E_c / E_c$
plastic	more plastic	f'_c	0.0	$= 0.0$
compress zone	unloading	$\sigma_i + E_c \Delta \varepsilon$	E_c	$= 1.0$
elastic	soften	$f_t + E_s(\varepsilon_{i+1} - \varepsilon_t)$	$(\sigma_{i+1} - \sigma_i) / \Delta \varepsilon$	< 1.0
soften	more soften	$\sigma_i + E_s \Delta \varepsilon$	E_s	< 0.0
soften	rupture	0.0	$-\sigma_i / \Delta \varepsilon$	< 0.0
rupture	more rupture	0.0	0.0	$= 0.0$

In the above table, the concrete-modulus ratio is defined as the chord modulus divided by the initial elastic modulus, $F'(y) = E'/E_c$. Thus, $F'(y)$ varies through the cross-section including negative values for integration points in the softening range.

Elastic unloading occurs from any compression zone whenever $|\varepsilon_{i+1}| < |\varepsilon_i|$ with the provision that neither strain is in the softening or rupture zone.

Once a point in the cross section begins to crack, the initial tensile strength is permanently reduced to the corresponding stress value on the softening leg of the stress-strain curve. Physically this means some tension damage has occurred changing the shape of the stress-strain path in the tension zone. When the tensile strain exceeds the rupture strain, the tension damage is complete and the stress-strain path is completely flat in tension for all future tensile loading conditions, implying the crack does not heal.

The above algorithm requires maintaining data records at each integration point to keep track of the cracking history and tension damage. It is also required to maintain a data record of plastic straining in compression in order to properly simulate unloading and reloading.

Steel chord modulus. Reinforcing steel is lumped at the inner and outer cage locations, measured by y_i and y_o . The chord modulus for steel at either location is easily deduced from the elastic-plastic relationship as shown in the following table.

Table 2.6.6-2. Steel chord modulus and ratio for specified starting and ending zones.

Starting Zone ε_i	Ending Zone ε_{i+1}	Corresponding Stress σ_{i+1}	Chord modulus E'_s	Modulus ratio $W' = E'_s / E_{st}$
elastic	elastic	$\sigma_i + E_{st} \Delta \varepsilon$	E_{st}	1.0
elastic	plastic	f_y	$(f_y - \sigma_i) / \Delta \varepsilon$	< 1.0
plastic	plastic	f_y	0.0	0.0
unloading	elastic	$\sigma_i + E_{st} \Delta \varepsilon$	E_{st}	1.0

In the above table, the steel-modulus ratio is defined as the chord modulus divided by the initial elastic steel modulus, $W' = E'_s / E_{st}$, where the ratio is in the range, $0 \leq W' \leq 1$.

To summarize, the relationships for chord moduli of concrete and steel are listed below:

$$E'(y) = E_c F'(y) = \text{concrete chord modulus at location } y \quad \text{Equation 2.6.6-1}$$

$$E'_{si} = E_{st} W'_i = \text{steel chord modulus at inner cage location, } y_i. \quad \text{Equation 2.6.6-2}$$

$$E'_{so} = E_{st} W'_o = \text{steel chord modulus at outer cage location, } y_o. \quad \text{Equation 2.6.6-3}$$

Re-expressing the steel chord moduli with concrete-transform parameters, we have

$$E'_{si} = n_i E_c W'_i \quad \text{Equation 2.6.6-4}$$

$$E'_{so} = n_o E_c W'_o \quad \text{Equation 2.6.6-5}$$

where, $n_i, n_o = E_{st}/E_c - 1$, if concrete is not cracked around the steel

$$n_i, n_o = E_{st}/E_c, \quad \text{if concrete is cracked around the steel}$$

The transform method expresses the elastic steel modulus as a multiple “n” of the concrete elastic modulus with the understanding that the uncracked concrete area needs to be reduced by the steel area to avoid double counting areas. On the other hand, if the concrete is already cracked then further reduction of concrete area by the steel area is not required.

Computing section properties. Section properties require area integration over the concrete cross section. To this end, the differential area is expressed as $dA = b(y)dy$ where $b(y)$ is the effective cross-section width per unit length as defined below.

$$b(y) = \left\{ \begin{array}{l} 1.0, \text{ if } y \text{ is in the slab zone} \\ (r_w + \frac{y}{h}(r_j - r_w))/r_s, \text{ if } y \text{ is in the rib zone} \end{array} \right\} \quad \text{Equation 2.6.6-6}$$

With the above understanding, the equations for the key section properties are expressed in transformed parameters as follows.

$$EA^* = E_c \left(\int_0^h F'(y)b(y)dy + n_i W_i A_{si} + n_o W_o A_{so} \right) \quad \text{Equation 2.6.6-7}$$

$$y^* = \left(\int_0^h F'(y)yb(y)dy + n_i W_i A_{si} y_i + n_o W_o A_{so} y_o \right) / A^* \quad \text{Equation 2.6.6-8}$$

$$EI^* = E_c \left(\int_0^h F'(y)(y-y^*)^2 b(y)dy + n_i W_i A_{si} (y_i - y^*)^2 + n_o W_o A_{so} (y_o - y^*)^2 \right) \quad \text{Equation 2.6.6-9}$$

The integrals over the concrete wall thickness are achieved with 11-point Simpson integration to evaluate the following three sums where $F'(y_i) \leq 1.0$ is the concrete modulus ratio at integration point i , and $b(y_i) \leq 1.0$ is the effective cross-section width per unit length.

$$S_1 = \int_0^h F'(y)b(y)dy = h/30[F'(y_1)b(y_1)+4F'(y_2)b(y_2)+2F'(y_3)b(y_3)+\dots+F'(y_{11})b(y_{11})] \quad \text{Equation 2.6.6-10}$$

$$S_2 = \int_0^h F'(y)yb(y)dy = h/30[F'(y_1)y_1b(y_1)+4F'(y_2)y_2b(y_2)+2F'(y_3)y_3b(y_3)+\dots+F'(y_{11})y_{11}b(y_{11})] \quad \text{Equation 2.6.6-11}$$

$$S_3 = \int_0^h F'(y)y^2b(y)dy = h/30[F'(y_1)y_1^2b(y_1)+4F'(y_2)y_2^2b(y_2)+2F'(y_3)y_3^2b(y_3)+\dots+F'(y_{11})y_{11}^2b(y_{11})] \quad \text{Equation 2.6.6-12}$$

Using the above integration results, the final results for the key section properties are expressed as,

$$EA^* = E_c(S_1 + n_i W_i A_{si} + n_o W_o A_{so}) \quad \text{Equation 2.6.6-13}$$

$$y^* = (S_2 + n_i W_i A_{si} y_i + n_o W_o A_{so} y_o) / A^* \quad \text{Equation 2.6.6-14}$$

$$EI^* = E_c(y^{*2} S_1 - 2y^* S_2 + S_3 + n_i W_i A_{si} (y_i - y^*)^2 + n_o W_o A_{so} (y_o - y^*)^2) \quad \text{Equation 2.6.6-15}$$

The above calculations are carried out in subroutine Conmax, which is called by subroutine Conrib. Iterations within the load step continue until successive calculations for EA^* , y^* and EI^* are within 1% relative error for all cross sections.

2.6.7 CONRIB Model Behavior and Parameter Identification

When comparing the stress-strain models of plain concrete model with the ductile CONRIB model, it may seem that the load capacities of the two models would be the same if the tensile strength and compressive strength were the same. Indeed, this observation is true for test specimens loaded in pure axial tension or pure axial compression. For these cases, the ultimate axial load is easily computed as recorded below and is independent of ductility parameters.

$$T = f_t A = \text{ultimate tensile load} \quad \text{Equation 2.6.7-1}$$

$$C = f_c' A = \text{ultimate compressive load} \quad \text{Equation 2.6.7-2}$$

where, f_t = tensile strength of concrete

f_c' = compressive strength of concrete

A = cross-sectional area of the test specimen.

However, for a test specimen loaded in pure bending, it is quite remarkable that the ultimate moment capacity of the ductile CONRIB model is appreciably greater than the plain concrete model depending on the value of the ductility strain ratio defined as follows.

$$r = \varepsilon_r / \varepsilon_t = \text{ductility strain ratio } (r \geq 1) \quad \text{Equation 2.6.7-3}$$

where, ε_r = rupture strain

ε_t = initial cracking strain

When the ratio $r = 1$, there is no ductility and the CONRIB model behaves like plain concrete, exhibiting an abrupt loss of the internal moment once the initial cracking moment is reached. However, for $r > 1$, the moment capacity increases with r and exhibits gradual strength loss.

2.6.8 Derivation of moment capacity in pure bending

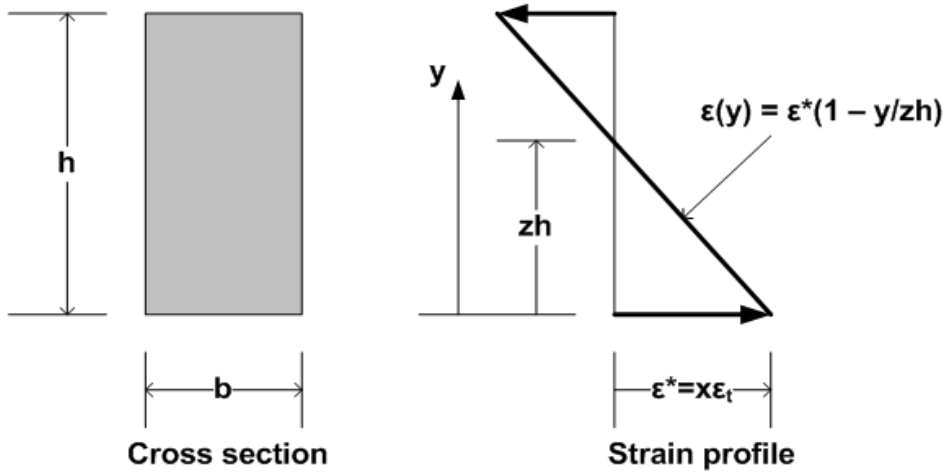
Consider a beam specimen in pure bending with a rectangular cross-section of height h and width b as shown in Figure 2.6.8-1. Because planes remain plane in bending, the strain profile is linear through the height of the cross section for all load levels as shown in the figure. The linear strain profile $\varepsilon(y)$ is completely defined by two points for which we choose the bottom fiber and the neutral axis.

$\varepsilon^* = x\varepsilon_t = \text{specified strain at bottom fiber, } y = 0$

$zh = \text{location of neutral axis at which } \varepsilon(zh) = 0$

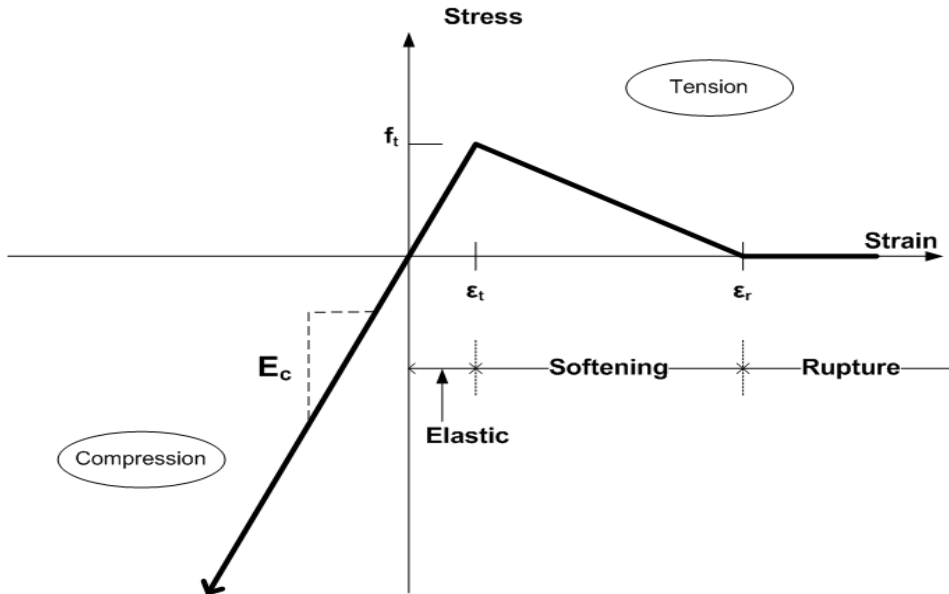
where x = specified multiplier of tensile cracking strain.
 z = fraction of h locating neutral axis.
 y = vertical coordinate, $0 \leq y \leq h$

Figure 2.6.8-1 Linear strain profile over cross section driven by the bottom strain, ϵ^*



At the bottom fiber, the strain is prescribed as $\epsilon(0) = \epsilon^*$ where ϵ^* is quantified by an x -multiplier of the initial cracking strain ($\epsilon^* = x\epsilon_t$). The location of the neutral axis z (as a fraction of h) is dependent on the resulting stress distribution in the cross section such that the net tensile force from 0 to zh is equal to the net compressive force from zh to h . Recall that the tensile stresses are described by the three piecewise linear regions as shown below.

Figure 2.6.8-2 Tension portion of CONRIB model with ductility (fiber reinforcement)



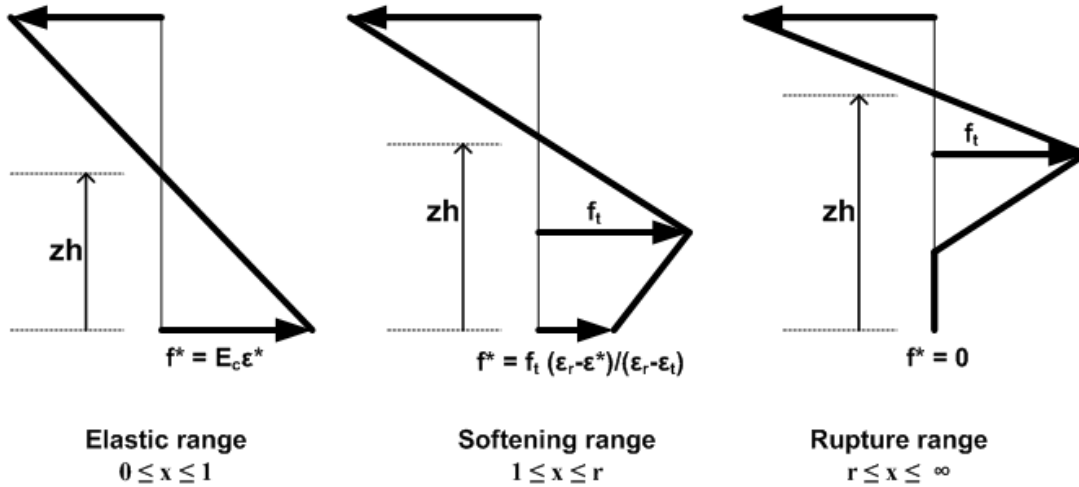
With the above understanding, the applied maximum tensile strain on the bottom fiber ϵ^* is in one of three ranges depending on the magnitude of x .

1. ϵ^* is in the uncracked elastic range, $0 \leq x \leq 1$
2. ϵ^* is in the softening range, $1 \leq x \leq r$

3. ϵ^* exceeds the rupture strain, $r \leq x \leq \infty$

The corresponding stress distributions for these three ranges are illustrated in Figure 2.6.8-3 wherein it is reasonably assumed that maximum compressive stress in the top fiber remains within the elastic range.

Figure 2.6.8-3 Stress distributions corresponding to the three ranges of ϵ^*



Since the stress profiles are due to pure bending, the neutral axis (z-fraction of h) is found by equating the net tensile force to the net compressive force. The center column in Table 2.6.8-1 gives the equation for z as a function of x and r.

Table 2.6.8-1 Neutral axis location and internal moment values as a function of x and r

Range of x-multiplier ($\epsilon^* = x \epsilon_t$)	Neutral axis location (zh)	Internal Moment ($M_t = f_t b h^2 / 6$)
Linear range $0 \leq x \leq 1$	$z = 1/2$	$M = M_t x$
Softening range $1 \leq x \leq r$	$z = ((1+a)^{1/2} - 1)/a$ where, $a = (x-r)/(r-1)/x^2 - 1 + (2r-x-1)/(r-1)/x$	$M = M_t [2(1-z)^3 x / z + z^2 (3r-2x-r/x^2) / (r-1)]$
Rupture range $r \leq x \leq \infty$	$z = 1 / (1 + r^{1/2} / x)$	$M = M_t [2x(1-z)^3 / z + z^2 (r^2 + r) / x^2]$

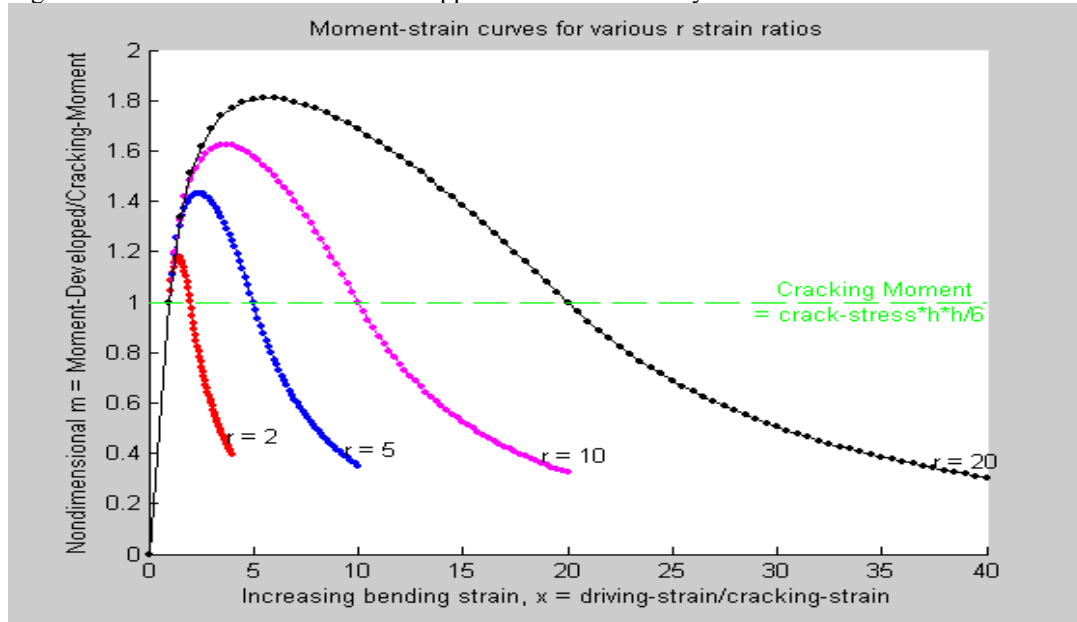
After determining the location of the neutral axis, the internal moment is computed by multiplying the force resultants times the lever-arm distance to the neutral axis. The last column in the above table gives the equation for the resulting moment as a function z, x and r and the initial cracking moment as defined below.

$$M_t = f_t b h^2 / 6 \quad \text{Equation 2.6.8-1}$$

M_t is the moment that causes initial tensile cracking on the bottom fiber when $x = 1$ and is the maximum moment capacity for the case $r = 1$ (plain concrete).

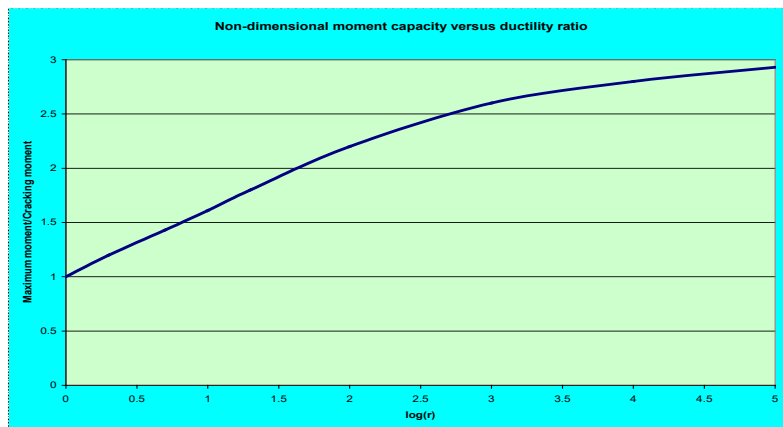
Except for the linear range, the equations for the internal moment do not lend themselves to easy interpretation without graphical aid. Figure 2.6.8-4 shows plots of the non-dimensional moment, $m(x) = M/M_t$, for a family of ratios, $r = 2, 5, 10, \text{ and } 20$. All families trace the same straight line in the linear range $0 \leq x \leq 1$, then diverge into separate bell-shaped curves in the softening range $1 \leq x \leq r$, and asymptotically approach zero in the rupture range, $r \leq x \leq \infty$. It is evident that the peak moment (maximum moment capacity) occurs in the softening range and increases with r . For $r = 20$, it is observed that the moment capacity is 1.8 times that of plain concrete.

Figure 2.6.8-4 Moment ratio versus applied strain for a family of r -values.



The foregoing development illustrates the increase in bending moment capacity is 80% as the ductility strain ratio increases modestly from 1 to 20. For steel fiber reinforced concrete, experimental evidence indicates that r -values can be as high as 500 or more depending on the percentage and type of steel fibers. Figure 2.6.8-5 shows a plot of the non-dimensional moment capacity as a function of $\log(r)$ wherein it is observed that the theoretical limit of moment capacity is $3.0M_t$ as the ratio r approaches infinity.

Figure 2.6.8-5 Maximum moment capacity versus strain ductility ratio r



2.6.9 Model parameter identification

The compression parameters of the CONRIB stress-strain model may be determined from standard load-deformation tests ($P-\Delta$) on cylindrical compression specimens in the same manner as ordinary concrete. Specifically, the compression parameters are determined as follows.

$$f'_c = P_{\max}/A = \text{compressive strength}$$

$$\epsilon_c = \Delta_c/L = \text{strain at initial compressive strength}$$

$$\epsilon_y = \Delta_e/L = \text{strain at initial yield (end of elastic range)}$$

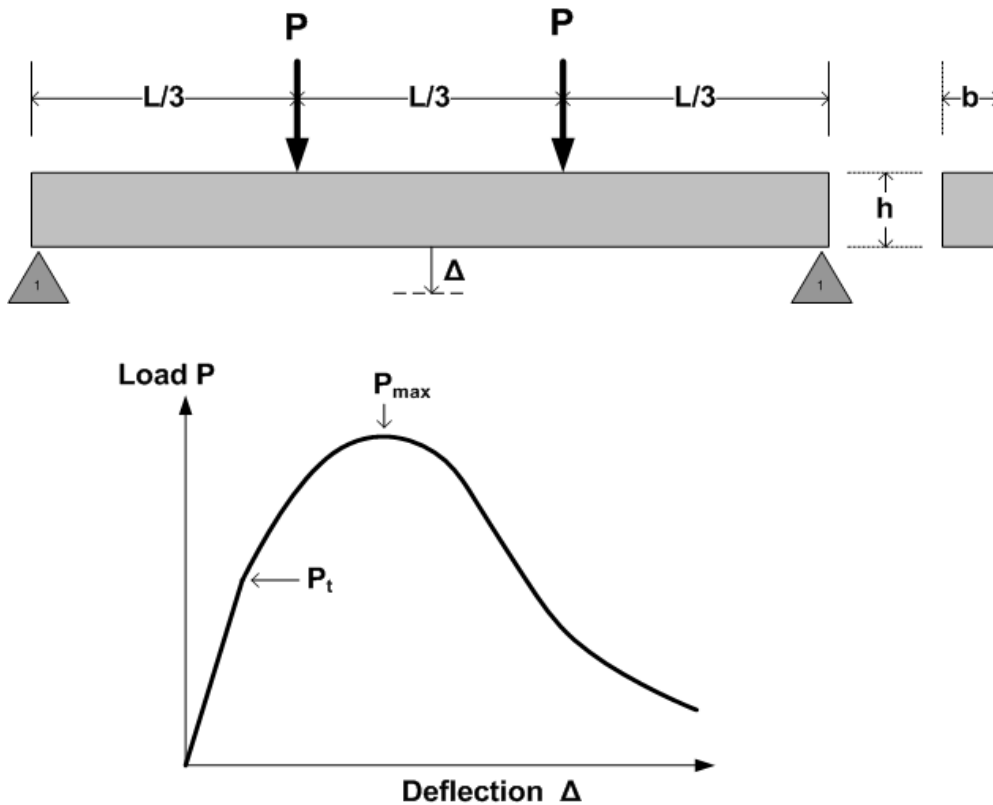
$$E_e = (P_e/A)/\epsilon_y = \text{Elastic Young's modulus}$$

where, P_e, P_{\max} = load at end of elastic range, and ultimate load, respectively
 Δ_e, Δ_c = deflection at end of elastic range, and at ultimate load, respectively.
 A = cross-sectional area of test specimen
 L = length of test specimen

Tension strain parameters ϵ_t and ϵ_r are best determined from beam bending tests in three-point loading as illustrated in Figure 2.6.91. The objective is to determine the beam loading levels indicated in the load-deformation plot as defined below.

P_t = beam load causing initial tensile cracking.
 P_{\max} = beam load at maximum capacity.

Figure 2.6.9-1 Experimental test for tension strain parameters ϵ_t and ϵ_r



Knowing the beam load causing initial tensile cracking, the initial cracking strain parameter is determined from simple beam theory by assuming the beam is uncracked and linear elastic as shown below

$$\varepsilon_t = \frac{2P_t L}{E_c b h^2} \quad \text{Equation 2.6.9-1}$$

where L = beam length
b = beam width
h = beam height

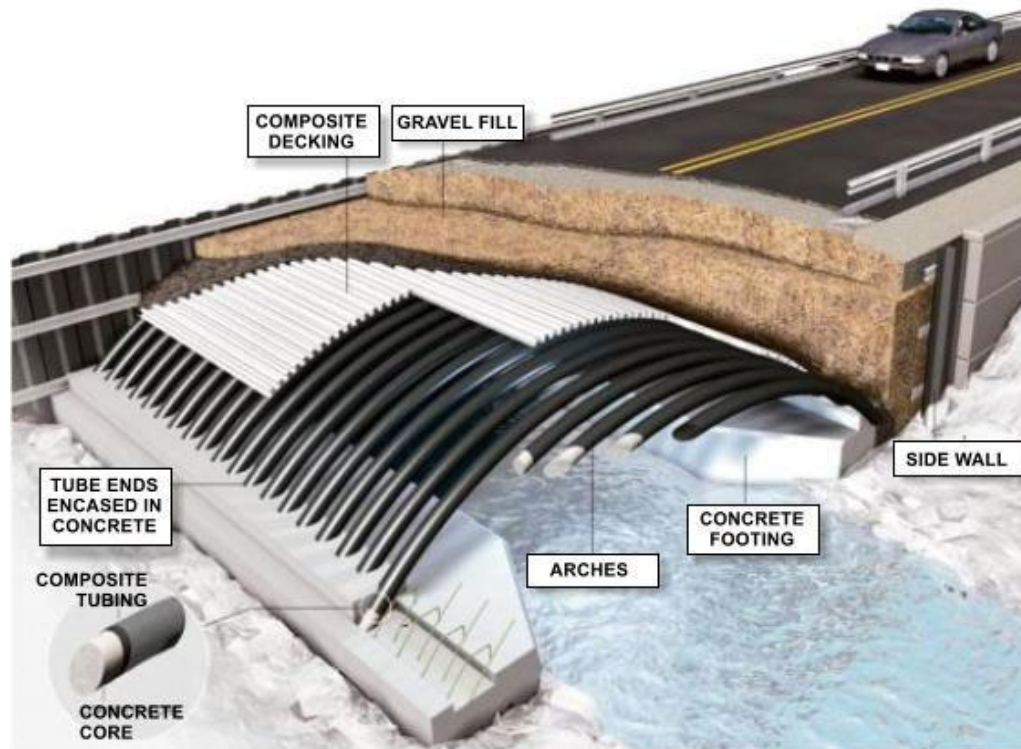
Lastly to determine the value of the rupture strain, we make use of the development in the previous section by determining the moment ratio and using Figure 2.6.8-5 to find ductility ratio r from which we obtain ε_r . Specifically the steps are,

1. Evaluate experimental moment ratio as, $m = M_{\max} / M_t = P_{\max} / P_t$
2. Enter Figure 2.6.8-5 with “m-value” and read $\log(r)$ value.
3. Recover r value as, $r = \log^{-1}(\log(r))$
4. Compute rupture strain as, $\varepsilon_r = \varepsilon_t r$

This completes the section on the CONRIB model.

2.7 Contube Pipe Type

The figure below shows a contube system that may be generally regarded as a long-span culvert system that is an alternative to other soil-bridge concepts such as monolithic reinforced concrete arch units or field-assembled corrugated metal arches. The unique feature of this system is that the arches are spaced at discrete intervals and composed of concrete-filled FRP tubes. The acronym CONTUBE refers to the circular concrete cross section contained in a thin-walled tube.

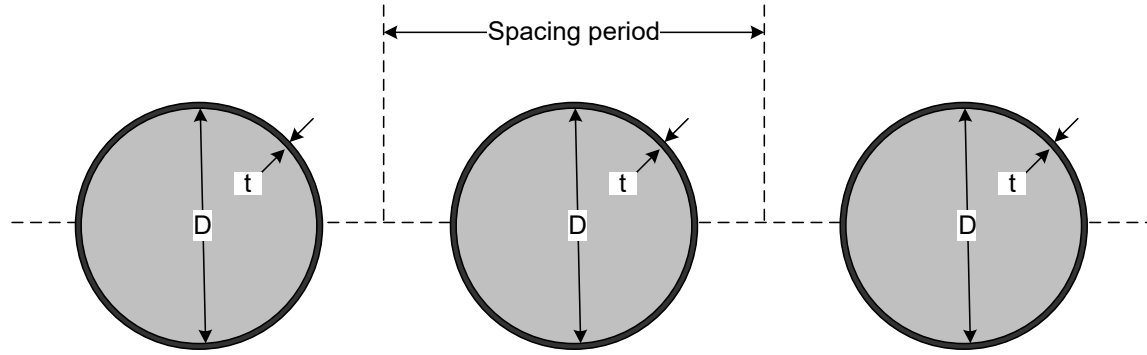


Another application of the CONTUBE pipe type is to represent a row of piles supporting the footing of a culvert system. Additional applications are provided in AASHTO publication, “*LRFD Guide Specifications for Design of Concrete-filled FRP tubes for Flexural and Axial Members, 1st edition 2012*”.

This section provides a detailed formulation of the CONTUBE pipe type using the same presentation outline that is used for all other pipe-types. The reader is referred back to Section 2.1 of this manual to review the general background development for the beam-column element, which is applicable to all pipe types. Here the ultimate goal is to derive the incremental axial stiffness EA^* and bending stiffness EI^* along with the nonlinear solution strategy for CONTUBE.

2.7.1 Overview of CONTUBE Model

The overall cross-sectional geometry is shown in the figure below which is completely defined by three measurements; D , t and S as shown in the figure below.



Where, D = diameter of concrete core
 t = thickness of tube
 S = spacing of tubes on center

The concrete stress-strain model is nonlinear in compression, simulated with a tri-linear stress-strain curve. In tension, concrete behavior is linear up to a specified tensile cracking strain limit. Thereafter tensile stress is released at a rate dependent on a tensile strain parameter called the rupture strain. Details of the concrete stress-strain model are discussed in a subsequent section.

The FRP tube is modeled as a linear elastic material in tension and compression for all levels of stress. However, specified stress-strength limits are used in the CANDE program to assess whether or not the maximum tube stress is beyond safety limits (design criterion).

2.7.2 Design Criteria for Concrete and Tube

CANDE prints out an evaluation of all appropriate design criteria at the end of each load step so that the user may assess the structural safety throughout the loading process. The design criteria in Table 2.7.2-1 are in general accordance with AASHTO publication, “LRFD Guide Specifications for Design of Concrete-filled FRP tubes for Flexural and Axial Members, 1st edition 2012”.

Table 2.7.2-1 Proposed design criteria for CONTUBE

Design Criterion (Strength limits)	Demand	Capacity
(1) Tube stress failure (psi)	f_{max} = max tube stress	f_y = tube strength
(2) Concrete crushing (psi)	σ_{max} = max compression	f'_c = compressive concrete strength
(3) Combined shear failure(lbs.)	V_{max} = max shear force	V_{ult} = combined shear capacity
Performance Limits (At Service Load)		
(4) Allowable crack width (in)	CW_{max} = max width	CW_{Allow} = allowable (0.01inch)

The above design criteria are equally applicable to working stress or LRFD design methodologies. For the working stress approach, the demand and the capacity quantities are unfactored, and the design evaluation is given by safety factors defined as capacity divided by demand. Typically, safety factors on the order of 2.0 are desirable for strength-related criteria. For the LRFD approach, the demand and the capacity quantities are factored and the design evaluation is given by ratios of demand-to-capacity. Demand-to-capacity ratios less than or equal to 1.0 are acceptably safe. Further discussion on the design criteria is provided below.

- (1) Tube failure. The maximum outer-fiber tube stress demand is determined from the computed beam-column strains at the inner and outer fibers multiplied by the tube's linear-elastic Young's modulus. On the capacity side, the tubes strength is an input value, nominally 150,000 psi.
- (2) Concrete crushing. On the demand side, the maximum outer-fiber concrete compressive stress is determined directly from the nonlinear concrete model as a result of thrust and bending. The ultimate compressive strength or capacity is an input or default value, typically 6000 psi.
- (3) Shear failure. The maximum shear-force demand acts on the combined concrete-tube cross section and is obtained directly from the CANDE solution output. The ultimate shear capacity is the combined sum of the tube and the concrete resistances, given by;

$$V_{ult} = \beta \sqrt{f'_c} A_{uncracked} + f_v A_{tube} \quad \text{Shear capacity equation}$$

where, β = concrete-shear factor typically in the range of 2 to 5 (producing psi units)

f'_c = concrete compressive strength (psi units)

$A_{uncracked}$ = uncracked area of concrete computed by CANDE (in²)

f_v = shear strength of tube cross section (psi)

A_{tube} = cross sectional area of tube material (in²)

Note, $A_{uncracked}$ is determined accurately based on the computed crack depth.

- (4) Allowable crack width. The allowable crack width at service loading is generally taken as 0.01 inches for unconfined concrete (AASHTO 12.10.3); however, much higher values may be reasonable for CONTUBE. CANDE's empirical strain-based crack width prediction is given by,

$$CW = L_S (\varepsilon_{tension} - \varepsilon_{crack}) \quad \text{Crack width equation}$$

where, $\varepsilon_{tension}$ = computed tensile strain in outer fiber of concrete.

ε_{crack} = tensile strain at initial concrete cracking, a concrete model property.

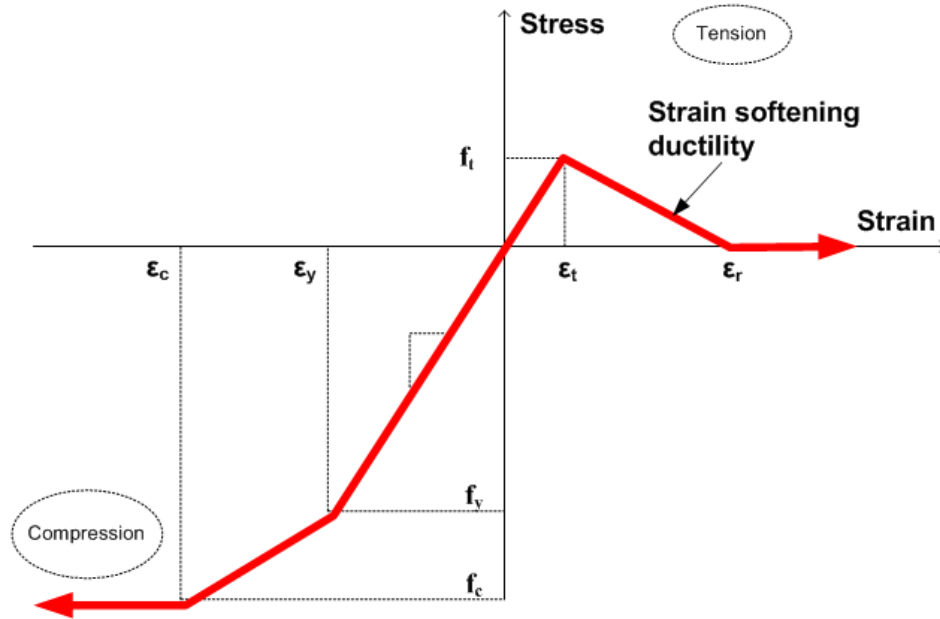
L_S = characteristic length for crack spacing, nominally about 10 inches.

Note that crack width is an approximation whereas crack depth is determined from first principles.

2.7.3 Concrete stress-strain model.

As shown in Figure 2.7.3-1, the CONTUBE concrete model is a tri-linear curve in compression exactly the same as the CONCRETE model for plain concrete. In the tension zone, however, the CONTUBE model has the capability of simulating varying amounts of ductility depending on the values assigned to the initial cracking strain and rupture strain parameters. If the rupture strain parameter is set equal to the initial tension cracking strain, then there is no ductility and the CONTUBE model behaves like plain concrete with an abrupt loss of all tensile stress once the initial cracking strain is reached. On the other hand, if the rupture strain parameter is assigned a value larger than the initial cracking strain, the model exhibits a ductile behavior with a gradual loss of tensile stress such that the larger the value of the rupture strain the greater the amount of ductility.

Figure 2.7.3-1 Concrete stress-strain model and parameters.



Primary model input parameters are defined below along with typical values shown in parenthesis

- ϵ_c = concrete strain at onset of unconfined compressive strength (0.002 in/in)
- ϵ_y = concrete strain at initial elastic limit in compression (0.0006 in/in)
- ϵ_t = concrete strain at initial tensile cracking (0.0001 in/in)
- ϵ_r = concrete strain at tensile rupture (.001 in/in)
- f'_c = unconfined compressive strength of concrete (6,000 psi)
- E_c = Young's modulus of concrete in elastic zone (4,700,000 psi)

Using the above input variables, four additional parameters are derived as follows:

- $E_2 = (f'_c - E_c \epsilon_y) / (\epsilon_c - \epsilon_y)$ = Young's modulus in compression yielding zone
- $f_{yc} = E_c \epsilon_y$ = compressive stress at initial yielding (3,000 psi)
- $f_t = E_c \epsilon_t$ = tensile strength at initial cracking and rupture (470 psi)
- $E_3 = -f_t / (\epsilon_r - \epsilon_t)$ = tension-softening modulus (negative)

The above model has the following behavior characteristics. For initial compression loading, the concrete behaves linearly until the stress level reaches the initial yield strength f_{yc} after which plastic hardening begins to occur in the yield zone. Perfect plasticity occurs when the stress level reaches compressive strength f'_c . Unloading is elastic and with permanent plastic strain, and reloading is elastic until the stress reaches its previous maximum value after which it follows the original stress-strain curve.

In tension, the concrete is linear until the initial tensile strain exceeds the cracking strain limit ϵ_t . After tensile cracking occurs, the tensile stress is reduced in the softening range at a rate depending on the softening modulus (negative value). Finally, when the strain exceeds the rupture strain all stress is released at this point. When this occurs, the crack is assumed not to heal so that there is no future tensile strength at this point. However, if the strain is reversed prior to reaching the

rupture strain, then the remaining tension stress is preserved and the ductile zone is characterized with a reduced tensile strength for future tensile loading.

2.7.4 Tube stress-strain model

The assumed stress-strain behavior for FRP tube material is shown in Figure 2.7.4-1. Tube material is assumed to be linear elastic at all stress levels and behavior in compression and tension is identical. Nominal failure strengths are defined for evaluation of design criteria; however, the actual CANDE model is always linear elastic. Thus, the input parameters are

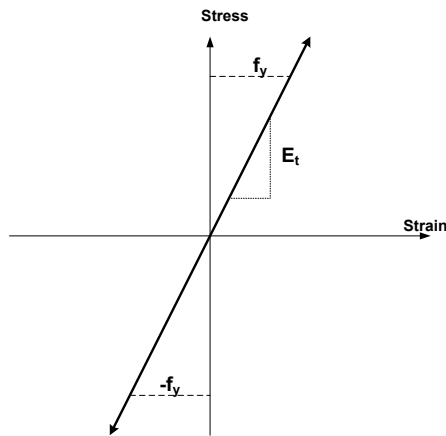
E_t = Young's modulus for tube

f_y = Nominal axial failure strength (evaluation only)

f_v = Nominal shear failure strength (evaluation only)

It is noted that the Young's moduli of the concrete and the tube are not converted to the standard plane-strain form using the Poisson factor, $1/\sqrt{1-\mu^2}$. This is because the arch tubes are spaced at a periodic distance S , which is better represented by a plane-stress assumption.

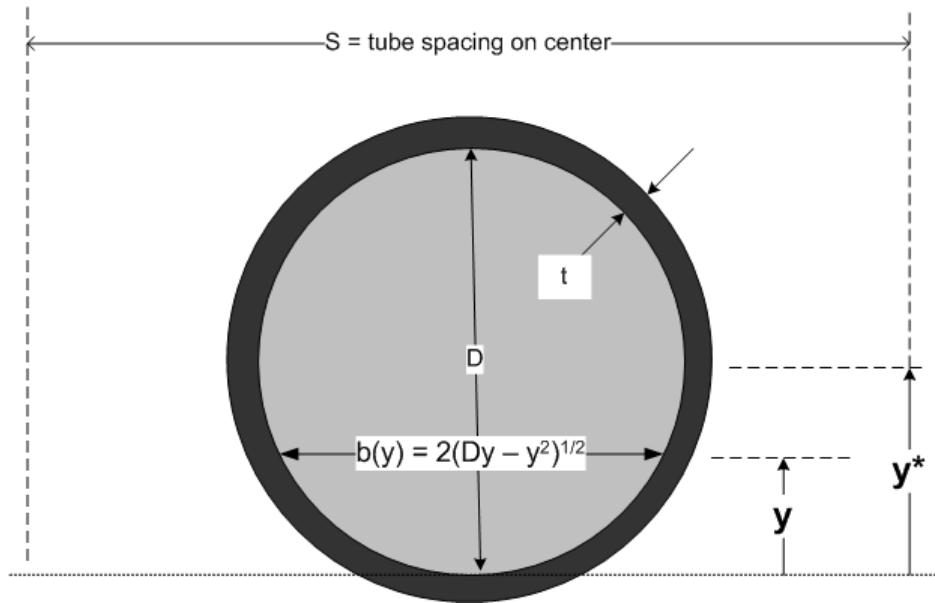
Figure 2.7.4-1 Linear-elastic stress-strain model for tube material.



2.7.5 Section stiffness properties for CONTUBE

Shown in the figure below is the composite CONTUBE cross-section configuration wherein the coordinate y is measured from the bottom concrete-tube interface. The variable y^* denotes the distance to the neutral axis and is also referenced to the concrete-tube interface at the base. Thus, prior to concrete cracking or any nonlinear behavior, y^* is at the centroid of the CONTUBE cross-section, i.e., $y^* = D/2$.

Figure 2.7.5-1 Composite CONTUBE cross section.



As stated in Section 2.1.9, the key section properties are; EA*(effective axial stiffness), y* (location of current neutral axis) and EI*(effective bending stiffness). These properties are the heart of all pipe type algorithms and are specialized in the following equations for the CONTUBE cross-section. Integrals representing concrete properties are denoted with a subscript c and integrals representing tube properties are denoted with a subscript t.

$$EA^* = \left(\int_{A_c} E' dA_c + \int_{A_t} E_t dA_t \right) / S \quad \text{Effective axial stiffness (lbs/inch)}$$

$$y^* = \left(\int_{A_c} E' y dA_c + \int_{A_t} E_t y dA_t \right) / EA^* \quad \text{Neutral axis (inches)}$$

$$EI^* = \left(\int_{A_c} E' (y^* - y)^2 dA_c + \int_{A_t} E_t (y^* - y)^2 dA_t \right) / S \quad \text{Effective bending stiffness (in-lbs/inch)}$$

In the above equations Young's modulus for concrete is denoted by E' implying that it is variable quantity within the cross-section. Later, E' is defined in detail in the context of a chord modulus.

Tube section properties (always elastic). Since the tube material is assumed to be linear elastic, the three tube integrals listed above may be integrated exactly to get the solutions for once and for all:

$$\int_{A_t} E_t dA_t = E_t \pi (D+t)t \quad \text{Tube axial stiffness}$$

$$\int_{A_t} E_t y dA_t = E_t \pi (D/2)(D+t)t \quad \text{Tube 1st moment about interface at base}$$

$$\int_{A_t} E_t (y^* - y)^2 dA_t = E_t \pi \left((y^* - D/2)^2 (D+t)t + \frac{(D/2+t)^4 - (D/2)^4}{4} \right) \text{ Tube bending stiffness about } y^*$$

Note that y^* is dependent on combined influence of the concrete and the tube together. Therefore, the tubes contribution to the total moment of inertia (last equation) is coupled with the nonlinear concrete behavior via the variable y^* .

Initial concrete section properties. Initially, when the concrete is unloaded and uncracked, the section properties for area, 1st moment, and moment of inertia are easily calculated. Again, referring to Figure 5.3.3-1, the three integrals for concrete in the linear range are evaluated below.

$$\int_{A_c} E_c dA_c = E_c \pi (D/2)^2 \quad \text{Linear-elastic concrete axial stiffness}$$

$$\int_{A_c} E_c y dA_c = E_c \pi (D/2)^2 (D/2) \quad \text{Linear-elastic concrete 1st moment}$$

$$\int_{A_c} E_c (y - y^*)^2 dA_c = E_c \pi \left((y^{*2} - (D/2)^2) (D/2)^2 + \frac{(D/2)^4}{4} \right) = E_c \pi D^4 / 64$$

Linear-elastic concrete bending stiffness about y^*

When both the tube and the concrete are in the linear-elastic range, we have $y^*=D/2$ so that the concrete contribution to the total bending stiffness is given by right most expression in the last equation.

Composite elastic properties per unit length. The CANDE plane-strain formulation requires that the elastic properties of the combined tube and concrete section properties be divided by the spacing distance S . Thus, the combined elastic properties per unit length for axial stiffness, neutral axis and bending stiffness are prescribed as follows.

$$EA^* = \left(E_t \pi (D+t)t + E_c \pi (D/2)^2 \right) / S \quad \text{Combined elastic axial stiffness}$$

$$y^* = D/2 \quad \text{Combined neutral axis (elastic)}$$

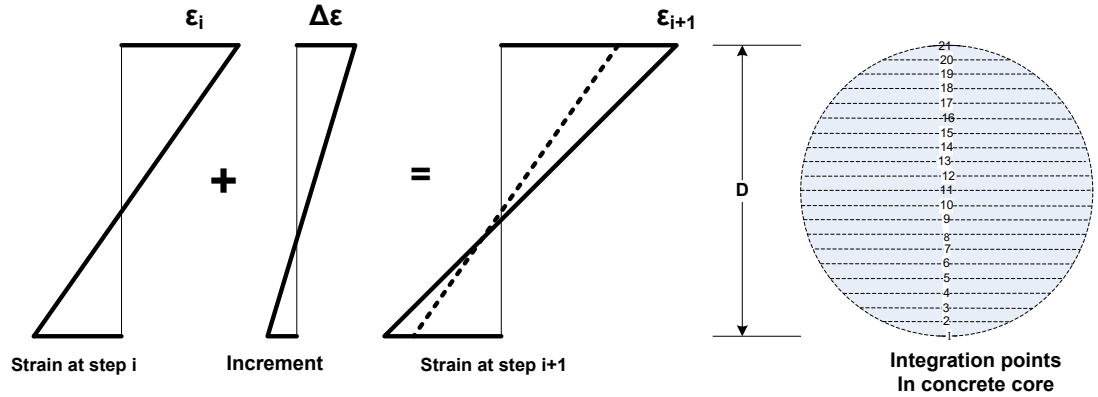
$$EI^* = \left(E_t \pi \left(\frac{(D/2+t)^4 - (D/2)^4}{4} \right) + E_c \pi \left(\frac{(D/2)^4}{4} \right) \right) / S \quad \text{Combined elastic bending stiff.}$$

The above composite section properties are valid as long the concrete does not enter the nonlinear range either by initial cracking or concrete compression yielding. When the concrete enters the nonlinear range, we invoke the nonlinear algorithm described below which means that section properties EA^* , y^* and EI^* must be iteratively recomputed for each element that experiences concrete cracking or compression yielding.

2.7.6 Nonlinear solution strategy.

We assume we have a converged solution at load step i and we seek an incremental solution for load step $i+1$. Using the values of EA^* , y^* and EI^* from the previous load step, a trial solution is obtained for the first iteration using the previous values and thereby providing new estimates of the strain distribution at each element cross-section. To compute the next estimate for EA^* , y^* and EI^* , numerical integration is used over the concrete core in order to cope with the nonlinear chord modulus as illustrated in the figures below.

Figure 2.7.6-1 Strain profile from step i to i+1 and 31-point Simpson integration



Concrete chord modulus. The effective chord modulus, E' , from the known stress-strain state (σ_i, ϵ_i) to the estimated stress-strain state $(\sigma_{i+1}, \epsilon_{i+1})$ is computed at each integration point using the concrete stress-strain curve. As discussed in the following sections, the chord modulus is determined iteratively.

The Figure 2.7.6 -2 illustrates various chord moduli, E' , which connects a known starting point (σ_i, ϵ_i) to the estimated end point $(\sigma_{i+1}, \epsilon_{i+1})$. Here, ϵ_{i+1} is obtained from the trial incremental solution, $\epsilon_{i+1} = \epsilon_i + \Delta\epsilon$, and σ_{i+1} is the corresponding stress determined from the stress-strain relationship as quantified in the Table 2.7.6-1.

Figure 2.7.6-2 Illustration of concrete chord moduli in zone transitions

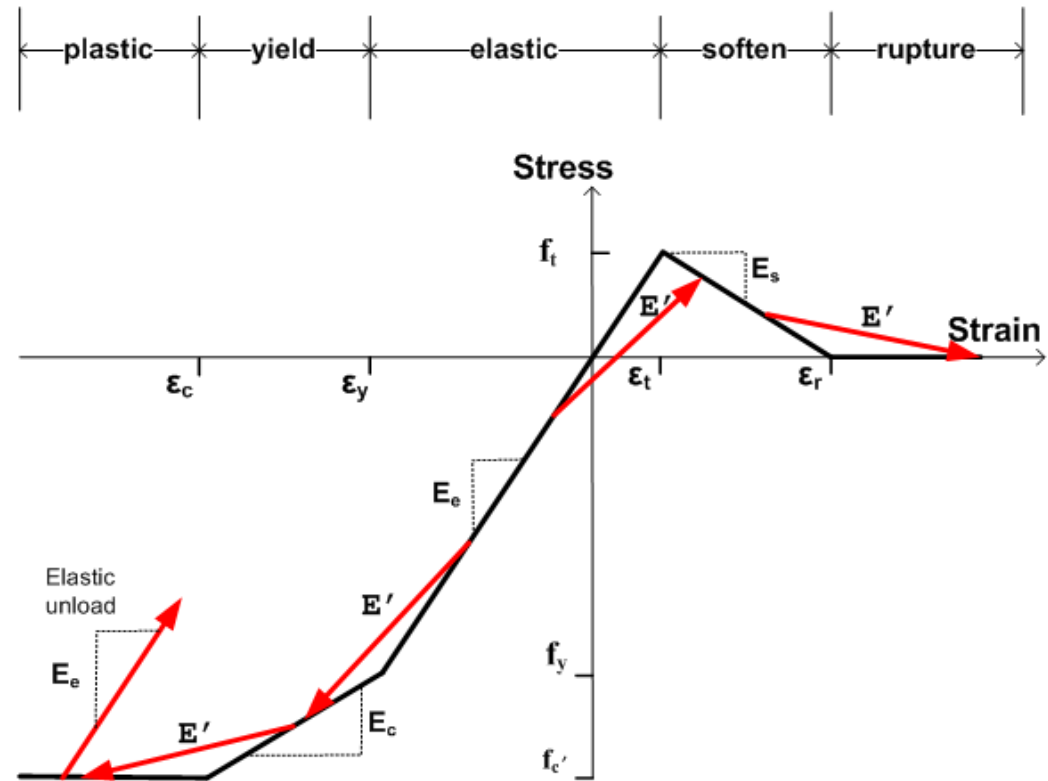


Table 2.7.6-1. Concrete chord modulus and ratio for specified starting and ending zones.

Starting Zone ϵ_i	Ending Zone ϵ_{i+1}	Corresponding Stress σ_{i+1}	Chord modulus E'	Modulus ratio $F'(y) = E'/E_e$
elastic	more elastic	$\sigma_i + E_c \Delta \epsilon$	E_c	$= 1.0$
elastic	yield	$f_y + E_c(\epsilon_{i+1} - \epsilon_y)$	$(\sigma_{i+1} - \sigma_i) / \Delta \epsilon$	< 1.0
elastic	plastic	f_c'	$(f_c' - \sigma_i) / \Delta \epsilon$	< 1.0
yield	more yield	$\sigma_i + E_c \Delta \epsilon$	E_c	$= E_c / E_e$
yield	plastic	f_c'	$(f_c' - \sigma_i) / \Delta \epsilon$	$< E_c / E_e$
plastic	more plastic	f_c'	0.0	$= 0.0$
compress zone	unloading	$\sigma_i + E_c \Delta \epsilon$	E_c	$= 1.0$
elastic	soften	$f_t + E_s(\epsilon_{i+1} - \epsilon_t)$	$(\sigma_{i+1} - \sigma_i) / \Delta \epsilon$	< 1.0
soften	more soften	$\sigma_i + E_s \Delta \epsilon$	E_s	< 0.0
soften	rupture	0.0	$-\sigma_i / \Delta \epsilon$	< 0.0
rupture	more rupture	0.0	0.0	$= 0.0$

In the above table, the concrete-modulus ratio is defined as the chord modulus divided by the initial elastic modulus, $F'(y) = E'/E_e$. Thus, $F'(y)$ varies through the cross-section including negative values for integration points in the softening range.

Elastic unloading occurs from any compression zone whenever $|\epsilon_{i+1}| < |\epsilon_i|$ with the provision that neither strain is in the softening or rupture zone.

Once a point in the cross section begins to crack, the initial tensile strength is permanently reduced to the corresponding stress value on the softening leg of the stress-strain curve. Physically this means some tension damage has occurred changing the shape of the stress-strain path in the tension zone. When the tensile strain exceeds the rupture strain, the tension damage is complete and the stress-strain path is completely flat in tension for all future tensile loading conditions, implying that cracks do not heal.

The above algorithm requires maintaining data records at each integration point to keep track of the cracking-depth history and tension damage. It is also required to maintain data records of plastic straining in compression in order to properly simulate unloading and reloading.

To summarize, all the above rules for the concrete chord modulus are implied in the following expression,

$$E'(y) = E_e F'(y) \quad \text{Chord modulus representation}$$

wherein E_e is constant and may be removed from integrals, and $F'(y)$ may be evaluated at each integration point in accordance with the above table.

Computing section properties. Section properties require area integrations over the concrete cross section. To this end, the differential area is expressed as $dA = b(y)dy$ where $b(y)$ is the concrete cross-section width as defined below.

$$b(y) = 2\sqrt{Dy - y^2} \quad \text{Circle width as a function of } y$$

With the above understanding, the key section properties are a combination of the tube (integrated exactly) plus the concrete core (integrated numerically) as expressed below.

$$EA^* = \left(E_t \pi (D+t)t + E_c \int_0^h F'(y)b(y)dy \right) / S$$

$$y^* = \left(E_t \pi (D/2)(D+t)t + E_c \int_0^h F'(y)yb(y)dy \right) / EA^*$$

$$EI^* = \left(E_t \pi \left((y^*-D/2)^2 (D+t)t + \frac{(D/2+t)^4 - (D/2)^4}{4} \right) + E_c \left(\int_0^h F'(y)(y-y^*)^2 b(y)dy \right) \right) / S$$

The integrals over the concrete core are achieved with 31-point Simpson integration to evaluate the following three sums where $F'(y_i)$ is the concrete modulus ratio at integration point i , and $b(y_i)$ is the cross-section width of the concrete core.

$$Sum_1 = \int_0^D F'(y)b(y)dy = D/90[F'(y_1)b(y_1)+4F'(y_2)b(y_2)+2F'(y_3)b(y_3)+...+F'(y_{31})b(y_{31})]$$

$$Sum_2 = \int_0^D F'(y)yb(y)dy = D/90[F'(y_1)y_1b(y_1)+4F'(y_2)y_2b(y_2)+2F'(y_3)y_3b(y_3)+...+F'(y_{31})y_{31}b(y_{31})]$$

$$Sum_3 = \int_0^D F'(y)y^2b(y)dy = D/90[F'(y_1)y_1^2b(y_1)+4F'(y_2)y_2^2b(y_2)+2F'(y_3)y_3^2b(y_3)+...+F'(y_{31})y_{31}^2b(y_{31})]$$

Using the above integration results, the final results for the key section properties (effective axial stiffness, current neutral axis, and effective moment of inertia) are expressed as,

$$EA^* = (E_t \pi (D+t)t + E_c Sum_1) / S$$

$$y^* = (E_t \pi (D/2)(D+t)t + E_c Sum_2) / EA^*$$

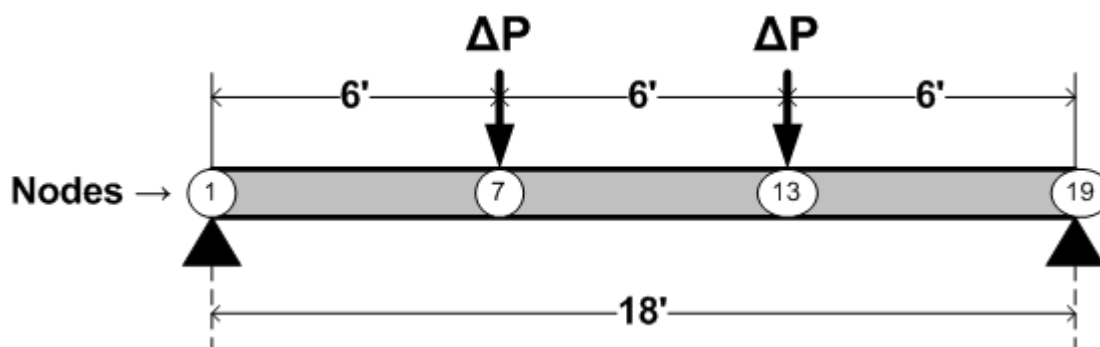
$$EI^* = \left(E_c (y^{*2} Sum_1 - 2y^* Sum_2 + Sum_3) + E_t \pi \left((y^*-D/2)^2 (D+t)t + \frac{(D/2+t)^4 - (D/2)^4}{4} \right) \right) / S$$

The above calculations are carried out in subroutine CONCIRCLE, which is called by subroutine CONTUBE. Iterations within the load step continue until successive calculations for EA^* , y^* and EI^* are within 1% relative error for all cross sections.

2.7.7 Simple Illustrative Example

To complete the development, the CONTUBE pipe type is tested as a simply supported beam under 3rd point loading as shown in the figure below. Eighteen beam-column elements are used to model the 18-foot beam with nodes 1 and 19 assigned to pinned supports and nodes 7 and 13 prescribed with equal increments of external loading in addition to the beam's self-weight.

Figure 2.7.7-1 Illustrative example of simply supported beam



Cross-section properties are the standard CONTUBE default values as identified in the CANDE-2022 user manual except that the tube spacing distance is set to 1.0 so that only a single beam's actual cross-sectional is modeled.

Recall that the concrete confinement by the tube is believed to increase the concrete tensile strength and tensile ductility. Accordingly, the purpose of this study is to demonstrate the parametric influence of the concrete cracking strain value on the load-deformation behavior of the beam model. Moreover, this procedure can be used to experimentally determine the tensile strain parameters of the CONTUBE model.

The CANDE-2022 output report provides a complete assessment of the CONTUBE design criteria as well as stress-strain diagnostics for concrete and tube at each node including combined shear evaluations. For purposes of this study, we restrict our attention to the load-deformation plots in Figure 2.2.7-2.

The figure's center curve (blue line) is the standard (default) value for cracking strain (0.0001 in/in), which is referred to as STNMAT(1) in line B-2 of the CANDE input instructions. In this case the initial elastic response begins to soften at a reaction load of about 2000 pounds as initial concrete cracking begins. The upper curve (red line) is the result of doubling the cracking strain (0.0002 in/in), and the lower curve (green line) is the result of reducing the cracking strain by an order of magnitude (0.00001 in/in).

Clearly, we see that the cracking strain has a pronounced influence on the load-deformation plots. By comparing experimental data with plots similar to those above, the actual value of the concrete cracking strain may be determined by numerical investigation. In the above plots the concrete rupture strain, which is referred to as STNMAT(4) in line B-2 of the CANDE input instructions, is maintained at the default value of 10 times the cracking strain. If lower values of the rupture strain are used, the softening curvature is more sharply acute, which may result in two equilibrium positions for a given load. If this should occur, it is recommended to impose the loading by prescribed displacements rather than by prescribed forces.

Figure 2.2.7-2 Load-deformation curves for three values of cracking strain.



As a final comment, it is believed that the CONTUBE model installed in CANDE-2022 is capable of correctly modeling the behavior concrete-filled tubes; however, this needs to be demonstrated in controlled laboratory experiments and in real-world applications.

3 SOIL MODELS

Soil models, or constitutive forms, define a relationship between stress and strain based on phenomenological observations of material behavior at the macroscopic level. The term soil model and constitutive form are used interchangeably throughout this chapter. CANDE-2022 offers the following suite of soil models; isotropic elastic, orthotropic elastic, overburden dependent, Duncan and Duncan/Selig, and extended Hardin. The common feature of these models, which have proven effective in simulating the soil layers in culvert installations, is that the models are based on elastic-like or variable modulus constitutive forms as opposed to plasticity based constitutive forms.

Each of the soil models is discussed in subsequent sections. However, in order to properly set the stage, we first discuss the basic formulation of the continuum elements in which the soil models are contained.

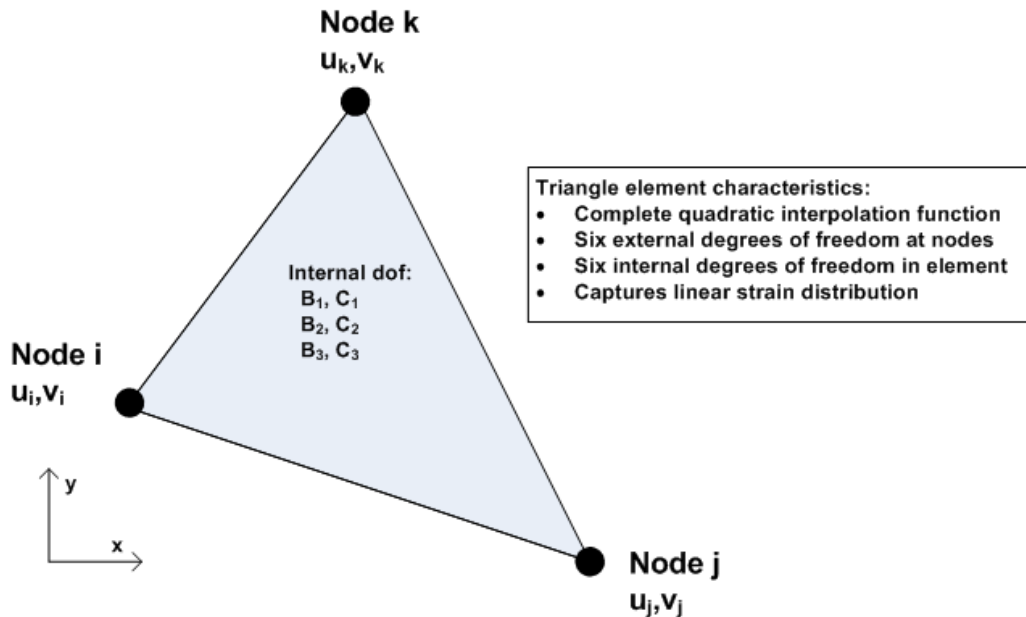
3.1 Continuum Elements

Plane-strain continuum elements are used to represent the soil zones in the soil-structure system. Two continuum element shapes are available in CANDE, triangular and quadrilateral. Both element shapes utilize identical interpolation functions and are classified as non-conforming elements. These elements, developed by Herrmann in Reference 11, have superior qualities in all basic deformation modes and outperform the well-known linear strain triangle and eight-node isoperimetric quadrilateral, respectively. For example, one row of CANDE's quadrilateral elements is capable of properly replicating beam-bending behavior.

3.1.1 Triangle elements

The triangular element, shown below, employs area coordinates (the natural coordinate system for triangles) to define interpolation functions for the x-displacement function $u(x,y)$ based on 3-external nodal degrees of freedom at the triangle vertices and 3-internal element degrees of freedom. Similarly, the y-displacement function $v(x,y)$ is based on 3-external and 3-internal degrees of freedom.

Figure 3.1.1-1. Characteristics of triangular continuum element



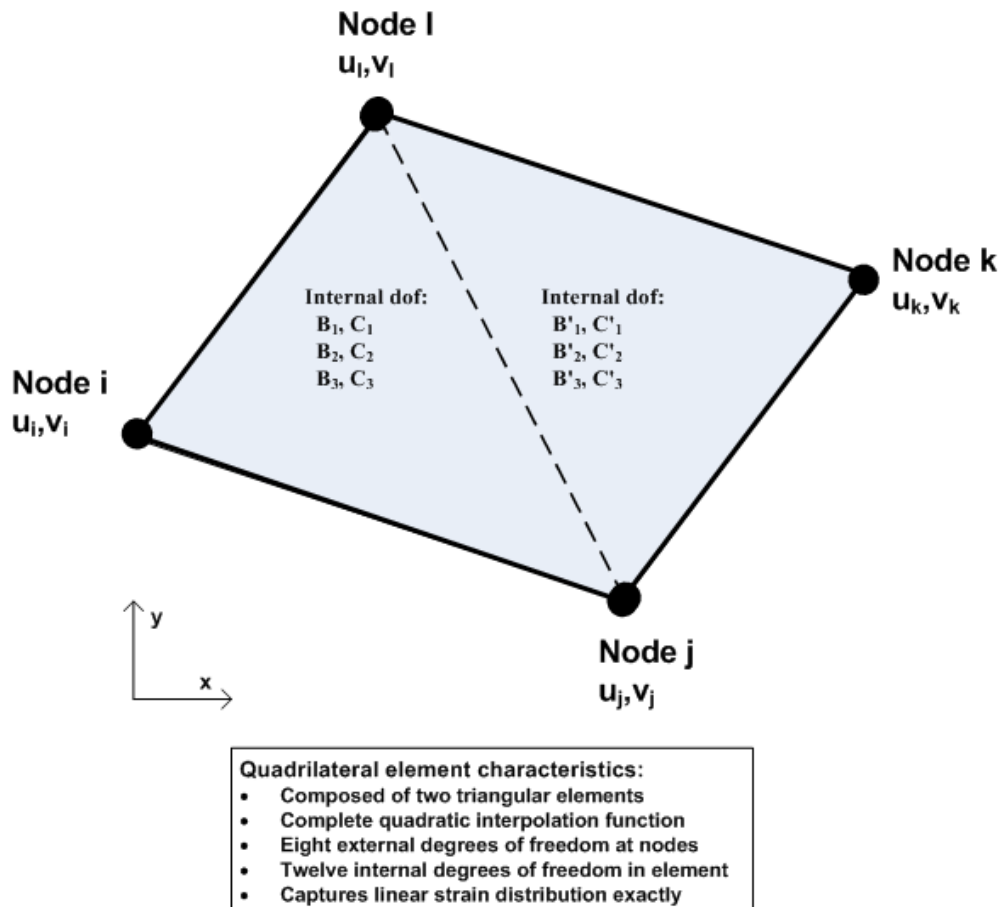
Linear interpolation functions are used for the external nodal degrees of freedom, which by themselves are equivalent to a constant strain triangle. Superimposed on the linear displacement functions are complete quadratic interpolation

functions associated with internal degrees of freedom within the element. Constraint equations are applied to the internal degrees of freedom so that the element is convergent when the element size approaches zero and passes the patch test. The internal degrees of freedom are statically condensed at the element level resulting in a 6x6 element stiffness matrix and a 6x1 body-load vector associated with the external degrees of freedom, and ready for global assembly.

3.1.2 Quadrilateral elements

As shown in the figure below, the quadrilateral element is composed of two triangles wherein the x-displacement function $u(x,y)$ is based on 4-external nodal degrees of freedom at the vertices and 6-internal degrees of freedom within the element. Similarly, the y-displacement function $v(x,y)$ is based on 4-external and 6-internal degrees of freedom.

Figure 3.1.2-1. Characteristics of quadrilateral continuum element



To ensure that the quadrilateral element is convergent and passes the patch test, the influence of the internal degrees of freedom must approach zero as the element becomes vanishingly small. This requirement places three constraints on the twelve internal degrees of freedom, resulting in nine internal degrees of freedom. The nine internal degrees of freedom are statically condensed at the element level resulting in an 8x8 element stiffness matrix and an 8x1 body-load vector associated with the external degrees of freedom, and ready for global assembly.

3.1.3 Finite element development

Interpolation functional forms. The interpolation functions used for triangle and quadrilateral elements may be generically expressed using the notation presented in Chapter 1 as,

$$\Delta u_e = N \Delta \hat{u}_e \quad \text{Equation 3.1-1}$$

$$\Delta v_e = N \Delta \hat{v}_e \quad \text{Equation 3.1-2}$$

where, $\Delta u_e, \Delta v_e$ = displacement functions for x- and y-directions in triangle or quadrilateral element.

$\Delta \hat{u}_e, \Delta \hat{v}_e$ = column-vector of degrees-of-freedom for x and y displacement functions in element.

N = row-vector of interpolation functions in area coordinates, also expressible in x and y variables.

Of course, the length of the interpolation row-vector is larger for the quadrilateral element than for the triangle element, as are also the lengths of the degree-of-freedom column-vector.

Strain-displacement relationship. Small strain and small deformation theory are used for all continuum elements. Accordingly, the strain components for plane strain are given by the partial derivatives of the displacement functions as expressed in the matrix relationship below,

$$\begin{pmatrix} \Delta \varepsilon_x \\ \Delta \varepsilon_y \\ \Delta \gamma \end{pmatrix} = \begin{pmatrix} N,x & 0 \\ 0 & N,y \\ N,y & N,x \end{pmatrix} \begin{pmatrix} \Delta \hat{u}_e \\ \Delta \hat{v}_e \end{pmatrix} \quad \text{Equation 3.1-3}$$

where, $\Delta \varepsilon_x, \Delta \varepsilon_y, \Delta \gamma$ = strain increments for x-direction, y-direction and shear components, respectively.

N,x & N,y = partial derivatives of interpolation functions in the row vector with respect to x and y.

Stress-strain relationship. All soil models conform to a general constitutive form relating increments of stress to increments of strain via a matrix of variable coefficients dependent on the stress-strain state at step i and step i+1 as indicated below,

$$\begin{pmatrix} \Delta \sigma_x \\ \Delta \sigma_y \\ \Delta \tau \end{pmatrix} = \begin{pmatrix} C_{11} & C_{12} & C_{13} \\ C_{21} & C_{22} & C_{23} \\ C_{31} & C_{32} & C_{33} \end{pmatrix} \begin{pmatrix} \Delta \varepsilon_x \\ \Delta \varepsilon_y \\ \Delta \gamma \end{pmatrix} \quad \text{Equation 3.1-4}$$

where, $\Delta \sigma_x, \Delta \sigma_y, \Delta \tau$ = stress increments for x-direction, y-direction and shear components, respectively.

C_{ij} = variable coefficients generally dependent on current stress and strain state.

Components of the constitutive matrix are symmetric ($C_{ij} = C_{ji}$) and are explicitly defined for each soil model in subsequent sections.

Element stiffness matrix. Using the above relationships, the element stiffness for the triangle or quadrilateral is obtained by integrating the following matrix products,

$$\underline{k}_e = \int_A \begin{pmatrix} N,x & 0 \\ 0 & N,y \\ N,y & N,x \end{pmatrix}^T \begin{pmatrix} C_{11} & C_{12} & C_{13} \\ C_{21} & C_{22} & C_{23} \\ C_{31} & C_{32} & C_{33} \end{pmatrix} \begin{pmatrix} N,x & 0 \\ 0 & N,y \\ N,y & N,x \end{pmatrix} dA \quad \text{Equation 3.1-5}$$

Integration of the interpolation functions is performed exactly using area coordinates whereas the components of the constitutive matrix are taken as constant within the element based on the stress-strain state at the center of the element.

After the internal degrees of freedom are statically condensed from the element, the element stiffness for the triangle element is a 6x6 matrix associated with the 6-external degrees of freedom, two per node. The quadrilateral element stiffness is an 8x8 matrix, associated with the 8-external degrees of freedom, two per node.

3.2 Isotropic Linear Elastic

The linear elastic soil model in isotropic form is the simplest soil model. Linear elastic implies the soil stiffness remains constant irrespective of the stress state, and isotropic implies the soil stiffness is uniform in all spatial directions. The model is useful for characterizing stiff in-situ soils and pre-consolidated soils such as the soil remaining after excavation. Moreover, when the exact character of the soil is not well known, the linear-elastic isotropic soil model is useful for parametric studies and/or to conservatively represent soil stiffness with modest moduli values. The isotropic form of the elastic constitutive matrix is expressed by the following incremental stress-strain relationship,

$$\begin{pmatrix} \Delta\sigma_x \\ \Delta\sigma_y \\ \Delta\tau \end{pmatrix} = \begin{pmatrix} C_{11} & C_{12} & 0 \\ C_{12} & C_{11} & 0 \\ 0 & 0 & C_{33} \end{pmatrix} \begin{pmatrix} \Delta\varepsilon_x \\ \Delta\varepsilon_y \\ \Delta\gamma \end{pmatrix} \quad \text{Equation 3.2-1}$$

where, C_{11} , C_{12} and C_{33} are material constants defined by two elastic parameters. In the above matrix, the C_{22} coefficient is identified as C_{11} to emphasize they are identical in value for the isotropic case.

In CANDE, the elastic parameters used to characterize C_{11} , C_{12} and C_{33} are Young's modulus and Poisson ratio as shown in the second column of Table 3.2-1. The exact equivalent using other pairs of elastic parameters are shown in the third column for the confined modulus and lateral coefficient, and in the fourth columns for the bulk modulus and shear modulus.

Table 3.2-1 Components for constitutive matrix defined by elastic parameters

Components of Constitutive matrix	Elastic parameter equivalent pairs		
	E = Young's modulus v = Poisson ratio (E, v)	M_s = confined modulus K_0 = lateral coefficient (M_s, K_0)	B = bulk modulus G = shear modulus (B, G)
$C_{11} =$	$E(1-v) / (1+v)(1-2v)$	M_s	$B + (4/3)G$
$C_{12} =$	$Ev / (1+v)(1-2v)$	$M_s K_0$	$B - (2/3)G$
$C_{33} = (C_{11}-C_{22})/2 =$	$E / 2(1+v)$	$M_s (1-K_0)/2$	G

The inference in the above table is that if any two elastic pairs are known, they may be equivalently expressed with any other elastic pairs using the above relationships.

Depending on the soil quality and compaction, representative ranges of Young's modulus and Poisson ratio are shown in Table 3.2-2 for three broad classes of soil.

Table 3.2-3 Representative ranges of Young's modulus and Poisson ratio

Soil type	Elastic parameters, nominal range	
	Young's modulus, E psi	Poisson ratio, v (-)
Granular	600 to 2000	0.30 to 0.35
Mixed	400 to 1400	0.30 to 0.40
Cohesive	200 to 400	0.33 to 0.40

Well-compacted soils are characterized by the high-range values of Young's modulus, whereas poorly compacted soils are characterized by the low-range values.

3.3 Orthotropic Linear Elastic

Like the isotropic model above, the linear-elastic designation means the stiffness of the orthotropic model remains constant irrespective of the stress state. However, unlike the uniform isotropic model, the stiffness of the orthotropic model may be different in one direction, say x' , than it is in an orthogonal direction say, y' . Some stratified sedimentary soil deposits exhibit orthotropic properties, but this is rather rare in culvert installations. A more common occurrence of orthotropic stiffness is due to man-made inclusions in soils such as reinforced earth and geo-textile fabrics.

The orthotropic form of the elastic constitutive matrix is expressed by the following incremental stress-strain relationship wherein the x-y coordinate system is assumed to be aligned with the principal material axis.

$$\begin{pmatrix} \Delta\sigma_x \\ \Delta\sigma_y \\ \Delta\tau \end{pmatrix} = \begin{pmatrix} C_{11} & C_{12} & 0 \\ C_{12} & C_{22} & 0 \\ 0 & 0 & C_{33} \end{pmatrix} \begin{pmatrix} \Delta\epsilon_x \\ \Delta\epsilon_y \\ \Delta\gamma \end{pmatrix} \quad \text{Equation 3.3-1}$$

C_{11} , C_{22} , C_{12} and C_{33} are four independent material constants, however their values are constrained by the requirement the constitutive matrix must be positive definite. If the x-y coordinate system is not coincident with the principal material directions, then the angle between the two coordinate systems is used to transform the constitutive matrix to the x-y system.

3.3.1 Orthotropic properties from testing specimens

Direct measurements to characterize C_{11} , C_{22} , C_{12} and C_{33} in naturally occurring orthotropic soils can be achieved with a tri-axial testing machine by performing K_0 -tests wherein the axial load is applied and the confining pressure is adjusted so that there is no net lateral strain, also called a confined compression test, or uniaxial strain test. For the case when the material x-axis is aligned with specimen's vertical axis, the results of the K_0 -test may be used to determine the following three coefficients,

$$C_{11} = \sigma_{\text{axial}} / \epsilon_{\text{axial}} \quad \text{Equation 3.3-2}$$

$$C_{12} = \sigma_0 / \epsilon_{\text{axial}} \quad \text{Equation 3.3-3}$$

$$C_{33} = (\sigma_{\text{axial}} - \sigma_0) / 2\epsilon_{\text{axial}} \quad \text{Equation 3.3-4}$$

where, σ_{axial} = net axial stress including confining pressure,

ϵ_{axial} = net axial strain including confining strain,

σ_0 = confining pressure.

In a similar manner, the K_0 -test may be repeated with the test specimen rotated 90 degrees such that the material y-axis is aligned with the vertical direction in order to determine the last coefficient C_{22} as,

$$C_{22} = \sigma_{\text{axial}} / \epsilon_{\text{axial}} \quad \text{Equation 3.3-5}$$

This second set of test results may also be used to confirm the previously computed results for C_{12} and C_{33} .

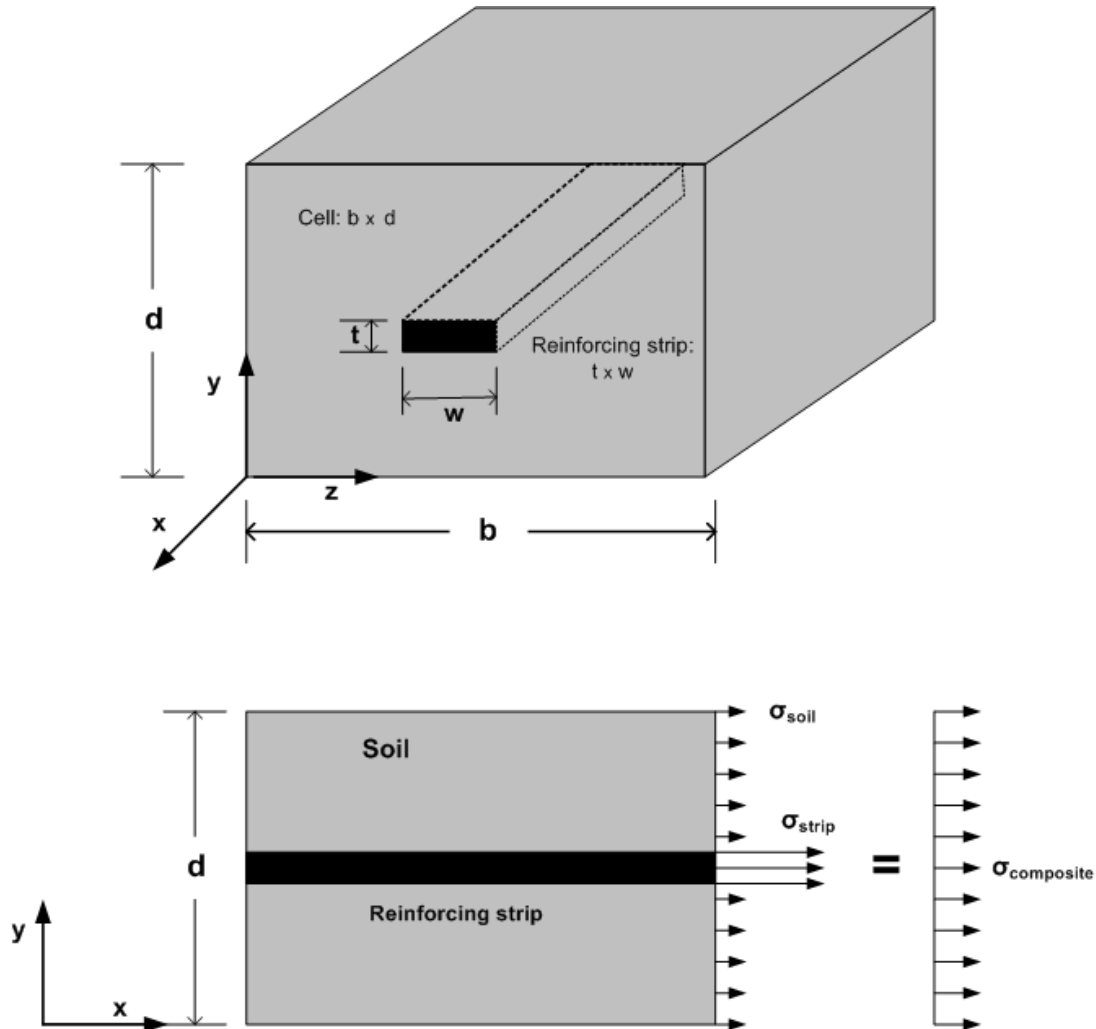
3.3.2 Orthotropic properties for reinforced soil

Placing strips of metal or geo-textile fabrics into soil has proven to be very effective in improving the directional stiffness of soils in embankments and pavement systems. Directional soil reinforcement has also been studied for use in long-span culvert installations in Reference 18. As developed Reference 18 and outlined below, the orthotropic model is useful for simulating the directional stiffness obtained from reinforced soil. This is based on the unit cell concept.

The upper portion of Figure 3.3.2-1 illustrates a unit cell of soil with a single reinforcing strip at the center of the cell extending in the x-direction. The y-z face of the cell measures d inches by b inches with the inference that the

reinforcement strips repeat themselves every d inches in the y -direction and every b inches in the z -direction to form a uniform grid in some large zone of soil.

Figure 3.3.2-1 Unit cell concept for modeling reinforced earth



Assuming the reinforcing strips act as one-dimensional elements and remain bonded to the soil, the composite stiffness in the x -direction is determined by applying a uniform strain ϵ_x while holding all other strains in the soil cell to zero. As illustrated in the bottom of Figure 3.3.2-1, the uniaxial straining produces stresses in the soil and the reinforcing strip as expressed below.

$$\sigma_{\text{soil}} = M_s \epsilon_x \tag{Equation 3.3-6}$$

$$\sigma_{\text{rs}} = E_{\text{rs}} \epsilon_x \tag{Equation 3.3-7}$$

where, $\sigma_{\text{soil}}, \sigma_{\text{rs}}$ = stress in x -direction for soil and reinforcing strip, respectively.

M_s = confined modulus of isotropic soil

E_{rs} = Young's modulus of reinforcing strip

To determine the composite stress-strain modulus in the x direction, we evoke force equilibrium such that the net force from the composite stress over the cell face is equal to force contributions from the soil and reinforcement,

$$A_{\text{cell}}\sigma_x = A_{\text{soil}}\sigma_{\text{soil}} + A_{\text{rs}}\sigma_{\text{rs}} \quad \text{Equation 3.3-8}$$

where, $A_{\text{cell}} = bd = \text{area of unit cell face}$

$A_{\text{soil}} = bd - wt = \text{soil area per unit cell}$

$A_{\text{rs}} = wt = \text{reinforcing strip area per unit cell}$

Replacing σ_{soil} , σ_{rs} in the above equilibrium equation with their strain equivalents, we have the key stress-strain expression for the x-direction as,

$$\sigma_x = (M_s + \alpha(E_{\text{rs}} - M_s))\epsilon_x \quad \text{Equation 3.3-9}$$

where, $\alpha = wt/bd = \text{ratio of reinforcement area to unit cell area.}$

To simplify and summarize, let the second term in the above expression be written as, $R = \alpha (E_{\text{rs}} - M_s)$, which is the contribution of reinforcing strip to the C_{11} component of the constitutive matrix for a unit cell area of soil. Thus, the final form of the orthotropic constitutive matrix may be written as,

$$\begin{pmatrix} \Delta\sigma_x \\ \Delta\sigma_y \\ \Delta\tau \end{pmatrix} = \begin{pmatrix} M_s + R & M_s K_0 & 0 \\ M_s K_0 & M_s & 0 \\ 0 & 0 & G \end{pmatrix} \begin{pmatrix} \Delta\epsilon_x \\ \Delta\epsilon_y \\ \Delta\gamma \end{pmatrix} \quad \text{Equation 3.3-10}$$

where, $R = \alpha(E_{\text{rs}} - M_s) = \text{additional soil modulus stiffness in x-direction due to reinforcing strips}$

$\alpha = wt/bd = \text{ratio of reinforcement area to area of unit cell}$

$E_{\text{rs}} = \text{Young's modulus of reinforcing strips}$

$M_s = \text{confined modulus of isotropic soil} = E(1 - \nu)/(1 + \nu)(1 - 2\nu)$

$K_0 = \text{lateral coefficient of isotropic soil} = \nu/(1 - \nu)$

$G = \text{shear modulus of isotropic soil} = E/2(1 + \nu)$

To apply the above in the CANDE program, input $C(1,1) = M_s + R$, $C(1,2) = M_s K_0$, $C(2,2) = M_s$, and $C(3,3) = G$.

3.4 Overburden Dependent Soil Model

The overburden-dependent model is the application of the isotropic elastic model in a series of steps. Each step represents an increment of soil fill or overburden pressure so that the elastic moduli are modified at each step to account for an increased stiffness due to increased confining pressure.

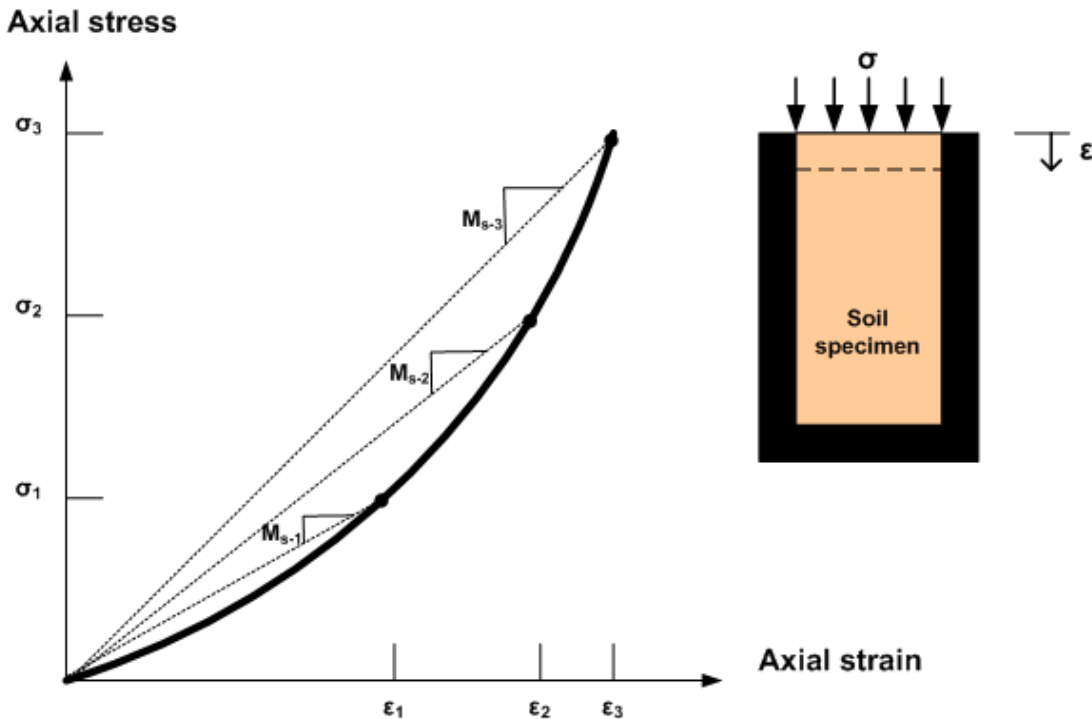
Implicit in the model is the assumption that soil stiffness increases with overburden pressure. This assumption holds true when the soil is in a state of confined compression (one-dimensional straining), wherein increased overburden pressure further increases the lateral confining pressure and the soil tends to stiffen. On the other hand, if the soil is unconfined, then increased overburden pressure will not stiffen the soil but, on the contrary, stiffness will be reduced due to shear straining as observed in standard tri-axial tests.

The significant point is that overburden-dependent models are only valid insofar as the soil is predominantly in a state of confined compression. Generally, gravity loading of the soil promotes states of confined compression; however, in regions of strong interaction, such as certain areas in the vicinity of the pipe or around other inclusions, the assumption of confined compression is questionable.

3.4.1 Input data for overburden dependent model

The overburden-dependent model is characterized using the stress-strain data obtained from a confined compression test as illustrated in Figure 3.4.1-1. In this test, increasing levels of axial stress are applied to the top surface of the soil specimen and the corresponding axial strains are measured for each stress level, all other normal strains are zero due to the confining chamber.

Figure 3.4.1-1 Illustration of confined compression test data and secant confined moduli



As illustrated in the figure, the secant confined modulus is defined as, $M_{si} = \sigma_i / \epsilon_i$, and generally increases as overburden pressure increases. The word secant is used to denote that M_{si} is the slope of total stress to total strain, not an incremental relationship. Experimental results from confined compression test are used to compute and list secant moduli values as function of overburden pressure as depicted in the table below for n data points.

Table 3.4.1-1 Data table of secant moduli versus overburden pressure.

Overburden Pressure (Vertical stress)	Secant confined Modulus $M_{si} = \sigma_i/\epsilon_i$	Secant Young's modulus $E_{si} = M_{si} (1+\nu)(1-2\nu)/(1-\nu)$
σ_1	M_{s1}	E_{s1}
σ_2	M_{s2}	E_{s2}
σ_3	M_{s3}	E_{s3}
*	*	*
*	*	*
*	*	*
σ_n	M_{sn}	E_{sn}

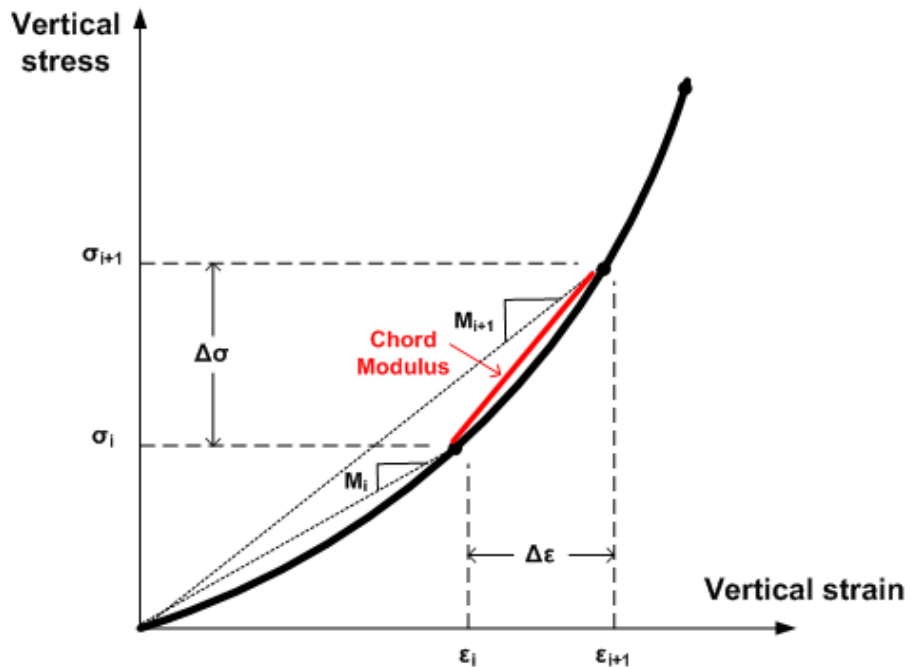
For most soils the lateral soil pressure exerted on the sides of the chamber typically increases in direct proportion to the overburden pressure. Thus, the lateral coefficient K_0 , which is the ratio of lateral pressure to vertical stress, remains practically constant for all levels of vertical stress. Since Poisson ratio $\nu = K_0/(1+K_0)$, a constant value of Poisson ratio is used to provide the second elastic parameter for the overburden dependent model. Accordingly, as shown in the last column of the above table, secant values for Young's moduli are easily computed by multiplying secant confined moduli by a constant factor $\beta = (1+\nu)(1-2\nu)/(1-\nu)$, which is derived from elasticity parameter equivalent relationships (see Table 3.2.1-1).

To briefly recap, Table 3.4.1-1 is representative of the data needed to exercise the overburden model in a typical soil-structure problem. CANDE-2022 has "canned tables" of secant Young's moduli corresponding to increasing values for overburden pressure for typical soils that may be used in lieu of actual test data.

3.4.2 Overburden model development

To incorporate the overburden pressure data into the incremental stress-strain relationship, it is necessary to convert the secant moduli data into chord moduli relating increments of vertical stress to increments of vertical strain in going from load step i to step $i+1$ as illustrated in the figure below.

Figure 3.4.2-1 Incremental stress-strain relationship and chord modulus



Specifically for each plane-strain element in the soil system, the incremental constitutive matrix has the form,

$$\begin{pmatrix} \Delta\sigma_x \\ \Delta\sigma_y \\ \Delta\tau \end{pmatrix} = \begin{pmatrix} C_{11} & C_{12} & 0 \\ C_{12} & C_{11} & 0 \\ 0 & 0 & C_{33} \end{pmatrix} \begin{pmatrix} \Delta\varepsilon_x \\ \Delta\varepsilon_y \\ \Delta\gamma \end{pmatrix} \quad \text{Equation 3.4-1}$$

where C_{11} , C_{12} , and C_{33} are chord moduli dependent on the stress state at load step i and step $i+1$.

Letting σ_i and ε_i represent the known vertical stress and strain at load step i in element $\#n$, the increment of vertical stress in element $\#n$ is estimated by determining the vertical pressure contributions of all elements above element $\#n$ that enter the soil system in load step $i+1$. Tersely, this is stated as,

$$\Delta\sigma \approx \text{increment of overburden pressure from added soil elements above element } \#n$$

The algorithm that computes the estimate for $\Delta\sigma$ utilizes the finite element mesh topology and element material property data to determine which elements entering the system during load step $i+1$ are above element $\#n$ along with their contributing pressures. The algorithm is laborious but straightforward.

Once the estimate for $\Delta\sigma$ is obtained, the chord moduli (see above figure) may be determined as,

$$C_{11} = \frac{\Delta\sigma}{(\sigma_i + \Delta\sigma)/M_{i+1} - \varepsilon_i} \quad \text{Equation 3.4-2}$$

$$C_{12} = K_0 C_{11} \quad \text{Equation 3.4-3}$$

$$C_{33} = \frac{1}{2}(1-K_0)C_{11} \quad \text{Equation 3.4-4}$$

where, σ_i , ε_i = known stress and strain values in element $\#n$ at load step i .

M_{i+1} = secant confined modulus interpolated from data table at pressure $\sigma_i + \Delta\sigma$.

$K_0 = \nu/(1-\nu)$ = constant lateral coefficient (ν = Poisson ratio)

Herein lies the advantage of an overburden-dependent model over the nonlinear models to be described next. That is, to advance the solution from step i to $i+1$, the overburden-dependent chord moduli are determined based on the soil layering within the finite element mesh, not on a trial solution. Thus, there are no iterations within the load step and convergence is not an issue with the overburden dependent soil model.

3.4.3 Overburden dependent secant moduli data tables in CANDE

For reference, reasonable ranges of Young's secant moduli are provided in Table 3.4.3-1 along with suggested values for Poisson ratio. The table offers three broad categories of soil; granular, mixed and cohesive for two compaction levels, fair and good.

Table 3.4.3-1 – Secant Young's modulus versus overburden pressure

Soil Class→ Compaction→ MATNAM→	Granular		Mixed		Cohesive	
	Good	Fair	Good	Fair	Good	Fair
	GGOOD	GFAIR	MGOOD	MFAIR	CGOOD	CFAIR
Overburden Pressure psi	Young's Modulus psi	Young's Modulus psi	Young's Modulus psi	Young's Modulus psi	Young's Modulus psi	Young's Modulus psi

5	1,100	550	600	400	250	150
10	1,300	750	850	550	325	200
15	1,500	850	1,000	600	375	225
20	1,650	1,000	1,100	700	375	250
25	1,800	1,100	1,200	750	400	250
30	1,900	1,150	1,250	800	400	250
40	2,100	1,300	1,350	900	400	250
50	2,250	1,400	1,450	900	400	250
Poisson ratio (pressure independent)	0.30 to 0.35		0.30 to 0.40		0.33 to 0.40	

The above values are a composite of seven different references as well as experimental data from the original CANDE investigation (Reference 1). As a whole the data values are conservative (low side) and are suitable for design if actual soil data is not available.

3.5 Duncan and Duncan/Selig Soil Models

The original Duncan and Duncan/Selig soil models are variable-modulus elasticity formulations using stress-dependent equations for Young’s modulus and bulk modulus. The Duncan form and Duncan/Selig form are very similar, differing slightly in the expression for the bulk modulus function. Both forms of the soil models are considered to be very representative of actual soil behavior particularly for representing the stress-dependent behavior of backfill soil in culvert installations. Basically, the models exhibit stiffening of constitutive moduli when confining stress increases and softening when shear stress increases.

Duncan’s original work for the Young’s modulus formulation, which is based on a hyperbolic stress-strain relationship, dates back to 1970 (Reference 19) and remains today as originally developed. In 1978 (Reference 20), Duncan and his colleagues introduced a variable bulk modulus to serve as the second constitutive parameter, replacing the previous assumption of a constant Poisson ratio. The bulk modulus function is based on a power law function of confining pressure. Today, Duncan’s original Young’s modulus formulation together with the power-law bulk modulus function is referred to as the Duncan soil model.

Selig proposed an alternative form of the bulk modulus function in 1988 (Reference 21). Selig’s bulk modulus function is based on an observed hyperbolic relationship between volumetric strain and hydrostatic pressure from soil specimens in hydrostatic compression. Thus, the so-called Duncan/Selig soil model is based on Duncan’s original Young’s modulus formulation and Selig’s hyperbolic bulk modulus formulation. Selig also performed independent tests to characterize the parameters of the Duncan/Selig model.

In 2015 Katona introduced a Modified form of Duncan and Duncan/Selig soil models to simulate plastic-like behavior with permanent deformation upon unloading (Reference 29). That is, although the original model is excellent in tracking the nonlinear behavior of soils in loading environments, it retraces the same stress-strain path upon unloading. Consequently, the original model does not predict residual deformation, which is invariably observed in laboratory soil specimens following a load-unload cycle. The new modified Duncan/Selig model produces permanent deformations upon unloading similar to advanced plasticity models. No new material parameters are introduced into the modified formulation; thus, the large existing data base of Duncan/Selig parameters remains valid for the modified formulation.

In the following sections, the original Duncan and Duncan/Selig models are presented first followed by the Katona modification given in the last section. The CANDE-2022 computer program provides the option to “turn on” or “turn off” the modified formulation at the user’s discretion.

3.5.1 Plane-strain constitutive matrix

From an overall perspective, the Duncan and the Duncan/Selig soil models are used to define the nonlinear components of an isotropic, elasticity-based constitutive matrix for plane-strain conditions as expressed below.

$$\begin{pmatrix} \Delta\sigma_x \\ \Delta\sigma_y \\ \Delta\tau \end{pmatrix} = \begin{pmatrix} C_{11} & C_{12} & 0 \\ C_{12} & C_{11} & 0 \\ 0 & 0 & C_{33} \end{pmatrix} \begin{pmatrix} \Delta\varepsilon_x \\ \Delta\varepsilon_y \\ \Delta\gamma \end{pmatrix} \quad \text{Equation 3.5-1}$$

where, $\Delta\sigma_x, \Delta\sigma_y, \Delta\tau$ = stress increments for x-direction, y-direction and shear components, respectively
 $\Delta\varepsilon_x, \Delta\varepsilon_y, \Delta\gamma$ = strain increments for x-direction, y-direction and shear components, respectively
 C_{11}, C_{12}, C_{33} = nonlinear coefficients dependent on Young's modulus and bulk modulus functions.

The table below shows the relationship between the constitutive matrix components and the elastic functions.

Table 3.5.1-1 Components for constitutive matrix relationship to moduli functions

Components of Constitutive matrix	E = Young's modulus B = bulk modulus (E, B)	E = Young's modulus v = Poisson ratio (E, v)
$C_{11} =$	$\frac{3B(3B + E)}{9B - E}$	$\frac{E(1 - v)}{(1 + v)(1 - 2v)}$
$C_{12} =$	$\frac{3B(3B - E)}{9B - E}$	$\frac{Ev}{(1 + v)(1 - 2v)}$
$C_{33} =$	$\frac{3BE}{9B - E}$	$\frac{E}{2(1 + v)}$

The middle column in the above table defines the matrix coefficients C_{11} , C_{12} and C_{13} in terms of Young's modulus and bulk modulus, which are the elastic parameter functions developed in the current Duncan and Duncan Selig models. The third column defines the matrix coefficients in terms of Young's modulus and Poisson ratio, which was the 1970 form of the Duncan model. We will return to the implications of the constitutive matrix after the functional forms of Young's modulus and bulk modulus are presented.

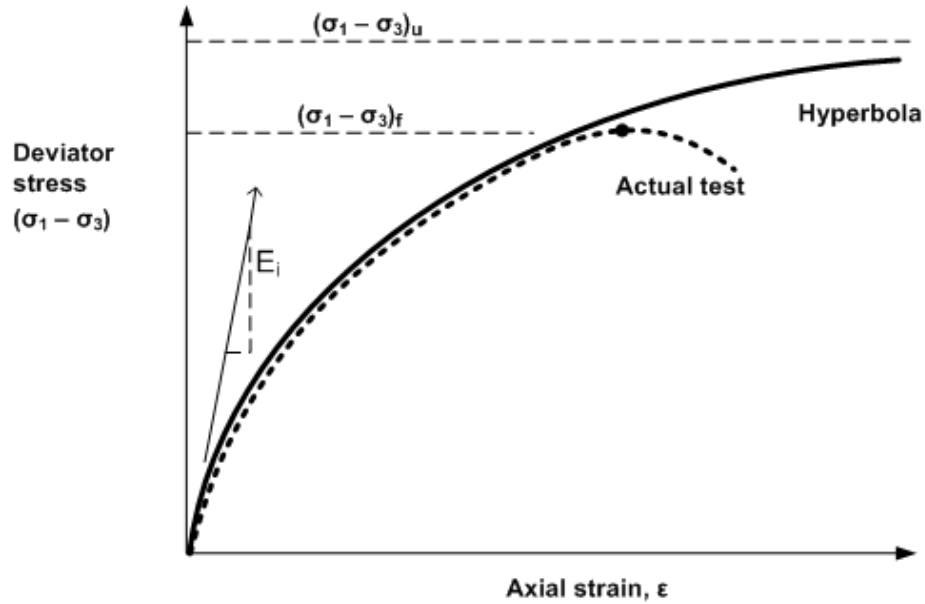
3.5.2 Duncan Young's modulus development

Duncan's formulation is based on experimental observations of soil behavior from standard tri-axial tests. A standard tri-axial test is conducted by placing a cylindrical soil specimen in a pressure chamber and initially subjecting the specimen to a uniform hydrostatic pressure, called σ_3 . Next a steadily increasing axial load is applied to the specimen producing a net axial stress, called σ_1 , which includes the hydrostatic pressure. Note that σ_3 and σ_1 are principal stresses in the lateral and axial directions, respectively. The difference in principal stresses $\sigma_1 - \sigma_3$ is called the deviator stress and is equal to twice the maximum shear stress occurring on 45-degree plane.

As the axial stress increases, axial strain is computed by measuring the axial shortening of the specimen divided by the specimen length. Note the measured axial strain does not include the initial hydrostatic strain.

The dashed curve in Figure 3.5.2-1 is a plot of deviator stress versus axial strain for a typical tri-axial test. Here, $(\sigma_1 - \sigma_3)_f$ is the measured maximum deviator stress at failure, and E_i is the initial slope representing Young's modulus at zero deviator stress. As discussed subsequently, $(\sigma_1 - \sigma_3)_f$ and E_i are dependent on the hydrostatic stress level.

Figure 3.5.2-1 Deviator stress versus axial strain for tri-axial test and hyperbolic approximation



Duncan hyperbolic function. Duncan's fundamental insight is that the experimental curve is fairly well approximated by equating the deviator stress to a hyperbolic function of axial strain as follows,

$$\sigma_1 - \sigma_3 = \frac{\varepsilon}{\frac{1}{E_i} + \frac{\varepsilon}{(\sigma_1 - \sigma_3)_u}} \quad \text{Equation 3.5-2}$$

where, E_i = initial slope for Young's modulus (dependent on minimum principal stress)

$(\sigma_1 - \sigma_3)_u$ = ultimate deviator stress from hyperbolic model (dependent on minimum principal stress)

ε = axial strain, not including initial hydrostatic strain

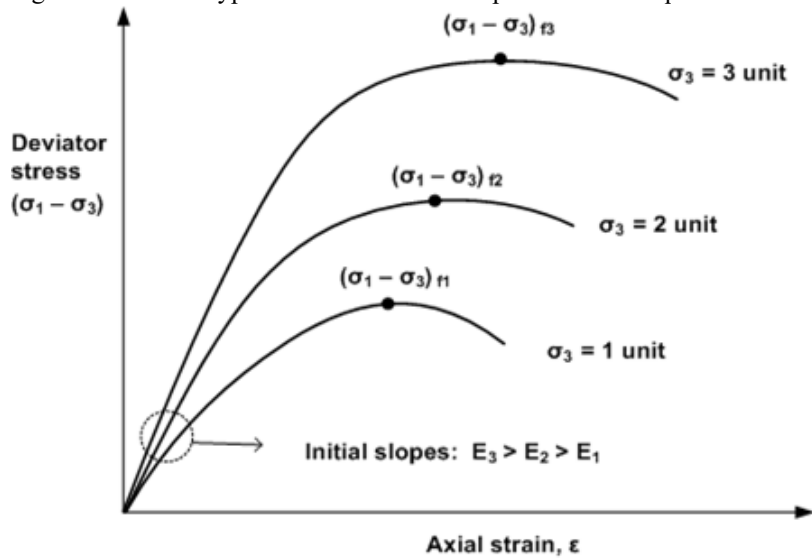
As illustrated in by the solid curve in the above figure, the hyperbolic function provides a good representation of the actual test data up to the point of actual failure, $(\sigma_1 - \sigma_3)_f$. Thereafter the hyperbolic function tends to overshoot the actual softening behavior as the hyperbolic function asymptotically approaches the limit, $(\sigma_1 - \sigma_3)_u$. In order to preserve the good curve-fit from zero to actual failure, it should be evident that $(\sigma_1 - \sigma_3)_u$ cannot, in general, be set equal to the actual failure deviator stress, $(\sigma_1 - \sigma_3)_f$. Rather, the Duncan model introduces a model parameter called the failure ratio defined as,

$$R_f = \frac{(\sigma_1 - \sigma_3)_f}{(\sigma_1 - \sigma_3)_u} \leq 1.0 \quad \text{Equation 3.5-3}$$

Given that $(\sigma_1 - \sigma_3)_f$ is characterized from actual experimental data, then Equation 3.5-3 may be used to define $(\sigma_1 - \sigma_3)_u$ for the hyperbolic function.

To complete the hyperbolic model, functional forms for $(\sigma_1 - \sigma_3)_f$ and E_i must be defined based on a sequence of tri-axial tests. Figure 3.5-2 illustrates the typical behavior of a specific soil specimen subjected to a series of tri-axial tests with increasing confining pressure.

Figure 3.5.2-2 Typical behavior of a soil specimen in a sequence of tri-axial tests.



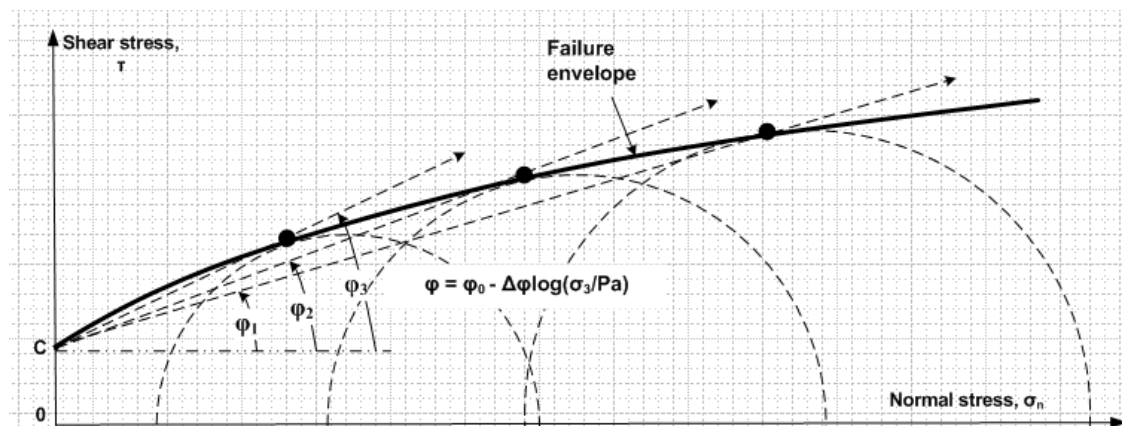
Initial Young’s modulus. Based on a wide variety of soil tests as typified by the above figure, the initial modulus is observed to increase with confining pressure according to the following power law,

$$E_i = K P_a (\sigma_3 / P_a)^n \tag{Equation 3.5-4}$$

- where, E_i = initial Young’s modulus when deviator stress = 0
- K = dimensionless magnitude of initial Young’s modulus
- P_a = atmospheric pressure used to nondimensionalize parameters K and n
- n = power-law coefficient usually less than 1.0
- σ_3 = confining pressure, minimum magnitude of principle stress

Mohr-Coulomb failure envelope. As portrayed in the Figure 3.5-2, the deviator stress at failure increases with confining pressure. Based on the well-known Mohr-Coulomb failure theory, the $(\sigma_1 - \sigma_3)_{fi}$ data points define a failure envelope in terms of normal stress and shear stress as depicted in the figure below.

Figure 3.5.2-3 Failure envelope in normal and shear stress space



Typically, the Mohr-Coulomb failure surface is a straight line defined by two constants, C and ϕ_0 , representing the cohesion intercept and a constant soil friction angle, respectively. As illustrated in the above figure, a more general form of the Mohr-Coulomb failure surface is used in this development wherein the soil friction angle is a decreasing function of the confining pressure. Often, this is a better representation of actual soil behavior.

Based on the generalized Mohr-Coulomb theory, the tri-axial deviator stress at failure is characterized as follows,

$$(\sigma_1 - \sigma_3)_f = \frac{2C \cos\phi + 2\sigma_3 \sin\phi}{1 - \sin\phi} \quad \text{Equation 3.5-5}$$

where, $\phi = \phi_0 - \Delta\phi \log_{10}(\sigma_3/P_a)$ = variable soil friction angle Equation 3.5-6

C = cohesion intercept, units of stress

ϕ_0 = Reference soil friction angle at $\sigma_3/P_a = 1$

$\Delta\phi$ = reduction of soil friction angle for 10-fold increase in σ_3

Tangent Young's modulus. Tangent Young's modulus is equal to the derivative of axial stress to axial strain under the conditions of tri-axial testing wherein the confining stress is constant. Since all the terms are now identified in Equation 3.5-2, we can compute tangent Young's modulus by forming the derivative $d\sigma_1/d\varepsilon$ and replacing strain values with equivalent stresses via Equation 3.5-2 to arrive at,

$$E_t = E_i \left[1 - \frac{R_f (1 - \sin\phi)(\sigma_1 - \sigma_3)}{2(C \cos\phi + \sigma_3 \sin\phi)} \right]^2 \quad \text{Equation 3.5-7}$$

where, E_t = tangent Young's modulus dependent on stress state

σ_1 = maximum compressive principal stress

σ_3 = minimum compressive principal stress

Equation 3.5.7 is fundamental for both the Duncan soil model and the Duncan/Selig soil model.

3.5.3 Bulk modulus formulations

By definition, the tangent bulk modulus is the change in mean stress divided by the change in volumetric strain, which is expressed as

$$B_t = \frac{d\sigma_m}{d\varepsilon_{vol}} \quad \text{Equation 3.5-8}$$

where, B_t = tangent bulk modulus, usually stress dependent for soils.

$\sigma_m = (\sigma_{11} + \sigma_{22} + \sigma_{33})/3$ = mean average stress, also called hydrostatic stress

$\varepsilon_{vol} = dV/V_0 = \varepsilon_{11} + \varepsilon_{22} + \varepsilon_{33}$ = volumetric strain

Duncan bulk modulus function. Duncan used tri-axial test data including measurements of volumetric strain to obtain experimental values for the tangent bulk modulus computed as,

$$B_{measured} = \frac{1}{3} \Delta\sigma_{axial} / \Delta\varepsilon_{vol} \quad \text{Equation 3.5-9}$$

For a given confining pressure, the change in axial stress and corresponding change in volumetric strain are measured when the axial stress reaches 70% of the failure stress or the volumetric strain peaks in contraction, whichever occurs first.

Based on a series of tri-axial tests with increasing confining pressure, Duncan proposed a power-law function (very similar to the initial Young's modulus function) to describe the tangent bulk modulus as,

$$B_t = K_b P_a (\sigma_3 / P_a)^m \quad \text{Equation 3.5-10}$$

where, K_b = dimensionless magnitude of tangent bulk modulus

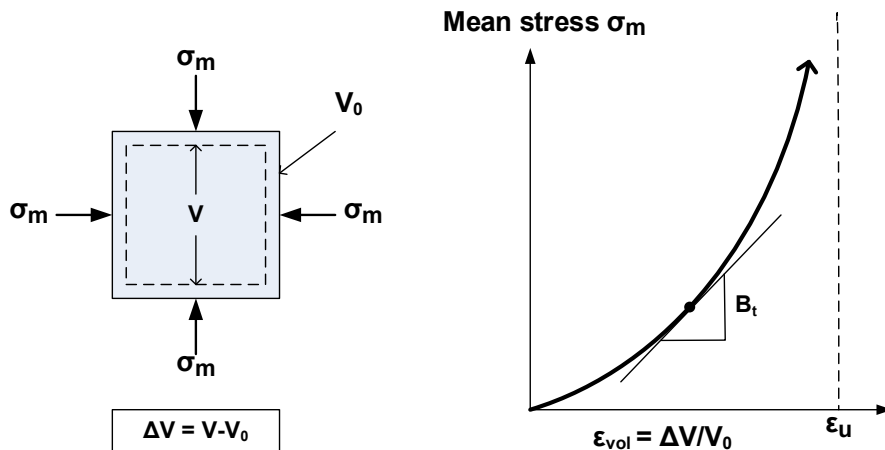
P_a = atmospheric pressure used to nondimensionalize parameters K_b and m

m = power-law coefficient usually less than 1.0

σ_3 = confining pressure or minimum magnitude of principle stress

Selig bulk modulus function. Selig developed an alternate form of the tangent bulk modulus function based on hydrostatic tests. In the hydrostatic test the soil specimen is compressed under increasing confining pressure applied equally in all directions and the change of volume is measured as function of confining pressure as depicted in the figure below.

Figure 3.5.3-1 Hydrostatic test and Selig's hyperbolic model



Selig observed that the experimental curves relating mean stress to volumetric strain is reasonably described by a hyperbolic equation in the form,

$$\sigma_m = \left(\frac{B_i}{1 - \epsilon_{vol} / \epsilon_u} \right) \epsilon_{vol} \quad \text{Equation 3.5-11}$$

where, B_i = initial tangent bulk modulus when volumetric strain = 0.

ϵ_u = ultimate volumetric strain at large hydrostatic stress.

As illustrated in Figure 3.5.3-1, the tangent bulk modulus is determined by forming the derivative $d\sigma_m / d\epsilon_{vol}$ and again using Equation 3.5-11 to replace volumetric strain with hydrostatic stress to get the final result,

$$B_t = B_i [1 + \sigma_m / (B_i \varepsilon_u)]^2 \quad \text{Equation 3.5-12}$$

where, B_t = Selig form of tangent bulk modulus dependent on mean hydrostatic stress.

3.5.4 Summary of Original Duncan and Duncan/Selig soil models.

To summarize the tangent Young's modulus function, Equation 3.5-7 is written in a more compact form as shown by Equation 3.5-13.

$$E_t = E_i \left[1 - \frac{\sigma_d}{\sigma_{dMax}} \right]^2 \quad \text{Equation 3.5-13}$$

Where, $E_i = K P_a \left(\frac{\sigma_3}{P_a} \right)^n \quad \text{Equation 3.5-14}$

$$\sigma_{dMax} = \frac{2(C \cos \phi + \sigma_3 \sin \phi)}{R_f (1 - \sin \phi)} \quad \text{Equation 3.5-15}$$

$$\phi = \phi_0 - \Delta \phi \log_{10} (\sigma_3 / P_a) \quad \text{Equation 3.5-16}$$

Definitions of the symbols are listed below.

- E_t = tangent Young's modulus dependent on complete stress state,
- E_i = initial Young's modulus dependent on minimum compressive stress,
- σ_{dMax} = Maximum deviatoric stress at failure
- ϕ = angle of internal friction dependent on minimum compressive stress,
- σ_1 = maximum compressive principal stress,
- σ_3 = minimum compressive principal stress,
- P_a = atmospheric pressure, a constant for units of stress.

Material properties required for the above tangent Young's modulus functions are,

- K = dimensionless magnitude of initial Young's modulus,
- n = power-law coefficient for initial modulus usually less than 1.0,
- C = cohesion intercept for failure, units of stress,
- ϕ_0 = initial soil friction angle of failure surface,
- $\Delta \phi$ = reduction of soil friction angle for 10-fold increase in σ_3 ,
- R_f = failure ratio of actual to model failure stress usually less than 1.0.

For the second elasticity function, the choice is between Duncan's tangent bulk modulus power law or Selig's tangent bulk modulus derived from a hyperbolic relationship between hydrostatic pressure and volumetric strain.

Duncan's tangent bulk modulus power-law function is given by,

$$B_t = K_b P_a (\sigma_3 / P_a)^m \quad \text{Equation 3.5-17a}$$

Material properties required for Duncan's tangent bulk modulus power law are,

- K_b = dimensionless magnitude of tangent bulk modulus,
- m = power-law coefficient usually less than 1.0.

Alternatively, Selig's tangent bulk modulus function is written compactly as,

$$B_t = B_i \left[1 + \frac{\sigma_m}{\sigma_{mRef}} \right]^2 \quad \text{Equation 3.5-17b}$$

where, $\sigma_m = \frac{1}{3}(\sigma_1 + \sigma_2 + \sigma_3)$ = average principal stress.

and, $\sigma_{mRef} = B_i \varepsilon_u$ = reference stress (a constant)

Material properties required for Selig's tangent bulk modulus function are,

B_i = initial tangent bulk modulus when hydrostatic stress is zero,

ε_u = ultimate volumetric strain at large hydrostatic stress.

See Section 3.58 for plastic-like unload/reload formulations.

3.5.5 Behavioral characteristics and special considerations

The behavioral characteristics and limitations of the Duncan and the Duncan/Selig soil model are nearly identical and are enumerated below along with discussions on special treatments for limiting cases. Recall that maximum shear stress is equal to half the difference in principal stresses, $(\sigma_1 - \sigma_3)/2$.

If confining pressure increases while shear stress is held constant, E_t and B_t become stiffer. However, if maximum shear increases with constant confining pressure, E_t becomes softer while B_t remains constant.

Shear failure is said to occur when E_t approaches zero as shear stress increases to the failure limit. To avoid numerical problems, the bracketed term in Equation 3.5-13, which varies from 1.0 to 0.0 as shear stress increases, is limited to the minimum value 0.05 so that $E_t = 0.0025E_i$ is the minimum tangent Young's modulus, which is effectively a near-zero stiffness.

Tension failure is said to occur when the minimum compressive stress σ_3 becomes tensile wherein most soils breakdown and lose all stiffness. This is simulated in the soil models by assigning a small limiting value to the minimum compressive stress, $\sigma_3/Pa = 0.1$, so that E_t and B_t are near-zero stiffness values whenever the minimum principal stress approaches tension.

Although E_t and B_t are developed as two independent functions, energy considerations require constraints between the functions (e.g., see Table 3.5-1). The soil models programmed in CANDE satisfy the energy constraints by enforcing,

$$E_t > 0, \text{ and } E_t/3 < B_t < 8E_t.$$

Lower and upper limits on B_t are equivalent to maintaining Poisson ratio in the range, $0 < \nu < 0.48$. The programmed soil models also have the option to use a constant Poisson ratio instead of the tangent bulk modulus functions.

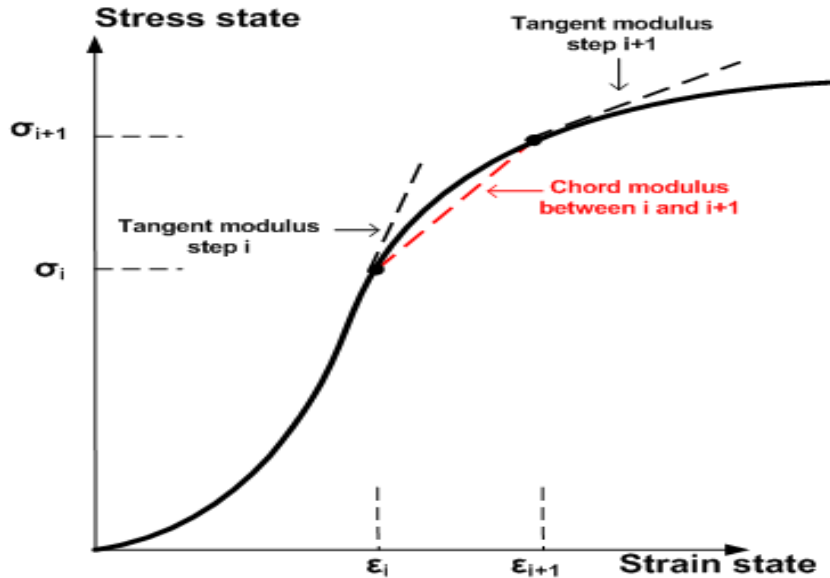
It should be noted that the original Duncan and Duncan/Selig soil models are nonlinear elastic and behave the same in loading or unloading. For the record, it is noted that some investigators have attempted to incorporate ad hoc unloading algorithms into the Duncan soil model. Some of these algorithms, which are not based on plasticity concepts, violate the continuity principal of load path.

Section 3.5.8 presents a thermodynamically admissible algorithm for unloading and reloading the Duncan and Duncan/Selig soil models based on plasticity concepts that satisfy the continuity principle. This formulation, called the Katona modification of Duncan/Selig soil models, is programmed into CANDE and be selected at the user's discretion.

3.5.6 Implementation of soil models and nonlinear solution strategy

Recall that Equation 3.5-1 is the fundamental plane-strain constitutive matrix relating stress increments to strain increments from a known stress-strain state at load step i to the unknown stress-strain state at load step $i+1$. Accordingly, the matrix coefficients, C_{11} , C_{12} and C_{13} are chord moduli as notionally illustrated on the stress-strain curve in the figure below along with the tangent moduli at the beginning and end of the load step.

Figure 3.5.6-1 Chord and tangent moduli on a notional stress-strain curve.



Chord moduli representation. To convert the Duncan and Selig tangent Young's modulus and tangent Bulk modulus to chord moduli suitable for defining C_{11} , C_{12} and C_{13} , the following averaging technique is used,

$$E_c = (1-r)E_{t_i} + rE_{t_{i+1}} \quad \text{Equation 3.5-18}$$

$$B_c = (1-r)B_{t_i} + rB_{t_{i+1}} \quad \text{Equation 3.5-19}$$

where E_c, B_c = chord moduli for Young's modulus and bulk modulus, respectively

$E_{t_i}, E_{t_{i+1}}$ = tangent Young's moduli at load step i and $i+1$, respectively

$B_{t_i}, B_{t_{i+1}}$ = tangent bulk moduli at load step i and $i+1$, respectively

r = averaging ratio usually taken as $1/2$.

The justification for averaging the tangent moduli to obtain the chord moduli follows from the mean-value-theorem of differential calculus, which implies that the process becomes exact as the size of the load step decreases. Generally, the averaging ratio is taken as $r = 1/2$. However as explained in the next paragraph, it is reasonable to set $r = 1$ when in situ soil elements enter the structural system for the first time. For this reason, the averaging ratio is treated as a material input parameter.

Entering soil elements. Soil elements enter the structural system in one of two categories. The first category applies to pre-existing or in-situ soil elements in which an initial state of stress exists but is generally not known prior to the solution. Elements entering in this category are typically part of the initial configuration and are assigned to the first construction increment.

The second category applies to fill soil elements, i.e., soil layers added to the system in a predefined construction schedule. Here, the initial stress state is non-existent prior to entry into the system. Both categories present special starting

problems for the iteration scheme because the initial stress state is unknown in the first category or nonexistent in the second category.

For the first category, the initial stress state can be determined iteratively by assuming the pre-existing soil zone is a construction increment loaded with its own body weight (and, if desired, a consolidation pressure). In this case the averaging ratio should be set to 1.0, so that, E_c and B_c are equal to the tangent values at the end of the load step because this corresponds to the existing stress state. When $r = 1$, the tangent moduli at the beginning of the load step have no influence on the averaging process. After the first construction increment is complete, the algorithm automatically changes $r = 1/2$ so that all subsequent moduli calculations represent chord values in going from a known stress state to an unknown stress state.

For the second category, soil layers entering the system for the first time have zero initial stress and zero initial stiffness at the beginning of the load step but gain stiffness at the end of the load step from self-weight and/or compaction load. In this case, using $r = 1/2$ implies the effective chord moduli during the load step is equal to one-half the tangent moduli at the end of the load step, which is considered to be a reasonable assumption. For all load steps following the initial load step, there is no longer any ambiguity and we set $r = 1/2$ because we know the stress state at the start of each subsequent load step.

To start the iteration process for entering elements of either category, some initial guess must be made for the end-of-load-step tangent moduli because the start-of-load step moduli are zero. Thus, in order to construct the first trial stiffness matrix, "dummy" principal stresses are used to get the first trial moduli value. The dummy principal stresses have no effect on the final converged solution, but they do influence the number of iterations required to achieve convergence. After an element has entered the system, the initial guess for end-of-load-step tangent moduli for all subsequent load steps are equated to the last calculated values and the use of dummy principal stresses is not required.

Nonlinear solution summary. Based on the forgoing discussion, a summary on the nonlinear solution strategy is provided in the flowchart shown in Figure 3.5.6-2. The flow chart depicts the iteration cycle to determine the constitutive matrix of a soil element wherein the principal stresses from the last iteration are used make closer and closer estimates of the chord moduli until convergence occurs. Convergence of the algorithm occurs when the chord moduli obtained from two successive iterations differ by no more than 1% for all elements.

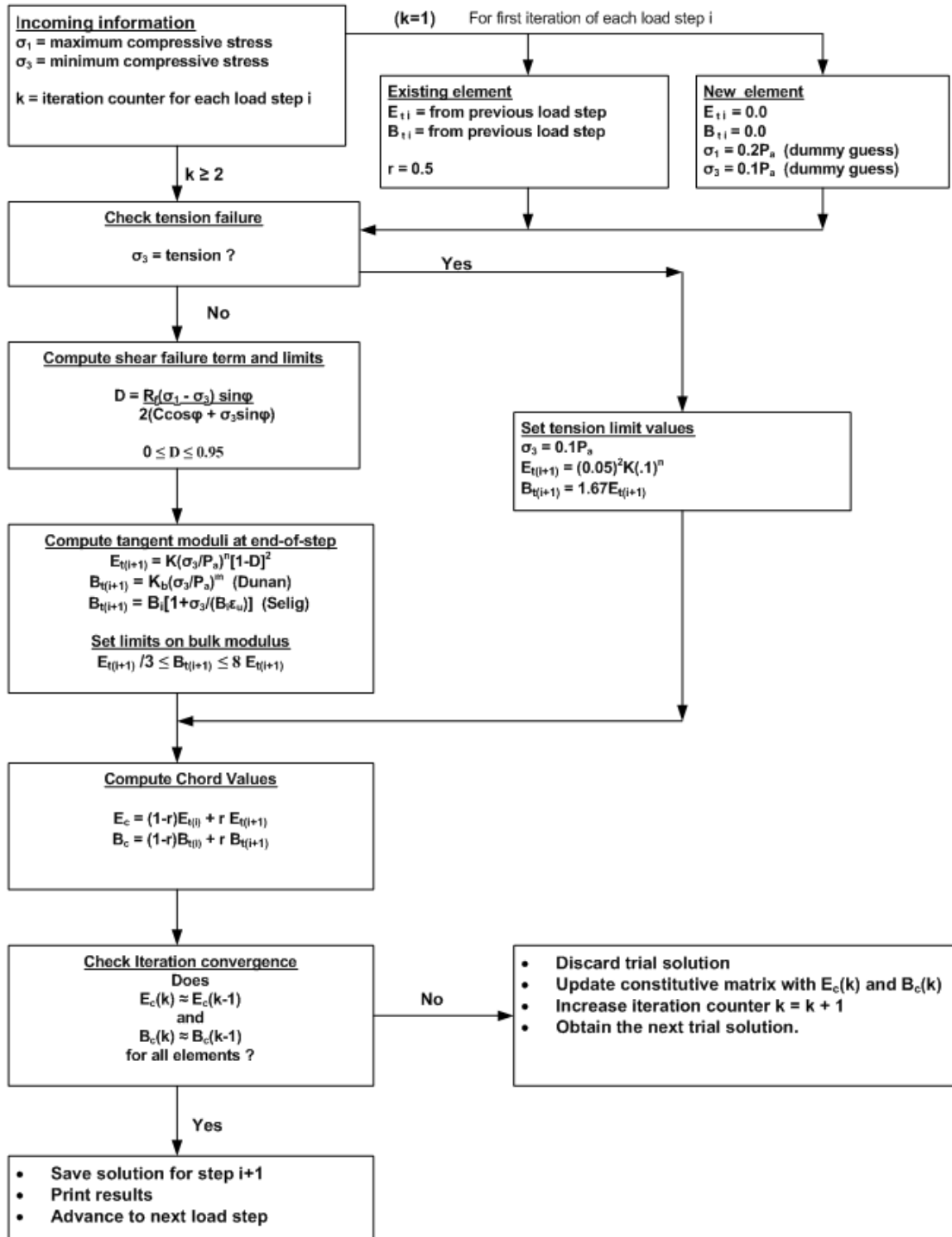
Two additional features of the algorithm not shown in the flow chart are listed below.

An under-relaxation scheme to improve the rate of convergence for the tangent moduli comes into play after the second iteration wherein each estimate of the end-of-load-step tangent moduli is a weighted average of the current estimate and the previous iteration estimate. This feature takes advantage of the observation that convergence occurs in an oscillatory manner.

A constant Poisson ratio option may be chosen by the user that replaces the tangent bulk modulus formulation. When the constant Poisson ratio option is exercised, the bulk modulus formulations are bypassed. Otherwise, the algorithm is essentially the same.

Figure 3.5.6-2 Duncan and Duncan/Selig flow chart for computing constitutive matrix.

Algorithm for Duncan and Duncan/Selig soil model from load step i to i+1



3.5.7 Recommended Duncan and Duncan/Selig parameters for standard soils

Whenever possible, the Duncan and/or Duncan Selig soil model parameters should be determined directly from tri-axial test equipment using established curve-fitting procedures. In many instances, however, tri-axial data may be unavailable, and so, it is convenient to establish standard parameter values for various types of soil and degrees of compaction.

Table 3.5.7-1 provides parameter values for the Duncan soil model for four soil classifications, each with three levels of compaction. These standard values, extracted from References 19 and 20, are conservative in the sense that they are the lower bounds of strength and moduli values observed from numerous tri-axial tests for each soil type. An independent study at the University of Notre Dame utilizing the same database verified that the table parameters give a good but conservative representation of the experimental data.

Table 3.5.7-1 Duncan soil model parameters (from Duncan Reference

Soil type and compaction	Young's Tangent Modulus Parameters						Bulk Parameters		Density reference (lb/ft ³)
	K	n	C	ϕ_0	$\Delta\phi$	R_f	K_b	m	
	(--)	(--)	(psi)	(deg)	(deg)	(--)	(--)	(--)	
CA105	600	0.40	0.0	42	9	0.7	175	0.2	150
CA95	300	0.40	0.0	36	5	0.7	75	0.2	140
CA90	200	0.40	0.0	33	3	0.7	50	0.2	135
SM100	600	0.25	0.0	36	8	0.7	450	0.0	135
SM90	300	0.25	0.0	32	4	0.7	250	0.0	125
SM85	150	0.25	0.0	30	2	0.7	150	0.0	120
SC100	400	0.60	0.5	33	0	0.7	200	0.5	135
SC90	150	0.60	0.3	33	0	0.7	75	0.5	125
SC85	100	0.60	0.2	33	0	0.7	50	0.5	120
CL100	150	0.45	0.4	30	0	0.7	140	0.2	135
CL90	90	0.45	0.2	30	0	0.7	80	0.2	125
CL85	60	0.45	0.1	30	0	0.7	50	0.2	120

In the above table the soil type is defined as follows: CA = Coarse Aggregates, SM = Silty Sand, SC = Silty-Clayey Sand and CL = Silty Clay. The compaction number is percent relative compaction, per AASHTO T-99. As an example, SM100 means silty sand compacted to 100% relative density per T-99.

In a similar manner Table 3.5.7-2 provides parameter values for the Duncan/Selig soil model for three soil classifications, each with five levels of compaction. These values were computed by Selig in Reference 21 and are generally conservative. The bulk modulus parameters were determined from hydrostatic tests which, according to Selig, tend to be more conservative than those determined from standard tri-axial tests.

Table 3.5.7-2 Duncan/Selig soil model parameters (from Selig Reference)

Soil type and compaction	Young's Tangent Modulus Parameters						Bulk Parameters		Density reference (lb/ft ³)
	K	n	C	ϕ_0	$\Delta\phi$	R_f	B_t/P_a	ϵ_u	
	(--)	(--)	(psi)	(deg)	(deg)	(--)	(--)	(--)	
SW100	1300	0.90	0.0	54	15	0.65	108.8	0.01	148
SW95	950	0.60	0.0	48	8.0	0.70	74.8	0.02	145
SW90	640	0.43	0.0	42	4.0	0.75	40.8	0.05	140
SW85	450	0.35	0.0	38	2.0	0.80	12.7	0.08	130
SW80	320	0.35	0.0	36	1.0	0.90	6.1	0.11	120
ML95	440	0.40	4.0	34	0.0	0.95	48.3	0.06	135
ML90	200	0.26	3.5	32	0.0	0.89	18.4	0.10	130
ML85	110	0.25	3.0	30	0.0	0.85	9.5	0.14	122
ML80	75	0.25	2.5	28	0.0	0.80	5.1	0.19	115
ML50	16	0.95	0.0	23	0.0	0.55	1.3	0.43	66
CL95	120	0.45	9.0	15	4.0	1.00	21.2	0.13	130
CL90	75	0.54	7.0	17	7.0	0.94	10.2	0.17	125
CL85	50	0.60	6.0	18	8.0	0.90	5.2	0.21	120
CL80	35	0.66	5.0	19	8.5	0.87	3.5	0.25	112

In the above table the soil type is defined as follows: SW = Gravelly sand, ML = Sandy silt, and CL = Silty Clay. The compaction number is percent relative compaction, per AASHTO T-99. As an example, SW95 means gravelly sand compacted to 95% relative density per T-99.

In the old CANDE-1989 documentation, Selig presented less conservative values for the tangent bulk modulus parameters by uniformly increasing the parameter B_t/P_a by a factor of 2.5 and uniformly decreasing ϵ_u by the factor 0.71. However, in recent years most researchers prefer the original hydrostatic data given in the above table.

3.5.8 Modified Duncan/Selig models for plastic deformation (Katona)

The Original Duncan and Duncan/Selig formulation is a nonlinear elastic model that travels the same stress-strain path in loading and unloading. Although the original model does an excellent job in capturing the nonlinear loading behavior, actual soil samples exhibit linear-like unloading and reloading similar to some plasticity-based constitutive models. In particular, the so-called PLAXIS soil hardening model employs a plasticity-based hardening rule that was developed to mimic the Duncan/Selig variable-modulus model under loading conditions along with elastic unloading and reloading behavior (Reference 30). One short coming of the PLAXIS model is that it requires new model material parameters that are not defined in the existing Duncan/Selig data base for typical soils and levels of compaction.

Clearly it is a desirable objective to modify the Duncan/Selig soil model to simulate the observed plastic-like behavior of soils in unloading and reloading conditions without introducing additional model parameters and retaining the variable modulus formulation. Specifically, the objective is to modify the model to unload and reload with appropriate linear elastic stiffness and to establish the criteria to define loading stress space versus unload/reload stress space. Underlying this objective is the requirement to prove that the modified model meets all thermodynamic restrictions for constitutive theories.

To achieve the objective, concepts from advanced plasticity theory are introduced into the original Duncan/Selig formulation such as stress-dependent history variables. However, the modified Duncan/Selig model remains a variable modulus formulation without explicitly dividing the strain into elastic and plastic components. The proposed formulation must satisfy thermodynamic restrictions, which under the assumptions of time and temperature independence, are reduced to the following two requirements:

Positive work. Work must be positive during any load increment without creation of energy during any load cycle. In this study it is shown that the modified Duncan/Selig formulation satisfies Drucker's postulate, which is a sufficient condition to satisfy this thermodynamic requirement.

Stress-strain continuity. Infinitesimal changes in the orientation of an incremental stress vector must result in small changes in the incremental strain vector; i.e., no discontinuous jumps in strain magnitude. In this study a plasticity-like normality factor is introduced into the variable Young's modulus function in order to satisfy the continuity requirement.

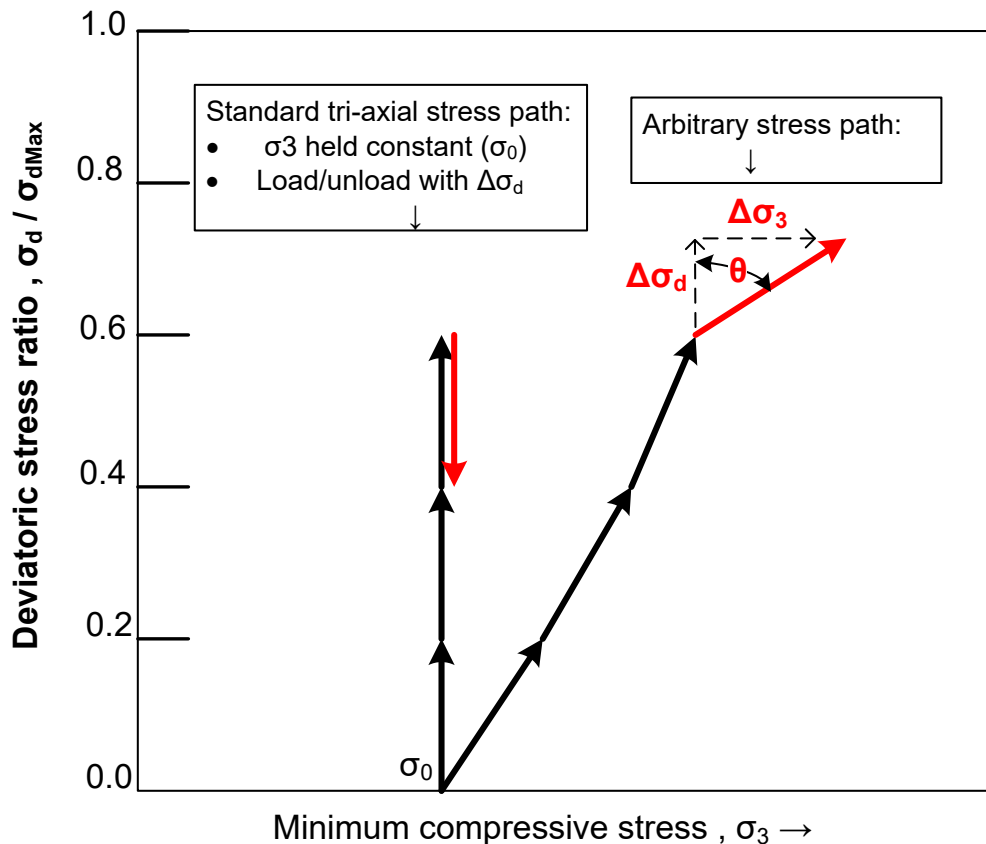
Young's Modulus Loading/Unloading Modification. To satisfy the stress-strain continuity requirement, Equation 3.5-13 is modified by inserting a continuity factor called β , where $0 \leq \beta \leq 1$, as defined below.

$$E_t = E_i \left[1 - \beta \frac{\sigma_d}{\sigma_{dMax}} \right]^2 \quad \text{Equation 3.5-20}$$

$$\beta = \text{Maximum} \left(\frac{\Delta\sigma_d}{\sqrt{\Delta\sigma_d^2 + \Delta\sigma_3^2}}, 0 \right) \quad \text{Equation 3.5-21}$$

The continuity factor is similar to the consistency condition in plasticity theory that asserts the growth of the yield surface is proportional to the applied stress vector acting in the direction normal to yield surface (dot product). To illustrate how the continuity factor accounts for loading and unloading consider the two stress paths shown in the figure below.

Figure 3.5.8-1. Illustration of load/unload stress paths for tri-axial and arbitrary conditions.



First consider the standard tri-axial stress path shown on the left side of the above figure wherein deviatoric load increments $\Delta\sigma_d$ are shown with vertical black arrows (since $\Delta\sigma_3 = 0$). For each of these loading steps, Equation 3.5-21 gives $\beta = \Delta\sigma_d / |\Delta\sigma_d| = 1$. Therefore, the tangent Young's modulus represents a pure loading condition exactly according to the original formulation, Equation 3.5-13, wherein the stiffness is decreasing. However, the fourth load increment shown with the red arrow is unloading (negative increment) so that we find, $-\Delta\sigma_d / |\Delta\sigma_d| = -1$, which means $\beta = 0$.

Therefore, the tangent Young’s modulus becomes $E_t = E_i$ satisfying the objective to unload elastically with the initial stiffness function.

It is important to realize that the reversal of stress at step 4 constitutes a “large” change in orientation because the direction of the stress vector is turned 180 degrees. Consequently, the abrupt change in stiffness from loading ($E_t \ll E_i$) to unloading ($E_t = E_i$) does not violate the continuity principle because the stress reversal is a “large” change in loading direction.

To demonstrate the continuity principle is satisfied for small changes in stress, consider the arbitrary stress path shown on the right side of Figure 3.5.5-1. Here each of the four load steps is associated with an arbitrary incremental stress vector with components $\Delta\sigma_3$, $\Delta\sigma_d$ that define an angle θ as illustrated in the last load step shown in red. Since $\beta = \cos \theta$ when θ is between -90 degrees and + 90 degrees, it is evident that a “small” change in θ from load step to load step will produce a small change in β and, hence a small change in the stiffness function; thereby satisfying the continuity requirement.

Based on the above concepts, loading and unloading definitions are summarized in the table below where it is observed the stiffness increases smoothly from the maximum loading angle $\theta = 0$ degrees to the neutral loading angles $\theta = \pm 90$ degrees.

Table 3.5.8-1. Loading definitions dependent on angle of stress-components θ

Loading Definitions	$\theta = \cos^{-1} \frac{\Delta\sigma_d}{(\Delta\sigma_d^2 + \Delta\sigma_3^2)^{1/2}}$	β Normality factor	E Tangent Young’s Modulus
Maximum loading	$\theta = 0^0$	$\beta = 1$	$E = E_i \left[1 - \frac{\sigma_d}{\sigma_{dMax}} \right]^2$
Intermediate loading	$-90^0 < \theta < 90^0$	$0 < \beta = \cos\theta < 1$	$E = E_i \left[1 - \beta \frac{\sigma_d}{\sigma_{dMax}} \right]^2$
Neutral loading	$\theta = \pm 90^0$	$\beta = 0$	$E = E_i$
Unloading	$ \theta > 90^0$	$\beta = 0$	$E = E_i$

Unload/Reload Range. Next, we need to establish the stress range wherein the initial elastic modulus E_i function is used for further unloading or reloading steps. This problem is solved by borrowing another plasticity concept called “isotropic hardening” that defines a load-history variable that tracks the largest growth of the yield surface over all past loading steps to present. In accordance with the original Duncan formulation, the yield function is the deviatoric stress. Therefore, we define the load-history variable $z_{(n)}$ to track the largest deviatoric stress obtained over load steps 1, 2, n, where n is the current load step number. Starting with $z_{(0)} = 0$, the load-history variable is updated at the end of each converged load step as shown below.

$$z_{(n)} = \text{Max} (z_{(n-1)}, \sigma_{d(n)}) \quad \text{Equation 3.5-22}$$

Note that $z_{(n)}$ increases if and only if load-step n results in a deviatoric stress greater than the previous high value; otherwise, $z_{(n)}$ does not change in value. Thus $z_{(n)}$ defines the current boundary separating the linear unload/reload domain from the nonlinear loading domain. During the iterative solution process for load step n+1, the trial solution $\sigma_{d(n+1)}$ is compared with $z_{(n)}$ to determine the appropriate equation for tangent Young’s modulus for the next iteration as shown below.

$$\text{If } \sigma_{d(n+1)} > z_{(n)}, \text{ then } E_{(n+1)} = E_i \left[1 - \beta \frac{\sigma_d}{\sigma_{dMax}} \right]^2 \quad (\text{loading domain}) \quad \text{Equation 3.5-23a}$$

$$\text{If } \sigma_{d(n+1)} \leq z_{(n)}, \text{ then } E_{(n+1)} = E_i \quad (\text{unload/reload domain, } \beta = 0) \quad \text{Equation 3.5-23b}$$

When operating in the unload/reload elastic domain, the initial modulus function E_i (Equation 3.5-4) is evaluated with the minimum stress value σ_3^* that is associated with the stress state of $z_{(n)}$. In other words, σ_3^* is a second load-history variable that is saved along with $z_{(n)}$. Thus, E_i is constant value for a specific unload/reload cycle.

Effective Young's Modulus. By definition E_n and E_{n+1} are the tangent modulus values at the end of load steps n and $n+1$, respectively. The effective modulus value $E_{\text{effective}}$ assigned to the incremental stress-strain matrix (Equation 3.5-1) is an appropriate weighted average of these two values depending on loading/unloading conditions as shown in the equation below with the weighted averaging ratio r_E defined in Table 3.5.8-2.

$$E_{\text{effective}} = (1 - r_E) E_{(n)} + r_E E_{(n+1)} \quad \text{Equation 3.5-24}$$

Table 3.5.8-2 Weighted averaging ratio ($0 \leq r_E \leq 1$) as defined below.

Loading Conditions	r_E value	Criteria for condition
(1) Pure loading	1/2	$z_{(n)} = \sigma_{d(n)}$ and $\sigma_{d(n+1)} - \sigma_{d(n)} > 0$
(2) Pure unloading	1/2	$z_{(n)} > \sigma_{d(n)}$ and $\sigma_{d(n+1)} - \sigma_{d(n)} < 0$
(3) Load-to-unload transition	1	$z_{(n)} = \sigma_{d(n)}$ and $\sigma_{d(n+1)} - \sigma_{d(n)} < 0$
(4) Reload-to-load transition	$r_E = \frac{\sigma_{d(n+1)} - z_{(n)}}{\sigma_{d(n+1)} - \sigma_{d(n)}}$	$z_{(n)} > \sigma_{d(n)}$ and $\sigma_{d(n+1)} > z_{(n)}$

The above table applies to all iterations while solving for incremental stresses from load-step n to $n+1$ until convergence is achieved. For loading conditions 1 and 2, the averaging ratio is $1/2$, which places equal weight on the beginning and ending tangent moduli in conformance with the mean value theorem of calculus for smooth functions. Case 3 places the total weight on the ending modulus (elastic) in order to simulate the abrupt change in stiffness upon load reversal. Finally, case 4 assigns r_E equal to the proportion of the stress increment that exceeds the linear range; conversely, $(1-r_E)$ is the proportion within the linear range. These weights generate an accurate stress-strain response for all load/unload/reload conditions.

Bulk Modulus Loading/Unloading Modification. The bulk modulus function, either the power law form (Equation 3.5-17a) or the hyperbolic form (Equation 3.5-17b) monotonically increases in value during hydrostatic loading conditions. That is, the bulk modulus becomes steadily stiffer as the hydrostatic stress increases, which is in accordance with experimental observations. Upon unloading, however, experimental evidence indicates that the response is linear with a constant bulk modulus approximately equal to the current tangent bulk modulus of the loading curve. Thus, the proposed modification to the original bulk modulus function is to unload and reload with a constant bulk modulus equal to the tangent of the loading curve.

Based on the above, the proposed bulk modulus formulation inherently satisfies the continuity principle because the loading, unloading and reloading bulk modulus values are identical at the common point of departure/return on the loading curve. Therefore, the bulk modulus loading function, Equation 3.5-17a or b, does not need to be modified as was required for the Young's modulus function with the insertion of a continuity factor.

Bulk Modulus Unload/Reload Range. Similar to the Young's modulus formulation, we need to establish and track the current stress range wherein the linear bulk modulus remains valid for subsequent unloading or reloading steps. Here again we use the plasticity concept of a load history variable $q_{(n)}$ representing the largest historical value of average stress

σ_m or minimum stress σ_3 , depending on whether the Selig or Duncan bulk modulus function is selected. The following equations are for the Selig bulk modulus function with the understanding that the Duncan form is very similar. Starting with $q_{(0)} = 0$, the load-history variable is updated at the end of each converged load-step n as shown below.

$$q_{(n)} = \text{Max}(q_{(n-1)}, \sigma_{m(n)}) \quad \text{Equation 3.5-25}$$

The variable $q_{(n)}$ increases if and only if load-step n results in a positive loading increment of average stress; otherwise, $q_{(n)}$ does not change in value. Thus $q_{(n)}$ defines the current average-stress level separating the unload/reload domain from the loading domain. Hence during the iterative solution process for load step $n+1$, the trial solution $\sigma_{m(n+1)}$ is compared to $q_{(n)}$ to determine the appropriate equation for the bulk modulus on the next iteration as shown below.

$$\text{If } \sigma_{m(n+1)} > q_{(n)}, \text{ then } B_{(n+1)} = B_i \left[1 + \frac{\sigma_m}{\sigma_{m\text{Ref}}} \right]^2 \quad (\text{loading domain}) \quad \text{Equation 3.5-26a}$$

$$\text{If } \sigma_{m(n+1)} \leq q_{(n)}, \text{ then } B_{(n+1)} = B_i \left[1 + \frac{q_{(n)}}{\sigma_{m\text{Ref}}} \right]^2 \quad (\text{unload/reload domain}) \quad \text{Equation 3.5-26b}$$

Note Equation 3.5-26b provides a constant tangent bulk modulus in the unload/reload domain because $q_{(n)}$ remains a fixed value until σ_m re-enters the loading domain.

Effective Bulk Modulus. Since B_n and B_{n+1} are the tangent bulk modulus values at the end of load steps n and $n+1$, respectively, the effective modulus value $B_{\text{effective}}$ assigned to the incremental stress-strain matrix (Equation 3.5-1) is taken as the average value. This is expressed in the equation below that is in conformance with the mean value theorem of calculus for smooth functions.

$$B_{\text{effective}} = \frac{1}{2} (B_{(n)} + B_{(n+1)}) \quad \text{Equation 3.5-27}$$

Modification Summary. This completes the development of the Modified Duncan and Duncan/Selig model to simulate realistic unloading and reloading of soils. It has been shown that the Modified model satisfies the stress-strain continuity requirement by introducing the continuity factor β in the Young's modulus function. Continuity is automatically satisfied for the bulk modulus function by using the tangent modulus at the point of departure as a constant bulk modulus in the unload/reload region.

Finally, the thermodynamic requirement of positive work (no energy creation) is ensured by the fact that the unloading modulus is always greater or equal to the loading modulus for both Young's modulus and bulk modulus functions over any load cycle. Expressed formerly, we require that for any load/unload cycle:

$$\oint \underline{\sigma}^T d\underline{\varepsilon} \geq 0 \quad \text{Equation 3.5-28}$$

Intuitively it can be seen that the area under the nonlinear stress-strain curve during loading is greater than the negative area under the steeper linear curve during unloading. Therefore, Equation 3.5-28 is satisfied thereby satisfying the thermodynamic on positive work.

Finally, it is important to note that no new material parameters have been introduced into the formulation so that the existing Duncan/Selig parameter data base presented in Section 3.5.7 remains valid for the modified formulation. Subroutines in the CANDE computer program relating to the Duncan/Selig model have been rewritten to incorporate the history variables and logic for the new formulation. Users are given the option to select the Original or the Modified Duncan/Selig with one simple input command (NEWDSK).

3.5.9 Performance of Modified Duncan/Selig model

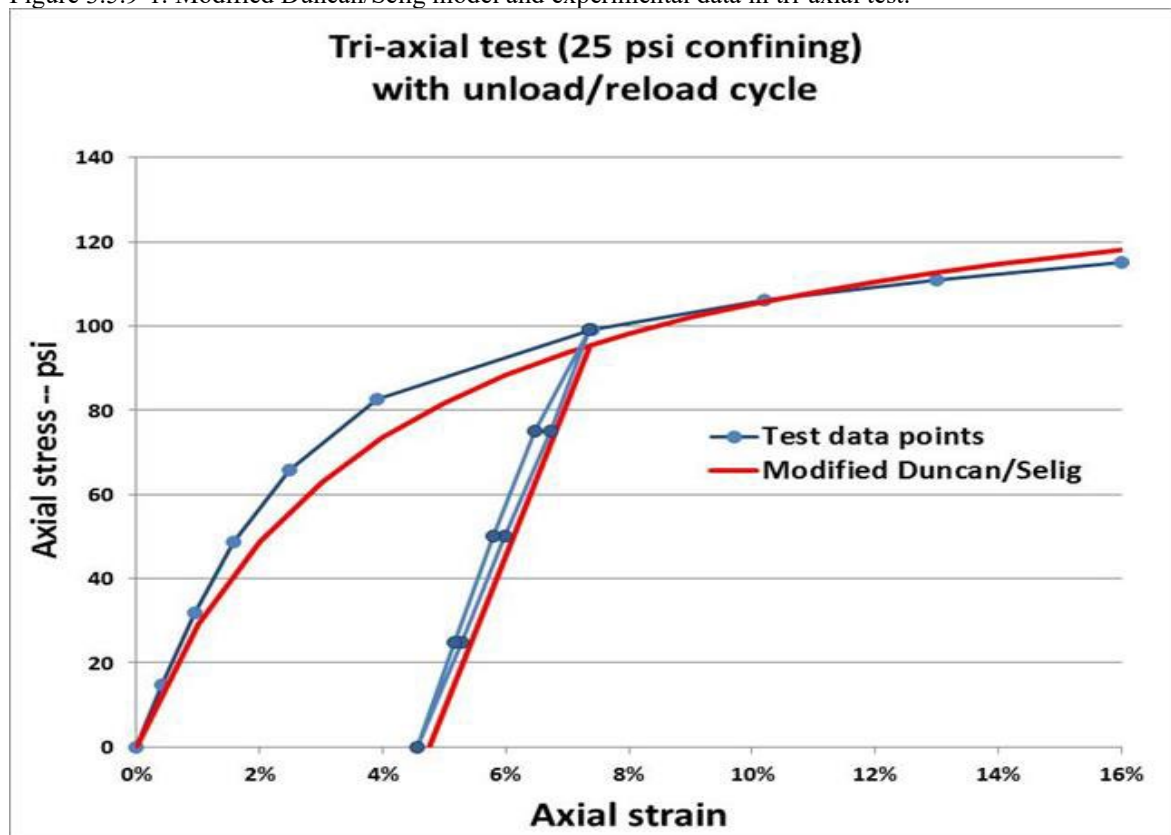
As the result of a previous study (Reference 28), the Duncan/Selig model parameters have been identified to best replicate the experimental loading curves of Cooks Bayou sand that included three standard triaxial tests with confining pressures

of 25, 50 and 100 psi and one hydrostatic test. The experimental tests also included unload-reload cycles, which of course, could not be replicated by the Original Duncan/Selig soil model. Clearly, the Cooks Bayou experimental data verifies the veracity of the Modified Duncan/Selig model.

Triaxial test performance. Figure 3.5.9-1 compares the Modified Duncan/Selig model with tri-axial test data for Cooks Bayou sand at 25 psi confining pressure. The predicted loading curve, which is identical for the Original and Modified forms of the Duncan/Selig model, matches the experimental plot starting with the initial tangent slope and tracking to the maximum capacity.

Midway along the loading curve, the Cooks Bayou test specimen is subjected to an unload/reload cycle that produces a narrow hysteresis loop as shown in the figure. The Modified model simulates the unload/reload cycle with a linear elastic response that is a close approximation to the hysteresis loop. It is re-emphasized that the Modified model only employs the model parameters determined from loading tests so that the predicted unload/reload line is just the initial modulus function evaluated at 25 psi.

Figure 3.5.9-1. Modified Duncan/Selig model and experimental data in tri-axial test.

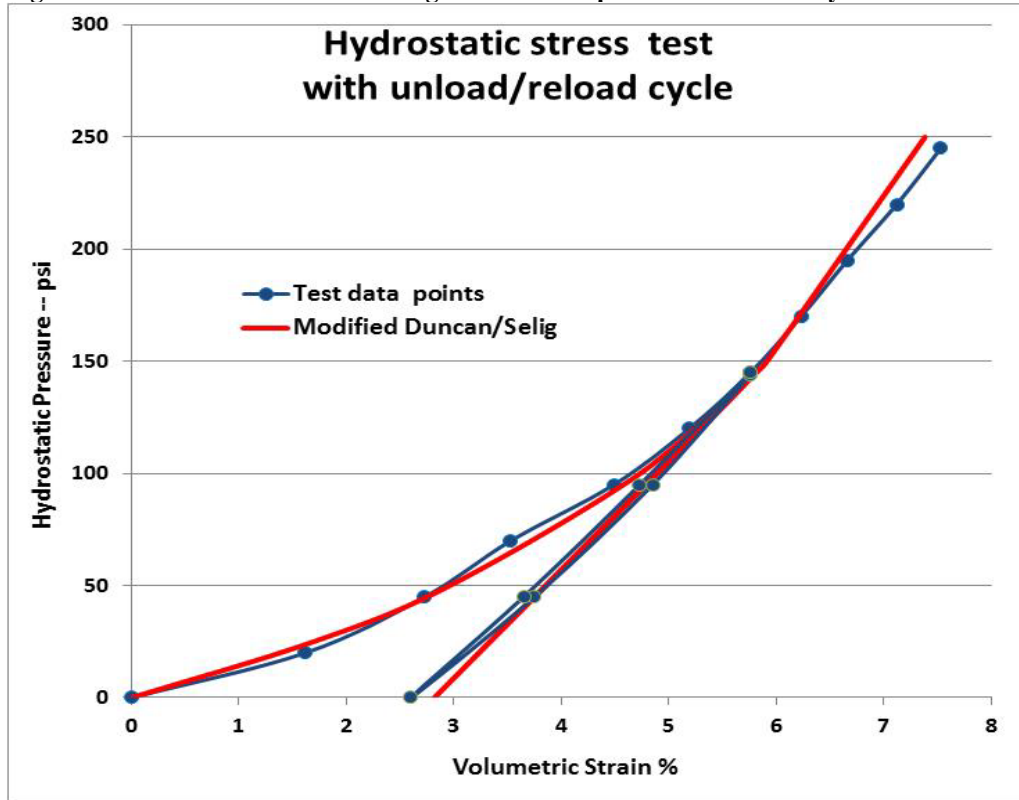


Hydrostatic test performance. In a similar manner, Figure 3.5.9-2 compares the Modified Duncan/Selig model with hydrostatic test data for Cooks Bayou sand. The predicted loading curve, which is identical for the Original and Modified forms of the Duncan/Selig model, tracks well with the experimental loading plot starting with the initial tangent slope and along the steadily increasing curve as the bulk modulus increases its stiffness.

Starting at hydrostatic pressure of 145 psi on the loading curve, the Cooks Bayou test specimen is subjected to an unload/reload cycle producing the near linear-like response shown in the figure below. The Modified model simulates the unload/reload cycle with a linear elastic response that closely approximates the experiment data. Again, it is re-

emphasized that the Modified model only employs the model parameters determined from loading tests wherein the predicted unload/reload linear slope is equal to the slope of the loading curve at the point of departure/return.

Figure 3.5.9-2. Modified Duncan/Selig model and experimental data in hydrostatic test.



Additional examples on the performance of Katona’s modified Duncan/Selig soil model are provided in Reference 29 wherein it is shown that the Modified model provides a realistic approach to simulate compaction loading on soil layers without using the artificial squeeze layer technique.

3.6 Extended Hardin Soil Model

The extended Hardin soil model is a variable-modulus elasticity formulation using stress/strain-dependent functions for the shear modulus and Poisson ratio. Basically, the model exhibits stiffening of constitutive moduli when confining stress increases and softening when shear strain increases.

Hardin's original work for the variable shear modulus formulation, which is based on a hyperbolic relationship between shear stress and shear strain, is summarized in a 1973 Air Force technical report (Reference 22). In 1974 a variable Poisson ratio function was developed to be the companion elasticity function so that together the two elasticity functions, shear modulus and Poisson ratio, are referred to as the extended Hardin soil model. Reference 1 documents the development of the variable Poisson function as well as validation of the shear modulus function against an independent set of experimental data.

In many ways the extended Hardin model is similar in behavior to the Duncan and Duncan/Selig models, although the later models are more popular and are supported by a larger database of soil parameters dependent on soil quality and compaction. However, a unique feature of the extended Hardin model is that the soil parameters for the shear modulus function are characterized in terms fundamental soil properties including void ratio, plasticity index and percent saturation of the soil.

From an overall perspective, the extended Hardin soil model functions are used to define the nonlinear components of an isotropic, elasticity-based constitutive matrix for plane-strain conditions as expressed below.

$$\begin{pmatrix} \Delta\sigma_x \\ \Delta\sigma_y \\ \Delta\tau \end{pmatrix} = \begin{pmatrix} C_{11} & C_{12} & 0 \\ C_{12} & C_{11} & 0 \\ 0 & 0 & C_{33} \end{pmatrix} \begin{pmatrix} \Delta\varepsilon_x \\ \Delta\varepsilon_y \\ \Delta\gamma \end{pmatrix} \quad \text{Equation 3.6-1}$$

where, $\Delta\sigma_x, \Delta\sigma_y, \Delta\tau$ = stress increments for x-direction, y-direction and shear components, respectively
 $\Delta\varepsilon_x, \Delta\varepsilon_y, \Delta\gamma$ = strain increments for x-direction, y-direction and shear components, respectively
 C_{11}, C_{12}, C_{33} = nonlinear coefficients dependent on shear modulus and Poisson ratio functions.

The table below shows the relationship between the constitutive matrix components and the shear modulus and Poisson ratio functions that define the extended Hardin model.

Table 3.6.1-1 Components for constitutive matrix relationship to moduli functions

Components of Constitutive matrix	G = shear modulus v = Poisson ratio (G, v)	G = shear modulus B = bulk modulus (G, B)
$C_{11} =$	$\frac{2G(1-v)}{1-2v}$	$B + \frac{4}{3}G$
$C_{12} =$	$\frac{2Gv}{1-2v}$	$B - \frac{2}{3}G$
$C_{33} =$	G	G

The middle column in the above table defines the matrix coefficients C_{11} , C_{12} and C_{13} in terms of shear modulus and Poisson ratio, which are the elastic parameter functions directly developed for the extended Hardin soil model. The third column defines the matrix coefficients in terms of shear modulus and bulk modulus, which is a more natural pair of

elasticity functions and often easier to implement. The equivalence between column 2 and 3 is given by the elasticity relationship,

$$B = G \frac{2(1 + \nu)}{3(1 - 2\nu)} \quad \text{Equation 3.6-2}$$

The motivation for choosing Poisson ratio as second elasticity function is because it easy to develop a smooth function that ensures Poisson ratio remains within the admissible bounds, $0 \leq \nu \leq \frac{1}{2}$. In contrast, the constraints on an independent bulk modulus function requires that $B > \frac{2}{3} G$, which is more difficult to achieve with a smooth function.

3.6.1 Hardin shear modulus development

Hardin's formulation is based on experimental observations of soil behavior from standard tri-axial tests. A standard tri-axial test is conducted by placing a cylindrical soil specimen in a pressure chamber and initially subjecting the specimen to a uniform hydrostatic pressure, called σ_3 . Next a steadily increasing axial load is applied to the specimen producing a net axial stress, called σ_1 , which includes the hydrostatic pressure. Note that σ_3 and σ_1 are principal stresses in the lateral and axial directions, respectively. The difference in principal stresses $\sigma_1 - \sigma_3$ is equal to twice the maximum shear stress occurring on 45-degree plane.

As the axial stress increases, axial strain ε_1 is computed by measuring the axial shortening of the specimen divided by the specimen length. Similarly, the lateral strain ε_3 is measured at each load step so that the maximum shear strain is equal to $\varepsilon_1 - \varepsilon_3$. Note that ε_1 and ε_3 do not include the initial hydrostatic strain and the algebraic signs must be strictly observed in computing differences. The above concepts are summarized below.

$$\tau = \frac{1}{2}(\sigma_1 - \sigma_3) \quad \text{Equation 3.6-3}$$

$$\gamma = \varepsilon_1 - \varepsilon_3 \quad \text{Equation 3.6-4}$$

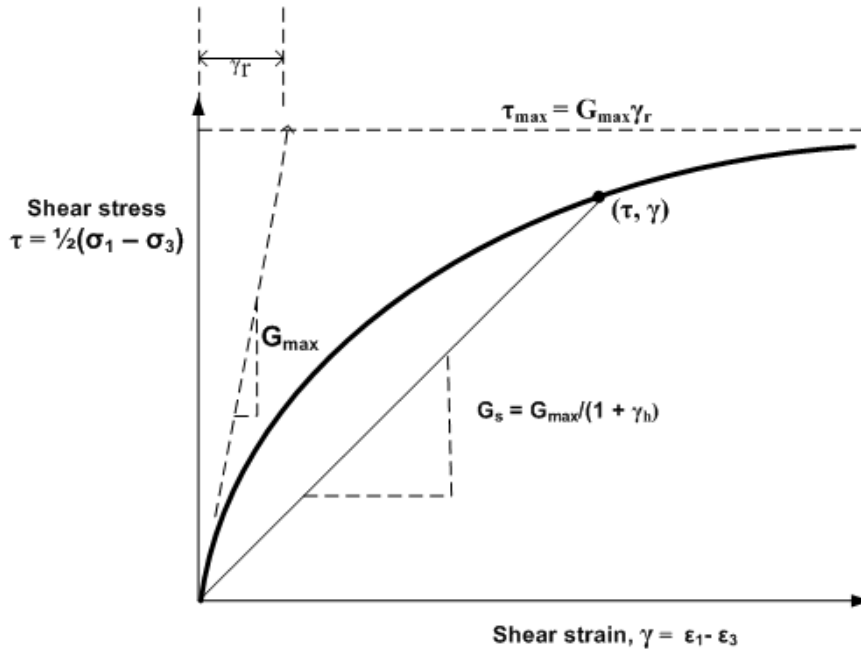
$$\tau = G_s \gamma \quad (\text{implied nonlinear relationship}) \quad \text{Equation 3.6-5}$$

where, τ = accumulated shear stress from tri-axial test

γ = accumulated shear strain from tri-axial test

G_s = secant shear modulus, a function of stress and strain

The curve in Figure 3.6.2-1 is an idealized plot of shear stress versus shear strain for a typical tri-axial test. Here, G_{\max} is the initial slope at zero shear strain and τ_{\max} is the maximum shear strain at failure. As discussed subsequently, G_{\max} and τ_{\max} are dependent on the hydrostatic stress level.

Figure 3.6.2-1 Idealized shear stress-strain curve for tri-axial test

Hardin hyperbolic function. Hardin's fundamental insight is that for any tri-axial test, the shear stress-strain curve is fairly well approximated by equating the shear stress to a hyperbolic function of shear strain as follows,

$$\tau = \frac{G_{\max}}{1 + \gamma_h} \gamma \quad \text{Equation 3.6-6}$$

$$\gamma_h = \frac{\gamma}{\gamma_r} \left(1 + \frac{\alpha}{\exp\left(\frac{\gamma}{\gamma_r}\right)^{0.4}} \right) \quad \text{Equation 3.6-7}$$

$$\gamma_r = G_{\max} / C_1 \quad \text{Equation 3.6-8}$$

where, G_{\max} = initial slope for shear modulus (dependent on hydrostatic stress)

γ_h = hyperbolic strain function

γ_r = reference shear strain

α = dimensionless soil parameter, related to soil type and percent saturation.

C_1 = soil parameter with units of stress, related to void ratio, percent saturation, and plasticity index.

As shear strain increases to infinity, the shear stress in Equation 3.6-6 approaches an asymptotic limit representing the maximum shear stress (or shear failure stress) given by,

$$\tau_{\max} = G_{\max} \gamma_r \quad \text{Equation 3.6-9}$$

Initial shear modulus. Based on a wide variety of soil tests as typified by the above figure, Hardin discovered that the initial shear modulus increased in proportion with the square root of the initial tri-axial confining pressure as expressed below.

$$G_{\max} = S_1 \sqrt{\sigma_m} \quad \text{Equation 3.6-10}$$

where, G_{\max} = initial shear modulus when shear strain = 0

S_1 = soil parameter related to void ratio (units in $\sqrt{\text{psi}}$)

$\sigma_m = 1/3(\sigma_{11} + \sigma_{22} + \sigma_{33})$ = hydrostatic stress (psi)

Equations 3.6-6 through 3.6-10 form the complete mathematical description of the Hardin secant shear modulus function, which is characterized by three soil model parameters, C_1 , S_1 and α . The direct method of determining the soil model parameters is to conduct a series of tri-axial tests on the particular soil being investigated. Alternatively, Hardin has developed an indirect method for determining soil parameters based on fundamental soil properties. Both the direct and indirect methods are presented below.

Direct method of soil parameter identification. Clearly the most accurate way to determine the shear modulus parameters, C_1 , S_1 and α , is to perform a series of tri-axial tests on the soil under investigation. For each confining pressure σ_3 , it is required to plot an experimental stress-strain curve similar to Figure 3.6.2-1 and then follow the steps below.

1. Construct the initial tangent at zero shear strain and denote its value as G_{\max} . Based in Equation 3.6-10, the parameter S_1 may be computed as follows.

$$S_1 = G_{\max} / \sqrt{\sigma_3} \quad \text{Equation 3.6-11}$$

Ideally each confining pressure would produce the same value for S_1 . However, since the model is not perfect, the final value for S_1 should be the average value determined from all initial confining pressures.

2. Using the measured value of G_{\max} from step 1 along with the experimentally observed max shear stress τ_{\max} , the parameter C_1 may be computed by combining Equations 3.6-8 and 3.6-9 as follows.

$$C_1 = G_{\max}^2 / \tau_{\max} \quad \text{Equation 3.6-12}$$

In an ideal world, the computed value of C_1 should be the same for all confining pressures. However, since the model is not perfect, the final value for C_1 should be the average value determined from all initial confining pressures.

3. The third and last soil parameter α controls the shape (concavity) of the shear stress-strain curve in Figure 3.6.2-1. Since all parameters of the secant shear modulus model are known except α , Equation 3.6-6 may be applied at a single experimental data point (τ^* , γ^*) to provide an algebraic equation to solve for α . A natural data point to select is midway in the stress range, $\tau^* = 1/2 \tau_{\max}$ along with the corresponding experimentally measured shear strain γ^* .

Indirect method of soil parameter identification. A particularly useful result of Hardin's work is that he developed an indirect method for determining soil parameters based on fundamental soil properties. This was accomplished by correlating the results of many tri-axial tests for many types soil with basic soil properties including void ratio, percent saturation, and plasticity index.

Listed below are the expressions he developed to quantify the soil parameters C_1 , S_1 and α for three broad classes of soil, granular, mixed and cohesive.

$$C_1 = \frac{F^2 R^2}{0.6 - 0.25(\text{PI})^{0.6}} \quad (\text{units psi}) \quad \text{Equation 3.6-13}$$

$$S_1 = 1230 F \quad (\text{units } \sqrt{\text{psi}}) \quad \text{Equation 3.6-14}$$

$$\alpha = \begin{cases} 3.2 & \text{for granular soil} \\ 2.54(1+0.02S) & \text{for mixed soil} \\ 1.12(1+0.02S) & \text{for cohesive soil} \end{cases} \quad (\text{dimensionless}) \quad \text{Equation 3.6-15}$$

where, $F = \frac{(2.973 - e)^2}{1 + e}$ for all soil types

$$R = \begin{cases} 1100 & \text{for granular soil} \\ 1100 - 6.0 S & \text{for mixed and cohesive soil} \end{cases}$$

and, e = void ratio ($0 \leq e \leq 1$)
 S = percent saturation ($0 \leq S \leq 100$)
 PI = plasticity index ($0 \leq \text{PI} \leq 1$)

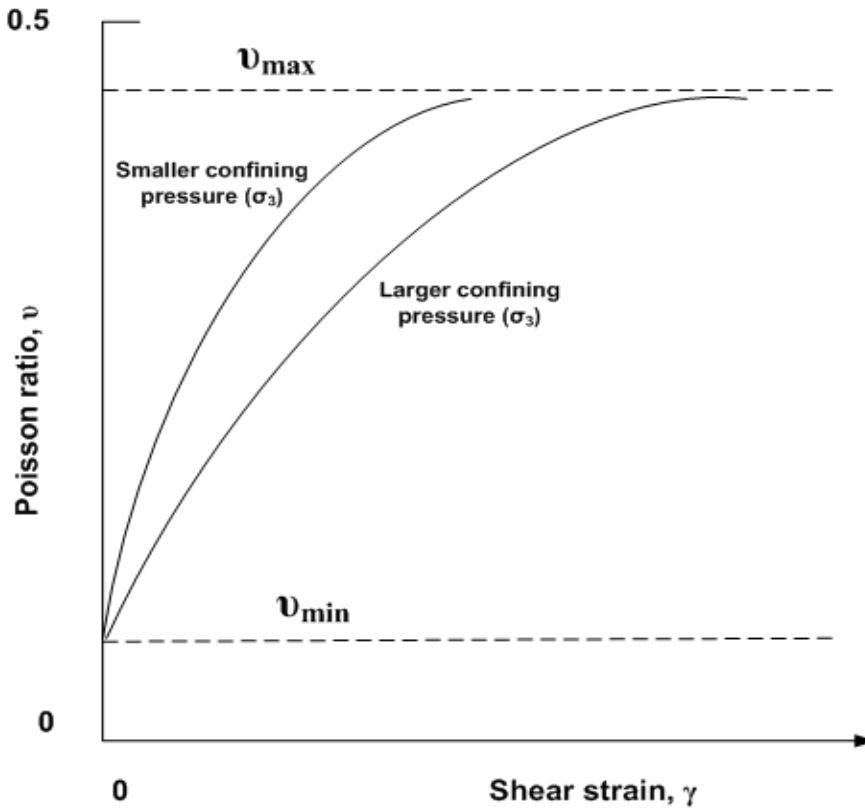
Thus, knowing the type of soil, void ratio, percent saturation, and plasticity index, Hardin's secant shear modulus function is completely characterized without the need of a tri-axial test.

3.6.2 Poisson ratio development

Poisson ratio may be back calculated from tri-axial test data providing that principal stresses and principal strains are measured during the test. Reference 1 presents a study showing back-calculated values of Poisson ratio for a sequence of tri-axial tests with increasing confining pressure. Two significant findings from this study are summarized below.

For each individual tri-axial test with a specified confining pressure, the measured Poisson ratio increases as shear strain increases. Starting at a low value of approximately 0.01, the measured Poisson ratio asymptotically approaches an upper limit, nominally equal to 0.49, as the shear strain approaches the shear failure limit.

When confining pressure is increased, the starting and ending values of Poisson ratio remain the same as noted above, however the rate of increase of Poisson ratio with shear strain increases as confining pressure increases. Said another way, the measured value of Poisson ratio at a given level of shear strain is inversely related to the confining pressure. The above two observations are illustrated in Figure 3.6.3-1.

Figure 3.6.3-1 Illustration of measured Poisson ratio from tri-axial tests.

Poisson ratio function. A Poisson ratio function that simulates the above two observations is shown below, wherein γ_p is a scaled measure of shear strain.

$$v = \frac{v_{\min} + \gamma_p v_{\max}}{1 + \gamma_p} \quad \text{Equation 3.6-16}$$

$$\gamma_p = \frac{q}{\gamma_r} \gamma \quad \text{Equation 3.6-17}$$

where, v = Poisson ratio function.

γ_p = scaled shear strain measure.

γ_r = Hardin reference shear strain (= G_{\max}/C_1 from Equation 3.6-8)

and, v_{\min} = Poisson function parameter denoting minimum value (dimensionless constant)

v_{\max} = Poisson function parameter denoting maximum value (dimensionless constant)

q = Poisson function parameter controlling curve shape (dimensionless constant)

Upon inspecting the Poisson ratio function, it is clear that when shear strain is zero, $v = v_{\min}$, and when shear strain becomes very large, $v = v_{\max}$. Thus, the Poisson ratio function satisfies the first observation noted above. The second observation is achieved by defining γ_p with Hardin reference strain γ_r in the denominator as shown in Equation 3.16-7.

Since γ_r is proportional to G_{\max} and G_{\max} is an increasing function of confining pressure, γ_p is reduced for tests with higher confining pressures so that the Poisson ratio function behaves as illustrated in the above.

It is important to realize that the predicted and observed variation in Poisson ratio as portrayed in Figure 3.6.3-1 is only for the case of a standard tri-axial loading environment. When Equation 3.6-16 is used to predict the behavior of Poisson ratio in a uniaxial-strain loading environment (K_0 -test), the Poisson ratio prediction remains nearly constant as axial strain (or shear strain) increases. This is because the steadily increasing confining pressure increases the value of G_{\max} at nearly the same rate as the increase in strain so that γ_p remains nearly constant in accordance with observed behavior.

Parameter identification. The Poisson ratio function requires identifying values for three model parameters, v_{\min} , v_{\max} and q . The study presented in Reference 1 measured Poisson ratio values from five tri-axial tests with confining pressures ranging from 25 psi to 250 psi. The soil specimens were dry, dense sand, and the model parameters identified as,

$$v_{\min} = 0.10$$

$$v_{\max} = 0.49$$

$$q = 0.26$$

Choosing values for v_{\min} and v_{\max} are straightforward observations from the experimental data, and the selection of the shape parameter q is determined by standard curve fitting techniques. The study concludes that the Poisson ratio function with the above parameter values is in excellent agreement with the measured Poisson ratio data points for all five tri-axial tests.

Of course, it is always best to conduct tri-axial tests on new soils to identify the parameters of the Poisson ratio function. However, experience has shown that v_{\min} , v_{\max} and q are not overly sensitive to the type of soil and soil properties, thus if no other data is available the above parametric values are fairly reasonable for all soil types.

3.6.3 Summary of extended Hardin soil model functions

The extended Hardin soil model is composed of the secant shear modulus function and the Poisson ratio function both of which are functions of maximum shear strain and hydrostatic pressure.

The secant shear modulus function is given by the following function and sub functions.

$$G_s = \frac{G_{\max}}{1 + \gamma_h} = \text{shear modulus function} \quad \text{Equation 3.6-18}$$

$$\gamma_h = \frac{\gamma}{\gamma_r} \left(1 + \frac{\alpha}{\exp\left(\frac{\gamma}{\gamma_r}\right)^{0.4}} \right) = \text{hyperbolic strain function} \quad \text{Equation 3.6-19}$$

$$\gamma_r = G_{\max} / C_1 = \text{reference shear strain} \quad \text{Equation 3.6-20}$$

$$G_{\max} = S_1 \sqrt{\sigma_m} = \text{initial shear modulus when shear strain} = 0 \quad \text{Equation 3.6-21}$$

where, γ = maximum shear strain

$$\sigma_m = 1/3(\sigma_{11} + \sigma_{22} + \sigma_{33}) = \text{hydrostatic stress (units psi)}$$

and, S_1 = soil parameter related to void ratio (units in $\sqrt{\text{psi}}$)

α = soil parameter, related to soil type and percent saturation (dimensionless)

C_1 = soil parameter related to void ratio, percent saturation, and plasticity index (units psi)

Parameter identification for C_1 , S_1 and α may be accomplished directly with tri-axial tests as outlined in the discussion associated with Equations 3.6-11 and 3.6-12. Alternatively, the parameters may be quantified by the indirect method outlined with the discussion associated with Equations 3.6-13, -14, and -15.

The Poisson ratio function is given by the following function and sub functions.

$$v = \frac{v_{\min} + \gamma_p v_{\max}}{1 + \gamma_p} = \text{Poisson ratio function} \quad \text{Equation 3.6-22}$$

$$\gamma_p = \frac{q}{\gamma_r} \gamma = \text{scaled shear strain measure} \quad \text{Equation 3.6-23}$$

where, γ_r = Hardin reference shear strain (= G_{\max}/C_1 from Equation 3.6-20)

and, v_{\min} = Poisson function parameter denoting minimum value (dimensionless constant)

v_{\max} = Poisson function parameter denoting maximum value (dimensionless constant)

q = Poisson function parameter controlling curve shape (dimensionless constant)

Parameter identification for v_{\min} , v_{\max} and q may be accomplished with tri-axial tests as outlined in the discussion in Section 3.6.3. If no independent test data is available, the default values, $v_{\min} = 0.1$, $v_{\max} = 0.49$, and $q = 0.26$ are reasonable for all soil types.

The overall behavior of the extended Hardin soil model mimics the actual behavior of soil. The model exhibits a stiffening behavior when confining pressure dominates shear strain, and conversely a softening behavior when shear strain dominates confining pressure.

Lastly, it is emphasized the extended Hardin soil model is a nonlinear elasticity model and behaves the same in loading or unloading. Like the Duncan and Duncan/Selig soil models, additional research needs to be done in order to incorporate plasticity-like concepts into the model so that unloading behavior can be simulated without violating energy theorems and continuity principles.

3.6.4 Implementation of Harden model and nonlinear solution strategy

To implement the extended Hardin model into the plane-strain constitutive matrix given by Equation 3.6-1, it is more convenient to use the bulk modulus function with the shear modulus function (G , B) rather than the Poisson ratio function (G , v) as was indicated in Table 3.6.1-1. The bulk modulus function is related to the extended Hardin functions by elasticity identity relationships as,

$$B_s = G_s \frac{2(1+v)}{3(1-2v)} \quad \text{Equation 3.6-24}$$

where, B_s = secant bulk modulus function

G_s = secant shear modulus function (Equation 3.6-18)

v = Poisson ratio function (Equation 3.6-22)

Letting σ_1 , σ_2 , σ_3 be the total principal stresses and ε_1 , ε_2 and ε_3 the corresponding total principal strains, then, the secant moduli (G_s , B_s) relate total stress quantities to total strain quantities as follows.

$$\tau = G_s \gamma \tag{Equation 3.6-25}$$

$$\sigma_m = B_s \varphi \tag{Equation 3.6-26}$$

where, $\tau = (\sigma_1 - \sigma_3)/2 =$ maximum shear stress

$\gamma = \epsilon_1 - \epsilon_3 =$ maximum shear strain

$\sigma_m = (\sigma_1 + \sigma_2 + \sigma_3)/3 =$ mean stress or hydrostatic stress

$\varphi = \epsilon_1 + \epsilon_2 + \epsilon_3 =$ volumetric strain

Chord moduli representation. To progress from load step i to load step $i+1$, the moduli must be expressed as incremental chord moduli, which are related to secant moduli as illustrated in the figures below.

Figure 3.6.5-1 Chord modulus relationship to secant modulus for shear modulus.

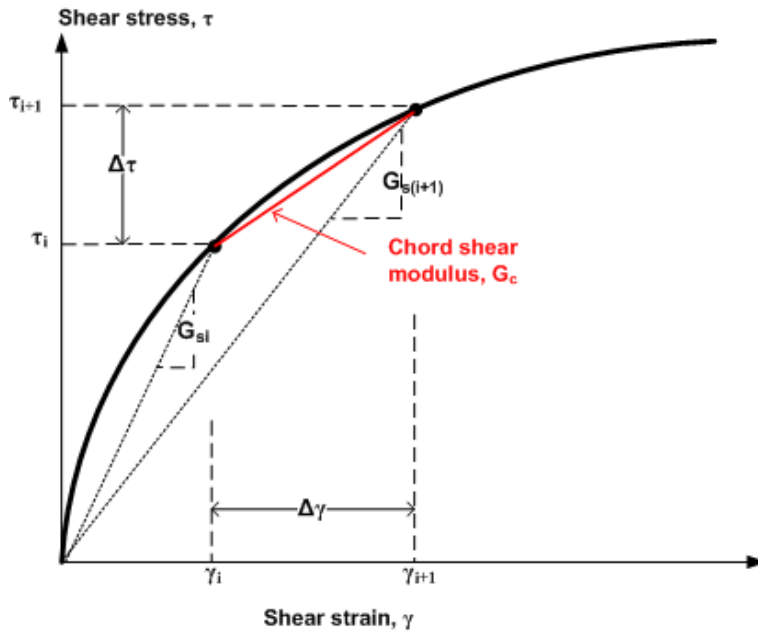
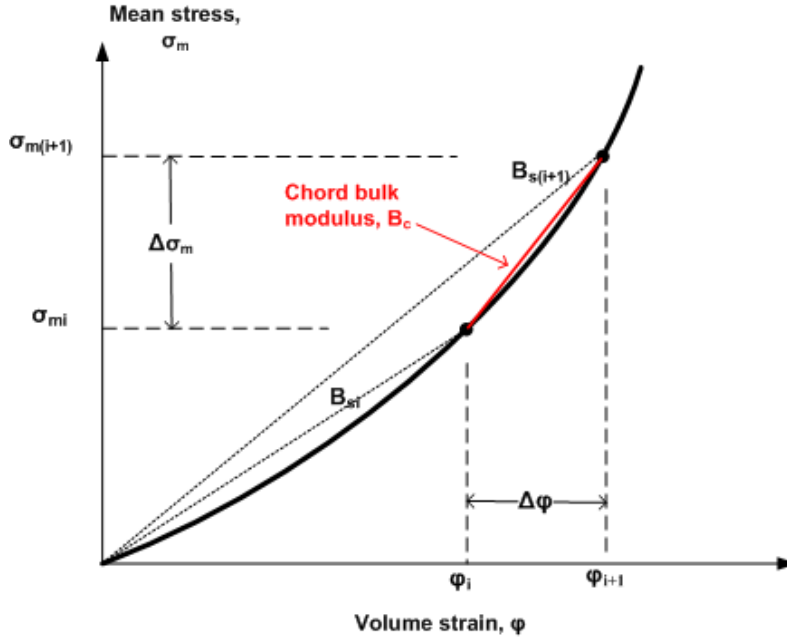


Figure 3.6.5-2 Chord modulus relationship to secant modulus for bulk modulus



The incremental relationships between load steps i and $i+1$ as portrayed in the above figures are defined below.

$$\Delta\tau = G_c \Delta\gamma \quad \text{Equation 3.6-27}$$

$$\Delta\sigma_m = B_c \Delta\phi \quad \text{Equation 3.6-28}$$

$$G_c = \frac{G_{s(i+1)} \gamma_{i+1} - \tau_i}{\gamma_{i+1} - \gamma_i} \quad \text{Equation 3.6-29}$$

$$B_c = \frac{B_{s(i+1)} \phi_{i+1} - \sigma_{m(i)}}{\phi_{i+1} - \phi_i} \quad \text{Equation 3.6-30}$$

where, G_c = chord shear modulus from load step i to $i+1$

B_c = chord bulk modulus from load step i to $i+1$

$\Delta\tau = \tau_{i+1} - \tau_i$ = shear stress increment

$\Delta\gamma = \gamma_{i+1} - \gamma_i$ = shear strain increment

$\Delta\sigma_m = \sigma_{m(i+1)} - \sigma_{mi}$ = mean stress increment

$\Delta\phi = \phi_{i+1} - \phi_i$ = volumetric strain increment.

Nonlinear solution strategy. The solution strategy is based on a direct iterative approach, also called trial and error. We begin with the understanding that we have a converged solution at load step i so that we know the total stress and total strain state, $\underline{\sigma}_i$ and $\underline{\varepsilon}_i$, respectively. Our objective is to advance the solution to load step $i+1$ following the steps below.

To obtain the first trial solution, assume the values for G_c and B_c remain the same as they were for load step i for each individual element.

Construct the element stiffness matrix using G_c and B_c to define the current constitutive matrix for each element (Equation 3.6-1)

Assemble the global stiffness matrix and load increment vector for step $i+1$. Solve the system for a trial solution and recover current estimates for increments of stress and strain vectors. Update trial vectors for total stress and strain as indicated below.

$\Delta \underline{\underline{\epsilon}}$ = incremental strain vector determined from strain-displacement relationship.

$\Delta \underline{\underline{\sigma}}$ = incremental stress vector determined from current constitutive matrix

$$\underline{\underline{\epsilon}}_{i+1} = \underline{\underline{\epsilon}}_i + \Delta \underline{\underline{\epsilon}}$$

$$\underline{\underline{\sigma}}_{i+1} = \underline{\underline{\sigma}}_i + \Delta \underline{\underline{\sigma}}$$

Based on the known stress-strain state at step i and the estimated stress-strain state at step $i+1$, compute new estimates for G_c and B_c .

$$G_c = \frac{G_{s(i+1)} \gamma_{i+1} - \tau_i}{\gamma_{i+1} - \gamma_i} \quad (\text{see Equation 3.6-18})$$

$$B_c = \frac{B_{s(i+1)} \phi_{i+1} - \sigma_{m(i)}}{\phi_{i+1} - \phi_i} \quad (\text{see Equations 3.6-18, -22, -24})$$

If G_c and B_c computed in the last step are sufficiently close to the previous estimates, say within 1% difference, then the load step has converged, the solution is saved, and control shifts back to step 1 to advance to the next load step. Otherwise, the iterative process continues wherein the incremental solution is discarded and control shifts back to step 2 to repeat the load increment using the new values for G_c and B_c to get a new trial solution.

Typically, the above algorithm converges for all elements in three to ten iterations for each load step, depending on the scope of the problem. Convergence means that static equilibrium and the constitutive matrix are simultaneously satisfied.

3.7 Mohr/Coulomb Plasticity Model with Tension Cutoff

3.7.1 Pros and Cons of Mohr/Coulomb Model

The classical Mohr/Coulomb elastic-perfectly plastic constitutive model is often used by geotechnical engineers to simulate soil shear-failure when analyzing soil-structure systems such as in-situ soil beneath footings and walls. The use of this classical model is supported by popular commercial finite programs such as ABAQUS, NASTRAN and FLAX3D, which recommend the use of the Mohr/Coulomb elastic-perfectly plastic model for soil-structure analysis. An inherent attribute of the plasticity formulation is that it includes permanent deformation when unloading from the plastic domain as opposed to nonlinear elasticity models that retrace the same load/unload path. In spite of these attributes, the classical Mohr/Coulomb plasticity model is less than ideal because it predicts shear failure to occur as an abrupt, rather than a gradual, phenomena as observed in most soils used for backfill. Another shortcoming is that the model does not exhibit increasing stiffness with increased confining pressure as generally observed in soils.

In contrast, the Duncan/Selig soil model captures the entire suite of observed soil behavior for all loading environments. Moreover, the Katona modified form of the Duncan/Selig model also captures the linear-like unload/reload response of soils similar to plasticity models. For the record, the finite element program PLAXIS offers a sophisticated plasticity-based hardening model whose hardening rule was developed to mimic the Duncan/Selig variable-modulus model under loading conditions (Reference 30). Accordingly, the Modified Duncan/Selig model and the PLAXIS hardening soil model are judged equivalent for loading and unloading environments and are well suited for modeling the backfill soil around culverts.

Irrespective of the limitations of the classical Mohr/Coulomb model to simulate the full range of soil behavior, this section is devoted to the development of the Mohr/Coulomb model and its implementation in the CANDE-2022 program. Although it is generally recommended to use the Duncan/Selig model to represent fill-soil behavior, the motivation for developing and offering the classical Mohr/Coulomb constitutive model is threefold:

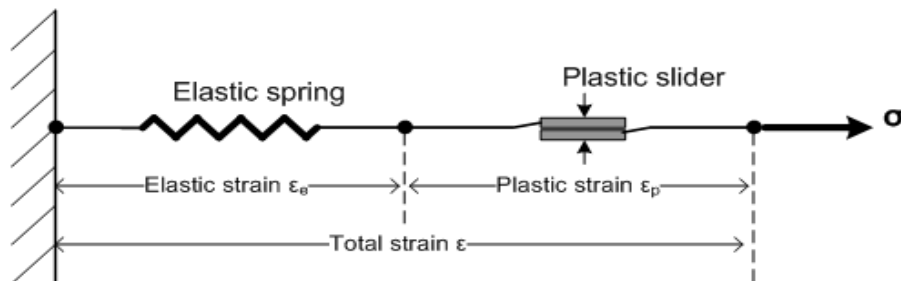
1. Some in-situ soils such as stiff clays are well represented by the Mohr/Coulomb model.
2. Since some finite element programs are limited to the classical Mohr/Coulomb plasticity soil model, it is convenient to include the model in CANDE in order to make direct comparisons.
3. Materials other than soils, such as metals, are well represented by the Tresca form of the Mohr/Coulomb model ($\phi = 0$).

With the above understanding, the Mohr/Coulomb plasticity model as offered in CANDE is developed in the following paragraphs. The last section provides a comparison of the performance of the Mohr/Coulomb and the Duncan/Selig soil models with experimental data for Cooks Bayou sand in tri-axial, hydrostatic and confined compression loading environments.

3.7.2 Basic Plasticity Concepts

From a one-dimensional view point the Mohr-Coulomb model may be viewed as an elastic spring in series with a plastic slider that is abruptly activated when the shear stress exceeds a stress dependent limit as depicted in Figure 3.7.1-1 below.

Figure 3.7.2-1. One dimensional analogue of Mohr/Coulomb elastic-plastic model



As illustrated, the total strain is the sum of the elastic and the plastic parts. Since the elastic spring and the plastic slider are in series, they experience the same stress; therefore, stress is always equal to the elastic stiffness times the elastic strain, not the total strain. When the stress level exceeds the activation limit of the plastic slider, slipping deformation occurs, thereby causing plastic strain, which adds to elastic strain to form the total strain. These basic concepts apply to the two-dimensional plane formulation developed below.

3.7.3 Stress and Strain Components for Plane Strain Plasticity

For two-dimensional plane strain, the elastic and plastic strains are expressed as incremental vectors wherein the total incremental strain is sum of the two increments as expressed below.

$$\underline{\Delta \varepsilon} = \underline{\Delta \varepsilon}_e + \underline{\Delta \varepsilon}_p \quad \text{Equation 3.7-1a}$$

Or equivalently, the above equation may be written in expanded vector notation for an x-y coordinate system as shown below.

$$\begin{pmatrix} \Delta \varepsilon_x \\ \Delta \varepsilon_y \\ \Delta \gamma \end{pmatrix} = \begin{pmatrix} \Delta \varepsilon_x \\ \Delta \varepsilon_y \\ \Delta \gamma \end{pmatrix}_e + \begin{pmatrix} \Delta \varepsilon_x \\ \Delta \varepsilon_y \\ \Delta \gamma \end{pmatrix}_p \quad \text{Equation 3.7-1b}$$

where the following symbols are used throughout this development.

- Δ = an incremental quantity (small load step)
- e = vector subscript denoting elastic response
- p = vector subscript denoting plastic response
- $\varepsilon_x, \varepsilon_y, \gamma$ = normal x, y and shear strain components
- σ_x, σ_y, τ = normal x, y and shear stress components

The elastic stress-strain relationship for isotropic materials is expressed below in compact vector notation and re-expressed in expanded notation for plane-strain geometry. Note these equations relate the total stress increment to the elastic strain increment by a linear relationship that is persistently valid irrespective of plastic deformation.

$$\underline{\Delta \sigma} = \underline{D}_e \underline{\Delta \varepsilon}_e \quad \text{Equation 3.7-2a}$$

Or equivalently in expanded notation,

$$\begin{pmatrix} \Delta \sigma_x \\ \Delta \sigma_y \\ \Delta \tau \end{pmatrix} = \begin{pmatrix} D_{11} & D_{12} & 0 \\ D_{12} & D_{11} & 0 \\ 0 & 0 & D_{33} \end{pmatrix} \begin{pmatrix} \Delta \varepsilon_x \\ \Delta \varepsilon_y \\ \Delta \gamma \end{pmatrix} \quad \text{Equation 3.7-2b}$$

Components of the elastic constitutive matrix \underline{D}_e , (i.e., D_{11} , D_{12} , and D_{33}) may be defined by any convenient pair of elasticity parameters as shown in Table 3.7.3-1, which remain constant for all stress and strain increments.

The last row in the table shows constraints for the elasticity parameters in order that thermodynamic restrictions are satisfied (e.g., positive definite matrix). This development uses the parameters Young's modulus E and Poisson ratio ν for the linear elastic formulation.

TABLE 3.7.3-1. Popular pairs of elastic parameters for constitutive matrix.

Elastic matrix component	M = Confined mod. K ₀ = Lateral coeff.	E = Young’s mod ν = Poisson ratio	B = Bulk mod. G = Shear mod.	E = Young’s mod. B = Bulk mod.
D ₁₁ =	M	$E(1-\nu)/(1+\nu)(1-2\nu)$	$B + (4/3)G$	$B(9B+3E)/(9B-E)$
D ₁₂ =	M K ₀	$E\nu/(1+\nu)(1-2\nu)$	$B - (2/3)G$	$3B(3B-E)/(9B-E)$
D ₃₃ = (D ₁₁ - D ₁₂)/2 =	M(1-K ₀)/2	$E/2(1+\nu)$	G	$3EB/(9B-E)$
Constraints	M > 0 0 ≤ K ₀ ≤ 1	E > 0 0 ≤ ν ≤ 1/2	B > 0 0 ≤ G ≤ (3/2)B	E > 0 E/3 ≤ B < ∞

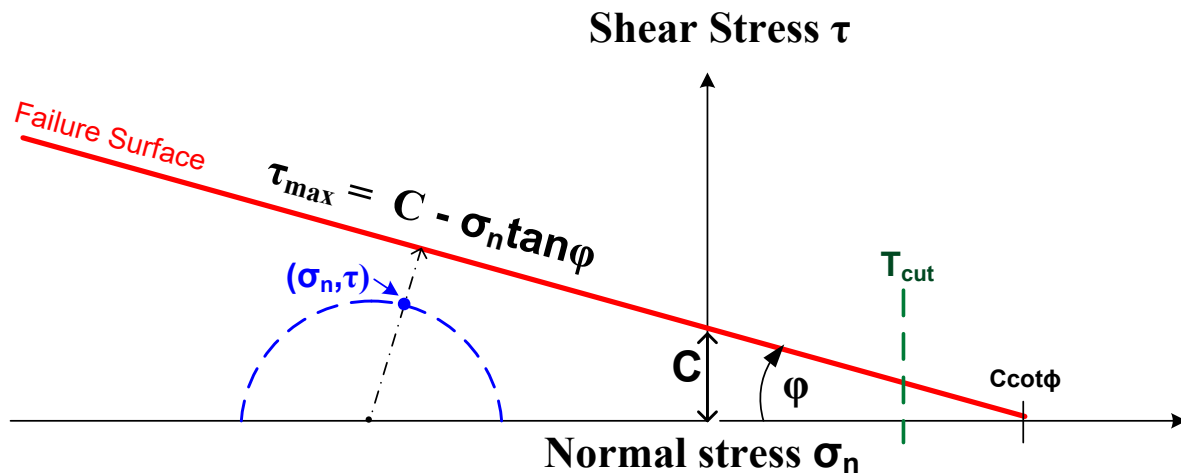
3.7.4 Plastic failure surface of Mohr/Coulomb Model

The classical Mohr/Coulomb formulation employs a non-hardening yield surface equivalently called the failure surface. Like the Tresca failure criterion that is defined by a maximum shear stress “c”, the Mohr/Coulomb failure surface is also a shear-based failure criterion; however, shear strength increases linearly with the compressive normal stress acting on the failure plane. This concept is like the theory of Coulomb friction, which linearly increases sliding resistance in proportion to the compressive normal force. The Mohr-Coulomb shear strength equation is shown below and depicted in Figure 3.7.4-1. Note that the development follows the standard sign convention wherein positive normal stresses are in tension and negative stresses are in compression.

$$\tau_{max} = C - \sigma_n \tan\phi \tag{Equation 3.7-3}$$

- where, τ_{max} = absolute maximum achievable shear stress
- C = cohesion of material (stress units, user defined)
- ϕ = angle of internal friction (radians, user defined)
- σ_n = normal stress on plane of failure (*negative stress is compressive*)
- T_{cut} = Tension cutoff (tensile stress, user defined)

Figure 3.7.4-1 Mohr/Coulomb failure surface in (σ_n, τ) stress space.



3.7.4.1 Mohr/Coulomb Yield Function

The yield function is a measure of how close the normal and shear stress components (σ_n , τ) are to the failure surface and is defined as:

$$F(\sigma_n, \tau) = |\tau| + \sigma_n \tan \phi - C \quad (\text{Yield function}) \quad \text{Equation 3.7-4}$$

Here it is understood that σ_n and τ are acting in a rotated coordinate system that minimizes the absolute value of the yield function as illustrated by the stress point (σ_n , τ) in Figure 1. Evaluating the yield function for any stress point (σ_n , τ) has three possibilities listed below.

$$F(\sigma_n, \tau) < 0 \quad \text{Stress state is inside failure surface (elastic zone)}$$

$$F(\sigma_n, \tau) = 0 \quad \text{Stress state is on failure surface (plastic zone)}$$

$$F(\sigma_n, \tau) > 0 \quad \text{Stress state is above failure surface (plastic failure, producing large plastic strains)}$$

By making use of Mohr-circle transformations, the normal and shear stress components (σ_n , τ) may be expressed in terms of the x-y stress state (σ_x , σ_y , τ_{xy}) by the equations,

$$\sigma_n = \frac{1}{2}(\sigma_x + \sigma_y) + R \sin \phi \quad \text{Equation 3.7-5}$$

$$\tau = R \cos \phi \quad \text{Equation 3.7-6}$$

$$\text{where, } R = \sqrt{\left(\frac{\sigma_x - \sigma_y}{2}\right)^2 + \tau_{xy}^2} = \text{radius of the Mohr circle.}$$

Thus, the yield function (Equation 3.7-4) may be equivalently expressed in x-y stress components as,

$$F(\sigma_x, \sigma_y, \tau_{xy}) = \frac{R}{\cos \phi} + \frac{\sigma_x + \sigma_y}{2} \tan \phi - C \quad \text{Equation 3.7-7}$$

When a stress vector $\underline{\sigma}$ moves from one point on the failure surface, $F = 0$, to a neighboring point $\underline{\sigma} + \Delta \underline{\sigma}$ on the failure surface, we still must have $F + \Delta F = 0$. Thus, it is evident that ΔF must also equal zero. This is called the consistency requirement and is expressed as,

$$\Delta F = \underline{\mathbf{n}}^T \Delta \underline{\sigma} = 0 \quad \text{Equation 3.7-8}$$

$$\text{where, } \underline{\mathbf{n}} = \begin{pmatrix} \mathbf{n}_x \\ \mathbf{n}_y \\ \mathbf{n}_{xy} \end{pmatrix} = \begin{pmatrix} \partial F / \partial \sigma_x \\ \partial F / \partial \sigma_y \\ \partial F / \partial \tau_{xy} \end{pmatrix} = \begin{pmatrix} (\sigma_x - \sigma_y) / 4R \cos \phi + (\tan \phi) / 2 \\ -(\sigma_x - \sigma_y) / 4R \cos \phi + (\tan \phi) / 2 \\ \tau_{xy} / R \cos \phi \end{pmatrix} \quad \text{Equation 3.7-9}$$

The last equation infers that the direction of vector $\underline{\mathbf{n}}$, as defined in stress space, is normal to the failure surface. Therefore, the consistency requirement (Equation 3.7-8) implies that the direction of stress increments is parallel to the failure surface during plastic deformation.

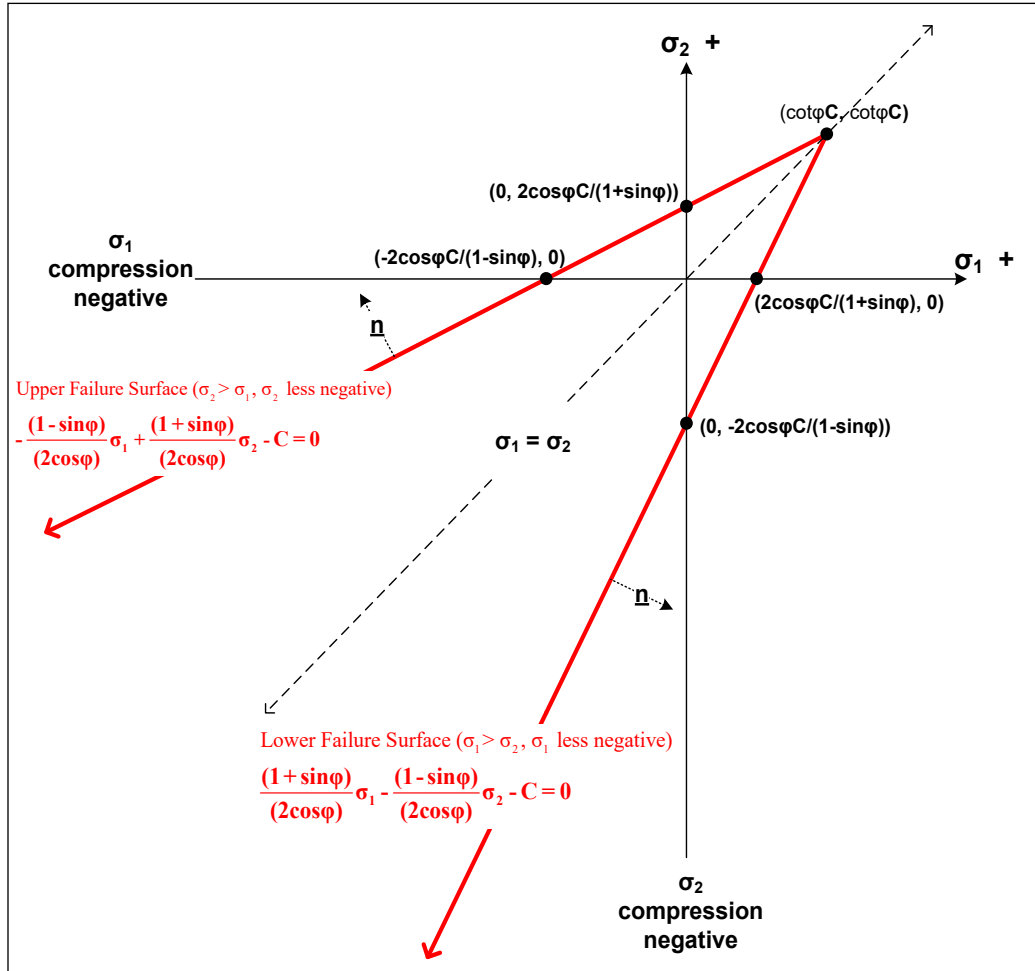
3.1.1.2 Principal Stress Space.

The forgoing development applies to a general stress-state $\sigma_x, \sigma_y, \tau_{xy}$ in any x-y coordinate system. To gain visual insight, it is useful to consider the case of principal stresses wherein $\sigma_x = \sigma_1, \sigma_y = \sigma_2$, and $\tau_{xy} = 0$. For a stress state expressed in principal stress, the normal components to the yield surface are not dependent on stress magnitudes but only on the signs of the principal stresses as shown below.

$$\underline{n} = \begin{pmatrix} n_1 \\ n_2 \\ n_{xy} \end{pmatrix} = \begin{pmatrix} \text{sign}(\sigma_1 - \sigma_2)/2\cos\phi + (\tan\phi)/2 \\ -\text{sign}(\sigma_1 - \sigma_2)/2\cos\phi + (\tan\phi)/2 \\ 0 \end{pmatrix}$$

In principal stress space, the Mohr-Coulomb failure surface is wedge shaped as shown in the figure below by the red lines, which are symmetric about the hydrostatic path $\sigma_1 = \sigma_2$. Also shown are the normal vectors in principal stress space, one for the upper surface and one for the lower surface.

Figure 3.7.6-1. Mohr-Coulomb failure surfaces in principal stress space.



The Mohr-Coulomb failure surface in principal stress space will be used to throughout this writing to illustrate the zones of elasticity, plasticity and tension cutoff.

3.7.5 Flow Rule – Associative and Non-associative.

The final ingredient required to define the plasticity formulation is the adoption of a flow rule that dictates the direction of plastic straining. In vector form the flow rule is expressed as,

$$\Delta \underline{\varepsilon}_p = \Delta \lambda \underline{\mathbf{m}} \quad \text{Equation 3.7-10a}$$

The term $\Delta \lambda$ is the yet-to-be-determined scalar magnitude of the plastic strain increment to be developed. The vector $\underline{\mathbf{m}}$ predefines the direction of the plastic strain increment in stress/strain space. There are two fundamental categories for the choices for $\underline{\mathbf{m}}$:

- **Associative flow rule:** $\underline{\mathbf{m}} = \underline{\mathbf{n}} = \partial F / \partial \underline{\boldsymbol{\sigma}}$. This choice implies the plastic strain flows in the direction normal to the yield surface, i.e., in the direction of the potentially expanding yield surface. This choice is generally found to be valid for metals and results in symmetric plasticity stress-strain matrices; however, geological granular materials are generally not well characterized with this assumption.
- **Non-associative flow rule:** $\underline{\mathbf{m}} = \partial G / \partial \underline{\boldsymbol{\sigma}}$. For this category $\underline{\mathbf{m}}$ is the normal vector to another potential surface in stress space, denoted as $G(\underline{\boldsymbol{\sigma}})$. For granular materials $G(\underline{\boldsymbol{\sigma}})$ is usually taken as a straight line just like the failure surface except that the angle ψ , usually prescribed as the soil's angle of dilatancy, replaces the angle ϕ . The downside of the non-associative flow rule is that it results in non-symmetric stress-strain matrices; however, it will be shown how to maintain a symmetric matrix at the expense of increasing the degree of nonlinearity.

In expanded notation, the flow rule is expressed as,

$$\begin{pmatrix} \Delta \varepsilon_x \\ \Delta \varepsilon_y \\ \Delta \gamma \end{pmatrix}_p = \Delta \lambda \begin{pmatrix} \mathbf{m}_x \\ \mathbf{m}_y \\ \mathbf{m}_{xy} \end{pmatrix} \quad \text{Equation 3.7-10b}$$

3.7.6 Development of Elastic-Plastic Constitutive Relationship

Having stated the assumptions and ingredients of classical Mohr/Coulomb plasticity theory, the final objective is to derive the stress-strain relationship between a stress increment and a total strain increment for implementation into the CANDE program.

Beginning with Equation 3.7-2a, the elastic strain is replaced with the total strain minus plastic strain (Equation 3.7-1a) to get the following relationship.

$$\Delta \underline{\boldsymbol{\sigma}} = \underline{\mathbf{D}}_e (\Delta \underline{\boldsymbol{\varepsilon}} - \Delta \underline{\boldsymbol{\varepsilon}}_p) \quad \text{Equation 3.7-11}$$

Using the flow rule (Equation 3.7-10a), the above relationship may be re-written as follows.

$$\Delta \underline{\boldsymbol{\sigma}} = \underline{\mathbf{D}}_e (\Delta \underline{\boldsymbol{\varepsilon}} - \Delta \lambda \underline{\mathbf{m}}) \quad \text{Equation 3.7-12}$$

In order to determine the scalar $\Delta \lambda$, the consistency requirement demands that the scalar product $\underline{\mathbf{n}}^T \Delta \underline{\boldsymbol{\sigma}} = 0$ when plastic deformation occurs. Thus, performing the dot product on Equation 3.7-12 and rearranging terms, $\Delta \lambda$ is determined in terms of the total strain increment as shown below.

$$\Delta\lambda = \frac{\underline{\mathbf{n}}^T \underline{\mathbf{D}}_e \Delta\underline{\boldsymbol{\varepsilon}}}{\underline{\mathbf{n}}^T \underline{\mathbf{D}}_e \underline{\mathbf{m}}} \quad \text{Equation 3.7-13}$$

Again, returning to Equation 3.7-12 with above value of $\Delta\lambda$, we obtain the desired general stress-strain relationship shown below,

$$\Delta\underline{\boldsymbol{\sigma}} = (\underline{\mathbf{D}}_e - \underline{\mathbf{D}}_p) \Delta\underline{\boldsymbol{\varepsilon}} \quad \text{Equation 3.7-14}$$

wherein $\underline{\mathbf{D}}_p$ is the plasticity matrix given by,

$$\underline{\mathbf{D}}_p = \left(\frac{1}{\alpha}\right) \underline{\mathbf{D}}_e \underline{\mathbf{m}} \underline{\mathbf{m}}^T \underline{\mathbf{D}}_e \quad \text{Equation 3.7-15}$$

and, alpha is a scalar given by, $\alpha = \underline{\mathbf{n}}^T \underline{\mathbf{D}}_e \underline{\mathbf{m}}$.

As described by Equation 3.7-15, $\underline{\mathbf{D}}_p$ is a non-symmetric matrix because $\underline{\mathbf{m}} \underline{\mathbf{m}}^T$ is not symmetric unless an associative flow is assumed where $\underline{\mathbf{m}} = \underline{\mathbf{n}}$. There is a clever trick to convert $\underline{\mathbf{D}}_p$ into a symmetric matrix for the non-associative flow rule as follows. We begin by expressing the vector product of the plasticity matrix times the strain increment vector to get:

$$\underline{\mathbf{D}}_p \Delta\underline{\boldsymbol{\varepsilon}} = \frac{1}{\alpha} \underline{\mathbf{D}}_e \underline{\mathbf{m}} \underline{\mathbf{m}}^T \underline{\mathbf{D}}_e \Delta\underline{\boldsymbol{\varepsilon}} = \frac{1}{\alpha} \underline{\mathbf{D}}_e \underline{\mathbf{m}} (\underline{\mathbf{n}}^T \underline{\mathbf{D}}_e \Delta\underline{\boldsymbol{\varepsilon}}) \quad \text{Equation 3.7-16a}$$

Note that the term in parenthesis ($\underline{\mathbf{n}}^T \underline{\mathbf{D}}_e \Delta\underline{\boldsymbol{\varepsilon}}$) is a scalar quantity which can be moved as desired. Next if we multiply the above equation by unity by means of multiplying and dividing with a new scalar ($\underline{\mathbf{m}}^T \underline{\mathbf{D}}_e \Delta\underline{\boldsymbol{\varepsilon}}$), then the above equation may be expressed as,

$$\underline{\mathbf{D}}_p \Delta\underline{\boldsymbol{\varepsilon}} = \frac{1}{\alpha} \underline{\mathbf{D}}_e \underline{\mathbf{m}} (\underline{\mathbf{m}}^T \underline{\mathbf{D}}_e \Delta\underline{\boldsymbol{\varepsilon}}) \frac{(\underline{\mathbf{n}}^T \underline{\mathbf{D}}_e \Delta\underline{\boldsymbol{\varepsilon}})}{(\underline{\mathbf{m}}^T \underline{\mathbf{D}}_e \Delta\underline{\boldsymbol{\varepsilon}})} = \frac{\kappa}{\alpha} [\underline{\mathbf{D}}_e \underline{\mathbf{m}} \underline{\mathbf{m}}^T \underline{\mathbf{D}}_e] \Delta\underline{\boldsymbol{\varepsilon}} \quad \text{Equation 3.7-16b}$$

Thus, the plasticity matrix with non-associative flow rule is now in a symmetric form as shown below.

$$\underline{\mathbf{D}}_p = \frac{\kappa}{\alpha} \underline{\mathbf{D}}_e \underline{\mathbf{m}} \underline{\mathbf{m}}^T \underline{\mathbf{D}}_e \quad \text{symmetric plasticity matrix.} \quad \text{Equation 3.7-17}$$

$$\text{where, } \kappa = \frac{(\underline{\mathbf{n}}^T \underline{\mathbf{D}}_e \Delta\underline{\boldsymbol{\varepsilon}})}{(\underline{\mathbf{m}}^T \underline{\mathbf{D}}_e \Delta\underline{\boldsymbol{\varepsilon}})} \quad \text{scalar dependent on strain increment.} \quad \text{Equation 3.7-18}$$

$\underline{\mathbf{D}}_p$ is symmetric because the product $\underline{\mathbf{m}} \underline{\mathbf{m}}^T$ is a symmetric matrix as is $\underline{\mathbf{D}}_e$. The penalty for symmetry is that the scalar multiplier κ causes another level of nonlinearity because it contains the unknown strain increment. Therefore, more iterations to convergence are generally required. However, it has been shown that the time and storage efficiency of symmetric equation solvers more than makes up for additional iterations.

In expanded notation, the individual components of the 3x3 plasticity matrix are shown below for the general case of a non-associative flow rule.

$$\underline{D}_p = \frac{\kappa}{\alpha} \begin{pmatrix} (D_{11}m_x + D_{12}m_y)^2 & (D_{11}m_x + D_{12}m_y)(D_{12}m_x + D_{11}m_y) & (D_{11}m_x + D_{12}m_y)D_{33}m_{xy} \\ (D_{12}m_x + D_{11}m_y)(D_{11}m_x + D_{12}m_y) & (D_{12}m_x + D_{11}m_y)^2 & (D_{12}m_x + D_{11}m_y)D_{33}m_{xy} \\ D_{33}m_{xy}(D_{11}m_x + D_{12}m_y) & D_{33}m_{xy}(D_{12}m_x + D_{11}m_y) & (D_{33}m_{xy})^2 \end{pmatrix}$$

where $\alpha = D_{11}(n_x m_x + n_y m_y) + D_{12}(n_x m_y + n_y m_x) + D_{33}(n_{xy} m_{xy})$

$$\kappa = \frac{n_x(D_{11}\Delta\varepsilon_x + D_{12}\Delta\varepsilon_y) + n_y(D_{12}\Delta\varepsilon_x + D_{11}\Delta\varepsilon_y) + n_{xy}(D_{33}\gamma_{xy})}{m_x(D_{11}\Delta\varepsilon_x + D_{12}\Delta\varepsilon_y) + m_y(D_{12}\Delta\varepsilon_x + D_{11}\Delta\varepsilon_y) + m_{xy}(D_{33}\gamma_{xy})}$$

For the special case of the associative flow rule, we have $\underline{m} = \underline{n}$ and $\kappa = 1$, and the plasticity matrix is given by:

$$\underline{D}_p = \frac{1}{\alpha} \begin{pmatrix} (D_{11}n_x + D_{12}n_y)^2 & (D_{11}n_x + D_{12}n_y)(D_{12}n_x + D_{11}n_y) & (D_{11}n_x + D_{12}n_y)D_{33}n_{xy} \\ (D_{12}n_x + D_{11}n_y)(D_{11}n_x + D_{12}n_y) & (D_{12}n_x + D_{11}n_y)^2 & (D_{12}n_x + D_{11}n_y)D_{33}n_{xy} \\ D_{33}n_{xy}(D_{11}n_x + D_{12}n_y) & D_{33}n_{xy}(D_{12}n_x + D_{11}n_y) & (D_{33}n_{xy})^2 \end{pmatrix}$$

where $\alpha = D_{11}(n_x^2 + n_y^2) + 2D_{12}n_x n_y + D_{33}n_{xy}^2$

In summary, the fundamental constitutive relationship given by Equation 3.7-14 is repeated below along with a new scalar parameter β that is a multiplier of the plasticity matrix where $0 \leq \beta \leq 1$.

$$\Delta \underline{\sigma} = (\underline{D}_e - \beta \underline{D}_p) \Delta \underline{\varepsilon} \quad \text{Equation 3.7-19}$$

The purpose of the β multiplier is to control the percentage of the plasticity matrix that is applied in any iteration of a particular load step. For example, if the starting and ending stress states remain within the elastic domain, then $\beta = 0$. Conversely if the stress increment starts and remains in the plastic zone, then $\beta = 1$. As will be discussed in the subsequent section on nonlinear solution strategy, transitioning from the elastic zone to the plastic zone requires determining a fractional value of β . However, the transition from the plastic zone to the elastic zone is always done with $\beta = 0$ because this is what produces permanent plastic deformation as observed in laboratory experiments (i.e., elastic unloading).

3.7.7 Development of Tension Cutoff Methodology

The Mohr-Coulomb failure surface does not mimic the complicated soil behavior that occurs when the stress state becomes predominantly tensile wherein soil particles separate and become discontinuous. To deal with this problem, a special tension cutoff methodology is introduced that simulates two important phenomena; the loss of stiffness and the inability to sustain additional tensile stress. Conversely, if the stress state changes direction and becomes compressive, then the tension cutoff model allows a gradual increase in stiffness and the ability to carry compressive stresses as the stress-state returns to the zones controlled by the Mohr-Coulomb failure surface.

Tension cutoff is simulated with a plasticity-based constitutive model whose yield surface is a straight line, orthogonal to the hydrostat ($\sigma_x = \sigma_y$), and intersecting the hydrostat at the point $\sigma_x = \sigma_y = T_{cut}$. Specifically, the tension cutoff yield function, which is independent of shear stress, is defined by Equation 3.7-20 and illustrated in Figure 3.7.7-1.

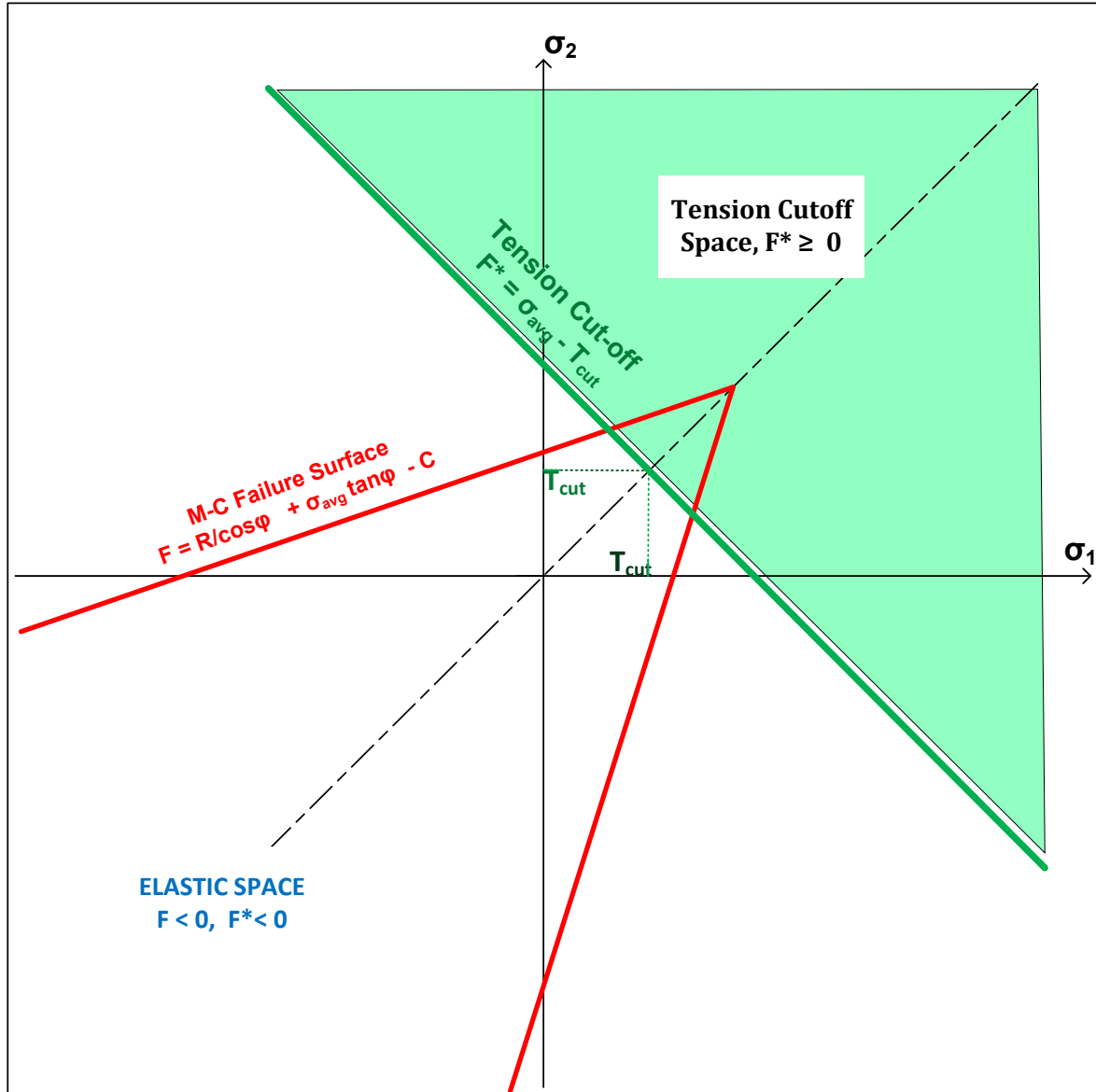
$$F^*(\sigma_x, \sigma_y) = \sigma_{\text{avg}} - T_{\text{cut}} \quad \text{Equation 3.7-20}$$

where, F^* = Tension cutoff yield function.

$\sigma_{\text{avg}} = \frac{1}{2}(\sigma_x + \sigma_y)$ = average (hydrostatic) stress, i.e., center of Mohr circle.

T_{cut} = Limit of average tensile stress, a model parameter, $0 \leq T_{\text{cut}} \leq C \cot \phi$

Figure 3.7.7-1. Illustration of tension cutoff zone



Note that the asterisk symbol “*” is used to distinguish tension cutoff symbols from the corresponding Mohr-Coulomb symbols. Evaluation of the tension yield function for any stress state has two possible results listed below.

$F^*(\sigma_x, \sigma_y) < 0$ Stress state is in Mohr-Coulomb domain - tension cutoff not activated.

$F^*(\sigma_x, \sigma_y) \geq 0$ Stress state is on or above tension cutoff surface (green) – tension plasticity activated.

As recorded below, the normal vector components to the tension cutoff surface are easily calculated because they are constant and independent of the stress state.

$$\underline{\mathbf{n}}^* = \begin{pmatrix} \mathbf{n}_x^* \\ \mathbf{n}_y^* \\ \mathbf{n}_{xy}^* \end{pmatrix} = \begin{pmatrix} \partial F_{TC} / \partial \sigma_x \\ \partial F_{TC} / \partial \sigma_y \\ \partial F_{TC} / \partial \tau_{xy} \end{pmatrix} = \begin{pmatrix} 1/2 \\ 1/2 \\ 0 \end{pmatrix} \quad \text{Equation 3.7-21}$$

A fluid-like elasticity matrix is assigned to the tension cutoff space in order to limit the development of shear stresses and, as will be shown with the inclusion of the plasticity matrix, to also limit the normal stresses. Specifically, the elasticity matrix for the tension zone employs the original bulk modulus value along with a very weak shear modulus, i.e., one-thousandth of the original shear modulus.

$$\underline{\mathbf{D}}_e^* = \begin{pmatrix} (B + \frac{4}{3}G^*) & (B - \frac{2}{3}G^*) & 0 \\ (B - \frac{2}{3}G^*) & (B + \frac{4}{3}G^*) & 0 \\ 0 & 0 & G^* \end{pmatrix} \quad \text{Equation 3.7-22}$$

Where, $\underline{\mathbf{D}}_e^*$ = Tension elasticity matrix (3x3) composed of elastic parameters B, G*
 B = bulk modulus of original soil model.
 G* = G/1000, reduced shear modulus of original soil model.

Following the same plasticity development resulting in Equation 3.7-17 for the Mohr-Coulomb failure surface, the plasticity matrix for the tension cutoff failure surface is recorded below wherein the associative flow rule is assumed.

$$\underline{\mathbf{D}}_p^* = \left(\frac{1}{\alpha^*} \right) \underline{\mathbf{D}}_e^* \underline{\mathbf{n}}^* \underline{\mathbf{n}}^{*T} \underline{\mathbf{D}}_e^* = \begin{pmatrix} (B + \frac{1}{3}G^*) & (B + \frac{1}{3}G^*) & 0 \\ (B + \frac{1}{3}G^*) & (B + \frac{1}{3}G^*) & 0 \\ 0 & 0 & 0 \end{pmatrix} \quad \text{Equation 3.7-23}$$

In summary, the fundamental constitutive relationship generically expressed by Equation 3.7-14 is re-expressed below along with a new scalar parameter ρ that is a multiplier of the entire composite matrix where $0 \leq \rho \leq 1$.

$$\Delta \underline{\boldsymbol{\sigma}} = \rho (\underline{\mathbf{D}}_e^* - \underline{\mathbf{D}}_p^*) \Delta \underline{\boldsymbol{\varepsilon}} \quad \text{Equation 3.7-24}$$

The purpose of the ρ multiplier is to control the percentage of the composite tension matrix that is applied in any iteration of a particular load step. For example, if the starting and ending stress states remain within the Mohr-Coulomb domain where $F^* < 0$, then $\rho = 0$. Conversely if the stress increment starts and remains in the tensile zone, then $\rho = 1$. Upon inspecting the composite elastic-plastic constitutive matrix, $\mathbf{C}_{ep}^* = \mathbf{D}_e^* - \mathbf{D}_p^*$, it may be observed that the bulk modulus

parameters cancel. Consequently, large volumetric strains only produce very small increases in hydrostatic stress, σ_{avg} , which is one objective the tension cutoff methodology.

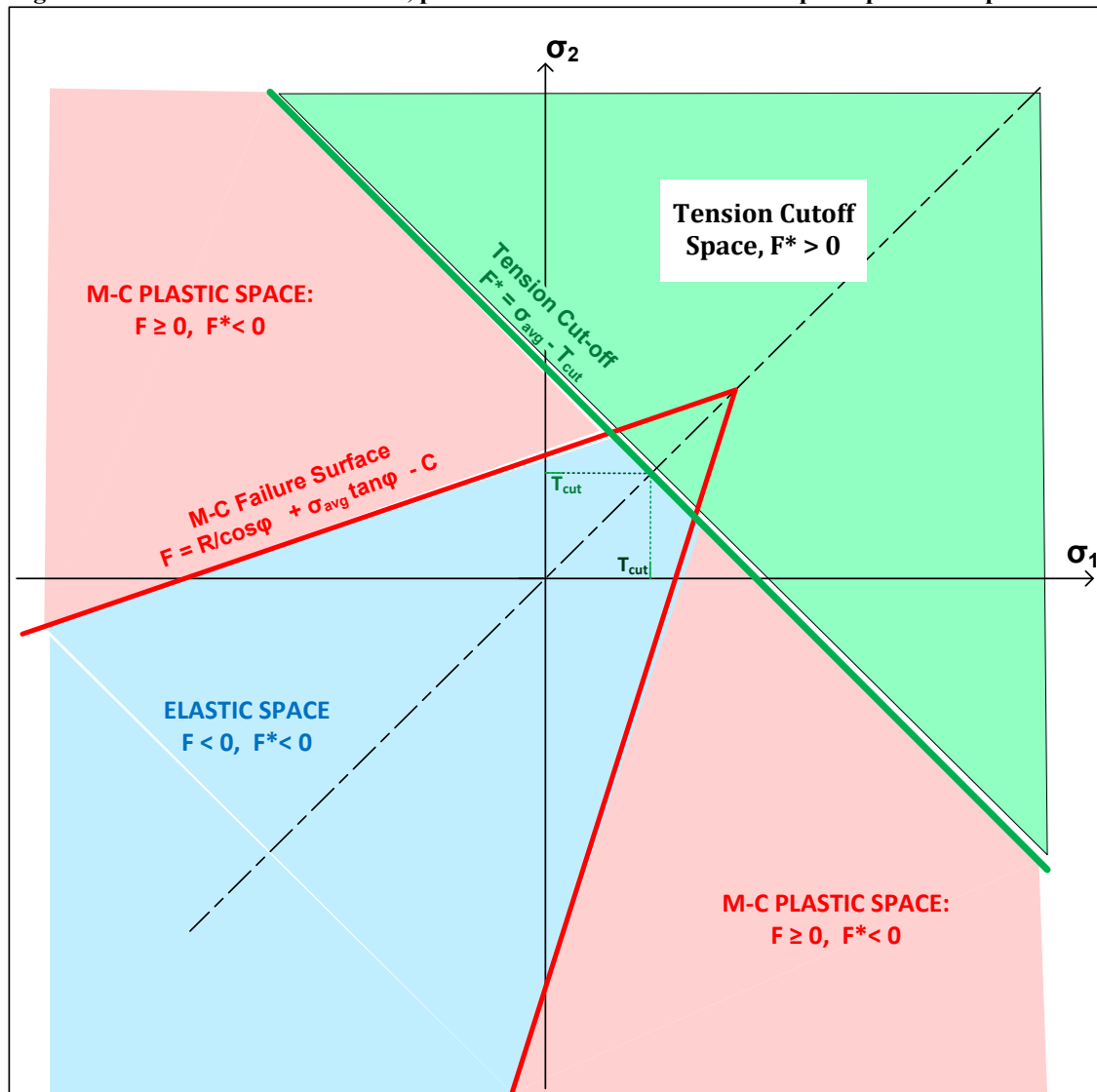
As will be discussed in the subsequent section on nonlinear solution strategy, transitioning from the Mohr-Coulomb zone to the tension cutoff zone requires determining the fractional value of the parameter ρ . Unlike the Mohr-Coulomb strategy, unloading from the tension zone is accomplished with the full C^*_{ep} matrix, rather than just the elastic matrix. The reason for this approach is to allow the tensile-rarified soil to smoothly recombine in a nonlinear-elastic manner without creating abrupt changes in stiffness and permanent volume-metric strains.

3.7.8 Nonlinear Solution Strategy for Mohr-Coulomb Plasticity with Tension Cutoff.

Recap of entire model

The previous developments established constitutive matrices that are applicable within the elastic, plastic and tension-cutoff zones of stress space. These zones are illustrated in the figure below for principal stresses.

Figure 3.7.8-1. Illustration of elastic, plastic and tension cutoff zones in principal stress space



The zone boundaries are defined by the Mohr-Coulomb yield function, $F=0$ and the tension-cutoff yield function $F^*=0$. For any arbitrary stress state, $\underline{\sigma} = \langle \sigma_x, \sigma_y, \tau_{xy} \rangle^T$, the zone to which this stress state belongs is determined by the following criteria;

- (1) Elastic zone, $F(\underline{\sigma}) < 0$ and $F^*(\underline{\sigma}) < 0$, with constitutive matrix, $\underline{C}_m = \underline{D}_e$ (From Equation 3.7-2)
- (2) Plastic zone, $F(\underline{\sigma}) \geq 0$ and $F^*(\underline{\sigma}) < 0$, with constitutive matrix, $\underline{C}_m = \underline{D}_e - \underline{D}_p$ (From Equation 3.7-14)
- (3) Tension-cutoff zone, $F^*(\underline{\sigma}) \geq 0$, with constitutive matrix, $\underline{C}_m = \underline{D}_e^* - \underline{D}_p^*$ (From Equation 3.7-24)

If the stress increment begins and ends in the same zone, then the constitutive matrix is as defined above. However, if the stress increment transitions from one zone to another during any load step, the parameters β and ρ enter into the constitutive matrix for general form expressed below.

$$\underline{C}_m = (1-\rho)(\underline{D}_e - \beta \underline{D}_p) + \rho(\underline{D}_e^* - \beta \underline{D}_p^*) \quad \text{Equation 3.7-25}$$

where, β = fraction of stress increment in plastic zone ($0 \leq \beta \leq 1$)
 ρ = fraction of stress increment in tension-cutoff zone ($0 \leq \rho \leq 1$)

As discussed next, convergence is dependent on achieving stable constitutive matrices for all elements, which in turn is dependent upon obtaining stabilized values for β and ρ .

Incremental-iterative procedure and convergence.

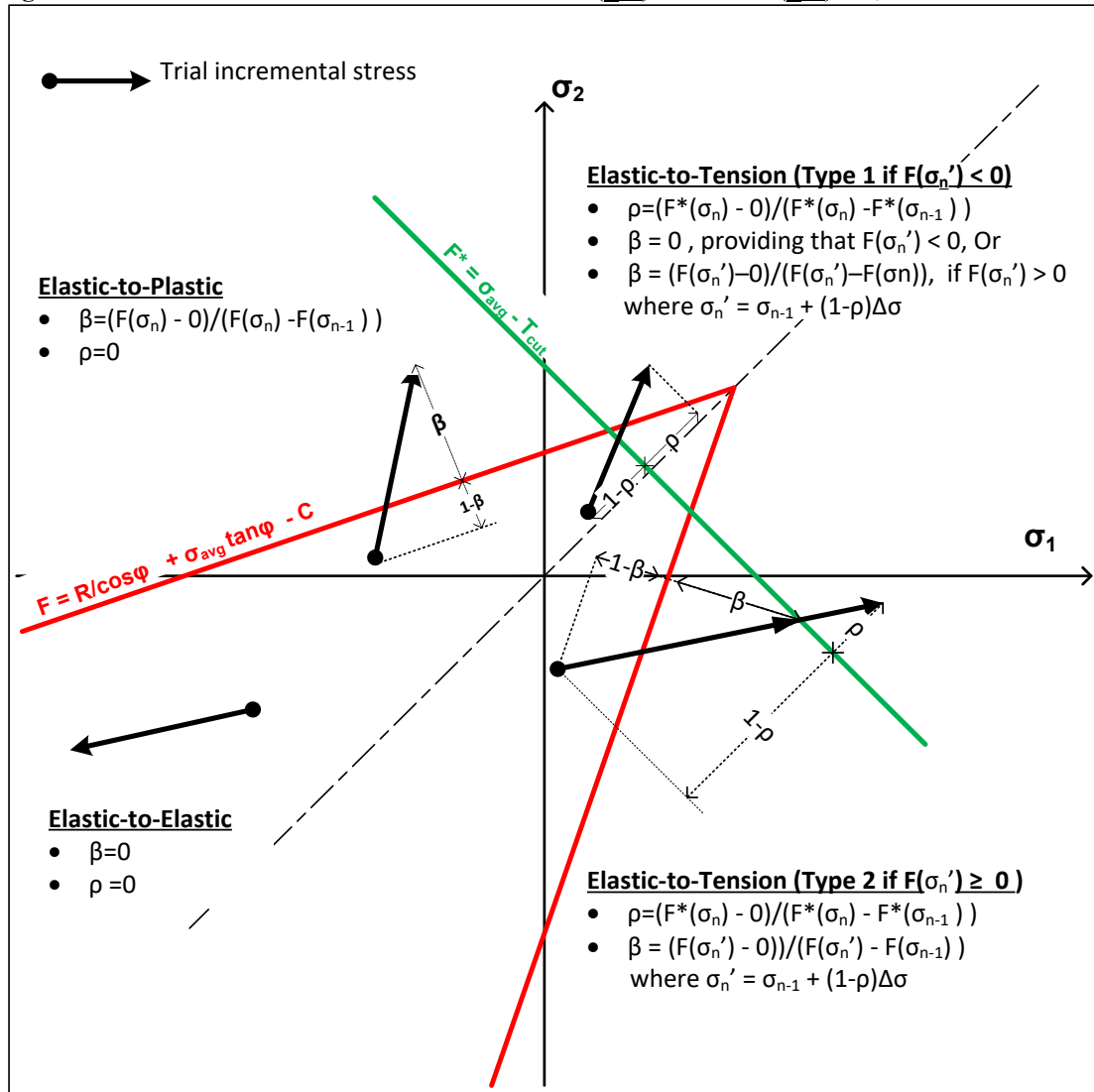
CANDE, like most finite element programs, is a displacement-based formulation wherein body loads and boundary loads are applied in a prescribed series of load steps. Each load-step requires the global assembly of the current estimate of the element stiffness matrices and a trial solution for displacement increments is obtained. Next, incremental strains are computed from the displacements and then incremental stresses are computed from the strains based on the current estimate of the stress-strain relationship. The new stress/strain state is used to update the stress-strain relationship and the whole solution process repeated until convergence is achieved. Repeated solutions within a load-step are called iterations.

With the above understanding, the basic algorithm is developed at the element stress-strain level wherein all elements must converge during each load step before progressing to the next load step. The algorithm begins with the premise that a valid solution has been obtained for each element at the previous load step n-1, and the objective is to advance the solution to load step n.

The constitutive matrix assigned to each individual element is dependent on the known stress-state defining the starting zone (elastic, plastic or tension-cutoff) and the ending zone of the trial stress increment. The following three sets of figures with tables offer complete set of conditions to define the constitutive matrix for all starting and ending stress states.

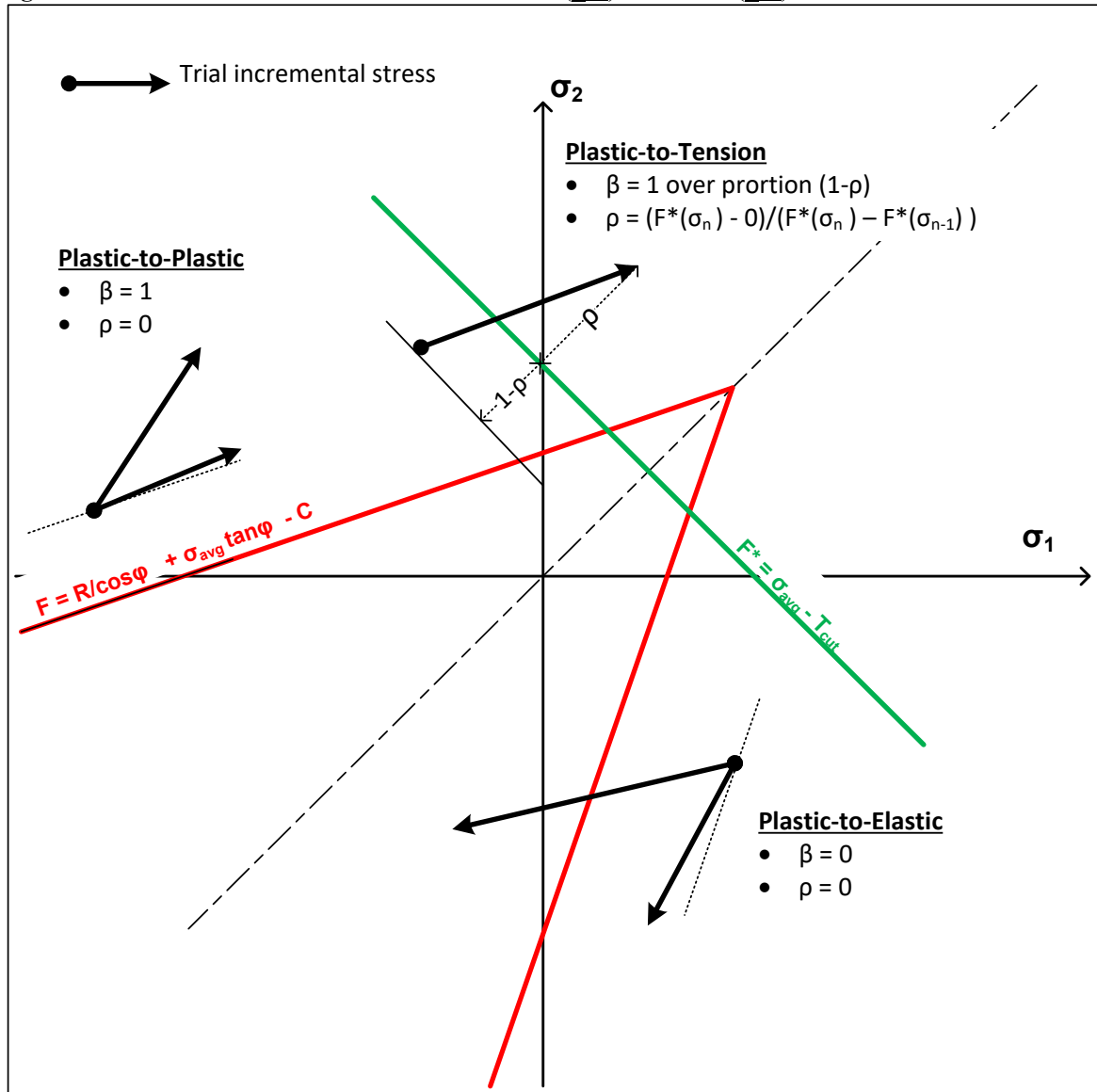
Strictly speaking the non-hardening Mohr Coulomb model cannot sustain a stress state above the failure surfaces without producing unrestrained plastic flow. To avoid these singular constitutive matrices which produce infinitely large strains and displacements, the CANDE algorithm increases the elasticity matrices \underline{D}_e by 1/1000 whenever $\beta = 1.0$. Likewise for \underline{D}_e^* whenever $\rho = 1.0$. Thus, completely plastic responses are accompanied by large increases in strain magnitude, but not infinite NaN numbers.

Figure 3.7.8-2 Case 1. Paths for Elastic Zone Start: $F(\underline{\sigma}_{n-1}) < 0$ and $F^*(\underline{\sigma}_{n-1}) < 0$,



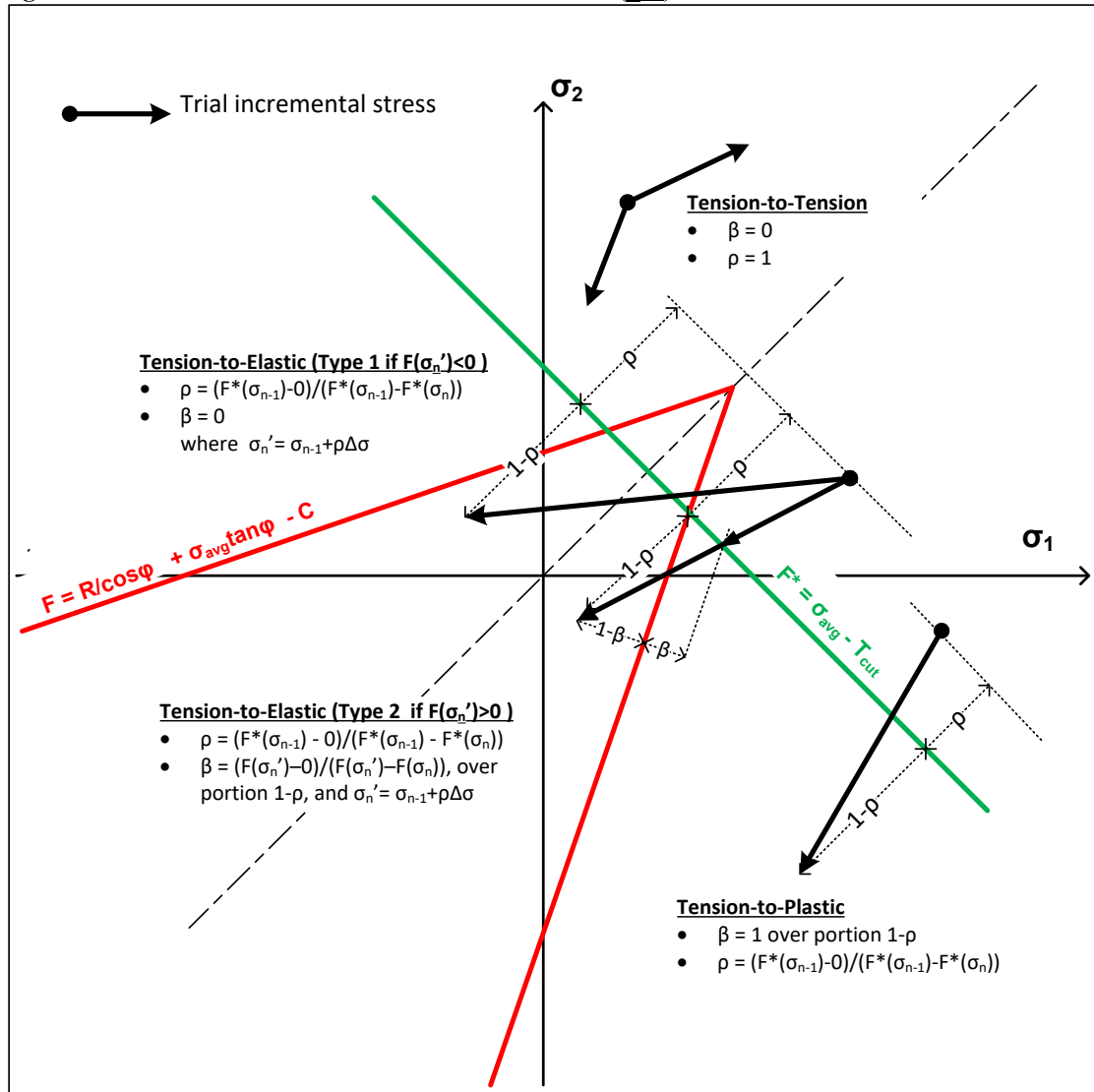
Stress State Ending Zone	Criteria for Ending Zone	Plasticity parameter β	Tension-cutoff parameter ρ	Constitutive matrix \underline{C}_m
Elastic	$F(\underline{\sigma}_n) < 0$, and $F^*(\underline{\sigma}_n) < 0$	0	0	\underline{D}_e
Plastic	$F(\underline{\sigma}_n) \geq 0$, and $F^*(\underline{\sigma}_n) < 0$	$(F(\underline{\sigma}_n) - 0) / (F(\underline{\sigma}_n) - F(\underline{\sigma}_{n-1}))$	0	$\underline{D}_e - \beta \underline{D}_p$
Tension (Type 1)	$F(\underline{\sigma}'_n) \leq 0$, and $F^*(\underline{\sigma}_n) \geq 0$	0	$(F^*(\underline{\sigma}_n) - 0) / (F^*(\underline{\sigma}_n) - F^*(\underline{\sigma}_{n-1}))$	$(1-\rho)\underline{D}_e + \rho(\underline{D}^*_e - \underline{D}^*_p)$
Tension (Type 2)	$F(\underline{\sigma}'_n) > 0$, and $F^*(\underline{\sigma}_n) \geq 0$	$(F(\underline{\sigma}'_n) - 0) / (F(\underline{\sigma}'_n) - F(\underline{\sigma}_{n-1}))$	$(F^*(\underline{\sigma}_n) - 0) / (F^*(\underline{\sigma}_n) - F^*(\underline{\sigma}_{n-1}))$	$(1-\rho)(\underline{D}_e - \beta \underline{D}_p) + \rho(\underline{D}^*_e - \underline{D}^*_p)$

Figure 3.7.8-3 Case 2. Paths for Plastic Zone Start: $F(\underline{\sigma}_{n-1}) \geq 0$ and $F^*(\underline{\sigma}_{n-1}) < 0$



Stress State Ending Zone	Criteria for Ending Zone	Plasticity parameter β	Tension-cutoff parameter ρ	Constitutive matrix \underline{C}_m
Elastic	$F(\underline{\sigma}_n) < F(\underline{\sigma}_{n-1})$, and $F^*(\underline{\sigma}_n) < 0$	0	0	\underline{D}_e
Plastic	$F(\underline{\sigma}_n) \geq F(\underline{\sigma}_{n-1})$, and $F^*(\underline{\sigma}_n) < 0$	1	0	$\underline{D}_e - \underline{D}_p$
Tension	$F^*(\underline{\sigma}_n) \geq 0$	1	$(F^*(\underline{\sigma}_n) - 0) / (F^*(\underline{\sigma}_n) - F^*(\underline{\sigma}_{n-1}))$	$(1-\rho)(\underline{D}_e - \underline{D}_p) + \rho(\underline{D}_e^* - \underline{D}_p^*)$

Figure 3.7.8-4 Case 3. Paths for Tension Zone Start: $F^*(\underline{\sigma}_{n-1}) \geq 0$



Stress State Ending Zone	Criteria for Ending Zone	Plasticity parameter β	Tension-cutoff parameter ρ	Constitutive matrix \underline{C}_m
Elastic (Type 1)	$F(\underline{\sigma}_n) < 0$, and $F(\underline{\sigma}'_n) < 0$, and $F^*(\underline{\sigma}_n) < 0$	0	$(F^*(\underline{\sigma}_{n-1}) - 0) / (F^*(\underline{\sigma}_{n-1}) - F^*(\underline{\sigma}_n))$	$(1-\rho)\underline{D}_e + \rho(\underline{D}^*_e - \underline{D}^*_p)$
Elastic (Type 2)	$F(\underline{\sigma}_n) < 0$, and $F(\underline{\sigma}'_n) \geq 0$, and $F^*(\underline{\sigma}_n) < 0$	$(F(\underline{\sigma}'_n) - 0) / (F(\underline{\sigma}'_n) - F(\underline{\sigma}_n))$	$(F^*(\underline{\sigma}_{n-1}) - 0) / (F^*(\underline{\sigma}_{n-1}) - F^*(\underline{\sigma}_n))$	$(1-\rho)(\underline{D}_e - \beta \underline{D}_p) + \rho(\underline{D}^*_e - \underline{D}^*_p)$
Plastic	$F(\underline{\sigma}_n) \geq 0$, and $F^*(\underline{\sigma}_n) < 0$	1	$(F^*(\underline{\sigma}_{n-1}) - 0) / (F^*(\underline{\sigma}_{n-1}) - F^*(\underline{\sigma}_n))$	$(1-\rho)(\underline{D}_e - \underline{D}_p) + \rho(\underline{D}^*_e - \underline{D}^*_p)$
Tension	$F^*(\underline{\sigma}_n) \geq 0$	0	1	$\underline{D}^*_e - \underline{D}^*_p$

The logic associated with above figures and charts produce a fairly robust algorithm that usually converges, even when large strains occur due to stress states that are imposed above the failure surfaces. CANDE deduces convergence when the constitutive matrices of all elements are stabilized i.e., remains essentially constant over two iterations. Sometimes elements may chatter, meaning that the element oscillates between one end state and another. When this occurs, CANDE has been equipped with logic to choose the most likely state. However, there are times when Mohr-Coulomb does not converge, when this occurs the following suggestions are offered:

1. Set ITMAX = -50 in line A-1. The minus sign forces CANDE to continue processing each load step even if convergence is not achieved.
2. Set IWRT = 4 in line C-2 of Level 3 (or appropriate C-line in Level 2 options). This command provides a trace printout in the CANDE output report for each iteration of all the Mohr-Coulomb elements showing the convergence errors.
3. Rather than applying increments of force to represent live loads, apply displacement increments. The equivalent incremental force can be determined by applying the displacement increment through a link element.

This completes the Mohr-Coulomb model development.

3.8 Comparison of Duncan/Selig and Mohr/Coulomb Soil Models

The remainder of this soil-model Chapter is devoted to a comparative study between the Duncan/Selig and Mohr/Coulomb soil models. The comparative study includes the following components.

1. *Experimental data suite.* Summary tables of experimental results for Cooks Bayou sand are provided to document the data base, which includes three triaxial tests, one hydrostatic test, and one confined compression test. All data is for loading, not unloading.
2. *Parameter identification.* Model parameters for the Mohr/Coulomb and Duncan/Selig model are computed to best fit the triaxial data and parameter identification techniques are discussed.
3. *Comparative plots.* The Mohr/Coulomb and Duncan/Selig model predictions are plotted against the corresponding experimental data and the models are judged accordingly.

Each of the above components is addressed, in turn, in the following subsections.

3.8.1 Experimental Data Suite

Experimental test data used in this study was generated by the US Army Core of Engineers at the Waterways Experiment Station in the 1970s using vintage triaxial testing equipment. All soil samples were taken from a natural sand quarry called Cook's Bayou wherein the sand is fairly well graded with a small amount of fines. Soil samples were tested in dry conditions with initial density of 112 pcf. Although the test data is old, it is considered very reliable.

The suite of experimental tests includes three standard tri-axial tests with confining pressures of 25, 50 and 100 psi as presented in Table 3.8.1-1 wherein all responses are referenced to zero after the confining pressure is applied so that deviator stress is equal to axial stress. The deviator stress at failure is highlighted in yellow, which is closely correlated with the radial stain approaching $\frac{1}{2}$ of the axial stain, i.e., Poisson ratio approaching 0.5.

TABLE 3.8.1-1. Standard tri-axial test data for confining pressures = 25, 50 and 100 psi

Confining stress = 25 psi			Confining stress = 50 psi			Confining stress = 100 psi		
Axial Stress psi	Axial Strain %	Radial Strain %	Axial Stress psi	Axial Strain %	Radial Strain %	Axial Stress psi	Axial Strain %	Radial Strain %
0.00	0.00	0.00	0.00	0.00	0.00	0.00	0.00	0.00
14.80	0.41	-0.04	13.11	0.33	-0.04	25.49	0.63	-0.04
31.80	0.94	-0.18	30.14	0.65	-0.11	76.45	1.91	-0.22
48.78	1.57	-0.40	64.17	1.74	-0.37	127.32	3.33	-0.58
65.72	2.48	-0.80	98.10	3.23	-0.91	178.02	5.04	-1.24
82.58	3.92	-1.54	131.85	5.61	-1.87	228.31	7.31	-2.48
99.18	7.40	-3.33	164.82	10.30	-4.83	277.73	10.75	-4.86
110.84	13.01	-6.40	176.00	13.95	-7.18	310.07	13.55	-6.95
113.00	14.09	-6.99	-	-	-	314.00	17.08	-9.57

Next, Table 3.8.1-2 contains the results of a hydrostatic test on Cook's Bayou sand. The right column is the computed secant bulk modulus determined by dividing the current hydrostatic pressure by the current volumetric strain.

TABLE 3.8.1-2 Hydrostatic test data for Cook’s Bayou sand

Hydrostatic Pressure psi	Volume change %	Secant Bulk Modulus psi
0	0	--
20	1.62	1235
45	2.73	1648
70	3.53	1983
95	4.49	2116
120	5.12	2344
145	5.67	2557
170	6.23	2729
195	6.66	2928
220	7.12	3090
245	7.53	3254

Lastly, Table 3.8.1-3 contains the experimental results for a uniaxial strain test, also called a confined compression test, also called a K_0 test. For this experiment a uniform hydrostatic pressure is applied, then axial stress is increased until the observed radial strain is zero. By definition, the secant confined modulus (M_s) is equal to the total axial stress divided by the total axial strain, and the lateral coefficient (K_0) is the radial stress divided by the axial stress. These calculations are shown in the last two columns, respectively.

TABLE 3.8.1-3. Uniaxial strain data for Cook’s Bayou sand .

Total axial stress psi	Total radial stress psi	Total axial strain %	Secant Confined Modulus psi	Lateral Coefficient, K_0 -
0	0	0	--	--
25.2	8	1.36	1853	0.317
50.71	18	2.25	2254	0.355
78.59	28	3.15	2495	0.356
129.78	48	4.31	3011	0.370
204.9	73	5.72	3582	0.356
273.24	98	6.8	4018	0.359
345.48	123	7.89	4379	0.356
413.66	148	8.79	4706	0.358
481.5	173	9.65	4990	0.359

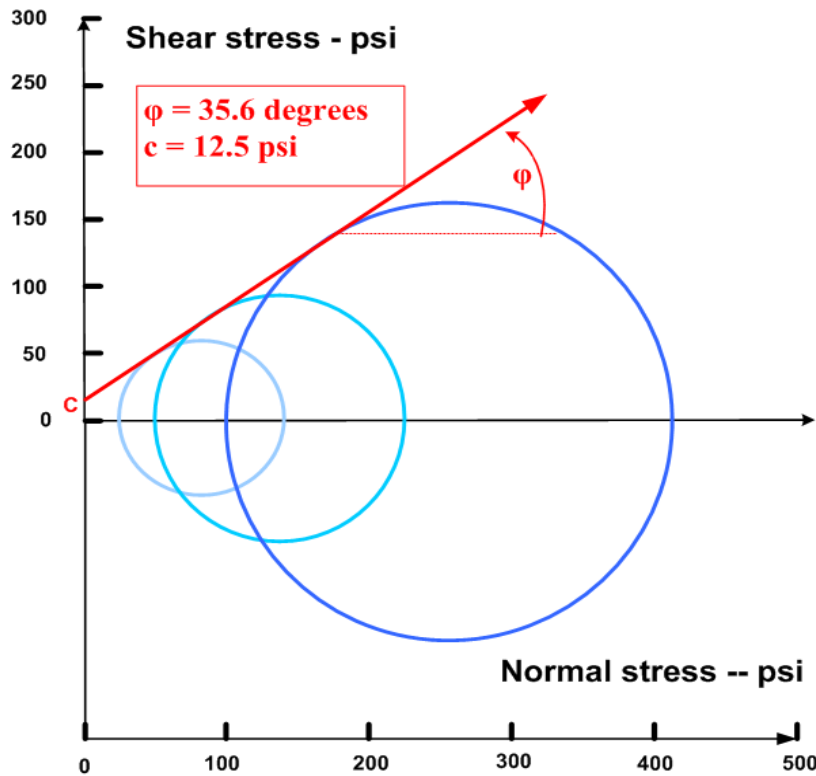
Subsequently, the tabular data in the above tables will be shown as plots versus soil model predictions. However, the raw data in the above tables will be useful to researchers to extend this study to include other soil models.

3.8.2 Parameter Identification

The tri-axial test data in Table 3.8.1-1 is used to determine values for the elastic parameters E and ν , the Mohr/Coulomb parameters c and ϕ , and all parameters for Duncan Young’s modulus. Hydrostatic test data in Table 3.8.1-2 is used to determine Selig bulk modulus parameters, B_1 and ϵ_u . Uniaxial strain data in Table 3.8.1-3 is not used for parameter identification; hence, this data serves as a blind test for the predictive capability of each soil model.

The three deviatoric failure stresses highlighted in Table 3.8.1-1 (113, 176, and 314 psi) are used to construct Mohr circles for each failure state as illustrated in the figure below. In this case, the Mohr-Coulomb failure surface forms a straight line with $c = 12.5$ psi and $\phi = 35.6^\circ$, these parameters apply to both the Mohr/Coulomb and Duncan/Selig models with $\Delta\phi = 0$.

FIGURE 3.8.2-1. Mohr-Coulomb failure surface determined from tri-axial test data.



Initial values for Young’s modulus are determined by dividing initial axial stress by initial axial strain, which produces $E = 3069, 3972$ and 4046 psi for each confining pressure, respectively. For the linear-elastic and the Mohr/Coulomb elastoplastic soil models, the average value $E = 3876$ psi is assigned to Young’s modulus. Likewise, Poisson ratio is $\nu = 0.30$ is the average result from all ratios of radial strain to axial strain. Table 3.8.2-1 summarizes the parameter values used for the linear elastic and Mohr/Coulomb elastoplastic models.

TABLE 3.8.2-1 . Linear Elastic and Mohr/Coulomb parameters for Cooks Bayou Sand.

Parameter Name	Symbol	Values based on best fit to data
Cohesion strength	c	12.5 psi
Internal friction angle	φ	35.6°
Young’s modulus	E	3876 psi
Poisson’s ratio	ν	0.30

Initial Young’s modulus for the Duncan/Selig model is defined by a power law and the best fit to the initial moduli data is $K = 238$ and $n = 0.0823$ so that the initial modulus may be expressed as $E_i = 3500(\sigma_3/14.7)^{0.0823}$. Finally, the bulk modulus function is determined by least-squares best fit to hydrostatic data in Table 3.8.1-2 resulting in $B_i = 1263$ psi and $\epsilon_{v0} = 0.1177\%$. Table 3.8.2-2 summarizes the 8 parameter values for the Duncan/Selig soil model.

Table 3.8.2-2. Duncan/Selig 8 parameters for Cooks Bayou Sand.

Parameter Name	Symbols	Values based on best fit to data
Cohesion strength	c	12.5 psi
Internal friction angle	ϕ_0	35.6°
Reduction of angle	$\Delta\phi$	0.0
Magnitude of E_i	K	238 (atmospheres) KPa = 3500 psi
Exponent for E_i	n	0.0823 $E_i = 3500(\sigma_3/14.7)^{0.0823}$
Ratio of failure	R_f	0.80
Initial Bulk modulus	B_i	1263 psi ($B_i/Pa = 85.92$)
Ultimate vol. strain	ϵ_u	0.1177%

The parameter R_f was determined by trial and error to best fit the observed failure stress.

3.8.3 Compare Soil Models with Experiments

Figures 3.8.3-1a, b & c show model predictions and experimental measurements for axial (deviatoric) stress versus axial strain for the three tri-axial tests at 25, 50 and 100 psi confining pressures.

The Duncan/Selig model tracks well with the experimental data; however, the curves are generally on the conservative side, slightly under-predicting the axial stress. Not surprisingly, the linear elastic model is highly unconservative, over-predicting axial stress except near the origin. Finally, the Mohr/Coulomb model initially follows the linear-elastic path until deviatoric stress reaches the failure surface after which the response is perfectly plastic (zero stiffness). Thus, the Mohr/Coulomb model is initially unconservative (overly stiff) followed by a conservative phase response of zero stiffness.

Figure 3.8.3-1a. Comparisons of axial stress versus axial strain at 25 psi confining pressure.

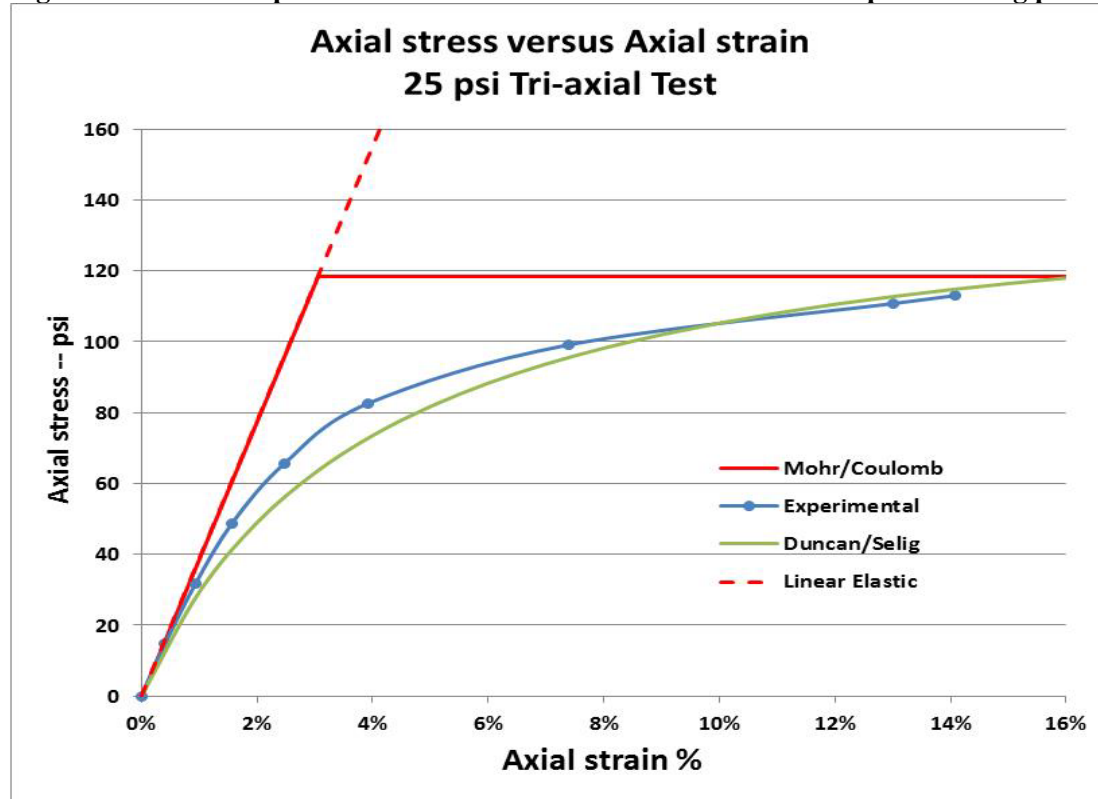


Figure 3.8.3-1b. Comparisons of axial stress versus axial strain at 50 psi confining pressure.

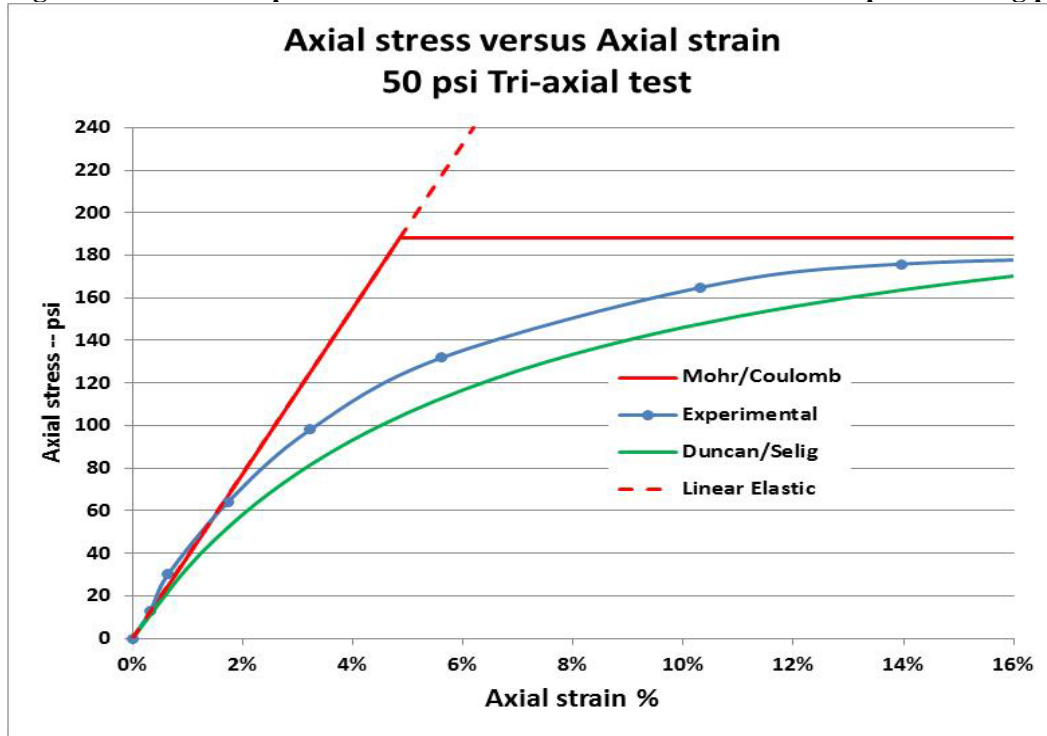


Figure 3.8.3-1c. Comparisons of axial stress versus axial strain at 100 psi confining pressure.

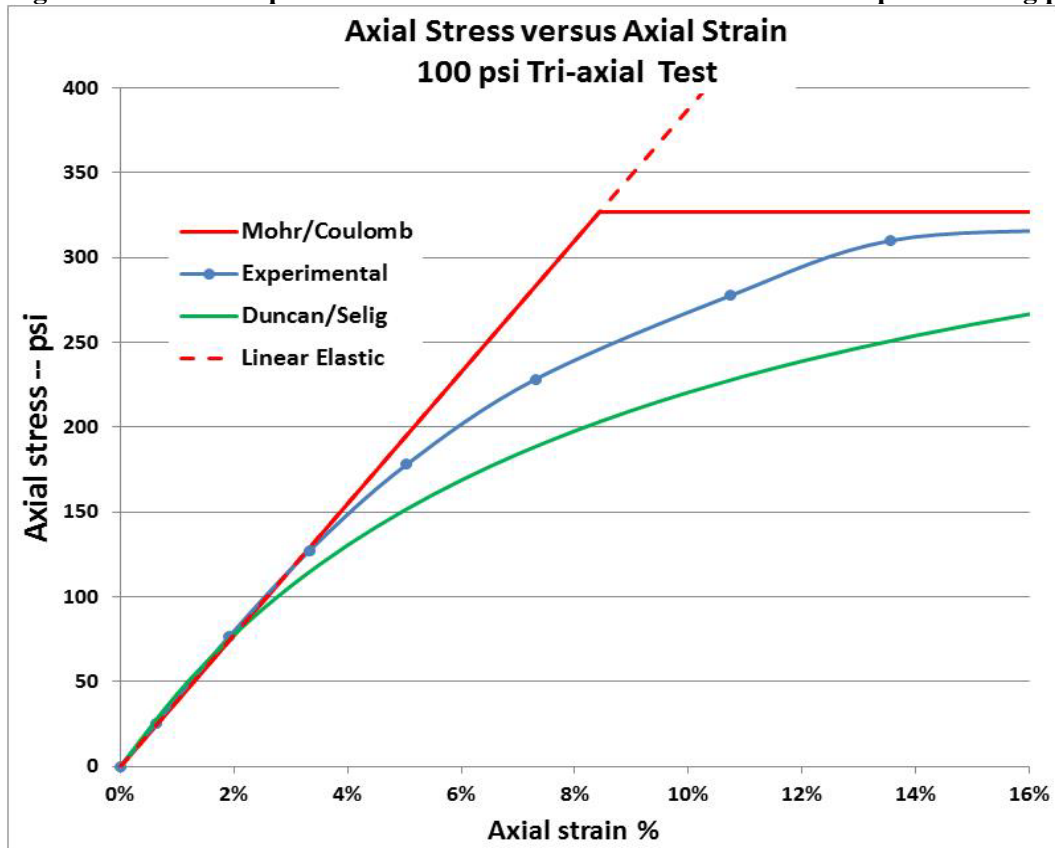
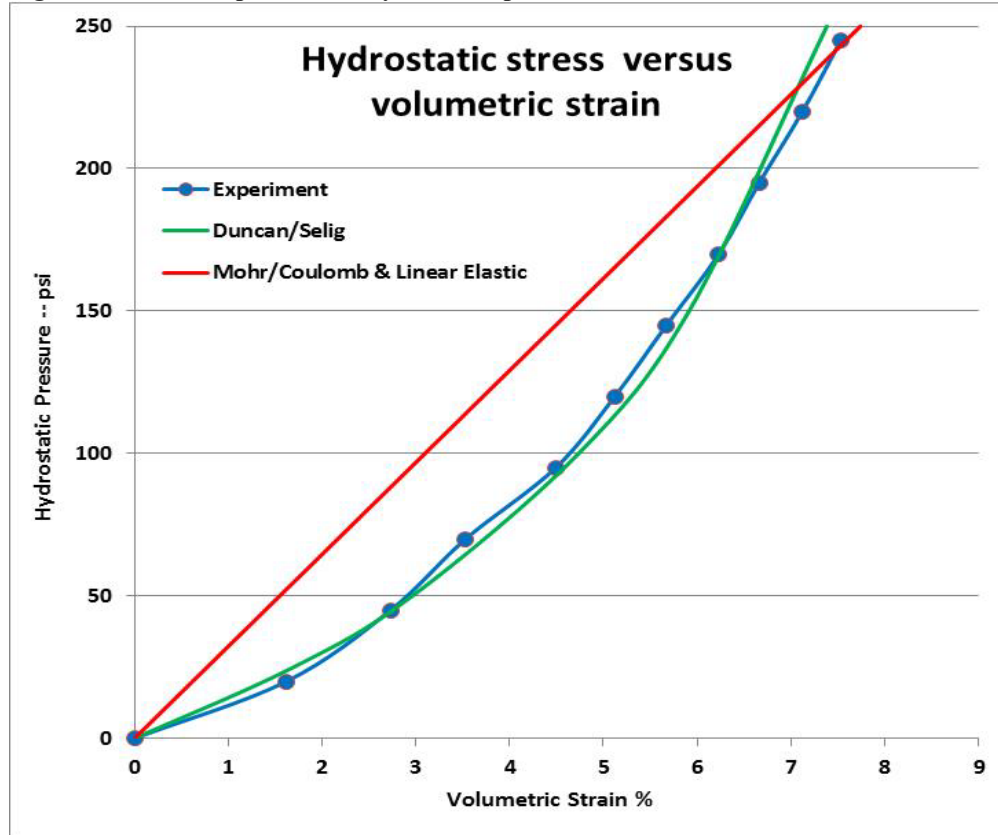
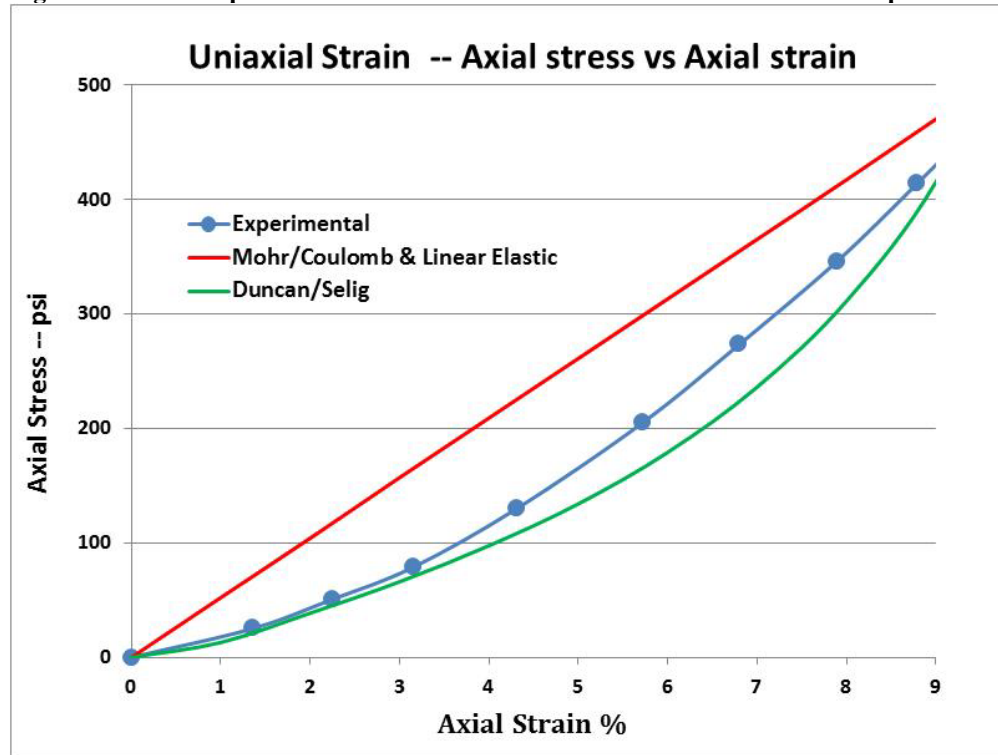


Figure 3.8.3-2 shows the soil-model predictions and experimental measurements for hydrostatic pressure versus volume strain. Under hydrostatic loading conditions, the Mohr/Coulomb model remains elastic for all pressure levels resulting in a straight-line prediction with a constant bulk modulus of 3250 psi. In contrast, the experimental data and the Duncan/Selig model exhibit a changing bulk modulus whose initial value is one half the Mohr/Coulomb value and increases to twice the Mohr/Coulomb value at 8% volumetric strain. Since the Bulk modulus function in the Duncan/Selig model was fitted to the experimental model, it is not surprising the model does a good job in replicating the experimental data.

Figure 3.8.3-2 Comparisons of hydrostatic pressure versus volumetric strain



Finally, Figure 3.8.3-3 shows the soil-model predictions for the uniaxial strain experiment. Unlike the previous comparisons, experimental data from the uniaxial strain test was not used to characterize the parameters for any soil model. Thus, these comparisons are a true test of each soil model’s predictive capability (a.k.a. a blind experimental comparison). Once again it is observed that the Mohr/Coulomb model remains linear elastic because the maximum shear stress remains within the failure surface due to the fact that the lateral stress increases in proportion to the axial stress. In contrast, the Duncan/Selig model exhibits a stiffening response that simulates the experimental data.

Figure 3.8.3-3 Comparisons of axial stress versus axial strain in confined compression.

The overall conclusion from all the above comparisons is that the Duncan/Selig soil-model performs the best in replicating soil loading behavior. The Mohr/Coulomb performs exactly like the linear elastic model for hydrostatic and confined compression loading. For triaxial tests (deviatoric stress loading), the Mohr Coulomb model responds with a sharp dogleg (elastic-perfectly plastic), which is a crude approximation to the gradually decreasing stiffness exhibited by the experimental data.

A more profound question is, “What difference does the three soil models make when it comes to predicting the distress in culvert installations?” This question is studied and answered for corrugated metal, reinforced concrete, and plastic pipe in deep and shallow burial in Reference 28. The bottom-line answer is that the Duncan/Selig model is preferable because it leads to conservative predictions.

4 INTERFACE AND LINK ELEMENTS

This chapter presents the development of the interface element and the link element, which have similar derivations based on constraint equations. The interface element is a friction-contact surface that simulates frictional slippage, separation, and re-bonding of two bodies mating at a common interface and subsequently deforming under an arbitrary static loading schedule. Constraint equations between mating pairs of nodes and the general principle of virtual work are used to formulate the interface element for a finite element solution methodology. The practical application of the interface elements is to mimic the behavior of the interface between the culvert exterior and backfill soil by simulating frictional slippage of the soil over the culvert wall during the backfilling operations. Similarly, the model is useful for simulating the slippage of backfill soil along trench walls for steep walled trench installations. More recently, the interface element formulation was extended to include the option of assigning an initial gap between the contact bodies. In general, the interface element requires a nonlinear solution process to determine the correct interface state (fixed, slip or free) and the correct interface forces.

Link elements are special constraints placed on degrees of freedom associated with two independent nodes. It is a simple linear operation. For example, the “rigid link” element enforces two beam nodes to experience the same x and y translation and a rotation, as if the beam nodes formed a welded connection. As another example, the “pinned” link element only enforces the same x and y translation without constraining rotations. Still another example is the so-called composite link element that may be used to join two parallel beam groups to act as a single beam group with a pre-defined percentage of composite action.

Perhaps the greatest utility of the link elements is the so-called element death option that is triggered by a user-defined load step. Simply put, this means the link element forces are removed and the element no longer exists when the load step number reaches the user-specified death step number. The link element death option has many practical applications such as removing temporary construction bracing, creating void openings in soil zones, and simulating the deterioration of structural segments.

4.1 Interface Element Introduction

CANDE’s interface element dates back to its original development in 1976, which is documented in Reference 1 and published in the open literature in Reference 24. Today, the interface element remains as originally developed with a few minor modifications to enhance convergence. Engineering literature contains a variety of interface element formulations; however, they can generally be classified as either a stiffness approach (e.g., directionally stiff elements) or a constraint approach typically formulated with the use of Lagrange multipliers. The constraint approach is used in this development, however rather than using Lagrange multipliers, the development is based on a novel extension of virtual work, which in itself became a contribution to FEM technology. Motivations for adopting the constraint approach include, avoidance of numerical round-off problems inherent in the stiffness approach, direct control of interface forces and relative movements, accuracy, and ease of FEM implementation.

The interface element is capable of responding to a general step-by-step loading history, such that tensile separation, frictional sliding, or complete bonding (or re-bonding) is possible during any load step. Two nodes, one on either side of an interface, defined by the interface angle, are used to establish the interface element along with a third “dummy node” to represent interface forces. By selectively applying constraint equations to the interface nodes in an incremental-iterative solution procedure, the behavior of a contact-friction interface is simulated.

Two computational advantages are inherent in the interface element. First, unlike the traditional Lagrange-multiplier method that requires a minimization principle, the virtual work formulation is not restricted to conservative systems. Secondly, the formulation results in an element 'constraint matrix' and element 'load vector' analogous to a typical element stiffness matrix and load vector. Thus, the interface element can be assembled into the global equations by standard techniques.

4.2 Interface Virtual Work and Constraint Equations

In Chapter 1, the traditional virtual work formulation is presented without constraints resulting in the classical, stiffness-based finite equations expressed in a scalar virtual work statement repeated here as,

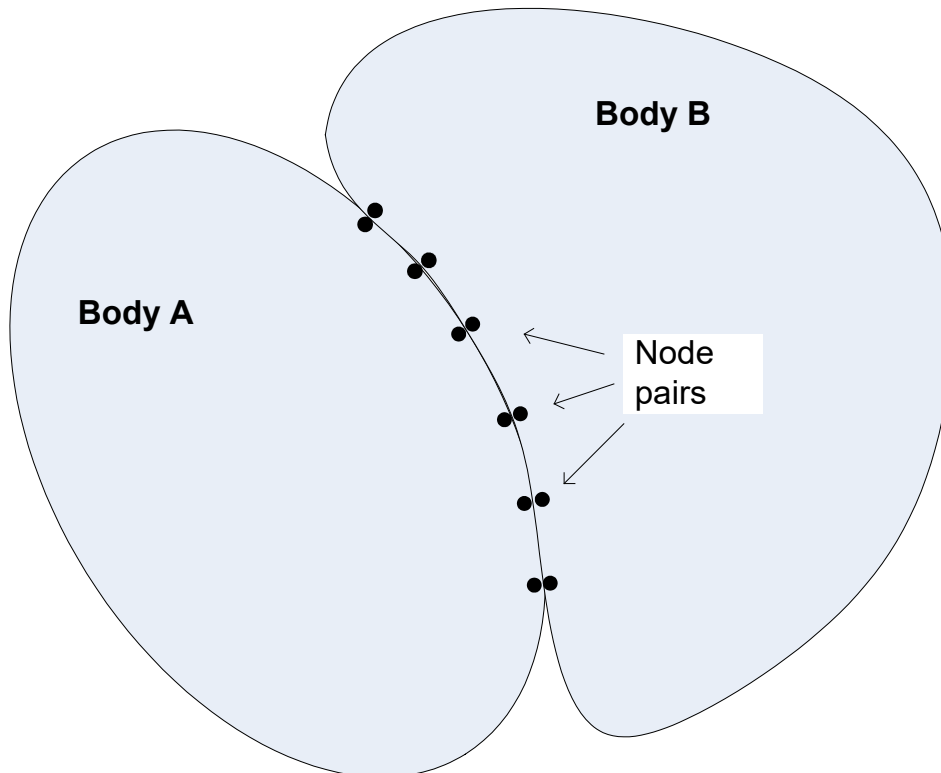
$$\delta \hat{\mathbf{u}}^T (\underline{\mathbf{K}} \Delta \hat{\mathbf{u}} - \Delta \mathbf{P}) = 0 \quad \text{Equation 4.2-1}$$

where, $\Delta \hat{\mathbf{u}}$ = incremental unknown nodal displacements
 $\underline{\mathbf{K}}$ = current global stiffness matrix (generally nonlinear)
 $\Delta \mathbf{P}$ = incremental load vector.

Since $\delta \hat{\mathbf{u}}^T$ is an arbitrary virtual displacement, the satisfaction of Equation 4.2-1 requires that $\underline{\mathbf{K}} \Delta \hat{\mathbf{u}} = \Delta \mathbf{P}$, usually solved iteratively to find displacements.

If Equation 4.2-1 represented a finite element model of two separate bodies initially in contact at node pairs as suggested in Figure 4.2-1, then the bodies can deform independently resulting in overlapping and/or separation along the interface. At the other extreme, if the node pairs at the interface are constrained to move together, a completely bonded response is obtained. Between these two extremes, a slipping response can be obtained by constraining only the displacements normal to the interface at each node pair.

Figure 4.2-1 Idealization of two bodies with initially mating node pairs along interface



4.2.1 Constraint equations general form

To achieve the above, the immediate objective is to incorporate an arbitrary set of constraint equations into a global virtual work statement. Formally, any set of algebraic nodal point constraint equations can be expressed as:

$$\underline{C}\Delta\hat{u} - \Delta\hat{a} = \hat{0} \quad \text{Equation 4.2-2}$$

where, \underline{C} = constraint coefficient matrix

$\Delta\hat{u}$ = subset of nodal degrees of freedom being constrained

$\Delta\hat{a}$ = vector of specified constants (for example, displacement gaps)

$\hat{0}$ = vector of zeroes, one zero for each constraint equation.

To fix ideas by means of a simple example, suppose it is desired to constrain one node in body A to be glued (fixed) to the partner node in body B with no displacement gap between the node pair. In this case, Equation 4.2-2 would be written in expanded notation as,

$$\begin{pmatrix} -1 & 0 & 1 & 0 \\ 0 & -1 & 0 & 1 \end{pmatrix} \begin{pmatrix} u_{Ax} \\ u_{Ay} \\ u_{Bx} \\ u_{By} \end{pmatrix} - \begin{pmatrix} 0 \\ 0 \end{pmatrix} = \begin{pmatrix} 0 \\ 0 \end{pmatrix}$$

In the above example we are simply imposing the two constraint equations, $u_{Ax} = u_{Bx}$ and $u_{Ay} = u_{By}$, which forces the x and y displacement component of the node in body A to be equal to those of the paired node in body B.

Associated with each constraint equation, there exists an unknown internal constraint force λ enforcing the constraint. For convenience, Equation 4.4-2 can be expressed in a scalar (work) form as:

$$\delta\hat{\lambda}^T (\underline{C}\Delta\hat{u} - \Delta\hat{a}) = 0 \quad \text{Equation 4.2-3}$$

where, $\hat{\lambda}$ = vector of interface constraint forces, one force component for each constraint equation.

Since $\delta\hat{\lambda}$ is an arbitrary variation of the constraint force vector, Equation 4.2-3 is satisfied if and only if the constraint equations are satisfied.

As yet the virtual work of constraint forces has not been established or defined. To this end, we argue that the internal constraint forces produce internal virtual work when the constraint is given a small virtual movement (variation) as follows.

$$VW_{\text{constraint}} = \delta(\underline{C}\Delta\hat{u} - \Delta\hat{a})^T \Delta\hat{\lambda} = \delta\hat{u}^T \underline{C}^T \Delta\hat{\lambda} \quad \text{Equation 4.2-4}$$

In the above definition for the incremental virtual work of constraints, we assume the system is equilibrium at load step i and moves to a new equilibrium position at load step $i+1$ consistent with the incremental constraint equations, which in turn generate incremental constraint forces, $\Delta\lambda$. When the constraints are given a small virtual disturbance (variation), the constraint forces perform virtual work as they move with the virtual disturbance. Physically, this is analogous to imposing constraints with stiff springs between node pairs wherein the internal spring force corresponds to the constraint force. However, in this case the constraint forces are primary unknowns.

4.2.2 Global virtual work statement with constraints

With the above understandings, we complete the formulation by adding the internal virtual work of constraints (Equation 4.2-4) to the standard virtual work statement in Equation 4.2-1 and append the constraint requirement in Equation 4.2-3 to get the general virtual work statement including constraints.

$$\begin{pmatrix} \delta \hat{\mathbf{u}} \\ \delta \hat{\boldsymbol{\lambda}} \end{pmatrix}^T \left(\begin{pmatrix} \underline{\mathbf{K}} & \underline{\mathbf{C}}^T \\ \underline{\mathbf{C}} & \underline{\mathbf{0}} \end{pmatrix} \begin{pmatrix} \Delta \hat{\mathbf{u}} \\ \Delta \hat{\boldsymbol{\lambda}} \end{pmatrix} - \begin{pmatrix} \Delta \mathbf{P} \\ \Delta \hat{\mathbf{a}} \end{pmatrix} \right) = 0 \quad \text{Equation 4.2-5}$$

Since the virtual displacements and virtual constraint forces are arbitrary, the virtual work statement leads to the following global system of equations.

$$\begin{pmatrix} \underline{\mathbf{K}} & \underline{\mathbf{C}}^T \\ \underline{\mathbf{C}} & \underline{\mathbf{0}} \end{pmatrix} \begin{pmatrix} \Delta \hat{\mathbf{u}} \\ \Delta \hat{\boldsymbol{\lambda}} \end{pmatrix} = \begin{pmatrix} \Delta \mathbf{P} \\ \Delta \hat{\mathbf{a}} \end{pmatrix} \quad \text{Equation 4.2-6}$$

The coupled set of global matrix equations is to be solved for nodal displacements and constraint forces. Note that the separate partitioning of the global system into $\Delta \mathbf{u}$ and $\Delta \boldsymbol{\lambda}$ is a mere formality and not required in actual global assembly.

4.2.3 General element constraint matrix and load vector

Recalling that the global stiffness equations are formed from the summation element stiffness matrices and load vectors based on the element's contributions to total virtual work, we can in the same manner construct an element constraint matrix and load vector based on the constraint element's contribution to the virtual work as shown below.

$$\delta V_{\text{constraint element}} = \begin{pmatrix} \delta \hat{\mathbf{u}}_e \\ \delta \hat{\boldsymbol{\lambda}}_e \end{pmatrix}^T \left(\begin{pmatrix} \underline{\mathbf{0}} & \underline{\mathbf{C}}_e^T \\ \underline{\mathbf{C}}_e & \underline{\mathbf{0}} \end{pmatrix} \begin{pmatrix} \Delta \hat{\mathbf{u}}_e \\ \Delta \hat{\boldsymbol{\lambda}}_e \end{pmatrix} - \begin{pmatrix} \hat{\mathbf{0}} \\ \Delta \hat{\mathbf{a}}_e \end{pmatrix} \right) \quad \text{Equation 4.2-7}$$

Since the above expression represents the contribution of a general constraint element to the global virtual work statement given by Equation 4.2-5, the element-level constraint matrix and load vector are established as follows.

$$\underline{\mathbf{C}}^* = \begin{pmatrix} \underline{\mathbf{0}} & \underline{\mathbf{C}}_e^T \\ \underline{\mathbf{C}}_e & \underline{\mathbf{0}} \end{pmatrix} \quad \text{Equation 4.2-8}$$

$$\hat{\mathbf{f}} = \begin{pmatrix} \hat{\mathbf{0}} \\ \Delta \hat{\mathbf{a}}_e \end{pmatrix} \quad \text{Equation 4.2-9}$$

where, \mathbf{C}^* = symmetric element constraint matrix, dimension $(n+m) \times (n+m)$

$\underline{\mathbf{C}}_e$ = constraint coefficient matrix for element, dimension $m \times n$

$\hat{\mathbf{f}}$ = incremental load vector of zeros and displacement gaps, dimension $n+m$

$\Delta \hat{\mathbf{a}}$ = specified incremental displacement gaps, dimension m

m = number of constraint equations associated with element ($m = 2$ for interface element)

n = number of constrained degrees of freedom within element ($n = 4$ for interface element)

Just as the global stiffness matrix is assembled by a summation of element stiffness matrices $\underline{\mathbf{k}}^*$, the global constraint matrix is assembled by a summation of element constraint matrices $\underline{\mathbf{C}}^*$. Similarly, the global constraint load vector is assembled by a summation of element load vectors $\hat{\mathbf{f}}$.

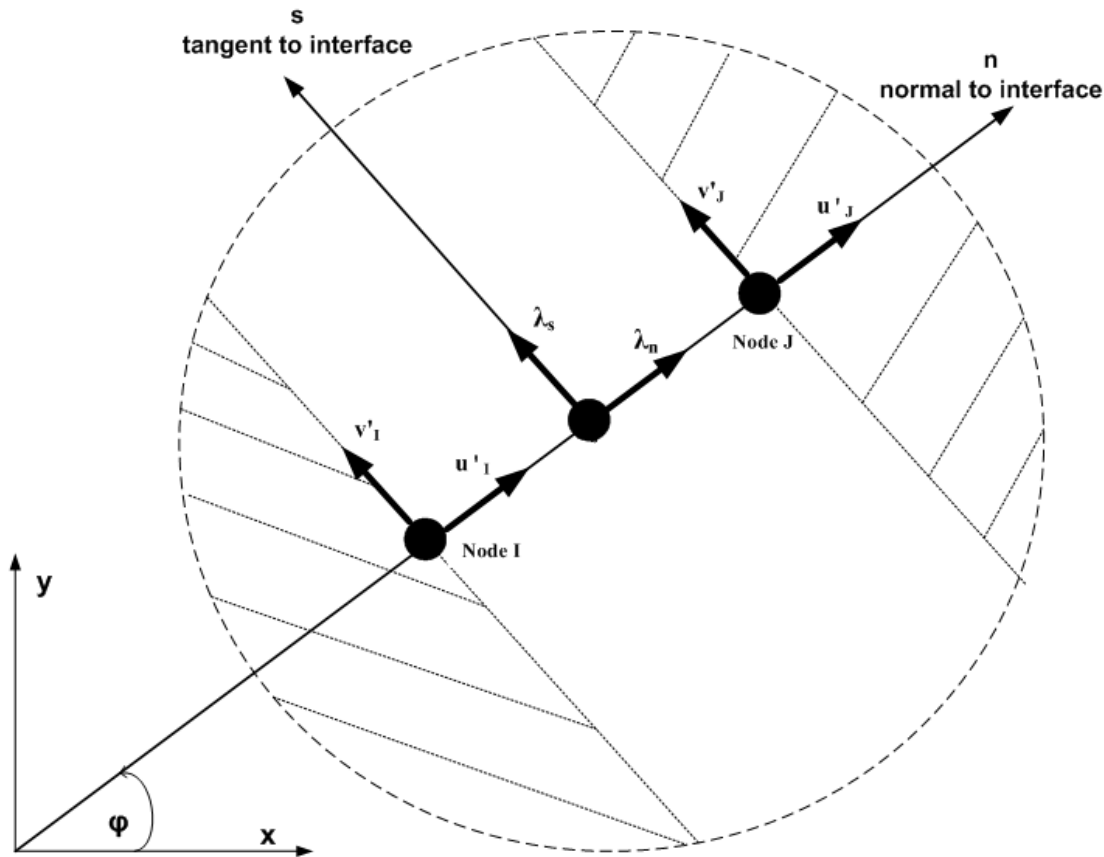
4.3 Interface Element Matrix and Load Vector

To specialize the foregoing to friction-contact interfaces, we assume that any interface can be modeled as a sequence of node pairs (Figure 4.2-1), so that attention can be focused on a single node pair that forms an interface element.

4.3.1 Definition of interface element

The interface element is composed two nodes on either side of a common interface plus an interior node (a stand-alone node K) that represents interface forces. Figure 4.3.1-1 shows an exploded view of the interface element.

Figure 4.3.1-1 Interface element exploded view defining normal and tangential directions



Here, the interface element is defined in the local n, s coordinates, rotated φ degrees from the global x, y coordinate system. Node I belongs to the body on one side of the interface and Node J belongs to the body on the other side of the interface. Node I and J are initially assigned to the same x, y coordinate location prior to loading. The positive normal direction is in the direction of travel from node I to node J. Nodal displacement components in the n - s system are marked with a prime to distinguish them from the unprimed components in the x - y system.

Physical properties assigned to the interface element are listed below.

- μ = coefficient of friction (Coulomb type)
- β = tensile rupture force (typically = 0)
- φ = angle of the interface normal with respect to x -axis

The coefficient of friction and tensile rupture force are discussed subsequently; however, it should be evident that if these properties are assigned very large numbers the interface will remain bonded (fixed) regardless of the interface angle and internal forces.

4.3.2 Incremental and total responses (notation)

As with all developments in this manual, the interface element is an incremental relationship from load step i to load step $i+1$. Letting the symbol q represent any interface response, we adopt the following notation for incremental relationships.

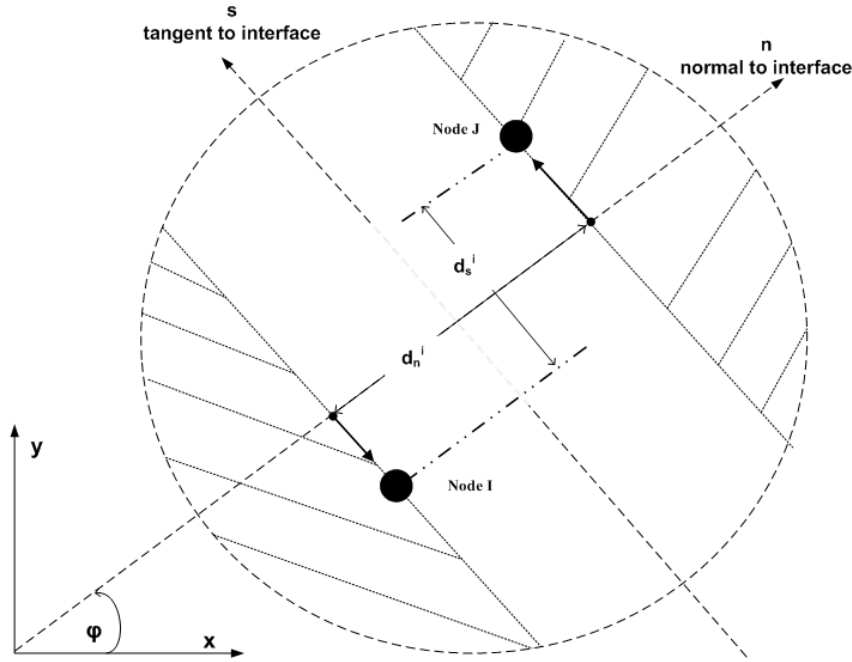
$$q^{i+1} = q^i + \Delta q \quad \text{Equation 4.3-1}$$

where, q^{i+1} = total response at load step $i+1$
 q^i = total response at load step i
 Δq = incremental response from step i to $i+1$

The following list defines interface response notation represented by the symbol q

u'_I = displacement of node I in the normal direction.
 u'_J = displacement of node J in the normal direction
 v'_I = displacement of node I in the tangent direction.
 v'_J = displacement of node J in the tangent direction.
 λ_n = normal force between node I and J
 λ_s = tangent force between node I and J
 u_I = displacement of node I in the global x direction.
 u_J = displacement of node J in the global x direction
 v_I = displacement of node I in the global y direction.
 v_J = displacement of node J in the global y direction.
 d_n = interface gap distance in normal direction
 d_s = interface gap distance in tangent direction

Interface gap distances are illustrated in the figure below for load step i wherein the two bodies have separated at nodes I and J producing normal and tangential gaps between the nodes.

Figure 4.3.1-1 Interface element in separated state at load step i.

The total normal gap and the total tangential gap at load step i are determined by the difference of nodal displacement components in the n - s coordinates as given below.

$$d_n^i = u_J^i - u_I^i \quad \text{Equation 4.3-2a}$$

$$d_s^i = v_J^i - v_I^i \quad \text{Equation 4.3-2b}$$

4.3.3 Element constraint matrices and load vectors for three interface states.

We now identify three 'interface states' that may be imposed during a load step depending on the current responses of the interface element. The three states are called fixed, slip, and free. In each case we will define the element constraint matrix and load vector.

Fixed State. The fixed state means that nodes I and J are constrained to move during the load step such that specified incremental gaps will occur in the normal and tangential direction (usually the incremental gaps are specified to be zero). In the local n - s coordinates system the fixed state is expressed with the following two constrain equations.

$$-\Delta u_I' + \Delta u_J' = \Delta a \quad \text{Equation 4.3-3}$$

$$-\Delta v_I' + \Delta v_J' = \Delta b \quad \text{Equation 4.3-4}$$

where, Δa = specified normal gap increment (often zero)
 Δb = specified tangential gap increment (often zero)

Since the global equations require that displacement components be expressed in x - y coordinates, the primed displacement components are transformed to x - y displacement components by standard coordinate transformation techniques so that the above constraint equations become,

$$\begin{pmatrix} -\cos\varphi & -\sin\varphi & \cos\varphi & \sin\varphi \\ \sin\varphi & -\cos\varphi & -\sin\varphi & \cos\varphi \end{pmatrix} \begin{pmatrix} \Delta u_I \\ \Delta v_I \\ \Delta u_J \\ \Delta v_J \end{pmatrix} = \begin{pmatrix} \Delta a \\ \Delta b \end{pmatrix} \quad \text{Equation 4.3-5}$$

Here the 2x4 matrix is the constraint coefficient matrix \underline{C}_c that is imbedded in the symmetric element constraint matrix \underline{C}^* defined by Equation 4.2-8. The right-hand side is the specified incremental gap vector for the element load vector defined in Equation 4.2-9. If Δa and Δb are both specified zero, then the normal gap and tangential gap do not change during the load step, i.e., both nodes experience identical displacement increments. If, on the other hand, we wish to return the nodes to their initial position (no gaps), we specify Δa and Δb equal to the total displacement gaps defined in Equations 4-3-2a,b.

The fixed state is summarized in the top portion of Table 4.3.3-1, which explicitly defines the element constraint matrix \underline{C}^* and the element load vector. These may be assembled in the global system just like element stiffness matrix.

Table 4.3.3-1 Element constraint matrix \underline{C}^* (6x6) and load vector \hat{f} (6x1) for three interface states.

State	Δu_I	Δv_I	Δu_J	Δv_J	$\Delta \lambda_n$	$\Delta \lambda_s$	\hat{f} (load)
Fixed	0	0	0	0	-c	s	0
	0	0	0	0	-s	-c	0
	0	0	0	0	c	-s	0
	0	0	0	0	s	c	0
	-c	-s	c	s	0	0	Δa
	s	-c	-s	c	0	0	Δb
Slip	0	0	0	0	-c	0	$-s\Delta T$
	0	0	0	0	-s	0	$c\Delta T$
	0	0	0	0	c	0	$s\Delta T$
	0	0	0	0	s	0	$-c\Delta T$
	-c	-s	c	s	0	0	Δa
	0	0	0	0	0	1	ΔT
Free	0	0	0	0	0	0	$c\Delta N - s\Delta T$
	0	0	0	0	0	0	$s\Delta N + c\Delta T$
	0	0	0	0	0	0	$-c\Delta N + s\Delta T$
	0	0	0	0	0	0	$-s\Delta N - c\Delta T$
	0	0	0	0	1	0	ΔN
	0	0	0	0	0	1	ΔT

$c = \cos\varphi$, and $s = \sin\varphi$

Slip State. The slipping state is defined by constraining the normal displacement increments of nodes I and J such that a specified incremental gap will occur in the normal direction during the load increment. The tangential displacement constraint is suppressed and replaced with a specification for the incremental interface force in the tangent direction. Specifically, the slip state is expressed with the following constraint equation and force equation in the n-s system.

$$-\Delta u'_I + \Delta u'_J = \Delta a \quad \text{Equation 4.3-6}$$

$$\Delta \lambda_s = \Delta T \quad \text{Equation 4.3-7}$$

where, Δa = specified normal gap increment (often zero)
 ΔT = specified increment of tangential force between nodes I and J

Since other types of elements share nodes I and J, the n-s displacement components must be transformed to the common x-y system for global assembly and solution. Thus, the above constraint equation is transformed to x-y system as shown below.

$$\begin{pmatrix} -\cos\phi & -\sin\phi & \cos\phi & \sin\phi \end{pmatrix}^T \begin{pmatrix} \Delta u_1 \\ \Delta v_1 \\ \Delta u_j \\ \Delta v_j \end{pmatrix} = \Delta a \quad \text{Equation 4.3-8}$$

With regard to the force equation (Equation 4.3-7), it may be retained in the n-s coordinate system because the dummy node K containing the interface forces is not shared with any other element.

Whenever we suppress a constraint and specify $\Delta\lambda_s = \Delta T$, we must also assign a positive ΔT force to node I and a negative ΔT force to node J thereby effecting the interface force on the nodes. Also, we must transform these forces to x-y system for proper assembly in the global load vector as shown in the load vector column in Table 4.3.3-1.

The slipped state is summarized in the central portion of Table 4.3.3-1. Here the \underline{C}^* matrix contains one constraint equation and force equation ($\Delta\lambda_s = \Delta T$), wherein the matrix size remains 6 x 6 for computational convenience. As discussed above, the load vector includes force components at nodes I and J from the specified interface force, ΔT .

To simulate a friction-contact interface, Coulomb-type friction is assumed so that the maximum possible interface tangent force in advancing from load step i to i+1 is a function of the normal compressive force and given by,

$$F^{i+1} = \mu \left| \lambda_n^{i+1} \right| \text{sgn}(\lambda_s^{i+1}) \quad \text{Equation 4.3-9}$$

where, F^{i+1} = maximum Coulomb frictional force at step i+1 (signed)
 μ = coefficient of friction

$$\text{sgn}(\lambda_s^{i+1}) = \begin{cases} +1, & \text{for } \lambda_s^{i+1} > 0 \\ -1, & \text{for } \lambda_s^{i+1} < 0 \end{cases}$$

With the above understanding, a frictional slipping interface requires that the specified incremental tangent force from load step i to i+1 satisfy the equilibrium condition as written below.

$$\Delta T = F^{i+1} - \lambda_s^i \quad \text{Equation 4.3-10}$$

where, λ_s^i = known tangential interface force at load step i.

Of course, ΔT is recomputed by iterating within the load step until two successive values of F^{i+1} are acceptably close, say within 1%.

Free State. The free state is defined by suppressing both constraint equations and specifying the normal and tangent interface force increments as shown below.

$$\Delta\lambda_n = \Delta N \quad \text{Equation 4.3-11}$$

$$\Delta\lambda_s = \Delta T \quad \text{Equation 4.3-12}$$

where, ΔN = specified increment of normal force between nodes I and J
 ΔT = specified increment of tangential force between nodes I and J

Again, the above force equations may be expressed in the n-s coordinate system because the dummy node K containing the interface forces is not shared with any other element. In addition, the specified interface forces ΔN and ΔT must be assigned to nodes I and J, positive for node I and negative for node J. Also, these forces must be transformed to x-y system for proper assembly in the global load vector.

The free state is summarized in the bottom portion of Table 4.3.3-1. Here the \underline{C}^* matrix is all zeros except $\underline{C}^*(5,5) = \underline{C}^*(6,6) = 1$ that enforces the equations $\Delta\lambda_n = \Delta N$ and $\Delta\lambda_s = \Delta T$. Again, the matrix size remains 6 x 6 for computational convenience. Lastly, the load vector includes x-y force components at nodes I and J from the specified interface forces.

4.4 Interface Nonlinear Solution Strategy

The problem is posed as follows. We assume we know the interface solution at end of load step i, which includes converged solutions for the following accumulated interface responses.

λ_n^i, λ_s^i = total interface normal and tangent interface forces at end of load step i.
 d_n^i, d_s^i = total interface normal and tangent displacement gaps at end of load step i.

We seek to determine an incremental solution ($\Delta\lambda_n, \Delta\lambda_s, \Delta d_n,$ and Δd_s) to achieve a valid solution for the total interface responses at the end of load step i+1 computed as follows.

$$\lambda_n^{i+1} = \lambda_n^i + \Delta\lambda_n \quad \text{Equation 4.4-1}$$

$$\lambda_s^{i+1} = \lambda_s^i + \Delta\lambda_s \quad \text{Equation 4.4-2}$$

$$d_n^{i+1} = d_n^i + \Delta d_n \quad \text{Equation 4.4-3}$$

$$d_s^{i+1} = d_s^i + \Delta d_s \quad \text{Equation 4.4-4}$$

By a valid solution we mean the physical compatibility and equilibrium conditions of the contact-friction interface are satisfied. In general, the valid solution must be determined iteratively wherein a particular state (fixed, slip, or free) is assumed and solved to obtain a trial solution. The trial solution is used to determine if the assumed state is correct, and if not, what state is more likely to be correct. At the same time, the trial solution is used to estimate new parameters for the trial load vector associated with trial interface state as listed below.

- Fixed state load parameters = $\Delta a, \Delta b$
- Slip state load parameters = $\Delta a, \Delta T$
- Free state load parameters = $\Delta N, \Delta T$

Recall that Δa and Δb are specified incremental displacement gaps in normal and tangential directions, respectively, and ΔN and ΔT are specified incremental interface forces in normal and tangential directions, respectively.

4.4.1 Selecting a new trial interface state

Table II offers an exhaustive set of physical criteria to test the validity of an assumed state. The table may be viewed as a 3 x 3 decision matrix wherein the previously assumed state forms rows and the new candidate states form columns.

Table 4.4.1-1 Decision matrix for selecting new trial interface state during iteration cycle from load step i to i+1

New trial state →	Fix	Slip	Free
Previous trial state ↓	↑	↑	↑
(1) Fix →	$\lambda_n^{i+1} < \beta$ and $\lambda_s^{i+1} < F^{i+1}$	$\lambda_n^{i+1} < \beta$ and $\lambda_s^{i+1} > F^{i+1}$	$\lambda_n^{i+1} > \beta$
(2) Slip →	$\lambda_n^{i+1} < \beta$ and $\Delta d_s F^{i+1} < 0$	$\lambda_n^{i+1} < \beta$ and $\Delta d_s F^{i+1} > 0$	$\lambda_n^{i+1} > \beta$
(3) Free →	$d_n^{i+1} < 0$	--	$d_n^{i+1} > 0$

To illustrate the decision matrix, if the previously assumed state was fixed, then row 1 of the decision matrix is entered from the left. The first query determines if the fixed state is correct by checking if the current normal interface force is compressive (or less than the tensile rupture force β) and the magnitude of the tangential force is less than the current frictional resistance calculated from Equation 4.3-9. If both of these inequalities are satisfied then the fixed state is correct, and the fixed state is assumed for the next iteration. Otherwise, we proceed to query the slip conditions to see if the tangential force exceeds the frictional resistance while the interface normal force is compressive. If both of these conditions are satisfied, then we select the slip state for the next iteration. The only remaining possibility is that the normal force exceeds the tensile resistance, implying the interface is prone to separate so that we choose the free state for the next iteration.

If the previous state was slip, we enter row 2 of the decision matrix to determine the most likely state for the next iteration. The first query determines whether or not we should shift to a fixed state based on the conditions that the normal force remains compressive, but there is a change in the direction of relative slip determined by the sign of the product of the slip increment, Δd_s , and the signed value of frictional resistance from Equation 4.3-9. This somewhat subtle argument is based on the observation that relative slip movement cannot reverse its direction until the passive frictional force totally reverses its direction. Therefore, a fixed state for the next iteration is assumed. On the other hand, if the product of the slip increment and the frictional resistance is positive (that is, they have the same sign), then we assume the slip state remains correct for the next iteration. The only remaining possibility is that the normal force exceeds the tensile resistance implying the interface is prone to separate so that we choose the free state for the next iteration.

Lastly if the previous state was free, we enter row 3 to determine whether or not to remain in the free state or shift to a fixed state for the next iteration. We shift to a fixed state if the current normal gap is less than zero meaning that the two bodies have incorrectly penetrated each other at this point. Otherwise, we remain in the free state for the next iteration. Note that row 3 does not provide a direct path from a free state to a slip state. This does not mean a slip state cannot be reached from a free state; it simply means a slip state must be reached by the iterative path, free to fix to slip.

Recapping, the decision matrix provides the choice for the next assumed state, thereby dictating the form of the element constraint matrix \underline{C}^* defined in Table 4.3.3-1. Before we can obtain the next trial solution, we must determine the constraint load parameters as discussed next.

4.4.2 Computing load vector parameters for next iteration

Given that we know the interface state (fixed, slip or free) from the converged solution at load step i and the new trial interface state from the above decision matrix, then the trial parameters for the new load vector may be determined by referring to Table 4.4.2-1. That is, go directly to the unique row/column position in the table where row = known state at step i, and column = current trial state for step i+1.

Table 4.4.2-1 Specified incremental parameter values for trial constraint load vector

New trial state for load step $i+1 \rightarrow$	Fix (a, b)	Slip (a, T)	Free (N, T)
Load step $i \downarrow$			
Fix	$\Delta a = 0$ $\Delta b = 0$	$\Delta a = 0$ $\Delta T = F^{i+1} - \lambda_s^i$	$\Delta N = -\lambda_n^i$ $\Delta T = -\lambda_s^i$
Slip	$\Delta a = 0$ $\Delta b = 0$	$\Delta a = 0$ $\Delta T = F^{i+1} - \lambda_s^i$	$\Delta N = -\lambda_n^i$ $\Delta T = -\lambda_s^i$
Free	$\Delta a = -d_n^i$ $\Delta b = \Delta d_s \left d_n^i / \Delta d_n \right $	$\Delta a = -d_n^i$ $\Delta T = F^{i+1}$	$\Delta N = 0$ $\Delta T = 0$

For example, if a slip state existed at the end of load step i and the next iteration for step $i+1$ is to be assumed free, then we locate slip/free table position and set ΔN and ΔT equal to the negative value of the interface forces existing at the end of load step i . As a consequence, the trial solution will result in net zero values for the interface forces, which must be the case for a free interface state.

Recall that the specification for ΔT under the slip column has already been addressed in the development of Equation 4.3-10. The remaining entries in Table 4.4.2-1 are generally self-explanatory except, perhaps, for the free/fix table position. Here the implication is that the node pair began in a free state at the end load step i , however interface penetration is observed in the decision matrix so that we are assuming a fixed state (re-bonding) for the next iteration. To this end, the normal gap is closed by specifying Δa equal to the negative of existing normal gap, which is physically correct, resulting in zero normal gap at the end of load step $i+1$. With regard to specifying the slip gap increment, we observe that the ratio existing-gap/incremental gap must be less than 1, otherwise penetration would not have been observed. Thus, it is reasonable to assume that the slip gap increment can be specified by reducing the incremental slip gap in the same proportion, which explains the logic for the Δb specification.

4.4.3 Algorithm summary and convergence

The following step-by-step algorithm summarizes the solution strategy and convergence criteria. As always it is assumed that a valid solution exists for a load step i , and we seek an incremental solution to advance the solution to load step $i+1$.

1. At the beginning of each new load step assume each interface element remains in the same state (fixed, slip or free) as determined by the converged solution of the previous load step. Therefore, the element constraint matrix is initially known (Table 4.3.3-1) and the constraint element load vector is set to zero for the first iteration. (For the very first load step, all constraints elements are initially assumed to be in the fixed state)
2. Assemble the global system matrix (see Equation 4.2-6) and solve the system for incremental displacements and incremental interface forces. Form a temporary trial solution for load step $i+1$ by summing the interface responses as shown in Equations 4.4-1 to 4.4-4.
3. Using the decision matrix in Table 4.4.1-1, evaluate each constraint element to see if it changed state with respect to the previous iteration. Assign new constraint matrices to all elements that changed state and keep a record of how elements changed state.
4. Using Table 4.4.2-1, compute a new load vector for each element. For each constraint element currently in a slipping state, compare the current value of frictional resistance (F^{i+1} in Equation 4.3-9) with the value determined in the previous iteration and record the number of elements that have relative differences higher than 1%.

5. Check for convergence.

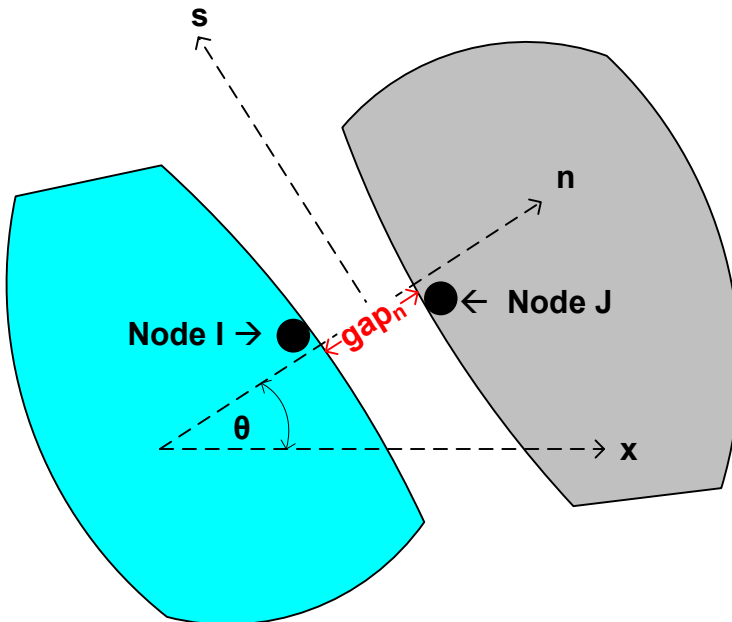
- Convergence is achieved if all constraint elements remain in the same state for two successive iterations, and the frictional resistance of all slipping elements is within 1 % tolerance on successive iterations. When this occurs the load step is converged and we proceed to step 6.
- Otherwise, if convergence is not achieved, we through away the trial solution, and return to step 2 for another iteration.

6. Update the solution by permanently adding the incremental solution to the previous converged solution and return to step 1 to solve for the next load step until all load steps have been processed.

4.4.3 Interface element with initial gap

The original interface element application assumed that the contact nodes I and J were initially located at a common point with the same x and y coordinates, i.e., no initial gap. In the year 2011, the application was extended to include the option to specify an initial gap across the interface as illustrated in Figure 4.4.4-1. This implies the two bodies move independently of each other until the relative deformations of node I and J in the normal direction close the distance “gap_n”. All the forgoing equations still apply, the only difference is that when gap_n is specified nonzero, the initial interface state is assumed to be free with $\Delta a = \text{gap}_n$.

Figure 4.4.4-1 Illustration of new interface element initial gap capability.



Note the specified gap distance need not match the distance between the x-y coordinates of nodes I and J. This means nodes I and J need not exactly lie on the normal axis. Also, in the case of beam elements, the independent specification of gap_n allows accounting for the thickness of beam elements which is not contained in the nodal (x-y) coordinates. For example, if the lateral gap distance between two 12-inch-thick concrete columns, spaced 30-inch on centerline, is 18 inches, then, the user would specify gap_n as 18 inches, not the x-coordinate difference of 30 inches, which is distance between column centerlines.

In summary, the user-defined properties of the interface element are the three original interface properties; angle θ , coefficient of friction, and tensile rupture force (lbs/inch), plus a new property gap_n . If gap_n is left unspecified (i.e., default $gap_n = 0$), then the interface behaves exactly as the original model.

In closing this chapter, the reader is referred References 1 and 24 for practical applications of the using constraint elements to successful predict the performance real-world culvert installations.

4.5 Link Element Introduction

The remainder of this chapter presents the development of CANDE's link elements that offer the modeling capabilities listed below.

(1) Simple links:

- Pinned link – constrain any two nodes to translate together in x and y direction.
- Rigid link - constrain any two beam nodes to translate in x and y and rotate together.

(2) Composite links

- Transverse link – constrain node pairs from two beam groups to act as a composite.
- Longitudinal link – a companion to the transverse link for complete composite action.

(3) Link element death option

- Simple link death – remove subassemblies from structural system at specified step.
- Composite link death – disconnect composite beam groups at specified load step.

Like the interface element, the link element is formulated with constraint equations operating on specified degrees of freedom. The constraints are expressed in a virtual work statement that results in an element constraint matrix analogous to an element stiffness matrix so that it can be assembled into the global system matrix by standard techniques. Herein lies one advantage of the constraint approach, not only are the constraints imposed but also the corresponding constraint forces and moments are determined at the same time. The last feature simplifies the link element death option because the existing constraint forces can be removed by applying their negative value to the system load vector.

4.6 Link Virtual Work and Constraint Equations

The traditional virtual work formulation, without constraints, results in the classical, stiffness-based, global equations expressed in a scalar virtual work statement as shown below.

$$\delta \hat{u}^T (\underline{K} \Delta \hat{u} - \Delta P) = 0 \quad \text{Equation 4.6-1}$$

where, $\Delta \hat{u}$ = incremental nodal displacement vector

\underline{K} = current global stiffness matrix

ΔP = incremental load vector.

Since $\delta \hat{u}^T$ is an arbitrary virtual displacement, the satisfaction of Equation 4.6-1 requires that $\underline{K} \Delta u = \Delta P$, which is solved to find displacements.

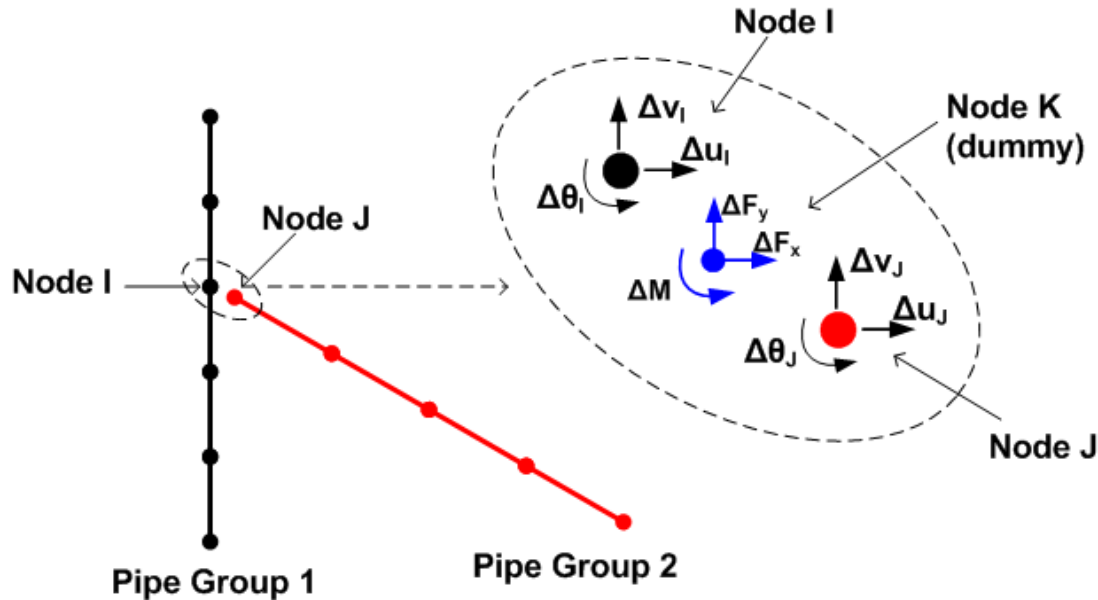
If Equation 4.6-1 represented a finite element model of two separate bodies such as the two pipe-type groups depicted in Figure 4.6-1, then the two pipe-type groups will deform independently possibly penetrating each other or becoming more separated. On the other hand, if nodes I and J shown in the figure are constrained to move together, then the two pipe groups are connected and cannot penetrate or separate from each other, but rather move together as a coupled structural system.

The simplest way to connect the two pipe groups is to redefine the node numbering so that both pipe-type groups share one common node, say node I, and eliminate the extraneous node number J. If this is done, then the connection is

inherently “fixed” meaning that the two pipe groups experience the same x-displacement, y-displacement and rotation at the common node I.

Alternatively, the pipe groups may be connected by means of constraints equations wherein nodes I and J remain as independent node numbers, but their degrees of freedom are constrained to move together. One advantage of the constraint approach is that connection may be pinned or fixed depending on whether the constraint equations are applied only to the translational degrees of freedom or to all three degrees of freedom, respectively. Another advantage is that nodes I and J do not need to reside in the same physical location although they generally do.

Figure 4.6-1 Two pipe groups to be connected at nodes I and J



4.6.1 Constraint equations

To illustrate the general concept of constraints, the simple constraints associated with rigid and pinned link elements are used as an example. Referring to the above figure, the two constraint equations to force the incremental x- and y-displacements at node J to be equal to those of node I to form a pinned connection may be simply expressed as shown below.

$$-\Delta u_I + \Delta u_J = 0 \quad \text{Equation 4.6-2}$$

$$-\Delta v_I + \Delta v_J = 0 \quad \text{Equation 4.6-3}$$

where, $\Delta u_I, \Delta u_J$ = horizontal displacement increment at node I and J

$\Delta v_I, \Delta v_J$ = vertical displacement increment at node I and J.

Similarly, the third constraint equation to force the incremental rotation at node J to equal that at node I to form a fixed moment connection is shown below.

$$-\Delta \theta_I + \Delta \theta_J = 0 \quad \text{Equation 4.6-4}$$

where, $\Delta \theta_I, \Delta \theta_J$ = rotation increment at node I and J.

The above constraint equations as well as any set of constraints, can be expressed generally in matrix notation as follows.

$$\underline{C}\Delta\hat{u} = \hat{0} \quad \text{Equation 4.6-5}$$

where, \underline{C} = constraint coefficient matrix
 $\Delta\hat{u}$ = vector of nodal degrees of freedom being constrained
 $\hat{0}$ = vector of zeroes, one zero for each constraint equation.

For example, in the case of the pinned constraints, \underline{C} is a 2 x 4 rectangular matrix (2 equations x 4 d.o.f.), and for the case of rigid constraints, \underline{C} is a 3 x 6 rectangular matrix (3 equations x 6 d.o.f). In the general case, Equation 4.6-5 represents any set of constraint equations.

4.6.2 Constraint forces and virtual work

Associated with each constraint equation, there exists an unknown internal constraint force enforcing the constraint. For example, the rigid link constraint equations are associated with the following constraint forces (previously illustrated in figure 4.6-1).

$$\Delta F_x = \text{Horizontal force between nodes to maintain } -\Delta u_1 + \Delta u_j = 0$$

$$\Delta F_y = \text{Vertical force between nodes to maintain } -\Delta v_1 + \Delta v_j = 0$$

$$\Delta M = \text{Moment required between nodes to maintain } -\Delta \theta_1 + \Delta \theta_j = 0$$

In the above example the constraint forces can be written in vector notation as

$$\hat{\lambda} = \langle \Delta F_x, \Delta F_y, \Delta M \rangle^T$$

In preparation for the general virtual work statement, the general constraint equations (Equation 4.6-5) may be expressed in a scalar (work) form as:

$$\delta \hat{\lambda}^T (\underline{C}\Delta\hat{u}) = 0 \quad \text{Equation 4.6-6}$$

where, $\hat{\lambda}$ = vector of interface constraint forces, one force component for each constraint.

Since $\delta \hat{\lambda}$ is an arbitrary variation of the constraint force vector, Equation 4.6-6 is satisfied if and only if the constraint equations are satisfied.

As yet the virtual work of constraint forces has not been established or defined. To this end, we argue that the internal constraint forces produce internal virtual work when the constraint is given a small virtual movement (variation) as follows.

$$VW_{\text{constraint}} = \delta(\underline{C}\Delta\hat{u})^T \Delta\hat{\lambda} = \delta\hat{u}^T \underline{C}^T \Delta\hat{\lambda} \quad \text{Equation 4.6-7}$$

In the above definition for the incremental virtual work of constraints, we assume the system is in equilibrium at load step i and moves to a new equilibrium position at load step $i+1$ consistent with the incremental constraint equations, which in turn generate incremental constraint forces, $\Delta\lambda$. When the constraints are given a small virtual disturbance (variation), the constraint forces perform virtual work as they move with the virtual disturbance. Physically, this is analogous to imposing constraints with stiff springs between node pairs wherein the internal spring force corresponds to the constraint force. However, in this case the constraint forces are primary unknowns.

4.6.3 Global virtual work statement with constraints

With the above understandings, we complete the global formulation by adding the internal virtual work of constraints (Equation 4.6-7) to the standard virtual work statement in Equation 4.6-1 and append the constraint requirement in Equation 4.6-6 to get the general virtual work statement including constraints.

$$\begin{pmatrix} \delta \hat{\mathbf{u}} \\ \delta \hat{\boldsymbol{\lambda}} \end{pmatrix}^T \left(\begin{pmatrix} \underline{\mathbf{K}} & \underline{\mathbf{C}}^T \\ \underline{\mathbf{C}} & \underline{\mathbf{0}} \end{pmatrix} \begin{pmatrix} \Delta \hat{\mathbf{u}} \\ \Delta \hat{\boldsymbol{\lambda}} \end{pmatrix} - \begin{pmatrix} \Delta \mathbf{P} \\ \mathbf{0} \end{pmatrix} \right) = 0 \quad \text{Equation 4.6-8}$$

Since the virtual displacements and virtual constraint forces are arbitrary, the virtual work statement leads to the following global system of equations.

$$\begin{pmatrix} \underline{\mathbf{K}} & \underline{\mathbf{C}}^T \\ \underline{\mathbf{C}} & \underline{\mathbf{0}} \end{pmatrix} \begin{pmatrix} \Delta \hat{\mathbf{u}} \\ \Delta \hat{\boldsymbol{\lambda}} \end{pmatrix} = \begin{pmatrix} \Delta \mathbf{P} \\ \mathbf{0} \end{pmatrix} \quad \text{Equation 4.6-9}$$

The coupled set of global matrix equations is to be solved for nodal displacements and constraint forces. Note that the separate partitioning of the global system into $\Delta \mathbf{u}$ and $\Delta \boldsymbol{\lambda}$ is a mere formality and not required in actual global assembly.

4.6.4 General constraint matrix

Recalling that the global stiffness equations are formed from the summation of element stiffness matrices and load vectors based on each element's contributions to total virtual work, we can in the same manner construct an element constraint matrix, based on the link element's contribution to the virtual work as shown below.

$$\delta V_{\text{link element}} = \begin{pmatrix} \delta \hat{\mathbf{u}}_e \\ \delta \hat{\boldsymbol{\lambda}}_e \end{pmatrix}^T \left(\begin{pmatrix} \underline{\mathbf{0}} & \underline{\mathbf{C}}_e^T \\ \underline{\mathbf{C}}_e & \underline{\mathbf{0}} \end{pmatrix} \begin{pmatrix} \Delta \hat{\mathbf{u}}_e \\ \Delta \hat{\boldsymbol{\lambda}}_e \end{pmatrix} \right) \quad \text{Equation 4.6-10}$$

The above expression represents the contribution of a link element to the global virtual work statement in Equation 4.6-9; therefore, the link element constraint matrix is defined as follows.

$$\underline{\mathbf{C}}^* = \begin{pmatrix} \underline{\mathbf{0}} & \underline{\mathbf{C}}_e^T \\ \underline{\mathbf{C}}_e & \underline{\mathbf{0}} \end{pmatrix} \quad \text{Equation 4.6-11}$$

where, $\underline{\mathbf{C}}^*$ = symmetric link element constraint matrix, dimension $(n+m) \times (n+m)$

$\underline{\mathbf{C}}_e$ = constraint coefficient matrix for link element, dimension $m \times n$

m = number of constraint equations associated with link element ($m = 2$ pin, or 3 fix)

n = number of constrained degrees of freedom ($n = 4$ pin, or 6 fix)

Equation 4.6-11 is the bottom-line result of the virtual work development. That is, $\underline{\mathbf{C}}^*$ is the basic link element constraint matrix that needs to be developed for each link type.

4.7 Simple Link Elements

The constraint equations for the rigid and pinned links have already been expressed in Section 4.6, therefore all that remains to be done is to develop the constraint element matrix.

4.7.1 Rigid link constraint matrix

For the rigid (fixed) link element, all the corresponding degrees of freedom of nodes I and J are constrained to move together. The element's degrees of freedom and internal forces are aligned in the standard x , y , and θ sequence as shown in the vectors below.

$$\Delta \hat{u}_e^T = \langle \Delta u_1, \Delta v_1, \Delta \theta_1, \Delta u_j, \Delta v_j, \Delta \theta_j \rangle$$

$$\Delta \hat{\lambda}_e^T = \langle \Delta F_x, \Delta F_y, \Delta M \rangle$$

Accordingly, the C^* matrix is constructed as shown in the table below based on three constraints.

Table 4.7-1 Link element constraint matrix C^* for fixed connections

Node I			Node J			Node K		
Δu_1	Δv_1	$\Delta \theta_1$	Δu_j	Δv_j	$\Delta \theta_j$	ΔF_x	ΔF_y	ΔM
0	0	0	0	0	0	-1	0	0
0	0	0	0	0	0	0	-1	0
0	0	0	0	0	0	0	0	-1
0	0	0	0	0	0	1	0	0
0	0	0	0	0	0	0	1	0
0	0	0	0	0	0	0	0	1
-1	0	0	1	0	0	0	0	0
0	-1	0	0	1	0	0	0	0
0	0	-1	0	0	1	0	0	0

4.7.2 Pinned link constraint matrix

For the pinned connection, the constrained degrees of freedom of nodes I and J are the x and y translations. The element's degrees of freedom and internal forces are ordered as shown in the vectors below.

$$\Delta \hat{u}_e^T = \langle \Delta u_1, \Delta v_1, \Delta u_j, \Delta v_j \rangle$$

$$\Delta \hat{\lambda}_e^T = \langle \Delta F_x, \Delta F_y \rangle$$

Accordingly, the C^* matrix is constructed as shown in the table below based on two constraints.

Table 4.7-2 Link element constraint matrix C^* for pinned connections

Node I		Node J		Node K	
Δu_1	Δv_1	Δu_j	Δv_j	ΔF_x	ΔF_y
0	0	0	0	-1	0
0	0	0	0	0	-1
0	0	0	0	1	0
0	0	0	0	0	1
-1	0	1	0	0	0
0	-1	0	1	0	0

The dimensions of the pinned constraint matrix are 6x6 whereas the rigid link matrix is 9x9. For computational convenience, the larger 9x9 matrix is used in CANDE to serve both link elements. This simply means that for the pinned condition the rows and columns associated with rotations and moments are filled with zeros.

Just as the global stiffness matrix is assembled by a summation of element stiffness matrices k^* , the constraints are assembled by a summation of element constraint matrices C^* . Since the link element is linear there are no iterations required to satisfy the link element. At the end of each load step the incremental intra-nodal forces are updated to total values and printed out with the Link element heading. This completes the simple link element development.

4.8 Composite Link Element

Introduction for User. The composite link element is used to combine two colinear beam element groups, called group A and group B, to react as a composite bending unit as if the two beam groups are welded together along the common interface. Or, at the user's discretion, a reduction factor may be specified to simulate an interface condition between fully bonded connection and frictionless interface, the later implying tandem action. Fully composite action means a significantly enhanced bending stiffness greater than the sum of the parts, whereas tandem action means the bending stiffness is the sum of the parts.

Beam groups A and B are illustrated in Figure 4.8-1a, wherein the centerline paths of groups A and B are separated by the distance “ h^* ” between node pairs. Note, h^* may vary from node pair to node pair depending on the pipe types selected for A & B. The composite link allows any two pipe types to be constrained into composite action irrespective of different materials and nonlinear behavior. For example, group A could represent a corrugated steel arch and group B a reinforced concrete stiffener affixed to the arch's crown region. Or, group A could be a concrete pipe and group B a circular plastic liner bonded to the pipe interior. Or, group A and B could be the same pipe type.

To utilize the composite link elements requires some pre-planning on the part of the user. For example, the coordinates of all node pairs, like I & J in the figures below, must lie in the transverse plane that is normal to the common interface. As illustrated in Figure 4.8-1b, both transverse and longitudinal constraints must be applied to achieve composite action. The transverse constraint elements connect node pairs from group A to group B (dashed red lines), whereas the longitudinal constraint elements connect successive beam nodes in group A (dashed green lines). CANDE's User manual provides explicit directions on defining the transverse and longitudinal constraint elements including nodal connectivity, dummy K nodes and material properties.

The remainder of this section is devoted to theory and development of the transverse and longitudinal constraint elements for composite action.

Figure 4.8-1 Portions of pipe groups A and B to be constrained into composite action.

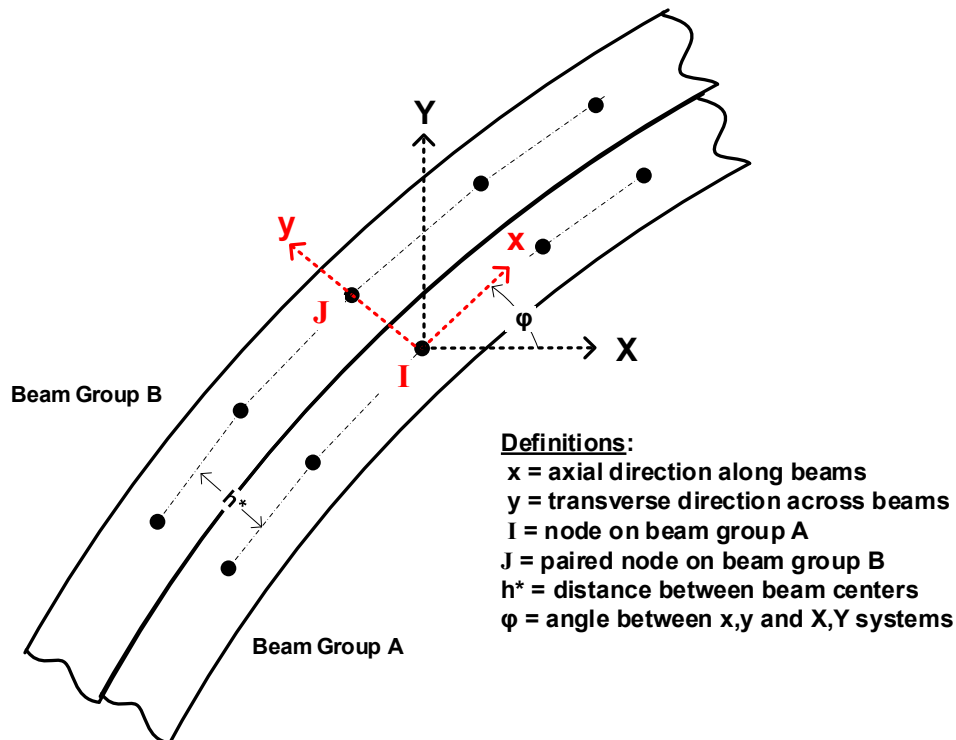
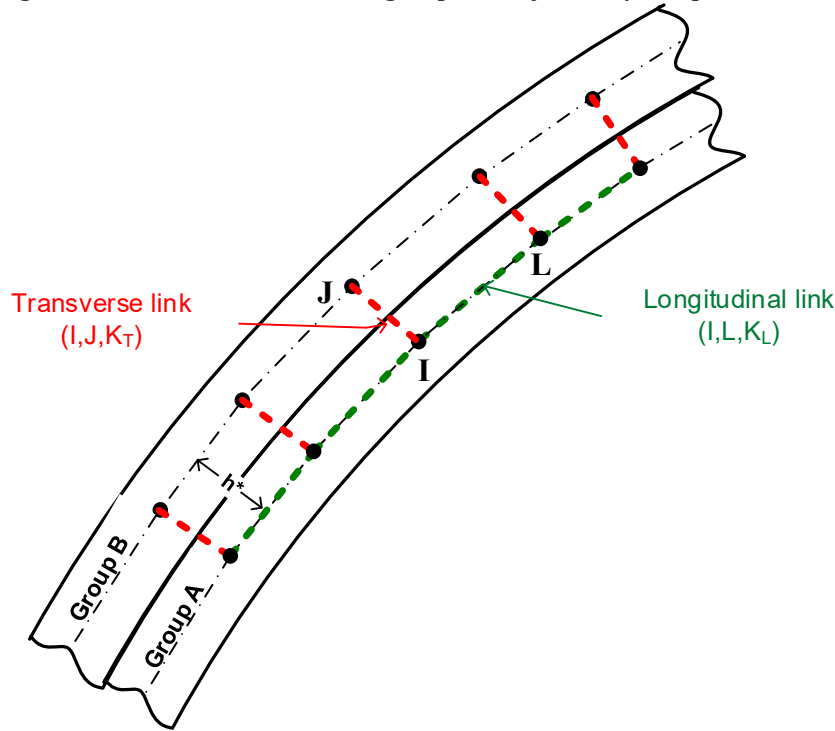


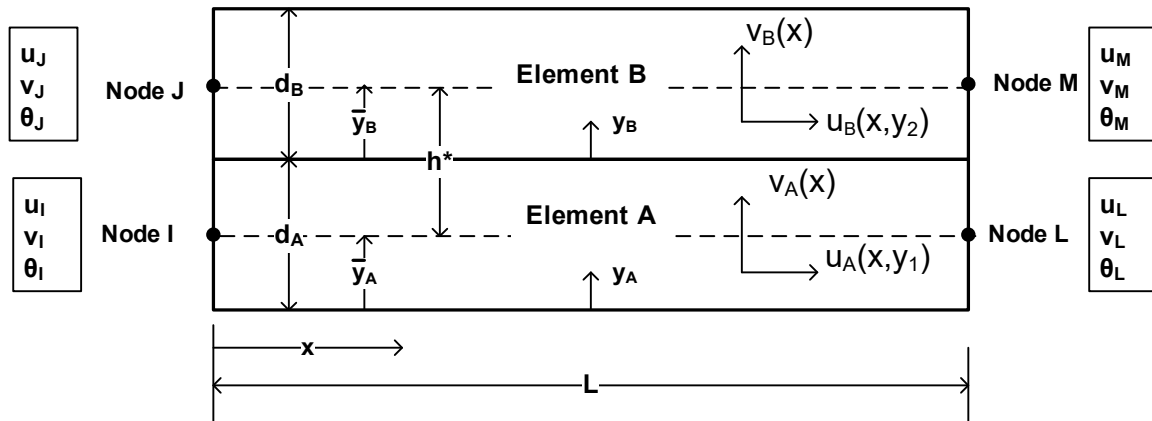
Figure 4.8.1. Illustration of beam groups to be joined by composite link elements



4.8.1 Composite constraint development

To develop constraint equations for composite behavior, we consider two beam elements stacked one upon the other representing one element from group A and one element from group B as shown in Figure 4.8-2. Element A is defined with nodes I and L and element B is defined with nodes J and M. Each node has three degrees of freedom as shown.

Figure 4.8-2 Illustration of two beam elements to be joined as a composite.



The Hermitian displacement functions $v_A(x)$ and $v_B(x)$, as developed in Chapter 2, are shown below in local beam coordinates for elements A and B. (Note that all displacement degrees of freedom are understood to be incremental quantities even though the incremental symbol Δ is not explicitly written to simplify the equations.)

$$\begin{aligned} v_A(x) &= \gamma_1(x)v_1 + \gamma_2(x)\theta_1 + \gamma_3(x)v_L + \gamma_4(x)\theta_L \\ v_B(x) &= \gamma_1(x)v_J + \gamma_2(x)\theta_J + \gamma_3(x)v_M + \gamma_4(x)\theta_M \end{aligned} \quad \text{Equation 4.8-1}$$

Where,

$$\begin{aligned} \gamma_1(x) &= 1 - 3(x/L)^2 + 2(x/L)^3 = \text{Hermitian interpolation function \#1} \\ \gamma_2(x) &= L(1 - x/L)^2 x/L = \text{Hermitian interpolation function \#2,} \\ \gamma_3(x) &= 3(x/L)^2 - 2(x/L)^3 = \text{Hermitian interpolation function \#3,} \\ \gamma_4(x) &= L(1 - x/L)(x/L)^2 = \text{Hermitian interpolation function \#4.} \end{aligned}$$

The first requirement for composite behavior is that the transverse displacement of element A is identical to element B, which is written in constraint form as,

$$v_B(x) - v_A(x) = 0 \quad \text{for } 0 \leq x \leq L \quad \text{Equation 4.8-2a}$$

Inserting the transverse displacement interpolation functions and regrouping nodal degrees of freedom, the above requirement may be written as,

$$\gamma_1(x)(v_J - v_1) + \gamma_2(x)(\theta_J - \theta_1) + \gamma_3(x)(v_M - v_L) + \gamma_4(x)(\theta_M - \theta_L) = 0. \quad \text{Equation 4.8-2b}$$

Since the interpolation functions are linearly independent functions of x , the above equation is satisfied if and only if the corresponding degrees of freedom at node pairs are equal, i.e.,

$$(v_J - v_1) = (\theta_J - \theta_1) = (v_M - v_L) = (\theta_M - \theta_L) = 0$$

Letting node I represent any node in element group A and letting node J represent the corresponding node pair in group B, we can enforce the above constraints for all elements by requiring,

$$-v_I + v_J = 0 \quad \text{Transverse Constraint 1}$$

$$-\theta_I + \theta_J = 0 \quad \text{Transverse Constraint 2}$$

where, I & J are all paired nodes along the portions of the beam groups being constrained into composite actions.

If we only imposed constraint equations 1 and 2 along the parallel beam groups, then the result would not be composite behavior because each beam bends about its own neutral axis resulting in relative axial motion (or slippage) at the common interface between beam groups.

To achieve full composite behavior with enhanced bending stiffness, we must introduce additional constraint equations that preclude relative axial motion at the interface and ensure planes remain plane over both cross sections. To this end, the Bernoulli-Euler kinematic approximation developed in Chapter 2, is re-expressed as,

$$\begin{aligned} u_A(x, y_A) &= a_A(x) + (\bar{y}_A - y_A)v_A'(x) \\ u_B(x, y_B) &= a_B(x) + (\bar{y}_B - y_B)v_B'(x) \end{aligned} \quad \text{Equation 4.8-3}$$

Where $a_A(x)$ and $a_B(x)$ are the axial displacement interpolation functions for beams A and B (to be further discussed).

And, \bar{y}_A = location of neutral axis of element A, y_A measured from element A bottom

\bar{y}_B = location of neutral axis of element B, y_B measured from element B bottom

Referring back to figure 4.8-2, the longitudinal displacement constraint to maintain continuity at the interface is stated as follows,

$$u_B(x, y_B = 0) - u_A(x, y_A = d_A) = 0 \quad \text{for } 0 \leq x \leq L \quad \text{Equation 4.8-4a}$$

Inserting the interpolation functions into the above equation and evoking the vertical constraint ($v_B'(x) = v_A'(x)$), we have the following longitudinal constraint requirement for $0 \leq x \leq L$.

$$a_B(x) - a_A(x) + \rho h^*(\gamma_1'(x)v_1 + \gamma_2'(x)\theta_1 + \gamma_3'(x)v_L + \gamma_4'(x)\theta_L) = 0 \quad \text{Equation 4.8-4b}$$

where $h^* = \bar{y}_2 - \bar{y}_1 + d_1$ distance between neutral axis of beams A & B
 $\rho = 1$ or less user-specified fraction of full composite behavior.

Note that h^* is the moment arm of the thrust-force couple generated by composite action between beams A and B, and the inserted multiplier ρ allows the user to reduce the degree of composite action, $0 \leq \rho \leq 1$. For $\rho = 1$, full composite behavior is obtained with enhanced bending stiffness, whereas for $\rho = 0$ simple tandem behavior is obtained with simple additive bending stiffness.

In order to identify the constrained degrees of freedom implied by the continuity requirement of Equation 4.8-4b, we must specify the interpolation functions for the axial displacements $a_A(x)$ and $a_B(x)$. Herein lies a special issue.

Issue with linear axial interpolation functions. As developed in Chapter 2, standard linear axial interpolation functions are used for all beam-column elements, which implies a constant thrust force within the element. Constant thrust force is a perfectly fine approximation as long as the neutral axis is established where thrust and moment are uncoupled, which is automatically done in the CANDE program for each beam element on each load step. However, the goal here is to constrain beams A and B into single-beam composite action, hence individual neutral axis of beams A and B are subject to the composite moment, which in turn, induces a linear varying thrust. For example, consider two identical beams A and B constrained into composite action with ends fixed at $x=0$, and a vertical load at $x=L$, i.e., a statically determinate cantilever beam. Although there is zero thrust in the single-beam composite, there are equal and opposite thrust forces along the neutral axis of beams A and B, and these thrusts form a couple that varies linearly with x .

Thus, the important revelation is that the interpolation function for axial displacements must include a quadratic function so that the derivatives $a_A'(x)$ and $a_B'(x)$ and hence thrust is at least linear in form.

Shown below are the expanded axial displacement interpolation functions for beams A & B. The first two sets of terms are linear functions associated with the standard nodal degrees of freedom. The new third terms are quadratic functions that equal zero when x equals 0 or L and are associated with nodeless degrees of freedom, u_A^* and u_B^* ,

$$\begin{aligned} a_A(x) &= (1-x/L)u_1 + (x/L)u_L + (x/L)(1-x/L)u_A^* \\ a_B(x) &= (1-x/L)u_j + (x/L)u_M + (x/L)(1-x/L)u_B^* \end{aligned} \quad \text{Equation 4.8-5}$$

where u_A^* = nodeless degree of freedom only associated with beam element A.
 u_B^* = nodeless degree of freedom only associated with beam element B.

Returning to the longitudinal-displacement continuity requirement given by Equation 4.8-4b and inserting the above axial interpolation functions, we arrive at the following equation that must be satisfied for all x , $0 \leq x \leq L$.

$$\begin{aligned} &(1-x/L)(u_j - u_1) + (x/L)(u_M - u_L) + (x/L)(1-x/L)(u_B^* - u_A^*) \\ &+ \rho h^* [(-6(x/L) + 6(x/L)^2) \frac{v_1}{L} + (1 - 4(x/L) + 3(x/L)^2) \theta_1 + (6(x/L) - 6(x/L)^2) \frac{v_L}{L} + (-2(x/L) + 3(x/L)^2) \theta_L] = 0 \end{aligned}$$

Regrouping in powers of x , we find the above expression is satisfied for all x if we enforce the following constraints on the degrees of freedom of beams A and B, (**composite planes remain plane**):

$$\begin{aligned} (u_J - u_I) + \rho h^* \theta_I &= 0 && \text{Transverse node-pair I\&J} \\ (u_M - u_L) + \rho h^* \theta_L &= 0 && \text{Transverse node-pair L\&M} \\ -(u_B^* - u_A^*) + 6\rho h^* \left(\frac{v_I}{L} + \frac{\theta_I}{2} - \frac{v_L}{L} + \frac{\theta_L}{2} \right) &= 0 && \text{Longitudinal nodeless d.o.f} \end{aligned}$$

The first two constraints are of identical form involving paired nodes from group A and group B; thus, we can enforce the first two equations for all elements by requiring,

$$-u_I + u_J + h^* \theta_I = 0 \quad \text{Transverse Constraint 3}$$

where, I & J are the paired nodes between beam groups A and B.

To summarize this section, four types of constraint equations have been developed that must be applied to the degrees of freedom associated beams A and B in order to achieve full composite action. Specifically, three transverse constraints and one longitudinal constraint as listed below.

$$\begin{aligned} -v_I + v_J &= 0 && \text{Transverse Constraint 1} \\ -\theta_I + \theta_J &= 0 && \text{Transverse Constraint 2} \\ -u_I + u_J + \rho h^* \theta_I &= 0 && \text{Transverse Constraint 3} \\ -u_B^* + u_A^* + 6\rho h^* \left(\frac{v_I}{L} + \frac{\theta_I}{2} - \frac{v_L}{L} + \frac{\theta_L}{2} \right) &= 0 && \text{Longitudinal Constraint 4} \end{aligned}$$

4.8.2 Composite constraint forces and solution approach

Associated with each of the four constraint equations, there is a corresponding constraint force that maintains the kinematic constraint. The constraint force and the associated virtual work are shown below and separated into two categories; transverse constraints (simple node pairs) and the complicated longitudinal constraint.

Transverse Constraint 1 - vertical displacements (local beam coordinates)

F_v = Vertical constraint force holding nodes I and J together in local vertical direction.

$VW_{\text{Constraint-1}} = \delta(-v_I + v_J)F_v$ = virtual work of constraint #1.

F_v is a solved-for variable contained in the dummy node K_T of the transverse link element.

Transverse Constraint 2 – Nodal rotations.

M_θ = Rotational constraint moment forcing nodes I and J to rotate the same amount.

$VW_{\text{Constraint-2}} = \delta(-\theta_I + \theta_J)M_\theta$ = virtual work of constraint #2.

M_θ is a solved-for variable contained in the dummy node K_T of the transverse link element.

Transverse Constraint 3 – Axial displacement at nodes I & J (local beam coordinates).

F_a = Axial constraint force maintaining horizontal nodal displacement continuity

$$VW_{\text{Constraint-3}} = \delta(-u_I + u_J + \rho h^* \theta_I) F_a = \text{virtual work of constraint \#3.}$$

F_a is a solved-for variable contained in dummy node K_T of the transverse link element.

Longitudinal Constraint 4 - Axial displacement continuity of nodeless variables along interface (planes remain plane).

Z^* = Interface constraint force per unit length maintaining continuity of u_A^* & u_B^* along interface.

$$VW_{\text{Constraint-4}} = \delta[-u_B^* + u_A^* + 6\rho h \left(\frac{v_I}{L} + \frac{\theta_I}{2} - \frac{v_L}{L} + \frac{\theta_L}{2} \right)] Z^* = \text{virtual work of constraint \#4.}$$

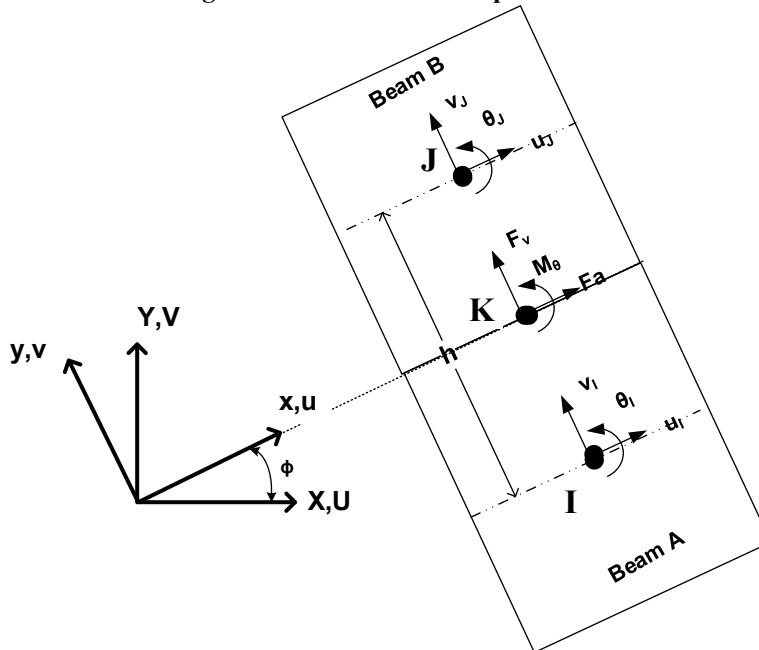
Z^* will be re-expressed in terms of a composite stiffness matrix using static condensation techniques.

Unlike the simple transverse node-pair constraints, constraint #4 includes nodeless degrees of freedom u_A^* & u_B^* as well as bending degrees of freedom at both ends of beam A. Hence, a different strategy is used in developing the longitudinal composite link element that is presented in detail in Section 4.8.4 after the simpler transverse constraints presented next.

4.8.3 Transverse composite link constraint matrix

Transverse constraints 1, 2 and 3 combine into one transverse matrix for each I & J node pair being constrained between beam groups A & B. But first the local degrees of freedom in beam coordinates must be transformed to global degrees of freedom for proper assembly of all elements into global equilibrium equations. Figure 4.8.3 shows the geometry and symbols for local and global degrees of freedom.

Figure 4.8-3. Local and global coordinates of composite beam elements.



Definitions

$u, v,$ and θ = local degrees of freedom at nodes I & J in beam coordinates.

$U, V,$ and θ = global degrees of freedom at node I & J in global coordinates.

h = distance between beam centers

x, y = local coordinates

X, Y = global coordinates

ϕ = angle between x, y and X, Y systems

Thus, the basic transformation of local to global degrees of transformation is given by,

$$\begin{aligned} u &= \cos\phi U + \sin\phi V \\ v &= -\sin\phi U + \cos\phi V \\ \theta_{\text{local}} &= \theta_{\text{global}} \end{aligned} \quad \text{Equation 4.8-6}$$

Note there is no need to transform the constraint forces F_a and F_v to global values because these are stand-alone forces in the system matrix associated with dummy K_T nodes that are not shared with any other elements.

Using the above transformation, the three transverse-composite link constraint equations between nodes I & J are expressed in global degrees of freedom and listed in standard order (U,V, θ) as shown below,

Axial displacement constraint in global coordinates for typical node pair I & J

$$-\cos\phi U_I - \sin\phi V_I + \cos\phi U_J + \sin\phi V_J + \rho h^* \theta_I = 0$$

Vertical displacement constraint in global coordinates for typical node pair I & J

$$\sin\phi U_I - \cos\phi V_I - \sin\phi U_J + \cos\phi V_J = 0$$

Rotation constraints (same in x,y and X,Y systems) for typical node pair I & J

$$-\theta_I + \theta_J = 0$$

Recall that the unknown quantities at node I (U_I, V_I, θ_I), node J (U_J, V_J, θ_J) and node K (F_a, F_v, M_θ) are incremental values associated with the current load step. With the above understanding, the constraint matrix for the transverse-composite link element is written in standard form as shown in Table 4.8-1 wherein the bottom three rows are the constraint equations, and the three columns under node K_T are the transpose of the constraint equations.

Table 4.8-1. Transverse composite link element matrix C^* (CANDE code 10)

Node I			Node J			Node K_T		
U_I	V_I	θ_I	U_J	V_J	θ_J	F_a	F_v	M_θ
0	0	0	0	0	0	-c	s	0
0	0	0	0	0	0	-s	-c	0
0	0	0	0	0	0	ρh^*	0	-1
0	0	0	0	0	0	c	-s	0
0	0	0	0	0	0	s	c	0
0	0	0	0	0	0	0	0	1
-c	-s	ρh^*	c	s	0	0	0	0
s	-c	0	-s	c	0	0	0	0
0	0	-1	0	0	1	0	0	0

Where,

$$c = \cos\phi$$

$$s = \sin\phi$$

$$\rho \leq 1$$

$$h^* = \bar{y}_2 - \bar{y}_1 + d_1$$

Local-global cosine and sine transformations

User specified fraction of full composite action.

Distance between neutral axis of beams at node pair I & J.

In the CANDE output report the constraint forces are printed under the heading *link element output* as well as with the K_T nodes under the heading *nodal displacement data*.

4.8.4 Longitudinal composite link constraint matrix

The fourth and last constraint is repeated below followed by the virtual work expression of the constraint force Z^* ,

$$\text{Longitudinal Constraint-4} = -u_B^* + u_A^* + 6\rho h^* \left(\frac{v_I}{L} + \frac{\theta_I}{2} - \frac{v_L}{L} + \frac{\theta_L}{2} \right) = 0$$

$$\text{VW}_{\text{Constraint-4}} = \left[-\delta u_B^* + \delta u_A^* + 6\rho h^* \left(\frac{\delta v_I}{L} + \frac{\delta \theta_I}{2} - \frac{\delta v_L}{L} + \frac{\delta \theta_L}{2} \right) \right] Z^*$$

Clearly constraint-4 is more complicated than the simple node-pair transverse constraints because the constrained degrees of freedom include the node-less, transverse components u_A^* and u_B^* and longitudinal components at nodes I and L of group A. However, we can take advantage of the fact that u_A^* and u_B^* are internal degrees of freedom that only exist in elements A and B, respectively, as does the unknown longitudinal constraint force Z^* . That is, the unknowns u_A^* , u_B^* and Z^* are not shared with any other elements in the entire systems; hence, u_A^* , u_B^* and Z^* can be eliminated at the element level (static condensation) and replaced with the equivalent composite bending stiffness matrix.

To achieve the above, we seek the complete virtual statement associated with the virtual movements δu_A^* and δu_B^* that includes the axial virtual work for elements A and B and the virtual work of the constraint force Z^* from the 1st part of $\text{VW}_{\text{Constraint-4}}$. After u_A^* , u_B^* and Z^* are resolved, we return to the 2nd part dealing with longitudinal nodes I & L.

Axial virtual work component. With the introduction of the new quadratic interpolation fiction for axial displacements presented in Equation 4.8-5, the axial virtual work and axial stiffness matrices for beams A and B are rederived as shown below.

$$\text{VW}_{\text{axial-A}} = \int_{V_A} \delta u' \sigma_A dV = \langle \delta u_I \delta u_L \delta u_A^* \rangle \underline{K}_{aA} \begin{pmatrix} u_I \\ u_L \\ u_A^* \end{pmatrix}$$

$$\text{VW}_{\text{axial-B}} = \int_{V_B} \delta u' \sigma_B dV = \langle \delta u_J \delta u_M \delta u_B^* \rangle \underline{K}_{aB} \begin{pmatrix} u_J \\ u_M \\ u_B^* \end{pmatrix}$$

Where \underline{K}_{aA} and \underline{K}_{aB} are the axial stiffness matrices for beams A and B as shown below,

$$\underline{K}_{aA} = \frac{E_A A_A}{L} \begin{pmatrix} 1 & -1 & 0 \\ -1 & 1 & 0 \\ 0 & 0 & 1/3 \end{pmatrix} \quad \text{and,} \quad \underline{K}_{aB} = \frac{E_B A_B}{L} \begin{pmatrix} 1 & -1 & 0 \\ -1 & 1 & 0 \\ 0 & 0 & 1/3 \end{pmatrix}$$

Remarkably, the new quadratic degrees of freedom u_A^* is uncoupled from the external degrees of freedom u_I and u_J of beam A, as is u_B^* uncoupled from the external degrees of freedom in beam B. This makes static condensation relatively simple as shown next.

Collecting all virtual work terms for δu_A^* and δu_B^* from VW_{axial} and from the 1st portion of $\text{VW}_{\text{constraint-4}}$ and understanding that no traction loads or body forces are assigned to the nodeless variables, we have the following equilibrium equations,

$$\delta u_A^* \left(\frac{1}{3} k_A u_A^* + Z^* \right) = 0 \quad \text{where } k_A = \frac{E_A A_A}{L_A}$$

$$\delta u_B^* \left(\frac{1}{3} k_B u_B^* - Z^* \right) = 0 \quad \text{where } k_B = \frac{E_B A_B}{L_B}$$

Since δu_A^* and δu_B^* are arbitrary virtual variations, the parenthetical expressions must be zero, which implies,

$$u_A^* = - \frac{3}{k_A} Z^*$$

$$u_B^* = + \frac{3}{k_B} Z^*$$

Equation 4.8-7

Inserting the above into constraint equation 4, provides a solution for the interface force Z^* in terms of the bending degrees of freedom as shown below,

$$Z^* = 2 \frac{k_A k_B}{k_A + k_B} \rho h^* \left(\frac{v_I + \theta_I}{L} - \frac{v_L + \theta_L}{L} \right)$$

Equation 4.8-8

Or, in vector notation

$$Z^* = 2 \frac{k_A k_B}{k_A + k_B} \rho h^* \left\langle \frac{1}{L} \quad \frac{1}{2} \quad -\frac{1}{L} \quad \frac{1}{2} \right\rangle \begin{Bmatrix} v_I \\ \theta_I \\ v_L \\ \theta_L \end{Bmatrix}$$

At this point, we have accounted for all aspects of the virtual work statement dealing with u_A^* , u_B^* . Now we return to 2nd portion of $VW_{\text{constraint-4}}$ to account for the virtual work of the constraint force Z^* undergoing the virtual movements of the bending degrees of freedom at longitudinal nodes I and L

$$VW_{\text{Constraint-4}} = 6 \rho h^* \left(\frac{\delta v_I}{L} + \frac{\delta \theta_I}{2} - \frac{\delta v_L}{L} + \frac{\delta \theta_L}{2} \right) Z^*$$

Inserting the results for Z^* and using vector notation, we have,

$$VW_{\text{Constraint-4}} = 12 \frac{k_A k_B}{k_A + k_B} (\rho h^*)^2 \left\langle \delta v_I \quad \delta \theta_I \quad \delta v_L \quad \delta \theta_L \right\rangle \begin{Bmatrix} 1/L \\ 1/2 \\ -1/L \\ 1/2 \end{Bmatrix} \left\langle \frac{1}{L} \quad \frac{1}{2} \quad -\frac{1}{L} \quad \frac{1}{2} \right\rangle \begin{Bmatrix} v_I \\ \theta_I \\ v_L \\ \theta_L \end{Bmatrix}$$

Thus, the virtual statement may be written in standard stiffness matrix form in local beam coordinates as,

$$VW_{\text{Constraint-4}} = \langle \delta v_I \quad \delta \theta_I \quad \delta v_L \quad \delta \theta_L \rangle [\underline{K}^*] \begin{Bmatrix} v_I \\ \theta_I \\ v_L \\ \theta_L \end{Bmatrix}$$

Where,

$$\underline{K}^* = (\rho h^*)^2 \left(\frac{k_A k_B}{k_A + k_B} \right) \begin{bmatrix} \frac{12}{L^2} & \frac{6}{L} & -\frac{12}{L^2} & \frac{6}{L} \\ \frac{6}{L} & 3 & -\frac{6}{L} & 3 \\ -\frac{12}{L^2} & -\frac{6}{L} & \frac{12}{L^2} & -\frac{6}{L} \\ \frac{6}{L} & 3 & -\frac{6}{L} & 3 \end{bmatrix}$$

The K^* stiffness matrix replaces the formal constraint equations and virtual work associated with the degrees of freedom u_A^* , u_B^* and the constraint force Z^* . Hence, as shown in table 4.8-2, the matrix for the longitudinal composite link element is reconfigured as a stiffness matrix rather than containing constraint equations and constraint forces. Accordingly, the constraint forces associated the dummy node K_L are not applicable and set to zero.

Table 4.8-2. Composite longitudinal link element matrix \underline{K}^* in local coordinates (Code 11)

Node I			Node L			Node K_L		
u_I	v_I	θ_I	u_L	v_L	θ_L	F_x n/a	F_y n/a	M n/a
0	0	0	0	0	0	0	0	0
0	$12\alpha/L^2$	$6\alpha/L$	0	$-12\alpha/L^2$	$6\alpha/L$	0	0	0
0	$6\alpha/L$	3α	0	$-6\alpha/L$	3α	0	0	0
0	0	0	0	0	0	0	0	0
0	$-12\alpha/L^2$	$-6\alpha/L$	0	$12\alpha/L^2$	$-6\alpha/L$	0	0	0
0	$6\alpha/L$	3α	0	$-6\alpha/L$	3α	0	0	0
0	0	0	0	0	0	1	0	0
0	0	0	0	0	0	0	1	0
0	0	0	0	0	0	0	0	1

$$\alpha = (\rho h^*)^2 \left(\frac{k_A k_B}{k_A + k_B} \right)$$

$$k_A = \frac{E_A A_A}{L_A} = \text{axial stiffness of element in group A}$$

$$k_B = \frac{E_B A_B}{L_B} = \text{axial stiffness of element in group B}$$

$$h^* = \bar{y}_2 - \bar{y}_1 + d_1 = \text{distance between neutral axis of beam elements A and B}$$

$$\rho \leq 1 = \text{User-specified fraction of full composite action.}$$

Since \underline{K}^* is expressed in local beam coordinate, the standard local-to-global coordinate transformation is applied to \underline{K}^* in order to assemble all element stiffness matrices in the common coordinate system for the global degrees of freedom, U, V and θ (reference Figure 4.8-3),

$$\underline{K}_{\text{Global}}^* = \underline{T}^T \underline{K}^* \underline{T}$$

Where the transformation matrix is.

$$\underline{T} = \begin{pmatrix} \cos\phi & \sin\phi & 0 & 0 & 0 & 0 \\ -\sin\phi & \cos\phi & 0 & 0 & 0 & 0 \\ 0 & 0 & 1 & 0 & 0 & 0 \\ 0 & 0 & 0 & \cos\phi & \sin\phi & 0 \\ 0 & 0 & 0 & -\sin\phi & \cos\phi & 0 \\ 0 & 0 & 0 & 0 & 0 & 1 \end{pmatrix}$$

Material Properties. The composite link elements require “material property” input data to define the two beam groups for which at least a portion of their lengths are being combined into composite action. Also, the material data defines the desired fraction of composite action, $0 \leq \rho \leq 1$. To this end, Material Type #7 has been introduced into the CANDE program for input on line D-1 along with the material number(s) assigned to the composite link element on input-lines C-4. The material property input for line D-2 includes the two beam group numbers being combined as well as the fraction of composite action, ρ .

This completes the development the composite longitudinal link element stiffness matrix; however, another issue must be addressed for beam elements that exhibit nonlinear behavior.

4.8.5 Revised Nonlinear Solution Strategy

The composite link formulation as presented above works perfectly for all pipe groups A and B that behave linearly and do not require iterations to update the section properties EA^* , EI^* and \bar{y} . However, if any beam element in pipe group A or B enters the nonlinear range, the iteration process results in the divergence of equal interface strains along the A-B interface, and the discrepancy grows as the number iterations increase.

CANDE’s original nonlinear algorithm utilizes the current trial solution increments for thrust (ΔN) and moment (ΔM) at each node to determine inner-fiber and outer-fiber strain increments as shown below for any nonlinear beam element,

$$\varepsilon_{\text{Inner}} = \frac{\Delta N}{EA^*} + \bar{y}^* \frac{\Delta M}{EI^*} = \text{incremental strain at bottom fiber (inner) of beam element.}$$

$$\varepsilon_{\text{Outer}} = \frac{\Delta N}{EA^*} + (\bar{y}^* - d_{\text{top}}) \frac{\Delta M}{EI^*} = \text{incremental strain at top fiber (outer) of beam element.}$$

Using the linear strain profile hypothesis, an updated nonlinear stress profile is computed and integrated to get updated section properties, which in turn provides a new trial solution for ΔN and ΔM and hence $\varepsilon_{\text{Inner}}$ and $\varepsilon_{\text{Outer}}$. Although this procedure has proven to be efficient and accurate for over forty years, this procedure ignores the kinematic constraint between groups A and B such that during any iteration cycle, section properties of groups A and B are updated independently of each other without knowledge of the composite link constraints. As a result, the predicted outer fiber strain of beam A does not match the inner fiber strain of beam B and gets worse on each iteration cycle.

To overcome this erroneous behavior an alternative nonlinear strategy is now enforced to predict strain for those beam elements constrained into composite action. Specifically, the strain increments at the inner and outer fibers of beams A and B are determined directly by the derivatives of the constrained displacement functions, i.e., $d(u_A(x,y))/dx$ and

$d(u_B(x,y))/dx$. The following developments identify the constrained functions u_A and u_B and the corresponding strains after the nodeless variables u_A^* and u_B^* have been removed by static condensation.

Horizontal displacement functions. The horizontal displacement functions of constrained beams A & B obey the Bernoulli-Euler kinematic assumption as previously expressed in Equation 4.8-3 wherein the axial interpolation functions have been increased to quadratic accuracy with the nodeless variables u_A^* and u_B^* as was shown in Equation 4.8-5. By means of static condensation (see Equations 4.8-7 and 4.8-8), the nodeless variables are expressible in terms of the composite element's bending degrees of freedom with the understanding as,

$$u_A^* = -6\rho h^* \left(\frac{k_B}{k_A + k_B} \right) \left(\frac{v_I}{L} + \frac{\theta_I}{2} - \frac{v_L}{L} + \frac{\theta_L}{2} \right)$$

$$u_B^* = +6\rho h^* \left(\frac{k_A}{k_A + k_B} \right) \left(\frac{v_I}{L} + \frac{\theta_I}{2} - \frac{v_L}{L} + \frac{\theta_L}{2} \right) \quad \text{using } v_J = v_I, \theta_J = \theta_I, \text{ etc.}$$

Accordingly, the Bernoulli-Euler horizontal displacement functions for beam elements A and B may be written as,

$$u_A(x, y_A) = (1-x/L)u_I + (x/L)u_L + [(\bar{y}_A - y_A) \gamma_1'(x) - \frac{k_B}{L} \beta^*(x)]v_I + [(\bar{y}_A - y_A) \gamma_2'(x) - \frac{k_B}{2} \beta^*(x)]\theta_I$$

$$+ [(\bar{y}_A - y_A) \gamma_3'(x) + \frac{k_B}{L} \beta^*(x)]v_L + [(\bar{y}_A - y_A) \gamma_4'(x) - \frac{k_B}{2} \beta^*(x)]\theta_L$$

and,

$$u_B(x, y_B) = (1-x/L)u_J + (x/L)u_M + [(\bar{y}_B - y_B) \gamma_1'(x) + \frac{k_A}{L} \beta^*(x)]v_I + [(\bar{y}_B - y_B) \gamma_2'(x) + \frac{k_A}{2} \beta^*(x)]\theta_I$$

$$+ [(\bar{y}_B - y_B) \gamma_3'(x) - \frac{k_A}{L} \beta^*(x)]v_L + [(\bar{y}_B - y_B) \gamma_4'(x) + \frac{k_A}{2} \beta^*(x)]\theta_L$$

where,

$$\beta^*(x) = \left(\frac{6\rho h^*}{k_A + k_B} \right) (x/L)(1-x/L) = \text{common quadratic function from nodeless variables}$$

$$k_A = \frac{E_A A_A}{L_A} = \text{axial stiffness of element in group A}$$

$$k_B = \frac{E_B A_B}{L_B} = \text{axial stiffness of element in group B}$$

Horizontal strain functions. Strains in elements A and B are formed by taking the derivative of the displacement functions, $d(u_A(x, y_A))/dx$ and $d(u_B(x, y_B))/dx$, to get,

$$\begin{aligned}
\varepsilon_A(x, y_A) &= \frac{u_L - u_I}{L} \\
&+ [(\bar{y}_A - y_A) \frac{6}{L^2} (-1 + 2x/L) - \frac{6\rho h^*}{L^2} \left(\frac{k_B}{k_A + k_B} \right) (1 - 2x/L)] v_I \\
&+ [(\bar{y}_A - y_A) \frac{2}{L} (-2 + 3x/L) - \frac{3\rho h^*}{L} \left(\frac{k_B}{k_A + k_B} \right) (1 - 2x/L)] \theta_I \\
&+ [(\bar{y}_A - y_A) \frac{6}{L^2} (1 - 2x/L) + \frac{6\rho h^*}{L^2} \left(\frac{k_B}{k_A + k_B} \right) (1 - 2x/L)] v_L \\
&+ [(\bar{y}_A - y_A) \frac{2}{L} (-1 + 3x/L) - \frac{3\rho h^*}{L} \left(\frac{k_B}{k_A + k_B} \right) (1 - 2x/L)] \theta_L
\end{aligned}$$

and,

$$\begin{aligned}
\varepsilon_B(x, y_B) &= \frac{u_M - u_J}{L} \\
&+ [(\bar{y}_B - y_B) \frac{6}{L^2} (-1 + 2x/L) + \frac{6\rho h^*}{L^2} \left(\frac{k_A}{k_A + k_B} \right) (1 - 2x/L)] v_J \\
&+ [(\bar{y}_B - y_B) \frac{2}{L} (-2 + 3x/L) + \frac{3\rho h^*}{L} \left(\frac{k_A}{k_A + k_B} \right) (1 - 2x/L)] \theta_J \\
&+ [(\bar{y}_B - y_B) \frac{6}{L^2} (1 - 2x/L) - \frac{6\rho h^*}{L^2} \left(\frac{k_A}{k_A + k_B} \right) (1 - 2x/L)] v_M \\
&+ [(\bar{y}_B - y_B) \frac{2}{L} (-1 + 3x/L) + \frac{3\rho h^*}{L} \left(\frac{k_A}{k_A + k_B} \right) (1 - 2x/L)] \theta_M
\end{aligned}$$

The function $\varepsilon_A(x, y_A)$ gives the strain in beam A for any x, y_A location between nodes I and L. Similarly, $\varepsilon_B(x, y_B)$ gives the strain in beam B for any x, y_B location between nodes J and M.

Along the common AB interface where $y_A = d_A$ and $y_B = 0$, it can be shown that $\varepsilon_A(x, d_A)$ is identically equal to $\varepsilon_B(x, 0)$ for all x . The proof of this identity is achieved by invoking the node-pair constraints; $v_I = v_J$, $\theta_I = \theta_J$, $v_L = v_M$, $\theta_L = \theta_M$,

$u_J = u_I - \rho h^* \theta_I$ and $u_M = u_L - \rho h^* \theta_L$, and then observing $\varepsilon_A(x, d_A) \equiv \varepsilon_B(x, 0)$. This identity ensures that strain continuity at the interface is maintained and that planes remain plane across the composite AB beam sections.

Inner and Outer Strains at Nodes. In order to facilitate CANDE's nonlinear procedure for updating section properties, the strain functions $\varepsilon_A(x, y_A)$ and $\varepsilon_B(x, y_B)$ need to be evaluated at the inner and outer fiber of each beam at their respective nodal locations. Listed below are the inner and outer strains at the nodes of beam A, followed by same information for beam B.

Beam A – Inner and outer strain at nodes I and L:

Node I: inner fiber at $x = 0$, $y_A = 0$, outer fiber at $x = 0$, $y = d_A$:

$$\begin{aligned}\varepsilon_{A\text{-inner}}(0,0) &= \left\{ \frac{u_L - u_I}{L} - \frac{3\rho h^*}{L} \left(\frac{k_B}{k_A + k_B} \right) \left(\frac{2}{L} v_I + \theta_I - \frac{2}{L} v_L + \theta_L \right) \right\} && \text{thrust component} \\ &\quad - \left\{ \frac{2\bar{y}_A}{L} \left(\frac{3}{L} v_I + 2\theta_I - \frac{3}{L} v_L + \theta_L \right) \right\} && \text{bending component} \\ \varepsilon_{A\text{-outer}}(0,d_A) &= \left\{ \frac{u_L - u_I}{L} - \frac{3\rho h^*}{L} \left(\frac{k_B}{k_A + k_B} \right) \left(\frac{2}{L} v_I + \theta_I - \frac{2}{L} v_L + \theta_L \right) \right\} && \text{thrust component} \\ &\quad - \left\{ \frac{2(\bar{y}_A - d_A)}{L} \left(\frac{3}{L} v_I + 2\theta_I - \frac{3}{L} v_L + \theta_L \right) \right\} && \text{bending component}\end{aligned}$$

Node L: inner fiber at $x=L$, $y_A=0$, outer fiber at $x=L$, $y=d_A$:

$$\begin{aligned}\varepsilon_{A\text{-inner}}(L,0) &= \left\{ \frac{u_L - u_I}{L} + \frac{3\rho h^*}{L} \left(\frac{k_B}{k_A + k_B} \right) \left(\frac{2}{L} v_I + \theta_I - \frac{2}{L} v_L + \theta_L \right) \right\} && \text{thrust component} \\ &\quad + \left\{ \frac{2\bar{y}_A}{L} \left(\frac{3}{L} v_I + \theta_I - \frac{3}{L} v_L + 2\theta_L \right) \right\} && \text{bending component} \\ \varepsilon_{A\text{-outer}}(L,d_A) &= \left\{ \frac{u_L - u_I}{L} + \frac{3\rho h^*}{L} \left(\frac{k_B}{k_A + k_B} \right) \left(\frac{2}{L} v_I + \theta_I - \frac{2}{L} v_L + \theta_L \right) \right\} && \text{thrust component} \\ &\quad + \left\{ \frac{2(\bar{y}_A - d_A)}{L} \left(\frac{3}{L} v_I + \theta_I - \frac{3}{L} v_L + 2\theta_L \right) \right\} && \text{bending component}\end{aligned}$$

Beam B – Inner and outer strain at nodes J and M:

Node J: inner fiber at $x=0$, $y_B=0$, outer fiber at $x=0$, $y=d_B$:

$$\begin{aligned}\varepsilon_{B\text{-inner}}(0,0) &= \left\{ \frac{u_M - u_J}{L} + \frac{3\rho h^*}{L} \left(\frac{k_A}{k_A + k_B} \right) \left(\frac{2}{L} v_I + \theta_I - \frac{2}{L} v_L + \theta_L \right) \right\} && \text{thrust component} \\ &\quad - \left\{ \frac{2\bar{y}_B}{L} \left(\frac{3}{L} v_I + 2\theta_I - \frac{3}{L} v_L + \theta_L \right) \right\} && \text{bending component} \\ \varepsilon_{B\text{-Outer}}(0,d_B) &= \left\{ \frac{u_M - u_J}{L} + \frac{3\rho h^*}{L} \left(\frac{k_A}{k_A + k_B} \right) \left(\frac{2}{L} v_I + \theta_I - \frac{2}{L} v_L + \theta_L \right) \right\} && \text{thrust component} \\ &\quad - \left\{ \frac{2(\bar{y}_B - d_B)}{L} \left(\frac{3}{L} v_I + 2\theta_I - \frac{3}{L} v_L + \theta_L \right) \right\} && \text{bending component}\end{aligned}$$

Node M: inner fiber at $x=L$, $y_B=0$, outer fiber at $x=L$, $y=d_B$:

$$\begin{aligned}\varepsilon_{B\text{-Inner}}(L,0) &= \left\{ \frac{u_M - u_J}{L} - \frac{3\rho h^*}{L} \left(\frac{k_A}{k_A + k_B} \right) \left(\frac{2}{L} v_I + \theta_I - \frac{2}{L} v_L + \theta_L \right) \right\} && \text{thrust component} \\ &\quad + \left\{ \frac{2\bar{y}_B}{L} \left(\frac{3}{L} v_I + \theta_I - \frac{3}{L} v_L + 2\theta_L \right) \right\} && \text{bending component}\end{aligned}$$

$$\begin{aligned} \epsilon_{B-Outer}(L, d_B) = & \left\{ \frac{u_M - u_J}{L} - \frac{3\rho h^*}{L} \left(\frac{k_A}{k_A + k_B} \right) \left(\frac{2}{L} v_I + \theta_I - \frac{2}{L} v_L + \theta_L \right) \right\} && \text{thrust component} \\ & + \left\{ \frac{2(\bar{y}_B - d_B)}{L} \left(\frac{3}{L} v_I + \theta_I - \frac{3}{L} v_L + 2\theta_L \right) \right\} && \text{bending component} \end{aligned}$$

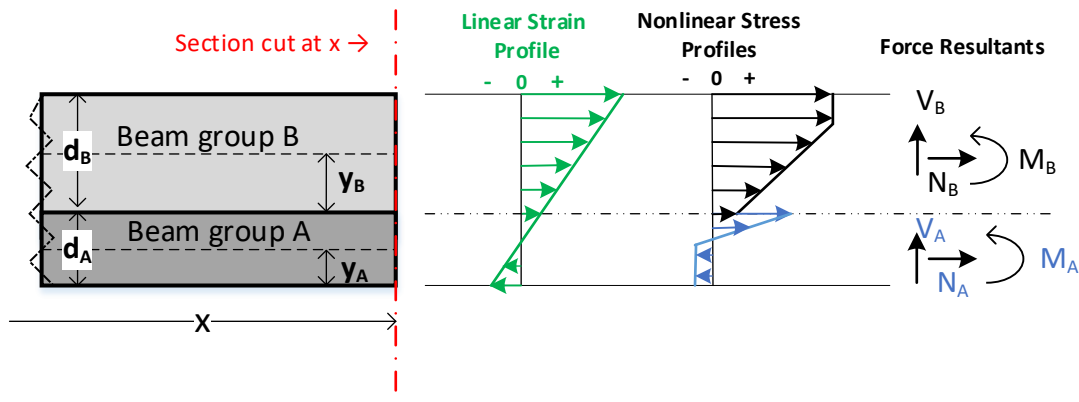
Subroutine RESPIP has been extended to compute the above inner and outer strains for all pipe elements that are joined in composite action. For interior nodes that are shared by two adjacent elements in either group A or in group B, the inner and outer strains are taken as the nodal average of the neighboring elements. The inner and outer strains for both nodes of each composite node pair are saved in the common statement “composlink.fi” and are shared with all pipe-type subroutines. Accordingly, the nonlinear algorithms in each pipe-type subroutine have been modified to update the nodal section properties of composite nodes based on the inner and outer strains stored in composlink.fi. Otherwise, for all other beam nodes not constrained into composite action, the former nonlinear algorithm remains in effect wherein inner and outer strain values are determined by their relationship to ΔN and ΔM. The revised nonlinear algorithm has been extensively tested and is working perfectly.

4.8.6 Interpreting CANDE output for beams with composite link elements.

CANDE’s printed output for each pipe type is the same whether or not the pipe group is constrained into composite action with another pipe group. Thus, for compositely joined pipe groups, structural responses such as moment, thrust and shear as well as stress, strain and all design criteria refer to the individual pipe group, not to the combined structural evaluation of the both groups together. That is, the structural evaluation of the composite is judged by the individual structural evaluations of each pipe group that forms the composite. For example, we may evaluate a reinforced concrete material in composite action with a plastic liner material and evaluate the combination based on the individual design criteria for the r/c pipe material and the design criteria for the thermoplastic pipe material. As another example, we could evaluate the effect of an aluminum circular tube compositely reinforced with an outer shell of corrugated steel wherein each metal (pipe group) is evaluated according to its own design criteria.

Structural Responses. Figure 4.8-4 shows a cross-section cut through beam groups A and B at an arbitrary location x. Also shown is an example linear strain profile for the combined composite section along with example stress profiles σ_A and σ_B that reflect different nonlinear materials.

Figure 4.8-4. Cross-section view of structural responses of composite beams A and B.



As derived in Section 2.1.3, the force resultants for thrust and moment in beams A and B are defined by integrating the stress profiles σ_A and σ_B as shown below.

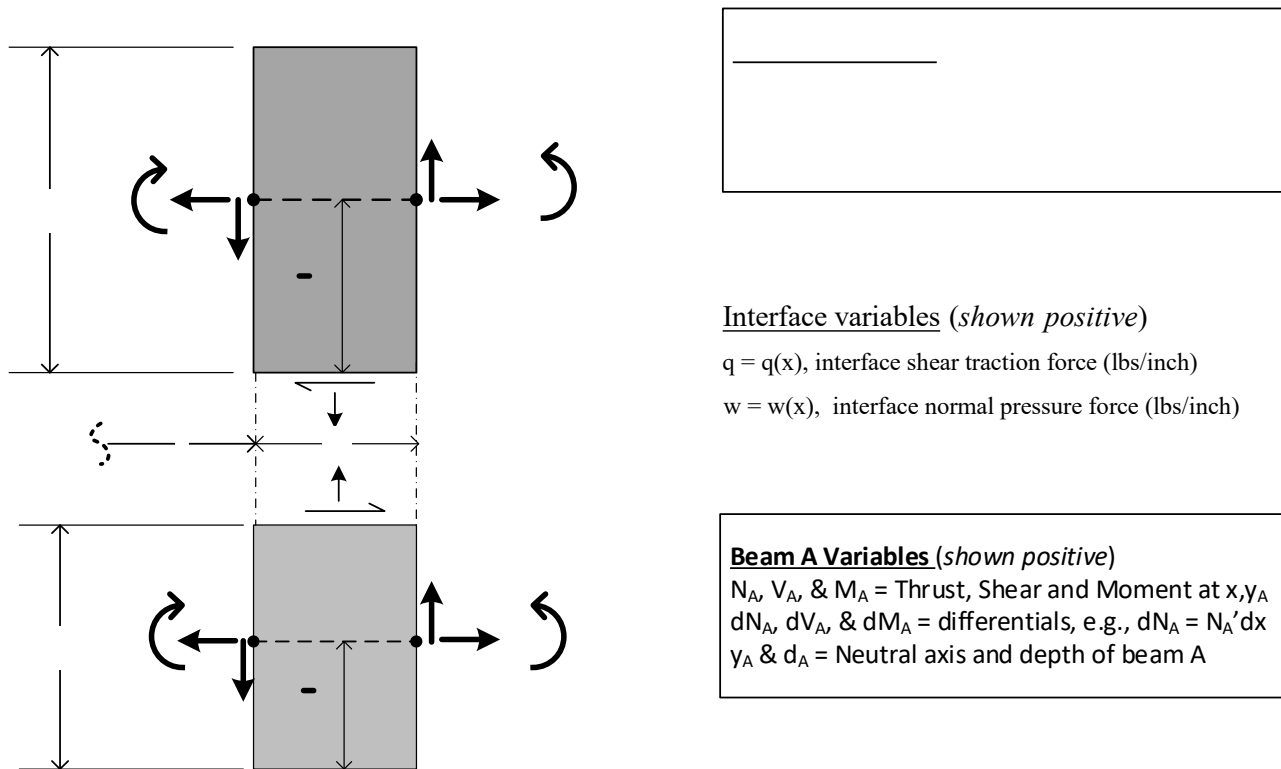
$$N_A = \int_{A_A} \sigma_A dA, \text{ and } M_A = \int_{A_A} (y - \bar{y}_A) \sigma_A dA_A$$

$$N_B = \int_{A_B} \sigma_B dA, \text{ and } M_B = \int_{A_B} (y - \bar{y}_B) \sigma_B dA_B$$

The force resultant integrations for N and M are carried out exactly or by numerical integration dependent the stress-strain model of the pipe type (see Chapter 2). Note that N and M are actually incremental quantities ΔN and ΔM ; however, as previously stated the Δ symbol has been dropped from all responses in order to minimize the large number of symbols used throughout this development of composite beams.

Shear Force Resultant. Unlike the thrust and moment resultants, the resulting shear force is not determined via a stress-strain relationship because the Bernoulli-Euler kinematics does not admit shear strain. Rather, the shear force is determined by moment equilibrium wherein for composite beams requires the inclusion of the interface traction stress q as illustrated in the Figure 4.8-5 and the following derivation.

Figure 4.8-5. Differential segment dx of composite beams A and B for individual moment equilibrium.



Note that internal body forces (lbs/inch) are not present in the above beam segments because the body force resultants (lbs) have already been assigned to the beam nodes as external loading.

Referring to the differential slice of Beam A and taking moment equilibrium about its neutral axis point (x, \bar{y}_A) produces the following shear force relationship,

$$-M_A + (M_A + M_A' dx) + (w dx) \frac{dx}{2} - (q dx)(d_A - \bar{y}_A) + (V_A + V_A' dx) dx = 0$$

Dividing by dx and then letting $dx \rightarrow 0$, gives the shear force V_A as,

$$V_A = -M_A' + q(d_A - \bar{y}_A)$$

Similarly, for Beam B taking moment equilibrium about its neutral axis point (x, \bar{y}_B) gives,

$$-M_B + (M_B + M_B' dx) + (w dx) \frac{dx}{2} - (q dx) \bar{y}_B + (V_B + V_B' dx) dx = 0$$

Dividing by dx and then letting $dx \rightarrow 0$, gives the shear force V_B as,

$$V_B = -M_B' + q \bar{y}_B$$

Recall that for a single non-composite beam all horizontal forces are presumed to act along the neutral axis thereby not contributing to the moment equilibrium equation, which produces the standard moment-shear relationship, $V = -dM/dx$. However, for composite beams the traction shear flow q at the interface surface contributes to the moment equilibrium via the moment arm to each beam's neutral axis. Thus, in addition to the standard moment-shear relationship the vertical shear forces V_A and V_B include a term dependent on shear flow q as shown in the above equations.

The shear flow is easily determined by force equilibrium in the x-direction from the differential beam segments as,

$$\text{For beam A, } q_A = -N_A' \quad (\text{lbs/inch})$$

$$\text{And beam B, } q_B = +N_B' \quad (\text{lbs/inch})$$

Note, $|q_A| = |q_B|$, and are defined positive in opposite x directions as shown in the above figure.

Since moment and thrust vary linearly within beams A and B, the derivatives N' and M' at each beam's center may be determined by using the known thrust and moment resultant values at nodes I and L for beam A and nodes J and M for beam B. Hence, for beam A we have,

$$N_A' = (N_L - N_I)/L_A$$

$$M_A' = (M_L - M_I)/L_A$$

And for beam B we have,

$$N_B' = (N_M - N_J)/L_B$$

$$M_B' = (M_M - M_J)/L_B$$

Therefore, the shear force at the center of beams A & B are determined as,

$$V_A = -M_A' - N_A'(d_A - \bar{y}_A)$$

$$V_B = -M_B' + N_B'(\bar{y}_B)$$

Lastly, the nodal values for shear forces V_I and V_J at each node pair I & J are determined in the usual manner by averaging the two composite beam elements that share node I or J, respectively. For the end nodes in a composite group the nodal shear force is taken to be the same as the element's center. (The above is performed in CANDE's subroutine RESPIP).

This completes the composite link development.

4.9 Link Element Death

The link element death option has many practical applications such as removing temporary construction bracing, creating void openings in soil zones, and simulating the deterioration of structural segments as illustrated in the MGK CANDE-2022 User manual.

The life and death of link elements are measured by the load-step counter, $IA = 1, 2, 3 \dots NINC$, where $NINC$ is the maximum number of load steps to be executed in a given problem. There are two key load-step numbers assigned to each link element by the user as defined below,

1. IAC = load-step number when link element enters the system (birth)
2. IAX = load-step number when link element is removed from system (death)

Where, it is required that $IAC < IAX$ so that the element is born before it dies.

4.9.1 Procedure for element death

Assuming the link element entered the system (born) at load-step number $IA = IAC$, then element death will be initiated when $IA = IAX$. Initiation of element death requires the following changes to the solution algorithm,

1. When $IA = IAX$, bypass the construction of the constraint matrix and skip the global assembly of the constraint matrix.
2. Create a link-element load vector containing the negative values of the element's accumulated constraint forces through load step $IAX-1$. To illustrate, the negative load vector for a rigid link is shown below (9 components).

$$\hat{\mathbf{f}} = \langle 0, 0, 0, 0, 0, 0, -F_x^*, -F_y^*, -M^* \rangle^T$$

3. Assemble the link element load vector into the global load vector and solve the global system as usual.
4. After the successful solution of load-step $IA = IAX$, the link element is no longer part of the system, the link-element's constraint forces are redistributed to the system, and the element's accumulated constraint forces are equal to zero.
5. For all load steps $IA > IAX$, the procedure is to simply bypass all operations with the constraint matrix and load vector associated with the dead link element.

As a side comment, it is noted that there is no theoretical problem in developing a similar death-element option for beam elements and continuum elements directly. However, the link-element has the special advantage that the accumulated constraint forces are already available in computer storage facilitating the construction of the negative load vector.

4.9.2 Programming strategy

Initial storage for the new variable IAX is logically resolved as an addition to the element property vector, IX . Specifically, the vector is extended from $IX(7)$ to $IX(8)$ as indicated by the data input line C-4 in Chapter 5 of the User Manual. This extension requires corresponding extensions in two other storage matrices as follows. In subroutine GENEL the element property array $NOD(7,Numel)$ is expanded to $NOD(8,Numel)$ to store the $IX(8)$ value. Similarly in subroutine HEROIC the array $MNO(3,Numel)$ is expanded to $MNO(4,Numel)$ for the same purpose.

5 LARGE DEFORMATIONS AND BUCKLING

This chapter presents the development of beam theory with large deformations that includes beam bending, column deformation, material nonlinearity, and incremental loading. The development is an extension on the small-deformation beam theory presented in Section 2.1 but removes the limitations of small deformation theory.

5.1 Updated Lagrange Formulation

The major assumptions and limitations are listed below:

1. Two-dimensional framework in a plane strain formulation.
2. Bernoulli-Euler beam kinematics without shear deformation.
3. Material nonlinearity is a function of normal stress and strain.
4. Incremental virtual work formulation with incremental stress-strain relationships and loading.
5. Updated Lagrange strain-displacement relationship appropriate for large rotations and small stretch.

5.1.1 Coordinates and incremental relationships.

Consider a beam element originally in an undeformed state that has experienced a sequence of load steps (1, 2, 3, ...i) and is in equilibrium after load step i. Let the nodes at either end of the element be labeled “a” and “b”, and let their current location in the global X-Y coordinate system be denoted as (X_{ai}, Y_{ai}) and (X_{bi}, Y_{bi}) , respectively.

Next, construct a local x-y coordinate system with the origin at node a. The x-axis extends from node a to node b along the base of the beam, and the y-axis is orthogonal to the x-axis with $y = 0$ at the bottom of the beam cross section. From this reference position we apply load step $i + 1$ and seek to determine the incremental structural responses. The local displacement increments in displacing from load step i to step $i + 1$ will be denoted as Δu in the x direction and Δv in the y direction.

Equilibrium of all the forces and moments acting on the element at load step $i + 1$ will be in reference to the x-y coordinate system of the previous load step i , not the element’s original position as assumed in small deformation theory.

5.1.2 Bernoulli-Euler beam kinematics.

Based on the assumption that cross-sectional planes remain plane in bending and axial deformation, the well-known Bernoulli-Euler assumption for displacement increments Δu and Δv at any station x along the beam length and at any point y in the beam’s cross section may be expressed as:

$$\Delta u(x, y) = \Delta a(x) + (y^* - y)\Delta v' \quad \text{Equation 5-1}$$

$$\Delta v(x) = \Delta v(x) \rightarrow \text{a function of } x \text{ only} \quad \text{Equation 5-2}$$

where, $\Delta u(x, y)$ = displacement in x direction from column and bending deformation
 $\Delta a(x)$ = uniform displacement in x direction from column, independent of y
 $\Delta v(x)$ = displacement in y direction as function of x , independent of y
 $\Delta v' = d(\Delta v)/dx$, derivative of Δv with respect to x (local deformation slope)
 y^* = a reference plane in the beam cross section at $y = y^*$, yet to be specified
 $()' = d()/dx$, prime symbol denotes derivative of any quantity with respect to x

5.1.3 Total Lagrangian strain for large rotations.

The total normal strain (x direction) at load step i at any station x along the beam length and at any point y in the beam’s cross section may be described by a truncated form of total Lagrangian strain given by,

$$E_i(x,y) = u_i' + \frac{1}{2}(v_i')^2 \quad \text{Equation 5-3a}$$

All quantities are in reference to the original undeformed position, $i = 0$. It is evident that u_i' is the standard definition of small strain in the x direction. The nonlinear term, $\frac{1}{2}(v_i')^2$, is a second order correction term that adds a uniform stretching strain to the axial strain as a result of beam rotation. The correction term may be visualized as the stretch that is induced in the leg of a right triangle as it is rotated into the position of the hypotenuse through an angle approximated by v_i' . The larger the value of v_i' the more inaccurate is the approximation of the angle.

If we express an increment of the total Lagrangian strain from step i to $i+1$ we obtain:

$$\Delta E(x,y) = E_{i+1}(x,y) - E_i(x,y) = \Delta u' + \frac{1}{2}(\Delta v')^2 + v_i' \Delta v' \quad \text{Equation 5-3b}$$

The last term in Equation 5-3b contains v_i' , which is not an incremental term but rather the approximated angle at step i in reference to the undeformed position at $i = 0$. Thus the incremental form of total Lagrangian strain, $\Delta E(x,y)$, produces the same error as Equation 5-3a when dealing with large rotations. Note that when determining the strain increment for the first load increment starting from $i = 0$, we have $v_i' = v_0' = 0$, because the reference configuration has no displacements or rotations.

5.1.4 Updated Lagrangian strain increments.

The so-called updated Lagrange formulation provides improved accuracy for calculating strains by updating the x and y coordinates of the beam element's position to step i prior to solving for step $i + 1$. In other words, the beam element's position at step i is taken as the reference position for equilibrium and for measuring additional displacements resulting from the loads that are imposed at step $i + 1$, which means $v_i' = 0$ for each load step from i to $i + 1$.

With the above understanding, we can rewrite Equation B-3 in the updated Lagrangian description as:

$$\Delta \varepsilon(x,y) = \Delta u' + \frac{1}{2}(\Delta v')^2 \quad \text{Equation 5-4a}$$

where the symbol $\Delta \varepsilon$ is used to represent updated Lagrangian strain increments in order to distinguish it from increments of total Lagrangian strain, ΔE .

Inserting the Bernoulli-Euler kinematical equations for Δu into the updated Lagrangian strain increment equation, we arrive at the incremental strain-displacement relationships for beams under large rotations, given as,

$$\Delta \varepsilon(x,y) = \Delta a' + (y^* - y) \Delta v'' + \frac{1}{2}(\Delta v')^2 \quad \text{Equation 5-4b}$$

Equation 5-4b is the new equation for this development. That is, the remainder of the basic equations for the nonlinear stress-strain model, internal force resultants, and virtual work remain valid as expressed in the small-deformation formulation. However, the interaction of these basic equations with Equation 5-4b results in new nonlinear governing equations for beam deformations.

5.1.5 Incremental stress-strain model.

The nonlinear stress-strain laws used in CANDE are specific to each pipe material such as corrugated metal and reinforced concrete, which are detailed in previous chapters. However, all these stress-strain models conform to the same generic form that may be expressed as

$$\Delta \sigma = E_c \Delta \varepsilon \quad \text{Equation 5-5}$$

where, $\Delta \sigma$ = increment of axial stress from load step i to $i + 1$, ($\Delta \sigma = \Delta \sigma(x,y)$)
 $\Delta \varepsilon$ = increment of axial strain from load step i to $i + 1$, ($\Delta \varepsilon = \text{Equation 5-4b}$)
 E_c = chord modulus of total stress-strain curve from load step i to $i + 1$

The chord modulus is dependent on the pipe material and the history of stress and strain throughout all loading steps. It is determined iteratively during each load step by repeating the solution process until the value of E_c converges for each element to a small tolerance of error.

Replacing $\Delta \epsilon$ in Equation 5-5 with Equation 5-4b, the fundamental stress-displacement relationship may be expressed as,

$$\Delta \sigma = E_c(\Delta a' + (y^* - y) \Delta v'' + \frac{1}{2}(\Delta v')^2) \quad \text{Equation 5-6}$$

Next, Equation 5-6 is used to define the internal thrust and internal moment acting on the cross section at any station x .

5.1.6 Internal thrust and moment increments.

As is customary, we define the thrust increment as the integral of $\Delta \sigma$ over the cross-section area A , and the moment increment as the integral of $\Delta \sigma (y^* - y)$ over the cross-section area A . Specifically,

$$\Delta N = \int_A \Delta \sigma \, dA = \int_A E_c(\Delta a' + (y^* - y) \Delta v'' + \frac{1}{2}(\Delta v')^2) \, dA \quad \text{Equation 5-7a}$$

$$\Delta M = \int_A \Delta \sigma (y^* - y) \, dA = \int_A E_c(\Delta a' + (y^* - y) \Delta v'' + \frac{1}{2}(\Delta v')^2) (y^* - y) \, dA \quad \text{Equation 5-7b}$$

where, ΔN = thrust increment from load step i to $i + 1$, ($\Delta N = \Delta N(x)$)
 ΔM = moment increment from load step i to $i + 1$, ($\Delta M = \Delta M(x)$)
 $dA = b(y)dy$, a differential area of cross section where $b(y)$ is the width with y measured from bottom.

The arbitrary reference position y^* is now chosen so that $\int_A E_c (y^* - y) \, dA = 0$, which simplifies Equations 5-7a,b, and gives the location of y^* measured from the bottom as,

$$y^* = \left(\int_A E_c y \, dA \right) / \left(\int_A E_c \, dA \right) \quad \text{Equation 5-8}$$

The remaining area integrals in Equation 5-7a,b relate to effective axial stiffness and effective bending stiffness and are defined as,

$$EA^* = \int_A E_c \, dA = \text{Effective axial stiffness of beam element} \quad \text{Equation 5-9}$$

$$EI^* = \int_A E_c (y^* - y)^2 \, dA = \text{Effective bending stiffness of beam element} \quad \text{Equation 5-10}$$

All of the integrals in Equations 5-8, 5-9, and 5-10 are computed numerically for every iteration within each load step until convergence is achieved.

With the above definitions for y^* , EA^* and EI^* , the thrust and moment increments (Equations 5-7a,b) simplify to the following equations,

$$\Delta N = EA^*(\Delta a' + \frac{1}{2}(\Delta v')^2) \quad \text{Equation 5-11}$$

$$\Delta M = EI^* \Delta v'' \quad \text{Equation 5-12}$$

Note that the moment-increment expression is the familiar bending stiffness-curvature relationship used in small deformation theory. However, the thrust-increment expression, in addition to the familiar column stiffness-deformation relationship, also contains a nonlinear stiffness term related to rotation, $\frac{1}{2}(\Delta v')^2$.

5.1.7 Virtual work for beam-column element.

The general concept of virtual work is fully developed in Chapters 1 and 2. Here the attention is focused on the internal virtual of beam-column elements.

The internal virtual work for the beam-column element under consideration may be expressed as the following volume integration at any load step $i + 1$:

$$\delta U_{i+1} = \int_V \delta \varepsilon_{i+1} \sigma_{i+1} dV \quad \text{Equation 5-13}$$

where, $\delta \varepsilon_{i+1}$ = virtual strain field arising from the imposed virtual displacements
 σ_{i+1} = stress field existing in beam element at load step $i + 1$
 $\int_V (\dots) dV$ = volume integration over the beam element

The virtual symbol δ means a small variation of the strain field. Similar to variational calculus, δ operates on the displacement variables like a total derivative. Thus, operating on the updated Lagrangian strain, the virtual strain field is determined as:

$$\delta \varepsilon_{i+1} = \delta [a' + (y^* - y) v'' + \frac{1}{2}(v')^2]_{i+1} = \delta a' + (y^* - y) \delta v'' + v'_{i+1} \delta v' \quad \text{Equation 5-14}$$

The displacement variables prefaced with the symbol δ are arbitrary motions and need not be associated with the values at load step $i+1$. However, the term v'_{i+1} is associated with load step $i+1$ and is equivalent to, $v'_{i+1} = \Delta v'$, since $v'_i = 0$ by virtue of the updated Lagrange formulation.

The incremental form of the element internal virtual work is defined by;

$$\delta \Delta U_e = \delta U_{i+1} - \delta U_i = \int_V (\delta \varepsilon_{i+1} \sigma_{i+1} - \delta \varepsilon_i \sigma_i) dV \quad \text{Equation 5-15}$$

Observing that $\delta \varepsilon_{i+1} = \delta \varepsilon_i + \Delta v' \delta v'$, the above becomes;

$$\delta \Delta U_e = \int_V \{ (\delta a' + (y^* - y) \delta v'') \Delta \sigma + \Delta v' \delta v' \sigma_{i+1} \} dV \quad \text{Equation 5-16}$$

Separating the volume integral into area and length integrals, $dV = dA dx$, we arrive at,

$$\delta \Delta U_e = \int_x \{ \delta a' \int_A \Delta \sigma dA + \delta v' \Delta v' \int_A \sigma_{i+1} dA + \delta v'' \int_A \Delta \sigma (y^* - y) dA \} dx \quad \text{Equation 5-17}$$

Here it is observed that the two area integrals involving $\Delta \sigma$ have already been identified as ΔN and ΔM in Equations 5-7a,b. The area integral involving σ_{i+1} will now be designated as N_{i+1} , which is the total thrust at step $i+1$ referred to the beam element's coordinate system at step i . Thus Equation 5-17 is written as;

$$\delta \Delta U_e = \int_x \{ \delta a' \Delta N + \delta v' \Delta v' N_{i+1} + \delta v'' \Delta M \} dx \quad \text{Equation 5-18}$$

Since we have already established expressions for ΔN and ΔM in terms of displacements in Equations 5-11 and 5-12, we replace the unknown force increments ΔN and ΔM in Equation 5-18 with the equivalent unknown displacements. However, with regard to N_{i+1} , which is nonlinear because it is coupled with $\Delta v'$, we choose to leave N_{i+1} as expressed to facilitate the nonlinear solution strategy. With the above replacements, Equation 5-18 becomes,

$$\delta \Delta U_e = \int_x \{ \delta a' EA \Delta a' + \delta a' EA \frac{1}{2} (\Delta v')^2 + \delta v' \Delta v' N_{i+1} + \delta v'' EI \Delta v'' \} dx \quad \text{Equation 5-19}$$

For the sake of clarity, we will express Equation 5-19 as the sum of four terms,

$$\delta \Delta U_e = \delta \Delta U_a + \delta \Delta U_r + \delta \Delta U_g + \delta \Delta U_b \quad \text{Equation 5-20}$$

where,

$$\delta \Delta U_a = \int_x \{ \delta a' EA \Delta a' \} dx \quad \text{Equation 5-20a}$$

$$\delta \Delta U_r = \int_x \{ \delta a' EA \frac{1}{2} (\Delta v')^2 \} dx \quad \text{Equation 5-20b}$$

$$\delta \Delta U_g = \int_x \{ \delta v' \Delta v' N_{i+1} \} dx \quad \text{Equation 5-20c}$$

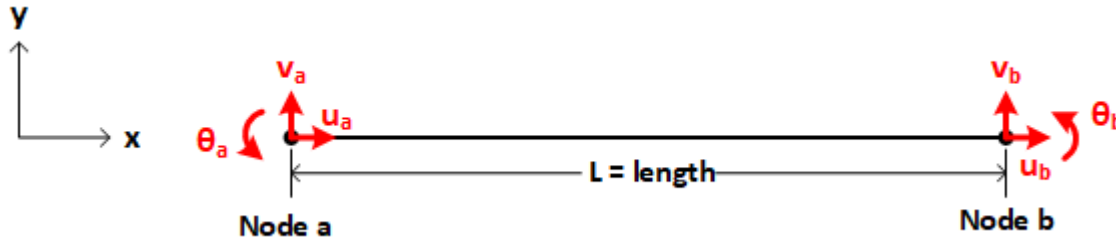
$$\delta\Delta U_b = \int_x \{\delta v'' EI \Delta v''\} dx \quad \text{Equation 5-20d}$$

Of the four terms in Equation 5-20, the first term is the familiar column stiffness term and the fourth term is familiar bending stiffness term identical to small deformation theory. The middle two terms are nonlinear and are associated with large deformations. As we shall see in the subsequent FEM development, the second term will be treated as a load vector and the third term will lead to the so-called geometric stiffness matrix.

5.2 Finite Element Development

5.2.1 Finite element interpolation functions.

Equation 5-20 is the incremental internal virtual work of a beam column element with large deformation without numerical approximations. To express this in a FEM formulation we introduce interpolation functions for the displacements that become exact as the element lengths become small. The interpolation functions are expressed in terms of unknown nodal variables shown in the sketch below.



where, $\Delta u_a, \Delta u_b$ = incremental nodal displacements in x direction at nodes a and b
 $\Delta v_a, \Delta v_b$ = incremental nodal displacements in y direction at nodes a and b
 $\Delta \theta_a, \Delta \theta_b$ = incremental nodal rotations in counter-clockwise direction at nodes a and b

The incremental axial displacement function is approximated with a linear interpolation function expressed in vector notation as;

$$\Delta a(x) = \langle \phi_1 \phi_2 \rangle \langle \Delta u_a \Delta u_b \rangle^T \quad \text{Equation 5-21}$$

where, $\phi_1(x) = 1 - x/L$
 $\phi_2(x) = x/L$
 $L = \text{element length}$

The incremental vertical displacement function is approximated by a cubic polynomial, known as a Hermitian interpolation function, and is expressed in vector notation by,

$$\Delta v(x) = \langle \gamma_1 \gamma_2 \gamma_3 \gamma_4 \rangle \langle \Delta v_a \Delta \theta_a \Delta v_b \Delta \theta_b \rangle^T \quad \text{Equation 5-22}$$

where, $\gamma_1(x) = 1 - 3(x/L)^2 + 2(x/L)^3$
 $\gamma_2(x) = L(1 - x/L)^2 x/L$
 $\gamma_3(x) = 3(x/L)^2 - 2(x/L)^3$
 $\gamma_4(x) = L(1 - x/L)(x/L)^2$

5.2.2 Element matrices and vectors

Taking the necessary derivatives of the approximating functions for $\Delta u(x)$ and $\Delta v(x)$, inserting them into the four internal virtual work terms of Equation 5-20, and integrating with respect to x over the element length L , we arrive at the following evaluations.

For the internal virtual work of the axial stiffness term we have,

$$\delta\Delta U_a = \langle \delta\Delta u_a \delta\Delta u_b \rangle \underline{\mathbf{K}}_a \langle \Delta u_a \Delta u_b \rangle^T$$

where the axial stiffness matrix is defined as,

$$\underline{\mathbf{K}}_a = (EA^*) \int_x [\langle \varphi'_1 \varphi'_2 \rangle^T \langle \varphi'_1 \varphi'_2 \rangle] dx \quad \text{Equation 5-23a}$$

and upon evaluating the integral, the axial stiffness matrix is determined as,

$$\underline{\mathbf{K}}_a = (EA^*/L) \begin{vmatrix} 1 & -1 \\ -1 & 1 \end{vmatrix} \quad \text{Equation 5-23b}$$

For the internal virtual work of the bending stiffness term we have,

$$\delta\Delta U_b = \langle \delta\Delta v_a \delta\Delta\theta_a \delta\Delta v_b \delta\Delta\theta_b \rangle \underline{\mathbf{K}}_b \langle \Delta v_a \Delta\theta_a \Delta v_b \Delta\theta_b \rangle^T$$

where the standard bending stiffness matrix is defined as,

$$\underline{\mathbf{K}}_b = (EI^*) \int_x [\langle \gamma''_1 \gamma''_2 \gamma''_3 \gamma''_4 \rangle^T \langle \gamma''_1 \gamma''_2 \gamma''_3 \gamma''_4 \rangle] dx \quad \text{Equation 5-24a}$$

and upon evaluating the integral, the standard bending stiffness matrix is determined as,

$$\underline{\mathbf{K}}_b = (EI^*/L) \begin{vmatrix} 12/L^2 & 6/L & -12/L^2 & 6/L \\ 6/L & 4 & -6/L & 2 \\ -12/L^2 & -6/L & 12/L^2 & -6/L \\ 6/L & 2 & -6/L & 4 \end{vmatrix} \quad \text{Equation 5-24b}$$

For the internal virtual work of the geometric stiffness term we have,

$$\delta\Delta U_g = \langle \delta\Delta v_a \delta\Delta\theta_a \delta\Delta v_b \delta\Delta\theta_b \rangle \underline{\mathbf{K}}_g \langle \Delta v_a \Delta\theta_a \Delta v_b \Delta\theta_b \rangle^T$$

where the geometric stiffness matrix is defined as,

$$\underline{\mathbf{K}}_g = (N_{i+1}) \int_x [\langle \gamma'_1 \gamma'_2 \gamma'_3 \gamma'_4 \rangle^T \langle \gamma'_1 \gamma'_2 \gamma'_3 \gamma'_4 \rangle] dx \quad \text{Equation 5-25a}$$

and upon evaluating the integral, the geometric stiffness matrix, which is dependent on the current thrust scalar is determined as,

$$\underline{\mathbf{K}}_g = (N_{i+1}) \begin{vmatrix} 6/5L & 1/10 & -6/5L & 1/10 \\ 1/10 & 2L/15 & -1/10 & -L/30 \\ -6/5L & -1/10 & 6/5L & -1/10 \\ 1/10 & -L/30 & -1/10 & 2L/15 \end{vmatrix} \quad \text{Equation 5-25b}$$

For the remaining internal virtual work term (rotational stretch vector), we have

$$\delta\Delta U_r = \langle \delta\Delta u_a \delta\Delta u_b \rangle \underline{\mathbf{r}}_c$$

wherein the rotational stretch vector is expressed as,

$$\underline{r}_e = \rho (EA^*/2L) \langle -1 \ 1 \rangle^T \quad \text{Equation 5-26a}$$

where, $\rho = \int_x (\Delta v')^2 dx = \langle \Delta v_a \Delta \theta_a \ \Delta v_b \Delta \theta_b \rangle \underline{K}_g^* \langle \Delta v_a \Delta \theta_a \ \Delta v_b \Delta \theta_b \rangle^T$

$$\underline{K}_g^* = \underline{K}_g \text{ without the multiplier } (N_{i+1})$$

Thus, the rotational stretch vector, which is dependent on the nonlinear scalar ρ , is determined as,

$$\underline{r}_e = \begin{bmatrix} r_a \\ r_b \end{bmatrix} = \rho (EA^*/2L) \begin{bmatrix} -1 \\ 1 \end{bmatrix} \quad \text{Equation 5-26b}$$

The above four terms of the element's internal virtual work, $\delta \Delta U_e$, may be brought together into a single 6 x 6 matrix along with 6-component vectors where the six nodal unknowns are listed in the following order $\langle \Delta u_a \ \Delta v_a \Delta \theta_a \ \Delta u_b \ \Delta v_b \Delta \theta_b \rangle$. Thus the finite element equivalent of Equation 5-20 is expressed as,

$$\delta \Delta U_e = \langle \delta \Delta u_a \ \delta \Delta v_a \ \delta \Delta \theta_a \ \delta \Delta u_b \ \delta \Delta v_b \ \delta \Delta \theta_b \rangle (\underline{K}_e \langle \Delta u_a \ \Delta v_a \Delta \theta_a \ \Delta u_b \ \Delta v_b \Delta \theta_b \rangle^T + \underline{r}_e)$$

where, \underline{K}_e = total effective element stiffness matrix (6 x 6) Equation 5-27

$$\underline{r}_e = \langle r_a \ 0 \ 0 \ r_b \ 0 \ 0 \rangle^T = \text{rotational stretch vector (1 x 6)} \quad \text{Equation 5-28}$$

Of course, it is understood that the components of \underline{K}_a , \underline{K}_b , and \underline{K}_g are added into the proper locations of the \underline{K}_e matrix corresponding to the ordering of nodal variables.

5.2.3 Transformation and global assembly.

The last step before adding the element's contribution of $\delta \Delta U_e$ into the entire system is to transform the nodal variables from local coordinates to global coordinates.

Let β = angle from global X-axis to local x-axis, then the local nodal variables may be expressed as global nodal variables by,

$$\underline{\Delta u}_e = \underline{T} \underline{\Delta u}_E \quad \text{Equation 5-29}$$

where, $\underline{\Delta u}_e = \langle \Delta u_a \ \Delta v_a \Delta \theta_a \ \Delta u_b \ \Delta v_b \Delta \theta_b \rangle^T$ local nodal variables for element

$$\underline{\Delta u}_E = \langle \Delta u_A \ \Delta v_A \Delta \theta_A \ \Delta u_B \ \Delta v_B \Delta \theta_B \rangle^T \text{ global nodal variables for element}$$

$$\underline{T} = \begin{bmatrix} C & S & 0 & 0 & 0 & 0 \\ -S & C & 0 & 0 & 0 & 0 \\ 0 & 0 & 1 & 0 & 0 & 0 \\ 0 & 0 & 0 & C & S & 0 \\ 0 & 0 & 0 & -S & C & 0 \\ 0 & 0 & 0 & 0 & 0 & 1 \end{bmatrix}$$

and, $C = \cos(\beta)$ and $S = \sin(\beta)$

With the above transformation matrix, the element stiffness matrix and rotational stretch vector may be expressed in global coordinates as,

$$\underline{K}_E = \underline{T}^T \underline{K}_e \underline{T} \quad \text{Equation 5-30}$$

$$\underline{r}_E = \underline{T}^T \underline{r}_e \quad \text{Equation 5-31}$$

It should be clear that lower-case subscripts are used for element quantities that are in expressed in local coordinates, whereas upper-case subscripts are used for element quantities that are in expressed in global coordinates.

The effective element stiffness matrix \underline{K}_E and the rotational stretch vector \underline{r}_E are in the proper form for global assembly wherein \underline{K}_E is added to the global effective stiffness matrix and \underline{r}_E is brought to the right-hand-side of the equations to be subtracted from the load vector.

5.3 Solution Strategy

The overall solution process is a direct iterative method as outlined below. The viewpoint is that we have a converged solution at load step i , and we seek a solution for load step $i+1$.

5.3.1 Iterative methodology

In obtaining a solution from load step i to $i+1$, we begin by assuming $N_{i+1} = N_i$ and $\rho = 0$ so that element matrices and vectors may be computed for each element. After global assembly, the current set of equations may be expressed for iteration k as

$$\underline{K}_{Gk} \Delta u_{Gk} = \Delta P_{Gk} \quad \text{Equation 5-32}$$

where, \underline{K}_{Gk} = global stiffness matrix for iteration k , i.e., collection of elements $\sum \underline{K}_{Ek}$

Δu_{Gk} = global vector of all unknown nodal variable increments for iteration k

ΔP_{Gk} = global vector of load increments for iteration k , including negative rotational-stretch vector.

k = iteration counter; 1, 2, 3, ...

The set of linear algebraic equations represented by Equation 5-32 is solved by Gauss Elimination for the displacement increments Δu_{Gk} . This trial solution is used to form a new and better estimates for N_{i+1} and ρ , which leads to revised values for \underline{K}_{Gk} and ΔP_{Gk} for the next iteration. When two successive iterations produce the same results within an acceptable tolerance, the solution has converged for load step $i + 1$, and all quantities are updated as,

$$q_{i+1} = q_i + \Delta q \quad \text{Equation 5-33}$$

where q stands for all structural responses such as displacements, stresses, strains, moments, thrusts, and so on. In addition, the updated Lagrange formulation implies that the global coordinate locations of each node are updated so that q also represents each (X,Y) nodal coordinate that are updated by the corresponding displacement increments.

5.3.2 Recovery of element forces

When load step $i+1$ converges to a solution, we want to recover the incremental internal forces at the ends of the element, that is, increments of thrust, shear and moment at the element's nodes. We can obtain these force increments in reference to "configuration i coordinates" by making use of virtual work.

Let, $\Delta T_a, \Delta T_b$ = Thrust force increments (x_i direction) at nodes a and b

$\Delta Q_a, \Delta Q_b$ = Shear force increments (y_i direction) at nodes a and b

$\Delta M_a, \Delta M_b$ = Moment increments at nodes a and b (invariant to x - y coordinates)

The incremental virtual external work of these end forces is given by;

$$\delta \Delta W_e = \langle \delta \Delta u_a \delta \Delta v_a \delta \Delta \theta_a \delta \Delta u_b \delta \Delta v_b \delta \Delta \theta_b \rangle \langle \Delta T_a \Delta Q_a \Delta M_a \Delta T_b \Delta Q_b \Delta M_b \rangle^T$$

With the element's incremental end loads defined, we can now express the net incremental virtual work of any element to be equal to zero; i.e.,

$$\delta\Delta V_e = \delta\Delta U_e - \delta\Delta W_e = 0$$

Using equation Equations 5-27 and 5-28 to express $\delta\Delta U_e$, we arrive at the following equations to determine the incremental end forces and moments:

$$\begin{pmatrix} \Delta T_a \\ \Delta Q_a \\ \Delta M_a \\ \Delta T_b \\ \Delta Q_b \\ \Delta M_b \end{pmatrix} = \left(\underline{\mathbf{K}}_a + \underline{\mathbf{K}}_b + \underline{\mathbf{K}}_{\text{ge}} \right) \begin{pmatrix} \Delta u_a \\ \Delta v_a \\ \Delta \theta_a \\ \Delta u_b \\ \Delta v_b \\ \Delta \theta_b \end{pmatrix} + \begin{pmatrix} r_a \\ 0 \\ 0 \\ r_b \\ 0 \\ 0 \end{pmatrix} \quad \text{Equation 5-34}$$

Thus the end forces can be recovered by multiplying the complete element stiffness matrix times the incremental displacements. For the end thrust forces we also add on the rotational stretch forces r_a and r_b . All of the above operations are carried out in reference to local the coordinate axis at step i .

5.3.3 Update coordinates

Before proceeding to the next load step, it is necessary to update all quantities to the new starting configuration. In particular we need to update the thrust associated with the geometric stiffness matrix. Let N^* represent the accumulation of all past thrust increments which is expressed in the x -direction of the previous step (i.e., $N^* = N_{i+1}$). Similarly let Q^* represent the accumulation of all past shear increments which is expressed in the y -direction of the previous step. The goal is to express in N^* in the x -direction and Q^* in the y -direction of the current position. The increment of rotation, say α , that the element experienced in moving from the previous step to the current step may be computed as:

$$L_{\text{new}} = (L_{\text{old}} + \Delta u_b - \Delta u_a)^2 + (v_b - v_a)^2)^{1/2} \quad (\text{new length of element}) \quad \text{Equation 5-35a}$$

$$\sin \alpha = (v_b - v_a) / L_{\text{new}} \quad \text{Equation 5-35b}$$

$$\cos \alpha = (L_{\text{old}} + \Delta u_b - \Delta u_a) / L_{\text{new}} \quad \text{Equation 5-35c}$$

Thus we can rotate the thrust and shear to the current configuration as

$$N^*_\alpha = \cos \alpha N^* + \sin \alpha Q^* \quad \text{Equation 5-36a}$$

$$Q^*_\alpha = -\sin \alpha N^* + \cos \alpha Q^* \quad \text{Equation 5-36b}$$

For the iteration process during the next load step, we use the following estimate for thrust in the geometric stiffness matrix;

$$N_{i+1} = N^*_\alpha + \Delta N \quad \text{Equation 5-37}$$

where N^*_α is a fixed value and ΔN is determined iteratively. For the first iteration we assume $\Delta N = 0$. In the absence of material nonlinearity, this process always converges in three load steps.

After all load steps are complete, the problem is finished and the load-deformation path of the structural system may be visualized. Note that this method of analysis by itself does not directly provide a critical buckling load like a linearized

buckling (Euler) analysis. Rather, the actual buckling load is observed by noting the peak load (e.g., soil height) when the system fails due to unbounded displacements. In order to predict the buckling capacity at the end of each load increment, we augment the large-deformation analysis with a linearized buckling solution as discussed next.

5.4 Buckling Capacity

At the end of each converged load step, we have stored in memory the current components for the standard stiffness matrix and the geometric stiffness matrix, which, when taken together, form the global stiffness matrix that is expressed in Equation 5-32. Thus, after convergence of load step $i+1$, we may write the global stiffness matrix in two parts as,

$$\underline{K}_G = \underline{K}_S + \underline{K}_{Geo}(\underline{N}_{i+1}) \quad \text{Equation 5-38}$$

where, \underline{K}_S = global standard stiffness matrix (small deformations)

$$\underline{K}_{Geo}(\underline{N}_{i+1}) = \text{global geometric stiffness matrix written as a function of element thrust values}$$

The known values for thrust \underline{N}_{i+1} as expressed in the above geometric stiffness matrix, have been determined iteratively during the solution for step $i + 1$. Thus, \underline{N}_{i+1} represents the current set of thrust values in the various beam-column elements at load step $i+1$.

If we temporarily assumed the matrices in Equation 5-38 remain constant except the geometric stiffness is scaled by a load parameter “c”, then we can determine what magnitude increase in the set of thrust values \underline{N}_{i+1} that would cause unlimited deformations, i.e., critical buckling. This will occur when the combined standard and geometric stiffness becomes singular (determinant = 0), which is dependent on the value of c.

To this end, let the global stiffness matrix be written as,

$$\underline{K}_G(c) = \underline{K}_S + c \underline{K}_{Geo}(\underline{N}_{i+1}) \quad \text{Equation 5-39}$$

and pose the problem as, find the value(s) c such that,

$$\text{Det } \underline{K}_G(c) = 0 \quad \text{Equation 5-40}$$

This, of course, is the classic eigenvalue problem for buckling bifurcation wherein the lowest eigenvalue “c” is a direct measure of the current buckling capacity. If, for example, the value of c is found to be 2.50, then the current set of thrust values \underline{N}_{i+1} could be increased by any factor up to 2.5 before buckling would occur. Thus we can say that the value of “c” is the predicted buckling capacity or equivalently the safety factor against buckling.

In CANDE-2022, a determinant search process finds the value of “c”. Starting with the guess $c = 1$, the determinant expressed in Equation 5-40 is evaluated. If the determinant is positive, meaning the matrix is structurally stable, then the value of c is steadily increased until the determinant is found to be negative, meaning the matrix structurally unstable. Knowing the correct value c lies in an interval bounded by the last two estimates, a binary-chop method is used to keep refining the estimate for “c” until it is accurate to two decimal places.

In summary, this chapter presents a complete derivation of a beam theory with large deformations that includes beam bending, column deformation, material nonlinearity, and incremental loading. The large deformation responses (forces, displacements, stresses and strain) are output at the end of each load step along with a prediction of the buckling capacity.

5.5 Illustration – Simply Supported Beam

This illustration compares the updated Lagrange CANDE-2022 solution and buckling prediction with a closed-form solution for an axially load, simply supported beam with initial constant end moment. The closed-form solution is theoretically equivalent to a one-step updated Lagrange solution (i.e., total Lagrange method) so that a direct comparison may be made if we limit the CANDE solutions to a single load step. Subsequently, we will obtain CANDE solutions with multiple load-steps to demonstrate a more realistic load-deformation behavior in contrast with the single-step solutions.

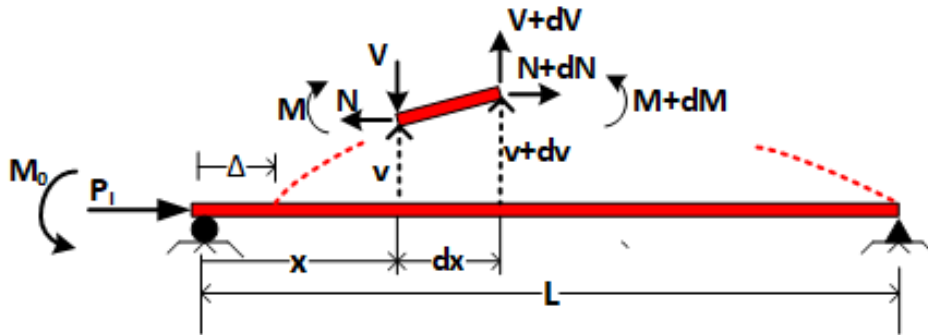
Thus, the specific objectives are:

1. Develop a closed form solution for a simply supported beam with an initial end moment and an increasing axial load based on total Lagrange formulation. Note a closed form Updated Lagrange solution is not tractable.
2. Compare CANDE load-deformation path and buckling prediction with the closed-form solution wherein the CANDE solution is obtained with a series of single load steps with increasing axial load (i.e., a series of total Lagrange solutions).
3. Show realistic load-deformation paths from CANDE solutions based on multiple steps to successively increase the axial load while updating the coordinates at the end of each load step (i.e., an updated Lagrange solution).

5.5.1 Development of closed-form solution

The idealized beam, shown in the figure below, is flexible in bending with bending stiffness EI and inextensible in axial elongation. The right end is pinned supported, and the left end is on a roller with a constant moment M_0 and an axially increasing thrust force, P_1 .

Figure 5.5.1-1 Simply supported beam with increasing axial load and fixed end moment.



A differential segment of the test beam is shown above for formulating the governing differential equation,

where, M, dM = moment and differential
 V, dV = shear and differential
 N, dN = thrust and differential
 v, dv = vertical displacement and differential
 x = horizontal coordinate
 $(.)' = d(.) / dx$ denotes derivative with respect to x

Horizontal and vertical equilibrium of the differential segment requires:

$$dN \equiv N' dx = 0 \quad (\text{Thrust is constant}) \quad \text{Equation 5-41}$$

$$dV \equiv V' dx = 0 \quad (\text{Shear is constant}) \quad \text{Equation 5-42}$$

Moment equilibrium of the differential segment is approximated by letting v' represent the tangent of the total rotation so that the differential equation remains linear as expressed below:

$$M' + Nv' + V = 0 \quad \text{Equation 5-43}$$

The Bernoulli-Euler moment-curvature relationship, wherein EI is the beam bending stiffness, is given by;

$$M = -EI v'' \quad \text{Equation 5-44}$$

Taking the first derivative of Equation 3 and the second derivative of Equation 4 and combining the results we arrive at (recalling that $N' = 0$ and $V' = 0$):

$$-EI v'''' + N v'' = 0 \quad \text{Equation 5-45}$$

Since N is constant, overall horizontal equilibrium requires that $N = -P$, where P is the applied axial force, positive in compression, and we define the positive quantity q as,

$$q^2 = P/EI \quad \text{Equation 5-46}$$

Using the above in Equation 5-45, we arrive at the governing ordinary differential equation written as,

$$v'''' + q^2 v'' = 0 \quad \text{Equation 5-47}$$

The general solution to Equation 5-47 is given by,

$$v(x) = C_1 + C_2 x + C_3 \cos qx + C_4 \sin qx \quad \text{Equation 5-48}$$

Where C_1 , C_2 , C_3 , and C_4 are constants determined from the four boundary conditions and written as,

$$v(0) = 0 \quad \text{Equation 5-49a}$$

$$v''(0) = -M_0/EI \quad \text{Equation 5-49b}$$

$$v(L) = 0 \quad \text{Equation 5-49c}$$

$$v''(L) = 0 \quad \text{Equation 5-49d}$$

After determining the constants, the final closed-form solution may be expressed as,

$$v(x) = (M_0/P) [-1.0 + x/L + \cos qx - (\cos qL/\sin qL) \sin qx] \quad \text{Equation 5-50}$$

Upon inspecting the last term in Equation 5-50, it is evident that the predicted vertical displacement becomes infinite when the divisor $\sin qL = 0$. This occurs when the load P reaches the first critical value, P_{critical} , such that $qL = \pi$. Or, making use of Equation 5-46, we arrive at the well-known critical buckling load for a simply supported beam,

$$P_{\text{critical}} = EI(\pi/L)^2 \quad \text{Equation 5-51}$$

The major approximation in the above derivation occurs in Equation 5-43 wherein the tangent of the rotation angle formed by the differential element with respect to the undeformed position is approximated by the derivative of the vertical displacement. This approximation is exactly equivalent to the total Lagrangian approach (truncated from) presented earlier in this chapter. Of course, this approximation becomes less and less accurate as the angle increases.

5.5.2 Example test problem for closed-form solution

To numerically illustrate the load-deformation behavior of Equation 5-50 as well as the critical buckling load given by Equation 5-51, hypothetical beam parameters are defined in the table below.

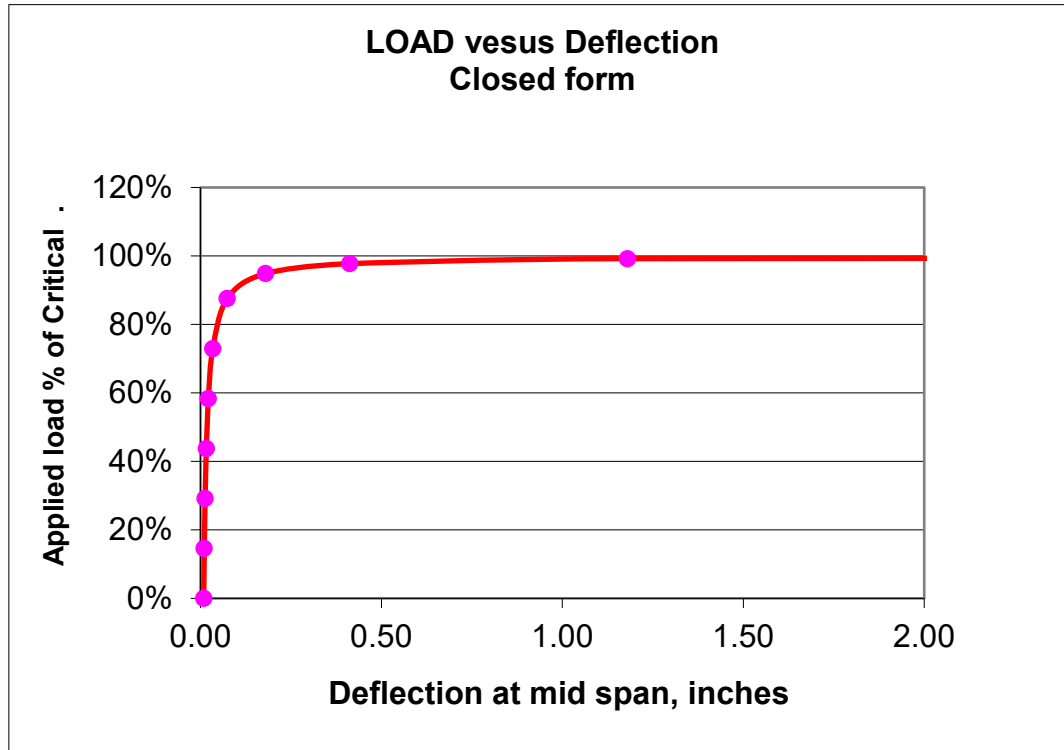
Table 5.5.2-1 Numerical values for test problem.

Beam Parameter	Parameter value
----------------	-----------------

Total Length, L	12 inches
Bending Stiffness, EI	1000 lbs-in ²
Initial end moment, M_0	1 in-lb
Axial load, P (variable)	0 to $P_{critical}$
$P_{critical}$ (Equation 5-51)	68.539 lbs

The following figure shows a plot of the applied load P versus mid-span deflection where the applied load is presented as percentage of the critical load (68.54 lbs)

Figure 5.5.2-1 Load-deformation curve from closed-form solution of test problem.



Deflections are observed to remain small until the applied load is near 80% of the critical load. After the 80% load level, the simple-theory solution predicts rapidly increasing displacements that become infinite as the load reaches 100% critical. The numerical values of displacements are less and less accurate as the displacements (and hence the rotations) increase in magnitude. The totally false prediction of an infinite displacement as the load approaches 100% of critical is a characteristic inaccuracy of this total Lagrangian formulation, which is limited to small rotations on the order of 5%. Another characteristic inaccuracy of total Lagrange is that for loads greater than 100% of critical is that predicted displacements are opposite in sign, which of course, is also obviously unrealistic.

Although the total Lagrange formulation does not give realistic predictions for the displacement values for loads near the critical load, the prediction of the critical load level where rapid changes in displacement occur is quite accurate. This finding, which is demonstrated in the next section, is significant because it gives credence to the buckling load prediction method used in CANDE for load schedules that are significantly below the critical load.

5.5.3 CANDE model of test problem

The corresponding CANDE model is shown in the figure below with parameters defined in the following table. Twelve beam-column elements are used to simulate the test problem. The same beam properties previously defined for the closed-form solution are assigned to the CANDE model except the CANDE model also includes axial deformation, which is not included in the closed-form formulation. In order to minimize the effect of axial deformation, the cross-sectional area is assigned a value two orders of magnitude larger than the moment of inertia so that bending deformation will dominate.

Figure 5.5.3-1 Twelve element CANDE model of test problem.

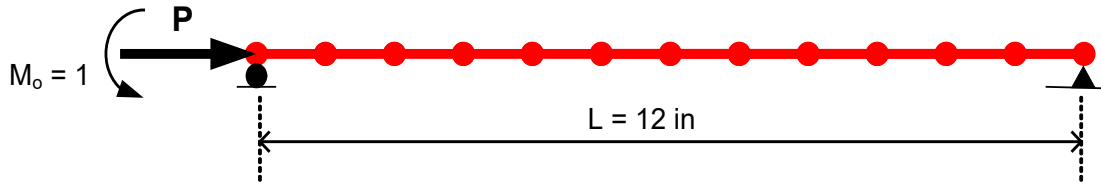


Table 5.5.3-1 Numerical values for CANDE model.

Beam Parameter	Parameter value
Total Length, L	12 inches
Young’s modulus, E	1000 psi
Moment of inertia, I	1.0 in ⁴
Cross-section area, A	100.0 in ²
Initial end moment, M ₀	1 in-lb
Axial load, P (variable)	0 to P _{critical}
P _{critical} (Equation 5-51)	68.539 lbs

5.5.4 CANDE simulating total Lagrange approach.

Although CANDE is developed for an updated Lagrange methodology, it is easy to simulate a total Lagrange solution by specifying only one load step so that the original configuration remains the reference configuration and coordinates are not updated. By solving a series of problems (each with one load step) the axial load P can be successively increased from zero to P_{critical}, while the initial end moment is held constant for each problem.

As shown in the table below, the predicted deflections from this series of CANDE solutions are found to be nearly identical to the closed form solution with agreement to three significant digits. The lower part of the table shows CANDE’s prediction for the critical buckling load at each axial load level.

Table 5.5.4-1a. Mid-span Deflections (inches) for increasing axial load % Critical Load

Axial load as percent of Critical	0%	29.18%	58.36%	87.54%	94.84%	99.21%	99.94%
Closed-form Deflections	0.0090	0.0128	0.0220	0.0742	0.1796	1.1803	16.357
CANDE (single-step) Deflections	0.0090	0.0128	0.0220	0.0742	0.1795	1.1800	16.170

Table 5.5.4-1b. CANDE prediction of Buckling load (lbs) at each axial load level

Predicted Buckling Load	N/A	68.6	68.4	68.4	68.3	68.8	69.2
-------------------------	-----	------	------	------	------	------	------

The rather remarkable agreement of deflection predictions and buckling load predictions suggests that the CANDE formulation for the geometric stiffness matrix, the rotational stretch vector and the nonlinear solution strategy is working properly. Typically, CANDE underwent three solution iterations per load level to achieve convergence. Buckling predictions typically required 8 determinant searches per problem to find the buckling load factor. The error tolerance on the determinant search algorithm is set at 2%.

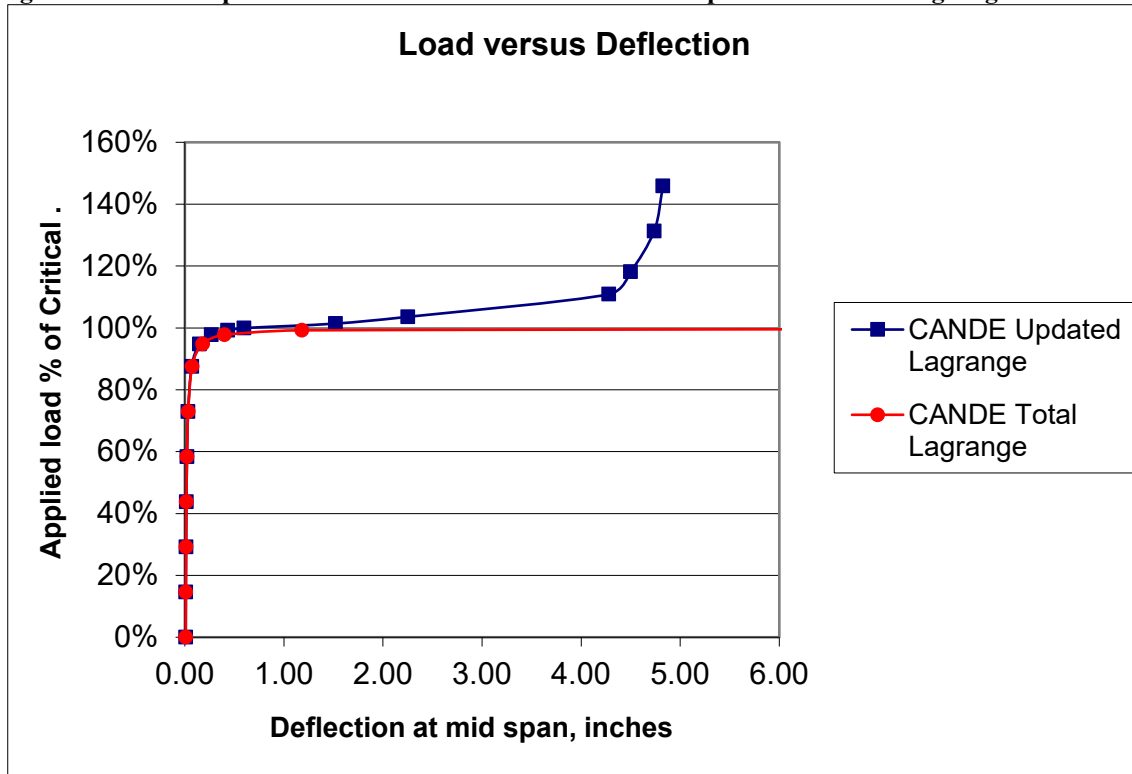
5.5.5 CANDE Solution for updated Lagrange approach.

In this more accurate approach, the CANDE solution is obtained by running a single problem wherein the axial load is increased on each load step with P starting at 0.0 and steadily increasing in value up to and well beyond $P_{critical}$.

The only difference between the previous total Lagrange methodology and the updated Lagrange methodology is that the beam's reference position is updated to the deformed position of the previous load step and the existing internal forces (thrust and shear) are transformed to be aligned with the deformed position.

Figure 5.5.5-1 shows load-deformation curves for mid-span deflection for the total and updated Lagrange methods. Recall that the total Lagrange solution as predicted by closed-form solution or by CANDE give nearly identical results.

Figure 5.5.5-1. Comparison of load-deformation curves from updated and total Lagrange.



Some pertinent observations from the above figure are noted below:

1. The size of the load increments for the updated Lagrange solution are indicated by the points shown in the figure. Smaller steps are required in the vicinity of the critical load where large displacements occur.
2. For axial loads below 80% of the $P_{critical}$, the deflections as predicted by total Lagrange are close but not identical to Updated Lagrange, differing at most by 4% at the 80% load level
3. When the axial load approaches $P_{critical}$, both the updated and total Lagrange solutions exhibit buckling-like behavior by showing rapid increases in displacement for small increases load.
4. The large displacements predicted by the total Lagrange solution are not realistic for loads close to $P_{critical}$ and incorrectly infers that there is no stable equilibrium position as the deflections become infinite. In contrast the updated Lagrange solution predicts realistic displacement and finds a stable position at about 110% of $P_{critical}$.
5. Although not shown, the buckling load predictions for updated and total Lagrange methods are very close for all load levels below $P_{critical}$. The updated Lagrange prediction for the buckling load when the axial load is very near $P_{critical}$ is about 2% higher than that predicted from the total Lagrange solution.

In summary for the simply supported beam example, the CANDE solution matches the closed form solution when restricted to one-step and loading. Under multi-step loading CANDE solutions are physically meaningful at load levels

near and above the critical buckling load whereas the closed-form solution is not. In all cases, the prediction of buckling capacity is accurate.

5.6 Illustration -- Soil-Structure Interaction

This illustration examines the effects of large deformations and buckling capacity in the presence of other nonlinearities for a corrugated steel culvert installation. The primary purpose is to compare and contrast small deformation solutions versus large deformation solutions in the presence of linear versus nonlinear corrugated metal behavior, linear versus nonlinear soil model behavior, and bonded versus frictionless soil-structure interface behavior.

Specifically, three separate studies are investigated for a corrugated steel pipe under progressively deep soil fill for the modeling conditions identified in the table below.

Study #	Deformation theory		Corrugated Metal		Soil Model		Interface	
	Small	Large	Linear	Elastic-plastic	Linear	Duncan/Selig	Bonded	Frictionless
1	✓		✓		✓		✓	
	✓			✓	✓		✓	
		✓	✓		✓		✓	
		✓		✓	✓		✓	
2	✓		✓			✓	✓	
	✓			✓		✓	✓	
		✓	✓			✓	✓	
		✓		✓		✓	✓	
3	✓		✓		✓			✓
	✓			✓	✓			✓
		✓	✓		✓			✓
		✓		✓	✓			✓

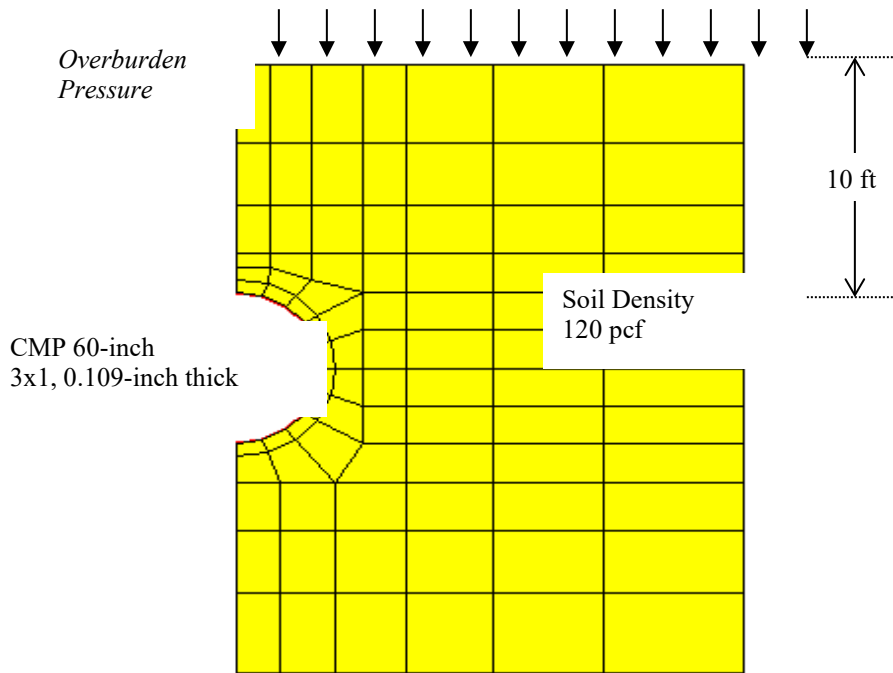
Each study contains four cases comparing small deformation solutions and large deformation solutions for linear and nonlinear corrugated metal models. Study #1 investigates the four cases under the assumption of a linear soil model and bonded interface. Study # 2 investigates the four cases under the assumption of a Duncan/Selig soil model and bonded interface. Study # 3 investigates the four cases under the assumption of a linear soil model and a frictionless interface.

5.6.1 CANDE soil-structure model and parameters

All the CANDE simulations are represented by finite element mesh shown in Figure 5.6.1-1 and have the following common features:

- Pipe is 60-inch corrugated steel, 3x1-inch corrugation, 0.109-inch thickness
- Soil is homogenous without bedding and weighs 120 pcf.
- Maximum soil height is 160 feet above the crown
- Truncated mesh height is 10 feet above crown (LEVEL 2 PIPE)
- Soil loading in excess of 10 feet is placed as equivalent increments of overburden pressure, where each increment represents 10 feet of soil.
- The first load increment includes the entire soil mass with 10 feet of fill followed by 15 increments of overburden pressure.

Figure 5.6.1-1. CANDE mesh of corrugated steel pipe (symmetric half)



Parameter values for the linear and nonlinear cases are identified in the table below.

Table 5.6.1-1. Linear versus nonlinear modeling assumptions.

System Component	Linear form	Non-linear form
Deformation theory	Small deformation theory (Standard engineering)	Large deformation theory (Updated Lagrange)
Corrugated metal stress-strain relationship:	Linear Elastic: Young's mod = 29,000,000 psi	Elastic-Plastic: Modulus = 29,000,000 psi Yield stress = 33,000 psi
Soil stress-strain relationship:	Linear Elastic: Young's mod = 1000 psi Poisson ratio = 0.3	Duncan/Selig Hyperbolic model for ML90
Soil-culvert interface assumption:	Fully Bonded	Frictionless slippage with tension separation allowed

In each study, comparison of the four cases are presented as vertical deflection versus fill height, maximum thrust stress versus fill height, and buckling safety factor versus fill height. These quantities along with plastic penetration constitute the design criteria for corrugated metal pipe.

5.6.2 Study # 1 -- Linear soil and bonded interface

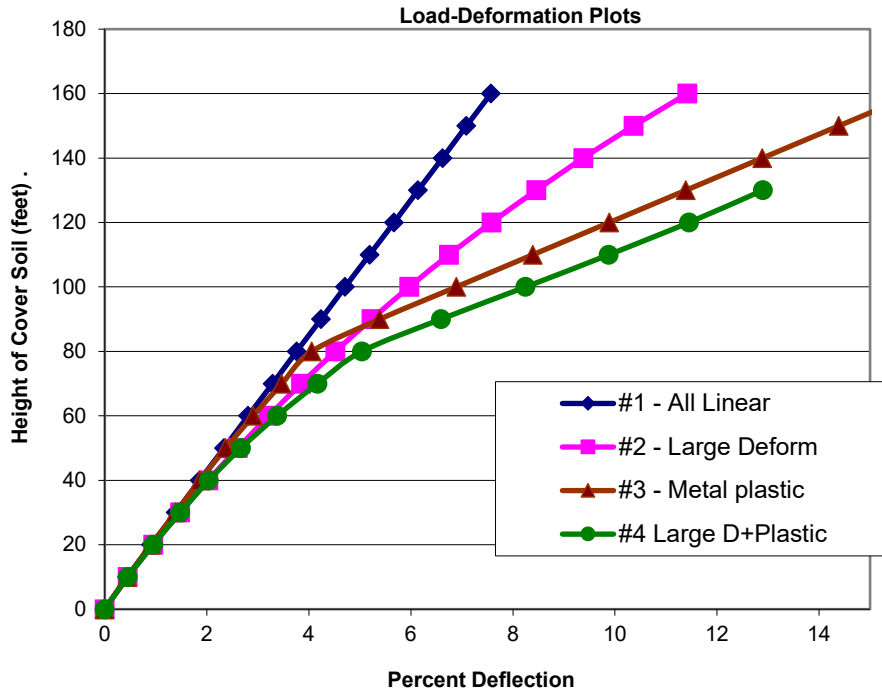
The first study assumes the culvert installation is defined by a linear elastic soil and a bonded soil-structure interface with the following four modeling cases:

- (1) linear steel material and small deformation theory
- (2) linear steel material and large deformation theory

- (3) nonlinear steel material and small deformation theory
- (4) nonlinear steel material and large deformation theory

Deflection. The following figure shows the vertical deflection of the corrugated steel pipe for four modeling cases.

Figure 5.6.2-1 Load-deflection plot – vertical deflection as percent of diameter (Study #1)

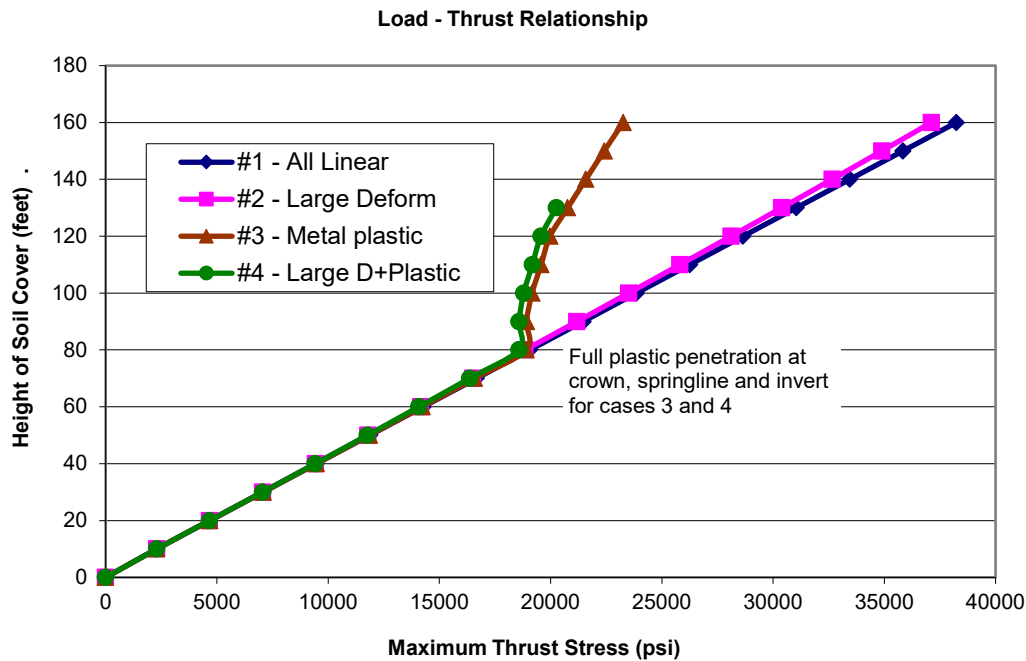


As expected, large deformation theory (case 2) produces deflections that progressively increase compared to the linear model (case 1). Although not shown, the large-deformation deflection curve becomes nearly flat at 300 feet of fill.

Case 3 shows that material nonlinearity by itself produces deflections that exceed case 2 after about 90 feet of fill. The dogleg bend in the deflection curve is caused by complete plastic hinging at crown, springline, and invert occurring at 80 feet of fill. Outer fiber compressive yielding first begins at the springline at 30 feet of fill, becomes a complete plastic hinge at 70 feet of fill, and finally forms a collapse mechanism at 80 feet of fill. After 80 feet fill the soil provides the elastic stiffness to resist complete collapse.

Case 4, which includes both material nonlinearity and large deformations, is presumably the most realistic case for applying the design criteria for deflection. Assuming 5% deflection is the allowable design limit, then 80 feet of fill is the maximum safe burial depth.

Thrust stress. The figure below shows the load-thrust plots for the same four cases wherein the maximum thrust occurs at the springline.

Figure 5.6.2-2 Load-Thrust stress plots of corrugated metal pipe (Study #1)

Comparing plots for cases 1 and 2, we observe that the large-deformation solutions are only slightly less than small deformation solutions. The same finding applies to comparing cases 3 and 4 so that it may be concluded that the thrust response is fairly insensitive to the large deformations.

In contrast to the above, when we compare cases 1 and 3 (or cases 2 and 4) we see that the thrust stress response is very sensitive to complete plastic penetration of the corrugated cross-section, causing an abrupt change of behavior. The abrupt change of thrust behavior in cases 3 and 4 is characterized by significantly smaller increases in thrust stress as increments of overburden pressure are applied. This behavior is to be expected because the combination of thrust and moment has produced complete plastic penetration of the corrugated cross-section at the crown, springline and invert so that the pipe now has minimal hoop stiffness (like slotted joints) which forces the soil to carry the bulk of the additional overburden pressure.

For the reasons described above, cases 3 and 4 do not produce a maximum thrust stress that approaches the yield stress value of 33,000 psi even at 160 feet of fill. This result reinforces the notion that the design criteria for corrugated metal should include a limit on the allowable plastic penetration because thrust stress alone can be misleading as evidenced in the above figure.

Buckling Stress and Safety Factor: The last comparison for Study # 1 is the buckling load and associated safety factor. Table 5.6.2-1 lists CANDE’s prediction for the thrust stress level that will produce a singular system matrix for each load increment. The buckling capacity is the maximum thrust stress value multiplied by the computed buckling factor “c”. Of course, the CANDE predictions, which are based on large deformation theory, only apply to cases 2 and 4.

For reference Table 5.6.2-1 also shows the simplified AASHTO prediction for buckling stress (LRFD specifications 12.7.2.4). The AASHTO equation for buckling stress is only dependent on the pipe diameter, modulus and cross-section geometry, it is not dependent on soil stiffness (assumed the same for all installations), nor is it dependent on metal yield stress. Thus, the predicted AASHTO buckling stress is the same for cases studied herein and is computed to be 42,867 psi, which is 30% greater than yield stress. Another reference value is the often-used Chelapatti-Allgood prediction, which predicts the buckling thrust equal to 54,275 psi. This prediction is based on the buckling of an elastic ring embedded in elastic springs (soil) and subjected to hydrostatic pressure.

Table 5.6.2-1 Buckling stress predictions

Fill Height (feet)	<i>Predicted Thrust Stress Level for Buckling-like Response (psi)</i>			
	CANDE – (Case 2) Linear steel	CANDE – (Case 4) Nonlinear steel	AASHTO Prediction	Chelapatti-Allgood
10	100,385	100,385	42,867	54,257
20	100,195	100,195	42,867	54,257
30	103,025	101,980	42,867	54,257
40	100,648	97,322	42,867	54,257
50	100,025	80,563	42,867	54,257
60	103,398	58,011	42,867	54,257
70	101,341	42,049	42,867	54,257
80	101,104	15,989	42,867	54,257
90	102,561	0	42,867	54,257
100	102,238	0	42,867	54,257
160	102,057	0	42,867	54,257

For the case of linear steel, CANDE's prediction for buckling stress remains nearly constant and is roughly twice the value of the AASHTO or Chelapati-Allgood approximations. However, for the case of nonlinear steel, the CANDE predictions for buckling capacity begin to steadily decrease as the steel begins to yield at about 30 feet of fill. When the complete collapse mechanism has formed at 80+ feet of fill, the buckling capacity approaches zero. Recall that CANDE's prediction of buckling stress is based on the current system stiffness matrix that becomes less and less robust as steel yielding increases with each load step.

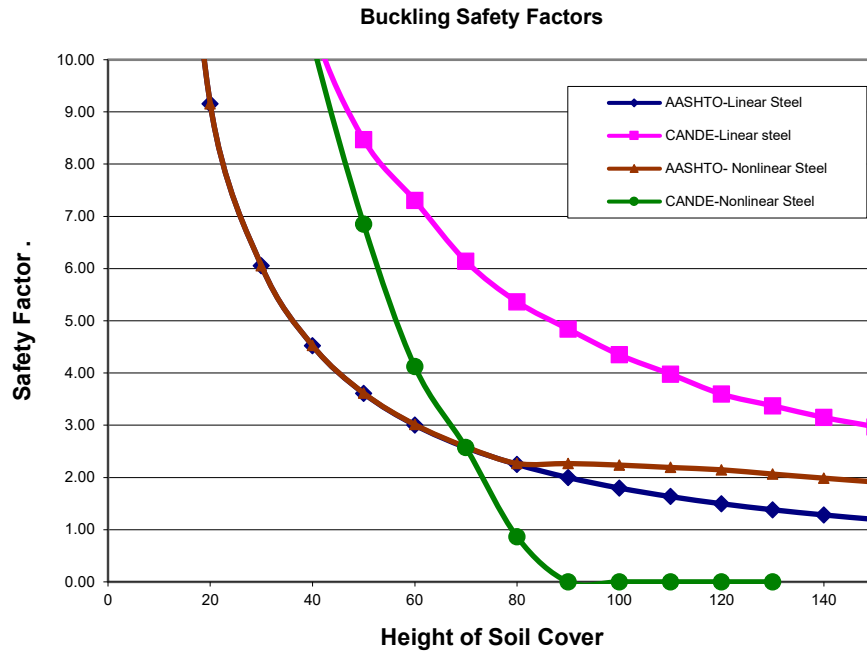
Figure 5.6.2-3 shows the buckling safety factors as a function of fill height. Safety factors are defined as the buckling stress capacity listed in Table 2 divided by the corresponding thrust stress shown in Figure 5.6.2-2. Note that the loading axis in the figure has been switched to the horizontal in order to illustrate the decrease in safety as fill height increases.

For the case of linear steel, it is evident that the AASHTO buckling safety factor is more conservative than CANDE prediction for all stages of fill height. However, when comparison is made for cases including nonlinear steel, the AASHTO safety factor predictions become less conservative after 80 feet of fill. That is the AASHTO safety factor tends to stay constant beyond 80 feet of fill due to the nearly constant thrust stress from the nonlinear steel solution.

In contrast the CANDE safety factor rapidly decreases due to the rapid loss of buckling capacity such that, after 70 feet of fill, CANDE provides a more conservative (and accurate) prediction of buckling safety than does the AASHTO prediction,

From the above study it is concluded that the AASHTO prediction for global is buckling is not always conservative.

Figure 5.6.2-3 Buckling safety factor versus fill height for corrugated steel pipe (Study # 1)



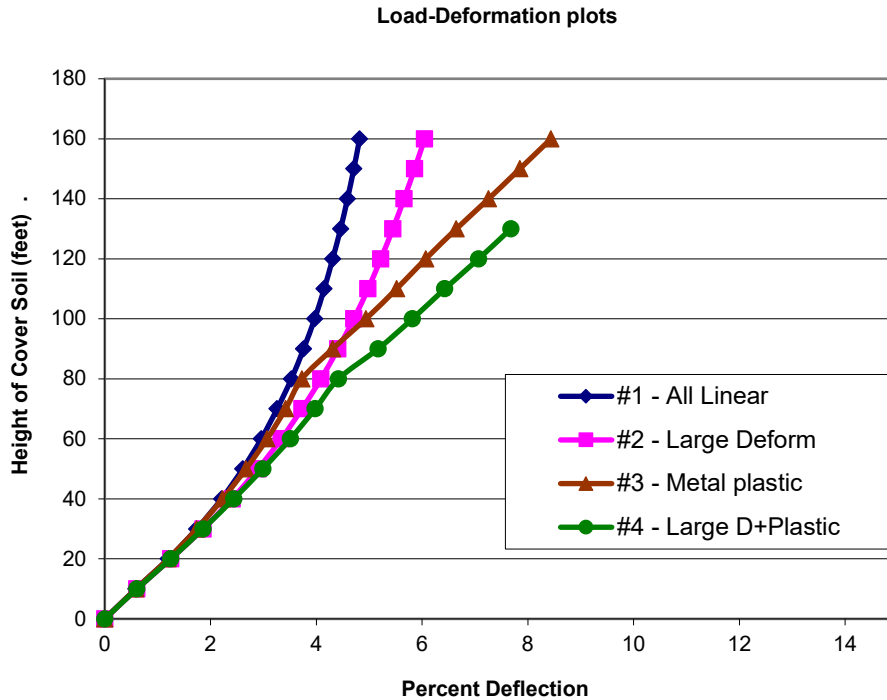
5.6.3 Study # 2 -- Nonlinear soil and bonded interface

This study assumes a nonlinear soil model while retaining the bonded soil-structure interface to define the test problem. Specifically, the nonlinear soil is called the Duncan/Selig hyperbolic formulation and represents silty sand compacted to 90% relative density (CANDE reference ML90).

Deflection. Figure 5.6.3-1 shows the vertical deflection of the corrugated metal pipe for four modeling cases composed small and large deformation theory and linear and nonlinear model for the corrugated steel. In this study the plot for case # 1 is not a linear response as it was in the previous study. Rather the curve exhibits a decreasing deflection as fill height increases. This, of course, is the influence of the soil model, which becomes stiffer under as confining pressure increases. Note, the soil model becomes less stiff under increasing shear strain, however the overall effect in this case is a stiffening of the soil mass.

Comparative observations between the deflection plots for four cases in are similar to Study #1. Specifically, large deformation theory (case 2) produces deflections that progressively increase as compared to the small deformation model (case 1). The dogleg bends in the deflection curves of cases 3 and 4 are caused by complete plastic hinging at crown, springline, and invert occurring at 80 feet of fill. Outer fiber compressive yielding first begins at the springline at 30 feet of fill, becomes a complete plastic hinge at 70 feet of fill, and finally forms a collapse mechanism at 80 feet of fill. After 80 feet of fill the ever-stiffening soil provides the stiffness to resist complete collapse.

Case 4, which includes both material nonlinearity and large deformations, is presumably the most realistic case for applying the design criteria for deflection. Assuming 5% deflection is the allowable design limit, then 90 feet of fill is the maximum safe burial depth.

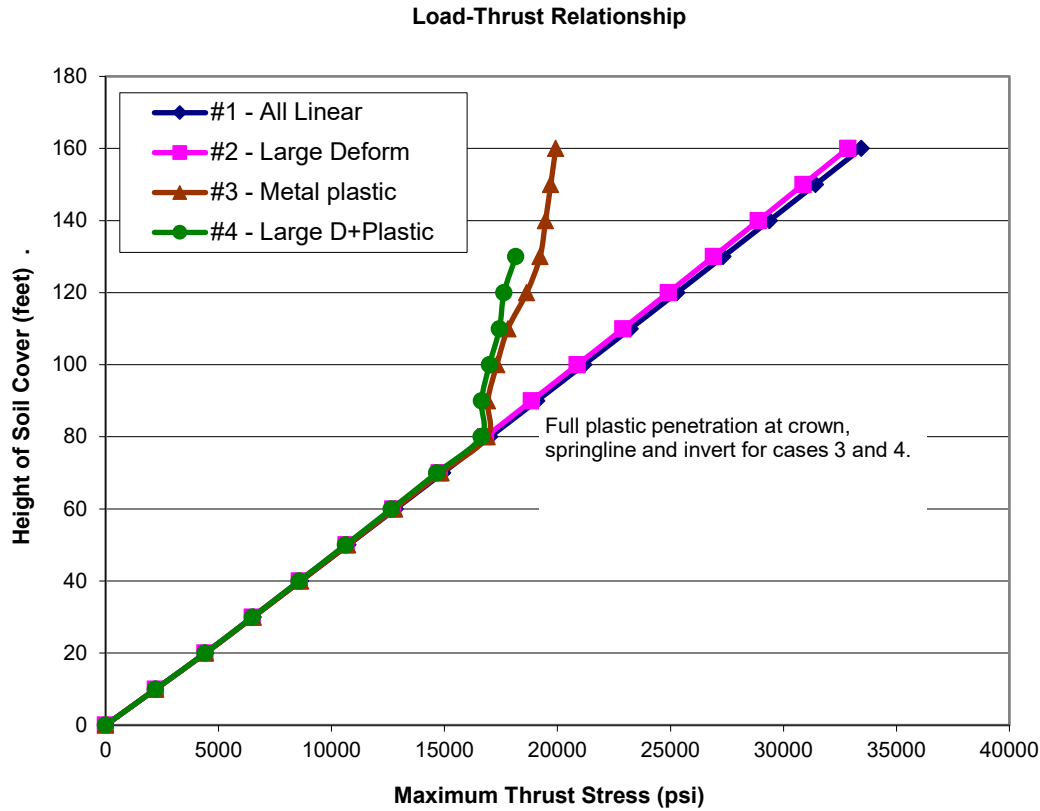
Figure 5.6.3-1 Load-Deflection plots of corrugated metal pipe (Study # 2)

Thrust stress. Figure 5.6.3-2 shows the load-thrust plots for the same four cases. In all cases the maximum thrust stress occurs at the springline. The thrust stress responses in this figure are very similar to Study #1. Overall, the effect of the nonlinear soil model is to reduce thrust stress values by about 5%, otherwise the shape of the curves and behavior is the same. Again, we conclude that the thrust response is fairly insensitive to large deformations.

As discussed in the previous study, the abrupt change of thrust behavior in cases 3 and 4 is to be expected because the combination of thrusts and moments has produced complete plastic penetration of the corrugated cross-section at the crown, springline and invert so that the pipe now has minimal hoop stiffness (like slotted joints) which forces the soil to carry the bulk of the additional overburden pressure.

As mentioned before, cases 3 and 4 do not produce a maximum thrust stress that approaches the yield stress value of 33,000 psi even at 160 feet of fill. This result reinforces the notion that the design criteria for corrugated metal should include a limit on the allowable plastic penetration because thrust stress alone can be misleading.

Figure 5.6.3-2 Load-Thrust stress plots of corrugated steel pipe (Study # 2).



Buckling Stress and Safety Factor. The last comparison for Study # 2 is the buckling load and associated safety factor. Table 5.6.3-1 lists CANDE’s prediction for the thrust stress level that will produce a singular system matrix for each load increment. Of course, the CANDE predictions, which are based on large deformation theory, only apply to cases 2 and 4.

As explained in Study # 1, the table also contains the simplified AASHTO prediction for ASSHTO buckling stress and the Chelapatti-Allgood prediction.

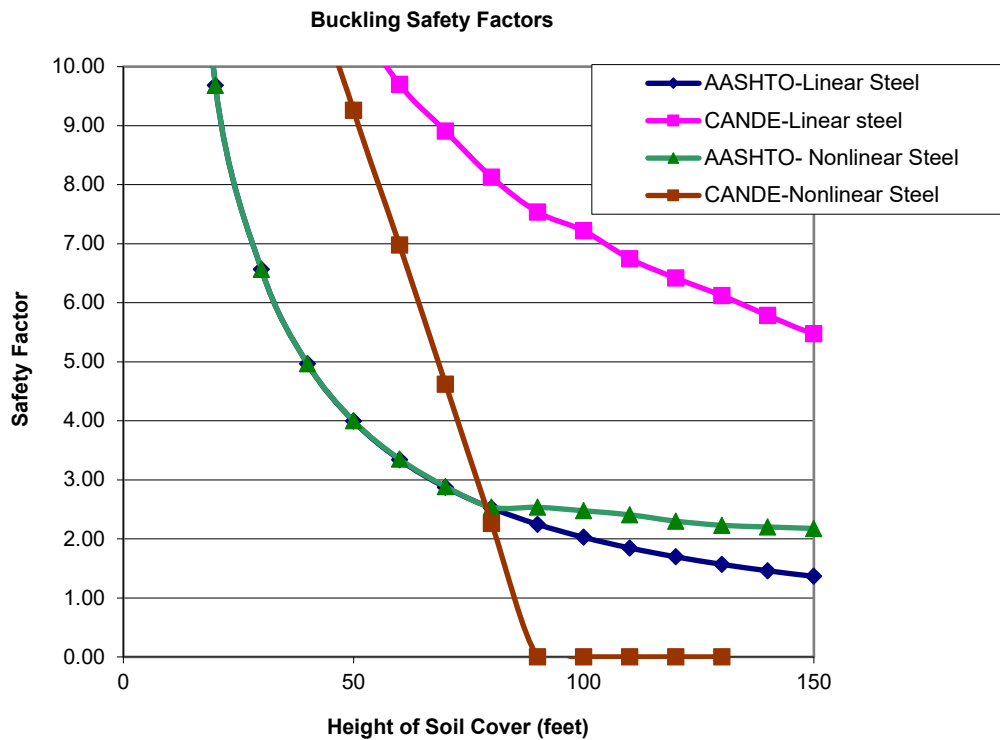
Table 5.6.3-1. Buckling stress predictions for Study # 2

Fill Height (feet)	Predicted Thrust Stress Level for Buckling-like Response (psi)			
	CANDE – (#2) Linear steel	CANDE – (#4) Nonlinear steel	ASSHTO Prediction	Chelapatti-Allgood
10	107174	107174	42,867	54,257
20	105029	105029	42,867	54,257
30	106067	109260	42,867	54,257
40	111191	102047	42,867	54,257
50	116490	98317	42,867	54,257
60	123310	88218	42,867	54,257
70	131538	67710	42,867	54,257
80	136658	37562	42,867	54,257
90	142060	0	42,867	54,257
100	150731	0	42,867	54,257
160	175659	0	42,867	54,257

For the case of linear steel, CANDE’s prediction for buckling capacity increases steadily at each load step because the soil stiffness is increasing without a loss in structural stiffness. However, for the case of nonlinear steel, the CANDE predictions for buckling stress begin to steadily decrease as the steel begins to yield at about 40 feet of fill. When the complete collapse mechanism has formed at 80+ feet of fill, the buckling capacity approaches zero. Recall that CANDE’s prediction of buckling stress is based on the current system stiffness matrix that becomes less and less robust as steel yielding increases with each load step.

The following figure shows the buckling safety factors as a function of fill height. Safety factors are defined as the buckling stress capacity listed in the above table divided by the corresponding thrust stress shown in Figure 5.6.3-2. Note that the loading axis in the figure has been switched to the horizontal in order to illustrate the decrease in safety as fill height increases.

Figure 5.6.3-3. Buckling safety factor versus fill height for corrugated steel pipe (Study #2)



In the above figure we can make the same observations as we did in Study # 1. Namely for the case of linear steel, the AASHTO buckling safety factor is more conservative than CANDE prediction for all stages of fill height. However, when comparison is made for cases including yielding steel, the AASHTO safety factor predictions become less conservative after 80 feet of fill. That is the AASHTO safety factor stays relatively constant due to the nearly constant thrust stress from the nonlinear steel solution.

In contrast to AASHTO, the CANDE safety factor rapidly decreases due to the rapid loss of buckling capacity such that, after 80 feet of fill, CANDE provides a more conservative (and accurate) prediction of buckling safety than does the AASHTO prediction. Again, it is concluded that the AASHTO prediction for global is buckling is not always conservative.

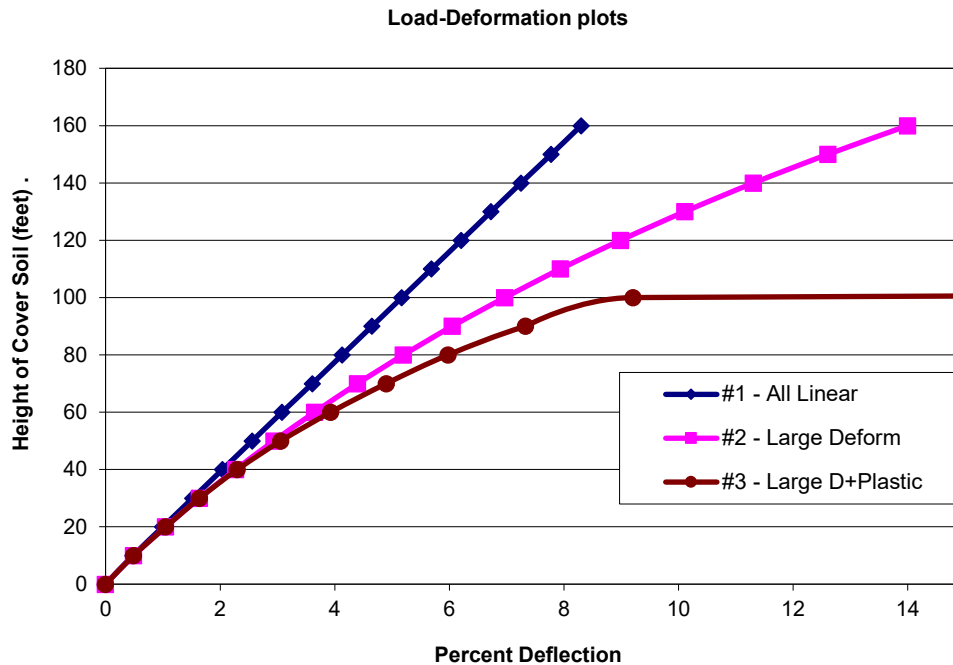
5.6.4 Study # 3 -- Linear soil and frictionless interface

Like the first study, Study # 3 uses a linear soil model, however the soil-structure interface is now assumed to be frictionless. The frictionless interface also infers that the culvert will separate from the soil if tension forces should occur.

Deflection. Figure 8 shows the vertical deflection of the corrugated metal pipe for three modeling cases: (the case of steel yielding with small deformations is no longer of interest)

- (1) linear steel material and small deformation theory
- (2) linear steel material and large deformation theory
- (3) yielding steel material and large deformation theory

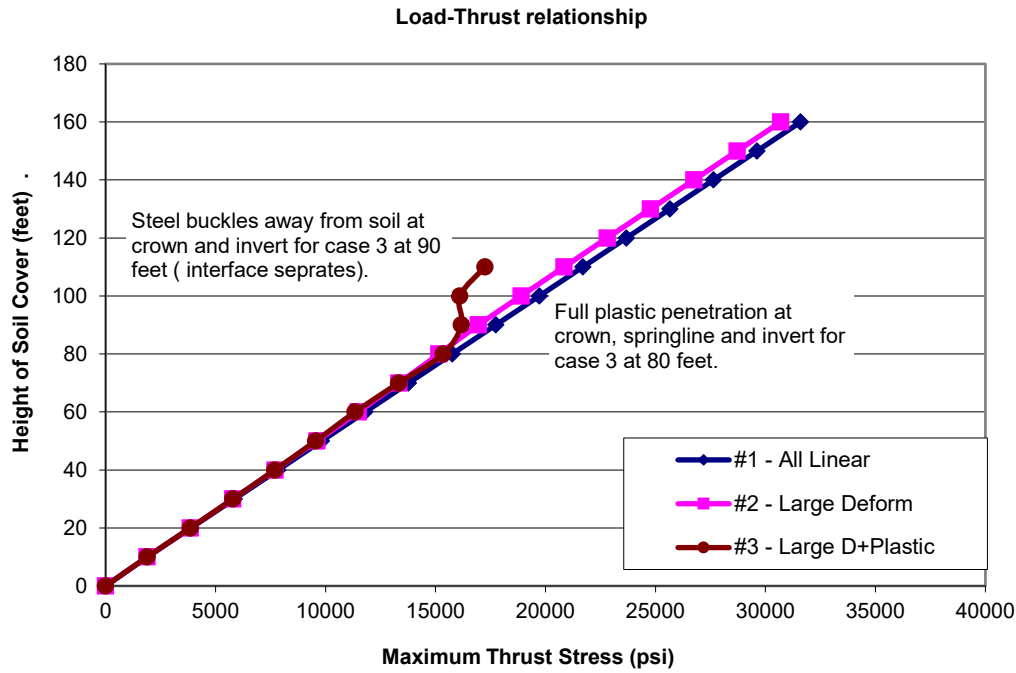
Figure 5.6.4-1 Load-Deflection plots of corrugated steel pipe (Study # 3)



The load-deflection curves for Study 3 are similar to the corresponding curves in Study 1 except that all displacements in the above figure are somewhat larger. In the case of combined large deformations and steel yielding, the deflections become excessive at 100 feet fill. This is because at 90 feet of fill the steel at the crown and the invert begin to buckle inward and separates from the soil due to tension break in the interface model. This causes the large displacement observed at 100 feet of fill in the above figure.

Thrust stress. Figure 5.6.4-2 shows the load-thrust plots for the same three cases. In all cases the maximum thrust stress occurs at the springline. Again, the thrust-load plots are similar to the corresponding plots in Study # 1 except that all thrusts are somewhat lower than the completely bonded case. This result is ascribed to loss of shear traction in the frictionless case. For case # 3, the combination of thrust and moment form a collapse mechanism at about 80 feet of fill so that further increase in thrust stress is retarded

Figure 5.6.4-2. Load-Thrust stress plots of corrugated metal pipe (Study # 3).



Buckling Stress and Safety Factor. The last comparison for Study # 3 is the buckling capacity and associated safety factor. Table 5.6.4-1 lists CANDE’s prediction for the thrust stress level that will produce a singular system matrix for each load increment. The table also contains the simplified AASHTO prediction for ASSHTO buckling stress and the Chelapatti-Allgood prediction.

Table 5.6.4-1 Buckling stress predictions for Study #3

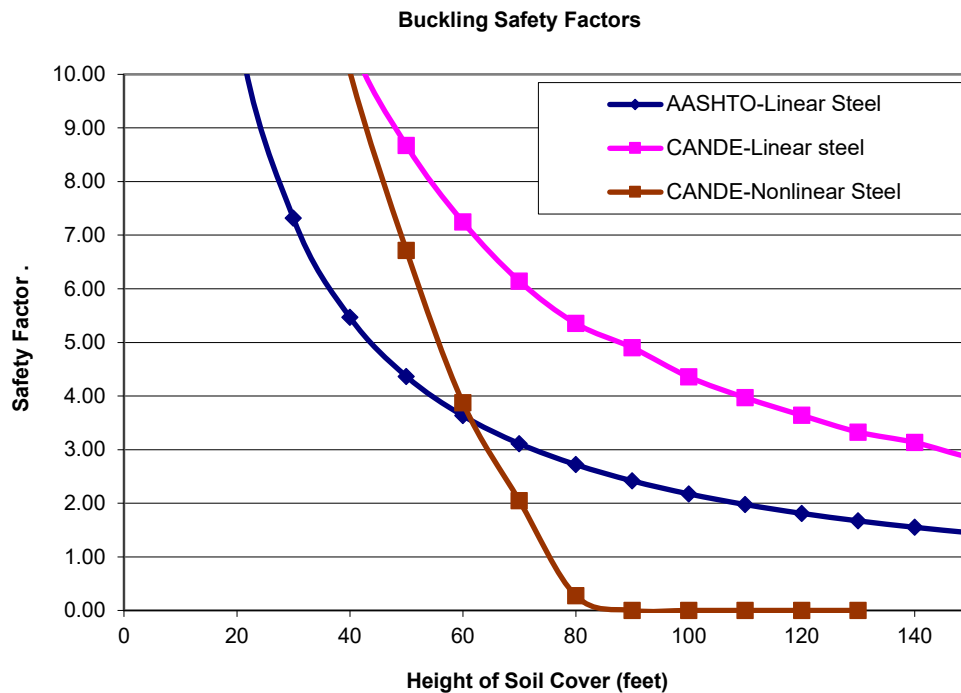
Fill Height (feet)	Predicted Thrust Stress Level for Buckling-like Response (psi)			
	CANDE – (#2) Linear steel	CANDE – (#3) Nonlinear steel	ASSHTO Prediction	Chelapatti-Allgood
10	84219	84219	42,867	54,257
20	84318	84318	42,867	54,257
30	83282	83663	42,867	54,257
40	82244	77324	42,867	54,257
50	83348	64154	42,867	54,257
60	83256	43962	42,867	54,257
70	81915	27274	42,867	54,257
80	81140	4196	42,867	54,257
90	83076	0	42,867	54,257
100	82295	0	42,867	54,257
160	83145	0	42,867	54,257

For the case of linear steel, the predicted buckling stress remains relatively constant at a nominal value of 83,000 psi, which is about 20% less than the corresponding predictions in Study # 1. The 20% reduction is attributed to the observation that the frictionless interface does not generate the same amount of shear stiffness in the soil as does the fully bonded condition. Note that the Chelapati-Allgood model is completely devoid of shear stiffness, which is one reason that their buckling predictions are on the low side.

As observed in the previous studies, the CANDE predictions for buckling stress in the presence of yielding steel begin to steadily decrease as the steel begins to yield between 30 and 40 feet of fill. When the complete collapse mechanism has formed at 80+ feet of fill, the buckling capacity approaches zero.

Figure 5.6.4-3 shows the buckling safety factors as a function of fill height. Safety factors are defined as the buckling stress capacity listed in the above table divided by the corresponding thrust stress shown in Figure 5.6.4-2. Again, it is observed that in the case of yielding steel, the CANDE safety factor rapidly decreases due to the rapid loss of buckling capacity. After 60 feet of fill, CANDE provides a more conservative (and accurate) prediction of buckling safety than does the AASHTO prediction.

Figure 5.6.4-3 Buckling safety factor versus fill height for corrugated metal pipe (Study #3)



5.6.5 Comparing Studies #1, #2 and #3 with design criteria

We conclude this chapter by comparing the maximum allowable fill heights for the three studies based on working-stress design criteria for corrugated steel pipe. Restricting the comparison to the cases of large deformation with steel yielding, which are presumably the most realistic CANDE solutions, the three studies are differentiated as follows:

- Study #1 = linear soil with bonded interface,
- Study #2 = nonlinear soil with bonded interface
- Study #3 = linear soil with frictionless interface

The design criteria and safety factors are given in the table below,

Table 5.6.5-1 Working stress design criteria for corrugated metal pipe

Design Criterion	Safety Factor	Allowable limit
Thrust yielding	2.0	Thrust stress = $\frac{1}{2}$ (yield stress)
Global buckling	2.0	Thrust stress = $\frac{1}{2}$ (buckling prediction)
Plastic penetration	1.5	Amount of wall yielding = $\frac{2}{3}$ of depth
Vertical deflection	1.0	Deflection = 5% of diameter

Using the above allowable limits and referring to the previous plots for the cases of large deformation with steel yielding, the maximum fill height may be determined for each design criterion. The results for each study are recorded in the table below.

Table 5.6.5-2. Allowable fill heights for each design criterion (feet)

Study #	Thrust Yielding	Global Buckling	Plastic Penetration	Vertical Deflection
1	73.0 ft	73.3 ft	55.2 ft	79.5 ft
2	79.4 ft	81.1 ft	49.7 ft	87.7 ft
3	88.9 ft	70.3 ft	53.9 ft	70.9 ft

Plastic penetration is the controlling design criterion for each study, which limits the maximum burial depth on the order of 50 feet. It is interesting to note that all three studies (installation conditions) have both strengths and weaknesses with regard to the design criteria.

As a final comment, the CANDE program performed in a robust manner to obtain converged solutions with several nonlinear models being exercised simultaneously

6 DESIGN CRITERIA AND LRFD DESIGN METHODOLOGY

Introduction. The probabilistic-based design philosophy known as load and resistance factor design (LRFD) has been adopted into the AASHTO LRFD Bridge Design Specifications (Reference 6) wherein the specifications for buried structures are primarily contained in Section 12. One of the tasks in the NCHRP CANDE Upgrade project was to incorporate LRFD methodology for all culvert materials into CANDE-2022 in addition to the traditional working stress design (WSD) methodology.

This chapter provides a succinct interpretation of the AASHTO LRFD specifications for buried structures with regard to defining factored loads and establishing design criteria. Tabularized values are summarized in this chapter for load factors and load modifiers to quantify dead loads, earth loads, and live loads, which are required for a LRFD analysis to produce the factored demands. The contents of this chapter are published in the Transportation Research Record No. 2028, Reference 23.

Also presented are tabularized descriptions of the design criteria and the corresponding factored capacities, which are defined and quantified herein for corrugated metal, reinforced concrete, and plastic pipe materials. In some cases, the design criteria have been generalized to provide mechanistically meaningful statements that are compatible with comprehensive analysis methods like CANDE.

Although this chapter is focused on LRFD design methodology, the fundamental design criteria presented herein are also used for CANDE's WSD methodology. The WSD approach uses service loads and unfactored capacities to compute safety factors defined as capacity divided by service-load demand. The LRFD approach uses factored loads and factored capacities to compute ratios of factored demand divided by factored capacity for strength related design criteria, and service-load demand divided by performance limits for service-related design criteria.

The objectives of this chapter are as follows:

- Summarize the loading definitions and load factors for LRFD methodology that are applicable to the comprehensive solution approach embodied in the CANDE-2022 program.
- Provide a clear and concise set of design criteria for buried structures for corrugated metal, reinforced concrete and plastic pipe that are mechanistically consistent with AASHTO LRFD specifications, but are not dependent on simplified design equations.
- Identify areas where improvements in the current AASHTO specifications are desirable and offer suggestions for a more generalized statement of the design criteria.

LRFD methodology for buried structures includes both service limit states and strength limit states. One consequence of the two limit states when using a comprehensive solution method is that two separate solutions may need to be obtained, one with service loading and one with factored loading. The definitions of service loading and factored loading are provided in the following discussion along with tables summarizing the specified load factors. To augment this discussion, guidance is provided on applying these factored loads in the context of a comprehensive finite element solution methodology.

6.1 Service Loads for Performance Criteria

A common example of performance criteria under service loading is the allowable deflection of flexible culverts. In the case of rigid culverts, a common example is the allowable concrete crack width. Later, the exact form of these and other design criteria will be discussed and quantified. For present purposes it is only necessary to understand that a solution at the service load level is required in order to evaluate the service limit design criteria. For a culvert system to successfully pass the service load design criteria, the predicted response such as the percent deflection must be less than or equal to the allowable limit.

The service load level is the actual design load experienced by the culvert system as if one were performing a working stress analysis. Service loads include the following conditions:

1. Dead load of structure
2. Earth load on the soil
3. Live load pressure on the structure transmitted through soil
4. Live load multiplier due to vehicle impact
5. Live load multiplier due to multiple lane presence
6. Other design load considerations such as hydrostatic or thermal loading

In terms of finite element modeling, the structure dead load (body weight of the culvert) is typically applied in the first load step after consideration of in situ soils, followed by a sequence of load steps composed of soil element layers, which are placed around and above the culvert up to the design cover height. Each soil layer is loaded with its own body weight according to the soil density associated with the region. Live loads are typically applied in the last load step(s) on the soil surface as a pressure boundary condition, representing the tire footprint pressures from the design-truck. AASHTO specifications also require that service-load tire pressures be increased by multipliers to account for dynamic impact and the effects of multiple lane presence, which are prescribed as follows:

- $\text{Impact multiplier} = 1 + 0.33(1.0 - H/8.0) \geq 1.0$ Equation 6-1
where, H is height of soil cover above the crown in feet.

- $\text{Multiple-lane-presence multiplier} = 1.2$ Equation 6-2

The multiple lane presence factor is 1.2 for a single loaded lane and considers that a single truck has a high likelihood of being overloaded. While LRFD allows reduced values of the multiple presence factor when more than one lane is loaded, calculations for culverts under live load show that the single loaded lane condition virtually always controls the design.

As a side comment, it is noted that the prescription of the basic live load tire pressure presents a special problem for two-dimensional, plane strain finite element programs because the tire foot print area extends to infinity in the out-of-plane direction, thereby overestimating the actual loading on the culvert as compared to the actual footprint width of finite dimensions. One way to correct for this problem is to reduce the surface pressure using the procedure described in Reference 12 and Reference 13. Other methods are currently being invested under NCHRP Project 15-29.

6.2 LRFD Loads for Strength-limit States

For strength limit states such as the yield strength, ultimate strain, or global buckling capacity of the soil-structure system, the LRFD methodology assigns net multiplying factors to the service loads. The resulting structural responses, which are at higher levels of stress than the service load responses, are called the factored demands. Concurrently, resistance factors, whose values are typically 1.0 or less, are multiplied by the strength values and the resulting products are called factored capacities. The test of a successful culvert design using the LRFD methodology is that the factored capacities are greater or equal to the corresponding factored demands for all the strength-state design criteria. In a simplistic sense, the ratio of the effective load factor to the resistance factor is comparable to the safety factor concept used in working stress design methodology. However, it is generally accepted that LRFD methodology offers a more logical design assessment than WSD methodology.

The net multiplying factor applied to service loads is product of two terms called the load factor and the net load modifier. Stated explicitly, the net factored load at any load step may be written as:

- Factored load = $\gamma \eta$ (Service load)
where, γ is the specified load factor, and η is the net load multiplier.

6.2.1 Load Factors.

The load factor term, symbolically denoted as γ , is currently specified in AASHTO LRFD specifications as shown in the table below. A general observation that should fit well with reader's intuition is that γ_{\max} (on average) increases in value from the dead load case to the earth load case to the live load case. This increase in load factor value roughly corresponds with our lack-of-confidence in knowing the actual load value in these three cases.

TABLE 6.2.1-1 Load factors and load modifiers for buried structures

Culvert Type	Dead Load Culvert (DC)			Earth fill Loading (EB)			Live Load (LL)	
	γ_{\max}	γ_{\min}	η_{DC}	γ_{\max}	γ_{\min}	η_{EB}	γ_{\max}	η_{LL}
Reinforced Concrete pipe	1.25	0.9	1.05	1.3	0.9	1.05	1.75	1.00
Reinforced Concrete box	1.25	0.9	1.05	1.3	0.9	1.05	1.75	1.00
Reinforced Concrete arch	1.25	0.9	1.05	1.3	0.9	1.05	1.75	1.00
Corrugated metal pipe or arch	1.25	0.9	1.05	1.95	0.9	1.05	1.75	1.00
Corrugated metal box	1.25	0.9	1.05	1.50	0.9	1.05	1.75	1.00
Plastic pipe (HDPE or PVC)	1.25	0.9	1.05	1.95	0.9	1.05	1.75	1.00

Symbols:

γ_{\max} = maximum load factor dependent on load case and culvert type.

γ_{\min} = minimum load factor dependent on load case and culvert type.

η_{DC} = net load modifier for DC load case = {(ductility)(redundancy)(importance)}

η_{EB} = net load modifier for EB load case = {(ductility)(redundancy)(importance)}

η_{LL} = net load modifier for LL load case = {(ductility)(redundancy)(importance)}

Two observations about the load factors in Table 1 that require further explanation are; (1) there are two values, γ_{\max} and γ_{\min} , listed for each load case, and (2) the load factors are dependent on the type of culvert material and shape.

With regard to the first observation, the maximum load factor, γ_{\max} , is generally the value used in an analysis to produce the worst-case structural response. However, during the sequence of load steps in a comprehensive solution method, it is conceivable that for some load steps the consistent application of γ_{\max} may not produce a worst-case scenario for a given design criteria. For example, if the earth-fill layers of soil are heavily compacted along the sides of the culvert so that lateral pressure causes an inward movement, the resulting change in moments in the culvert may become less than the

initial moment caused by the dead load of culvert in step 1, and also counter to the sign of the moments that will be added into the culvert when subsequent earth-fill layers are placed on top of the culvert. Thus, in the spirit of seeking the worst-case LRFD loading scenario, it may be reasonable to use γ_{\min} for those load steps wherein earth-load layers are placed along the sides of the culvert.

The second observation, i.e., the load factor values are dependent on culvert type and shape, does not have a rational explanation except to say the AASHTO specifications represent work-in-progress. It is certainly reasonable to assign different resistance factors to different structural materials; however, it is difficult to argue why the load factors, such as those for vertical earth load, should be different. Perhaps at some time in the future, the load factors will be uniform for all buried structures. However, until that time comes, Table 1 serves as the reference for load factors.

6.2.2 Load Modifiers.

The so-called net load modifier, symbolically denoted as η , is a product of three sub-factors related to ductility, redundancy and operational importance that are described in AASHTO LRFD Specifications 1.3.2.1. For buried structures it is customary to assign the sub-factors associated with ductility and operational importance to be 1.0. However, for the redundancy sub-factor the LRFD specification suggests that value should be 1.05 for buried structures under dead loads and earth loads, but not live loads.

Based on the above discussion, the values in Table 6.4.1-1 for η_{DC} and η_{EB} are recommended to be 1.05 when the maximum load factor γ_{\max} is being used. On the other hand, if the minimum load factor γ_{\min} is assigned to a particular load step, then the corresponding load modifier is the inverse value, e.g., load modifier = $1/1.05 = 0.95$.

The load modifier for operational importance is a function of the specific structure being designed, thus, while often set to 1.0, other values may be appropriate.

The above loading conditions are not a recipe for all culvert problems because worst loading scenario depends on the structure type, installation, and the governing limit state. However, the beauty of comprehensive solution procedures like CANDE is that it is easy to re-run the same problem with different load factors to find the worst loading condition.

6.2.3 LRFD load factors and nonlinear soil models.

A long-standing issue with regard to LRFD analysis is whether or not nonlinear soil models should be driven by stresses and strains from factored loading or from service loading. Although there is no question that factored loads are required to produce the factored demands to evaluate the LRFD design criteria against the factored capacities, some engineers argue that the factored soil stresses and strains cause the nonlinear soil models to become overly stiff due to the increased confining pressure from factored loads, especially for the case of deep burial wherein nonlinear soil models like the Duncan/Selig hyperbolic soil models generally result in substantially increased soil stiffness due to “artificially” increased confining stress from the earth load factor. Others argue that the LRFD philosophy implies that factored loads have some “real” probability of occurring so that the increased soil stiffness is the proper analysis approach. Of course, this dilemma only applies to nonlinear soil models because linear soil models are insensitive to the level of stress.

Rather than adopting only one method or the other in the CANDE-2022 program, the Duncan/Selig soil model is programmed to operate by either method at the user’s option. Specifically, the input variable called NON in the Duncan/Selig input instructions allows the user to choose whether "service stresses" (NON = 0) or "factored stresses" (NON = 1) are used to compute the Duncan/Selig stiffness values for Young’s modulus and Bulk modulus. Thus, even though factored loads are input into CANDE and the solution output are actual factored structural responses, for the case NON = 0, the stiffness calculations performed within the Duncan/Selig subroutine are based on service stresses at each load step. This is achieved by dividing the factored stress and strain increments by the corresponding load factor for that load step and maintaining a running total of the service stresses and strains to drive the nonlinear soil model.

6.3 Design Criteria for Culvert Materials

In the following paragraphs, the AASHTO LRFD design criteria are regrouped into three material types called corrugated metal, reinforced concrete, and plastic pipe. The design criteria are summarized in tables followed by a discussion of each design criterion. The tables list the resistance factors, factored capacities and the corresponding reference to AASHTO LRFD Specification. We believe the tabularized design criteria accurately reflect the intentions of the AASHTO specifications; however, in some cases, denoted with an asterisk, we have generalized the criterion to be mechanistically compatible with comprehensive solution methods like CANDE-2022.

6.3.1 Corrugated metal

Corrugated steel and corrugated aluminum have the same general AASHTO design criteria, differing only by the numerical value of design criterion limits such as the yield stress. The table below is applicable to both types of corrugated metal. The criterion for plastic penetration is a generalization of the AASHTO specifications and is discussed below.

Table 6.3.1-1 Corrugated Metal LRFD Design Criteria.

Design Criterion (Strength limits)	Resistance Factor	Factored Capacity	Definition and AASHTO Reference
(1) Thrust stress (psi)	$\phi_1 = 1.0$	$\phi_1 F1$	F1 = metal yield strength (Equation 12.7.2.3-1.)
(2) Global Buckling (psi)	$\phi_2 = 1.0$	$\phi_2 F2$	F2 = buckling thrust stress (Equations 12.7.2.4-1-2)
(3) Seam strength (psi)	$\phi_3 = 0.67, 1.0$	$\phi_3 F3$	F3 = seam strength (Section 12.7.2.5)
(4) Plastic Penetration *(%)	$\phi_4 = 0.90$	$\phi_4 F4$	F4 = fully plastic (100%) (Replaces 12.9.4.3.1)
Performance Limits (Service Load)			
(5) Allowable deflection *(%)	--	P5	P5 = 5%, (2% LS)

1. The thrust stress limit value, F1, is typically 33,000 psi for steel and 24,000 psi for aluminum. The thrust stress criterion is based on AASHTO LRFD equation 12.7.2.3-1.
2. The thrust stress level that causes global buckling, F2, may be conservatively approximated from the simplified AASHTO LRFD equations 12.7.2.4-1-2. A more accurate alternative is to utilize the new large deformation formulation with buckling capacity prediction available in CANDE-2022
3. If seams are not present, the factored seam strength value $\phi_3 F3$ may be set equal to F1. If longitudinal seams are present, F3 should represent the measured seam capacity and $\phi_3 = 0.67$
4. Failure from full plastic penetration occurs when the cross section becomes fully plastic due to plastic hinging, which occurs when the internal moment approaches the plastic moment capacity ($F4 = 100\%$). The recommended LRFD resistance factors are 0.90 for steel and 0.85 for aluminum, respectively. This criterion is a generalization of the original AASHTO LRFD equation 12.9.4.3.1 for structural plate box culverts.

AASHTO specifications are silent on limiting moments or plastic hinging for corrugated metal structures other than structural plate box structures. As implied in the above table, the plastic penetration design criterion is offered for consideration for all corrugated metal structures including pipes, arches and long spans.

5. The service load limit for allowable deflection, P5, is generally taken as 5% for all corrugated metal structures except long spans, which are usually limited to 2% of the vertical rise. Although AASHTO Bridge Specification does not currently specify deflection limits, experience has shown that deflections greater than 5% indicate that the backfill type and/or compaction are below standard

6.3.2 Reinforced concrete

The AASHTO design criteria for reinforced concrete are the most challenging criteria to generalize because the criteria are masked in simplified solution methods and are differentiated for various culvert shapes. In Table 6.3.2-1 and the ensuing discussion, it is believed that the proposed design criteria faithfully represent the intent and, in some cases, improve the clarity of the criteria as presented in the AASHTO LRFD specifications.

Table 6.3.2-1 Reinforced Concrete LRFD Design Criteria

Design Criterion (Strength limits)	Resistance Factor	Factored Capacity	Definition and AASHTO Reference
(1) Steel yielding (psi)	$\phi_1 = 0.90$	$\phi_1 F_1$	F1 = reinforcement strength (Alternative to 12.10.4.2.4a-1)
(2) Concrete crushing* (psi)	$\phi_2 = 0.75$	$\phi_2 F_2$	F2 = concrete strength (New proposed criterion)
(3) Shear failure (lb/in)	$\phi_3 = 0.90$	$\phi_3 F_3$	F3 = concrete shear strength (Multiple AASHTO equations)
(4) Radial tension failure (psi)	$\phi_4 = 0.90$	$\phi_4 F_4$	F4 = radial tension strength (Adapted from 12.10.4.2.4c-1)
Performance Limits (Service Load)			
(5) Allowable crack width* (in)	--	P5	P5 = 0.01 inch (Recommendation)

- The steel yielding stress limit value, F1, is nominally 60,000 psi for deformed bars and 65,000 psi for smooth wire fabric. This criterion is a generalization of AASHTO LRFD Equation 12.10.4.2.4a-1 and more fundamental than the AASHTO equation for steel area. Note that the AASHTO equation specifies the required steel area for the steel-yielding criterion based on a simplified solution method.
- The outer-fiber concrete crushing stress limit value, F2, is the ultimate compressive strength f_c' . A concrete compression criterion is explicitly stated in the AASHTO LRFD specifications because it is assumed that reinforcing steel is designed to yield prior to the load level causing the concrete to begin crushing. Here it is proposed that concrete crushing should be retained as a direct design criterion and the specified resistance factor for concrete crushing be less than specified the resistance factor for steel yielding, with values of 0.75 and 0.90, respectively.
- The shear capacity, F3, is the shear force causing diagonal tension failure at a given cross-section. If the shear demand exceeds the shear capacity, then transverse reinforcement (stirrups) is required. The value of F3 is specified differently by AASHTO depending on structural shape and burial depth.
 - For concrete pipes and arches, the shear strength is specified by Equations 12.10.4.2.5, which yield a variable value for F3 dependent on the values for moment, thrust and shear around the culvert wall.
 - For boxes and 3-sided structures with 2 or more feet of soil cover, the shear strength is specified by Equations 5.14.5.3-1 wherein the value for F3 is dependent on moment and shear (not thrust).
 - For boxes and 3-sided structures with less than 2 feet of soil cover, the shear strength is specified by equations in Section 5.8.3.3 that, in some cases, depend on the nature of the transverse reinforcement (stirrups).

Clearly there is a need for unifying the AASHTO LRFD specifications for the shear strength capacity because rational mechanics suggests that shear strength capacity should be a function of the cross-section properties and state of loading, not on the culvert shape or depth of burial. Hopefully this remark may stimulate a future research study to develop a more fundamental criterion, which is the root cause of diagonal cracking. However, until that time, we propose that AASHTO Equation 12.10.4.2.5 is the best predictor of shear strength capacity for culverts because of the large experimental data base upon which it was developed (Reference 14).

4. The radial tension failure stress, F_4 , is related to the tension strength of concrete and the structure span. The criterion is adapted from AASHTO LRFD equation 12.10.4.2.4c-1. It is restated here in psi units as:

- $F_4 = 37.92(f_c'/1000)^{1/2} F_{rt}$

where F_{rt} is a scale factor dependent on structure span, which is specified in the paragraphs following Equation 12.10.4.2.4c-1.

The corresponding factored demand is the average radial tensile stress that the curved inner cage exerts on the inside concrete cover thickness. This is automatically determined in CANDE-2022 by dividing the interior cage steel force (maximum tensile force per unit length) by the radius of curvature of the steel cage.

5. The allowable crack width at service loading is generally taken as 0.01 inches in accordance with AASHTO LRFD specification 12.10.3. An empirical formula to predict crack width, developed by Heger and McGrath (Reference 15), has been adopted by AASHTO in the form of Equation 12.10.4.2.4d-1. For purposes of this paper, the authors reworked the equation in a more fundamental form, which linearly relates crack width to the tension stress in the reinforcing steel once it exceeds the surrounding concrete tensile strength. The revised equation is:

- $CW = (t_{bs1}/2n)^{1/3} \{f_s - 0.0316C_1(h/d)^2 \sqrt{f_c'} / \rho\} / 3000$

where, CW is crack width in inches, ≥ 0

f_s is tension steel stress in ksi units

f_c' is concrete strength in ksi units

All other symbols are section properties defined in Section 12.10.4.2.4d

CANDE-2022 predicts the crack width at each point around the culvert by feeding the computed tension steel stress f_s into Equation 5.6 thereby producing a semi-empirical prediction. This procedure has been well calibrated for crack widths of approximately 0.01 in. and becomes increasingly uncertain as the crack width varies from this value. As an alternative, CANDE provides the option to use the older Gergely-Lutz formula instead of Equation 6-5.

6.3.3 Plastic pipe

The design criteria for plastic pipe, summarized in Table 6.3.3-1, are straightforward interpretations of the AASHTO LRFD specifications. Said another way, the AASHTO fundamental design criteria are easily understood and not confounded with the simplified methods that are offered to predict the factored demands. The main difficulty in applying the plastic pipe design criteria is deciding whether to use the long-term or short-term material properties. Typically, an engineer would select short-term material properties if live loads were the major concern. On the other hand, for deep burial situations long-term properties are appropriate. In some cases, it may be prudent to solve the problem twice, once with short-term properties and once with long-term properties. This is a relatively easy task with CANDE-2022.

Table 6.3.3-1 Plastic Pipe LRFD Design Criteria.

Design Criterion (Strength limits)	Resistance Factor	Factored Capacity	Definitions and AASHTO Reference
(1) Thrust failure (psi)	$\phi_1 = 1.0$	$\phi_1 F_1$	F_1 = plastic yield strength (Equation 12.12.3.5.1)
(2) Global buckling (psi)	$\phi_2 = 1.0$	$\phi_2 F_2$	F_2 = thrust stress for buckling (Equation 12.12.3.5.2-1)
(3) Combined strain (in/in)	$\phi_3 = 1.0$	$\phi_3 F_3$	F_3 = fiber strain limit (Equation 12.12.3.5.4a-1)
Performance Limits (Service Load)			
(4) Allowable displacement (%)	--	P4	P4 = 5% (Recommendation)
(5) Allowable tensile strain (in/in)	--	P5	P5 = 0.05 (for HDPE) (Table 12.12.3.3-1)

1. The thrust stress limit or ultimate strength, F_1 , is dependent on the type plastic and the load duration. Types of plastic identified by AASHTO include high-density polyethylene (HDPE) and polyvinyl chloride (PVC) with characteristic material properties for short-term or long-term loading. Nominal values, taken from the AASHTO LRFD specifications and elsewhere, are shown in Table 6.3.3-2. Thrust load capacity is also influenced by profile geometry, which can reduce section capacity due to susceptibility to local buckling as discussed below.

Table 6.3.3-2 Recommended plastic properties for short and long-term loading

Type of plastic	Effective Young's Modulus (PE)		Ultimate strength (PU)	
	Short-term (ksi)	Long-term (ksi)	Short-term (ksi)	Long-term (ksi)
HDPE –	110.0	22.0	3.00	0.90
PVC –	400.0	140.0	6.00	2.60
PP –	135.0	27.0	3.10	1.00

- The thrust stress level that causes local global buckling, F_2 , may be conservatively approximated from the simplified AASHTO LRFD equations 12.7.2.4-1-2. A more accurate alternative is to utilize the new large deformation formulation with buckling capacity prediction available in CANDE-2022.
- The combined strain limit value (combined thrust and bending), F_3 , is specified by AASHTO LRFD Equation 12.12.3.5.4a-1 and is equal to 1.5 times the long-term strength divided by the long-term modulus. Accordingly, HDPE ~ 0.06 in/in, PVC ~ 0.028 in/in. and PP ~ 0.045 in/in.
- The service load value for allowable deflection, P4, is generally taken as 5% of the diameter for all plastic pipes; however, the deflection limit is not directly specified in the AASHTO LRFD Design Specifications.
- The service load value for maximum allowable tensile strain, P5, is specified in AASHTO LRFD table 12.12.3.3-1 and is 0.05 in/in for HDPE and 0.035 or 0.05 in/in for PVC depending on cell class.

Local Buckling. Local buckling is not a direct design criterion for plastic pipe, but it does influence the demands and capacities of the design criteria listed above. Local buckling is a nonlinear phenomenon caused by compressive forces that induce the sub elements of profile wall pipe to deform out-of-plane in a wrinkled pattern. Similar to corrugated metal pipe wherein some amount of outer fiber yielding is permitted, some amount of local buckling is

permitted in plastic profile pipe. Chapter 2 provides a description of the CANDE’s nonlinear model to account for local buckling based on Section 12.12.3.5.3 of AASHTO LRFD specifications. The procedure simulates the effect of local buckling by reducing the effective area of the sub elements dependent upon the average level of compressive strain in each sub element. Thus, local buckling increases the demand and/or decreases the capacity of design criteria listed above.

6.4 Illustration of LRFD Factors and Evaluation with CANDE

This example is for a concrete arch with straight legs installed in a trench-like installation with backfill soil placed in eight layers to a final cover height of 2 feet above the crown. A live load is placed over the arch centerline on the ninth and last load increment. To evaluate this problem under LRFD design methodology, CANDE’s Level-2 arch mesh option is used to automatically construct a symmetric finite element mesh with nine construction increments with the load factors taken from Table 6.2.1-1 and computed as described in the following paragraphs.

6.4.1 Construction increment number 1.

As shown in Figure 6.4.1-1, the first construction increment includes the surrounding in situ soil (red), concrete footing (yellow), and reinforced concrete arch culvert (black). The in-situ soil and the footing are assigned appropriate stiffness values, but with zero body weight. That is, since the in-situ soil and footing are in place before the arch is constructed, the arch is only loaded with its own self-weight. Thus, the arch is assigned a body weight of 150 pcf, representing body weight of concrete. LRFD analysis requires the user to define the load factor for each construction increment. In this case, the first load step represents dead load ($\gamma = 1.25$ and $\eta = 1.05$) so that the net load factor = $1.25 * 1.05 = 1.31$.

6.4.2 Construction increment numbers 2 through 8

Figure 6.4.2-1 shows construction increments 2 through 8, which are all associated with earth loading. The 2nd increment is shown as two rows of orange elements, the 3rd increment is shown in yellow, the 4th in green and so on up to the final cover height. Each of these layers of soil is assigned the actual body weight (120 pcf) of the fill soil. Also, each increment is assigned the same load factor based on earth loading, computed as $(\gamma = 1.30$ and $\eta = 1.05) = 1.37$. CANDE applies the load factor to the earth loads in steps 2 through 8 so that the accumulated solution is the factored demand at the end of each step.

Figure 6.4.1-1 Concrete arch installation for first construction increment (net load factor =1.31)

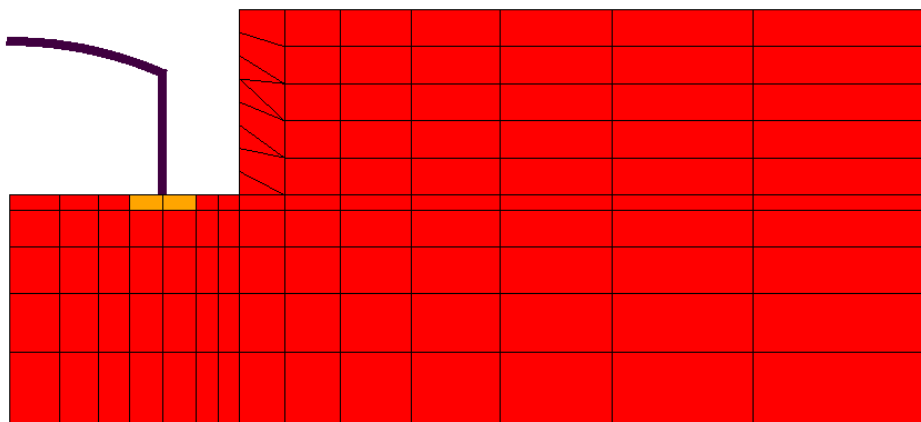
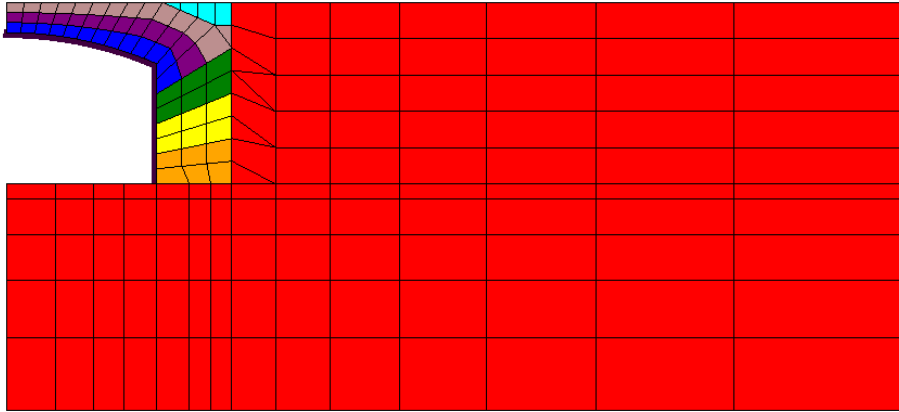


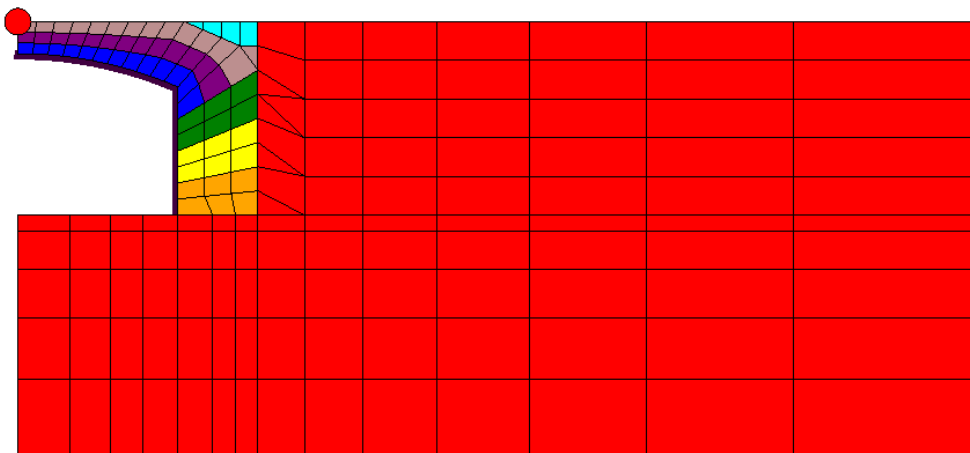
Figure 6.4.2-1 Concrete arch installation for construction increments 2-8 (net load factor =1.31)



6.4.3 Construction increment number 9 (live load).

The last construction increment represents a live load as illustrated by the red circle in the figure below. The load is applied in the 9th step without additional soil loading as a downward force (boundary condition) representing the actual service load of a design truck, but reduced for plane-strain considerations. In this case the net load factor is computed as ($\gamma = 1.75$ and $\eta = 1.05$) = 1.84. CANDE applies this load factor to the service load as prescribed in the boundary condition. Thus, CANDE's final accumulated solution at the end of load step 9 is the total factored demand.

Figure 6.4.3-1 Concrete arch installation for ninth construction increment (net load factor =1.84)



6.4.4 Final evaluation of LRFD design criteria

The final evaluation of the reinforced concrete arch is shown Figure 6.4.4-1 in terms of the design criteria for reinforced concrete. CANDE prints out this evaluation at each load step but our interest is focused on the last load step because it represents the worst case. Here we observe that the concrete arch is safe for the proscribed loading conditions because all demand-to-capacity ratios are less than 1.0. In this example, the steel yielding design criterion is called the controlling design criterion because it has the highest ratio. The controlling node number in the evaluation summary identifies the location in the concrete arch where each design criterion has the maximum demand-to-capacity ratio. Although not shown here, the evaluation summary also includes a performance assessment including the predicted crack width under service load conditions.

Figure 6.4.4-1 LRFD evaluation summary for concrete arch after load step 9 (copy from CANDE)

LRFD SUMMARY EVALUATION FOR GROUP 1, LOAD STEP 9				
DESIGN-CRITERION	CONTROL NODE	FACTORED DEMAND	FACTORED CAPACITY	RATIO VALUE
STEEL YIELDING (psi)	1	46450.1	54000.0	0.860
CONCRETE CRUSHING (psi)	12	1934.2	3000.0	0.645
SHEAR FAILURE (lbs/in)	11	460.5	782.7	0.588
RADIAL-TENSION FAIL (psi)	1	7.8	54.6	0.142

(Print out from CANDE)

7 BANDWIDTH MINIMIZATION

A bandwidth minimizer is installed in CANDE-2022 that reduces the maximum bandwidth of the system of equations characterizing the finite element mesh topology. Bandwidth minimization is achieved by strategically renumbering the node numbers that were originally input by the user. Node renumbering is accomplished heuristically by swapping node numbers, a pair at a time, starting with the node number with the highest bandwidth and exchanging it with another node number that optimally reduces the maximum bandwidth at the first location while not generating a bandwidth at the second location that is greater or equal to the original maximum bandwidth.

7.1 Background and Objectives

Background. For any given finite element problem solved by CANDE, the number of rows in the global stiffness matrix is dictated by the number of nodal unknowns, which defines the number of equations. In contrast, the number of rows in the global stiffness matrix is dependent on the maximum bandwidth, which depends on the nodal numbering pattern, not the number of equations. By judiciously numbering the nodal pattern, the maximum bandwidth can be reduced. The motivations for reducing the maximum bandwidth are, (1) to reduce storage space for the global stiffness matrix whose size is equal to the number of equations times the maximum bandwidth, and (2) to reduce the time required to solve the system of equations, which is proportional to the number of equations times the square of the bandwidth.

For Level 2 operations, which use “canned” finite element meshes, a bandwidth minimizer is not necessary because the nodal numbering pattern has been optimized once and for all time. On the other hand, for Level 3 operations, which implies a user-defined mesh topology, a bandwidth minimizer can be useful. Although experienced users usually construct nodal numbering patterns that are reasonably close to an optimum pattern, there are situations in which the nodal numbering pattern may differ substantially from optimum. For example, when a pre-existing finite element mesh is altered to include more elements and nodes in a local area, the added nodes are likely to have node numbers that are numerically much larger than the existing nodes in this neighborhood, thereby resulting in an excessively large bandwidth.

The bandwidth minimization problem may be formally stated as follows. Given a sparse, $n \times n$, matrix A with components a_{ij} , find a permutation of rows and columns (node renumbering pattern) such that all the non-zero components of matrix A reside in a band that is close as possible to the main diagonal. Or expressed mathematically, Minimize $\{ |i-j| \text{ for } i, j = 1 \text{ to } n: a_{ij} \neq 0 \}$.

Beginning in the 1950s, the bandwidth minimization problem received a lot of attention from mathematicians due to the emergence of the computer for solving large systems of equations representing a wide range of applications. The classical Cuthill-McKee algorithm, published in 1969, employs the breadth-first search method to construct a level structure in the context of graph theory. A similar but more efficient algorithm, known as Gibbs-Poole-Stockmeyer, was published in 1976, and remains very popular.

Although the above and many other general-purpose bandwidth minimization algorithms are available in the literature, the following development is unique and takes advantage of the finite element assembly methodology to systematically reduce the bandwidth. To the best of the author’s knowledge the bandwidth minimization algorithm presented herein is novel.

Objectives. Within the context of the CANDE finite element program and mesh topology, the objectives are;

1. Develop a robust algorithm to convert an arbitrary node-numbering input pattern into a new node-numbering pattern that minimizes the maximum bandwidth.
2. Display all printed and graphical output from the CANDE solutions in terms of the original node-numbering pattern so that the user does not need to learn the new node number scheme, i.e., transparent to user.

Like other finite element programs, CANDE's finite element methodology has three properties that are extremely useful for the bandwidth minimization algorithm:

- First, the global system matrix is symmetric so that bandwidth minimization is restricted to one side of the matrix diagonal.
- Second, each node number represents a group of nodal unknowns (e.g., x-displacement, y-displacement, and rotation) each with the same bandwidth. Thus, bandwidth minimization is reduced to reordering the node-number pattern as opposed to the entire set of equations.
- Third, all the information required to minimize the bandwidth is contained in the so-called element connectivity matrix, which simply identifies the node numbers associated with each element.

The above advantages are exploited in the following development.

7.2 Bandwidth Minimization Methodology in CANDE

7.2.1 Element connectivity matrix

The element connectivity matrix contains the node numbers that are attached to each element and is symbolically denoted and dimensioned as $NOD(NET, NDX)$, where NET is the total number of elements and NDX is the maximum number of nodal locations as required by the various element types. In the CANDE program, for example, $NDX = 4$ to accommodate the 4-noded quadrilateral elements, which has more nodes than the other types of elements as shown in the table below.

Element Type (connected nodes)	NOD(NE,1)	NOD(NE,2)	NOD(NE,3)	NOD(NE,4)
Beam-column (nodes=2)	Node-1	Node-2	0	0
Triangle (nodes=3)	Node-1	Node-2	Node-3	0
Interface & Link (nodes=3)	Node-1	Node-2	Node-3	0
Quadrilateral (nodes=4)	Node-1	Node-2	Node-3	Node-4

Letting NE be a counter from 1 to NET , then the components of element connectivity matrix are identified as:

- $NOD(NE,1)$ = node number assigned to location 1 of element NE
- $NOD(NE,2)$ = node number assigned to location 2 of element NE
- $NOD(NE,3)$ = node number assigned to location 3 of element NE (depending on element type)
- $NOD(NE,4)$ = node number assigned to location 4 of element NE (depending on element type)

If, for example, element number 10 is a beam element with the two end-nodes numbered 33 and 43, then $NOD(10,1) = 33$ and $NOD(10,2) = 43$. The remainder of the nodal list for element 10 is equal to 0.

7.2.2 Algorithm Cycle.

With the above information as a starting point, bandwidth minimization is accomplished by swapping node numbers, a pair at a time, starting with a node number that has the highest bandwidth and exchanging it with another node number that optimally reduces the maximum bandwidth at the first node location while not generating a bandwidth at the second location that is greater or equal to the original maximum bandwidth.

The process is presented in the following four steps. These steps are repeated iteratively until no additional node pairs can be found to further reduce the bandwidth.

Step 1. Use the current NOD connectivity matrix to create a new matrix denoted and dimensioned as $MT(NDT,3)$ where NDT is the total number of nodes in the mesh. Letting N represent each node number in turn, the three components of the MT matrix are defined as follows:

- $MT(N,1)$ = Maximum node number among all nodes that are attached to any element that is also attached to node N . $MT(N,1)$ is referred to as $NDMAX$.
- $MT(N,2)$ = Minimum node number among all nodes that are attached to any element that is also attached to node N . $MT(N,2)$ is referred to as $NDMIN$.
- $MT(N,3)$ = Maximum of $\{ILEFT \text{ or } IRITE\}$, where $ILEFT = N - NDMIN$, which is the bandwidth to the left of node N , and $IRITE = NDMAX - N$, which is the bandwidth to the right of node N . $MT(N,3)$ is referred to as $MAXB$, which is the largest bandwidth associated with node N .

The computational key to establishing the MT matrix is to start with an outer do-loop for each node number (referred to as the pivot node). Insert an imbedded do-loop for the element numbering and use the NOD connectivity array. If any of the element's connectivity nodes match the pivot node, then record the maximum and minimum nodal values found in that element's connectivity array. Replace the maximum and/or minimum nodal values by node numbers from subsequent element connectivity arrays if the node values are more extreme than the previously recorded values. At completion of the element loop, the values of $NDMAX$, $NDMIN$ and $MAXB$ for the current pivot node are stored in the MT matrix.

Step 2. Search the $MT(N,3)$ column to find the maximum bandwidth of all nodes. Denote and save this value as $MAXALL$, (i.e., $MAXALL = \text{Maximum of } \{MT(N,3), N=1 \text{ to total number of nodes}\}$). It is often the case that several nodes share the same maximum bandwidth value, $MAXALL$. Accordingly, each of these node numbers is a candidate for the current nodal position to be called node-1. The primary goal is to optimally reduce the bandwidth at the node-1 position by interchanging the node-1 number with an as yet undetermined node number, called node-2. Of course, the insertion of the node-1 number into the node-2 position must also be considered as explained in the next step.

Step 3. The purpose of step 3 is to select an optimum pair of nodes, called node-1 and node-2, such that the interchange of their node numbers reduces the local bandwidth at node-1, while maintaining the bandwidth at node-2 to be less than $MAXALL$. A candidate number for node-1 is labeled $N1$ and a candidate number for node-2 is labeled $N2$. We begin with an outer do-loop for all nodes using the node counter $N1$, and we exclude all $N1$ node numbers such that $MT(3,N1) \neq MAXALL$. Thus, the $N1$ nodes that are not excluded are candidates for node-1. For node-2 candidates, we use an inner do-loop wherein we restrict our search for $N2$ node numbers in the sequential range;

$$N2(\text{start}) = MT(1,N1) - MAXALL + 1$$

$$N2(\text{end}) = MT(2,N1) + MAXALL - 1$$

This restricted range of $N2$ contains the only node numbers that will reduce the bandwidth at the $N1$ position.

If the candidate node pair, $N1$ and $N2$, were interchanged such that number $N2$ is assigned to position 1 and number $N1$ is assigned to position 2, then the new bandwidths at these two positions can be respectively determined as;

$$MAXB1 = \text{Maximum of } \{N2 - MT(N1,2) \text{ or } MT(N1,1) - N2\}$$

$$MAXB2 = \text{Maximum of } \{N1 - MT(N2,2) \text{ or } MT(N2,1) - N1\}$$

The next step within the inner loop is to test whether or not the current candidate pair, $N1$ and $N2$, is a better choice than the best of the previous candidate pairs. This test is passed by satisfying two simultaneous requirements:

- (1) $MAXB1$ is smaller than that produced by any previous candidate pairs, and
- (2) $MAXB2$ is less than $MAXALL$

When all candidate node pairs have been tested, there are two possible outcomes, which dictate one of two possible courses of action:

- (1) A final node pair, node-1 and node-2, has been identified that reduces the bandwidth. In this case we proceed to Step 4 to update matrices and vectors to perform the node swapping.
- (2) No node pair could be found to reduce the current maximum bandwidth (MAXALL). In this case, we exit from the bandwidth minimization process because the job is done.

Step 4. Given a viable solution for node-1 and node-2, the purpose of this step is to update the element connectivity matrix with the current node swap. It is also useful to update a history vector that keeps track of all the nodal changes, called an “is-was” vector.

To update the connectivity matrix, we perform an outer loop search with element counter NE, and an inner loop search with node-location counter K. At any point during the update process, let node-x be the nodal value representing NOD(NE,K). The update is easily achieved by two successive if-then statements:

If node-x equals node-1, then set $NOD(NE,K) = \text{node-2}$

If node-x equals node-2, then set $NOD(NE,K) = \text{node-1}$

When the search loops are completed, the NOD connectivity matrix is completely updated and we may return to Step 1 to repeat the entire process with the new NOD matrix, which provides new starting conditions.

However, before returning to Step 1, it is useful to update a history vector that relates the current node numbering to the original node numbering defined by the user. To this end, denote and dimension a nodal vector ISWAS(NPT) and initialize $ISWAS(N) = N$, for N progressing from 1 to NPT. This initialization infers that new node numbers N are identical to the old node numbers ISWAS(N).

To update for each node swap, let $K1 = ISWAS(\text{node-1})$ and $K2 = ISWAS(\text{node-2})$, where K1 and K2 are the original node numbers that are currently represented by node-1 and node-2, respectively. Then nodal swap is easily updated and saved as

$$ISWAS(\text{node-1}) = K2$$

$$ISWAS(\text{node-2}) = K1$$

When all cycles of node swapping are complete (job done), the ISWAS vector will contain the final correspondence between the new node number N and the old node number ISWAS(N). Said another way, ISWAS(N) is the original node number that identifies the same nodal location that is now identified as N. As discussed in the next section, the ISWAS vector is useful for updating other nodal vectors such as nodal coordinates that must be converted to the new nodal numbering pattern.

This marks the end of Step 4 and the algorithm requires that we return to Step 1 for another cycle. The termination of cycles is decided in Step 3.

7.2.3 Post algorithm-cycle updates.

When the algorithm cycle is exited at Step 3, the maximum bandwidth has been minimized, and the updated NOD connectivity matrix and the ISWAS vector are complete. However, before the finite element solution process can begin, other nodal data that is defined in the original nodal numbering scheme must be converted to the new node numbering scheme such as nodal coordinate vectors and boundary condition vectors prescribing displacements and/or forces at nodes. The ISWAS vector is used to accomplish these conversions.

For vectors such as nodal coordinates, say X and Y, that implicitly reference the old nodal number by means of the vector index number N, it is necessary to first make the conversion to a temporary vector, say T, over a do loop N = 1 to NDT as shown below:

$$T(N) = X(ISWAS(N))$$

After this do-loop is completed, the X vector is converted to the new node numbers by a second do-loop over the same index range:

$$X(N) = T(N)$$

The two-step conversion is required so that information in X vector is not prematurely overwritten, which would occur in a one-step conversion.

For vectors that explicitly define old node numbers such as the list of nodes where boundary conditions are applied, say vector NB, the conversion can be made in one do-loop as,

$$NB(I) = NB(ISWAS(I))$$

where I = 1, to the number of boundary conditions.

After the last conversion of old node numbers to new numbers is completed, the ISWAS vector as previously defined is no longer useful. In preparation for the finite element solution phase, it is convenient to redefine the ISWAS vector to be the inverse of its original definition. That is, ISWAS (N) is the new node number corresponding to the old node number N. The inverse is accomplished in a two-step process using a temporary vector T, similar to the conversion of nodal coordinates. Specifically, for N = 1 to NDT:

$$T(ISWAS(N)) = N$$

Followed by a second do-loop to store inverse definition back into the ISWAS,

$$ISWAS(N) = T(N)$$

In summary, the entire process described above is easily executed in a single subroutine (called BMIZER in CANDE). The output from this subroutine includes the updated NOD matrix, the updated nodal vectors (X, Y, NB, etc.) and the ISWAS vector in its second definition, that is, ISWAS(N) is the new node number associated with old node number N. From this point on, the finite element assembly and solution routines will be working the new node numbering pattern.

7.3 Transparency of Node Numbers in Solution Output.

The second objective of this development is to list the solution output with reference to the original node numbers. A prime example is the tabular listing of displacements where, for example, the output displays values for N, U(N), V(N), where U(N) and V(N) are the x and y displacements at node N. Since U(N) and V(N) are in reference to the new node-numbering pattern, we must redefine the displacement indexes if N represents the sequential numbers of the old numbering pattern.

The proper indexes for the displacements are contained in the ISWAS vector (2nd definition). Therefore, to display the information by a write statement imbedded in a do-loop for N = 1 to NPT, the write statement would read as,

```
WRITE(*,*) N, U(ISWAS(N)), V(ISWAS(N))
```

Output of any other nodal data is handled in the same manner.

Fortunately, element output data such as stress and strain measures are referenced to element numbers, not node numbers. Thus, element output data is the same for either the old or new nodal number pattern.

7.4 Illustration of Bandwidth Minimization

A simple finite element mesh layout, resembling a house on stilts, is shown in Figure 7.5-1 and is used to illustrate the bandwidth minimization algorithm. The mesh contains a total of eight elements composed of 4 beam elements, 2 quadrilateral elements, and 2 triangular elements. The initial node-numbering pattern, subsequently referred to as the old node numbers, is shown in the figure with red numbers. A quick inspection of Figure 1 reveals that the initial node-numbering pattern is far from optimum because of the intentional disparity between node number values surrounding each node point. Thus, there is room for improvement from the bandwidth minimization algorithm.

Figure 7.5-1. Mesh topology for house-on-stilts showing elements and original node pattern

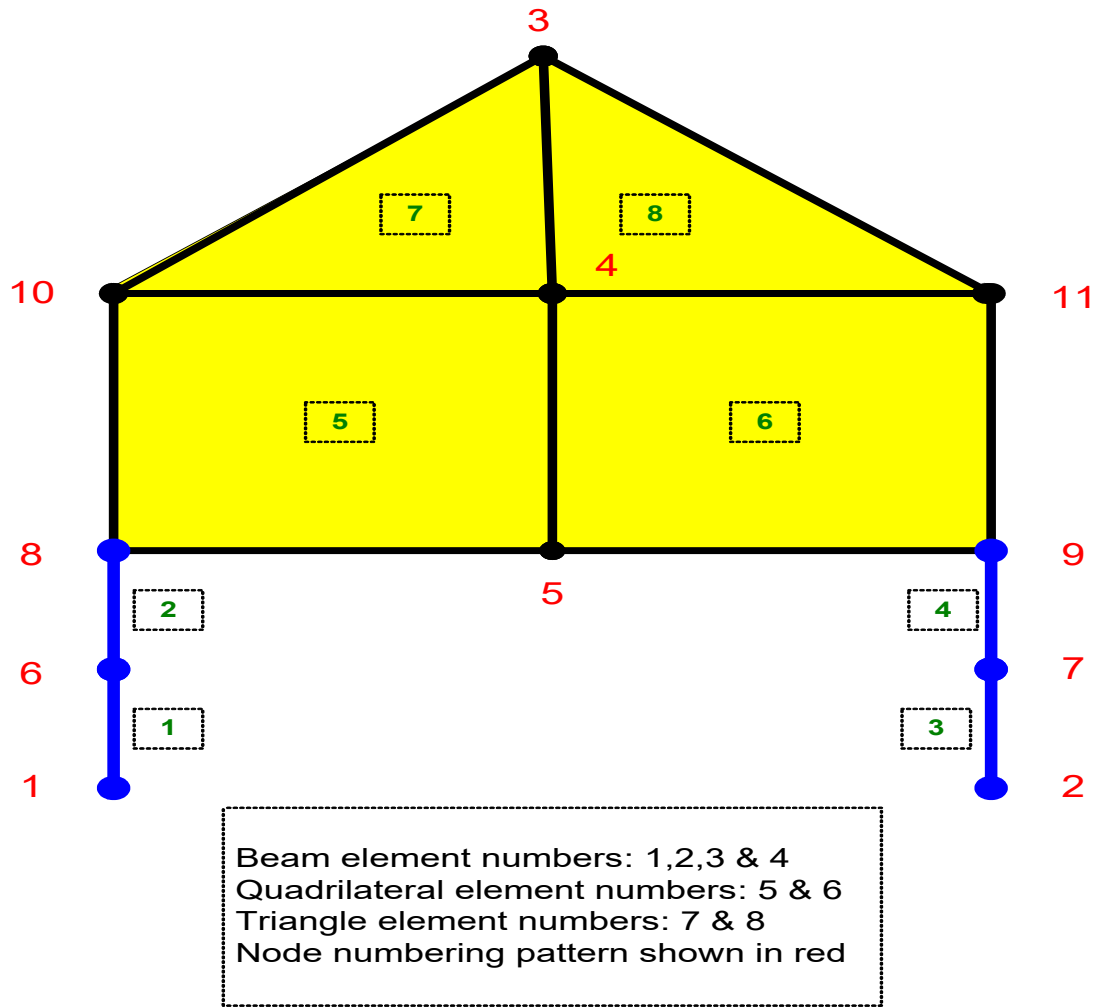


Table 7.5-1 shows the initial connectivity array for the eight elements that is easily deduced from the above figure. Also shown in the table is the initial MT Matrix that is constructed from the element connectivity array as described in Step 1 of the algorithm. For Step 2 it is observed from the last column in the MT matrix that the overall maximum bandwidth is eight (MAXALL = 8).

In Step 3, which is the heart of the algorithm, the MT matrix shows that both node #3 and node #11 are candidates for the primary swapping node because both have a maximum bandwidth equal to 8. For node #3, the candidate secondary node numbers are # 4 to #10, which is the node range that can reduce the bandwidth at node #3. Similarly for node #11, the candidate secondary node numbers are #4 to #10, which is the node range that reduces the bandwidth at node #11. Of

all the possible combinations of primary and secondary node pairs, the winning pair, passing the final test in Step 3, is shown at the bottom of Table 1 as primary node = #3 and secondary node = #7.

Table 7.5-1. NOD and MT Matrices for initial node numbering (Node swaps = 0)

NOD – Matrix (Element Connectivity)					MT-Matrix (Bandwidth Analysis)			
Element	Node a	Node b	Node c	Node d	Pivot Node	NDMAX	NDMIN	MAXB
1	6	1	0	0	1	6	1	5
2	8	6	0	0	2	7	2	5
3	7	2	0	0	3	11	3	8
4	9	7	0	0	4	11	3	7
5	10	8	5	4	5	11	4	6
6	4	5	9	11	6	8	1	5
7	10	4	3	0	7	9	2	5
8	4	11	3	0	8	10	4	4
					9	11	4	5
					10	10	3	7
					11	11	3	8
Results of Algorithm: Nodes to be swapped Node-1 = 3 Node-2 = 7								

Step 4 updates the element connectivity matrix NOD with the node pair #3 and #7. After the update is complete the process starts again at Step 1 to build a new MT matrix.

Table 7.5-2, like the previous table, shows the current NOD and MT matrices after the first node swap. The MT matrix shows that the bandwidth at node #3 was reduced from 8 to 6. However, the largest bandwidth among all nodes is now reduced to seven (MAXALL = 7), occurring at nodes #4 and #11.

Table 7.5-2. NOD and MT Matrices after 1st node swap (Node swaps = 1)

NOD – Matrix (Element Connectivity)					MT-Matrix (Bandwidth Analysis)			
Element	Node a	Node b	Node c	Node d	Pivot Node	NDMAX	NDMIN	MAXB
1	6	1	0	0	1	6	1	5
2	8	6	0	0	2	3	2	1
3	3	2	0	0	3	9	2	6
4	9	3	0	0	4	11	4	7
5	10	8	5	4	5	11	4	6
6	4	5	9	11	6	8	1	5
7	10	4	7	0	7	11	4	4
8	4	11	7	0	8	10	4	4
					9	11	3	6
					10	10	4	6
					11	11	4	7
Results of Algorithm: Nodes to be swapped Node-1 = 4 Node-2 = 8								

In like fashion Tables 7.5-3 to 7.5-7 show the algorithm results for five more successive node swaps.

Table 7.5-3. NOD and MT Matrices after 2nd node swap (Node swaps = 2)

NOD – Matrix (Element Connectivity)					MT-Matrix (Bandwidth Analysis)			
Element	Node a	Node b	Node c	Node d	Pivot Node	NDMAX	NDMIN	MAXB
1	6	1	0	0	1	6	1	5
2	4	6	0	0	2	3	2	1
3	3	2	0	0	3	9	2	6
4	9	3	0	0	4	10	4	6
5	10	4	5	8	5	11	4	6
6	8	5	9	11	6	6	1	5
7	10	8	7	0	7	11	7	4
8	8	11	7	0	8	11	4	4
					9	11	3	6
					10	10	4	6
					11	11	5	6

Results of Algorithm: Nodes to be swapped
 Node-1 = 10
 Node-2 = 7

Table 7.5-4. NOD and MT Matrices after 3rd node swap (Node swaps = 3)

NOD – Matrix (Element Connectivity)					MT-Matrix (Bandwidth Analysis)			
Element	Node a	Node b	Node c	Node d	Pivot Node	NDMAX	NDMIN	MAXB
1	6	1	0	0	1	6	1	5
2	4	6	0	0	2	3	2	1
3	3	2	0	0	3	9	2	6
4	9	3	0	0	4	8	4	4
5	7	4	5	8	5	11	4	6
6	8	5	9	11	6	6	1	5
7	7	8	10	0	7	10	4	3
8	8	11	10	0	8	11	4	4
					9	11	3	6
					10	11	7	3
					11	11	5	6

Results of Algorithm: Nodes to be swapped
 Node-1 = 3
 Node-2 = 6

Table 7.5-5. NOD and MT Matrices after 4th node swap (Node swaps = 4)

NOD – Matrix (Element Connectivity)					MT-Matrix (Bandwidth Analysis)			
Element	Node a	Node b	Node c	Node d	Pivot Node	NDMAX	NDMIN	MAXB
1	3	1	0	0	1	3	1	2
2	4	3	0	0	2	6	2	4
3	6	2	0	0	3	4	1	2
4	9	6	0	0	4	8	3	4
5	7	4	5	8	5	11	4	6
6	8	5	9	11	6	9	2	4
7	7	8	10	0	7	10	4	3
8	8	11	10	0	8	11	4	4
					9	11	5	4
					10	11	7	3
					11	11	5	6

Results of Algorithm: Nodes to be swapped
 Node-1 = 5
 Node-2 = 7

Table 7.5-6. NOD and MT Matrices after 5th node swap (Node swaps = 5)

NOD – Matrix (Element Connectivity)					MT-Matrix (Bandwidth Analysis)			
Element	Node a	Node b	Node c	Node d	Pivot Node	NDMAX	NDMIN	MAXB
1	3	1	0	0	1	3	1	2
2	4	3	0	0	2	6	2	4
3	6	2	0	0	3	4	1	2
4	9	6	0	0	4	8	3	4
5	5	4	7	8	5	10	4	5
6	8	7	9	11	6	9	2	4
7	5	8	10	0	7	11	4	4
8	8	11	10	0	8	11	4	4
					9	11	6	3
					10	11	5	5
					11	11	7	4

Results of Algorithm: Nodes to be swapped
 Node-1 = 5
 Node-2 = 6

Table 7.5-7. NOD and MT Matrices after 6th node swap (Node swaps = 6)

NOD – Matrix (Element Connectivity)					MT-Matrix (Bandwidth Analysis)			
Element	Node a	Node b	Node c	Node d	Pivot Node	NDMAX	NDMIN	MAXB
1	3	1	0	0	1	3	1	2
2	4	3	0	0	2	5	2	3
3	5	2	0	0	3	4	1	2
4	9	5	0	0	4	8	3	4
5	6	4	7	8	5	9	2	4
6	8	7	9	11	6	10	4	4
7	6	8	10	0	7	11	4	4
8	8	11	10	0	8	11	4	4
					9	11	5	4
					10	11	6	4
					11	11	7	4

Results of Algorithm: Nodes to be swapped
None (job done)
No further node swaps will reduce the maximum bandwidth less than 4

The algorithm exited after six node swaps, and Table 7.5-7 portrays the final element connectivity matrix and MT matrix. The final maximum bandwidth is 4, which is a 50% reduction of the original bandwidth.

It is reiterated here that the algorithm is intended to reduce the maximum bandwidth, not to minimize the skyline profile of all nodes, which in this example, includes eight different nodes sharing maximum the bandwidth. Indeed, it is possible to construct a node pattern for this example in which only one node has a maximum bandwidth of 4 and all other nodes have a bandwidth of 3 or less.

Table 7.5-8 shows the final ISWAS vector for both definitions discussed in the algorithm. The second definition is used to reference finite element output back to the original nodal numbering system so that the user need not be concerned with the new numbering system that is only used internally in the solution routines.

Table 7.5-8. Final results of new and old node numbering

ISWAS Definition # 1		ISWAS Definition # 2	
New Nodes	Old Nodes	Old Nodes	New Nodes
1	1	1	1
2	2	2	2
3	6	3	10
4	8	4	8
5	7	5	7
6	10	6	3
7	5	7	5
8	4	8	4
9	9	9	9
10	3	10	6
11	11	11	11

As a closing comment, it is not claimed that the above method provides an absolute global minimum to the bandwidth problem. However, all the results to date have produced node-numbering patterns that could not be further improved to reduce the maximum bandwidth.

8 MODELING TECHNIQUES

When applying CANDE to analyze or design any culvert installation (or more generally any soil structure interaction problem), modeling questions always arise. Some common questions are; what extent of the insitu soil should be included in the finite element mesh, what soil models should be used for insitu and backfill soil, should interface elements be included between structure and soil, how many construction increments should be used, and is large deformation theory required. There is no clear-cut answer to these and similar modeling questions because each problem is unique and modeling assumptions that are appropriate for one case may not be appropriate for another.

The best advice is to try as many modeling approaches as can be practically undertaken for a particular problem. Sometimes it will be found that the differences in solutions from alternative modeling assumptions are inconsequential. At other times, a particular modeling assumption may substantially alter the structural behavior, impacting the safety of the design. In all cases, however, useful information is obtained that guides our insight into soil-structure interaction and permits a more intelligent assessment of the problem.

The remainder of this chapter provides suggested techniques for modeling live loads, pipe-group connections and combinations, and construction increments and soil compaction. However, the “best advice” approach described above should always be kept in mind.

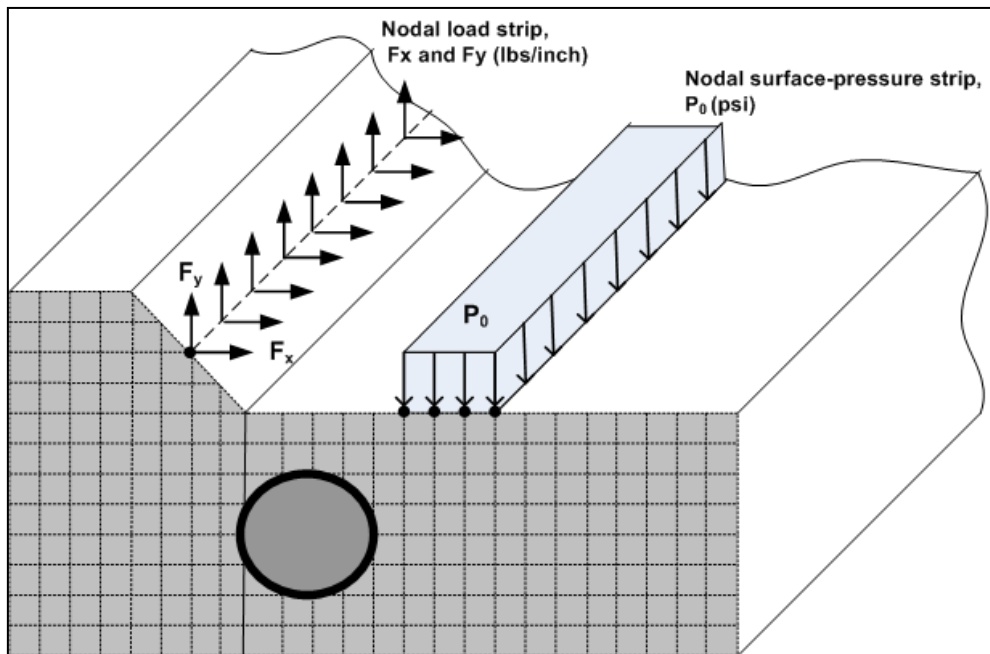
8.1 Live Loads

Live or external loads, as opposed to element body weight loads, are defined by boundary-condition input data described in CANDE’s user instructions. External loads typically represent vehicles traveling over the culvert installation; however, they could also represent temporary compaction loading or any specified loading condition.

8.1.1 Specifying Live Loads for 2D Plane Strain

As illustrated below, all external loads are ultimately applied at nodes with F_x and F_y force components in the global x and y directions per unit length in the z direction (lbs./inch), representing an infinitely long strip load in the z-direction.

Figure 8.1-1. Illustration of nodal strip load and surface-pressure strip load.



Similarly, if pressures are prescribed over the surface of one or more elements as illustrated above by the P_0 surface pressure strip, then the pressures are converted to nodal forces per unit length in the z-direction as described below. Pressure strip loadings are converted to equivalent nodal-force strip loads by distributing the pressure load acting on each element to the neighboring nodes and summing the results to determine the equivalent force strips, F_x and F_y . Figure 8.1-2 and the accompanying table shows an example of converting a pressure-strip load to nodal-strip loads in the negative y-direction.

Figure 8.1-2 Illustration of converting pressure strip to equivalent nodal forces

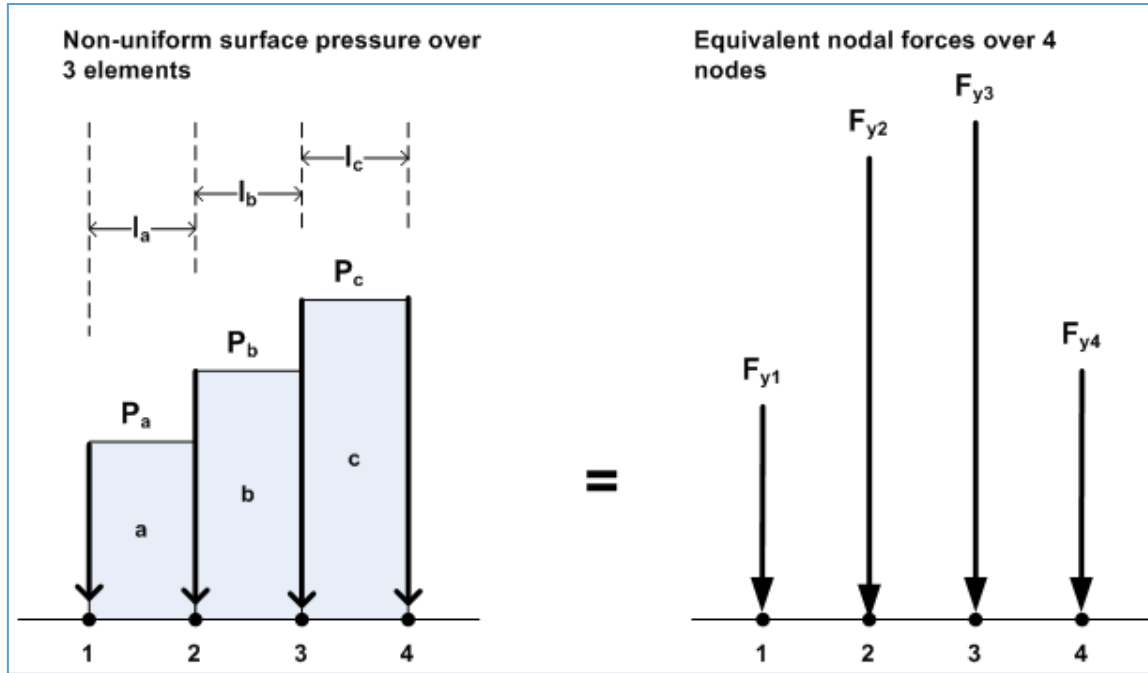


Table 8.1-1 Symbolic calculation of equivalent nodal forces

Contributing Element	Nodal force at nodes			
	Node 1 F_{y1}	Node 2 F_{y2}	Node 3 F_{y3}	Node 4 F_{y4}
a	$P_a l_a / 2$	$P_a l_a / 2$	0	0
b	0	$P_b l_b / 2$	$P_b l_b / 2$	0
c	0	0	$P_c l_c / 2$	$P_c l_c / 2$
Totals	$P_a l_a / 2$	$P_a l_a / 2 + P_b l_b / 2$	$P_b l_b / 2 + P_c l_c / 2$	$P_c l_c / 2$

In the above, P_a , P_b and P_c are the average pressures on each element surface, and l_a , l_b and l_c are the surface lengths of each element, respectively. The total force recorded at the bottom of the table is the boundary-condition y-force value to be entered as input data (negative) for each node under the total in-plane pressure length, $L = l_a + l_b + l_c$.

For large culverts, the surface lengths of elements are often greater than total in-plane length “L” of the pressure strip. In these cases, the strip pressure load is assigned to a single node with line load equal to $P_{avg}L$. Indeed, the single-node loading is often used for any mesh configuration because it is a conservative approximation due to focusing the entire load at a point.

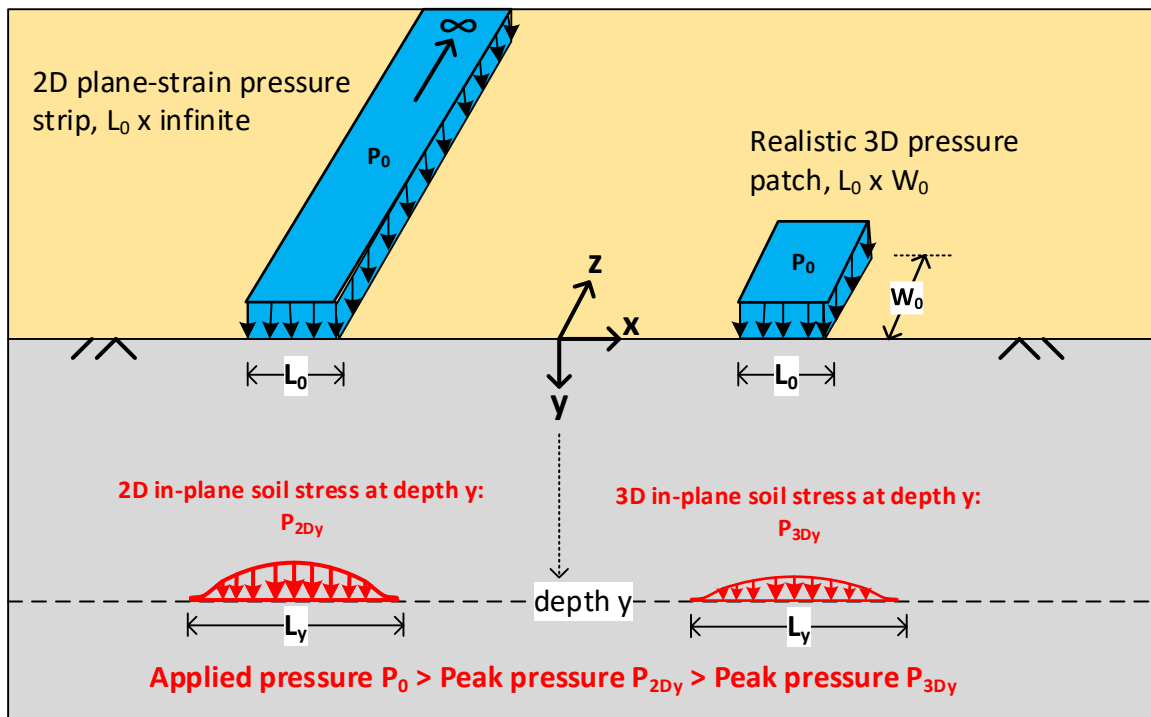
8.1.2 Live Load 2D Problems and Remedies

Problems. If the live load is actually in the form of a very long surface-pressure strip or line load, then there is no modeling problem; that is, the actual surface pressure is used to determine the equivalent boundary-condition nodal forces for the CANDE analysis. However, vehicular loads are transmitted through tire footprints, whose rectangular dimensions are a finite pressure-patch, $L_0 \times W_0$, that does not conform to long prismatic loading. The in-plane patch length L_0 is not an issue because the 2D finite element mesh configuration automatically simulates the ever-increasing, in-plane load spreading at deeper and deeper soil depths. However, the out-of-plane width W_0 presents a problem because the 2D plane-strain formulation inherently implies that the out-of-plane width is an infinitely long pressure strip, $W_0 = \infty$. Consequently, the plane-strain formulation does not simulate the additional load spreading that occurs in the out-of-plane direction.

Visually, the comparison between a 2D pressure strip ($L_0 \times \text{infinite}$) and the 3D pressure patch ($L_0 \times W_0$) is portrayed in Figure 8.1-3. As the 2D pressure-strip load is transmitted through the soil, the uniform surface pressure distribution P_0 spreads laterally as soil depth increases thereby increasing the length of the in-plane footprint from L_0 to L_y and decreasing the peak stress from P_0 to P_{2Dy} as illustrated by the red, dome-shaped distribution beneath the 2D pressure strip. However, 2D pressure strip does not spread longitudinally because every x-y plane is identically loaded resulting in the same pressure distribution.

In a similar manner, the 3D pressure patch spreads in-plane like the 2D pressure strip with the same footprint length L_y . However, the actual 3D load also spreads out-of-plane so that footprint width grows from W_0 to W_y and the peak pressure is further decreased from P_{2Dy} to the correct value P_{3Dy} . The in-plane 2D and 3D distributions shown in red differ in magnitude with the same shape over L_y . That is, the peak-stress reduction factor $r = P_{3Dy}/P_{2Dy}$ is the same reduction that is applied uniformly over the 2D distribution to obtain the 3D distribution.

Figure 8.1-3 Illustration of 2D pressure strip and 3D pressure-patch footprints



With the above understanding, the 2D modeling problem for live loads acting on buried culverts is now readily apparent. To wit, if the actual tire pressure P_0 acting on a realistic footprint is used in a straight-forward 2D plane-strain analysis, then the soil stress impinging on the culvert would be excessive and over conservative, resulting in over designing the culvert cross sections, and/or restricting truck travel due to incorrect load rating factors.

The 2D live-load modeling problem is further exacerbated when the soil surface is overlain with a stiff pavement or when 3D stiffness effects of the culvert need to be taken into account. These lesser-known issues will be discussed and remedied after introducing the basic remedies for correcting 2D solutions for out-of-plane load spreading through soil.

Remedies – an overview. To correct the 2D solution for 3D patch loads requires a reasonable load-spreading theory coupled with a procedure to adjust the magnitude of the 2D strip load to account for the reduction in soil stress due to out-of-plane (longitudinal) load spreading. As summarized below, there are two well-used theories for load spreading as well as two viable procedures for reducing the live-load pressure transmitted through the 2D soil model.

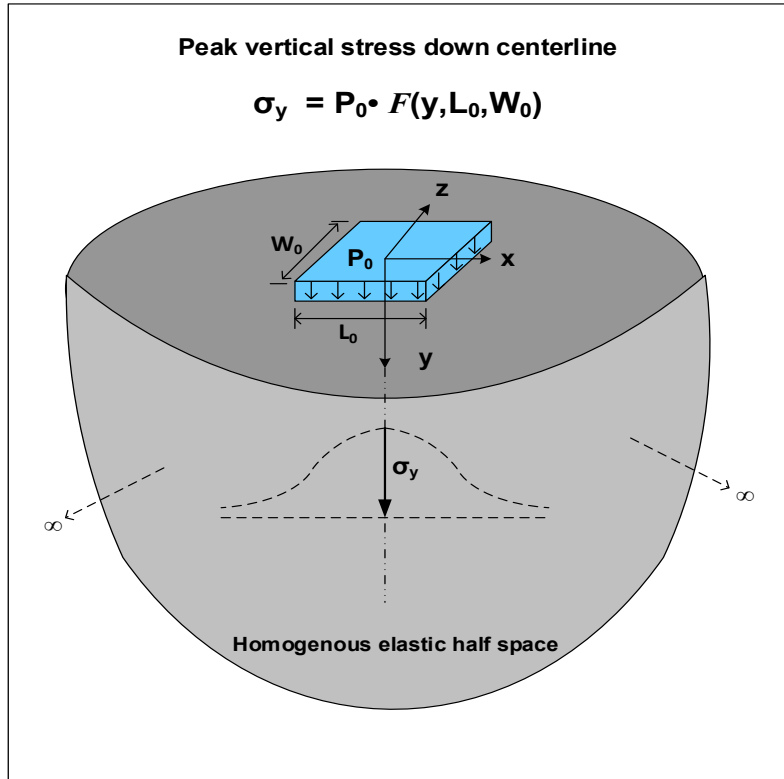
1. **Load spreading theories.** For a homogenous soil half space with a rectangular pressure-patch load:
 - (a) **Elasticity-based Method (EBM).** An exact elasticity solution for peak soil stress as function of soil depth and patch dimensions, $L_0 \times W_0$. That is, an exact closed form solution for the reduction of peak stress as function of soil depth beneath the loading centerline.
 - (b) **AASHTO Ad-hoc Method (AAM).** An approximate solution for peak soil stress as a function of soil depth and patch dimensions, $L_0 \times W_0$. AAM includes the ability to determine two-wheel interaction depths wherein the soil pressures from two separate wheels combine to exceed one-wheel peak pressure.
2. **Corrective procedures.** Procedures to adjust 2D loading magnitudes to simulate out-of-plane load spreading.
 - (a) **Reduced Surface Load (RSL).** This is the traditional procedure that has been used for many decades wherein the surface pressure or line load is judiciously reduced in magnitude so that the soil pressure at one specified depth matches that of the selected load-spreading theory.
 - (b) **Continuous Load Scaling (CLS).** This revolutionary procedure introduced in 2017 by Katona corrects the soil pressure at all soil depths. This is achieved by a modification to the CANDE program such that the unit thickness of each plane-strain element is amplified as a continuous function of soil depth wherein the amplifying factor is the inverse of the load-spreading reduction factor.

The next two section provides a thorough review of EBM and AAM load-spreading theories followed by sections describing the RSL procedure and the CLS procedure. Finally, the last sections present the methodology for pavement overlays, and the special case of 3D stiffness effects.

8.1.3 Elasticity Based Method (EBM) for Load Spreading

The geotechnical text by Poulos and Davis (Reference 25) provides a closed-form elasticity solution for the peak centerline stress as a function of soil depth y for a homogenous, elastic half-space with a rectangular pressure patch $L_0 \times W_0$ as shown in Figure 8.1-4.

This elasticity solution for peak, free-field, vertical soil stress (denoted as σ_y in the figure) was derived by Holl in the late 1940s at a time period when PhD students solved difficult partial differential equations rather than exploring numerical analysis. Holl's closed-form solution is shown in Equation 8.1-1.

Figure 8.1-4 Elasticity Based Model (EBM) for free-field stress beneath 3D pressure patch.**Closed Form Solution for Peak Soil Stress.**

$$\sigma(y)_{3D} = 2 \frac{P_0}{\pi} \left[\arctan\left(\frac{\alpha}{h\sqrt{1+\alpha^2+h^2}}\right) + \frac{\alpha h}{\sqrt{1+\alpha^2+h^2}} \left(\frac{1}{1+h^2} + \frac{1}{h^2+\alpha^2} \right) \right] \quad \text{Equation 8.1-1}$$

where, $\sigma(y)_{3D}$ = Peak vertical soil stress at soil depth y for arbitrary 3D patch footprint (L_0, W_0).

y = soil depth below center of pressure patch.

P_0 = surface patch pressure.

L_0 = patch length in x-y plane.

W_0 = patch width in y-z-plane.

with non-dimensional variables defined as,

$$\alpha = W_0/L_0 = \text{aspect ratio of patch width to length}$$

$$h = y/(L_0/2) = \text{non-dimensional soil depth in half-wheel lengths}$$

Important observations regarding Equation 8.1-1 for peak stress $\sigma(y)_{3D}$ are;

- This is an exact solution without approximation; however, the solution is limited to predicting peak stress down the centerline and not the stress distribution around the centerline.
- As might be expected, the peak stress σ_y along the centerline does not depend on any elastic material properties of the homogenous soil half space.

- Excluding the proportional pressure parameter P_0 , there are only 3 independent variables; the soil depth y and the 3D patch footprint dimensions L_0 and W_0 . That is, $\sigma(y)_{3D}/P_0 = \text{function of } (y, L_0, W_0)$

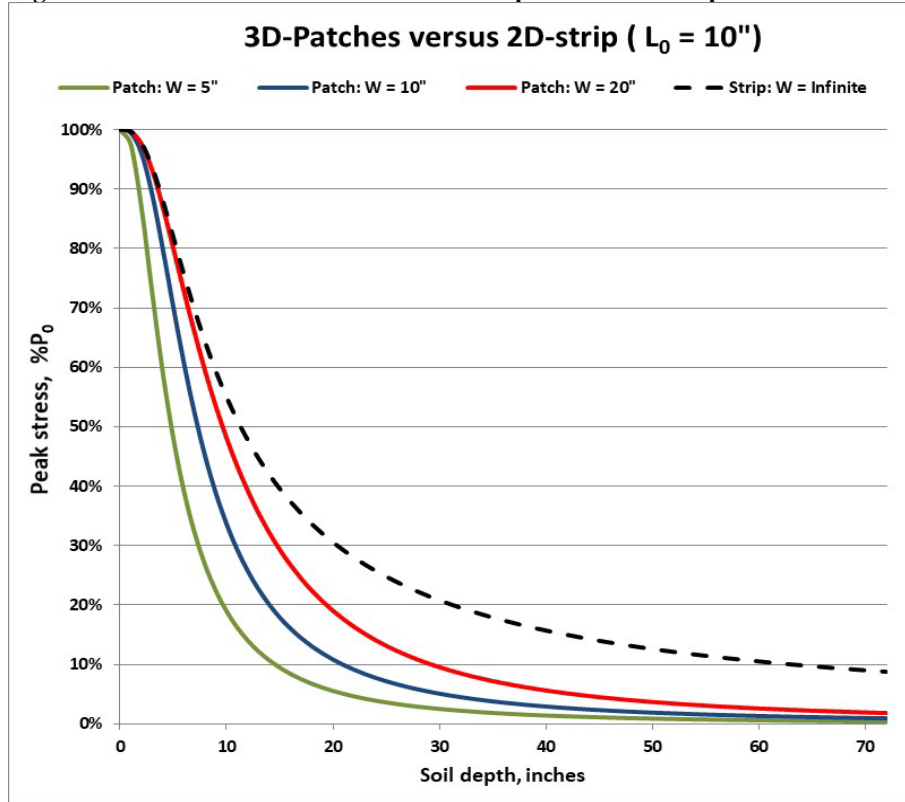
Most significantly, Equation 8.1-1 also contains the 2D plane-strain pressure strip solution as a special case. Specifically, if the patch width W_0 approaches infinity while L_0 remains constant, then $\alpha = W_0/L_0 \rightarrow \infty$, and Equation 8.1-1 reduces to the 2D solution $\sigma(y)_{2D}$ for an infinite pressure strip as expressed below.

$$\sigma(y)_{2D} = 2 \frac{P_0}{\pi} \left[\arctan\left(\frac{1}{h}\right) + \frac{h}{1+h^2} \right] \tag{Equation 8.1-2}$$

where, $\sigma(y)_{2D}$ = Peak vertical soil stress at soil depth y for arbitrary 2D pressure strip ($L_0 \times \infty$).
 $h = y/(L_0/2)$ = non-dimensional soil depth in half-wheel lengths

Peak Soil Stress Plots. Figure 8.1-5 illustrates the difference in peak soil stress plots for three 3D-patch cases, $W_0 = 5''$, $10''$ and $20''$, versus a 2D strip condition with $W_0 = \text{infinite}$. In all cases the footprint length is constant at $L_0 = 10''$.

Figure 8.1-5 EBM Peak soil stress vs. soil depth for three 3D-patches versus 2D strip loads.



Observations from above figure:

- The peak-stress plot for the 2D pressure strip (dashed line) exceeds each of the peak-stress plots for the 3D patches (solid lines) at all soil depths because the dashed line only exhibits in-plane (L_0) load spreading, whereas the solid lines exhibit both in-plane (L_0) and out-of-plane (W_0) load spreading.
- The vertical distance between the 2D dashed line and 3D solid lines at any soil depth is the 2D error in overpredicting the soil stress in terms of $\%P_0$. The 2D error is more pronounced for shallow depths than for deeper soil depths.

- Although the influence of increasing L_0 is not shown in the figure, it is intuitively clear that increasing L_0 would raise the stress plots for all cases. For example, consider the 3D patch dimensions $L_0 = 10''$ and $W_0 = 10''$ (solid blue line), and if we increase L_0 to $20''$, then the blue line would rise up to the solid red line. That is, the peak stress plot for $L_0 = 20''$ & $W_0 = 10''$ is identical to that of $L_0 = 10''$ and $W_0 = 20''$, which can be understood by the physical symmetry.

EBM Reduction Factor Equation. The peak stress equation for the 3D patch ($L_0 \times W_0$) divided by the equation for the 2D strip ($L_0 \times \infty$) produces a dimensionless expression called the reduction factor equation as shown below,

$$r_y = \frac{\sigma(y)_{3D}}{\sigma(y)_{2D}} = \frac{\arctan\left(\frac{\alpha}{h\sqrt{1+\alpha^2+h^2}}\right) + \frac{\alpha h}{\sqrt{1+\alpha^2+h^2}}\left(\frac{1}{1+h^2} + \frac{1}{h^2+\alpha^2}\right)}{\arctan\left(\frac{1}{h}\right) + \frac{h}{1+h^2}} \quad \text{Equation 8.1-3}$$

Where, r_y = reduction factor, a decreasing function of y , $r_y \leq 1$
 $\alpha = W_0/L_0$ = aspect ratio of patch width to length
 $h = y/(L_0/2)$ = non-dimensional soil depth in half-wheel lengths.

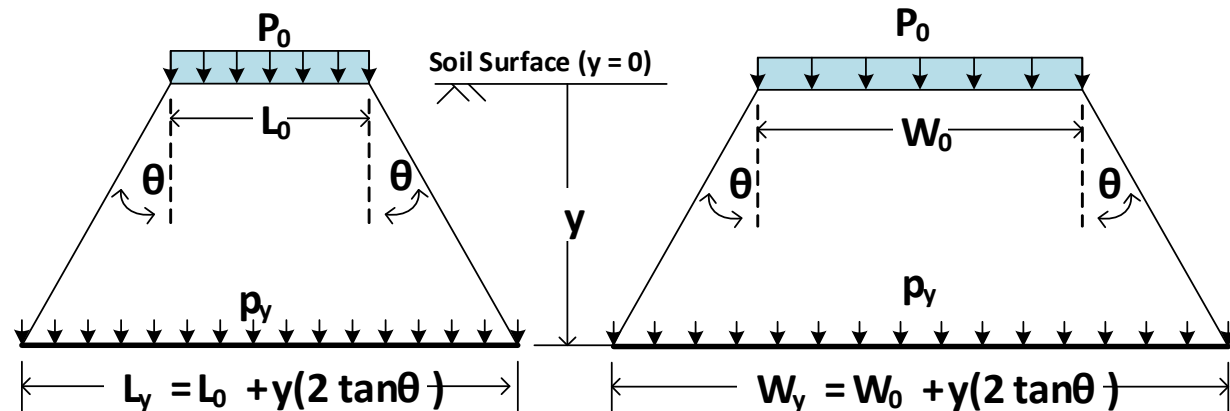
Although certainly not obvious in the above equation, the patch length L_0 cancels out in the division of 3D stress by 2D stress so that r_y is only a function of the soil depth y and the patch parameter W_0 . The reduction factor equation tells us how much the 2D solution needs to be reduced at each soil depth in order to match the correct 3D solution.

EBM Summary. EBM load spreading theory provides an exact solution for free-field peak stress beneath 3D patch centerline as well as an exact measure of error in peak-stress error from CANDE’s 2D plane-strain solution. Dividing the 3D peak stress equation by the 2D peak stress equation yields the important reduction factor equation r_y which is used to correct the 2D CANDE solution. One shortcoming of the EBM solutions is they do not provide information on the stress distribution around the centerline, which is required to determine two-wheel interaction soil stress. In contrast, the AAM load spreading method, presented next, offers an approximate solution to peak stress but includes a pseudo stress distribution suitable for the assessing the two-wheel interaction problem.

8.1.4 AASHTO Ad-hoc Method (AAM) for Load Spreading

The AAM load-spreading model is intended to predict peak soil stress at any soil depth within a semi-infinite, homogenous soil mass whose surface is loaded by a rectangular footprint area L_0W_0 with uniform pressure P_0 , i.e., AAM has the same objective as EBM. Figure 8.1-6 shows the simple geometry that defines AAM load-spreading for the in-plane direction (left side) and the out-of-plane direction (right side).

Figure 8.1-6 Geometry for AMM load spreading; L_y in-plane, and W_y out-of-plane.



Symbols in the figure are defined as follows:

P_0 = applied surface pressure to rectangular loading patch
 L_0 = in-plane length of patch footprint on surface
 W_0 = out-of-plane width of patch footprint on surface
 y = soil depth beneath surface
 θ = load spreading angle
 L_y = in-plane footprint length at soil depth y
 W_y = out-of-plane footprint width at soil depth y
 p_y = uniform pressure acting on footprint area $L_y W_y$ at soil depth y

Note that the AAM methodology conveniently assumes that p_y is uniformly distributed over the footprint area $L_y W_y$; hence, the peak pressure is equal to uniform pressure. Of course, the actual distribution is not uniform, but rather, it is a dome-shaped function with peak stress p_y occurring on the footprint centerline and decaying to zero at boundaries that exceed the compact AAM footprint area. However, the advantages of assuming a pseudo uniform pressure include the following,

- 1) Peak stress p_y , which is the primary objective, is identical to the uniform pressure.
- 2) Net vertical force on the surface and on soil footprints at depth y are easily derived as $p_0 L_0 W_0$ and $p_y L_y W_y$.
- 3) The soil depth wherein 2-wheel footprint superposition exceeds 1-wheel peak pressure occurs when the uniform pressure distributions begin to overlap each other.

AAM Fundamental Tenets. With the above understandings, the fundamental tenets behind the AAM formulation are; (1) enforcing vertical force equilibrium between the surface footprint load and soil footprint load. i.e.,

$$p_y L_y W_y = P_0 L_0 W_0 \quad \text{Equation 8.1-4}$$

And (2) L_y and W_y increase by the same increment as controlled by depth and spread angle. i.e.,

$$L_y = L_0 + y(2 \tan \theta) \quad \text{Equation 8.1-5}$$

$$W_y = W_0 + y(2 \tan \theta) \quad \text{Equation 8.1-6}$$

Combining the above Equations, the key AAM equation to predict peak soil stress for 3D patch loading is,

$$p_{y(3D)} = P_0 \frac{L_0 W_0}{L_y W_y} \quad \text{Equation 8.1-7}$$

The added subscript (3D) is used to denote 3D patch loading with finite footprint dimensions $L_0 \times W_0$. For the special case of 2D pressure strip loading, we have $W_0 = \infty$ so that $W_0/W_y = 1$. Thus, the above equation simplifies to peak soil stress for 2D strip loading as shown below.

$$p_{y(2D)} = P_0 \frac{L_0}{L_y} \quad \text{Equation 8.1-8}$$

Assuming L_0 , W_0 and P_0 are known along with a chosen soil depth y , Equations 8.1-7&8 predict the 3D & 2D peak stress providing that a value for θ is specified. Any choice of θ will satisfy equilibrium; however, the choice of θ has a profound influence on the accuracy of predicting p_y . Or said more succinctly, the accuracy of AAM methodology is totally dependent on the choice of spread angle θ and its dependence on the depth y .

For the last several decades, the AASHTO guidelines have specified that θ should be taken as constant 30° for all soil depths, which is referred to as the AAM- 30° model. In 2017, Katona (Reference 34) undertook a thorough investigation of the accuracy of the traditional AAM- 30° model in comparison with the exact Elasticity Based Method (EBM). Ideally, $p_{y(3D)}$ should match the exact EBM solution $\sigma(y)_{3D}$ at all soil depths; however, this is not the case as discussed below.

AAM-30° Accuracy Assessment. For the specific choice of a constant spread angle $\theta = 30^\circ$ that defines the AAM-30° model, the accuracy investigation resulted in the following significant findings:

- 1) EBM and AAM-30° predict the same peak-stress value only at one specific soil depth denoted as y^* . The soil depth y^* is proportional to the square root of the footprint area and is calculated as,

$$y^* = 44 \sqrt{\frac{L_0 W_0}{200}} \quad (\text{All units in inches}) \quad \text{Equation 8.1-9}$$

The above formula is valid for all footprint areas with aspect ratios in the range $\frac{1}{4} \leq W_0/L_0 \leq 4$, which encompasses the range of practical wheel footprint dimensions. As an example, for HL93 trucks where $L_0 = 10''$ and $W_0 = 20''$, we find $y^* = 44''$ so that $\frac{1}{2}y^* = 22''$.

- 2) For shallow soil depths, defined to be in the range $0 < y < \frac{1}{2}y^*$, the AAM-30° peak stress prediction is significantly less than the exact EBM peak stress by as much as 31.3% P_0 with an average error of 10.4% error over the shallow-depth range. Since AAM-30° underpredicts the actual stress, the pressure predictions are unconservative and should not be used in this range.
- 3) For moderate-to-deep soil depths, defined as $y \geq \frac{1}{2}y^*$, the AAM-30° peak stress prediction is acceptably close to the exact EBM peak stress. Specifically, the maximum peak-pressure error is just 3.8% P_0 at $y = \frac{1}{2}y^*$, and over the entire range $y \geq \frac{1}{2}y^*$, the average peak-pressure error is only 0.2% P_0 .

Based on the above three findings, it is concluded that the AAM-30° model is only acceptable for predicting peak stress for moderate-to-deep soil depths where $y \geq \frac{1}{2}y^*$. However, it is not acceptable for shallow soil depths where $y < \frac{1}{2}y^*$. Herein is the purpose of the new AAM- θ^* model, i.e., to improve the accuracy of the AAM-30° model in the shallow-depth range where $0 < y < \frac{1}{2}y^*$.

Introducing Improved AAM- θ^* Model. AAM- θ^* follows the same rules as AAM-30°. The two models only differ in the definition of θ , that is, $\theta = \text{constant } 30^\circ$ for AAM-30°, versus $\theta = \theta^*$ for AAM- θ^* wherein θ^* is a simple bi-linear function as defined below,

$$\theta^* = \begin{cases} \frac{y}{(1/2)y^*} 30^\circ & \text{if } y < (1/2)y^* \\ 30^\circ & \text{if } y \geq (1/2)y^* \end{cases} \quad \text{Equation 8.1-10}$$

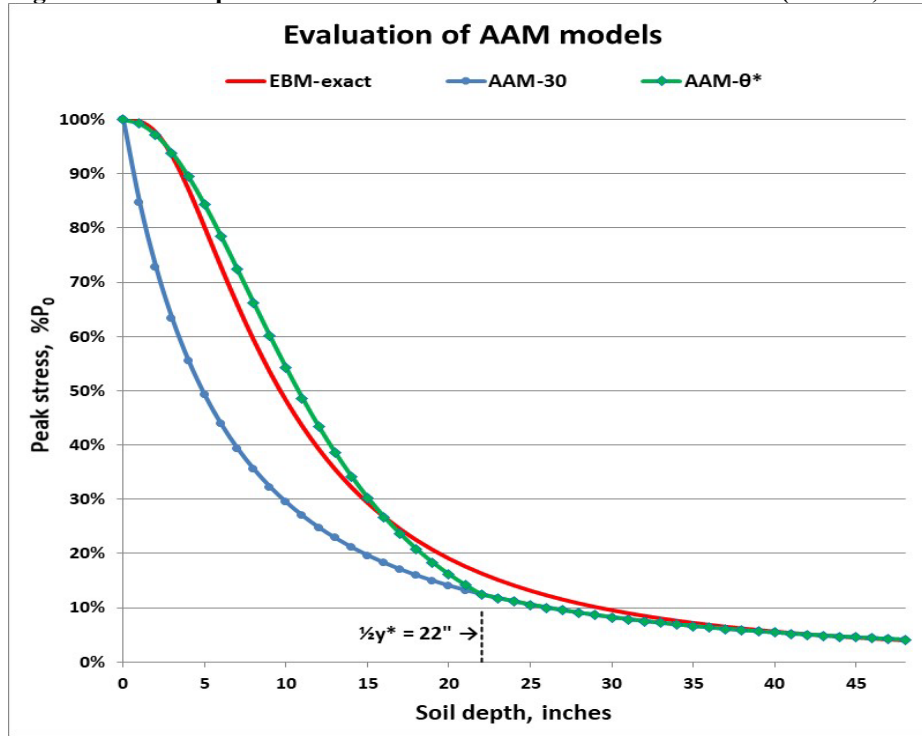
Figure 8.1-7 shows the visual comparison of peak stress plots for AAM-30° versus AAM- θ^* and the exact EBM solution for the ubiquitous 3D patch footprint dimensions $L_0 = 10''$ and $W_0 = 20''$.

As illustrated in the figure, the AAM- θ^* model is significantly more accurate than the non-conservative AAM-30° model in the shallow depth zone, $0 < y < \frac{1}{2}y^*$. In this example we have $\frac{1}{2}y^* = 22$ inches as determined from Equation 8.1-6 with footprint area $L_0 W_0 = 200 \text{ in}^2$. Oversize vehicles with larger wheel footprints and/or the amplified footprint areas caused by pavements can easily result in shallow depth zones to 50 inches or more. With this understanding, it is evident that the more accurate AAM- θ^* model must replace the AAM-30° model in the shallow depth zone to avoid overly non-conservative stress analysis.

Therefore, to maintain reasonable accuracy in all cases, the AAM- θ^* model is adopted with θ^* defined by the above equation so that L_y and W_y generically expressed by Equations 8.1-5 and 8.1-6 are explicitly written as,

$$L_y = L_0 + y(2\tan\theta^*)$$

$$W_y = W_0 + y(2\tan\theta^*)$$

Figure 8.1-7 Comparison of AAM models with exact EBM solution ($L_0=10''$, $W_0=20''$)

AAM- θ^* Reduction Factor Equation. The peak stress equation for the 3D patch ($L_0 \times W_0$) divided by the equation for the 2D strip ($L_0 \times \infty$) produces a dimensionless expression called the reduction factor equation for one wheel as shown below,

$$r_y^* = \frac{p_{y(3D)}}{p_{y(2D)}} = \frac{W_0}{W_y} = \frac{W_0}{W_0 + y(2 \tan \theta^*)} \quad \text{Equation 8.1-11}$$

where, r_y^* = one-wheel reduction factor equation, a decreasing function of y , $r_y \leq 1$
 W_0 = Actual 3D patch width of surface live load.

The AAM- θ^* reduction factor equation r_y^* tells us how much the 2D CANDE stress predictions need to be reduced at each soil depth in order to simulate a finite 3D patch width W_0 . Like r_y the exact EBM reduction factor equation, r_y^* is a function of the soil depth y and the patch parameter W_0 . The advantage of r_y^* is that it is much easier to calculate than the EBM r_y equation, and the AAM methodology permits calculating the 2-wheel interaction depth.

AAM- θ^* Summary. AAM- θ^* load spreading method provides a reasonably accurate solution for free-field peak soil stress for all soil depths, whereas the old AAM-30° is overly non-conservative in the shallow depth zone, $y < \frac{1}{2}y^*$. The key equations for AAM- θ^* are summarized below:

- $y^* = 44'' \sqrt{L_0 W_0 / 200}$ = specific soil depth where AAM-30° matches exact EBM solution.
- $\theta^* = 30^\circ \frac{y}{\frac{1}{2}y^*} \leq 30^\circ$ = AAM bilinear angle function best matching exact EBM solution
- $r_y^* = W_0 / (W_0 + y(2 \tan \theta^*))$ = 1-wheel reduction factor equation to convert 2D strip to 3D patch.

In the next section, the above AAM- θ^* equations and concepts are used to derive the two-wheel interaction depth H_{int} and the associated peak-stress adjustment factor called λ_y^* .

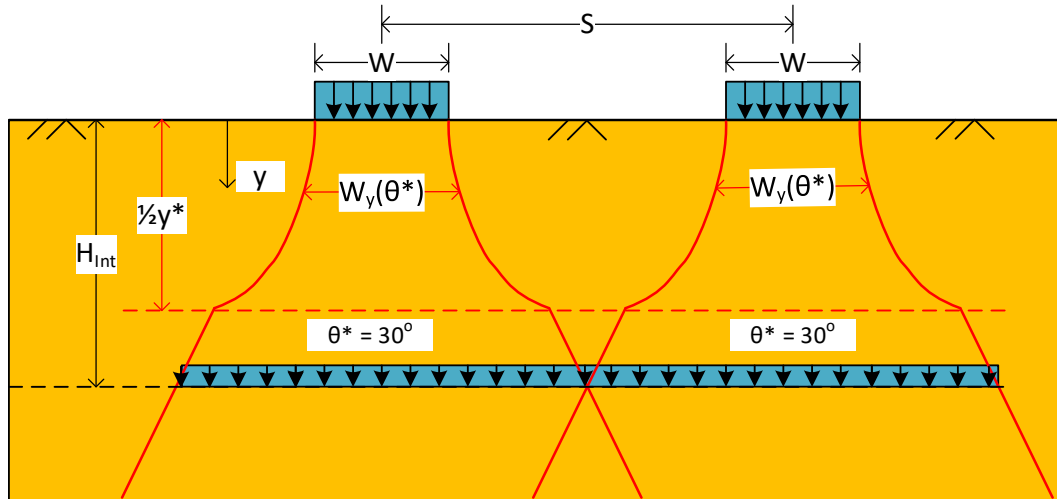
8.1.5 Two-wheel Interaction and Soil Depth H_{int}

We now extend the AAM- θ^* peak stress prediction for a single wheel to consider two wheels (or two wheel-pods) on truck axles. The CANDE analysis properly simulates multi-axial trucks traveling in the x-y plane, however, each axle's two wheels (or wheel-pods) are aligned in the out-of-plane direction and separated by a distance "S" between wheel-patch centers. These two axially-aligned footprints spread with soil depth such that at some depth the two stress distributions overlap a sufficient amount to produce a peak stress exceeding that of a single wheel. This depth is denoted as H_{int} , meaning the two-wheel interaction depth.

Although the actual soil-stress distribution under each wheel is dome shaped with footprints larger than the uniform-pressure AAM- θ^* footprint, the uniform pressure assumption provides a rational method to determine H_{int} . As will be illustrated, H_{int} is the soil depth at which the two W_y footprint widths initially merge together. At depths greater than H_{int} , the soil stress distribution is assumed to remain uniform and spread evenly over the merged footprint areas. Hence, equilibrium demands the peak pressure for soil depths greater than H_{int} is both wheel loads divided by the combined footprint area. This provides a continuous peak-stress prediction in transitioning from the one-wheel footprint at depth H_{int} to the two-wheel footprint; however, the rate of peak-stress reduction declines for $y > H_{int}$.

Determining H_{int} . Figure 8.1-8 illustrates the two-wheel scenario for two identical wheels with out-of-plane patch widths W_0 separated by distance S between wheel centers. The solid red lines depict the AAM- θ^* load spreading width $W_y(\theta^*)$ beneath each wheel wherein the spread angle θ^* becomes a constant 30° when $y \geq \frac{1}{2}y^*$.

Figure 8.1-8 AAM- θ^* two-wheel interaction soil depth H_{int}



The above figure illustrates that the two-wheel interaction depth H_{int} occurs at the soil depth where the individual footprint widths intersect each other (center red lines). Due to symmetry, the footprints intersect when each footprint's width W_y expands to equal the spacing distance S; that is, H_{int} is the depth y where $W_0 + y(2\tan\theta^*) = S$. Or, placing W_0 on the righthand side, the governing equation for H_{int} is,

$$y(2 \tan \theta^*) = S - W_0 \quad (\text{The solution for } y \text{ satisfying this equation is } H_{int}) \quad \text{Equation 8.1-12}$$

where, $\theta^* = 30^\circ \frac{y}{\frac{1}{2}y^*}$ if $y < \frac{1}{2}y^*$; otherwise, $\theta^* = 30^\circ$

Equation 8.1-12 contains three known parameters S, W_0 and y^* , and we observe the expression $y(2\tan\theta^*)$ is either linear or nonlinear in y because θ^* is either constant 30° or variable 0° to 30° depending on whether or not the solution H_{int} is

greater than $\frac{1}{2}y^*$ as is depicted in the above figure. For the pivotal case, we try $\theta^* = 30^\circ$, so that $2\tan 30^\circ = 1.15$ and solving Equation 8.1-12 gives $H_{\text{int}} = (S - W_0)/1.15$. Thus, if we find $(S - W_0)/1.15 \geq \frac{1}{2}y^*$, then we have the solution for H_{int} . Otherwise, a nonlinear solution is required. The solution process is summarized below.

$$\text{If } \frac{S - W_0}{1.15} \geq \frac{1}{2}y^*, \text{ then } H_{\text{int}} = \frac{S - W_0}{1.15} \quad \text{Equation 8.1-13a}$$

$$\text{If } \frac{S - W_0}{1.15} < \frac{1}{2}y^*, \text{ then } H_{\text{int}} = y, \text{ which solves; } y(2 \tan \theta^*) = S - W_0 \quad \text{Equation 8.1-13b}$$

For the nonlinear case where $(S - W_0)/1.15 < \frac{1}{2}y^*$, Equation 8.1-13b has solution $y = H_{\text{int}}$ in the range $0 < y < \frac{1}{2}y^*$, which may be determined by standard nonlinear methods such as Newton-Raphson or binary chop. Or more simply, a spreadsheet solution by evaluating $y(2\tan\theta_y^*)$ with successive values of y incremented by 1" until $y(2\tan\theta_y^*) = S - W_0$.

For the ubiquitous HL93 trucks where $L_0 = 10''$, $W_0 = 20''$ and $S = 72''$, and, we compute $(S - W_0)/1.15 = 45.2''$. which is greater than $\frac{1}{2}y^* = 22''$, therefore Equation 8.1-13a controls and we find $H_{\text{int}} = 45.2''$.

Determining 2-Wheel Peak Soil Stress. The combined effective footprint width for soil depths $y \geq H_{\text{int}}$ is the width between outer red lines, which is simply $S + W_y$. This is illustrated in Figure 8.1-8 for the case $H_{\text{int}} > \frac{1}{2}y^*$ but also applies for all depths of H_{int} . To determine the peak 2-wheel soil stress, the fundamental AAM equilibrium tenet is invoked to equate the total surface force $2p_0L_0W_0$ to the sub-surface force $p_yL_y(S + W_y)$ so that peak stress for $y \geq H_{\text{int}}$ is given by,

$$p_{y(2\text{-wheel})} = 2P_0 \frac{L_0 W_0}{L_y (S + W_y)} \quad \text{Two-wheel peak stress for } y \geq H_{\text{int}}$$

The above equation can be conveniently re-written in terms of the one-wheel peak pressure p_y multiplied by the depth-dependent peak-stress increase factor λ_y , i.e.,

$$p_{y(1 \text{ or } 2\text{-wheel})} = \lambda_y p_y = \lambda_y \left(P_0 \frac{L_0 W_0}{L_y W_y} \right) \quad \text{One or Two-wheel peak stress for all } y. \quad \text{Equation 8.1-14}$$

$$\text{where, } \lambda_y = \frac{2}{1 + S/W_y} \geq 1 \quad \text{One- or two-wheel rate factor, where } \lambda_y = 1 \text{ until } y \geq H_{\text{int}}, \quad \text{Equation 8.1-15}$$

At the depth $y = H_{\text{int}}$, we have $W_y = S$, so that $\lambda_y = 1.0$, which is the lower limit allowed for λ_y . Thus, we see that 1-wheel peak pressure smoothly transitions to 2-wheel peak pressure in a continuous manner. As y increases beyond H_{int} , the term S/W_y approaches zero and the factor λ_y approaches 2.0, which is the physical upper limit.

With the above definition for λ_y , the one-wheel reduction factor equation given by Equation 8.1-11 can be generalized to apply to one or two wheels depending on soil depth as expressed below,

$$r_y^* = \lambda_y \frac{W_0}{W_0 + y(2 \tan \theta^*)} \quad \text{One- or two-wheel reduction factor equation} \quad \text{Equation 8.1-16}$$

Summary Two-wheel Interaction. The above AAM- θ^* methodology provides a rational basis for determining the 2-wheel interaction depth, H_{int} , along with the 2-wheel, depth-dependent rate factor, λ_y that amplifies the 1-wheel peak stress prediction when $y > H_{\text{int}}$. Note that the λ_y factor can also be used to amplify the 1-wheel EBM peak stress prediction to account for 2-wheels on an axle. This is demonstrated in the next two sections on correcting the CANDE 2D strip loads to simulate 3D patch loads. The two corrective procedures are called, Reduced Surface Load (RSL) and Continuous Load Scaling (CLS).

8.1.6 Reduced Surface Load (RSL) Procedure

The RSL procedure is based on reducing the magnitude of the actual live loads to account for out-of-plane load spreading. To this end, the live-load reduction factor may be taken from the exact EBM reduction factor equation r_y (Equation 8.1-3) or the approximate AAM- θ^* reduction factor equation r_y^* (Equation 8.1-11). Because both of these reduction factor equations are dependent on soil depth y , we would ideally like to correct CANDE's 2D predictions at all soil depths. However, since the live-load magnitude assigned to each boundary-condition node can only be assigned one specific value, we must choose reduction factor based on one selected soil depth, say $y = h^*$. Herein lies the major shortcoming of the RSL procedure. That is, the magnitude of the live-load soil pressure is corrected for just the single soil depth h^* . For soil depths less than h^* , the 2D soil pressures are less than actual (unconservative), and for soil depths greater than h^* , the 2D soil pressures are greater than actual (conservative).

In spite of the above shortcomings, RSL-AAM is a very popular procedure for correcting 2D soil-structure models to account for longitudinal load spreading of live loads for the following reasons.

- Alternatives to RSL do not exist for 2D finite element program other than CANDE because the CLS procedure requires extensive modifications to the plane-strain formulation and is currently only available in CANDE.
- RSL-AAM is promoted and sanctioned in the AASHTO LFRD Specifications and includes guidance on selecting the specific correction soil depth h^* .
- The RSL-AAM correction factor is easier to calculate than the RSL-EBM correction factor, and since RSL only corrects for one selected soil depth, the improved accuracy of RSL-EBM is somewhat irrelevant.

Step by step instructions to implement the RSL-AAM- θ^* procedure are provided below followed by short description of the RSL-EBM procedure.

RSL-AAM- θ^* . The following step-by-step procedure utilizes the AAM- θ^* equations that have been derived and discussed in Sections 8.1.4 and 8.1.5. It is assumed the live-load patch dimensions L_0 & W_0 are known along with axle-wheel spacing S .

Step 1. Select the soil depth h^* for peak-stress equivalence of 2D-strip and 3D-patch loading.

AASHTO Guidance for live loads on or near culvert centerline;

- $h^* = "H"$, Cover over crown is a Legacy AASHTO specification.
- $h^* = "H + 0.0522(\text{Span})"$, AASHTO 2014 specification with span in inches.

Common Practices for live loads located away from centerline;

- $h^* =$ Legacy or 2014 AASHTO specifications - (generally a conservative approach)
- $h^* =$ vertical distance from surface load to culvert periphery - (a more realistic approach)

Step 2. Compute the AAM- θ^* shallow-depth zone $\frac{1}{2}y^*$;

$$\frac{1}{2}y^* = \frac{1}{2}(44" \sqrt{W_0 L_0 / 200})$$

Step 3. Compute two-wheel interaction depth H_{int} ;

$$\text{If } \frac{S-W_0}{1.15} \geq \frac{1}{2}y^*, \text{ then } H_{\text{int}} = \frac{S-W_0}{1.15}$$

If $\frac{S-W_0}{1.15} < \frac{1}{2}y^*$, then $H_{int} = y$, which solves; $y(2 \tan \theta_y^*) = S - W_0$

Step 4. Evaluate the AAM- θ^* y-dependent functions θ_y^* , λ_y and r_y^* at $y = h^*$;

$$\theta_h^* = \frac{h^*}{(1/2)y^*} 30^\circ \leq 30^\circ \quad \text{AAM-}\theta^* \text{ spread angle at } y = h^*$$

$$\lambda_h = \frac{2}{1+S/(W_0 + h^*(2 \tan \theta_h^*))} \geq 1 \quad \text{Two-wheel rate factor if } h^* > H_{int}, \text{ otherwise } \lambda_h = 1$$

$$r_h^* = \lambda_h \frac{W_0}{W_0 + h^*(2 \tan \theta_h^*)} \quad \text{RSL-AAM-}\theta^* \text{ reduction factor at } y = h^*.$$

Step 5 (last). Reduce the 2D strip load by the reduction factor r_h^* ;

The actual live-load wheel pressure P_0 is scaled down by the reduction factor r_h^* so that the 2D strip pressure $r_h^*P_0$ will simulate the actual 3D patch width W_0 at soil depth h^* . In CANDE the reduced pressure loads are input as force boundary conditions (lbs/inch) on those surface nodes corresponding to the location of the L_0 footprint. Often the L_0 length is small compared to mesh-node spacing so that a single node carries the reduced in-plane load.

RSL-EBM. Since the RSL procedure only corrects the 2D strip solution for one particular depth h , there is little to be gained by using RSL in combination with the exact peak-stress EBM reduction factor equation r_y . Consequently RSL-EBM is mainly of academic interest and seldom used in practice.

Although the EBM provides an exact solution for peak stress, the EBM solution is limited to 1-wheel loading. Thus, in order to account for 2-wheel interaction, the RSL-EBM procedure borrows from the RSL-AAM- θ^* procedure to determine the two-wheel interaction depth H_{int} and the two-wheel rate factor λ_h .

With the above understanding, the step-by-step procedure for RSL-EBM procedure are:

Steps 1 to 3. Exactly the same as the RSL-AAM- θ^* steps 1, 2, and 3.

Step 4. The same as step 4 of RSL-AAM- θ^* for determining θ_h^* and λ_h . However, for reduction factor use EBM Equation 8.1-3 evaluated at $y = h^*$, i.e.,

$$r_h = \lambda_h \frac{\arctan\left(\frac{1}{h}\right) + \frac{h}{1+h^2}}{\arctan\left(\frac{\alpha}{h\sqrt{1+\alpha^2+h^2}}\right) + \frac{\alpha h}{\sqrt{1+\alpha^2+h^2}} \left(\frac{1}{1+h^2} + \frac{1}{h^2+\alpha^2}\right)} \quad \text{RSL-EBM reduction at } y = h^*.$$

Where, r_h = EBM reduction factor, at $y = h^*$.
 $h = h^*/(L_0/2) =$ non-dimensional soil depth in half-wheel lengths.
 $\alpha = W_0/L_0 =$ aspect ratio of patch width to length

Step 5 (last). The same as step 5 of RSL-AAM- θ^* except replace r_h^* with r_h .

RSL Summary. The reduced surface load procedure reduces the magnitude of the applied 2D strip loading so that the 2D soil stress at one particular soil depth h^* matches the 3D stress as predicted by AAM- θ^* or EBM load spreading theory. Consequently, the 2D soil stresses for $y < h^*$ are underpredicted and the soil stresses for $y > h^*$ are overpredicted. Since the 2D solution is only corrected for the particular depth h^* , the easier but approximate AAM- θ^* load spreading is more commonly used than the exact and more difficult EBM load spreading theory.

8.1.7 Continuous Load Scaling (CLS) Procedure

The innovative idea behind CLS versus RSL is succinctly stated as follows. Rather than reducing the live-load magnitude to correct the CANDE solution for one specific soil depth (h^*), a more realistic operation is performed within the CANDE program that amplifies the unit thickness of the plane-strain slice as a continuous function of soil depth. Said another way, the CLS procedure increases the global stiffness matrix as a continuous function of soil depth, and the live-load vector is left unchanged with the actual service live load.

The amplifying function is the inverse of the depth-dependent reduction factor equations r_y for EBM or r_y^* for AAM- θ^* . Specifically, the inverse relationship is written as,

$$a_y = \frac{1}{r_y} \quad \text{or} \quad a_y^* = \frac{1}{r_y^*} \quad \text{Equation 8.1-17}$$

where, a_y = EBM amplifying equation for all soil depths, $a_y \geq 1$
 r_y = EBM reduction factor equation defined by Equation 8.1-3.
 a_y^* = AAM- θ^* amplifying equation for all soil depths, $a_y^* \geq 1$
 r_y^* = AAM- θ^* reduction factor equation defined by Equation 8.1-16.

The amplifying functions physically represent the rate of increase of the out-of-plane footprint width, which is simulated in CANDE by increasing the unit thickness of the plane strain slice by the amplifying factor as a continuous function of depth.

Since all the theory and developments for the reduction factor equations r_y and r_y^* have already been presented, the amplifying functions used for CLS-EBM and CLS-AAM- θ^* are simply recorded below for easy reference;

CLS-AAM- θ^* . The AAM- θ^* amplifying function is given by the inverse of Equation 8.1-16 as shown below,

$$a_y^* = \frac{1}{\lambda_y} \left(\frac{W_0 + y(2 \tan \theta^*)}{W_0} \right) \quad \text{AAM-}\theta^* \text{ amplifying function} \quad \text{Equation 8.1-18}$$

where, $\lambda_y = \frac{2}{1 + S/(W_0 + y(2 \tan \theta^*))} \geq 1$ Two-wheel rate factor when $y > H_{int}$

and $\theta^* = \frac{y}{\frac{1}{2}y^*} 30^\circ \leq 30^\circ$ Spread angle, 0° to 30°

CLS-EBM. Similarly, the EBM amplifying function is the inverse of Equation 8.1-3 as shown below,

$$a_y = \frac{1}{\lambda_y} \frac{\arctan\left(\frac{1}{h}\right) + \frac{h}{1+h^2}}{\arctan\left(\frac{\alpha}{h\sqrt{1+\alpha^2+h^2}}\right) + \frac{\alpha h}{\sqrt{1+\alpha^2+h^2}} \left(\frac{1}{1+h^2} + \frac{1}{h^2+\alpha^2}\right)} \quad \text{Equation 8.1-19}$$

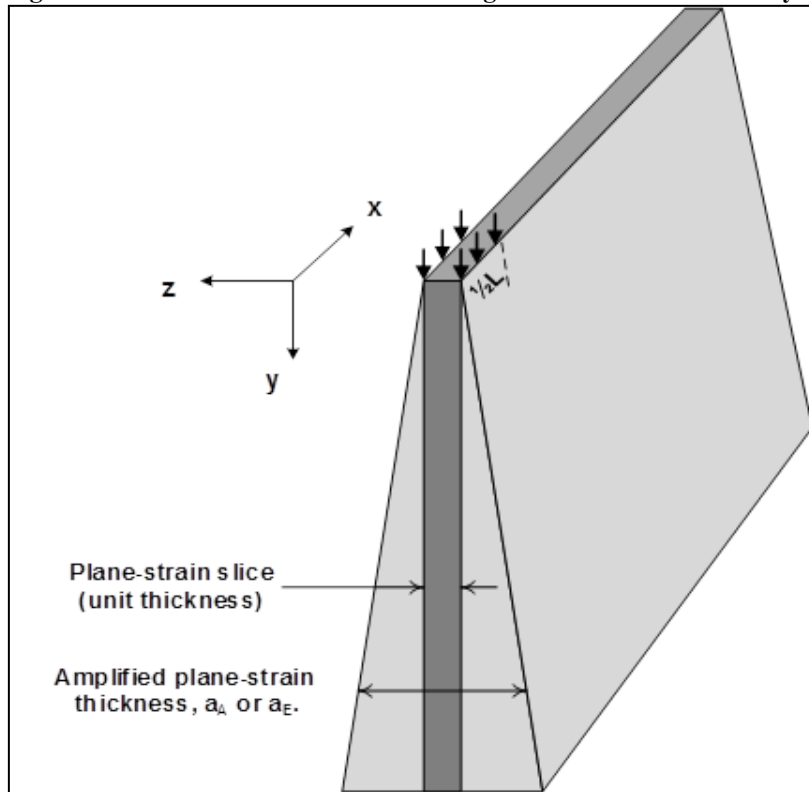
where, $h = y/(L_0/2)$ = non-dimensional soil depth in half-wheel lengths.
 $\alpha = W_0/L_0$ = aspect ratio of patch width to length
and λ_y as defined above for CLS-AAM- θ^* .

From a user's perspective, the data input for CSL is less complicated than for RSL because there is no requirement to compute reduction factors to define the surface loading magnitude. Rather, the user specifies the actual wheel-load magnitude along with wheel-axle dimensions, and the CANDE program computes the depth-dependent amplifying functions according to the user-selected method AAM- θ^* or EBM.

Like RSL, the user may activate any and all nonlinear models with CSL. The only difference is that the nonlinear models respond more realistically with CSL than with RSL. As an obvious example, consider a nonlinear soil element directly beneath the wheel load. Under the RSL approximation the stress magnitude imparted to this soil element is reduced to $r_h \cdot P_0$ instead of true stress $r_y P_0$ that is imparted by the CSL procedure.

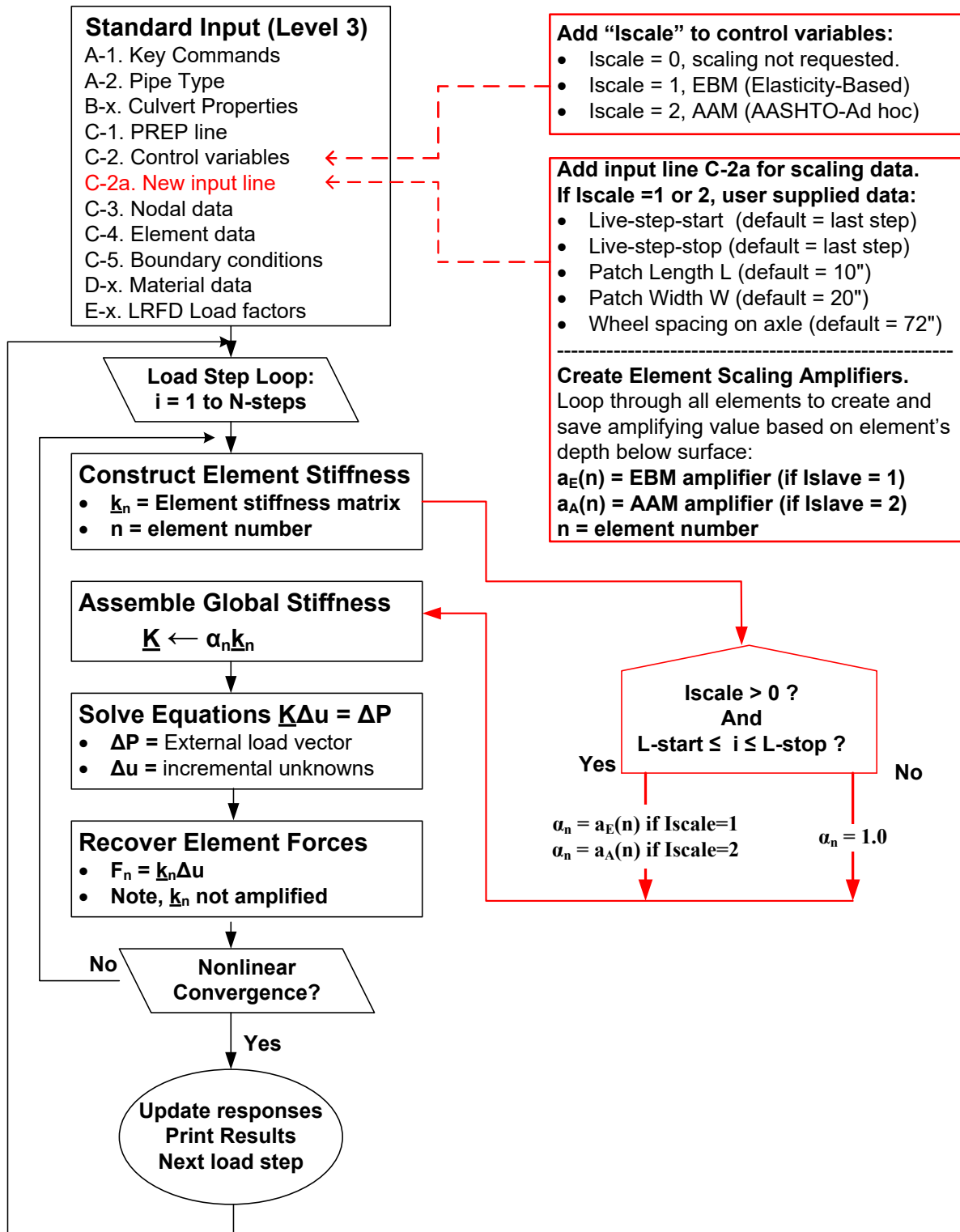
Figure 8.1-9 illustrates the depth-dependent effect of amplifying a unit with plane-strain finite element model, which is depicted as additional area outside the unit plane-strain slice. As the surface load is transmitted down through the soil and structure, load is increasingly diverted to the additional stiffness area so that the load in the original plane-strain slice is continuously reduced due to longitudinal load spreading. Consequently, the structural distress is significantly less than a standard plane-strain unit slice.

Figure 8.1-9. Illustration of CSL increasing the unit-slice thickness by the amplifying function.



CLS CANDE Modifications. The essential CANDE modification is within the subroutine that assembles the global stiffness matrix from all the individual elements. Specifically, as each element is assembled into the global stiffness matrix, whether it be continuum, structural or interface, the element stiffness is multiplied by the amplifying factor associated with the depth of the element's centroid below the surface. Physically this amplification is equivalent to increasing unit thickness of the plane-strain slice as a function of depth. Thus, upon solving the global set of equations, the computed displacement increments are progressively smaller with depth than would be achieved from the standard unit-thickness slice. Upon recovering each element's internal forces and stresses from the computed displacement increments, the original unit-thickness element stiffness matrix is employed. Figure 8.1-10 illustrates these changes in the CANDE program.

Figure 8.1-10 CANDE flow chart for implementing continuous load scaling - CLS (red boxes).



The red boxes in the above flow chart show the additional programming logic to incorporate the CLS procedure into the CANDE program and are discussed below.

1. The first red box introduces a new control parameter called “Iscale”, which must be input with a non-zero value if the user wishes to activate CLS. Otherwise, continuous scaling is not performed and the traditional RSL may be employed. Choosing Iscale = 1 activates the exact EBM amplifier, and Iscale = 2 activates the AAM- θ^* amplifier.
2. Assuming that Iscale > 0, the 2nd red box defines input to be supplied by the user. Specifically, the user identifies the starting and ending load step numbers that correlates with the live loads to be continuously scaled. Also, the wheel’s footprint dimensions L_0 & W_0 must be defined as well as the wheel spacing S on the axle. Lastly, a node on the travel surface is required to establish the surface elevation. The above data is used to compute and save the amplifying value $a_A(n)$ or $a_E(n)$ for each element n , dependent on depth of the element’s centroid. The one or two-wheel rate-increase factors $\lambda(n)$ are computed based on the element’s depth and H_{int} , which is automatically determined by CANDE
3. During the assembly of the global stiffness matrix each element stiffness matrix is multiplied by the element’s individual amplifying value providing that CLS is turned on (Iscale > 0) and the load step counter is within the range of the declared live load steps. Otherwise, the amplification factor is set to 1.0.

It is worth emphasizing that CLS does not change the algorithms for recovery of element forces or the nonlinear solution strategy. Indeed, it is important to use the original element stiffness (unit thickness) in order to properly compute the reduced internal forces resulting from the reduced displacements.

Finally, a programming subtlety not shown in Figure 8.1-10 is required for special elements based on constraint equations, such as CANDE’s interface and link elements. For these specialized elements the primary unknowns are intra-node forces, and the elements’ right-hand-side “load vector” may contain non-zero displacement gaps. In these cases, the element load vector is scaled with same amplification factor as the element stiffness matrix in order to impose the correct displacement gaps.

CLS Summary. Continuous Load Scaling is more accurate and easier to use than RSL and CLS is the recommended procedure for simulating patch loads like HL-93 truck tires. The choice of the exact EBM vs the approximate AAM- θ^* amplifying factors to be used in conjunction with CLS is largely a matter personal preference because the CANDE solutions tend to be very similar, differing by less than 5%.

8.1.8 Pavements and Live Loads (RSL and CLS)

It is well known that inserting a stiff pavement on the soil surface in the finite element model significantly reduces the culvert’s structural distress from live loads. This has been demonstrated with 3D FEM solutions and verified with field tests in the NCHRP project report on Load Rating (Reference 35), wherein the report concludes that the full benefits of pavements should be incorporated into LRFR culvert analysis software programs in order to avoid falsely predicting unsafe load rating factors.

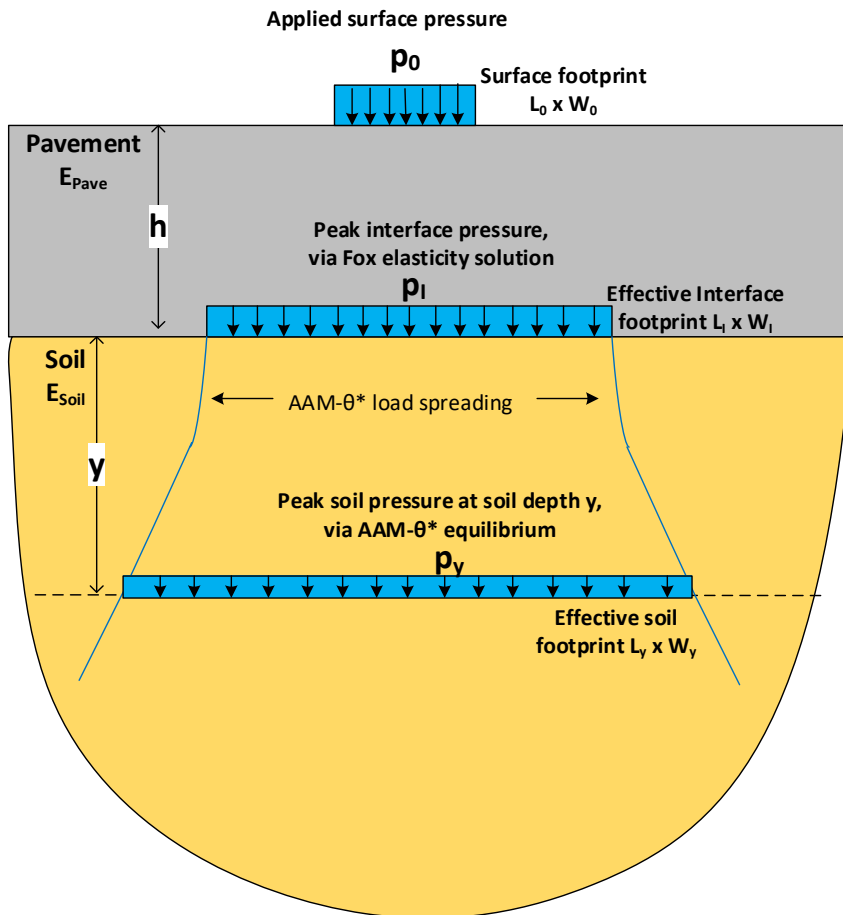
Full Benefits of Pavements. Stiff pavements reduce the culvert’s distress from live loads due to the enhanced load-spreading that occurs through the pavement’s thickness, which is significantly greater than the load spreading that would occur through the same thickness of soil. Of course, the enhanced load spreading from pavements occurs both in-plane and out-of-plane. However, 2D-FEM soil-structure models just capture the enhanced in-plane load spreading from pavements, they do not capture the enhanced out-of-plane load spreading. Thus, one option is to obtain just the partial in-plane benefit and ignore the out-of-plane benefit by using the previously established EBM or AAM- θ^* load spreading theories through a homogenous soil half-space as previously presented. However, to get the full benefits of pavements we need a new load spreading theory that includes two layers, pavement and soil. Fortunately, a limited elasticity solution developed by Fox (Reference 36) provides the required information. The Fox elasticity solution provides the peak soil stress at the pavement-soil interface for a circular loading footprint as a graphical function of the pavement thickness and the pavement-to-soil Young’s modulus ratio.

Overview for Obtaining Full Benefit of Pavements (AAMP- θ^*). The goal is to develop a combined pavement & soil load spreading methodology by coupling the Fox two-layer elasticity solution with the AAM- θ^* procedure to simulate the enhanced out-of-plane load spreading of the combined pavement-soil system. This combined methodology is called **AAMP- θ^* (P for Pavement)** and is applicable for 2D FEM analysis of soil-culvert systems using either RSL or CLS procedures.

As illustrated in Figure 8.1-11 the AAMP- θ^* methodology is a two-part process:

- Part 1 begins with a rectangular wheel footprint $L_0 \times W_0$ with uniform pressure p_0 and utilizes the Fox elasticity solution to determine the reduced peak stress p_I and increased footprint area $L_I \times W_I$ at the pavement-soil interface.
- Part 2 begins with the interface pressure patch and utilizes AAM- θ^* load-spreading theory to predict peak pressure p_y and effective footprint area $L_y \times W_y$ at any chosen soil depth y .

Figure 8.1-11 Overview of AAMP- θ^* two-part methodology

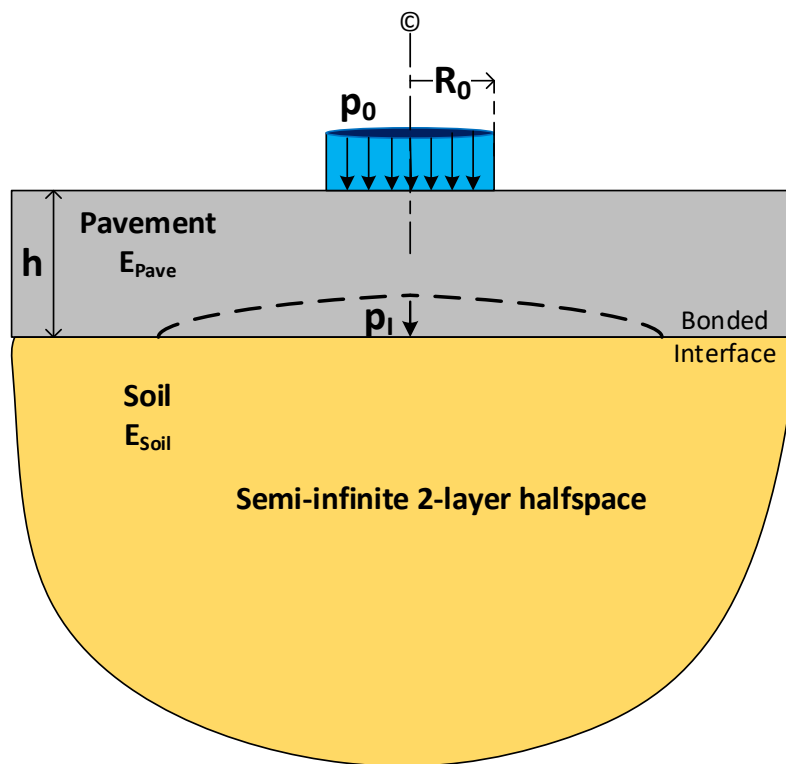


Detailed developments are presented in the following subsections wherein the subscript “0” denotes known quantities on the pavement surface, the subscript “I” denotes derived quantities at the pavement-soil interface, and the subscript “y” denotes derived quantities evaluated at soil depth y . The guiding philosophy throughout this development is to maintain accuracy while making sure that assumptions and approximations are on the conservative side to avoid over estimating the beneficial effects of pavements.

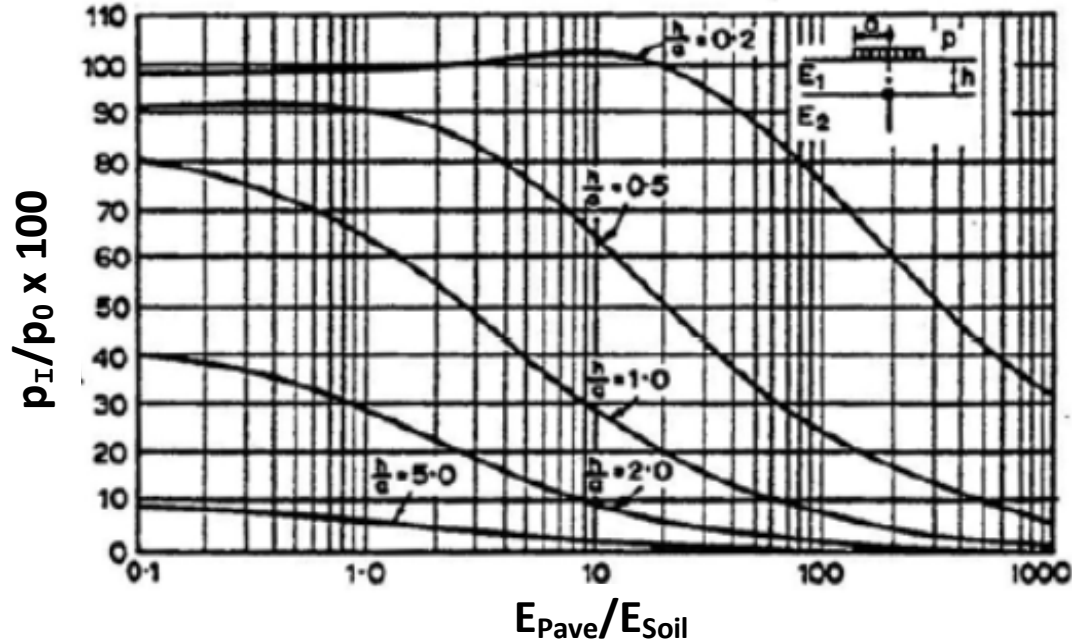
AAMP-0* Part-1: Fox two-layer elasticity problem. The two-layer elasticity problem is considerably more difficult than the homogenous EBM elastic half space problem. Consequently, a closed form elasticity solution for peak stress throughout the two-layer system is not tractable. Rather, Fox’s limited elasticity solution only provides peak stress at the pavement-soil interface in a graphical format. Moreover, the Fox elasticity problem only considers circular footprint loading so that assumptions and approximations are required to convert the Fox solution to equivalent rectangular footprints for the AAMP-0* methodology. As will be demonstrated, all assumptions and approximations are intentionally on the conservative side so that the beneficial effects of pavements are conservative and not overstated.

Figure 8.1-12 illustrates the parameters of the two-layer elasticity problem as solved by Fox. Note, the circular loading footprint is defined by the radius R_0 with uniform pressure p_0 . The pavement is defined by Young’s modulus E_{Pave} and thickness h , and the soil half-space is defined by Young’s modulus E_{Soil} . The Fox solution provides the peak stress p_I at the pavement-soil interface under the loading centerline.

Figure 8.1-12 Fox Two-layer boundary value problem with circular footprint radius R_0



Fox two-layer graphical solution for reduction factor. Figure 8.1-13 shows the Fox graphical solution for the peak vertical stress, which is presented as a reduction factor, $r_I = p_I/p_0$, that occurs directly below the loading center at the pavement-soil interface. The peak interface stress is determined graphically as a function of pavement-to-soil modulus ratio E_{Pave}/E_{Soil} along the horizontal axis for a family of five parametric curves. Each parametric curve represents a particular ratio of pavement thickness-to-loading radius. Specifically, the thickness-to-radius ratios are, $h/R_0 = 0.25, 0.5, 1.0, 2.0$ and 5.0 .

Figure 8.1-13 Fox graphical elasticity solutions for p_I/p_0 vs E_{Pave}/E_{Soil} for families of R_0/h .

Three issues exist with the Fox graphical solution as presented above with respect to the goal of this development:

- (1) We need to establish a rational method for converting Fox's circular loading area with radius R_0 to an equivalent rectangular surface loading area L_0W_0 .
- (2) Fox's graphical solution for peak stress is difficult to read and interpolate between parametric lines and curves. Hence, we need to establish a data table for reliable parameter identification and interpolation.
- (3) Given that the Fox solution will provide the correct peak pressure p_I for a set of chosen parameters, we need to devise a rational method to compute the effective AAM- θ^* footprint dimensions L_I and W_I at the interface.

These issues are resolved in a reliable and conservative manner as explained in the following developments.

Converting from circular to rectangular loading. To convert to a rectangular footprint, the Fox radius parameter R_0 needs to be expressed in terms of the specified rectangular dimensions $L_0 \times W_0$. This is achieved by equivalence of total force wherein each footprint has the same uniform pressure, which in turn requires equal area, $\pi R_0^2 = L_0W_0$, so that the characteristic radius is,

$$R_0 = \sqrt{L_0W_0 / \pi} \quad \text{Equation 8.1-20}$$

Although Equation 8.1-20 equates rectangular and circular surface loading area, an important question remains, "How does Fox's circular peak-stress solution relate to the desired rectangular solution for peak stress". This question has been answered in a previous homogenous soil investigation (Reference 34) wherein it is shown that a circular footprint produces a slightly higher peak stress than does an equivalent rectangular area for all aspect ratios in the range $\frac{1}{4} \leq W_0/L_0 \leq 4$. Specifically, the average conservative error is about 6% for the extreme aspect ratio of $\frac{1}{4}$ or 4 and reduces to near

zero error as the aspect ratio approaches 1 (square shape). In short, the Fox solution for peak interface stress applies to all practical rectangular loading patterns with the understanding the peak stress predictions are slightly conservative.

Fox solution Table for peak-stress reduction factor at interface. Table 8.1-2 contains the peak-stress reduction factors ($r_1 = p_1/p_0$) as taken from Fox's graphical Figure 8.1-13 for the five of pavement thickness-to-radius (h/R_0) parametric ratios and four pavement modulus-to-soil modulus (E_{Pave}/E_{Soil}) parametric ratios. The table encompasses the practical range of parametric ratios for all realistic pavement-soil systems.

Table 8.1-2 Fox peak-stress reduction $r_1 = p_1/p_0$, for parametric ratios of h/R_0 and E_{Pave}/E_{Soil} .

Thickness-to-Radius h/R_0 ($R_0 = \sqrt{L_0 W_0 / \pi}$)	Pavement-to-Soil Stiffness Ratio E_{Pave}/E_{Soil}			
	1	10	100	1000
0.2	1.00	1.00	0.75	0.32
0.5	0.91	0.63	0.24	0.06
1.0	0.65	0.28	0.08	0.02
2.0	0.29	0.09	0.02	0.01
5.0	0.06	0.02	0.01	0.01

Clearly the above table is easier to read than Fox's graphical figure. Moreover, linear interpolation between parametric rows of h/R_0 and/or columns of E_{Pave}/E_{Soil} may be undertaken with conservative confidence. That is, the linear interpolation between rows and/or columns results in peak stresses slightly greater than indicated by the graphical curves.

Effective footprint dimensions L_1 & W_1 at pavement-soil interface. The last issue is to determine the effective footprint dimensions L_1 and W_1 at the pavement-soil interface based on the AAM tenets. The first AAM tenet is the equilibrium equation that requires, $p_1 L_1 W_1 = p_0 W_0 L_0$. Since Table 8.1-2 accurately provides Fox's peak-stress reduction factor stress as, $r_1 = p_1/p_0$, we find total effective footprint area $L_1 W_1$ is given by,

$$L_1 W_1 = \frac{L_0 W_0}{r_1} \quad \text{Equation 8.1-21}$$

The above equilibrium equation prescribes the footprint area but not the individual dimensions L_1 and W_1 , which requires invoking the second fundamental AAM tenet that implies L_1 and W_1 increase by the same incremental amount as inferred by the common growth term, $y(2\tan\theta^*)$. To this end, let the unknown incremental amount be represented by an unknown dimensionless factor δ times the characteristic length $\sqrt{L_0 W_0}$ as shown below,

$$L_1 = L_0 + \delta \sqrt{L_0 W_0} = \beta_L L_0 \quad \text{Equation 8.1-22a}$$

$$W_1 = W_0 + \delta \sqrt{L_0 W_0} = \beta_W W_0 \quad \text{Equation 8.1-22b}$$

where, $\beta_L = (1 + \delta \sqrt{\frac{W_0}{L_0}})$ and $\beta_W = (1 + \delta \sqrt{\frac{L_0}{W_0}})$ are footprint amplification factors so that,

$$L_1 = \beta_L L_0 \quad \text{and} \quad W_1 = \beta_W W_0$$

To determine the unknown factor δ and hence the amplification factors β_L and β_W , we observe the product of Equations 8.1-22a and 8.1-22b must equal the right-hand-side of Equation 8.1-21 resulting in quadratic equation for δ that is solved in terms of the known aspect ratio W_0/L_0 & L_0/W_0 and reduction factor r_1 . Inserting the solution for δ in the above expressions for β_L and β_W , we have,

$$\beta_L = \frac{1}{2} \left(1 - \frac{W_0}{L_0}\right) + \frac{1}{2} \sqrt{\left(1 + \frac{W_0}{L_0}\right)^2 + 4 \frac{W_0}{L_0} \left(\frac{1}{r_1} - 1\right)} \quad \text{Equation 8.1-23a}$$

$$\beta_w = \frac{1}{2} \left(1 - \frac{L_0}{W_0}\right) + \frac{1}{2} \sqrt{\left(1 + \frac{L_0}{W_0}\right)^2 + 4 \frac{L_0}{W_0} \left(\frac{1}{r_1} - 1\right)}$$

Equation 8.1-23b

Table 8.1-3 presents the amplification factors β_L and β_W in a matrix format with the reduction factor (r_1) listed in rows and the initial footprint aspect ratio ($\alpha = L_0/W_0$ or W_0/L_0) listed in columns.

Table 8.1-3. Amplification factors β_L and β_W for select values of $r_1 = p_i/p_0$ and $\alpha =$ aspect ratio.

Reduction Factor $r_1 = p_i/p_0$	Aspect Ratio α : For $\beta_W \alpha = W_0/L_0$, Or for $\beta_L \alpha = L_0/W_0$						
	0.25	0.33	0.50	1.00	2.00	3.00	4.00
1.00	1.00	1.00	1.00	1.00	1.00	1.00	1.00
0.90	1.09	1.08	1.07	1.05	1.04	1.03	1.02
0.80	1.19	1.18	1.16	1.12	1.08	1.06	1.05
0.70	1.32	1.30	1.26	1.20	1.13	1.10	1.08
0.60	1.49	1.45	1.39	1.29	1.20	1.15	1.12
0.50	1.70	1.65	1.56	1.41	1.28	1.22	1.18
0.40	2.00	1.92	1.79	1.58	1.40	1.31	1.25
0.30	2.45	2.32	2.13	1.83	1.56	1.44	1.36
0.20	3.22	3.01	2.70	2.24	1.85	1.67	1.55
0.10	5.00	4.58	4.00	3.16	2.50	2.19	2.00
0.05	7.57	6.84	5.84	4.47	3.42	2.94	2.64
0.02	12.72	11.34	9.51	7.07	5.26	4.43	3.93
0.01	18.56	16.42	13.65	10.00	7.33	6.12	5.39

Table 8.1-3 is used in conjunction with reduction factor found in Table 8.1-2 to determine the corresponding effective footprint dimensions acting on the soil surface, L_1 & W_1 . For example, suppose from Table 8.1-2 we find the reduction factor $r_1 = 0.3$ with standard footprint $L_0 = 10''$ and $W_0 = 20''$. For β_L we use column $\alpha = L_0/W_0 = 0.5$ and find value $\beta_L = 2.13$. For β_W we use column $\alpha = W_0/L_0 = 2.0$ and find value $\beta_W = 1.56$. Therefore, the interface footprint dimensions are $L_1 = 2.13 \times 10'' = 21.3''$ and $W_1 = 1.56 \times 20'' = 31.2''$. Note the total area $L_1 W_1 = 21.3'' \times 31.2'' = 666 \text{ in}^2$, which is equal to $L_0 W_0 / r_1$ as required by Equation 8.1-21.

To summarize Part 1 of the 2-part AAMP- θ^* procedure, Tables 8.1-2 and 8.1-3 provides us with Fox’s correct peak interface stress p_i acting on the soil surface with effective footprint dimensions L_1 and W_1 based on AAM’s uniform pressure assumption. As previously emphasized, the assumed uniform pressure distribution is not realistic, but merely a convenient assumption to provide the correct peak stress and to account for two-wheel interaction.

AAMP- θ^* Part 2: Load Spreading through Soil beneath Pavement. As previously illustrated in Figure 8.1-11, Part 2 the AAMP- θ^* procedure is the straight forward application of AAM- θ^* load spreading through homogenous soil as previously developed in Section 8.1.4. Thus, no new derivations are required.

We begin with the interface pressure p_i and footprint dimensions $L_1 \times W_1$ as determined in Part 1 and our objective is predict the free-field peak soil stress and effective footprint area at any soil depth y , where y is measured from interface. The only change to the previously derived AAM- θ^* equations is to change the quantities with subscript 0 to subscript I, i.e., $p_0 \rightarrow p_i$, $L_0 \rightarrow L_1$, and $W_0 \rightarrow W_1$, where we have $L_1 = \beta_L L_0$ and $W_1 = \beta_W W_0$. Thus, we have the following equations;

- The AAM- θ^* shallow-depth boundary $\frac{1}{2}y^*$ and θ^* ;

$$\frac{1}{2}y^* = \frac{1}{2}(44''\sqrt{L_1 W_1/200})$$

$$\theta^* = \frac{y}{\frac{1}{2}y^*} 30^\circ \leq 30^\circ$$

Note $\frac{1}{2}y^*$ is deeper for pavements because $L_1 > L_0$ and $W_1 > W_0$.

- The two-wheel interaction depth H_{int} ;

$$\text{If } \frac{S-W_1}{1.15} \geq \frac{1}{2}y^*, \text{ then } H_{int} = \frac{S-W_1}{1.15}$$

$$\text{If } \frac{S-W_1}{1.15} < \frac{1}{2}y^*, \text{ then } H_{int} = y, \text{ which solves; } y(2 \tan \theta^*) = S - W_1$$

- Effective footprint dimensions at soil depth y ;

$$L_y = L_1 + y(2 \tan \theta^*)$$

$$W_y = W_1 + y(2 \tan \theta^*)$$

- Peak soil pressure p_y for any chosen soil depth y ;

$$p_y = p_1 \frac{L_1 W_1}{L_y W_y} \quad \text{for } y < H_{int} \text{ (1 wheel)}$$

$$p_y = 2p_1 \frac{L_1 W_1}{L_y (S+W_y)} \quad \text{for } y > H_{int} \text{ (2 wheels)}$$

Or more simply,

$$p_y = \lambda_y (p_1 \frac{L_1 W_1}{L_y W_y}) \quad \text{where, } \lambda_y = \frac{2}{1+S/W_y} \geq 1, \text{ i.e., } \lambda_y = 1 \text{ until } y \geq H_{int},$$

- Finally, for 2D FEM strip loading with surface pressure p_0 , the out-of-plane load spreading reduction factor r_y at any soil depth y is given by dividing $p_{y(3D)}$ by $p_{y(2D)}$ to get;

$$r_y = \lambda_y \frac{W_0}{W_y} = \lambda_y \frac{W_0}{W_1 + y(2 \tan \theta^*)} \quad \text{where, } \lambda_y = \frac{2}{1+S/W_y} \geq 1$$

We can replace W_0 with W_1/β_w to get the reduction factor equation expressed in terms of the interface footprint width W_1 as shown below,

$$r_y = \frac{\lambda_y}{\beta_w} \left(\frac{W_1}{W_y} \right) \quad \text{where } \lambda_y = \frac{2}{1+S/W_y} \geq 1 \quad \text{Equation 8.1-24}$$

At the pavement-soil interface where $y = 0$, we have for Equation 8.1-24; $W_y = W_1$ and $\lambda_y = 1$ (usually) so that the full benefits of pavements immediately provide a reduction factor $r_y = 1/\beta_w$ versus no reduction ($r_y = 1$) for homogenous soil without pavement.

As a closing comment it is noted that EBM could be used as an alternative to AAM- θ^* load spreading through the soil. However, since the tenets of AAM- θ^* load spreading are required to determine the interface footprint dimensions L_1 and

W_1 as well as the two-wheel interaction depth, there is little justification for using the slightly more accurate but slightly less conservative EBM theory.

Applying AAMP- θ^* in 2D-FEM Analysis: RSL and CLS: The foregoing AAMP- θ^* developments for the full benefits of pavements are applicable to RSL and CLS procedures for correcting 2D-FEM soil-structure models representing 3D patch loads on the pavement surface. For the most part these corrective procedures follow the same format as previously presented for soil-structure systems without pavements.

RSL. The RSL method reduces the actual wheel's surface pressure p_0 (or point-strip load) by the out-of-plane load spreading reduction the factor, r_{h^*} obtained from Equation 8.1-24 where $y = h^*$ is a user selected soil depth measured from the pavement-soil interface. For clarity, r_{h^*} is explicitly expressed in Equation 8.1-25 and may represent 1-wheel or 2-wheel interaction depending on the choice of h^* .

$$r_{h^*} = \frac{\lambda_{h^*}}{\beta_w} \left(\frac{W_1}{W_{h^*}} \right) = \frac{\lambda_{h^*}}{\beta_w} \left(\frac{W_1}{W_1 + h^*(2 \tan \theta^*)} \right) \quad \text{where, } \lambda_{h^*} = \frac{2}{1 + S/W_{h^*}} \geq 1 \quad \text{Equation 8.1-25}$$

As discussed in Section 8.1.6 AASHTO provides guidance on the selection h^* for various culvert installations; however, the RSL method does nothing more than adjust the magnitude of the surface live load so that the live-load induced soil-stress is corrected for the single depth h^*

The advantage of the RSL method is its simplicity, its ease of use, and its applicability to all existing plane-strain FEM programs. However, the major shortcoming of the RSL method, is that the reduction factor r_{h^*} only adjusts the 2D wheel pressure for one selected soil depth, $y = h^*$. Consequently, the 2D solution underestimates soil pressures at soil depths less than h^* and overestimates soil pressures at soil depths greater than h^* .

CLS. Continuous Load Scaling overcomes the shortcoming of RSL's one-depth correction by correcting the plane strain solution for all soil depths y in a continuous manner. As previously discussed in Section 8.1.7, CLS requires reprogramming the plane-strain program wherein the plane-strain unit slice of every element is increased (amplified) as the soil depth increases, thereby allowing the surface load to spread in the out-of-plane direction in a natural manner similar to the 3D world.

The thickness of each soil and structural element is amplified in accordance with the individual element's centroidal depth beneath the pavement-soil interface ($y > 0$). The amplification factor for each element is simply the inverse the reduction factor as given in Equation 8.1-24. Or more explicitly the amplification factor is $a_y = r_y^{-1}$ and expressed as,

$$a_y = \frac{\beta_w}{\lambda_y} \left(\frac{W_y}{W_1} \right) = \frac{\beta_w}{\lambda_y} \left(\frac{W_1 + y(2 \tan \theta^*)}{W_1} \right) \quad \text{where } \lambda_y = \frac{2}{1 + S/W_y} \geq 1 \quad \text{Equation 8.1-26a}$$

At the interface where $y = 0$ and $\lambda_y = 1$ (assuming $S/W_1 > 1$); the interface amplification is $a_i = \beta_w$ as expected. However, the exact amplification factor at the centroid of the pavement elements, which by definition are above the interface ($y > 0$) is not provided by the Fox elasticity solution. Rather, the amplification factor assigned to the centroid of all pavement elements whether they be continuum or beam-column types, is the average amplification at the pavement surface (1.0) and at the pavement bottom (β_w). Thus, the amplification for pavement element centroids is taken as,

$$a_{\text{pavement}} = \frac{1}{2}(1 + \beta_w) \quad \text{Equation 8.1-26b}$$

At present time, CANDE is the only available 2D-FEM program that has been reprogrammed to accommodate Continuous Load Scaling including the AAMP- θ^* procedure for pavements. Validation of the AAMP- θ^* procedure is demonstrated in Reference 37 wherein CANDE CLS thrust and bending stress predictions are compared with strain gage measurements from live-load field tests on a real-world corrugated steel culvert with and without a pavement. The correlation between predictions and measurements were excellent and vividly demonstrates the beneficial effect of

pavements in reducing structural distress from live loads. Using the CANDE solutions to perform an LRFR analyses of the paved and unpaved models revealed the controlling load rating factor (RF) increased by over 50% for the paved model.

8.1.9 3D Stiffness Effects and Live Loads (RSL and CLS)

The so-called 3D stiffness effect (3DSE) is not well understood by the culvert engineering community mainly because the current AASHTO LRFD Specification 4.6.2.10 does not identify the special distribution width as a 3D stiffness effect. Rather, AASHTO simply presents a special live-load distribution width for reinforced concrete box and arch culverts in shallow burial conditions without explaining the associated physics. For completeness, the AASHTO special distribution width equation is reviewed below followed by a discussion on the physical meaning behind the equation. Lastly, the 3D stiffness effect is generalized and incorporated into 2D analysis using RSL and CLS procedures.

AASHTO Review. AASHTO Section 4.6.2.10 specifies a special longitudinal distribution width for reinforced concrete box and arch culverts when the soil cover H is less than 2 feet of fill as shown below,

$$E_{Axle} = 96" + 1.44 * \text{Span} \leq 2 \text{ lay-lengths for precast culverts} \quad \text{Equation 8.1-27}$$

where, E_{Axle} = Longitudinal distribution width for axle load (inches)
 Span = Reinforced concrete box or arch span distance expressed in feet.

To be consistent with the AAM 1-wheel-load spreading width, Equation 8.1-27 may be equivalently written for 1-wheel loading as,

$$E_{Wheel} = \frac{1}{2}(96" + 1.44 * \text{Span}) \leq 1 \text{ lay-length for precast culverts} \quad \text{Equation 8.1-28}$$

where, E_{Wheel} = Longitudinal distribution width for one wheel load (inches)
 Span = Reinforced concrete box or arch span distance expressed in feet.

Dividing the truck's axle load by E_{Axle} or the truck's wheel load by E_{Wheel} produces the same line-load intensity that AASHTO recommends for 2D analysis of r/c boxes and arches when $H < 2$ feet. However, for $H \geq 2$ feet, AASHTO specifies the traditional AAM soil-spreading distribution width, W_y . As a consequence, the line-load magnitude has a jump increase at $H = 2'$ because E_{Wheel} is significantly larger than the traditional AAM soil-spreading distribution width at $H = 2$ feet. This begs many questions. First and foremost, "Where does "Equation 8.1-27" come from?"

Equation 8.1-27 originates from the PennDOT sponsored study conducted in 2004 by SGH (Reference 32). The study was motivated by PennDOT's observation that shallow buried r/c box culverts appear to be much more robust under live loading than indicated by traditional 2D analysis. To pursue this question, the PennDOT study used NASTRAN to obtain 3D finite element solutions of reinforced concrete box culverts subject to HS20 truck loads. Overall, 31 linear box and slab model configurations were analyzed with spans ranging from 8 to 24 feet and cover heights from zero to two feet. By comparing the 3D solutions to 2D solutions, the PennDOT study proposed the special distribution width given by Equation 8.1-27 so that the 2D and 3D solutions predicted comparable results for the controlling internal forces.

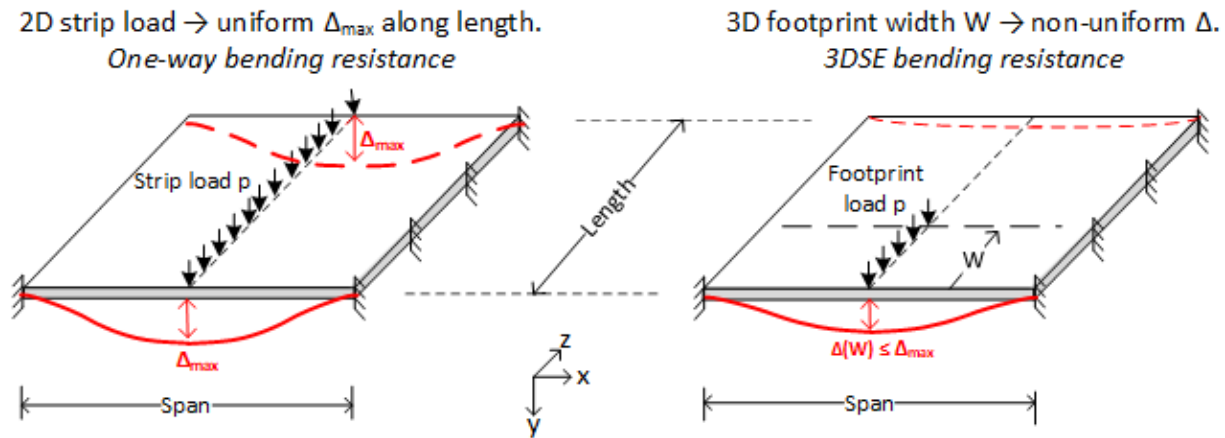
AASHTO adopted the recommendation from the PennDOT study and incorporated the special distribution width into Section 4.6.2.10 of the LRFD Bridge Specifications. However, the AASHTO commentaries do not provide a discussion on the physical meaning of this special distribution width. Clearly, the special distribution width is not related to load spreading through the soil because at the surface E_{Wheel} is much larger than the actual wheel width.

Physical Insights. The special distribution width (E_{Wheel}) compensates for the additional stiffness observed in the 3D world but is not realized in the 2D world. Said another way, the 2D model does not include the longitudinal bending and twisting stiffnesses that actually occurs when the longitudinal load width is relatively short compared to the culvert's

length. Accordingly, when the 2D model under-represents the actual stiffness, the 2D line load intensity is reduced by the W_0/E_{Wheel} so that worst-case structural response predicted by the stiffer 3D models agree with the 2D models.

The above concepts are clarified in the following paragraphs which are adapted from Reference 33. To simplify the understanding of 3DSE, consider two identical flat plates with span and length dimensions similar to the top slab of a precast box culvert. The plates are fixed along the left and right sides and free to deflect at the ends as shown in Figure 8.1-14. The left plate has a longitudinal line load of magnitude p (*force/length*) extending the entire length of the plate, and the right plate is loaded with same line load magnitude p but terminated at an arbitrary footprint width W , measured from the front end. In short, the left plate model is referred to as 2D strip loading and the right plate model as 3D footprint loading.

Figure 8.1-14. Rectangular plate model with partial and full line-load widths W with magnitude p (lbs./inch).



The red lines in the above figure illustrate the deformation patterns where the symbol Δ refers to the vertical deflection along the centerline's z axis. For the 2D strip loading, the plate deforms uniformly in one-way bending without variation along the z -axis with a constant centerline displacement Δ_{max} . Due to one-way plate bending, the deformed shape in the x - y plane is exactly equivalent to a fixed-end beam whose cross-section is a unit slice of the plate. Thus, the 2D resistance to deformation is supplied solely by the plate's in-plane bending stiffness about the z -axis.

In contrast, the 3D footprint loading produces a nonuniform deformed shape dependent on the footprint width W . The peak displacement $\Delta(W)$ occurs on the plate centerline at $z = 0$ and diminishes along the z -axis due to resisting longitudinal and twisting moments as explained by the following thought experiment. Imagine that the right plate is severed into two separate segments along the plane $z = W$ so that the forward segment contains the 3D footprint load and the rear segment is load free. Since the two plate segments are severed, no forces or moments are transmitted between the segments. Hence, the front segment deforms exactly like the 2D strip-load with uniform displacement Δ_{max} , and the rear segment is undeformed. Based on this thought experiment, we conclude that the unloaded portion of the intact plate provides additional bending and twisting stiffnesses that are not activated by the 2D strip load. This phenomenon is the meaning behind the term "3D stiffness effects" or 3DSE.

Plate Model Solution. Deeper insight into the plate's structural behavior is provided by a closed-form Ritz solution of the plate model developed by the author. The Ritz displacement solution is the product of beam-theory displacement function $\Delta(x)$ times a dimensionless function $f(z/l)$ where z is the longitudinal coordinate and l is the plate length so that $0 \leq z/l \leq 1$. The arguments of f include span-to-length ratio s/l , the footprint ratio W/l and the orthotropic bending-stiffness ratio D_x/D_z . The Ritz solution for centerline deflection is functionally expressed by Equation 8.1-17 assuming isotropic bending stiffness, $D_x = D_z = D$.

$$\Delta(z) = \Delta_{\text{max}} f\left(\frac{z}{l}, \frac{W}{l}, \frac{s}{l}\right) \quad \text{Equation 8.1-29}$$

- Δ_{max} = maximum 2D centerline displacement (same as beam theory for unit slice)
- p = line-load intensity (force per unit length)
- s = span of plate in x direction
- l = length of plate in z direction
- $D = EI/(1-\nu^2)$ = isotropic plate bending stiffness per unit width about x or z axis.
- f = dimensionless longitudinal function, range $0 \leq f \leq 1$.
- W/l = percentage of load footprint over plate length, $0 \leq W/l \leq 1$.

The dimensionless function f is fully expressed via Reference 33 and not written explicitly here because it is a cumbersome expression that provides little insight without visually plotting the behavior for various footprint widths, to be shown in the next section. However, for the special case $W = l$ (i.e., 2D strip load), then the function $f(z/l) \equiv 1$ for all z so that the above equation becomes $\Delta(z) = \Delta_{max}$ where Δ_{max} is given by simple beam bending theory as shown below.

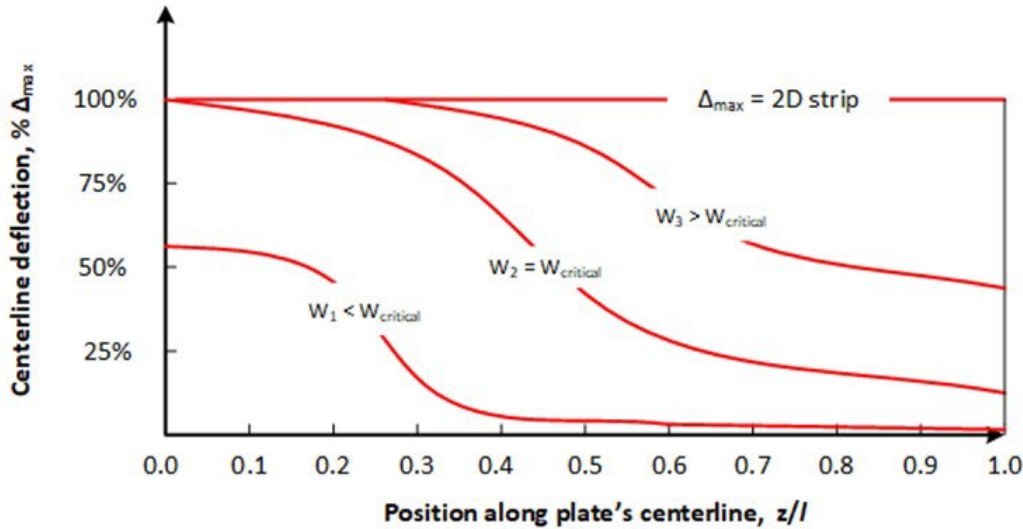
$$\Delta(z) = \Delta_{max} = p \frac{s^3}{192D} \tag{Equation 8.1-30}$$

Results from the plate model solution are used to define two important parameters that establish the load-width range of 3DSE influence. These two important parameters are called $W_{critical}$ and W_{min} .

Introducing $W_{critical}$. The critical distribution width called $W_{critical}$ is succinctly defined as follows. $W_{critical}$ is the minimum longitudinal footprint width W that produces a peak 3D displacement in the x-y plane at $z = 0$ that is equal to the displacement of the equivalent 2D unit slice with the same loading. Accordingly, when $W \geq W_{critical}$, 3DSE no longer has an impact on the 2D solution, rather only standard load spreading methods are required to adjust the 2D analysis. However, when $W < W_{critical}$, the benefits of 3DSE should be taken into account to correct the 2D analysis. Thus, $W_{critical}$ is the load width beyond which 2D solutions no longer benefit from 3DSE as illustrated next with plots of the plate model.

Figure 1.8-15 shows centerline displacement profiles $\Delta(z)/\Delta_{max}$ for three increasing sizes of 3D footprints; $W_1 < W_{critical}$, $W_2 = W_{critical}$, and $W_3 > W_{critical}$. Also shown is the uniform maximum 2D displacement profile when $W = l$. Keep in mind that all footprint widths are directly impinging on the plate surface with the same line-load intensity p acting over each width. Therefore, the successive curves may be interpreted as increasing load widths due to longitudinal load spreading; however, the load intensity p is held constant.

Figure 8.1-15 Deflection profiles (symmetric half) for four key choices of W .



As previously defined and implied in the above figure, $W_{critical}$ is the minimum distribution width producing a peak 3D displacement at $z = 0$ that is equal to the uniform maximum 2D displacement, Δ_{Max} . $W_{critical}$ is determined by forming the displacement ratio shown below and incrementally increasing the value of W until the ratio is equal to 1.

$$W_{\text{critical}} = \text{minimum } W \text{ such that } \frac{\Delta(W)}{\Delta_{\text{Max}}} = 1 \quad \text{Equation 8.1-31}$$

There is nothing magic about peak displacement because any other key structural response (e.g., maximum positive moment, maximum negative moment or peak shear) could be used in the above equation to produce the same value for W_{critical} . Note that W_{critical} is a physical property of the slab (culvert) irrespective of the soil or burial depth. Moreover, since W_{critical} is determined from a ratio as shown above, W_{critical} is not influenced by linear plate parameters such as plate stiffness because these parameters cancel out in the ratio. For an isotropic plate, W_{critical} is only dependent on span and length.

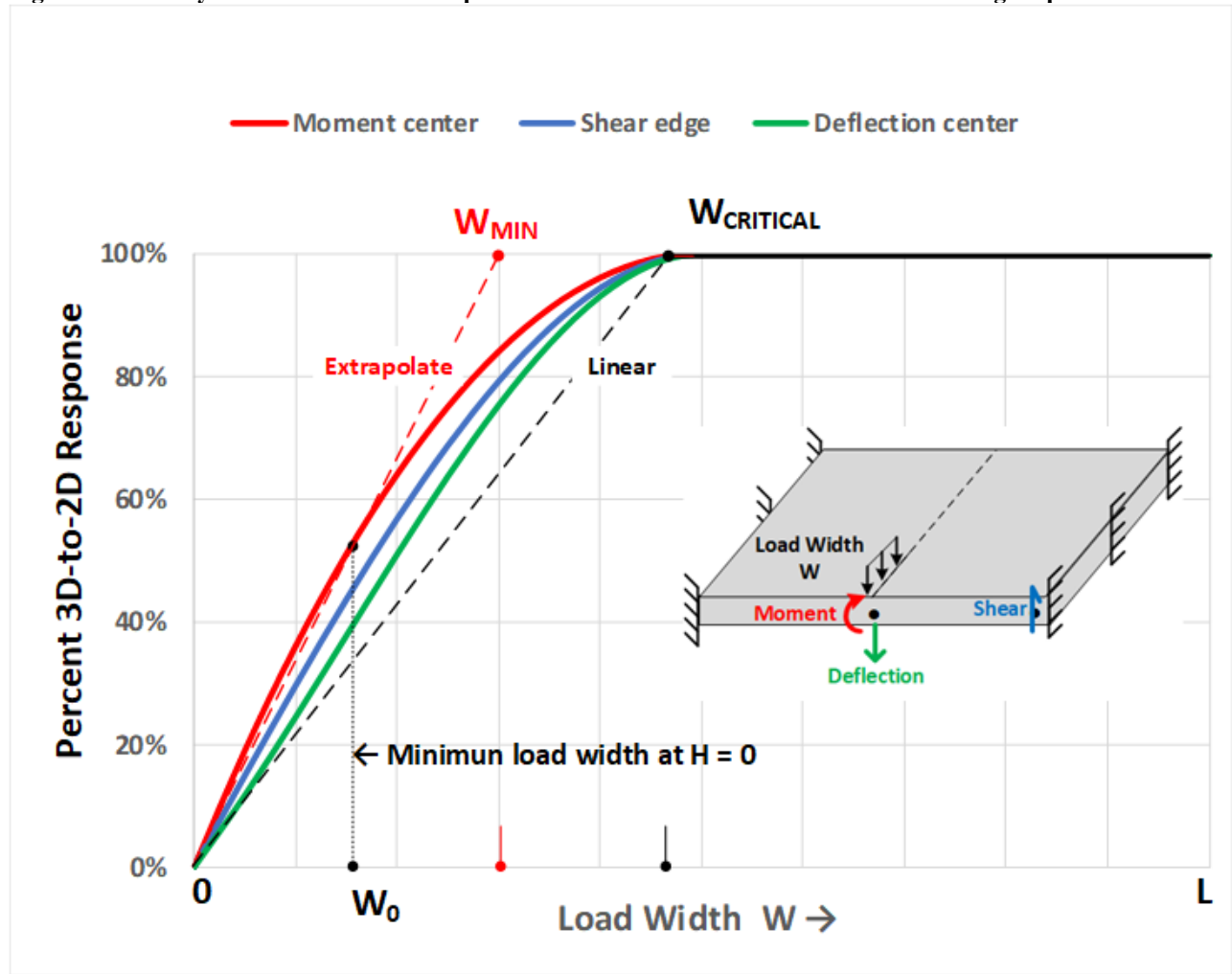
Once W_{critical} is known for a class of culverts, it is used in 2D analysis to define the transition soil depth, denoting the end of 3DSE benefits and the start of pure load spreading. The soil zone above the transition soil depth is where 3DSE controls the distribution width, and the soil zone below the transition soil depth is where standard load spreading controls the distribution width. When the structure has zero soil cover, the effective 3DSE distribution width is called W_{min} and is defined in the following section.

Introducing W_{min} . W_{min} is the minimum 3DSE distribution width associated with the minimum possible load width W_0 acting on the culvert. Like W_{critical} , W_{min} is a culvert property and is determined with aid of 3D solutions based on the worst-case 3D-to-2D structural response ratio as will be illustrated with the aid of the plate model Ritz solutions.

Figure 8.1-16 shows 3D-to-2D response ratios as function of load width W for 3 key structural responses in the transverse plane at $z = 0$; deflection at center, moment at center and shear at edge. Initially these key response ratios form distinct nonlinear curves with steep slopes that gradually decreases to zero as W approaches W_{critical} . When $W \geq W_{\text{critical}}$, all 3D-to-2D ratios are equal to 1.0, indicating the entire transverse section at $z = 0$ is distressed exactly like the 2D slice.

On the other hand, when $W < W_{\text{critical}}$ it is evident that 3D stiffness effects reduce the key structural responses in the 3D plate in comparison to the more-distressed 2D slice with same load intensity p . However, the 3DSE benefit is not the same for each key structural response; hence the highest curve (worst case) is used to conservatively determine W_{min} for load width W_0 . This procedure is illustrated in Figure 8.1-16.

Figure 8.1-16 Key 3D-to-2D structural response ratios versus load widths from 0 to L acting on plate.



In the above illustration, it so happens that the controlling key response ratio is “center moment” whose 3D-to-2D response ratio is 0.53 based on the wheel’s minimum load width W_0 . Therefore, to adjust the over-loaded 2D solution to replicate the worst-case 3D solution, the 2D surface pressure p is reduced by the factor, $r = 0.53$. Or, in terms of reduction factors based on footprint ratios, we have $r = W_0/W_{min} = 0.53$. This example demonstrates the concept of W_{min} and provides the logic behind the formal definition given below that is applicable to any culvert.

$$W_{min} = \frac{W_0}{\text{Controlling 3D/2D ratio}} \tag{Equation 8.1-32}$$

Where the controlling 3D/2D ratio is determined by finite element investigations for various classes of culverts, to be discussed.

To summarize, the proposed 3DSE distribution width starts at W_{min} on the soil surface ($H = 0$) and expands to $W_{critical}$ at the transition soil depth $H = H_{Trans}$ where load spreading $W(H_{Trans})$ is equal to $W_{critical}$. As a side comment, it interesting to note that if all the key structural response ratios increased linearly from $W = 0$ to $W_{critical}$ as indicated by the dashed line in the above figure, then the 3DSE distribution width would remain constant with $W_{min} = W_{critical}$.

Complete details for implementing 3DSE into the improved RSL and CLS procedures are presented in the next two sections. To this end, W_{min} and $W_{critical}$ are viewed as known quantities for the particular class of culverts being analyzed.

The final section discusses the current and future status of quantifying W_{min} and $W_{critical}$ for all culverts.

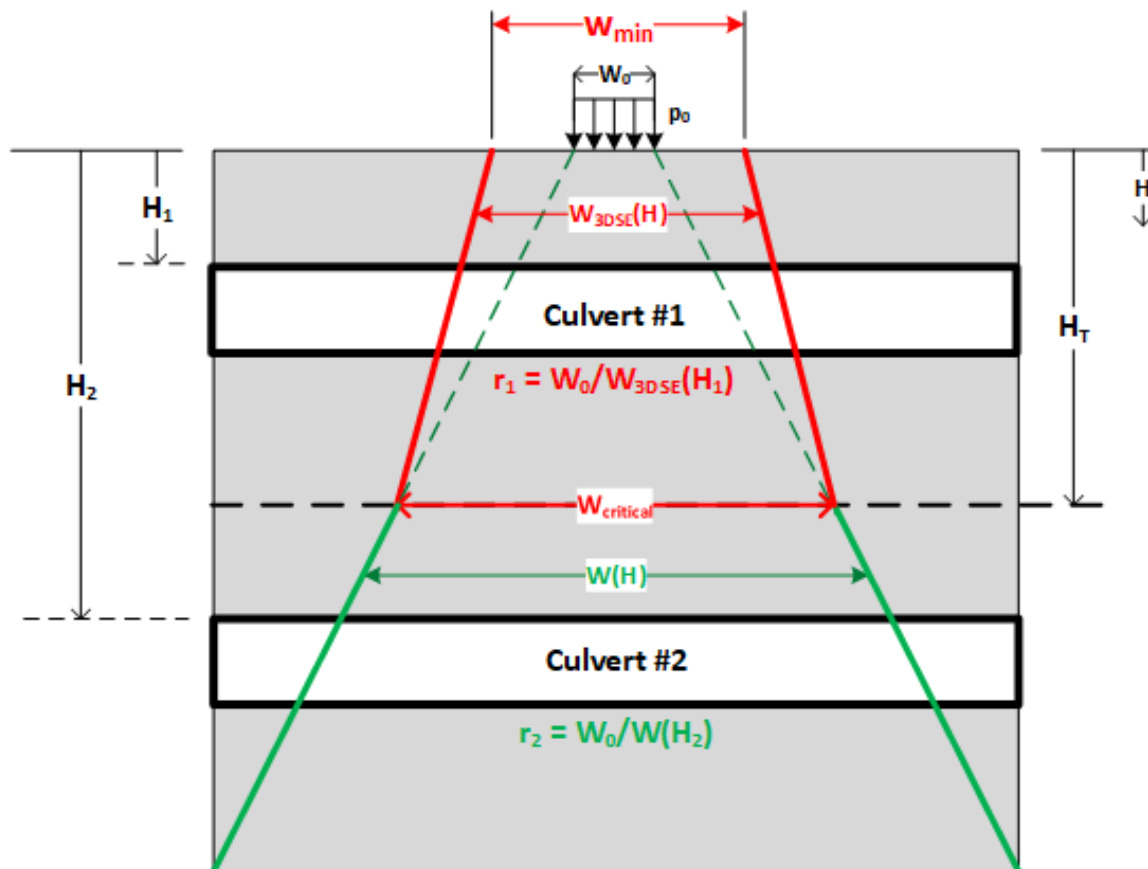
Revised RSL Procedure accounting for 3DSE. Recall that the traditional RSL procedure for “load spreading only” is summarized in Section 8.1.6 for AAM and EBM load spreading theories. The revised RSL procedure presented here melds 3DSE with load spreading in a consistent and seamless manner based on W_{min} and $W_{critical}$.

Figure 8.1-17 illustrates the revised procedure by showing the longitudinal view of two identical culverts, one representing shallow burial at depth H_1 and the other representing deeper burial at depth H_2 . A wheel load with line intensity p_0 is applied to the surface. The figure’s red lines define the special 3DSE distribution width denoted as $W_{3DSE}(H)$ that linearly increases from W_{min} on the surface to $W_{critical}$ at the transition depth ($H = H_{Trans}$), Thus the 3DSE distribution width is given by,

$$W_{3DSE}(H) = W_{min} + \frac{H}{H_{Trans}}(W_{critical} - W_{min}) \tag{Equation 8.1-33}$$

Shown with solid green lines is the load-spreading distribution width $W(H)$ representing the selected load spreading theory such as AAM or EBM as previously described. The red and green distribution widths are equal at the transition soil depth H_{Trans} where $W(H_{Trans}) = W_{critical}$, thereby ensuring continuity from the 3DSE zone to the load-spreading zone.

Figure 8.1-17 Longitudinal view of shallow and deeply buried culverts for improved RSL analysis.



The RSL procedure for 2D analysis simply requires determining a reduction factor for the surface line load that is dependent on a selected soil depth H , usually taken at or slightly below the cover over crown. For example, culvert #1 in the above figure with crown cover H_1 is governed by the 3DSE distribution width $W_{3DSE}(H_1)$, whereas culvert #2 with crown cover H_2 is governed by the load spreading width $W(H_2)$.

In short, the reduction factor for the improved RSL method for any particular choice of H is given by the alternatives in the equations below as governed by the transition depth H_{Trans} .

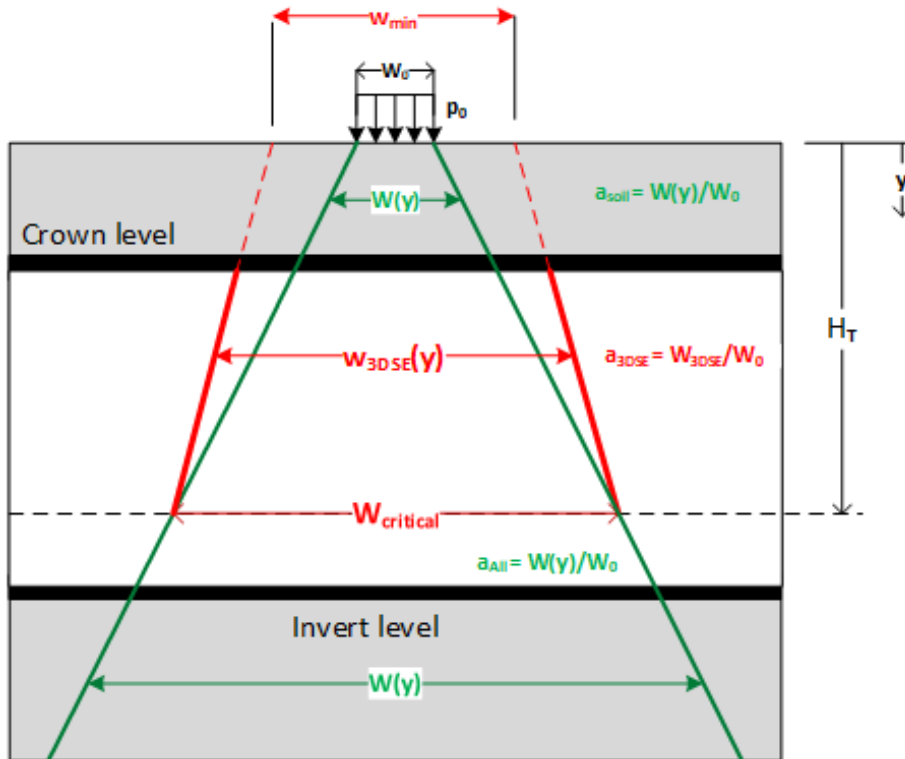
$$r(H) = \begin{cases} W_0/W_{3DSE}(H) \rightarrow \text{if } H < H_{Trans} \\ W_0/W(H) \rightarrow \text{if } H \geq H_{Trans} \end{cases} \quad \text{Equation 8.1-34}$$

Note that the load spreading width $W(H)$ is always taken as the load spreading width beneath one wheel for all depths H. Thus, if H is greater than the 2-wheel interaction depth, then $W(H)$ is taken as one-half of the combined two-wheel footprint width. It is understood that W_{min} and $W_{critical}$ are determined from 3D analysis accounting for full axle loading.

It is informative to consider the physical soil pressure acting upon the crowns of culvert #1 and culvert #2. The bottom culvert experiences a uniform reduced pressure distribution between the solid green lines. In contrast, the top culvert only experiences actual soil pressure between the dashed green lines. The additional distribution width to the solid red lines artificially increases the reduction factor to account for actual 3DSE behavior that is invisible in a 2D unit slice model. These incongruities do not occur with the CLS procedure, presented next.

Revised CLS Procedure accounting for 3DSE Recall that the CLS procedure for “load spreading only” is summarized in Section 8.1.7 for both AAM and EBM load spreading theories. The revised CLS procedure as presented here incorporates the additional 3DSE zone directly into the culvert element 2D stiffness matrices while at the same time simulating load spreading throughout the 2D soil-structure slice in a continuous manner. To emphasize the continuous nature of CLS versus RSL, the depth variable is denoted as y instead of H (specified depths) as shown in Figure 8.1-18.

Figure 8.1-18 Longitudinal view of a buried culvert for the improved CLS analysis procedure.



The above figure shows the longitudinal view of a culvert, wherein the solid red lines define the special 3DSE distribution width denoted as $W_{3DSE}(y)$ that linearly increases from W_{min} on the surface ($y = 0$) to $W_{critical}$ at the transition depth ($y = H_{Trans}$). Shown with solid green lines is the load spreading distribution width $W(y)$ representing the selected load spreading theory such as AAM or EBM as previously described. The red and green distribution widths are equal at the

transition soil depth H_{Trans} where by definition $W(H_{\text{Trans}}) = W_{\text{critical}}$, thereby ensuring continuity from the 3DSE zone to the load-spreading zone.

CLS mimics reality by amplifying the unit thickness (stiffness) of every soil element by the load-spreading amplification ratio $W(y)/W_0$. To account for 3DSE, which is strictly a property of the culvert, the superiority of CLS procedure becomes evident. Specifically, the stiffness of culvert elements above the transition depth H_{Trans} are amplified by the 3DSE ratio $W_{\text{3DSE}}(y)/W_0$, whereas the culvert element stiffnesses below H_{Trans} are amplified for load spreading only, $W(y)/W_0$.

To summarize, the CLS amplification factors are not only dependent on each element's depth below the surface, but also dependent on the type of element, soil or structure, as summarized below.

For each soil element the amplification factor is given by,

$$a(y) = \frac{W(y)}{W_0} \quad \text{where } y = \text{soil element's depth.} \quad \text{Equation 8.1-35a}$$

And for each culvert element the amplification is dependent on H_{Trans} and is given by,

$$a(y) = \begin{cases} W_{\text{3DSE}}(y)/W_0 & \rightarrow \text{if } y < H_{\text{Trans}} \\ W(y)/W_0 & \rightarrow \text{if } y \geq H_{\text{Trans}} \end{cases} \quad \text{where } y = \text{culvert element depth.} \quad \text{Equation 8.1-35b}$$

$$\text{in which, } W_{\text{3DSE}}(y) = W_{\text{min}} + \frac{y}{H_{\text{Trans}}}(W_{\text{critical}} - W_{\text{min}}) \quad \text{Equation 8.1-35c}$$

To remain consistent for all measures of load and distribution widths, $W(y)$ is defined as the soil-spreading width (AAM or EBM) beneath one wheel. Therefore, $W(y)$ is taken as one-half of the combined two-wheel footprint width when y is greater than the 2-wheel interaction depth, H_{int} . Accordingly, W_{min} and W_{critical} are culvert properties representing 3DSE widths associated with one wheel; however, the size of W_{min} and W_{critical} is influenced from two-wheel axle loading. This concept is fully explained in Reference 33 by describing how 3D FEM programs should be used to determine W_{min} and W_{critical} for any class of culverts.

Lastly, recall that Section 8.1.7 provided a detailed flow-chart on modifying the CANDE program to perform CLS for soil-load-spreading. Inspecting this flow chart, it should be evident that only small changes in the logic are needed to include the 3DSE amplification factor in accordance with Equation 8.1-35b. Accordingly, the revised CANDE-2022 program includes the CLS-3DSE option and is available at the CANDE website, CandeForCulverts.com. Refer to the CANDE-2022 User Manual, Level 3, line C-2 to activate the CLS options. Not too surprisingly, preliminary live-load studies comparing RSL versus CLS predictions for r/c box and arch culverts indicate CLS solutions are more accurate.

Current and future determination of W_{min} and W_{critical} . Currently, the only “sanctioned equation” for quantifying W_{min} is the AASHTO special distribution width for r/c boxes and arches, denoted as E_{Wheel} in Equation 8.1-28. It can be rigorously proven that the calculation procedure for E_{Wheel} is exactly equivalent to W_{min} as defined by Equation 8.1-32. AASHTO does not currently employ a parameter equivalent to W_{critical} . Rather, AASHTO assumes the 3DSE distribution width remains constant and equal to W_{min} . Therefore, to mimic current AASHTO using the new improved RSL and CLS procedures, W_{critical} is set equal to W_{min} and quantified by the following AASHTO equation.

$$W_{\text{min}} = W_{\text{critical}} = \frac{1}{2}[96" + 1.44*\text{Span}(\text{ft})] < 1 \text{ lay length (inches)} \quad \text{Equation 8.1-36}$$

The consequence of choosing $W_{\text{critical}} = W_{\text{min}}$ instead of a realistic larger value is that the 3DSE distribution widths are shorter than reality. Hence, this is a conservative approximation, which may be acceptable for design purposes but not desirable for load rating if false no-go rating factors are predicted.

The NCHRP project 15-54 final report made recommendations to AASHTO for improving 2D analysis procedures for load rating. The revised RSL and CLS procedures using W_{\min} and W_{critical} are compatible with the NCHRP 15-54 recommendations, and the recommendations to AASHTO include the following.

- Allow for the smooth transitions from 3DSE distribution width to soil load spreading depth at the proper transition soil depth. That is, eliminate the arbitrary and discontinuous transition depth at 2 feet.
- Pursue further research on r/c box culverts that include investigating the influence of span and lay length on the 3DSE distribution widths. (The original PennDOT study did not investigate the important effect of box lay length).
- Encourage new research on r/c arches to establish 3DSE distribution widths as a function of span and lay length. (The original PennDOT study did not investigate arch shapes, arches were simply assumed to behave like a box.)

Undoubtedly, future research efforts will continue to investigate the benefits of 3DSE for other culvert materials and shapes beyond r/c boxes and arches. To this end, Reference 33 provides a comprehensive step-by-step procedure for using 3D FEM programs to develop equations for W_{\min} and W_{critical} as function of gross geometry for each class of culverts.

The beauty of the CANDE-2022 program is that it can account for 3DSE benefits for any class of culverts providing there exists reliable equations for W_{\min} and W_{critical} for the culvert class being analyzed.

8.1.10 Big Picture Summary for Live Loads

It is recognized that this entire sub-chapter on Live Loads has introduced many new concepts for realistically modeling live loads in a 2D plane-strain FEM program. This big-picture summary simplifies, clarifies and recommends specific methods for the CANDE analysis of buried culverts with live loads. To begin with, it is strongly recommended to use AAM- θ^* theory for load-spreading through soils augmented by the two-step AAMP- θ^* theory when pavements are included in the CANDE model. These theories have been shown to be slightly conservative and acceptably accurate. In contrast, the older AAM-30° theory should not be used because of its large non-conservative error in the shallow-depth zone. Although EBM is the most accurate load spreading theory and of academic interest, it is not recommended for practical applications because the equation is cumbersome and requires using AAM tenets for 2-wheel interaction depth.

Perhaps the most confusing aspect of live-load corrections for 2D analysis is the distinction between AAM- θ^* load spreading through soil versus AASHTO's special 3DSE distribution widths for r/c box and arch culverts. These two distinctly different phenomena and their interactions are reviewed and fully explained in the following figures and discussions.

Review and Conceptual Overview. Figure 8.1-19 shows an out-of-plane view of a vehicle's axle with two wheels of width W_0 , that are spaced by a distance S between wheel centers, and acting on a pavement surface. Also shown are key soil-depth parameters, effective AAM- θ^* footprint widths, and 3DSE distribution widths. Summarized below are the definitions and equations associated with these variables as previously developed.

Key soil-depth parameters (vertical depths from soil surface in Figure 8.1-19)

- $\frac{1}{2}y^* = \frac{1}{2}(44 + \sqrt{L_1 W_1 / 200})$. AAM- θ^* shallow-depth zone limit (all units in inches).
- $H_{\text{int}} = y\text{-depth satisfying, } y(2\tan\theta_y^*) - (S - W_1) = 0$. The two-wheel interaction depth.
- $H_{\text{trans}} = y\text{-depth satisfying, } y(2\tan\theta_y^*) - (W_{\text{critical}} - W_1) = 0$. The 3DSE transition depth.

Effective load-spreading footprint widths (red line widths in Figure 8.1-19):

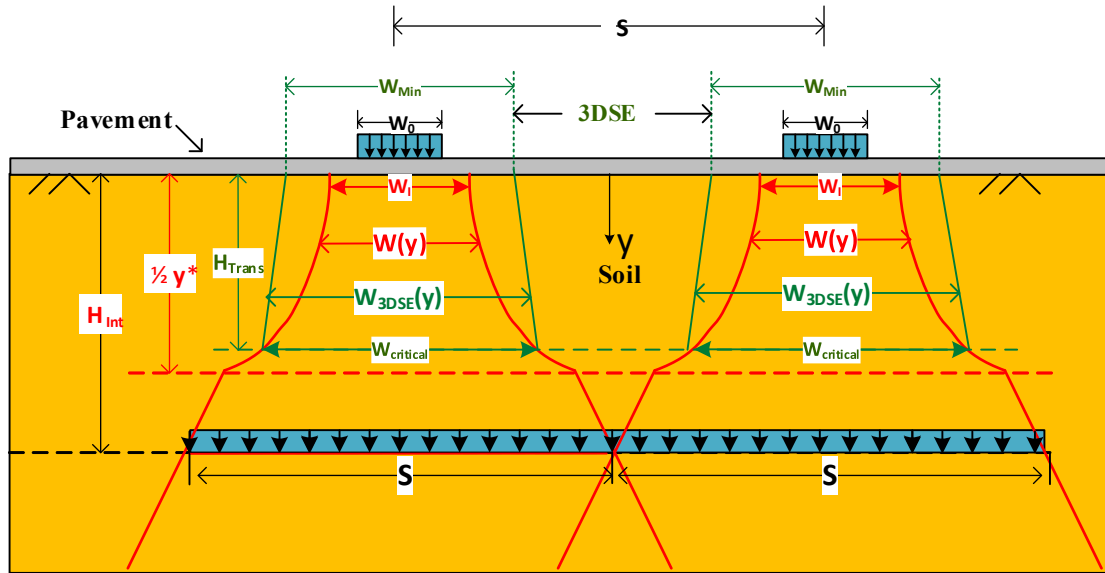
- $W_0 =$ Out-of-plane wheel width on loading surface, a specified value
- $W_1 = \beta_w W_0$. Effective wheel width at pavement-soil interface (β_w factor determined from Tables 8.1-3)

- $W(y) = W_1 + y(2\tan\theta_y^*)$. Single wheel AAM- θ^* effective footprint at depth y

3DSE distribution widths (green line widths in Figure 8.1-19):

- $W_{min} =$ AASHTO Specified 3DSE distribution width for W_0 wheel on surface, a culvert property.
- $W_{critical} =$ Load-spread width where 2D response is equal to maximum 3D response, a culvert property.
- $W_{3DSE}(y) = W_{min} + \frac{y}{H_{Trans}}(W_{critical} - W_{min})$. The 3DSE distribution width as a function of depth y .

Figure 8.1-19. Big picture illustration of key soil-depth parameters and effective distribution widths.



The red lines in the above figure depict the effective AAM- θ^* footprint width $W(y)$ in the soil beneath each wheel. On the soil surface where $y = 0$, we have $W(0) = W_1 = \beta_W W_0$, wherein $\beta_W = 1$ if there is no pavement, otherwise β_W is determined from Table 8.1-3 in combination with the peak pressure reduction at the pavement-soil interface determined from Table 8.1-2. At soil depth $y = \frac{1}{2}y^*$, the load spreading angle θ^* becomes a constant 30° so that $W(y)$ increases linearly for all $y > \frac{1}{2}y^*$. At the two-wheel interaction depth where $y = H_{int}$, we have $W(H_{int}) = S$, and the two separate wheel footprints merge into one long effective footprint with full axle load. Note that the above figure happens to depict H_{int} occurring at a deeper depth than the shallow zone limit $\frac{1}{2}y^*$; however, this not always the case, particularly when very stiff pavements result in large β_W values.

In contrast to the red lines, the green lines represent the 3DSE distribution width $W_{3DSE}(y)$ that accounts for a culvert’s additional out-of-plane stiffness properties in resisting longitudinal bending and twisting. On the soil surface $W_{3DSE}(y)$ is equal to W_{min} and increases linearly to $W_{critical}$ at $y = H_{Trans}$. By definition $W_{critical}$ is the minimum effective AAM-footprint width $W(y)$ acting on the culvert such that the peak 3D responses are equal to the uniform 2D responses. Thus, H_{Trans} is the soil depth that satisfies the equation $W(H_{Trans}) = W_{critical}$.

At present time, AASHTO only acknowledges 3DSE benefits for r/c box and arch culverts wherein $W_{min} = W_{critical}$ and is specified as, $W_{min} = W_{critical} = \frac{1}{2} (96" + 1.44 * \text{Span}(\text{ft})) < 1 \text{ lay length}$, Note Span is in feet but 3DSE widths are in inches.

Consistency check on 3DSE. As portrayed in Figure 8.1-19, the 3DSE transition depth H_{Trans} is correctly shown to be less than the two-wheel interaction depth H_{Int} , which is equivalent to saying $W_{critical}$ is less than the spacing S between wheels. At first thought it may seem reasonably possible to have $H_{Trans} > H_{Int}$, but this possibility is physically rejected

because when $y \geq H_{\text{int}}$ the two footprints merge into one large footprint such that $W(y) \geq 2S$. Under the reasonable assumption that $W_{\text{critical}} < 2S$, it is concluded that any potential benefits from 3DSE should not extend beyond $y = H_{\text{int}}$.

The above argument provides the rationale behind the 3DSE consistency check expressed below;

$$W_{\text{critical}} \leq S, \text{ and consequently } H_{\text{Trans}} \leq H_{\text{Int}} \quad \text{Equation 8.1-37}$$

Or stated more directly, if the specified value of W_{critical} is greater than S , then reset the value of W_{critical} equal to S . Note that redefining W_{critical} does not apply to W_{min} , i.e., W_{min} retains its original specified value.

The foregoing big-picture review (Figure 8.1-19) describes and illustrates the interactions between the potential 3DSE benefit and the ever-present AAM- θ^* load spreading benefit. To utilize these corrective benefits in a CANDE analysis the fundamental issue is to ascertain which benefit controls, 3DSE or AAM- θ^* . As always, the user has the option to apply the controlling benefit in the CANDE analysis using either RSL or CLS procedures, as discussed next.

Big-Picture RSL Procedure. The reduced surface load (RSL) procedure, which is fully developed in Section 8.1.6, reduces the 2D surface loading by the reduction factor of the controlling benefit (3DSE or AAM- θ^*) at a user-selected soil depth, $y = h^*$. To this end, it is presumed that the following parameters have been identified and calculated: vehicle data; W_0 and S , AAM- θ^* parameters; $W_I = \beta_W W_0$, $\frac{1}{2}y^*$ and H_{int} , and 3DSE parameters; W_{min} , W_{critical} and H_{Trans} .

With the above understanding on the choice of h^* , the RSL method proceeds as follows:

- 1) Evaluate effective AAM- θ^* load spreading width at $y = h^*$.

- $\theta_h^* = \frac{h^*}{(1/2)y^*} 30^\circ \leq 30^\circ$ AAM- θ^* spread angle at $y = h^*$
- $W(h^*) = W_I + h^*(2\tan\theta_h^*)$ AAM- θ^* spread width at $y = h^*$

- 2) Evaluate 3DSE distribution width at $y = h^*$.

- $W_{\text{3DSE}}(h^*) = W_{\text{min}} + \frac{h^*}{H_{\text{Trans}}}(W_{\text{critical}} - W_{\text{min}})$

- 3) Determine the single wheel controlling footprint width at depth $y = h^*$,

- $W_{\text{Control}} = \text{Max}(W(h^*), W_{\text{3DSE}}(h^*))$

- 4) Compute reduction factor r_y dependent on 1 or 2-wheel interaction,

- If $h^* \leq H_{\text{int}}$, $r_h^* = \frac{W_0}{W_{\text{Control}}}$ --- reduction applied to loaded surface nodes
- If $h^* > H_{\text{int}}$, $r_h^* = \frac{2W_0}{W_{\text{Control}} + S}$ --- reduction applied to loaded surface nodes

As previously stated, the shortcoming of the RSL procedure is that the magnitude of the live-load soil pressure is corrected for just the single soil depth h^* . For soil depths less than h^* , the 2D soil pressures are less than actual (unconservative), and for soil depths greater than h^* , the 2D soil pressures are greater than actual (conservative). Moreover, the RSL procedure is insensitive to the controlling benefit whether it be AAM- θ^* load spreading through soil or 3DSE stiffness enhancement of the culvert. These shortcomings are overcome with the physically correct CLS procedure discussed next.

Big-picture CLS Procedure. The continuous load scaling (CLS) procedure, which is fully developed in Section 8.1.7, is a more accurate methodology than RSL. Moreover, CLS is easier to use than RSL because the new CANDE-2022 program performs all the required calculations internally. CLS closely mimics reality by amplifying the unit thickness (stiffness) of every soil element by the load-spreading amplification ratio $W(y)/W_0$. To account for 3DSE, which is strictly a property of the culvert, the superiority of CLS procedure becomes evident. Specifically, the stiffness of culvert elements above the transition depth H_{Tran} are amplified by the 3DSE ratio $W_{3DSE}(y)/W_0$, whereas the culvert element stiffnesses below H_{Tran} are amplified for load spreading only, $W(y)/W_0$.

The required CANDE input to activate the CLS procedure includes the following data: vehicle axle data; L_0 , W_0 & S , Fox pavement amplification parameters; β_L & β_W ($\beta_L = \beta_W = 1$ for no pavement) and 3DSE parameters; W_{min} & $W_{critical}$. With this information, CANDE assigns to every element a depth-dependent amplification factor that increases element's thickness dependent on the element's centroid depth below the surface. Referring back to the CANDE algorithm illustrated in Figure 8.1-10, the amplification factors assigned to soil and culvert elements are expressed below where the soil depth y = individual element depth.

- 1) For paving elements identified by material number (where $y = 0$, or above soil surface)

- $a_y = \frac{1}{2}(1 + \beta_W)$ amplification assigned to pavement elements on or above soil surface.

- 2) For $0 < y \leq H_{int}$, 1-wheel amplification for all elements except pavements and culverts not modified for 3DSE.

- $a_y = \beta_W \frac{W_I + y(2 \tan \theta^*)}{W_I}$ amplification assigned to all elements in this range.

- 3) For $y > H_{int}$, 2-wheel amplification for all elements except pavements and culverts not modified for 3DSE.

- $a_y = \beta_W \frac{W_I + y(2 \tan \theta^*_y) + S}{2W_I}$ amplification assigned to all elements below soil surface

- 4) Lastly, for $0 < y < H_{tran}$, we address 3DSE for culvert elements only. If 3DSE is active, we assign the culvert elements the higher 3DSE amplification. (Remember consistency requires that $H_{tran} \leq H_{int}$)

- $a_y = \frac{W_{min} + \frac{y}{H_{Tran}}(W_{critical} - W_{min})}{W_0}$ culvert elements only, 3DSE trumps AAM- θ^* .

In closing this section on live loads, it is noted that the CANDE program allows the user to replace AAM- θ^* load spreading theory with the exact EBM load spreading theory using the control variable called I_{scale} . As a general rule it is recommended use the simpler AAM- θ^* load spreading theory because it is sufficiently accurate and compatible with the two-wheel interaction depth. With regard to the choice of RSL versus CLS, it is recommended to use CLS because it is significantly more accurate than RSL. Nonetheless, it is recognized that many users will use RSL because of its tradition and because AASHTO provides guidelines on choosing the sampling depth h^* .

8.2 Pipe Group Connections and Combinations

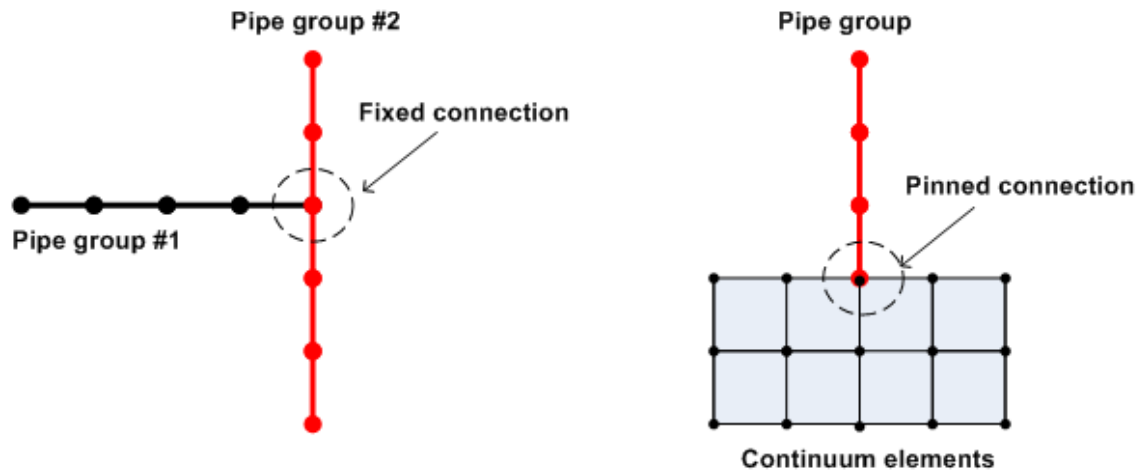
Finite element models utilizing multiple pipe groups is a powerful feature in CANDE-2022 that offers many modeling capabilities. Discussed below are several techniques for combing pipe groups with each other and soil elements to achieve various desired objectives. Topics include connection modeling (fixed, pinned, and roller), long-span stiffeners, culvert rehabilitation with liners, and other pipe group combinations.

8.2.1 Connections among element types

A pipe group is a connected sequence of beam-column elements joined head-to-toe at common nodes and tracing an arbitrary curvilinear path in x-y space. Each beam-column node has three degrees of freedom, x-displacement, y-displacement and a rotation. Continuum elements (triangle or quadrilateral) only have two degrees of freedom per node, x-displacement and y-displacement.

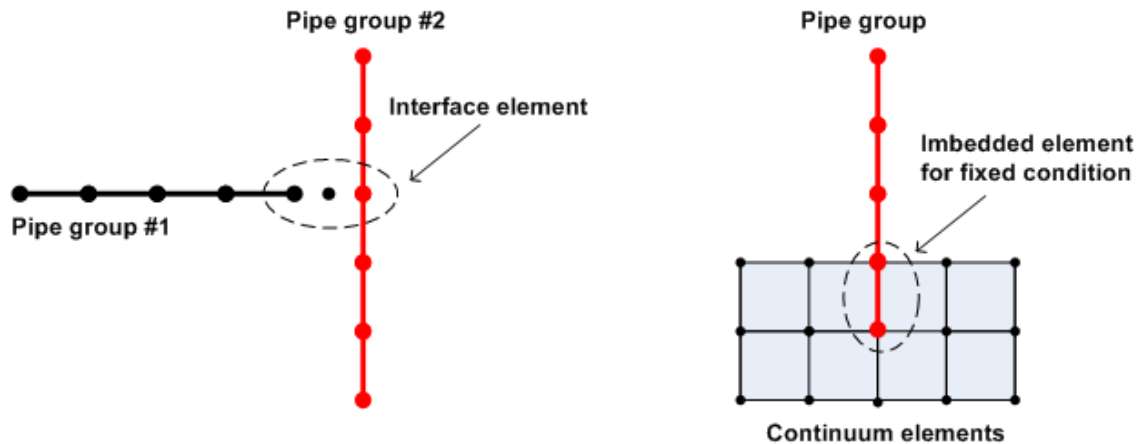
When two or more pipe groups are connected to a common node the connection is called fixed, meaning moment continuity is preserved at the junction node. On the other hand, when a pipe group is attached to a continuum element the connection is called pinned, meaning the moment at the junction node is zero. These fundamental connections, representing the default conditions, are illustrated in the figure below.

Figure 8.2.1-1 Connections made by sharing common node at junction.



If it is desired to simulate a pinned or roller connection between two pipe groups such as pipe group #1 and pipe group #2 in the above figure, then an interface element or a link element should be inserted at the junction of the two pipe groups. An interface element provides the most options to join two independent nodes as a pinned connection, friction connection, roller connection or gap connection depending on the properties assigned to the interface element. Figure 8.2.1-2 illustrates an interface element joining one node of pipe group #1 to one node of pipe group #2 along with the third interface node whose degrees of freedom are the interface forces required to enforce the desired connection.

Figure 8.2.1-2 Techniques to change connection conditions.



The assigned interface properties required to achieve various connection conditions are listed in the table below wherein the value 10^6 means a very large number such that frictional slippage or tensile rupture cannot occur.

Table 8.2.1-1 Interface property values to simulate various connection conditions

Desired Connection Type	Interface properties	
	Friction coefficient (μ)	Tensile breaking force (lbs/inch)
Pinned	10^6	10^6
Friction (no tensile separation)	0.3 (typical)	10^6
Friction (tensile separation)	0.3 (typical)	0.0
Roller (no tensile separation)	0.0	10^6
Roller (tensile separation)	0.0	0.0

Shown on the right side of Figure 8.2.1-2 is a modeling technique to simulate a fixed connection between a pipe group and a concrete footing (continuum elements). Here a beam-column element is added to the pipe group and imbedded in the concrete, mimicking reality.

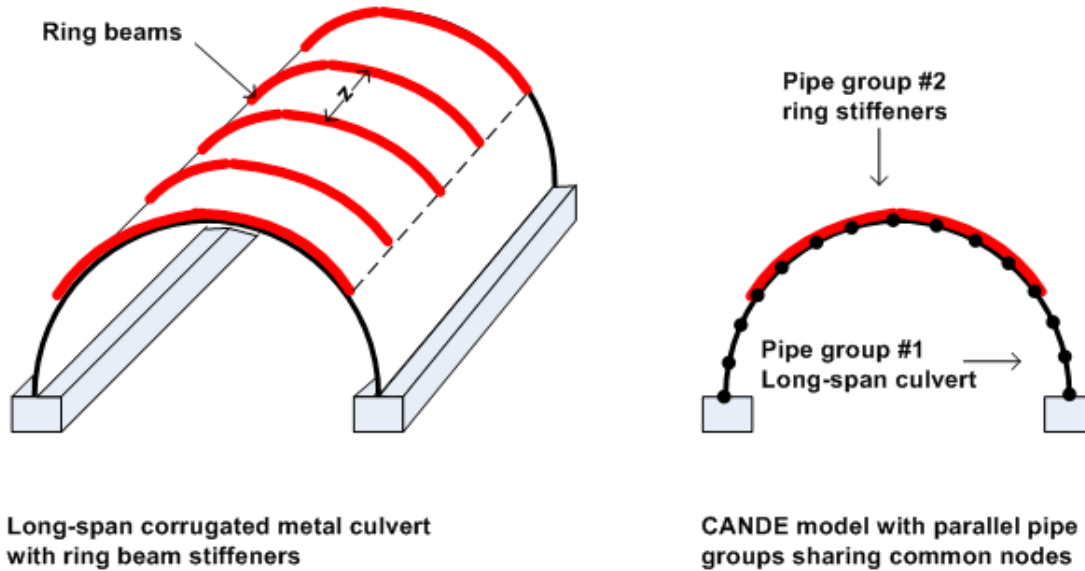
8.2.2 Stiffeners and culvert rehabilitation with parallel pipe groups

When two pipe groups share the same set of nodes, referred to as overlapping pipe groups, it is evident that both groups experience identical deformations (displacements and rotations) because both pipe groups are attached to the same nodes. The combined stiffness is additive, that is the combined thrust stiffness is $EA_1 + EA_2$ and the combined bending stiffness $EI_1 + EI_2$. Thus, even though overlapping pipe groups experience identical deformations, the resulting internal forces (moment, thrust and shear) and stresses in group #1 may differ substantially from group #2, depending on individual stiffness properties of each group.

Many types of culvert stiffeners can be reasonably and conservatively modeled with overlapping pipe groups with one pipe-group modeling the culvert and the second pipe-group modeling the stiffener. As noted above, a stiffener that is modeled as an overlapping pipe group provides additive bending stiffness as opposed to a larger composite bending stiffness that is achieved only when the stiffener is perfectly fused to the culvert ensuring a 100% bonding along the interface. Generally, it is recommended to model stiffeners with overlapping-pipe group(s) method as illustrated below.

Long-span stiffener. Long-span corrugated metal culverts are often reinforced with discrete ring-beam stiffeners periodically spaced along the top arch. Typically, the ring beams are lightly bolted to the corrugated metal so that the assumption of additive stiffness instead of composite stiffness is quite reasonable, erring slightly on the conservative side. Figure 8.2.2-1 illustrates how to model ring-beam stiffeners with overlapping pipe groups.

Figure 8.2.2-1 Modeling technique for long-span culvert with ring beam stiffeners



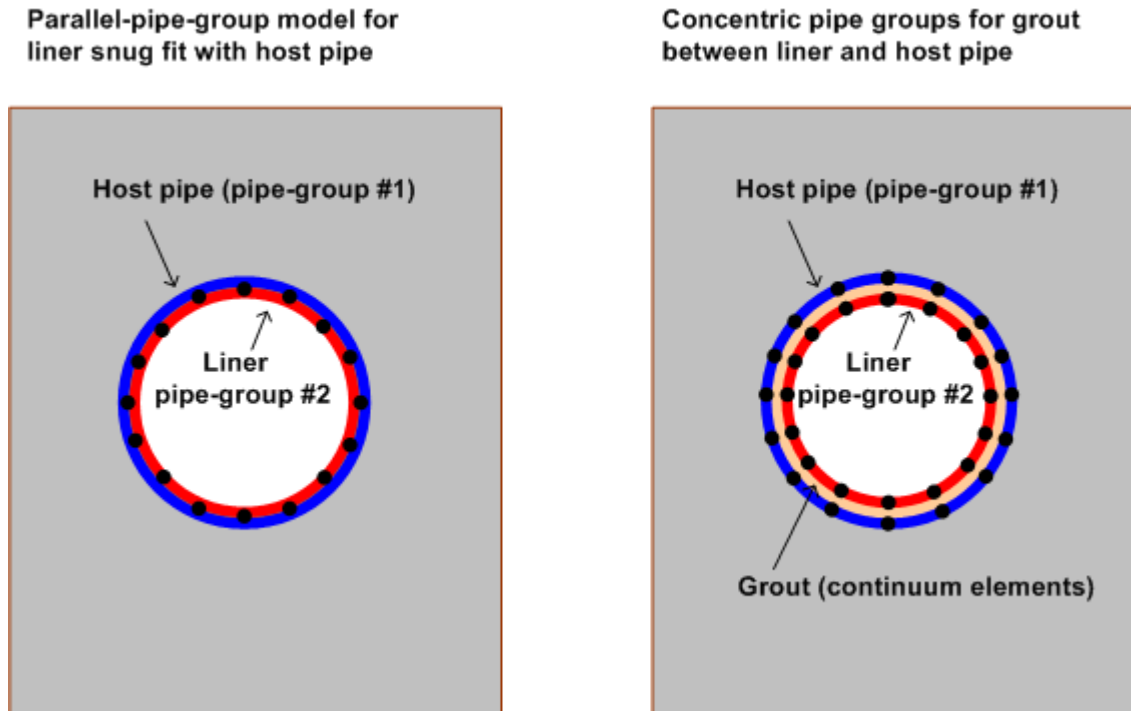
As shown in the table below input for the CANDE ring beam properties for pipe group #2 are smeared values based on a ring-beam spacing of z inches on center.

Section Properties of Ring Beam	Individual ring values	CANDE input values
Area	$A \text{ (in}^2\text{)}$	$A/z \text{ (in}^2\text{/inch)}$
Moment of Inertia	$I \text{ (in}^4\text{)}$	$I/z \text{ (in}^4\text{/inch)}$
Section Modulus	$S \text{ (in}^3\text{)}$	$S/z \text{ (in}^3\text{/inch)}$

Another advantage of the overlapping-pipe-group method is due to the fact that CANDE provides an individual assessment of each group so that the structural integrity of stiffener is evaluated in addition to the culvert.

Culvert rehabilitation stiffener. One method to rehabilitate structurally distressed culverts is to insert a pipe liner inside the old culvert to stiffen the old soil-culvert system. Typically, the liner is a smooth wall plastic pipe inserted into a host culvert such as corrugated metal or reinforced concrete pipe. If the plastic-pipe liner is inserted into the host pipe with a snug fit, it is reasonable to assume the combined stiffness of the host pipe and liner is properly simulated by overlapping pipe groups. The rationale is that the interface between the host pipe and liner does not have a sufficient shear bond for the two pipes to act in a composite manner. The left side of Figure 8.2.2-2 shows the recommended overlapping pipe-group method for modeling a snug fit liner wherein both pipe groups share the same nodes.

Figure 8.2.2-2 Modeling techniques for culvert rehabilitation with liners



The right side of the above figure shows an alternative rehabilitation method in which the outside diameter of the liner is several inches smaller than the inside diameter of the host pipe thereby creating an annular space that is filled with grout. In this case the combined stiffness of liner, host pipe and grout is significantly greater than the snug fit condition using parallel pipe groups. As illustrated in the figure, an accurate simulation is achieved by assigning the liner an independent set of nodes tracing its smaller diameter and modeling the grout with continuum elements.

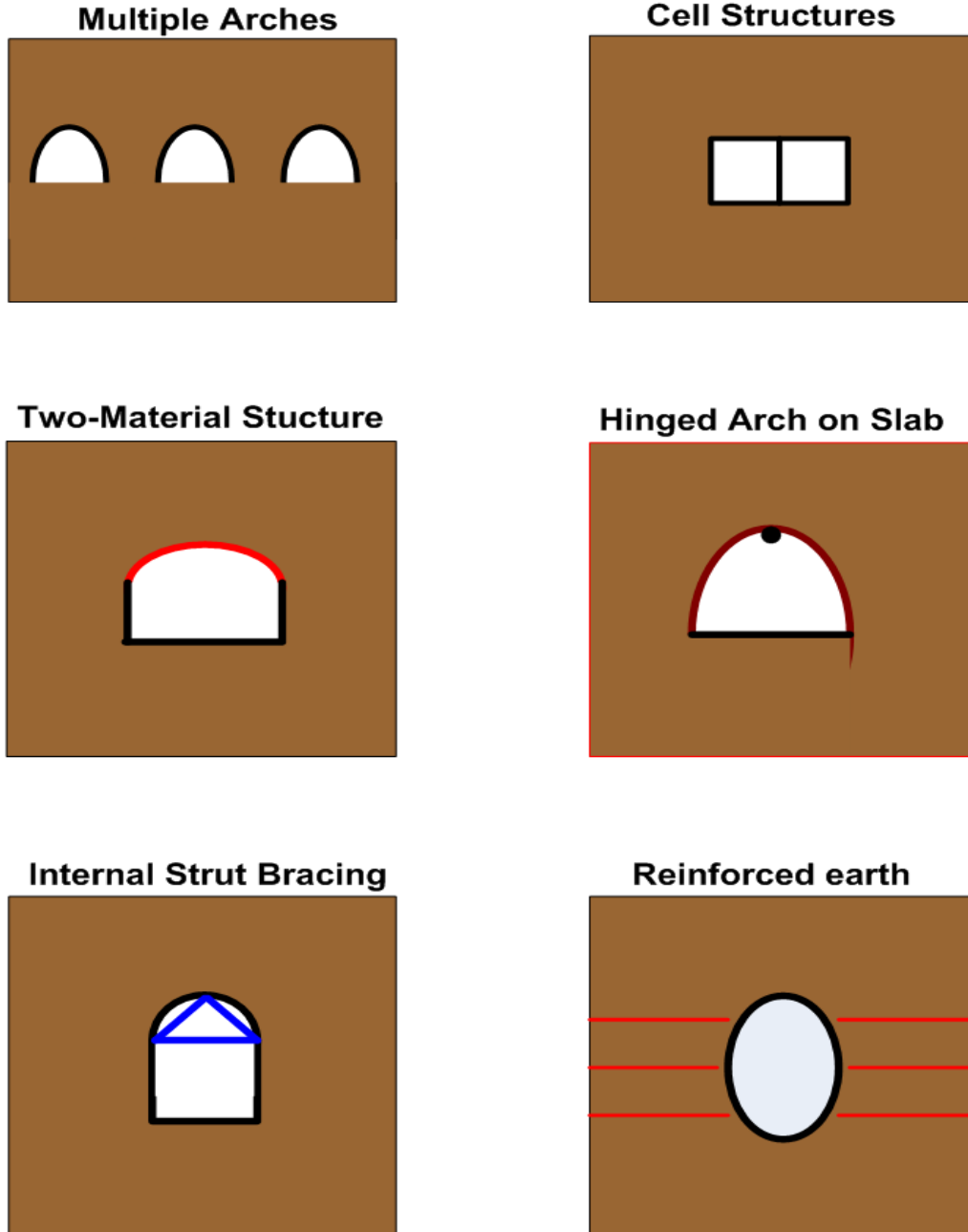
If the grout elements are assigned common nodes with the liner pipe and with the host pipe, the net effect is a composite bending stiffness that may be overly optimistic if the grout is not securely bonded both pipes. Therefore, a more conservative approach would be to assign independent node numbers to the grout elements and use frictional interface elements to connect the grout nodes to the pipe nodes, allowing relative slip along the pipe-grout boundaries.

Fully composite stiffeners and pipe groups. CANDE’s “composite link element” was developed specially to provide composite action between two pipe groups that are integrally attached with complete shear bonding along the interface. The “composite link” element is fully described in section 4.8 wherein the composite action is enforced by user-defined transverse and longitudinal link elements along the interface. Although the input data is somewhat tedious, the composite link element is a powerful and unique capability and only available in CANDE-2022.

8.2.3 Illustrations of pipe group combinations

In addition to the pipe group connections and combinations discussed above, additional pipe-group applications are illustrated in the Figure 8.2.3-1.

Figure 8.2.3-1 Illustrations of multiple pipe group applications



The above illustrations are intended to demonstrate the wide variety of modeling options that are possible with CANDE's multiple pipe-type capability. For example, the reinforced earth application (last figure) implies that pipe groups can be used to simulate soil reinforcement strips. If interface elements are inserted along these pipe groups, the model is capable of determining the ultimate pullout strength of the soil reinforcement.

8.3 Construction Increments

Incremental construction is the physical process of placing and compacting soil layers, one lift at a time, below, alongside and above the culvert as the installation is constructed. Analytically this is achieved by adding incremental solutions from successive finite element configurations, where each new configuration contains additional soil elements (and/or structural elements) that mimics the real-world buildup of the soil-structure system, one load step at a time.

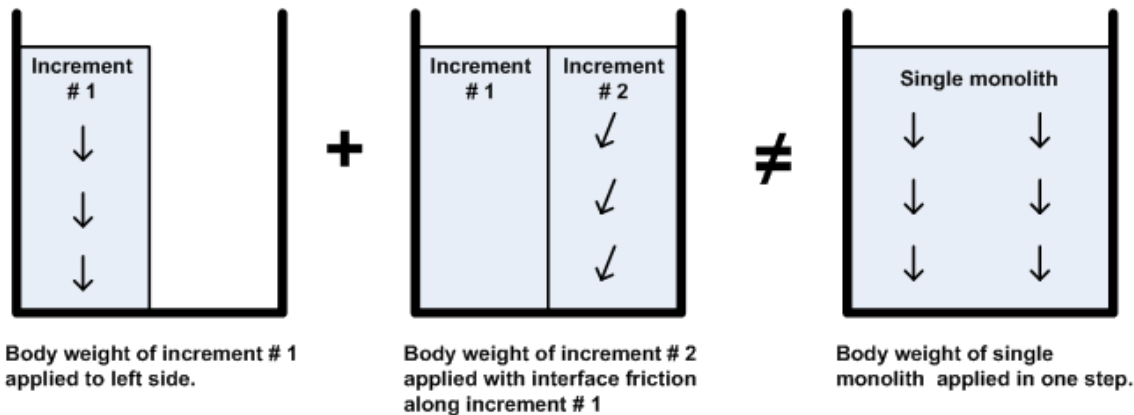
The terms “load step” and “construction increment” are closely related terms and are often used interchangeably, however they have slightly different meanings. Load step is an all-encompassing term referring to any incremental solution, which may or may not include a construction increment. For example, a load step may only include boundary-condition loads without additional elements added to the system. A construction increment is a special kind of load step wherein additional elements are added to the global stiffness matrix usually representing an additional layer of soil. The body weight of added elements forms the load increment associated with the load step along with any boundary loads such as soil compaction pressures, discussed subsequently.

8.3.1 Rules and insights for construction increments

With the above understanding, construction increments are subject to the following rules. Each element is assigned a construction increment number, which corresponds to the load step number that the element stiffness matrix and load vector is assembled into the global system. Once an element stiffness enters the system it remains active for all subsequent load steps (there is no element death, except for link element). Of course, the element body-load vector is only applied during the load step corresponding to the element construction increment number; it is not reapplied on subsequent load steps. Similarly, surface pressure and/or point loads (i.e., force boundary conditions) are also assigned a particular construction increment number and are only applied during the corresponding load step. Likewise, displacement boundary conditions are applied during the load step they are specified and remain fixed for all subsequent load steps. In short, the rules simulate reality.

Although the rules seem simple, it is easy to be fooled. For example, novices generally think that if all construction increments are linear elastic and no other nonlinearities are involved, then a structure built in several steps behaves no differently than a structure built as a monolith (all in one step). A simple example demonstrating this is not true is shown in the figure below.

Figure 8.3.1-1 Illustration of two construction increments versus a single monolith



The figure illustrates that after the first construction increment is set in place with roller boundary conditions on the sidewalls, the body weight produces a uniform stress distribution properly aligned in the vertical direction as expected. However, when the second construction increment is set in place (sharing common nodes with the first construction increment), some of the second construction increment’s body weight is transferred to the first construction increment’s stiffness. Therefore, the resulting stress and strain distribution in the two-step system is not uniform and differs from the uniform stress distribution in the single monolith system shown on the right.

The specific point of this simple example is that the sequence of construction increments is important and influences the structural behavior of the final system. More generally, when developing a finite element model for a particular soil-structure system, the sequence of construction increments should be modeled as realistically as practical.

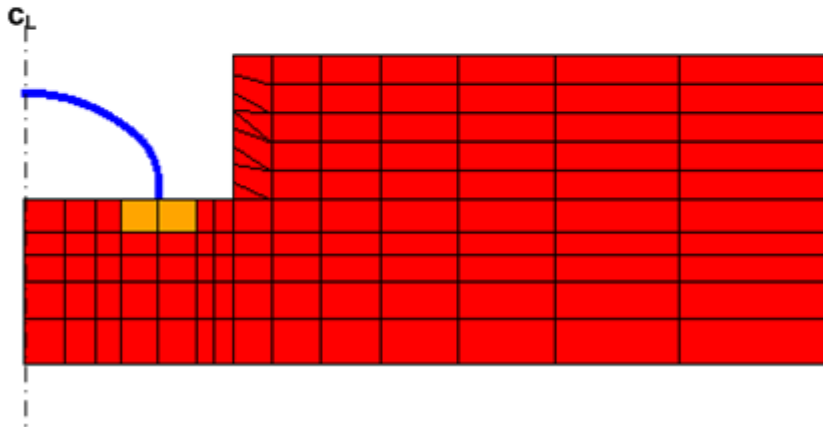
8.3.2 Techniques for initial construction increment

All too often the first construction increment is not modeled properly, causing incorrect deformation in the structure due to the insitu soil model. Proper modeling techniques depend on whether the insitu soil is linear or nonlinear and the assignment of body weight as discussed below.

Linear insitu soil. Generally, insitu soil can be realistically modeled with a linear elastic soil model because the existing soil is pre-consolidation and/or recently unloaded from excavation. In this case, the initial construction increment may include the insitu soil, footing or bedding and the structure as illustrated in the example below.

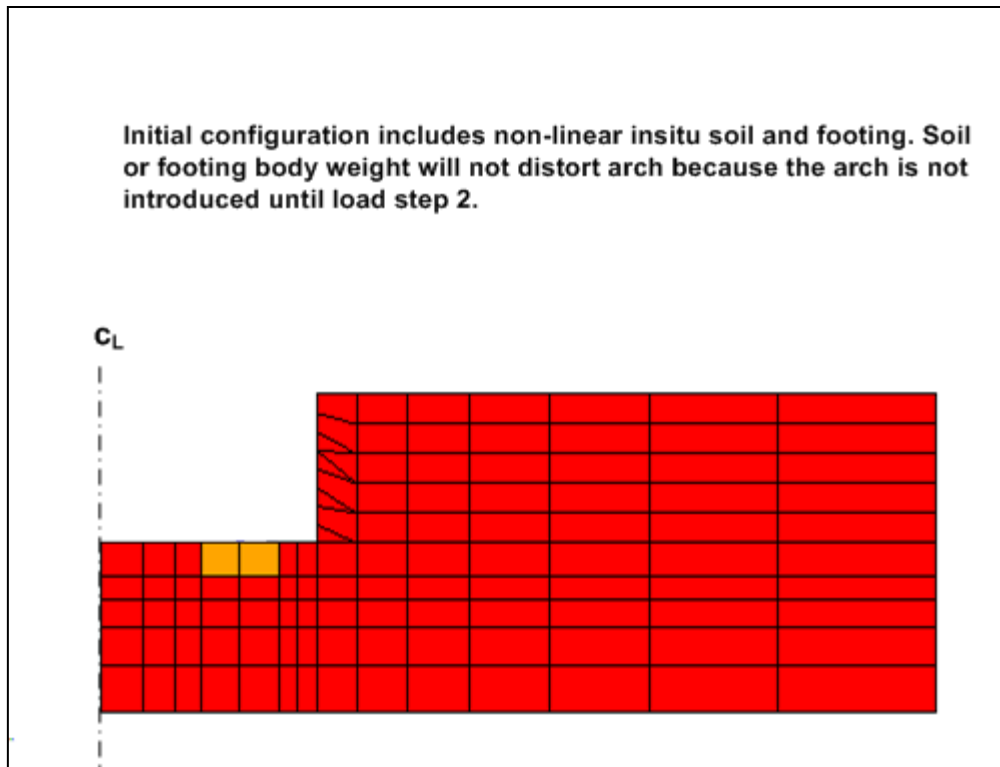
Figure 8.3.2-1 Initial configuration for an arch-trench installation with linear insitu soil

Initial configuration includes insitu soil, footing and arch structure (symmetric). Soil and footing body weight should be zero to avoid distorting structure in first load step.



Only the arch should be assigned a non-zero body weight for this initial configuration. A common mistake made by novices is to also assign body weight to the insitu soil and footing, which causes these components to deform under their own weight and introduce fictitious distortions into the arch. Physically we know the insitu soil and footing are at rest under their own weight before the arch is attached to the footing, thus only the arch body weight can cause deformations in the first load step.

Nonlinear insitu soil. If it is desired to model the insitu soil with a nonlinear soil model like Duncan/Selig, then the arch should be eliminated from the initial configuration and introduced in the second construction increment. In this case we need to assign the actual body weight to the insitu soil because the soil stiffness is dependent on the stress state caused by the soil body weight, requiring iteration within the load step. Figure 8.3.2-2 illustrates the proper initial configuration when nonlinear soil model is used for insitu soil.

Figure 8.3.2-2 Initial configuration for an arch-trench installation with nonlinear insitu soil

If the arch were included in the initial configuration, it would experience fictitious distortions due to deformation of the insitu soil by self-weight. Now however, after the initial configuration has converged and the insitu soil and footing are at rest in a deformed state, the arch may be correctly assigned to the second construction increment.

8.3.3 Soil compaction and construction increments

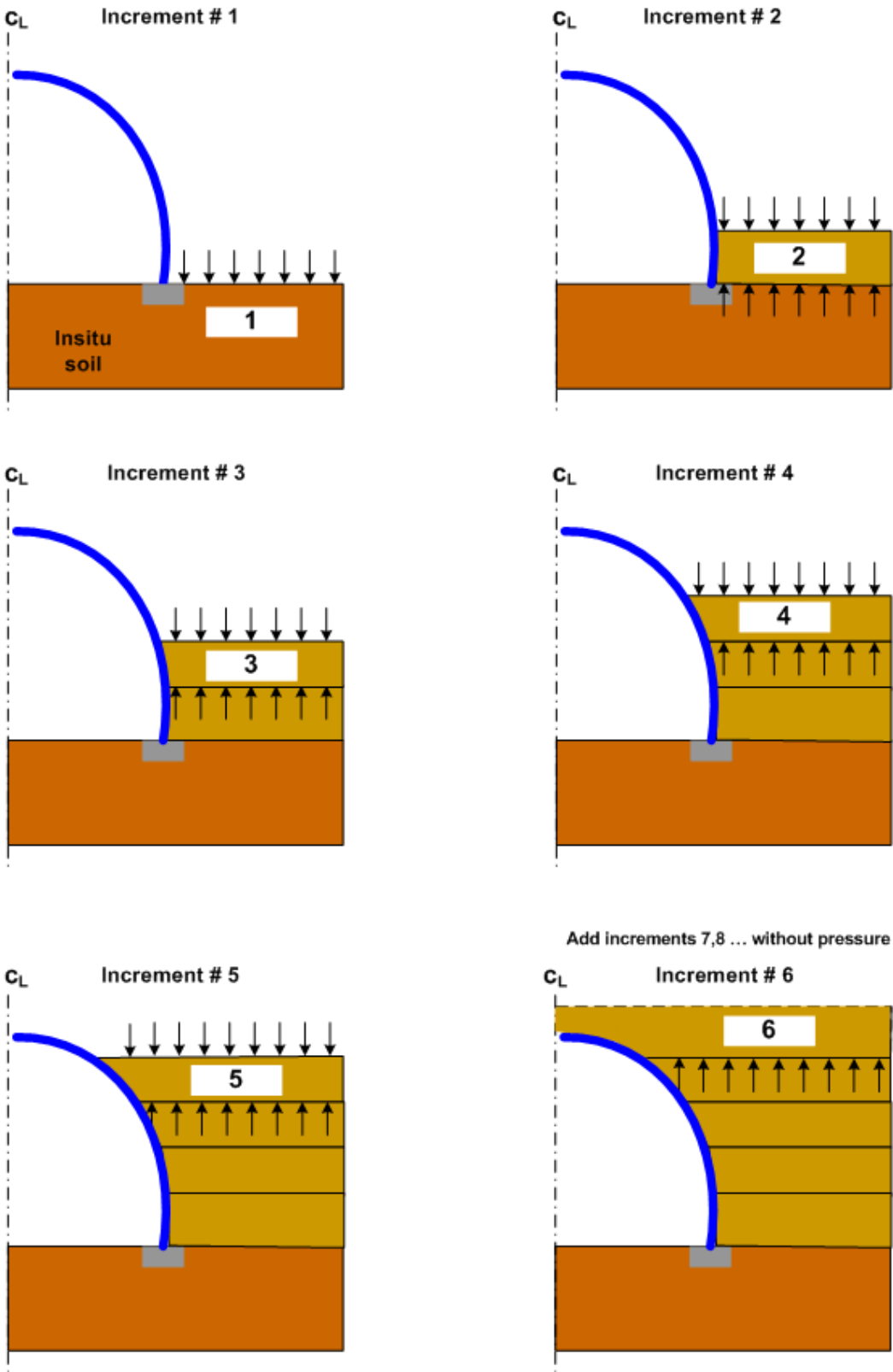
The last technique to be described is the modeling of soil compaction using the so-called squeeze layer method first introduced in Reference 18. The purpose of soil compaction is to densify soil after it is laid down in loose layers and then compacted to achieve a specified density usually stated in terms of AASHTO T-99 relative density.

Compaction equipment ranging from hand-held compactors to large-tracked bulldozers is used to compress each soil layer by creating a temporary vertical pressure to compact the soil. As the soil is compressed vertically (squeezed), it tends to expand laterally due to the Poisson effect, which creates horizontal pressure on the sides of the culvert. These lateral pressures cause inward movement of the culvert sides and peaking at the culvert crown, that is, a reverse deformation pattern from that caused by overburden loading. Large culverts such as long-span corrugated metal structures often experience as much as 2 % crown peaking as a result of compacting soil layers between the footing and the crown.

Compaction loads are beneficial not only in compacting the soil to achieve the desired soil stiffness properties but also in introducing reverse deformations and bending moments into the culvert, which provides the culvert with additional capacity to resist the opposite bending deformations that subsequently come from soil placed on top of the culvert.

The squeeze layer technique is a simple modeling concept that simulates the effect of soil compaction and is applicable to both linear and nonlinear soil models. The concept is illustrated in Figure 8.3.3-1.

Figure 8.3.3-1 Squeeze-layer method for compaction loads on long-span culvert.



A point-by-point discussion of the above figure is provided below.

1. To start, a uniform compaction pressure representing the compaction equipment, typically on the order 5-psi pressure, is placed on the surface of the insitu soil at the level of the footing.
2. Next, the 2nd construction increment (first layer of backfill soil with body weight) is added to the system along with another uniform compaction pressure applied to its top surface. At the same time, however, the first compaction pressure is removed by applying an equal but opposite compaction pressure to the bottom surface. These two opposing pressures squeeze the soil layer and increase the lateral pressure on the arch via the Poisson effect.
3. The intermediate construction increments 3rd, 4th and 5th are treated exactly like the 2nd construction increment so that each layer is squeezed, increasing lateral pressure on the arch and inducing more peaking. Note that after the 5th load increment (or more generally, the increment before the crown-level increment) all the temporary compaction pressures have been removed except the compaction pressure on the surface of 5th construction increment.
4. The squeeze layer process is terminated with the 6th construction increment (i.e., crown-level increment). As the 6th construction increment is added to the system with its stiffness and body weight, the last remaining compaction pressure from the 5th construction is removed.
5. All the remaining construction increments, representing soil layers above the crown, are added in the normal manner with body weight but without any compaction pressures.

Examples of applying the squeeze layer technique and the behavior of long-span culverts can be found in References 18, 26 and 27.

As an alternative to the squeeze layer technique, the plasticity Mohr-Coulomb and/or Duncan/Selig model with Katona modification may be used to model the backfill soil. In this case the compaction pressure is applied to the soil surface and then immediately removed in the next load step. Due to the permanent plastic deformation of these plasticity models, the unloading phase does not restore the soil layer to its original position and locked-in lateral forces are maintained on the structure.

9 REFERENCES

1. CANDE: A Modern Approach for the Structural Design and Analysis of Buried Culverts, Federal Highway Administration Report No. FHWA-RD-77-5, October 1976, (Authors: M. G. Katona, J. M. Smith, R. S. Odello, and J. R. Allgood).
2. CANDE User and System Manuals, Federal Highway Administration Report No. FHWA-RD-77-6, October 1976, (Authors: M. G. Katona and J. M. Smith).
3. CANDE-1980: Box Culverts and Soil Models, Federal Highway Administration, Report No. FHWA-RD-172, May 1981 (Authors: M. G. Katona, P. D. Vittes, C. H. Lee, and H. T. Ho).
4. CANDE-89: Culvert Analysis and Design computer program – User Manual, Federal Highway Administration Report No. FHWA-RD-89-169, June 1989. (Authors: S. C. Musser, M. G. Katona and E. T. Selig).
5. Predicting Performance of Buried Conduits, Report No. FHWA/IN/JHRP-81/3, Joint FHWA and Indiana State Highway Commission, June 1982. (Authors; G.A. Leonards, T.H. Wu, and C.H. Juang).
6. AASHTO Guidance, *AASHTO LRFD Bridge Design Specifications*, Current Edition, AASHTO, Washington, D.C. (Continually updated).
7. Burns, J. Q., and R. M. Richard, “Attenuation of Stresses for Buried Cylinders,” In Proc., *Symposium on Soil-Structure Interaction*, University of Arizona Engineering Research Laboratory, Tucson, 1964, pp. 378-392.
8. Herrmann, L. R., “User’s manual for plane strain incremental construction program,” Department of Civil Engineering, University of California, Davis, 1972.
9. Katona, M. G., and A. Y. Akl, “Analysis and Behavior of Buried Culverts with Slotted Joints,” *Transportation Research Record*, No. 1008, 1985, pp. 22-32.
10. Katona, M. G., and A. Y. Akl, “Structural Design of Buried Culverts with Slotted Joints,” *ASCE, Journal of Structural Engineering*, January 1987.
11. Herrmann, L. R., “Efficiency evaluation of a two-dimensional incompatible finite element,” *Journal of Computers and Structures*, vol 3, 1973, pp 1377-1395.
12. Katona, M. G., Minimum Cover Heights for Corrugated Plastic Pipe Under Vehicle Loading,” *Transportation Research Record*, No. 1288, 1990, pp. 127-135.
13. McGrath, T.J., I.D. Moore, E.T. Selig, M.C. Webb, and B. Taleb, Recommended Specifications for Large-Span Culverts, *NCHRP Report 473*, Transportation Research Board, Washington, DC, 2002.
14. Heger, F.J., and T.J. McGrath, Shear Strength of Pipe, Box Sections, and Other One-Way Flexural Members, *ACI Journal*, Proceedings Vol. 79, 1982, pp. 470-483.
15. Heger, F.J. and T.J. McGrath. Crack Width Control of Reinforced Concrete Pipe and Box Sections, *ACI Journal*, Proceedings Vol. 81, 1984, pp. 149-157.
16. Gergely, P. and L.A. Lutz. Maximum Crack Width in Reinforced Concrete Flexural Members, SP-20, American Concrete Institute, Detroit 1968, pp. 87-117
17. Katona, M. G., and P. D. Vittes, Soil-Structure Evaluation of Buried Box Culvert Designs, *Transportation Research Record*, No. 878, 1982, pp 1-7.

18. Katona, M. G., D. F. Meinhert, R. Orillac, and C. H. Lee, Structural Evaluation of New Concepts for Long-span Culverts and Culvert Installations, Report No. FHWA-RD-79-115, December 1979,
19. Duncan, J. M., and C. Y. Chang, Nonlinear Analysis of Stress and Strain in Soils, Journal of Soil Mechanics and Foundations, ASCE, vol. 96, No. SM5, September 1970, pp. 1629-1653.
20. Duncan, J. M., et. al., Strength, Stress-strain and Bulk modulus Parameters for Finite Element Analysis of Stresses and Movements in Soil Masses, Report University of California, Berkeley, GT 78-02 to National Science Foundation, April 1978.
21. Selig, E. T., Soil Parameters for Design of Buried Pipelines, Proceedings, Pipeline Infrastructure Conference, ASCE, 1988, pp 99-116.
22. Hardin, B. O., Effects of Strain Amplitude on the Shear Modulus of Soils, Air Force Weapons Laboratory Technical Report AFWL-TR-72-201, Kirtland AFB, NM, March 1973.
23. Katona, M. G., and T. J. McGrath, A Guideline for Interpreting AASHTO LRFD Specifications to Design or Evaluate Buried Structures with Comprehensive Solution Methods, Transportation Research Record, No. 2028, 2007, pp. 211-217.
24. Katona, M. G., “A Simple Contact-Friction Interface Element with Application to Buried Culverts, International Journal for Numerical and Analytical Methods in Geomechanics, Vol. 7, 1983, pp. 371-384.
25. H. G. Poulos and E. H. Davis, *Elastic Solutions for Soil and Rock Mechanics* (Holl, homogenous half-space, rectangular footprint solution, page 54), John Wiley, New York, 1980,
26. Katona, M. G., “On the Analysis of Long-span Culverts by the Finite Element Method,” Transportation Research Record, No. 678, 1978, pp. 59-66.
27. Katona, M. G., “CANDE: A Versatile Soil-Structure Design and Analysis Computer Program,” Journal of Advances in Engineering Software, Vol. 1, No. 1, 1978, pp. 3-9.
28. Katona, M. G., Influence of Soil Models on Performance of Buried Culverts, Paper presented at TRB 2015 annual meeting Session 614, January 13, 2015. Paper in TRB online Compendium; <http://AMOnline.TRB.org>
29. Katona, M. G., Modifying Duncan/Selig Soil Model for Plastic-like behavior, Transportation Research Record, No. 2511, 2015, pp. 53-62.
30. Brinkgreve, R.B.J. and Broere, W., Eds. Plaxis 3D Tunnel Version 2, Plaxis, Netherlands, 2004.
31. Katona, M. G., “Continuous Load Scaling: A New Method to Simulate Longitudinal Live-load Spreading for 2D Finite Element Analysis of Buried Culverts”, Transportation Research Record: No. 2642, Issue 1, 2017, pp. 77-90.
32. McGrath T. J. et. al., *Live Load Distributions for Design of Box Culverts*, A study for Pennsylvania Department of Transportation, prepared by Simpson Gumpertz and Heger Inc, Waltham Massachusetts, 2004.
33. Katona, M. G., “Improved Methods for Simulating Live Loads for 2D Structural Analysis of Buried Culverts”, Transportation Research Record, Vol. 2673(12), 2019, pp. 449-462.
34. Katona, M. G. “Assessment of AASHTO Load-Spreading Method for Buried Culverts and Proposed Improvement”, Transportation Research Record, Vol. 2675(11), 2021, pp. 877-887.
35. NCHRP Project 15-54 final Report, *Proposed Modifications to AASHTO Culvert Load Rating Specifications*. Washington, DC: The National Academies Press. <https://doi.org/10.17226/25673>, 2019.

36. H. G. Poulos and E. H. Davis, *Elastic Solutions for Soil and Rock Mechanics* (Fox, two-layer circular footprint graphical solution, page 138), John Wiley, New York, 1980,
37. Katona, M. G. “*Extension of AASHTO Load-Spreading Method to Include the Full Benefits of Pavements for Reliable Load Rating of Buried Culverts*”, Transportation Research Record, to be published 2022

10 CANDE ANALYSIS SOURCE CODE

The purpose of this chapter is to provide the reader with sufficient understanding of the CANDE Analysis Engine source-program architecture to enable the reader to modify, change and extend the program. Researchers are encouraged to modify and/or extend CANDE-2022 to investigate new soil models, pipe-material behavior and other new theories and concepts. By sharing new developments among the engineering community, CANDE will continue to grow in the future, in the same manner as it has grown in the past.

10.1 Overview of CANDE Analysis Engine Architecture

The CANDE-2022 source program is written in modern Fortran and developed with the following:

- Microsoft Visual Studio 2005, Version 8.0.50727.762 (SP.050727-7600)
- Intel Fortran Compiler version 9.1.3427.2005.
- Microsoft .NET Framework version 2.0.50727

The MVS framework permits grouping subroutines together to form projects and then grouping projects together to form a whole solution. CANDE's whole solution is composed of six projects described in the table below.

Table 10.1-1 CANDE-2022 projects contained in MVS solution

Project	Description	Number of programs or subroutines
1. Cande_dll	The primary executive routine controlling the overall solution strategy and calls to subroutines in other projects including input/output files and error messages. (dynamic link)	1
2. Engine	Contains all the engineering subroutines including all finite element formulations, equation solver, elasticity solution, soil models and pipe types with design logic and structural evaluations.	56
3. Inc	Contains all named common statements and parameter declarations whose variables are shared between subroutines by means of "Include statements".	25
4. Intel	Utility subroutines for controlling screen monitor.	3
5. IO	Utility subroutines for input/output message writing to print files and screen monitor for all output including error messaging.	27
6. Main	Dynamic link interface between Cande_dll and monitor screen to identify input file.	1

In the following discussion, the CANDE architecture is presented from a top down viewpoint, starting with the primary executive subroutine, Project Cande_dll, and then narrowing to specific subroutines in Project Engine.

10.2 Executive Routine (Cande_dll)

Overall, the executive routine is divided into three parts, input phase, solution phase and output phase. The executive routine defines the Fortran variable ICOME to communicate with other subroutines as to which phase is currently being addressed as follows.

- ICOME = 1 means input phase
- ICOME = 2 means solution phase
- ICOME = 3 means output phase

As might be expected, the solution phase is the most complicated wherein the executive routine must decide if the solution for the current load step is valid (converged) and how to proceed next. For this purpose another Fortran variable IEXIT is defined with one of four possible values as follows.

- IEXIT = 1 means entire problem is complete, normal exit from CANDE.
- IEXIT = 0 means current load step has converged, advance to next load step
- IEXIT = -1 means current load step has not converged, repeat load step.
- IEXIT = -2 means design-mode solution did not converge, repeat all load steps.

With the above understanding, Figure 10.2-1 shows a flow chart of the executive routine wherein the “ICOME divisions” are clearly evident on the left. Within each ICOME division, there are two colored boxes, one representing calls to pipe-type subroutines and one representing calls to solution-level subroutines. Both the pipe-type subroutines and the solution-level subroutines are contained in Project Engine and will be discussed in turn.

10.3 Pipe-type Subroutines

Currently there are five pipe types in CANDE’s pipe library. Each pipe-type is associated with one or more subroutines to accomplish the three basic functions, input, evaluating trial solution, and updating results. Table 10.3-1 identifies the subroutines associated with each pipe type.

Table 10.3-1 Subroutines associated with each pipe-type

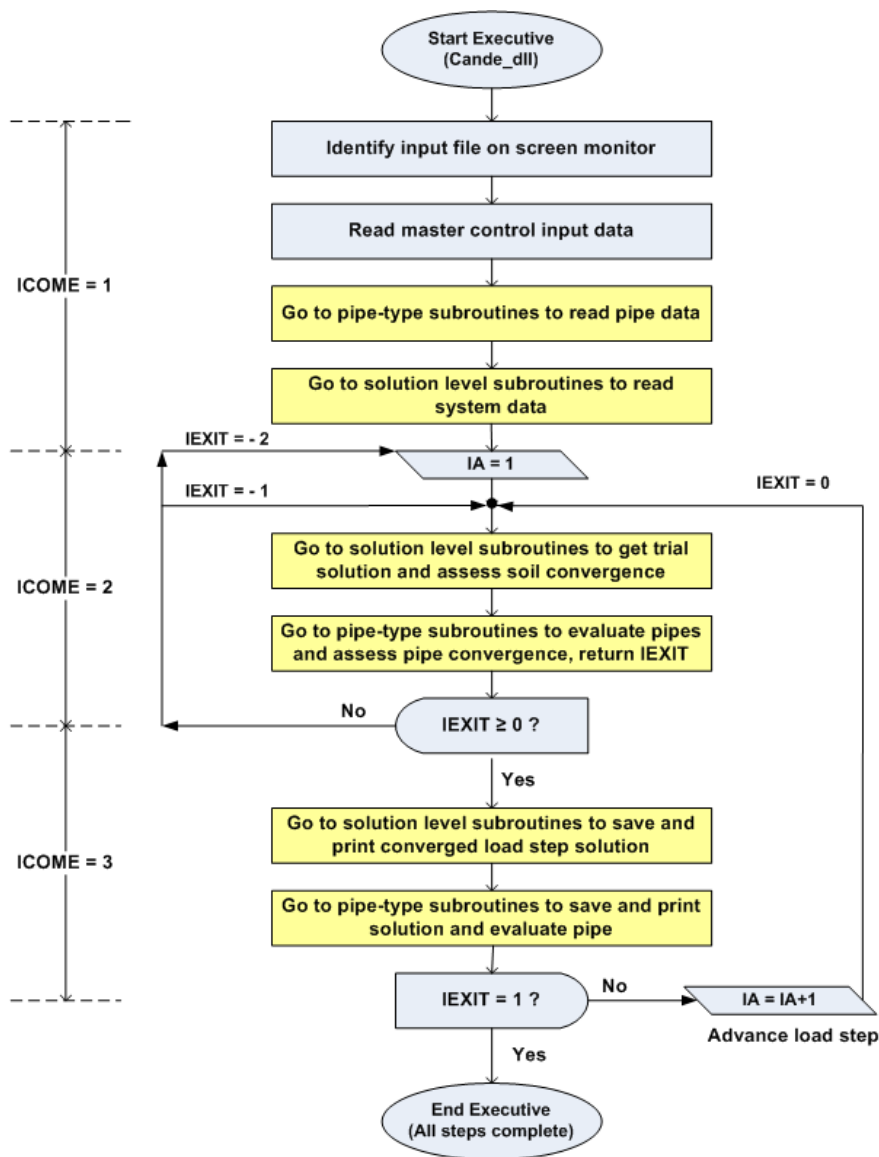
Pipe-type and material	Main pipe-type subroutine name	Auxiliary subroutines called by main pipe-type subroutine
Corrugated aluminum	alum	emod : calculates nonlinear section properties.
Corrugated steel	steel	emod : calculates nonlinear section properties. jmod : special model for slipping joints. slpjnt : process input/output for slotted joints.
Reinforced concrete	concre	conmat : calculates nonlinear section properties. conend : computes shear capacity, radial tension, and crack width.
Plastic pipe	plasti	plasbro : calculates section properties of profile wall. plsnbk : computes strains and local buckling losses.
Basic	basic	none
Concrete with ribs/fiber	conrib	conmax : calculates nonlinear section properties. conend : calculates shear capacity, radial tension and crack width predictions.
Concrete filled tubes	contube	concircle : calculates nonlinear section properties. converger : enhanced algorithm for convergence. (called by concircle)

Each of the main pipe-type subroutines listed above performs the same three basic functions as dictated by the executive routine via the variable ICOME. Table 10.3-2 lists the basic functions for a generic main pipe-type subroutine.

Table 10.3-2 Tasks performed by main pipe-type subroutines for each ICOME value.

ICOME value	Tasks performed in main pipe-type subroutine
1 (input phase)	<ul style="list-style-type: none"> • Read input properties for pipe group • Compute initial linear-elastic section properties.
2 (solution phase)	<ul style="list-style-type: none"> • Revise section properties based on current solution • Determine if nonlinear pipe group has converged • Send IEXIT value back to executive routine (-2,-1, or 0)
3 (output phase)	<ul style="list-style-type: none"> • Save and update pipe-group structural responses • Print safety evaluation for pipe group

Figure 10.2-1 Executive routine flow chart: input phase, solution phase, and output phase



10.4 Solution-level Subroutines

For any given problem, only one of the three solution levels is operative, that is, Level 1, Level 2 or Level 3. The closed-form Burns and Richard elasticity solution, Level 1, only employs one subroutine, named Burns. In contrast, the finite element solutions, Level 2 and Level 3, employ numerous subroutines. Level 2 and Level 3 share the same subroutines for the solution phase (ICOME = 2) and the output phase (ICOME = 3). For the input phase (ICOME = 1), Level 2 includes a separate set of subroutines to create an input file that is identical to a Level 3 input file. Hence, the subroutines employed for the Level 3 input phase (ICOME = 1) are also used to read the internally created Level 2 input file. The above comments are clarified in the following tables and charts.

10.4.1 Elasticity solution Level 1

As stated above, the Level 1 solution employs one subroutine called Burns that is not shared by any other solution level. The tasks performed by the Burns subroutine are shown in the table below in accordance with the calls from executive routine via the parameter ICOME.

Table 10.4-1 Burns subroutine tasks as called

ICOME value	Tasks performed by Burns subroutine
1 (input phase)	Read system input variables; pipe diameter, soil density, number of load steps, soil stiffness and fill heights, interface condition.
2 (solution phase)	Compute incremental trial solution for moments, thrusts and shear around the pipe and form trial total solutions for processing by pipe-type subroutine.
3 (output phase)	No action. (Soil responses are not computed in Burns subroutine, only pipe responses are computed which are processed in the pipe-type subroutine)

10.4.2 Finite element solutions Level 2 and Level 3

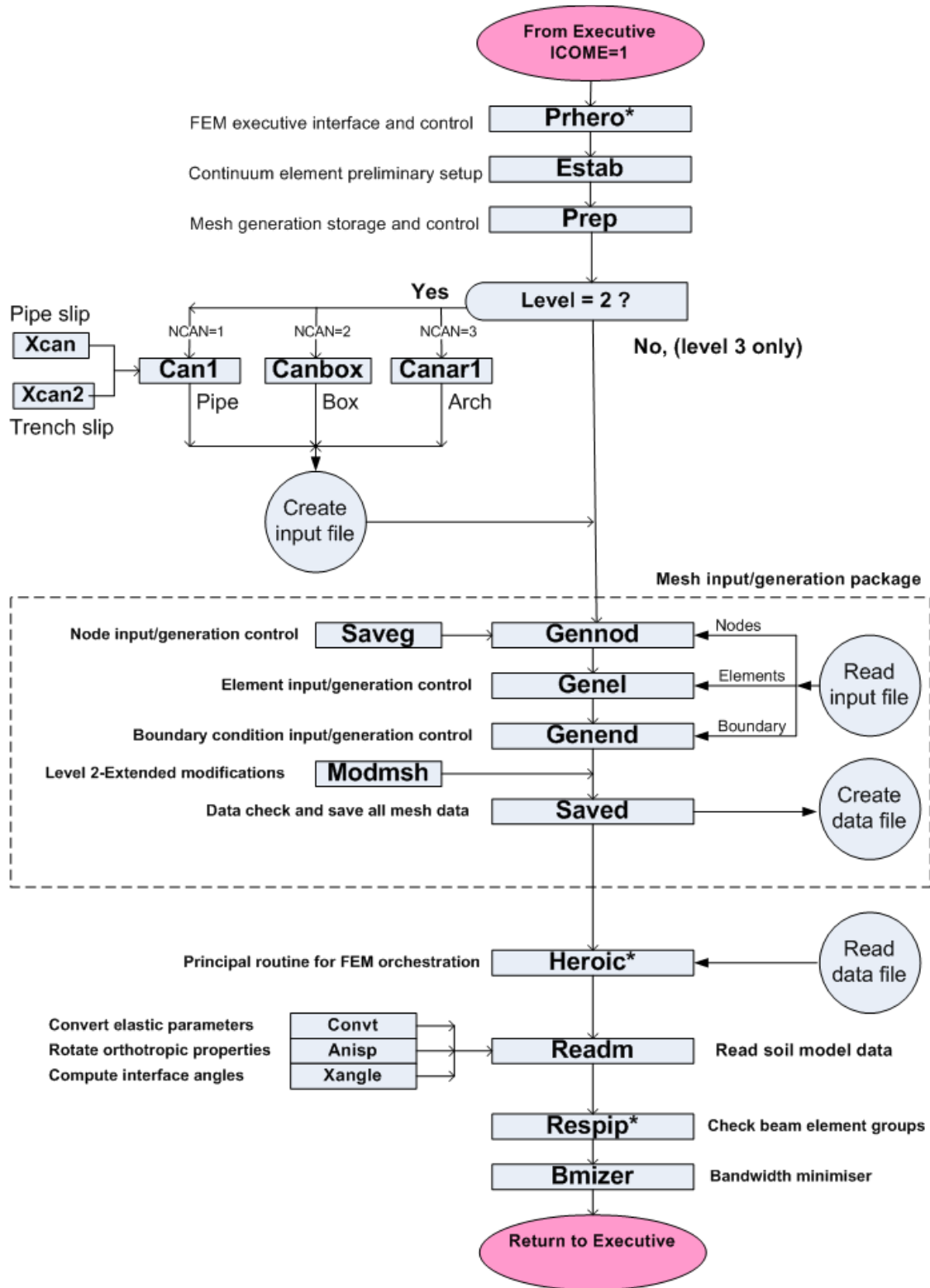
Solution levels 2 and 3 share most subroutines in common as illustrated in the following finite element flow charts. For clarity, the flow charts are broken down into the input phase (ICOME = 1), solution phase (ICOME = 2) and the output phase (ICOME = 3)

Input phase (ICOME = 1) When the executive routine calls for the finite element input phase, the sequence of subroutines shown in Figure 10.4.2-1 come into play. Note that the flow path shows a diversion path for Level 2 wherein one of the three canned-mesh subroutines are entered to create an input file identical to Level 3.

Solution phase (ICOME = 2) The sequence of subroutines that come into play for the solution phase is shown in Figure 10.4.2-2. Note there is no distinction between Level 2 and Level 3, the flow path is the same for both.

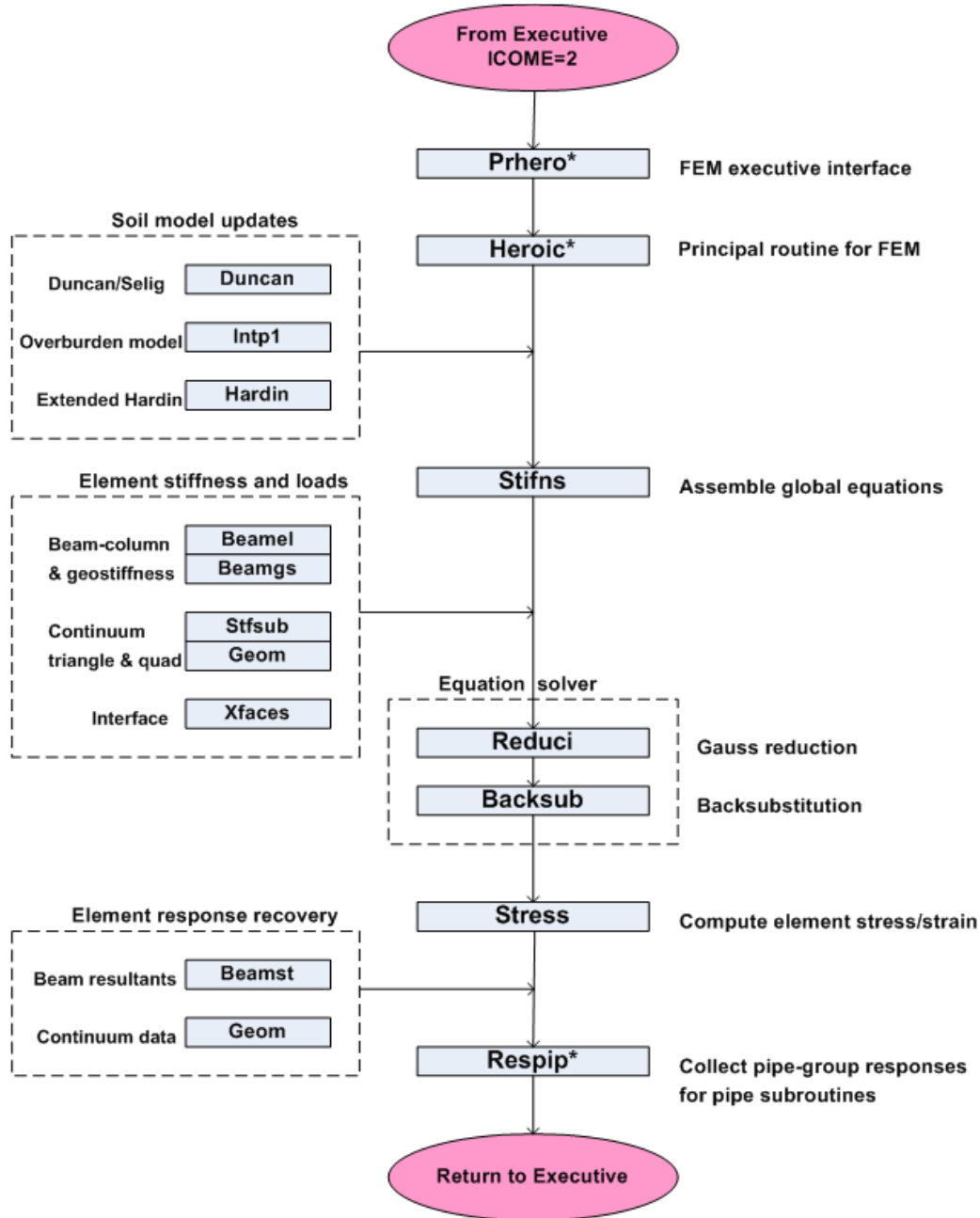
Output phase (ICOME = 3) When the executive routine determines that the load step has converged, ICOME is set equal to 3 to signal the printout of the solution. The sequence of subroutines for the output phase is shown in Figure 10.4.2-3. Again, there is no distinction between Level 2 and Level 3.

Figure 10.4.2-1 Subroutine flow chart for input phase of finite element solution Level 2 and Level 3.

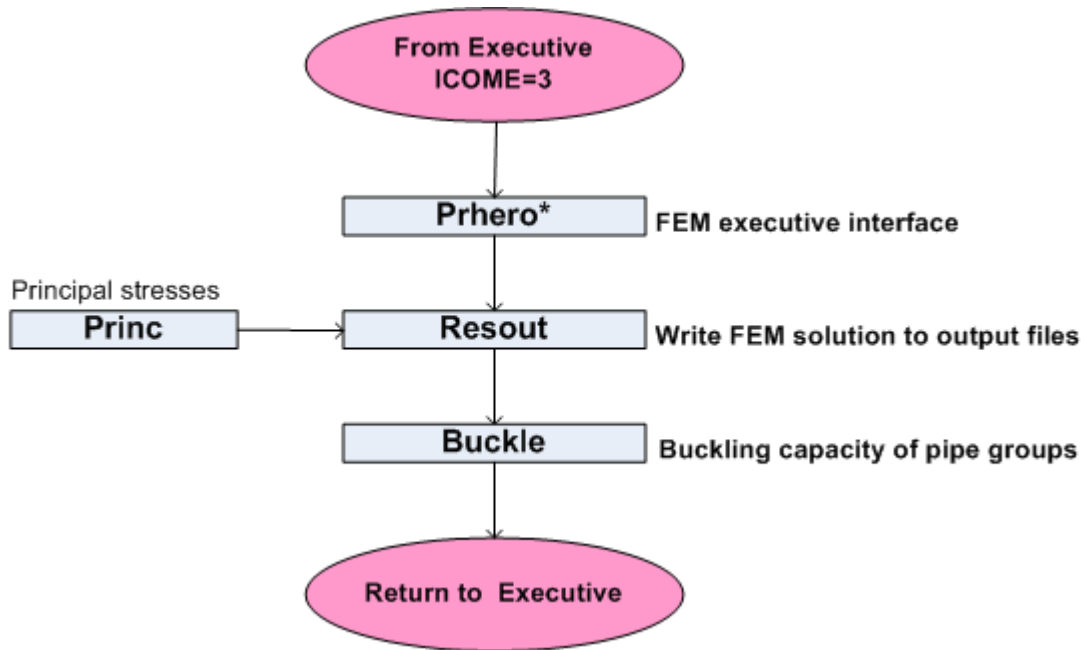


Asterisk (*) means subroutine serves in more than one phase

Figure 10.4.2-2 Subroutine flow chart for solution phase using finite element method



Asterisk (*) means subroutine serves in more than one phase ex

Figure 10.4.2-3 Subroutine flow chart for output phase using finite element method

10.5 Extensions to New Pipe Types, Soil Models and Canned Meshes

As stated at the beginning of this appendix, modifications and extensions to CANDE's capabilities are welcomed and encouraged. Based on CANDE's history, the three areas that are most likely to be extended are: (1) new pipe-type model, (2) new soil model and (3) new canned mesh model. Brief guidance for undertaking each of these endeavors is provided below.

10.5.1 New pipe-type model

The basic programming for installing a new pipe model is already included in CANDE-2022. The executive routine contains the Fortran name NEWPIP in the list of recognized pipe-type names that may be specified in the input data file on line A-2. In addition, the executive routine is programmed with calls to a subroutine called Newpip for the three executive phases; input, solution and output (i.e., ICOME = 1, 2, and 3).

The shell of subroutine Newpip along with its arguments is installed in Project Engine, therefore the researcher needs only to provide the programming within the Newpip subroutine. The programming logic should follow the structure outlined in Table 10.3-1, and the existing Basic subroutine, which is the simplest of the pipe types, is useful as a programming guide.

10.5.2 New soil models

To install a new soil model, the subroutines Readm and Heroic located in Project Engine need to be modified. Subroutine Readm is associated with the input phase wherein input parameters for all soil models are read and processed. For the first input line D-1, common to all soil models, the new soil model should be identified as ITYP = 7 because six other models already exist. The remaining input lines, D-2, D-3, etcetera, are defined as needed to read and process the input parameters associated with the new model. It is recommended to store the Fortran variables for the soil model in a new Include statement (named common statement) inserted in subroutines Readm and your new subroutine, say Newmud, called from subroutine Heroic as discussed next.

In the solution phase of subroutine Heroic (ICOME = 2), the appropriate soil-model subroutine is called to compute the updated modulus values for the element's constitutive matrix (see Chapter 3). Comment cards in subroutine Heroic

identify exactly where to insert the call to subroutine Newmud (ITYP = 7). Using the element's current stress /strain values as input (ST array), subroutine Newmud's job is to update moduli values and assign values to the incremental plane-strain constitutive matrix CP(3x3) stored in the include statement, materl.fi. See subroutine Duncan as an illustration for programming and for signaling convergence using the simple logic, ICONDS = 1 or 0. Note the array STHARD may be used as desired in subroutine Newmud.

10.5.3 New canned mesh for Level 2

Installing a new canned mesh requires a trivial modification to the executive routine, inserting a call to the new subroutine, say Newcan, in subroutine Prep, and programming the Newcan subroutine. Input line A-2 contains the input variable NPCAN, which is currently input as 1, 2, or 3, corresponding to the Level 2 choice of pipe mesh, box mesh, or arch mesh. To expand NPCAN to 4 choices requires modifying line 443 in the executive routine to avoid the error check.

As indicated in Figure 10.4.2-1, subroutine Prep directs the calling to the canned mesh subroutine based on the value of NPCAN. Accordingly, a new call statement to subroutine Newcan needs to be inserted in subroutine Prep immediately following line 62

Programming subroutine Newcan may seem daunting, particularly after inspecting other canned mesh subroutines. However, the fundamental goal is simple. Using physical input data describing the configuration shape being addressed, Newcan generates the entire finite element input stream and writes it to a data file (unit 11) in the same sequence and format as Level 3 input instructions. This means line C-1 (PREP), line C-2 (control), multiple lines C-3 (nodes), multiple lines C-4 (elements) and multiple lines C-5 (boundary conditions) are all written to unit 11. The mesh/generation package (Figure 10.4.2-1) reads the data file on unit 11 just the same as if it were a batch input file on unit 5.

11 CANDE GUI Source Code

The CANDE Graphical User Interface (GUI) source code is the topic of this chapter. While the source code itself is the ultimate documentation of the program, this chapter provides a simple guideline for using the code.

11.1 Overview of CANDE GUI Architecture

The CANDE-2007/11 source program is written in modern Fortran and developed with the following:

- Microsoft Visual Studio 2005, Version 8.0.50727.762 (SP.050727-7600)
- GUI written in .NET C# programming language
- Microsoft .NET Framework version 2.0.50727

The MVS framework permits grouping subroutines together to form projects and then grouping projects together to form a whole solution. CANDE's whole solution is composed of six projects described in the table below.

Table 11.1-1 CANDE-2022 projects contained in MVS solution

Project	Description	Files required to initiate the project
candel	This is the primary project and can be opened by opening the candel.sln project file. The primary functions of this project are as follow: <ul style="list-style-type: none"> ▪ Main CANDE GUI project that initiates the CANDE Multiple document interface (MDI) ▪ All other projects are instantiated from the main module Form1 ▪ Project also contains the input interface and all of the input screen forms ▪ Contains the help about screens and auxiliary forms 	
CANDEBeamResults	Contains the form that plots the beam results using a linear graphing tool. This project uses a third party graphing tool, Graphics server. This tool is distributable royalty free, but a license must be purchased in order to develop with it.	aaa_MeshGeom.xml aaa_BeamResults.xml
CANDEGraphics	This project drives all of the mesh plotting for CANDE. The viewer permits viewing of the mesh geometry without the results file.	aaa_MeshGeom.xml(required) (aaa_MeshResults.xml) Last file is optional but must be present to view analysis results.

Project	Description	Files required to initiate the project
CANDEImport	<p>This project provides support for importing external files into CANDE. The files currently supported are:</p> <ul style="list-style-type: none"> ▪ MeshGeom.XML – the format for this file is defined in the CANDE user manual. ▪ NASTRAN – The NASTRAN commands supported by the CANDE import are described in an appendix to the CANDE user manual. ▪ CANDE-89 – The CANDE-89 plot file import is supported. 	Requires an external import file of the type defined.
CANDEInputViewer	This project defines the form needed for the CANDE text input viewer. A Feature of this tool is the column-sensitive help.	Requires a CANDE input file with an extension .CID.
CANDENewInput	This project controls the CANDE input wizard screens. This form is generally made to be run in modal mode.	Generates a new CANDE input file.
CANDEOutputGenerator	The output generator project initiates the windows to dynamically generate CANDE output based on the data stored in the CANDE. The program provides the user with choices to customize the data stored in the three CANDE xml output files. The format of these files is described in the CANDE user manual.	aaa_MeshGeom.xml aaa_MeshResults.xml aaa_BeamResults.xml All three CANDE xml output files are required to run this module.
CANDEOutputViewer	<p>This project uses the CANDE table of contents file (ctc) and CANDE output file to create an interactive browser for CANDE output files. If the CANDE table of contents file is not present, the form will still work without a browser input tree.</p> <p>This form performs double duty as the viewer for the standard CANDE output file and the file produced by the CANDE output generator.</p>	CANDE output file CANDE table of contents file (ctc extension).
Utility Classes		
CANDEOutputClass	Classes used to build output files for the CANDE output generator.	
AbanGeometry, absngnrl	General geometry classes	
CANDE_InputData_ClassLibrary	Group of classes that reads/write the CANDE input file using the format described explicitly in the CANDE user Manual (Chapter 5). The classes are named according to the input names defined in the user manual.	
CANDE_XML_ClassLibrary	Library of classes for reading the various XML files used by CANDE.	
RTBExCs	Expanded rich text box control that supports printing.	
CANDE Setup	Project that builds the CANDE installation.	

11.2 CANDE Files

The CANDE-2007/11 GUI relies on a series of files to function properly; some are generated by the analysis engine, some are soft-coded and some are produced by the GUI. This section provides a guideline for these files.

11.2.1 CANDE Input Definition

The CANDE input definition XML file provides information used by the GUI to check ranges, determine context-sensitive help tags, short help descriptions, long help descriptions, and input formatting. The file is used primarily by the GUI input system and is read in when the input system is initiated. Each input item defined in Chapter 5 of the CANDE user manual has a <Data> entry in the CANDE input definition file. A sample of the XML file is shown below.

```
<?xml version="1.0" encoding="UTF-8"?>
<CANDEInputDefinition>
.
.
.
  <Data>
    <className>CLRFDLoadFactors E1</className>
    <ShortInputName>E-1</ShortInputName>
    <CANDEVariableName>FACTOR</CANDEVariableName>
    <CANDEInputLine>E-1</CANDEInputLine>
    <shortDescription>LRFD load factor applied to the load increments INCRS through
INCRL.</shortDescription>
    <longDescription>FACTOR is the net load factor applied to the load steps INCRS to INCRL
(inclusive). It is the user's responsibility to determine the appropriate value of FACTOR that correlates to each load step.
Table E-1 provides information on load factors based on the</longDescription>
    <inputColumnStart>11</inputColumnStart>
    <inputLength>10</inputLength>
    <inputFormat>F10.0</inputFormat>
    <ouputFormat>F10.0</ouputFormat>
    <unitsUS>.none.</unitsUS>
    <unitsSI>.none.</unitsSI>
    <defaultUS>1</defaultUS>
    <defaultSI>1</defaultSI>
    <lowerLimitUS_W>0</lowerLimitUS_W>
    <upperLimitUS_W>10</upperLimitUS_W>
    <lowerLimitSI_W>.none.</lowerLimitSI_W>
    <upperLimitSI_W>.none.</upperLimitSI_W>
    <lowerLimitUS_E>.none.</lowerLimitUS_E>
    <upperLimitUS_E>.none.</upperLimitUS_E>
    <lowerLimitSI_E>.none.</lowerLimitSI_E>
    <upperLimitSI_E>.none.</upperLimitSI_E>
    <HelpTag>5_7_1_E_1_LRFD_Net_Load_Factor_per_Load_step</HelpTag>
  </Data>
.
.
.
  <Data>
    <className>CPTTypeDef_AlumB2_A</className>
    <ShortInputName>B-2.Alum.A</ShortInputName>
    <CANDEVariableName>PA</CANDEVariableName>
    <CANDEInputLine>B-2</CANDEInputLine>
    <shortDescription>Area of pipe wall section per unit length</shortDescription>
    <longDescription>The cross-sectional area of one corrugation period divided by the period
length.</longDescription>
    <inputColumnStart>1</inputColumnStart>
```

```

    <inputLength>10</inputLength>
    <inputFormat>F10.0</inputFormat>
    <ouputFormat>F10.0</ouputFormat>
    <unitsUS>in^2/in</unitsUS>
    <unitsSI>mm^2/mm</unitsSI>
    <defaultUS>.none.</defaultUS>
    <defaultSI>.none.</defaultSI>
    <lowerlimitUS_W>.001</lowerlimitUS_W>
    <upperLimitUS_W>10</upperLimitUS_W>
    <lowerlimitSI_W>.none.</lowerlimitSI_W>
    <upperLimitSI_W>.none.</upperLimitSI_W>
    <lowerlimitUS_E>.none.</lowerlimitUS_E>
    <upperLimitUS_E>.none.</upperLimitUS_E>
    <lowerlimitSI_E>.none.</lowerlimitSI_E>
    <upperLimitSI_E>.none.</upperLimitSI_E>
    <HelpTag>5_4_1_2_B_2_Aluminum_Analysis_Section_Properties</HelpTag>
</Data>
.
.
.
<CANDEInputDefinition>

```

CANDE Input Definition Tag Descriptions.

Tag	Type	Description
className	string	Class name as defined in CANDE.
shortInputName	string	Short input name description. This name is generally the command name followed by the variable description.
CANDEVariableName	string	The CANDE variable name as defined in the CANDE user manual.
CANDEInputLine	string	CANDE input line command (e.g. E-1) as defined in Chapter 5 of the CANDE user manual.
shortDescription	string	Short description of the input item.
longDescription	string	More detailed description of the input item.
inputColumnStart	integer	The column that the input item starts in the input file.
inputLength	integer	The total length of an input item as it is written to the input file.
inputFormat	string	Input format defined in Chapter 5 of the user manual for each input item. The format in general follows FORTRAN guidelines for formatting. Currently used for the persistent help shown at the bottom of the input screen.
outputFormat	(not currently used)	
unitsUS	string	This value is used in labeling the US 'units' field on all CANDE input menus
unitsSI	string (set by not currently used)	This value is used in labeling the SI 'units' field on all CANDE input menus
defaultUS	string	The value set for a CANDE input file when initially generated.
defaultSI	(not currently used)	
lowerlimitUS_W	integer, double	lower limit for CANDE input for this particular input item. CANDE allows input with range violations but provides a warning message.
upperlimitUS_W	integer, double	upper limit for CANDE input for this particular input item. CANDE allows input with range violations but provides a warning message.
lowerlimitSI_W	(not currently used)	

Tag	Type	Description
upperlimitSI W	(not currently used)	
lowerlimitUS E	(not currently used)	
upperlimitUS E	(not currently used)	
lowerlimitSI E	(not currently used)	
upperlimitSI E	(not currently used)	
HelpTag	string	This tag is used by the GUI to set the help tag associated with the CANDE-2007.chm help file. When CANDE opens and input menu it uses this tag to search for context sensitive help.

11.2.2 CANDE analysis XML output files

The CANDE XML output files are described in detail in the CANDE User Manual and Guideline. Which modules use the files is described in a table in section 11.1 of this manual.

11.2.3 CANDE table of contents files

The CANDE analysis engine and the CANDE output generate produce a table of contents file that is used in tandem with the corresponding CANDE output files to create a ‘browsable’ output file. The format of the CANDE table of contents file is simple and could be applied to other programs that produce ASCII text based output. The format is as follows:

Format:

```

IIII|aaaa...
IIII|aaaa...
IIII|aaaa...

```

Where

IIII – the heading level to be used in the tree explorer

aaaa... - represents the key text to be searched for when the tree item is clicked.

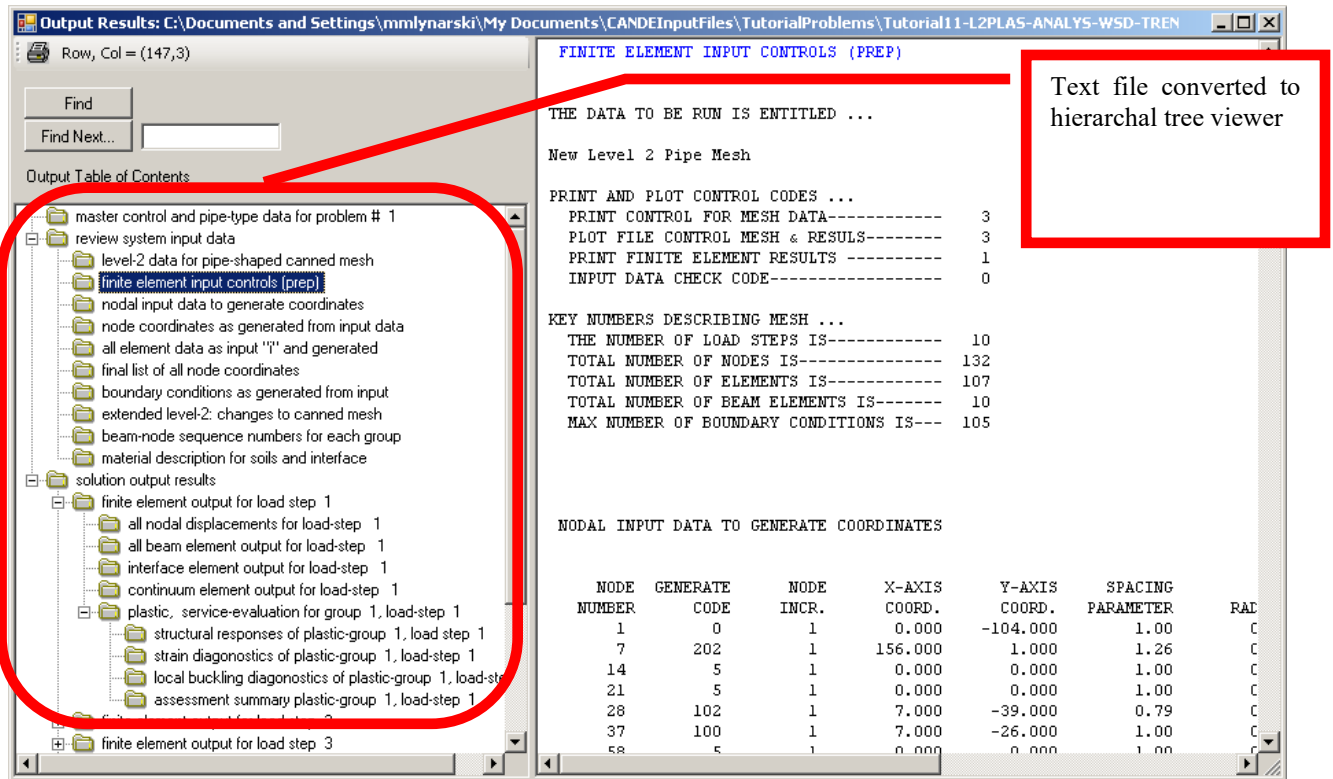
Perhaps the best way to demonstrate the use of this file is by example. The following is a snippet from a CANDE ctc file and demonstrates how it gets translated to a tree browser.

```

1|MASTER CONTROL AND PIPE-TYPE DATA FOR PROBLEM # 1
1|REVIEW SYSTEM INPUT DATA
2|LEVEL-2 DATA FOR PIPE-SHAPED CANNED MESH
2|FINITE ELEMENT INPUT CONTROLS (PREP)
2|NODAL INPUT DATA TO GENERATE COORDINATES
2|NODE COORDINATES AS GENERATED FROM INPUT DATA
2|ALL ELEMENT DATA AS INPUT "I" AND GENERATED
2|FINAL LIST OF ALL NODE COORDINATES
2|BOUNDARY CONDITIONS AS GENERATED FROM INPUT
2|EXTENDED LEVEL-2: CHANGES TO CANNED MESH
2|BEAM-NODE SEQUENCE NUMBERS FOR EACH GROUP
2|MATERIAL DESCRIPTION FOR SOILS AND INTERFACE
1|SOLUTION OUTPUT RESULTS
2|FINITE ELEMENT OUTPUT FOR LOAD STEP 1
3|ALL NODAL DISPLACEMENTS FOR LOAD-STEP 1
3|ALL BEAM ELEMENT OUTPUT FOR LOAD-STEP 1
3|INTERFACE ELEMENT OUTPUT FOR LOAD-STEP 1
3|CONTINUUM ELEMENT OUTPUT FOR LOAD-STEP 1
3|PLASTIC, SERVICE-EVALUATION FOR GROUP 1, LOAD-STEP 1
4|STRUCTURAL RESPONSES OF PLASTIC-GROUP 1, LOAD STEP 1

```

- 4|STRAIN DIAGNOSTICS OF PLASTIC-GROUP 1, LOAD-STEP 1
- 4|LOCAL BUCKLING DIAGNOSTICS OF PLASTIC-GROUP 1, LOAD-STEP 1
- 4|ASSESSMENT SUMMARY PLASTIC-GROUP 1, LOAD-STEP 1

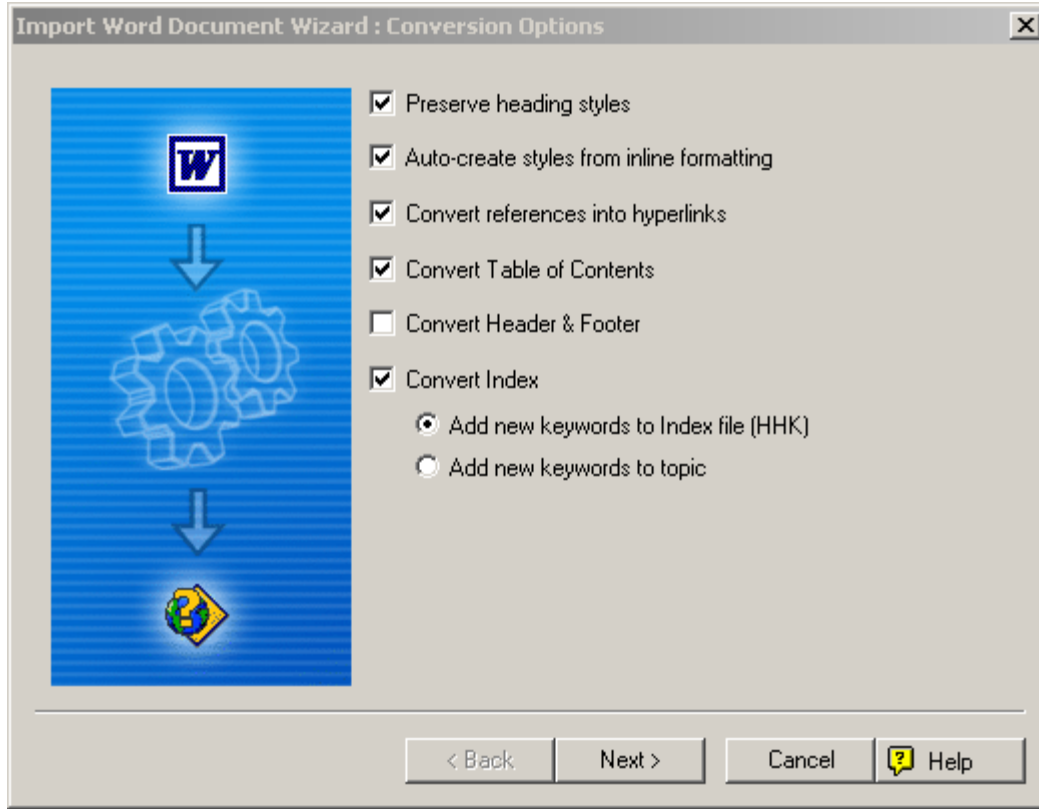


11.2.4 CANDE help files

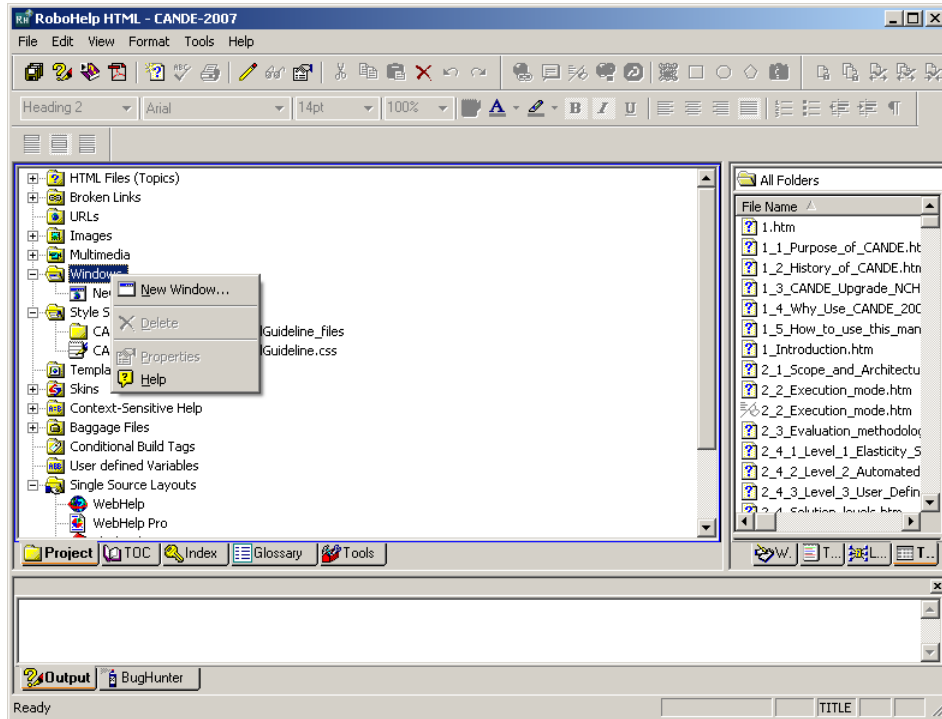
CANDE comes with a predefined CANDE help file CANDE-2007.chm. This file was generated using Adobe RoboHelp HTML 6, Build 99. The file was produced by taking the CANDE User Manual and Guideline Microsoft Word document and importing the document into Robohelp for HTML 6. Once the document is imported a small amount of cleanup is required to finalize the document.

To create the CANDE help file follow the following steps:

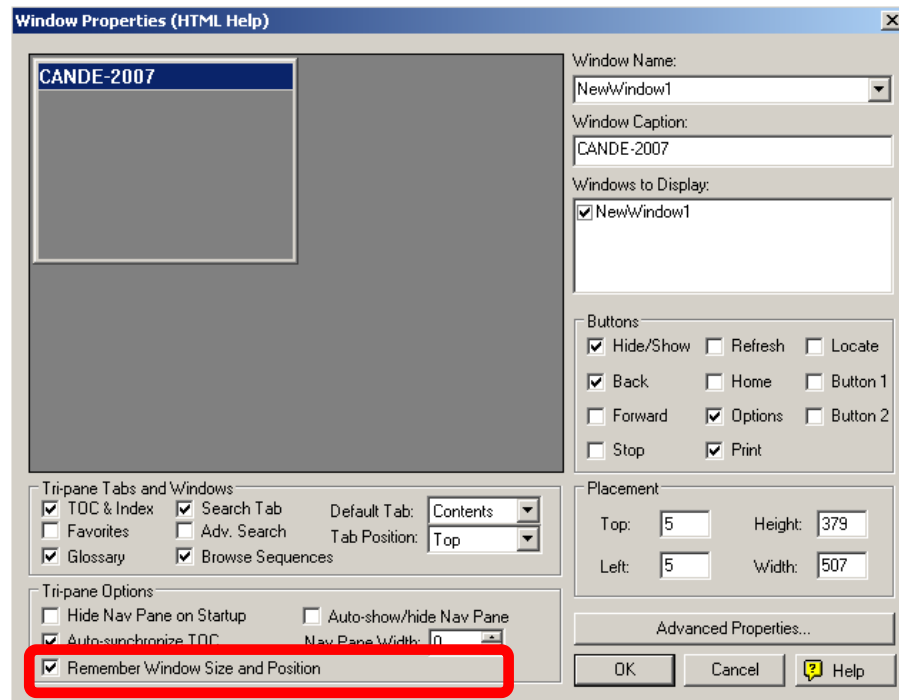
- Start up RoboHelp HTML
- Create a new project through 'File -> New Project'
- Select the 'Import' tab
- Select 'Word Document' as the import type
- Browse to the CANDEUserManualAndGuideline.doc file
- Import the document
- Follow the import wizard using the following settings



Once the project has been generated, select ‘New Window...’ by right-clicking on the ‘Windows’ icon in the RoboHelp HTML explorer (see below).



This will create a new instance of the RoboHelp project that can then be opened. Once opened select the option to 'Remember Window Size and Position' (see below).



Close the window and select the 'Generate' option from the 'File' menu.